Probing strongly correlated many-body systems with quantum simulation

Annabelle Bohrdt

Technische Universität München
Fakultät für Physik
Lehrstuhl für kollektive Quantendynamik

Probing strongly correlated many-body systems with quantum simulation

Annabelle Bohrdt

Vollständiger Abdruck der von der Fakultät für Physik der Technischen Universität München zur Erlangung des akademischen Grades eines

Doktors der Naturwissenschaften (Dr. rer. nat.)

genehmigten Dissertation.

Vorsitzende/-r: Prof. Dr. Christian Pfleiderer

Prüfende/-r der Dissertation:

1. Prof. Dr. Michael Knap

2. Prof. Dr. Johannes Knolle

Die Dissertation wurde am 07.12.2020 bei der Technischen Universität München eingereicht und durch die Fakultät für Physik am 27.01.2021 angenommen.

Thesis advisor: Michael Knap Annabelle Bohrdt

Probing strongly correlated many-body systems with quantum simulation

Abstract

We propose new schemes to implement and probe strongly interacting phases of matter in and out of equilibrium with quantum simulation experiments. We probe the Fermi-Hubbard model by studying higher-order correlations and the spectral function, and by applying pattern analysis and machine learning techniques. In the Bose-Hubbard model we study scrambling of information as well as thermalization and the absence thereof. We investigate the latter case in a quantum gas microscope and through interferometric probes accessible to superconducting qubits.

Thesis advisor: Michael Knap Annabelle Bohrdt

Probing strongly correlated many-body systems with quantum simulation

Kurzfassung

Wir schlagen neue Methoden vor um stark wechselwirkende Phasen im und außerhalb des Gleichgewichts mit Quantensimulationsexperimenten zu implementieren und zu untersuchen. Wir untersuchen das Fermi-Hubbard Modell indem wir Korrelationen höherer Ordnung und die Spektralfunktion betrachten und indem wir Mustererkennungs- und Machine Learning Techniken anwenden. Im Bose-Hubbard Modell studieren wir die Verwürfelung von Information sowie Thermalisierung und deren Abwesenheit. Wir erforschen letzteren Fall in einem Quantengasmikroskop und mithilfe von interferometrischen Untersuchungen, die mit supraleitenden Qubits zugänglich sind.

Contents

Listing of figures

Acknowledgments

Many individuals contributed to the great experience I had during my PhD. There is an African proverb that says that it takes a village to raise a child. According to Wikipedia, this means that 'an entire community of people must interact with children for those children to experience and grow in a safe and healthy environment'. While I was already pretty much grown up when I started my PhD, the same is in a way true for graduate students. I want to thank the people who provided this community for me during the last four years, letting me learn and try and struggle and fail and succeed at my own pace, giving me both space and support when I needed them.

I want to start by thanking Michael for making a somewhat unconventional PhD possible for me. Thank you for taking me in as a graduate student and letting me go to Boston before I even had funding. I deeply appreciate the freedom I had over the past four years, not only to do a long-distance PhD, but also to pursue whichever projects I found exciting.

I want to thank Simon, for welcoming me into the group in the beginning, for being patient and helpful with all questions, no matter how annoying, from bureaucracy to cluster troubles, and for many fun stories.

In my first project, I had the pleasure of working with Manuel Endres and Christian Mendl. I want to thank Manuel for his hospitality during our visit at Caltech and for sharing his ideas and insights. I am thankful to Christian for performing the numerical simulations, which I could only fully appreciate much later, for his patience, and for his ongoing interest in my work.

During my PhD, I spent a lot of time at Harvard as an exchange student. From the first day on I felt welcomed by the Harvard physics community and in particular the groups of Eugene Demler and Markus Greiner. I am deeply grateful to Eugene for his hospitality during a very long exchange as well as shorter visits. Moreover, I want to thank Eugene for his insights in many different areas of physics as well as in writing papers.

I am grateful to Yulia and Marton, for welcoming me at Harvard and for always being supportive. I additionally want to thank Marton for sharing his QMC code with me, which continues to be

helpful.
One of the first people I interacted with at Harvard was Daniel Greif. I first met Daniel at the DPG in 2016, a month after I started my PhD, and from the first day on, he was interested in my work and patient in explaining his. Daniel combines an incredible curiosity and knowledge of theoretical backgrounds with his expertise in cold atom experiments as well as his patience and his exceptional leadership skills. It has been a pleasure to work with Daniel and I am glad to have him as a friend.
I still vividly remember my first interaction with Markus Greiner: I was standing outside the LISE building, eating a waffle during social hour, when Markus (whom I did not know at the time) showed up and struck up a conversation with the words 'do you do something with fermions?'. Well, I did not, but through an incredible collaboration with his Lithium team I started working with fermions and I am very glad I did. I want to thank Markus for many interesting discussions and insights, his curiosity and persistence in certain questions, and for being so inclusive. Moreover, I want to thank the entire Greiner lab for being so welcoming and inclusive.
I had a fantastic time collaborating with the Lithium team in Markus Greiner's group, Christie, Geoffrey, Muqing and Daniel, in our quest to find string patterns. As a theorist, I mostly work on my own, and it has been a great experience to be part of a team, especially a team of such intelligent, curious and hard-working individuals. I highly appreciate that Christie, Geoffrey, Daniel and Muqing took an incredible amount of data, trusting Fabian and me that we could find what we were looking for. I enjoyed our (sometimes very long) discussions and learned a lot. I hope to be able to continue working together in the future. I am thankful for another great collaboration with the Lithium team, including Lev and Martin, on the dynamics of a single hole.
It has been a great pleasure working with Christie on various different projects, in particular devising the string pattern finding algorithm, developing the string game, and writing a popular science article about our work. I want to thank Christie for being an outstanding collaborator and friend.
During my time at Harvard, I was very happy to be included in the Harvard Women in Physics community. I am incredibly thankful to Anne for taking me to the WiP events in the first place, for always being there for me, and, most importantly, for being an exceptional friend. I want to thank Anne, Anjalika and Ana (A^3) for their hospitality, even if we kept breaking things, and their friendship. I am thankful to Lee, for always joining in all sorts of fun events, for being an integral part of Harvard physics soccer, for being a great friend even at times when I was annoying – simply for being the best man.
I enjoyed a lot of inspiring discussions with Julian. I am thankful to Julian, Sooshin and Matthew for their interest in my machine learning ideas and for all the data to support those. I also want to thank Matthew for borrowing all those towels for me.
All of my visits at Harvard would not have been possible without the help in bureaucratic matters from Bonnie and Liz. I am thankful for their as well as Karin's invaluable help and patience. I

promise I always tried my best.
I worked with Snir and Ahmed on a project that took us more than two years to finish, mostly because I never found the time to work on the stuff I promised to do, and I am grateful for their patience. I want to thank Snir for helping me with the DMRG code and my annoying questions. It has also been a pleasure working with Ahmed, who pays incredible attention to every detail and was very patient in explaining experimental capabilities.
A lot of the numerical work I did during my PhD was based on the TeNPy code and I want to thank Frank Pollmann, Johannes Hauschild and everybody involved for making this code available. I am thankful to Ruben for sharing his code with me and patiently answering all my questions about it.
I am grateful to Ben and Pedram for their hospitality during my visit in Santa Barbara and for their experimental efforts in our collaboration on MBL with superconducting qubits. I want to thank Ben for his patience in answering my questions about the measurements.
I greatly enjoyed working with Immanuel Bloch's Lithium quantum gas microscope team, Jayadev, Mim, Guillaume, Joannis, Sarah and Christian, on the observation of dynamical spin-charge separation. I am grateful for this opportunity and the many inspiring discussions and insights. I want to thank Jaya for being patient with my questions about the experiment, and Joannis for the soccer enthusiasm and for being a great collaborator. It has been a pleasure working with the Lithium team – including also Timon Hilker, Dominik Bourgund, Petar Bojovic, and Thomas Chalopin – on the breakdown of magnetic polarons in the two-dimensional Fermi-Hubbard model. I am thankful to Immanuel for being so inclusive and supportive.
I want to thank Ignacio and Claudius for a great collaboration on hole dynamics, in particular for putting in all the numerical effort and including me in this interesting project.
I enjoyed working with Cole and Eun-Ah on an exciting project about the interpretability of neural networks used to distinguish two competing theories, during which I learned a lot.
Between 2012 and 2019, the Studienstiftung des deutschen Volkes supported me financially. I highly appreciate the financial independence this has given me, in particular during my PhD. I am grateful for the opportunity to teach at the Sommerakademie in Leysin, which was a fantastic experience due to the extraordinary students in our group.
When I returned to Munich after a long time abroad, I was more than happy to join a terrific group, in particular Alex, Ella, Johannes, and Clemens. I am thankful for all the discussions about physics and other things, your enthusiasm and excitement, and to know that I can count on your help (assuming you happen to be in Munich).
I am thankful to Dennis for his friendship during all those years, and, among many other things, for always booking the best hotel and for never being boring.
I want to thank my family for their support, in particular Adrian and Janje for welcoming me in their home when I first arrived in Munich, my parents and Heiner and Ulrike for taking such great care

of all birds and turtles whenever I was gone, and Annika for the moral support every step along the way and for proofreading a lot of my (mostly boring) writing.
Most importantly, I am incredibly lucky to have Fabian as a partner in crime. You are the perfect collaborator in every project, and I am deeply grateful for your remarkable enthusiasm and optimism, your exceptional ability to make things work and your willingness to share your vast knowledge with me so patiently, especially when I am impatient.

Publications

Parts of the content of this thesis have been published in the following Refs. [1–18]. They contain large parts of the material presented here, partly with textual overlap. All of these publications are the result of fruitful collaborations of several authors. The author of this thesis has made significant and substantial contributions to these publications, ranging from the development of ideas, literature research, analytical calculations, design, development and implementation of numerical codes, data analysis, to the interpretation of results, and writing of the papers.

Publications in peer-reviewed journals

[1] Annabelle Bohrdt, Christian B. Mendl, Manuel Endres, Michael Knap: "Scrambling and thermalization in a diffusive quantum many-body system" – New J. Phys. 19, 063001 (2017) (NJP Highlight 2017)

[2] Annabelle Bohrdt, Daniel Greif, Eugene Demler, Michael Knap, Fabian Grusdt: "Angle-resolved photoemission spectroscopy with quantum gas microscopes" – Phys. Rev. B 97, 125117 (2018) (Editor's Suggestion, Featured in Physics)

[3] Fabian Grusdt, Marton Kanasz-Nagy, Annabelle Bohrdt, Christie S. Chiu, Geoffrey Ji, Markus Greiner, Daniel Greif, Eugene Demler: "Parton theory of magnetic polarons: Mesonic resonances and signatures in dynamics" – Phys. Rev. X 8, 011046 (2018)

[4] Fabian Grusdt, Annabelle Bohrdt, and Eugene Demler:"Microscopic spinon-chargon theory of magnetic polarons in the t-J model" – Phys. Rev. B 99, 224422 (2019)

[5] Annabelle Bohrdt, Christie S. Chiu, Geoffrey Ji, Muqing Xu, Daniel Greif, Markus Greiner, Eugene Demler, Fabian Grusdt, Michael Knap: "Classifying Snapshots of the Doped Hubbard Model with Machine Learning" – Nature Physics Vol. 15, pp. 921–924 (2019)

[6] Christie S. Chiu, Geoffrey Ji, Annabelle Bohrdt, Muqing Xu, Michael Knap, Eugene Demler, Fabian Grusdt, Markus Greiner, Daniel Greif: "String patterns in the doped Hubbard

model" – Science Vol. 365, Issue 6450, pp. 251-256 (2019)

[7] Jayadev Vijayan, Pimonpan Sompet, Guillaume Salomon, Joannis Koepsell, Sarah Hirthe, Annabelle Bohrdt, Fabian Grusdt, Immanuel Bloch, Christian Gross "Time-Resolved Observation of Spin-Charge Deconfinement in Fermionic Hubbard Chains" – Science 367, 186 (2020)

[8] Claudius Hubig, Annabelle Bohrdt, Michael Knap, Fabian Grusdt, J. Ignacio Cirac: "Evaluation of time-dependent correlators after a local quench in iPEPS: hole motion in the t-J model" – SciPost Phys. 8, 021 (2020)

[9] Annabelle Bohrdt, Ahmed Omran, Eugene Demler, Snir Gazit, Fabian Grusdt: "Multiparticle interactions for ultracold atoms in optical tweezers: Cyclic ring-exchange terms" – Phys. Rev. Lett. 124, 073601 (2020)

[10] Annabelle Bohrdt, Eugene Demler, Frank Pollmann, Michael Knap, and Fabian Grusdt: "Parton theory of ARPES spectra in anti-ferromagnetic Mott insulators" – Phys. Rev. B 102, 035139 (2020)

[11] Annabelle Bohrdt, Fabian Grusdt, Michael Knap: "Dynamical formation of a magnetic polaron in a two-dimensional quantum antiferromagnet" – New J. Phys. 22 123023 (2020)

[12] Annabelle Bohrdt, Yao Wang, Joannis Koepsell, Marton Kanasz-Nagy, Eugene Demler, and Fabian Grusdt:"Dominant fifth-order correlations in doped quantum anti-ferromagnets" – Phys. Rev. Lett. 126, 026401 (2021)

Publications submitted to peer-reviewed journals

[13] Benjamin Chiaro, Charles Neill, Annabelle Bohrdt, Michele Filippone, et al. [collaboration with the group of J. Martinis]: "Direct measurement of non-local interactions in the many-body localized phase" – arXiv:1910.06024

[14] Geoffrey Ji, Muqing Xu, Lev Haldar Kendrick, Christie S. Chiu, Justus C. Brüggenjürgen, Daniel Greif, Annabelle Bohrdt, Fabian Grusdt, Eugene Demler, Martin Lebrat, Markus Greiner: "Dynamical Interplay between a single hole and a Hubbard antiferromagnet" – arXiv:2006.06672

[15] Joannis Koepsell, Dominik Bourgund, Pimonpan Sompet, Sarah Hirthe, Annabelle Bohrdt, Yao Wang, Fabian Grusdt, Eugene Demler, Guillaume Salomon, Christian Gross, and Immanuel Bloch: "Microscopic evolution of doped Mott insulators from polaronic metal to Fermi liquid" – arXiv:2009.04440

[16] Cole Miles, Annabelle Bohrdt, Ruihan Wu, Christie Chiu, Muqing Xu, Geoffrey Ji, Markus Greiner, Kilian Q. Weinberger, Eugene Demler, and Eun-Ah Kim: "Correlator Convolutional Neural Networks: An Interpretable Architecture for Image-like Quantum Matter Data" – arXiv:2011.03474

[17] A. Bohrdt, S. Kim, A. Lukin, M. Rispoli, R. Schittko, M. Knap, M. Greiner, and J. Léonard: "Analyzing non-equilibrium quantum states through snapshots with artificial neural networks" – arXiv:2012.11586

[18] Yao Wang, Annabelle Bohrdt, Joannis Koepsell, Eugene Demler, and Fabian Grusdt: "Higher-Order Spin-Hole Correlations around a Localized Charge Impurity" – arXiv:2101.00721

The ability to reduce everything to simple fundamental laws does not imply the ability to start from those laws and reconstruct the universe. [...] At each level of complexity entirely new properties appear. We can now see that the whole becomes not merely more, but very different from the sum of its parts [19].

Philip Warren Anderson

1 Introduction

When simple constituents interact with each other, their collective behavior can lead to complex emergent phenomena. An illustrative example is a colony of ants: each ant has very little knowledge, and there is no central unit to make decisions. The interplay of many ants nonetheless yields a colony which as an entity exhibits complex behavior with regards to foraging, fighting off intruders and strategic planning. In science, it has for a long time been a central goal to understand the most elementary building blocks, such as how single ants behave, how individual synapses in the brain work, or how atoms or molecules are built up. Once the individual components are identified and well understood, a different question arises: how do these constituents interact, and what collective behavior emerges from their interplay? In condensed matter physics, one tries to understand or predict the macroscopic behavior of a large collection of simple constituents, such as atoms or electrons. Often, the microscopic laws governing the behavior of these constituents are well known. In quantum many-body physics, the relevant microscopic degrees of freedom can often be descibed by a Hamiltonian, which prescribes how the particles can move and interact.
In some cases, the qualitative physics is captured by approximating the impact of all other constituents on any given constituent as a single, averaged effect. In such a mean-field description, the many-body problem is thereby effectively reduced to a one-body problem. One example is a Bose-Einstein condenstate, where a significant fraction of bosonic particles occupies the lowest

available quantum state. If this happens, microscopic phenomena such as wavefunction interference become apparent macroscopically. After theoretical predictions by Bose and Einstein in 1924 [20, 21], this state was realized and probed more than 70 years later in experiments with cold atoms [22, 23], yielding a Nobel prize in 2001. Today, Bose-Einstein condensates are routinely produced experimentally, with one such experiment orbiting the Earth on board of the International Space Station [24].

The beauty and at the same time challenge of quantum many-body physics lies in the fact that even when we know the Hamiltonian describing a system, we do not necessarily see or understand all of the rich physics that it captures. This is particularly true for strongly correlated systems, where simple mean-field theories become insufficient and the single-particle description breaks down. An extreme example are one dimensional metallic systems, in which the fundamental excitations are of a collective nature [25], vastly different from the original constituents – in P.W. Anderson's words, the whole here really becomes very different from its parts [19].

The discovery of new phenomena in condensed matter physics often starts with an unexpected experimental observation, such as the exact quantization in integers of e^2/h of the Hall conductivity in cold, quasi-two-dimensional semiconductors in high magnetic fields found by von Klitzing in 1980 [26]. Only two years later, Tsui, Stormer and Gossard experimentally discovered the fractional quantum Hall effect, in which the Hall conductance shows precisely quantised plateaus at fractional values of e^2/h [27]. The ensuing theoretical research established the field of topological order and the associated emergent phenomena, such as fractional charge, fractional statistics and chiral edge states [28].

Experiments on real materials can however be hard to understand theoretically, because many different effects can play a role, such as phonons, multiple bands, and disorder in the sample. Taking all these effects and their interplay into account is often challening. Moreover, tunability in conventional solid state experiments is typically very limited, rendering a systematic comparison with theoretical models harder. Probably the most paradigmatic example are the cuprate materials, which exhibit high-temperature superconductivity. The completely unexpected discovery of this phenomenon by Bednorz and Müller in 1986 [29] led to a Nobel prize only a year later, and a wealth of theoretical as well as experimental research until today. High-temperature superconductors are materials that exhibit zero resistivity below a critical temperature, which can be high enough to be achieved by cooling with liquid nitrogen. There are numerous applications for high-temperature superconductors, such as levitating trains, magnetic resonance imaging, and high-efficiency electric power distribution. Since the discovery of the cuprate materials more than thirty years ago, physicists have sought to understand how superconductivity is possible in these systems. However, the mechanism underlying high-temperature superconductivity is still not understood, and this lack of comprehension remains a major obstacle in developing materials for practical use with higher crit-

ical temperatures and better material properties. The most widely agreed-upon model, believed to capture all essential features of the cuprate materials, is the Fermi-Hubbard model [30, 31]. Large parts of the community believe that this conceptually simple model contains all key ingredients to explain high-temperature superconductivity. To date there exists, however, no unifying theoretical description of the Fermi-Hubbard model, which could explain all the phases that emerge due to the complex interplay of spin and charge.

Exact numerical simulations of the Fermi-Hubbard model are hindered by the dimension of the Hilbert space, which grows exponentially with system size. While a variety of numerical methods exist, each of them has some drawback. Quantum Monte Carlo calculations of the Fermi-Hubbard model for example face the sign-problem, such that simulations at finite doping and low temperature are very difficult. Exact diagonalization calculations can access arbitrary doping and temperature regimes, but are limited to very small systems – typically a 4×4 system is the largest possible for the Fermi-Hubbard model.

As early as 1982, Feynman proposed quantum simulation as an alternative to the numerical simulation of quantum systems on classical computers [32]. There are two different approaches, analog and digital quantum simulation. A universal digital quantum simulator can basically simulate any given system through the application of the corresponding quantum gates. The basic idea of analog quantum simulation is to experimentally realize the quantum system described by the Hamiltonian under consideration in a well-controlled setting. In the past few decades, tremendous progress has been made in the field and today, several hundred quantum simulators exist worldwide [33], with platforms ranging from ultracold atoms, trapped ions and superconducting qubits, to quantum dots. In a quantum simulator, the relevant parameters are well controlled and can usually be tuned in a wide range. Moreover, they enable the measurement of quantities difficult or impossible to access in conventional materials, such as non-local observables, higher-order correlators and entanglement measures [6, 34–36]. Depending on the platform, complete access to the quantum state is possible. In quantum gas microscopes for examples, ultracold atoms trapped in optical potentials can be imaged with single site resolution, yielding snapshots of the quantum many-body state. These new experiments call for completely new ways to analyze data and make use of the wealth of information contained in the measurements, such as pattern recognition and machine learning techniques.

New experimental probes are furthermore possible through quantum quenches and non-equilibrium dynamics, which can be observed since the system is well isolated from the environment and thus evolves under its own intrinsic quantum dynamics. Non-equilibrium physics warrants completely new descriptions beyond the equilibrium paradigm with new research questions ranging from thermalization behavior, to spreading of quantum information, entanglement dynamics, non-thermaliz- ing behavior in integrable and disordered systems, to Floquet engineering. At the same

time, experimental tools have been developed to make dynamical processes accessible in condensed matter experiments, such as using photo-excitation of cuprate materials, leading for example to light-induced superconductivity [37]. Predicting, describing, and understanding the new phenomena that can emerge in non-equilibrium settings is a fascinating challenge of modern condensed matter theory. One example for non-equlibrium physics is the thermalization – or lack thereof – of closed quantum systems. Conserved quantities, such as total particle density and energy, can slow down thermalization, leading to hydrodynamic behavior at long times. In some cases, such as integrable systems or systems with strong disorder, there are extensively many conserved quantities, and the system does not thermalize at all. In experiments with cold atoms, the lack of thermalization on experimentally accessible time-scales has been observed for example in the case of an initially prepared density domain wall in a disordered two-dimensional bosonic system [38]. This experiment accesses long times in a large two-dimensional, interacting quantum many-body system without translational invariance, thus reaching regimes which are increasingly hard, if not impossible, to simulate numerically.
As a theorist, now is the time to work in the field of quantum simulation. Experiments are starting to explore unchartered territory by simulating parameter regimes which have not been accessed otherwise. Completely new measurements are possible and necessary to probe these regimes, and the interpretation of experimental data is becoming more challenging, as a direct comparison to numerical simulations is often not possible anymore. New observables allow for an in-detail comparison of experimental results to different model predictions, yielding completely new insights based on microscopic details into the emerging many-body phenomena.

The remainder of this thesis is organized as follows:

- In chapter 2, we give a brief introduction to quantum simulation in general and the platforms used in this work in particular.

- Part I deals with the Fermi-Hubbard model and begins with a general introduction of the phase diagram, experimental progress and related models, such as the $t-J$ model, in chapter 3.

  - Chapter 4 treats the one-dimensional Fermi-Hubbard model. In section 4.1, we introduce the squeezed space used in subsequent sections. Section 4.2 covers our proposal to experimentally access the spectral function as measured in angle resolved photoemission spectroscopy with a quantum gas microscope, as well as numerical results for the spectral function of the one-dimensional $t-J$ model [2]. In section 4.3, we present experimental and numerical results for time-resolved spin-charge deconfinement [7].

We conclude this chapter with a first step in two dimensions, as we consider cyclic ring-exchange on a ladder [9] in section 4.4.

- Chapter 5 contains our results for a single hole in the two-dimensional Fermi-Hubbard model. The results in this chapter build on the geometric string theory introduced in section 5.1, see [3, 4]. We find that emergent constituents – partons – can form, which carry fractions of the original fermion quantum numbers, and present newly accessible direct signatures for partons in such systems. In section 5.2 we introduce algorithms to find such signatures in the form of string patterns by analyzing single snapshots. In section 5.3, we study string patterns as well as higher-order correlation functions in the ground state of the $t - J$ model with a single hole [4, 12]. We extend our results to the spectral function in section 5.4 and are able to explain most low-energy features in the spectrum in the framework of the geometric string theory [10]. In section 5.5, we study the dynamics of a single hole created in a two-dimensional system. We explain the emergence of two different time-scales for the dynamics starting from the ground state, an infinite temperature state [11], and a finite temperature state [14]. In section 5.6, we proceed to the ground state of two holes and analyze the spin correlations relative to the holes.
- Chapter 6 extends these results to the case of the Fermi-Hubbard model at finite doping. In section 6.1, we introduce the pecularities of the experimental setup used in the remainder of the chapter [6]. In section 6.2, we discuss the π-flux RVB state, which constitutes a possible theoretical description of the doped Fermi-Hubbard model. We then analyze conventional observables, such as two-point spin correlation functions, for the experimental data as well as the π-flux and geometric string theory in section 6.3. Next, we search for string patterns in the three datasets in section 6.4. Finally, in section 6.5, we apply machine learning techniques to the snapshots in order to make full use of the information contained in the data [5].
- In chapter 7, we summarize our findings on the Fermi-Hubbard model and provide an outlook.

- Part II contains our results on the Bose-Hubbard model. We start with the introduction of the model and a brief discussion of thermalizing and non-thermalizing systems and their dynamics.
  - In chapter 8, we study the spread of quantum information in a system where quasiparticles cease to exist [1]. In particular, in section 8.1 we investigate out-of-time ordered correlation functions, which serve as a proxy for the scrambling of quantum information, with matrix product state techniques in the one-dimensional Bose-Hubbard

model at finite temperatures. In section 8.2, we compare our results to time-ordered correlation functions, which show significantly slower dynamics due to globally conserved quantities. We propose two different measurement protocols to access time-ordered as well as out-of-time ordered correlation functions in quantum simulation experiments in section 8.3.

  - Chapter 9 contains our results on many-body localization. We start with a brief introduction to many-body localization, the τ-bit picture and its entanglement properties. In section 9.2, we present our results on many-body localization in an experiment with superconducting qubits, where we directly probe entanglement properties as well as the non-local interactions in the τ-bit picture [13]. In section 9.3, we discuss applications of machine learning techniques to snapshots as obtained from a quantum gas microscope simulating the dynamics of the one-dimensional Bose-Hubbard model with quasi-periodic disorder.
  - In chapter 10, we summarize our findings on the Bose-Hubbard model and provide an outlook for interesting future research directions.

- Part III contains the appendices, which cover technical details on the results presented in the main text.

  - In chapter A, we provide an overview over the numerical methods used in this work. In particular, in section A.1, exact diagonalization is introduced and the details for spin 1/2 systems, the $t - J$ model, the Fermi-Hubbard model and the Bose-Hubbard model are discussed. We briefly introduce the Lanczos algorithm and elaborate on its application for time evolution, the spectral function, finite temperature and the spectral function at finite temperature. In section A.2, we give a very short introduction to matrix product states and operators, as well as simulating ground states and time evolution in this formalism. In section A.3 we discuss the Metropolis Monte Carlo algorithm used to sample snapshots, in particular from an MPS and from a Gutzwiller projected density matrix at finite temperature. In section A.4 we provide details on the analysis of single snapshots, both from numerical simulations and experimental data. In section A.5 we provide a brief overview over the neural network techniques used in our analysis.
  - In chapter B, we provide details on the spectral function in the one- and two-dimensional $t - J$ model and possible extensions of the measurement scheme to other quantities and models. We discuss momentum shifts in the spectral building principle in one dimension and details on the numerical simulations for the spectral function in two dimensions.

– In chapter C, we provide details on the results on the Bose-Hubbard model. We discuss the numerical simulations and data analysis for the out-of-time ordered correlation functions. We show additional experimental and theoretical data on our studies of many-body localization.

Nature isn't classical, dammit, and if you want to make a simulation of nature, you'd better make it quantum mechanical, and by golly it's a wonderful problem, because it doesn't look so easy.

Richard Feynman

2 Quantum Simulation

Some quantum many-body problems are so complex that not even the most powerful classical supercomputers can provide a solution [39]. The exponentially growing Hilbert space renders numerical simulations difficult, even if one employs clever algorithms. Experiments on real materials are on the other hand often limited by sample properties and quality as well as accessible observables. Moreover, the combination of many different – often uncontrolled – ingredients can make an interpretation challenging. Quantum simulation can bridge this gap between theory and real materials by directly probing the quantum many-body model under consideration in a clean and tunable setting. Beyond that, quantum simulation experiments can reach regimes and enable probes which are otherwise completely inaccessible.

In quantum simulation experiments, the general idea is usually to start with comparably simple elementary building blocks, such as ions, atoms or superconducting qubits, which we can understand and control very well. Using these 'simple' constituents, we then build the complex system we are trying to understand – as Markus Greiner likes to put it: "building and investigating quantum materials one atom at a time" [40]. In analogue quantum simulation, the resulting complex system directly simulates the Hamiltonian under consideration, i.e. for example the thermal state of the system, the real-time evolution of a given initial state, or the response of the system to a perturbation are determined by the Hamiltonian we wish to study. The parameters of the Hamiltonian,

such as the interaction strength, hopping amplitude, or filling, can usually be tuned within a wide range, thus allowing to probe different regimes. At the same time, the Hamiltonian parameters can typically be tuned or measured independently, which in real materials is often not the case.
The main challenges faced by quantum simulation experiments today are scalability – especially while keeping everything under control – and state preparation [33]. An important goal in a lot of quantum simulation setups is now to reach lower equilibrium temperatures and thus typically the most interesting part of the phase diagram.
Quantum simulation is nowadays a vast field of research with plenty of different platforms, each of which has its own advantages and drawbacks. Often, this difference between platform means that they can tackle complementary aspects of a problem. At the same time, the simultaneous development of different setups has the advantage that once unchartered territory, where numerical simulations are no longer possible, is reached, one quantum simulator can verify another.
A non-comprehensive list of current quantum simulation platforms includes

- Superconducting qubits, which will be discussed in more detail in section 2.2. The main drawback here is scalability, because each qubit has to be calibrated individually and potential sources of errors increase significantly with the system size. On the other hand, arbitrary read-outs and state preparations are possible, with a high repition rate.

- Cold atoms in optical lattices, which will be discussed in more detail – in particular in the context of quantum gas microscopy – in section 2.1. Cold atoms can simulate fermionic as well as bosonic models, and almost arbitrary lattice geometries are possible. Atoms come with the advantage that all of them are equal, and no more calibration is needed. Scalability is thus much easier. Currently one of the main challenges here is to reach lower temperatures.

- Atoms in optical tweezers, which allow for a large degree of spatial control. Interactions between individual atoms can for example be realized through excitation to Rydberg states. Depending on the spacing between the atoms, different interaction strengths can be realized [41].

- Cold molecules, which need to be either produced from individual atoms, or cooled down. Cooling down molecules is somewhat more complicated than cooling atoms due to their complex internal structure. Cold molecules however allow for a variety of interactions between molecules, and at the same time, the study of their internal degrees of freedom is by itself a fascinating application of quantum simulation [42].

- Trapped ions, which can simulate spin systems with long-range interactions and allow for a large degree of control for state preparation, such as superposition states, and readout [43]. One of the main challenges here is scalability.

- Color (e.g. nitrogen-vacancy) centers in diamond, which typically simulate a spin system with long-range (dipole-dipole) interactions. These experiments can be done without a high vacuum and at comparably high temperatures and feature long coherence times [44, 45]. The spin states can be prepared and read-out optically and the dynamics can be driven with resonant microwave excitations [46]. Due to inhomogeneities, either in diamond or in the placement of the defects, disorder can play a role here. Scalability, while maintaining control over the placement of defects, is one of the active areas of research here. These platforms are also employed for quantum metrology.

- Dopant atoms in silicon, which can simulate the Fermi-Hubbard model and easily achieve very low temperatures [47]. The Hamiltonian parameters are here fixed upon fabrication of a sample and currently, only small system sizes can be realized with a high degree of control [48]. Typical probes here are scanning tunneling microscopy and transport measurements. Snapshots of the quantum state, such as for example in a quantum gas microscope, are not possible.

- Quantum dot arrays, which are also natural candidates for the quantum simulation of the Fermi-Hubbard model, since they are described by the same Hamiltonian [49]. The quantum dots are realized by electrostatically confined conduction-band electrons and the Hamiltonian parameters, such as chemical potential and hopping amplitude, can be tuned through gate electrodes. Currently, only small system sizes can be realized and probed with high fidelity, but very low temperatures can be reached. Local charge occupation as well as global charge transport can be measured. Moreover, local spin degrees of freedom and nearest neighbor singlet-triplet correlations are in principle accessible [50].

2.1 Cold Atoms and Quantum Gas Microscopy

Experiments with cold atoms in optical lattices have evolved into a well-established field in the context of quantum simulation in the past two decades. Many excellent review articles [39, 51, 52] and theses, such as e.g. [53–56] to name but a few, have been written on the subject – most of them by the people who actually work on the experiments. The goal of this section is thus not to provide an in-depth introduction to the field, but rather to summarize the most important aspects and achievements from a theorist's point of view.
In experiments with ultracold atoms, dilute atomic gases are cooled down to the Nanokelvin range, usually by using a sequence of laser and evaporative cooling techniques. The atoms are then spatially confined in optical lattices. These setups allow for a large degree of control, where typically the hopping, interaction strength, and chemical potential can be tuned in a significant range. In

the following, we will briefly summarize the typical experimental procedure in a quantum gas microscope for the example of fermionic Lithium-6 atoms as used in the groups of Immanuel Bloch and Markus Greiner, which provided the experimental cold atom results presented in this thesis. Lithium is chosen in those experiments because it has a broad Feshbach resonance, which allows to tune interactions, and because – compared for example to Potassium – its mass is smaller, thus allowing for larger hopping amplitudes t. The main aspects of the experimental procedure presented here also apply to experiments with bosons.

2.1.1 Experimental sequence

The experiment starts with an atomic beam of Lithium produced from a heated block of Lithium. This beam then travels through a Zeeman slower into a vacuum chamber, where on the order of 10^8 atoms are loaded into a magneto-optical trap. Subsequently, the atoms are cooled down to approximately 60μK in a sequence of magneto-optical or dipole traps. At this point, the cloud is sufficiently cold to be loaded into an optical dipole trap. This trap is used to transfer the atoms from the magneto-optical trap to a transport beam, which is focused to a narrow waist. This transport beam is used to move the atoms from the magneto-optical trap to the glass cell, or science chamber, where the rest of the experiment happens. Once the atoms enter the science chamber, they are trapped by a beam angled with respect to the transport beam, yielding a crossed dipole trap. The next step is another stage of evaporative cooling by ramping the trap depth. A magnetic field gradient can be used to spill the most energetic atoms out of the trap.
In the experiments discussed in part I of this thesis, the Fermi-Hubbard model with spin up and spin down fermions is realized. To this end, two spin states are needed, and in principle there are different ways to obtain them, see e.g. Ref. [39]. Here, we discuss the realization with two different hyperfine states of Lithium-6, which is used in the discussed experiments. In principle, experiments with more than two spin components are possible by straightforward extension [52]. If an imbalance between spin up and spin down fermions occurs after the steps described thus far, one can use a microwave pulse to resonantly drive the transition between the two relevant hyperfine states to obtain an equal mixture.
At this point, e.g. the experiment in Markus Greiner's group has about 10^5 atoms in each spin state at a temperature of $T/T_F \approx 0.05$. However, in order to load a single layer in the accordion lattice in the next step, another evaporation step follows, leading to approximately 2000 atoms in the trap. Now, the temperature of the system can no longer be determined with the help of the absorption imaging system, as the latter is not sensitive enough at these densities. Therefore, the temperature is usually determined from site-resolved imaging after the lattice is loaded, for example by comparing the spin correlations to quantum Monte Carlo simulations. Another possibility that was recently

realized is the direct measurement of the equation of state, which allows for thermometry with the help of the fluctuation-dissipation theorem [57].
Next, the atoms are loaded into the accordion lattice and transported to the object plane of the high resolution imaging system. Just before loading the lattice, a final evaporation step is used in order to reach colder temperatures. The final trap depth is used to precisely control the atom number, and the magnetic bias is used to set the atomic scattering length and thus the interaction strength. Finally, the atoms are loaded into the optical lattice. Depending on the specific setup, the imaging is often parity projected, meaning that a site occupied by two fermions with opposite spin is imaged as empty. In order to determine the chemical potential corresponding to half-filling, i.e. one atom per site, one can thus tune the chemical potential μ and for each value of μ, count the number of singly occupied sites. At half-filling, this number is maximized. For finite doping in this type of setup, the doping value is then determined by fitting the singles density to quantum Monte Carlo simulations.

2.1.2 Interactions

In general, there are different ways interactions are implemented. For example, atomic species with large magnetic moments, polar molecules, and Rydberg atoms can realize long-range interactions. In the case of Lithium-6 discussed here, atoms in different hyperfine states interact via two-body van der Waals interactions. These interactions have a hard-core cut-off on a distance scale given by the atomic radius. In general, the extent of the atomic wave function is larger than the range of the inter-atomic potential. Therefore, the detailed shape of the short-range potential does not matter and only s-wave scattering plays a role. The potential between two different spin states can then be approximated as a pure contact interaction potential $V(r) = V_0\delta(r)$ [52, 54], where the strength is determined by the scattering length a,

$$V(r) = \frac{4\pi\hbar^2 a}{m}\delta(r). \tag{2.1}$$

Due to the Pauli principle, only two fermions with opposite spin can interact in this way. At low energies, scattering with non-zero angular momentum, such as p-wave scattering, is suppressed by the scattering centrifugal barrier. The scattering length a determining the strengh of the interaction potential can exhibit magnetic field dependent resonances, the so-called Feshbach resonances. These occur when a closed molecular channel energetically approaches the scattering state of an open channel of two colliding atoms [53, 55]. This energy difference between the bound state and the scattering state of two free atoms can be tuned by a magnetic field, if the corresponding states have different magnetic moments. The amplitude and sign of the scattering length a can thus be tuned.

The two hyperfine states of Lithium used in the described experiments have a broad Feshbach resonance, which has been measured out very well [58]. The on-site interaction U in the Hubbard model can thus be well controlled by tuning the magnetic field bias using Feshbach coils. In order to determine the actual value of U for a given magnetic field, the amplitude of the lattice in one direction can be modulated sinusoidally at a variable frequency ν for a given time and modulation depth. If the modulation frequency ν matches the interaction energy, $\nu = U/h$, more doubly occupied sites appear in the system. In the parity projected measurements in Markus Greiner's group, this leads to a reduction in the observed density. The value of the on-site interaction U is thus determined as the position of the resonances [53].

2.1.3 Optical lattices

Optical lattices are typically formed by interfering several laser beams of identical frequency, thus realizing a periodic light structure, which mimics the crystal lattice of a solid. For a laser with wavelength λ_L, the periodic potential obtained by shining two counter-propagating laser beams along e.g. the x axis is

$$V_x(x) = V_{0,x} \sin^2(\pi x/\lambda_L). \tag{2.2}$$

Atoms can be trapped in such periodic light fields because the alternating electric field of the laser light creates an oscillating atomic dipole parallel and proportional to the local electric field of the laser. The atomic dipole then interacts back to the same electric field via dipole interaction. Thus, an optical dipole potential

$$V_x(x) = d_0^2 \mathrm{E}(x)^2/4\hbar\delta \tag{2.3}$$

is created, where d_0 is the matrix element of the atomic dipole, $\mathrm{E}(x)$ is the amplitude of electric field, and $\delta = \omega_L - \omega_A$ is the detuning between laser and atomic angular frequencies [52]. The sign of the detuning δ determines whether the potential is attractive (red-detuned) or repulsive (blue-detuned) at the intensity maxima. The intensity and detuning of the laser can both be tuned experimentally, thus enabling control of the sign and amplitude of the potential. Moreover, with the help of more complicated laser configurations different geometries, dimensionality, spin dependence as well as disorder in the lattice can be realized [52]. The optical lattice has a Gaussian envelope due to the Gaussian profile of the laser beams, leading to a harmonic confinement, which is approximately quadratic at the center of the trap. In order to create a flat potential in the region used for the experiment, a digital micromirror device can be used to obtain an additional harmonic potential in the opposite direction. Note that misaligning the center of this compensating potential with the harmonic confinement from the lattice lasers leads to a linear potential gradient across the experimental region of interest. Another option is to not compensate for the harmonic potential

and instead employ the inhomogeneity: if the potential varies sufficiently slow, the local density approximation can be applied and the potential leads to a spatially varying effective chemical potential. The system then realizes a broad range of fillings in one experimental run, and thus many doping values can be scanned simultaneously.
In order to derive the Hubbard Hamiltonian, two approximations are commonly made:

(i) only the lowest band is occupied. This approximation is valid as long as the on-site interaction U, the thermal energy $k_B T$ and the chemical potential μ are smaller than the bandgap to the first excited band

(ii) the Wannier functions are sufficiently localized on one lattice site. This tight binding approximation is valid as long as the lattice potential is sufficiently deep.

The hopping amplitude t is then obtained from the integral over the Wannier functions, which decay fast with distance and the interaction strength U is given by the integral over Wannier functions on the same lattice site. For a non-vanishing overlap between Wannier functions at next nearest neighboring sites, the corresponding hopping amplitude t' is non-zero and can thus be tuned by the lattice depth. The Wannier states get narrower as the amplitude of the periodic potential is increased. This allows to vary the ratio of tunneling amplitude t to interaction strength U by tuning the lattice potential V_0, since the tunneling energy decreases with increasing localization of the Wannier functions, whereas the interaction energy increases. In particular, the Hamiltonian parameters scale as

$$\frac{t}{E_r} \simeq \frac{4}{\sqrt{\pi}} \left(\frac{V_0}{E_r}\right)^{3/4} \exp\left(-2\sqrt{V_0/E_r}\right) \qquad \text{and} \qquad \frac{U}{E_r} \simeq \sqrt{\frac{8}{\pi}} k_L a \left(\frac{V_0}{E_r}\right)^{3/4}, \tag{2.4}$$

where the recoil energy $E_r = \hbar^2 k_L^2 / 2m$ sets the energy scales of particles in the lattice and $k_L = 2\pi/\lambda_L$ is the laser wavevector. For a detailed derivation see Ref. [52] and references therein.

2.1.4 Imaging

The idea of site-resolved imaging is to collect sufficiently many fluorescent photons from each atom with a high-resolution imaging objective to be able to resolve the occupation on neighboring sites. One of the first quantum gas microscope experiments used large optical lattices to facilitate imaging, but this has the drawback of reducing the tunneling amplitude within the lattice during the experiment [59]. For a sizeable hopping amplitude t, the lattice spacing in the optical lattice needs to be small, which leads to lattice spacings close to the limit of optical resolution. As a consequence, several hundreds of fluorescent photons need to be collected per atom to faithfully determine whether a single site is occupied. In order to obtain a binarized image, a threshold value

is used to determine the occupation of a given lattice site. One challenge is to collect sufficiently many photons before the atoms hop between sites. Typically, this is resolved by employing deep optical lattices for imaging, which are ramped up sufficiently fast to freeze the atom distribution, as well as efficient cooling mechanisms. Note that the specifics of this ramp actually can change the observable physics: for example, in the Fermi-Hubbard model, virtual doublon-hole excitations exist. If the lattice is ramped up sufficiently slow, these doublon-hole pairs can recombine into two singly occupied sites, but also move apart from each other, thus displacing the spins in between.
After the first quantum gas microscopes were realized for bosonic Rubidium [60, 61], it took another six years for fermions to be imaged with single site resolution [62–65]. One of the reasons is that more elaborate laser cooling methods such as Raman-sideband cooling are necessary for site-resolved detection of fermions.
If a single site is occupied by two atoms, the imaging procedure leads to a light assisted collision, which results in the loss of both atoms. The collected fluorescence signal from this site is then identical to the signal from an empty sites, and thus the measurement is parity projected. In the Lithium quantum gas microscope experiment in Markus Greiner's group discussed in chapter 6, it is currently not possible to image both hyperfine states simultaneously. In order to obtain spin observables, one of the two hyperfine states can be removed before imaging by driving a nearly closed transition to a higher manifold with a resonant pulse, thus removing the atoms in the corresponding hyperfine state from the trap. This means, however, that in a given snapshot, only atoms in one spin state are visible, and empty sites in the image can be holes, doublons, or atoms in the other spin state. In the corresponding experiment in Immanuel Bloch's group discussed in section 4.3, the simultaneous detection of two hyperfine states is possible by spatially separating the states directly before imaging using a Stern-Gerlach setup. In Markus Greiner's Rubidium experiment the local occupation number can be resolved by letting the atoms expand in the second spatial dimension [66].
The microscope objective can additionally be used to project spatial patterns of light onto the system, thus creating a different potential landscape.

2.1.5 What has been achieved

In experiments with cold atoms in optical lattices, a broad range of milestones have been achieved in the past two decades and it is beyond the scope of this thesis to cover all of them. For a more comprehensive review and further reading, references [39, 67] are recommended. Here, we only want to highlight some of the many outstanding experiments in the field.
The starting point for the study of strongly correlated many-body physics with cold atoms was the observation of the superfluid to Mott insulator transition in the Bose-Hubbard model by tuning the

ratio of tunneling to interaction strength t/U, Ref. [68]. Later, the Higgs amplitude, which is the excitation mode corresponding to oscillations of the amplitude of the superfluid order parameter in the vicinity of the superfluid to Mott insulator transition was observed [69].
In 2008, Mott insulators of fermions were realized using potassium and probed through the compressibility, which vanishes as the number of atoms is varied, as well as the reduction of doubly occupied sites [70, 71]. Later, Mott insulators of lithium were realized, and the compressibility at this point could be measured by observing the change in the density profile throughout the trap [72]. As next steps, short range magnetic correlations were observed [73, 74], antiferromagnetic correlations in one-dimensional systems [75] as well as antiferromagnetism across the system in a two-dimensional Fermi-Hubbard system [76]. Inspired by experiments on real materials, transport measurements [77, 78] and angle-resolved photoemission spectroscopy [79] have been realized in the Fermi-Hubbard model.
In the description above, we focused on realizations of the Fermi-Hubbard model in a quantum gas microscope, and the work in part I of this thesis is concerned with the one and two dimensional Fermi-Hubbard model in a square lattice. However, different geometries, such as a triangular or honeycomb lattice are possible and different atomic species can be used. Today, rubidium [60, 61], ytterbium [80, 81], potassium [65, 82, 83] and lithium [64, 84, 85] have been imaged and more microscopes are being built. Additionally, very strong effective magnetic fields and complex tunneling parameters can be engineered. In the groups of Tilman Esslinger in Zurich, Immanuel Bloch and Monika Aidelsburger in Munich, and Klaus Sengstock and Christof Weitenberg in Hamburg, systems with topological order have been realized in this way [86–89].
The isolation from the environment possible in cold atom experiments also enables the observation of dynamical properties and non-equilibrium physics. The time evolution of a many-body system with disorder has been observed in one and two spatial dimensions. In both cases, a memory of the initial state could still be seen in the local occupation [90–92]. Moreover, configurational correlations related to the logarithmic growth of entanglement have been measured [35]. Using two copies of the system, the Renyi entropies can be measured [93], and the thermalization of a system was studied using entanglement properties [94]. Other out-of-equilibrium experiments include for example the study of the relaxation of a spin spiral imprinted onto the system [95] and the dynamics of a single mobile spin impurity [96].

2.2 Superconducting Qubits

In this section, we give a brief introduction to superconducting qubits and their application in quantum simulation. For more details we refer to the many excellent review articles and theses written on the subject, such as Ref. [97–99]. Superconducting qubits have been suggested as possible platform for quantum computing already in 1997 [100] and a lot of research and development is conducted among others by companies like Google, IBM, Rigetti and Intel.
Superconducting qubits are solid state electrical circuits. Their fabrication is based on technologies developed for conventional integrated circuits. Each qubit is a non-linear LC resonator. The non-linearity is needed to be able to separately adress the transitions between different levels. In a quantum harmonic oscillator, consisting of an inductor and a conductor, the levels are equally spaced with a frequency $\omega_0 = 1/\sqrt{LC}$ and transitions between different levels can thus not be adressed independently. In the non-linear LC circuits used as superconducting qubits, a Josephson junction is used as inductance. A Josephson junction consists of two superconductors, separated by a thin insulating layer, allowing for coherent tunneling of Cooper pairs. The insulator is usually fabricated through oxidation of the superconductor, yielding an insulating barrier a few tens of atoms thick [97]. The two superconductors can have a different phase. The current through the Josephson junction is given by

$$I = I_0 \sin\left(2\pi\Phi/\Phi_0\right), \tag{2.5}$$

with the superconducting flux quantum $\Phi_0 = h/2e$. This periodicity of the current is caused by the discreteness of Cooper pair tunneling across the junction. The energy stored in the junction, called the Josephson energy, is

$$E_J = \int I \cdot V \mathrm{d}t = -\frac{\Phi_0}{2\pi} I_0 \cos(2\pi\Phi/\Phi_0). \tag{2.6}$$

The Hamiltonian for a single qubit is

$$\hat{H} = \frac{\hat{Q}^2}{2C} - \left(\frac{\Phi_0}{2\pi}\right)^2 \frac{1}{L} \cos(2\pi\hat{\Phi}/\Phi_0) \tag{2.7}$$

with the charge $\hat{Q}$ of the capacitor. The energy separation of the system is large enough to work at temperatures of about 0.01K, which are reached in cryogenic refrigerators.
Additional inductors, capacitors and Josephson junctions can be added to the qubit architecture to achieve certain design goals. The circuit parameters are used to engineer various qubit properties. In the design of a qubit, a trade-off between different goals has to be made, such as the anharmonicity being large and the sensitivity to various noise sources being small. Choosing a higher impedance $Z_0 = \sqrt{L/C}$ yields a higher non-linearity, such that the system can be easily treated

as a two level system. This comes however at the price of a higher sensitivity to noise. A large resonance frequency is desirable to suppress thermal effects. If the resonance frequency is too high, the corresponding control electronics are not as common anymore and thus expensive [98].
There are three general superconducting qubit architectures: flux, phase and charge qubits. In the flux qubit, a superconducting loop with one or possibly several Josephson junctions is threaded with a magnetic field. Different integer numbers of magnetic flux quanta can be trapped in the superconducting loop. In the phase qubit, a current flowing through the Josephson junction alters the phase between the two sides of the junction. A charge qubit consists of a small superconducting island, which is connected to a large superconducting reservoir through a junction. The charge offset n_g used to tune the qubit frequency is controlled through a capacitively coupled gate voltage. The Hamiltonian for this type of circuit is

$$\hat{H} = 4E_C(\hat{N} - n_g)^2 - E_J \cos\hat{\Phi}, \tag{2.8}$$

where $\hat{N}$ are the excess Cooper pairs on the island and $\hat{\Phi}$ is the phase difference across the junction. The Josephson junction provides a valve for Cooper pairs and couples the two qubit states $|N\rangle$, $|N+1\rangle$, without and with an additional Cooper pair on the island. Charge qubits are particularly susceptible to charge noise. In the *transmon* qubit, this problem is avoided by adding a shunt capacitor. The circuit is described by the same Hamiltonian as above, but the ratio of E_J/E_C is tuned to values $\geq$ 50, thereby significantly reducing the sensitivity to charge noise. This however comes at the cost of reducing the anharmonicity to about -200MHz, which is only a few percent of the level spacing $\omega_{01} \propto$ 5GHz. Measurement, control and coupling of the qubits is achieved through microwave resonators with techniques from circuit quantum electrodynamics. In the Google experiments, each pair of neighboring qubits is inductively coupled to a coupler loop through a mutual inductance, see Fig. 2.2.1. The coupler loop has a Josephson junction, such that the inductance can be tuned by applying a magnetic flux through the coupler loop, yielding a variable coupling strength g_{ij} between the two qubits [101]. The circuits can be engineered such that the coupling current, induced by the first qubit in the coupler loop, is much smaller than the critical current of the coupling junction. Only a small, tunable fraction of the current in the first qubit is induced through the coupler in the second qubit. With this architecture, the coupling can be tuned to any value $-55\text{MHz} \leq g/2\pi \leq 5\text{MHz}$ and in particular also to zero [98]. This can for example increase the fidelity and coherence during the application of single qubit gates.
An array of coupled superconducting qubits is described by the Bose-Hubbard Hamiltonian [13],

$$H_{\text{BH}} = \sum_i^{n_Q} h_i a_i^\dagger a_i + \frac{U}{2}\sum_i^{n_Q} a_i^\dagger a_i (a_i^\dagger a_i - 1) + J\sum_{\langle i,j\rangle}\left(a_i^\dagger a_j + \text{h.c.}\right), \tag{2.9}$$

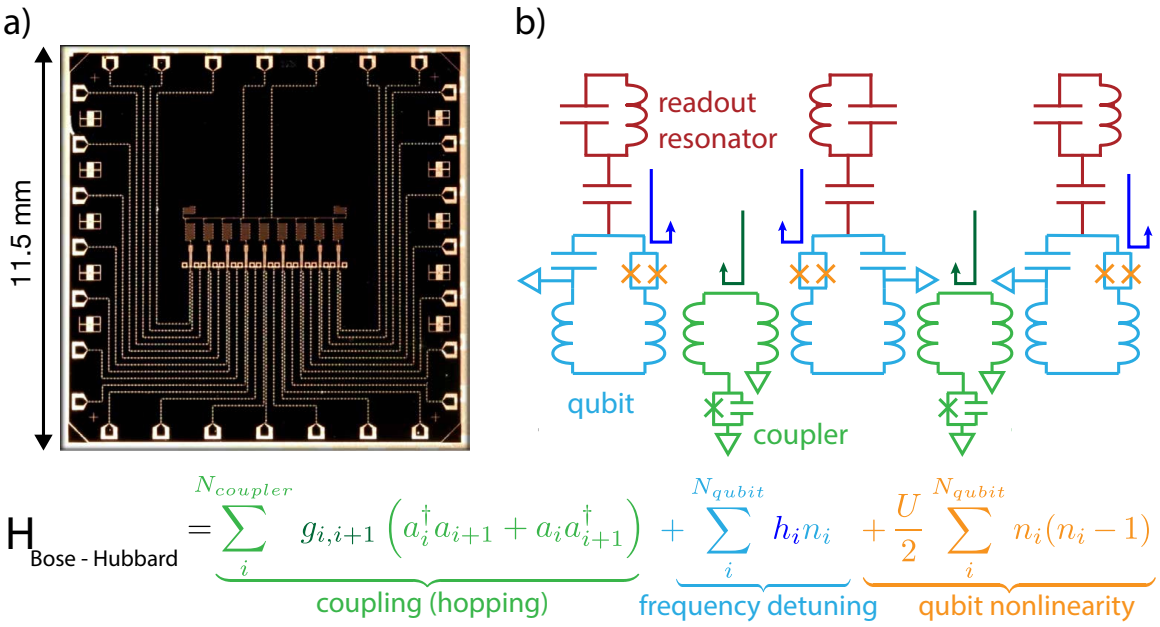

Figure 2.2.1: Superconducting qubit device used for part of the experimental results in section 9.2. a) Optical micrograph of the nine qubit linear-chain device. b) Circuit diagram for a three qubit subsection of the device, indicating which element controls which part of the Hamiltonian.

where $a^\dagger$ (a) denotes the bosonic creation (annihilation) operator, h_i is the on-site detuning, $J = g_{i,i+1}$ is the hopping rate between nearest neighbor lattice sites, U is the on-site Hubbard interaction, and n_Q is the number of qubits. The qubit frequency, the nearest neighbor coupling, and the nonlinearity set h_i, J, and U, respectively.

Circuit properties are not as exactly reproducible as for example the properties of isolated atoms, such that a newly fabricated circuit needs to be calibrated first. The values of the circuit model parameters, such as transition frequencies and coupling strength, are infered for example from spectroscopic measurements. In comparison to quantum gas microscopes, the repition rates for superconducting qubit experiments are very high and thus a large amount of measurements is easily possible.

2.2.1 What has been achieved

Quantum simulation with arrays of superconducting qubits is a relatively new field, such that important milestones have been achieved in the past few years. Besides analog quantum computation, superconducting qubits are also a promising platform for a quantum computer, and a lot of research is focused on the development of technology to obtain a universal quantum computer that can outperform a classical computer. Perhaps most prominently, the Google team recently reported a dramatic speed-up in the sampling from a probability distribution as compared to a

classical supercomputer [102]. The same technology, namely state preparation, high fidelity gate operations, and readout, can also be used for digital quantum simulation, where the Hamiltonian is typically trotterized into one- and two-qubit gate operations.

The paradigmatic Heisenberg and Ising interacting spin models have for example been implemented with superconducting qubits using digital quantum simulation [103]. The Fermi-Hubbard model has been realized, albeit for very small system sizes [104]. For the Fermi-Hubbard model, the local Hilbert space dimension is four as compared to two for a spin system. Therefore, usually two qubits are needed to simulate one lattice site in the fermionic system. The digital simulation is complicated further by the necessity to implement non-local Jordan-Wigner strings in order to obtain the correct fermionic commutation relations. Another field of research in digital quantum simulation is quantum chemistry. Superconducting qubits have for example been used to compute the energy surface of molecular hydrogen [105].

Analog quantum simulation experiments using arrays of superconducting qubits have shown a variety of physical phenomena. Among them is the realization of a quantum random walk of one and two excitations on a 12 site chain [106], and the implementation of synthetic gauge fields [101, 107]. Signatures of many-body localization have been observed by using a spectroscopic scheme to measure the eigenenergies of the underlying Hamiltonian [108].

Since the particles in the system are microwave photons, intrinsic particle losses are a potential problem in superconducting qubit arrays. One approach to make use of this property is dissipative preparation and manipulation of the quantum system, as for example in Ref. [109], where dissipation was used to stabilize a Mott insulator of photons.

Part I

The Fermi-Hubbard Model

3

Introduction

The Fermi Hubbard model is described by the Hamiltonian

$$\hat{H} = -t \sum_{\sigma=\uparrow,\downarrow} \sum_{\langle \mathbf{i},\mathbf{j} \rangle} \left(\hat{c}^{\dagger}_{\mathbf{i},\sigma} \hat{c}_{\mathbf{j},\sigma} + \text{h.c.} \right) + U \sum_{\mathbf{j}} \hat{c}^{\dagger}_{\mathbf{j},\uparrow} \hat{c}_{\mathbf{j},\uparrow} \hat{c}^{\dagger}_{\mathbf{j},\downarrow} \hat{c}_{\mathbf{j},\downarrow}, \tag{3.1}$$

which appears deceivingly simple: spin up and spin down fermions, described by fermionic creation and annihilation operators $\hat{c}^{(\dagger)}_{\mathbf{i},\sigma}$, hop between neigboring lattice sites with a hopping amplitude t. Two fermions of opposite spin occupying the same lattice site are associated with an interaction energy U. The Pauli exclusion principle prevents two fermions with the same spin to sit on the same lattice site. Here, we are interested in the regime $U \gg t$, but before – at half-filling – the Nagaoka regime is reached and the system becomes polarized [110].

The Fermi-Hubbard model was originally introduced in 1963 by John Hubbard [111] to describe the transition between conducting and insulating states. The discovery of high temperature superconductivity in the cuprates in 1986 by Bednorz and Müller [29] sparked an increased interest in the two dimensional Fermi-Hubbard model, which is believed to capture the main features of the cuprate phase diagram [30, 31]. High-temperature superconductors are materials which can have

critical temperatures T_c above 77K, reachable by cooling with liquid nitrogen[1]. Cuprate superconductors are high-temperature superconductors which consist of layers of copper oxides, alternating with layers of oxides of other metals. There exist a variety of cuprate materials, such as LBCO (lanthanum barium copper oxide), the material studied by Bednorz and Müller [29] and YBCO (yttrium barium copper oxide). The relevant physics is mostly based on the valence electrons of the copper atoms, and it is thus believed that most aspects of the cuprate phase diagram are captured by the two-dimensional Fermi-Hubbard model.

Intriguingly, the properties of the cuprate materials are not fully explained. The long-standing goal of the field is to understand the phase diagram and in particular, how to enhance superconductivity. Assuming the mechanism behind the high critical temperatures as well as possibly competing phases are understood, one can dream about engineering new materials which become superconducting at room temperature. The optimal material would moreover be easy to manufacture and handle, as opposed to mostly brittle cuprate materials.

However, despite its apparent simplicity and decades of research, the phase diagram of the Fermi-Hubbard model still poses many open questions. At half-filling, the model is comparably well understood. As the temperature is lowered, long-range antiferromagnetic correlations build up, which can extend across the entire system. Note that due to the Mermin-Wagner theorem, there cannot be true long-range order in the two-dimensional model. However, the correlation length can be exponentially large in the temperature and thus be bigger than the system sizes considered in numerical simulations and quantum simulation experiments. Going away from half-filling to finite doping in the phase diagram in Fig. 3.3.1, the situation becomes more complicated. In the cuprate materials, doping is realized by introducing foreign elements in the interleaved 'charge-reservoir' layers, thus adding or removing electrons in the copper-oxygen planes [112]. Within the Fermi-Hubbard model, (hole-)doping is simply described by having less than one particle per site. Even the properties of a single hole in an anti-ferromagnet are not fully agreed upon, let alone the mechanism that leads to the pairing of two charge carriers.

In conventional superconductivity, the interactions between electrons and phonons lead to the formation of Cooper pairs. As the Debye frequency of phonons depends on the mass of the lattice ions, the transition temperature of conventional superconductors varies for different isotopes. The corresponding dependence could not be shown in the cuprate materials, indicating that a different mechanism than electron-phonon interactions is at play. It is widely believed that antiferromagnetic spin fluctuations play a crucial role. The Fermi-Hubbard model describes the latter, while it does not include phonons.

In 1987, only a year after the discovery of high temperature superconductivity in the cuprates, An-

[1]Materials are sometimes called high temperature superconductors if their critical temperature is below 77K, but still much higher than expected from conventional theoretical descriptions.

derson proposed the resonating valence bond theory to describe the phenomenon [30]. A resonating valence bond state is an equal superposition of all possible coverings of the lattice with singlets. The holes then move freely through this covering of singlets, which comprises a spin liquid. This state can be expressed with the help of a Gutzwiller projection on a mean field level, as will be discussed in more detail in section 5.1 and A.3. Anderson proposed to use projected mean-field states as trial wavefunctions [30], where all components corresponding to doubly occupied sites are removed from the mean-field wavefunction. This projected state was found to be a good variational ground state of the $t - J$ model over a range of dopings [113].

Twenty years after the discovery of high-temperature superconductivity, already more than 100.000 papers had been published on the subject [114]. With this wealth of publications on the subject, an exhaustive review has become basically impossible. The literature is too vast for anyone to have a comprehensive overview. Different materials yield different experimental outcomes with properties like disorder, phonons, and interlayer couplings varying. Often it is difficult to scan the entire range of interesting doping values in one material. Early work often suffers from more inhomogenities and a less optimal fabrication process of samples. From a theory perspective, in a way even less is known about the Fermi-Hubbard model itself. While the quest to understand (or even map out!) its phase diagram has resulted in the development and improvement of several theoretical methods, its numerical simulation is still difficult. Analytical theories, or simple pictures, are either lacking, or highly debated, and people working in the field usually have strong opinions, thus rendering an objective review from an expert almost impossible. When Anderson was asked to write a review on the subject from his personal perspective in 2010, he already states in the abstract: *Also, their purpose was for it to serve as an "introduction to the more technical debates", but its message is that almost all of these are not relevant."* [115].

The remainder of this chapter is structured as follows. We start by introducing the descendants of the Fermi-Hubbard model considered in this thesis. We then briefly – and by no means exhaustively – discuss the experimental and numerical methods used to probe the cuprate materials and the Fermi-Hubbard model. Finally, we provide an overview over what is known (or not known) about the different phases in the phase diagram.

In chapter 4, we present results on the one-dimensional Fermi-Hubbard and $t - J$ model. We then move on to two dimensions and start in chapter 5 with a detailed description of the ground state and dynamical properties of a single hole. In chapter 6, we discuss many holes, going up to a doping of more than 30%. We conclude in chapter 7.

3.1 Descendants of the Fermi-Hubbard model

In order to describe the actual materials in more detail, sometimes the Fermi-Hubbard model with an additional t'-term is considered, which captures hopping to next nearest neighboring sites. In this thesis, we however only consider the 'pure' Fermi-Hubbard model, as described by Eq. 3.1.
In cuprate materials, the ratio of interaction strength U to hopping t is usually big, the most common case being $U/t = 12$. In the limit of $U \gg t$ and below half filling, the Fermi-Hubbard Hamiltonian (3.1) can be mapped to the $t-J^*$ model using a Schrieffer-Wolf transformation, as discussed in detail in Ref. [116]. We briefly summarize the transformation in the following.
The Hamiltonian (3.1) is written as sum of kinetic and interaction part $\hat{\mathcal{H}} = \hat{T} + \hat{V}$ with

$$\hat{T} = -t \sum_{\sigma=\uparrow,\downarrow} \sum_{\langle \mathbf{i},\mathbf{j} \rangle} \left(\hat{c}^\dagger_{\mathbf{i},\sigma} \hat{c}_{\mathbf{j},\sigma} + \text{h.c.} \right) \qquad \text{and} \qquad \hat{V} = U \sum_{\mathbf{j}} \hat{c}^\dagger_{\mathbf{j},\uparrow} \hat{c}_{\mathbf{j},\uparrow} \hat{c}^\dagger_{\mathbf{j},\downarrow} \hat{c}_{\mathbf{j},\downarrow}. \tag{3.2}$$

The kinetic part is further split up as

$$\hat{T} = \hat{T}_0 + \hat{T}_{-1} + \hat{T}_1, \tag{3.3}$$

where $\hat{T}_m$ changes the number of doubly occupied sites by m. It holds

$$\hat{T}^\dagger_m = \hat{T}_{-m} \qquad \text{and} \qquad [\hat{V}, \hat{T}_m] = mU\hat{T}_m, \tag{3.4}$$

since the interaction energy changes by mU after one of the hops in $\hat{T}_m$. A unitary transformation of the Hamiltonian can be written as

$$\hat{H}' = e^{i\hat{S}} \hat{H} e^{-i\hat{S}} = \hat{H} + \frac{1}{1!}[i\hat{S}, \hat{H}] + \frac{1}{2!}[i\hat{S}, [i\hat{S}, \hat{H}]] + \dots \tag{3.5}$$

In order to obtain a Hamiltonian without couplings between states with different numbers of doubly occupied sites up to a given order in t/U, we need to eliminate the last two terms from

$$\hat{H} = \hat{V} + \hat{T}_0 + \hat{T}_{-1} + \hat{T}_1. \tag{3.6}$$

This can be done by choosing

$$i\hat{S} = \frac{1}{U}(\hat{T}_1 - \hat{T}_{-1}), \tag{3.7}$$

yielding

$$\hat{H}' = e^{i\hat{S}} \hat{H} e^{-i\hat{S}} = \hat{V} + \hat{T}_0 + \frac{1}{U}([\hat{T}_1, \hat{T}_{-1}] + [\hat{T}_0, \hat{T}_{-1}] + [\hat{T}_1, \hat{T}_0]) + \mathcal{O}\left(\frac{1}{U^2}\right). \tag{3.8}$$

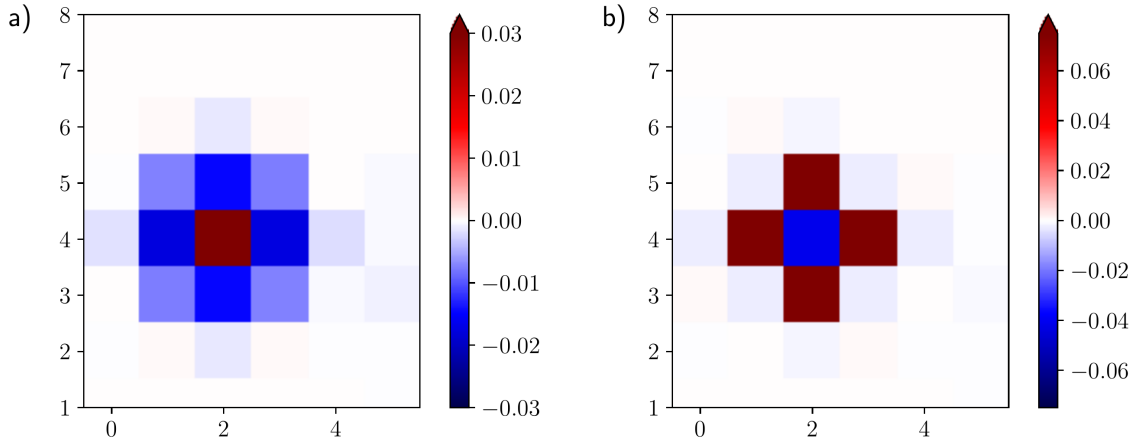

Figure 3.1.1: Doublon-doublon and doublon-hole correlations for the ground state of the Fermi-Hubbard model at half-filling and $U/t = 8$, obtained with DMRG on a 6×20 cylinder. The connected a) doublon-doublon and b) doublon-hole correlations are shown. Note that the colorscale is clipped in both cases to make features beyond nearest neighbors visible; the maximum value for the doublon-hole correlation is ± 0.244.

The procedure can be generalized to a recursive scheme to eliminate the corresponding terms up to any desired order in t/U, see Ref. [116]. Note that this transformation also gives a prescription on how to return from e.g. the groundstate of the Heisenberg model to the Fermi-Hubbard model at half-filling to a given order in t/U by introducing doublon-hole pairs accordingly. Due to the structure of the Hamiltonian, doublon-hole pairs on nearest neighbor sites dominate strongly for large U/t, see Fig. 3.1.1. Moreover, correlations between doublon-hole pairs only appear in the third order transformation.

Up to order $\mathcal{O}(t^2/U)$ the exact representation is

$$\hat{\mathcal{H}}_{t-J^*} = \mathcal{P}\left[-t\sum_{\langle \mathbf{i},\mathbf{j}\rangle,\sigma}\hat{c}^\dagger_{i,\sigma}\hat{c}_{j,\sigma} + J\sum_j\left(\hat{\mathbf{S}}_{j+1}\cdot\hat{\mathbf{S}}_j - \frac{\hat{n}_{j+1}\hat{n}_j}{4}\right) - \frac{J}{8}\sum_{\langle i,j,r\rangle,\sigma}^{i\neq r}\left(\hat{c}^\dagger_{i,\sigma}\hat{c}_{r,\sigma}\hat{n}_j - \sum_{\sigma',\tau,\tau'}\hat{c}^\dagger_{i,\sigma}\boldsymbol{\sigma}_{\sigma,\sigma'}\hat{c}_{r,\sigma'}\cdot\hat{c}^\dagger_{j,\tau}\boldsymbol{\sigma}_{\tau,\tau'}\hat{c}_{j,\tau'}\right)\right]\mathcal{P}, \quad (3.9)$$

see e.g. Ref. [117]. Here, $\mathcal{P}$ denotes the projection operator on the subspace without double occupancy, and $\langle i,j,r\rangle$ is a sequence of neighboring sites. The operator $\hat{c}^\dagger_{j,\sigma}$ creates a fermion with spin σ on site j and $\hat{n}_{j,\sigma} = \hat{c}^\dagger_{j,\sigma}\hat{c}_{j,\sigma}$ denotes the density operator of fermions with spin σ. The spin operators are defined by $\hat{\mathbf{S}}_j = \frac{1}{2}\sum_{\sigma,\sigma'}\hat{c}^\dagger_{j,\sigma}\boldsymbol{\sigma}_{\sigma,\sigma'}\hat{c}_{j,\sigma'}$, where $\boldsymbol{\sigma}$ denotes a vector of Pauli matrices. The first term in Eq. (3.9) describes tunneling of holes with amplitude t. The second term corresponds to spin-

exchange interactions of Heisenberg type, with anti-ferromagnetic coupling constant $J = 4t^2/U$. For a single hole, the term $\hat{n}_{j+1}\hat{n}_j$ leads to a constant shift in energy, which we will not include in the analysis in the following sections. Together these first two terms define the $t-J$ model. It is extended to the $t-J^*$ model by including the last term, which describes next-nearest neighbor tunneling of holes correlated with spin-exchange interactions. In our numerical simulations, we often consider the $t-J$ instead of the $t-J^*$ model, thus neglecting the term proportional to $J/8$. For the case of exactly one particle per site, the $t-J^*$ model reduces to the isotropic Heisenberg model,

$$\hat{\mathcal{H}}_J = J\sum_j \hat{\mathbf{S}}_{j+1}\cdot\hat{\mathbf{S}}_j. \tag{3.10}$$

The t-XXZ model is described by the Hamiltonian

$$\hat{\mathcal{H}}_{t-\mathrm{XXZ}} = \mathcal{P}\left[-t\sum_{\langle \mathbf{i},\mathbf{j}\rangle,\sigma}\hat{c}^\dagger_{i,\sigma}\hat{c}_{j,\sigma} + J_z\sum_j \hat{S}^z_{j+1}\hat{S}^z_j + \frac{J_\perp}{2}\sum_j\left(\hat{S}^+_{j+1}\hat{S}^-_j + \mathrm{h.c.}\right)\right]\mathcal{P}, \tag{3.11}$$

with the same terminology as introduced above. Hamiltonians closely related to Eq. (3.11) can be realized independently of the Fermi-Hubbard model in a quantum gas microscope using polar molecules [118], Rydberg dressing [119, 120] or by spin-dependent interactions [121]. In this case, there is no next-nearest neighbor hole hopping term. Furthermore, anisotropic spin coupling constants can also be realized with spin-dependent lattices [122]. In these types of setups, the coupling J/t can in principle be tuned to arbitrary values, including to $J/t > 1$. This case cannot be realized as an approximation of the Fermi-Hubbard model, since we assumed a large ratio of U/t in the mapping to the $t-J^{(*)}$ model.

The crossover from one to two dimensions in the Fermi-Hubbard model can be studied in a cold atom experiment by tuning the lattice depth in one spatial direction [123]. In this case, the interaction U stays constant while the ratio t_y/t_x is tuned, and upon mapping the Fermi-Hubbard model to the $t-J^{(*)}$ model, the spin exchange couplings become $J_y/J_x = t_y^2/t_x^2$, realizing the Hamiltonian

$$\hat{\mathcal{H}}^{\mathrm{1D2D}}_{t-J} = -\sum_{\mathbf{i},\sigma}\mathcal{P}\left(t_x\hat{c}^\dagger_{\mathbf{i},\sigma}\hat{c}_{\mathbf{i}+\mathbf{e_x},\sigma} + t_y\hat{c}^\dagger_{\mathbf{i},\sigma}\hat{c}_{\mathbf{i}+\mathbf{e_y},\sigma} + \mathrm{h.c.}\right)\mathcal{P} + \sum_{\mathbf{i}} J_x\hat{\mathbf{S}}_i\cdot\hat{\mathbf{S}}_{\mathbf{i}+\mathbf{e_x}} + J_y\hat{\mathbf{S}}_{\mathbf{i}}\cdot\hat{\mathbf{S}}_{\mathbf{i}+\mathbf{e_y}}. \tag{3.12}$$

3.2 Experimental and numerical probes

3.2.1 Experiments on the cuprate materials

A lot of progress in understanding the cuprates, and by extension the Fermi-Hubbard model, has been made through experiments. A common experimental probe in condensed matter physics is Angle Resolved Photoemission Spectroscopy (ARPES), where the photoemission of electrons from a sample is used to gain insights into the electronic structure. The excitation spectrum of cuprate materials measured with ARPES has for example revealed the *d*-wave nodes predicted by various theories [124–127]. For a comprehensive review on the method and experimental results up to 2003, we recommend Ref. [128]. In section 4.2, we discuss a protocol to perform ARPES in a quantum gas microscope, thus enabling the same experimental probe in a clean and well-controlled realization of the Fermi-Hubbard model.

Another typical probe is scanning tunneling microscopy (STM), where the local density of states is measured with atomic resolution. This method is in a way a complementary probe to ARPES, as it provides real-space information. STM has for example demonstrated the spatial inohmogeneities in many samples, which might also influence the results obtained with other experimental methods [129].

With the synthesis of large single crystals with controlled doping values, neutron scattering has become a valuable tool [130]. Neutron scattering can be used to probe the dynamical structure factor, which can exhibit evidence for antiferromagnetic correlations and stripe order.

Nuclear magnetic resonance (NMR) measurements of the Knight shift and its temperature and doping dependence have provided the first experimental probes of the elusive pseudogap phase.

Important insights have also been gained by transport and conductivity measurements. In order to understand transport properties, measurements of the Hall coefficient [131], which can be used to access the carrier density, are invaluable.

The competing phases at low temperatures in the cuprate phase diagram can be investigated by suppressing superconductivity with high magnetic fields. In the case of underdoping, i.e. a doping smaller than the optimal doping for superconductivity, quantum oscillations have been observed in the resistance, indicating well-defined quasiparticles with fermionic statistics [132]. Since then, quantum oscillations have been observed in other quantities, such as the specific heat [133]. Another method to suppress superconductivity is to introduce impurities in the sample.

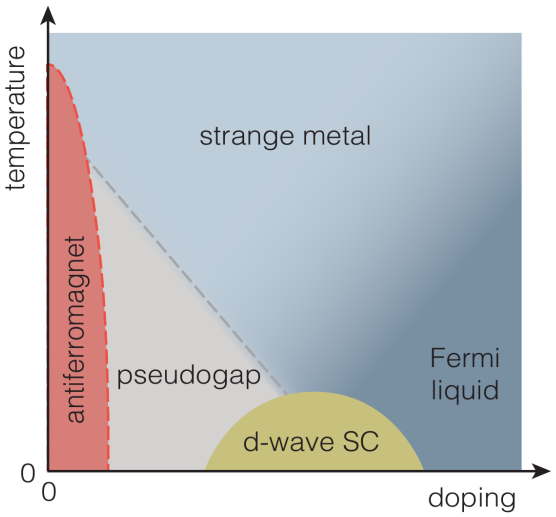

Figure 3.3.1: Conjectured phase diagram of the Fermi-Hubbard model. A schematic of the conjectured phase diagram of the finite-size 2D Fermi–Hubbard model [5].

3.2.2 Numerical Methods to probe the Fermi-Hubbard model

A lot of effort has been made to study the problem numerically. However, until today the exact simulation of the Fermi-Hubbard model remains challenging. We recommend Ref.[134] for a review of some of the most commonly used numerical methods. In quantum Monte Carlo simulations, the sign problem becomes apparent for low temperatures, high values of U/t, and finite doping. The local Hilbert space dimension of four limits exact diagonalization calculations to very small systems. Matrix product state algorithms are used to simulate the ground state of one dimensional systems, and while extensions to two spatial dimensions are possible, they usually come with some limitation, such as a cylinder geometry, which might favor certain states. Instead of describing the entire lattice, a different approach is taken in cluster approximations, such as cluster dynamical mean field theory: a single (small) cluster is treated exactly, while the surrounding system provides an external bath, which in turn influences the degrees of freedom of the small cluster [135]. The size of the small cluster can then be varied to some degree.

While definitive statements about the phase diagram of the Fermi-Hubbard model in the relevant parameter regime of $U \geq 6t$ remain scarce, all numerical methods agree on one thing: there are various competing states, which are close in energy [112].

3.3 Phase diagram

The Fermi-Hubbard model is believed to capture many aspects of the cuprate phase diagram, such as antiferromagnetism [136], its disappearance upon doping, stripes, the pseudogap phase [137] and pairing, see Fig. 3.3.1. One of the biggest mysteries of the phase diagram are the pseudogap and bad (or strange) metal regime, which defy a description in terms of conventional quasiparticles.
As mentioned above, the low temperature part of the cuprate phase diagram can be explored by applying a strong magnetic field, which suppresses superconductivity and thus enables the study of possibly competing phases. Moreover, the strength of the magnetic field necessary to suppress superconductivity at a given temperature and doping gives an indication of the competition at this point in the phase diagram [133].
Superconductivity and stripe formation for example seem to compete and coexist in the phase diagram [138, 139]. Numerical studies of the Fermi-Hubbard and the $t - J$ model have shown that this competition is strongly affected by extensions of the model, such as the next nearest neighbor hopping t' mentioned above [140, 141]. In order to investigate these phases which are so close in energy, numerical and experimental methods which are able to capture all phases under consideration without any bias are necessary.

3.3.1 Antiferromagnet

The parent compounds of the cuprate materials, i.e. samples without doping, and the half-filled two-dimensional Fermi-Hubbard model, are Mott insulators. This means that the system is insulating, even though the band is half filled and thus should be metallic according to band theory. The reason for the insulating behavior are strong interactions. In the case of the Fermi-Hubbard model, the Mott insulator is an antiferromagnet, because the virtual hopping, allowed by occupying a single site with a spin up and a spin down fermion, yields an energy gain of $4t^2/U$ for anti-aligned spins. The $t - J$ model introduced in section 3.1 with exactly one particle per site corresponds directly to the Heisenberg model.
Early numerical simulations, for example with quantum Monte Carlo, have shown that the ground state of the half-filled two-dimensional Fermi-Hubbard model had long-range antiferromagnetic order [136]. In order to make a statement about the ground state, successively lower temperatures were simulated and the result was extrapolated to the $T = 0$ limit. Experimentally, the antiferromagnetic state has been observed in neutron scattering experiments, where the two sublattice structure leads to Bragg peaks at momentum $\mathbf{k} = (\pi/a, \pi/a)$ [142–144]. Note that in two dimensions, there is no actual Néel temperature. However, in cuprate materials, the small interlayer coupling effectively leads to coupled two-dimensional layers. In pure two dimensional finite size systems, such as the one studied in a cold atom realization of the Fermi-Hubbard model in a quan-

tum gas microscope in Ref.[76], the antiferromagnetic correlations can span the entire system at sufficiently low temperatures.

3.3.2 Pseudogap

The pseudogap is probably the most mysterious and elusive part of the phase diagram. A variety of experimental observations hint towards certain properties, but their theoretical interpretation remains unclear and debated. There is no definite finite-temperature phase boundary, but instead a crossover at T^* for dopings $p < p^*$. The defining property of the pseudogap is that there is an energy gap in some properties, but not in others [129]. Phrased differently, increasing the temperature from the superconducting state, certain gap-like features persist in the normal state, i.e. without superconductivity. For a review of pseudogaps in a general context, see Ref. [145].
Early experiments on the cuprate materials showed gap-like behavior in the normal state above the superconducting phase in the uniform spin susceptibility, probed through NMR measurements of the Knight shift [146, 147]. In conventional superconductors, the Knight shift is temperature independent in the normal state. Below the critical temperature T_c for superconductivity, the pairing of electronic spins into superconducting Cooper pairs leads to a sharp drop in the Knight shift [148]. In the cuprate materials for doping below the optimal doping, the Knight shift drops at temperatures significantly higher than T_c. One possible conclusion is that pairs already form for temperatures $T > T_c$, which leads to a so-called spin gap [146]. Numerically, the temperature and doping dependence of the Knight shift has for example been observed in cluster DMFT studies of the two-dimensional Fermi-Hubbard model [149]. A similar signature has been found directly for the spin susceptibility, which exhibits a maximum at the temperature T^*, already at half-filling and in the Heisenberg model [150].
One picture of the pseudogap is thus as follows: the observed gap is due to paring, but long-range order is not yet established. The phase stiffness is comparably small, and thermal fluctuations therefore easily inhibit the ability to carry a supercurrent [130]. However, definite proof for pairing correlations up to high temperatures is still lacking and even difficult to define precisely [112]. Numerically, the d-wave pairfield susceptibility has been used to probe the pre-formed pairs [151].
Apart from the spin susceptibility, a pseudogap has also been seen in a variety of other experiments, maybe most prominently in ARPES measurements. In the superconducting phase, the spectral function at the antinodal point $\mathbf{k} = (0, \pi)$ exhibits a narrow peak, which is a signature of a well-defined quasiparticle [130]. The onset of this peak is found above the Fermi energy, thus indicating the presence of a gap. As the temperature is increased through the critical temperature T_c, the quasiparticle peak disappears. The gap, however, persists. One possible conclusion is that the quasiparticle in the superconducting phase exists due to the phase coherence, which is lost in the pseudogap phase [130]. The formation of a pseudogap near the antinodal point has been

observed numerically for example with determinantal quantum Monte Carlo simulations [152]. Around the nodal points $\mathbf{k} = (\pm\pi/2, \pm\pi/2)$, so-called Fermi-arcs have been seen experimentally [153]. These arcs of high spectral weight appear like a part of a small Fermi surface, but they have two end points and the backside of the putative Fermi surface is invisible. In a Fermi-liquid state, one would expect a closed Fermi surface. The microscopic origin of the Fermi arcs is poorly understood. For example, it remains unclear whether the observed arcs are due to inherent many-body effects, or whether they emerge in the many-body system merely by renormalizing parameters in a putative effective single-particle theory. Furthermore, it remains unclear whether there exist states on the backside of the Fermi arcs whose spectral weight is strongly suppressed. If this is the case, and the Fermi-arcs can be understood as being part of a Fermi surface, this will have some intriguing consequences: The expected area enclosed by the putative Fermi surface would violate Luttinger's theorem [154], indicating the existence of either a hitherto unknown broken translational symmetry or of topological excitations [155]. If the latter was the case, it would imply striking consequences for the nature of the constituents that determine the physics of strongly correlated cuprate compounds [156, 157].

Another route to probe the pseudogap phase are transport measurements. In particular, in high magnetic fields, which suppress superconductivity, the Hall coefficient has been measured at low temperatures. Starting from high doping, the carrier density is $n = 1 + p$, corresponding to the number of holes relative to a maximally filled system. With decreasing doping p, one enters the pseudogap phase. This is accompanied by a rapid drop in the Hall coefficient n_H, yielding a carrier density of $n = p$ in the pseudogap phase [133]. Correspondingly, the resistivity shows a large upturn at low temperatures for samples in a high magnetic field. This is consistent with a loss of carrier density [133]. Note that only the density of charge carriers is reduced, while their mobility does not change significantly [158].

3.3.3 Strange metal

The state at dopings higher than p^* is a so-called strange metal for a range of dopings, until it becomes a normal metal or a Fermi liquid [133]. In the strange or bad metal regime, the conductivity at temperatures much higher than T_c is almost two orders of magnitude smaller than in a simple metal [112]. At low temperatures, the resistivity scales linearly with temperature, as opposed to the quadratic scaling predicted by Fermi liquid theory. In Fermi liquid theory, the charge is carried by the quasiparticles and the conductivity corresponds to the current of those carriers. As a consequence, the resistivity should scale as T^2 at low temperatures. Moreover, the mean free path of a quasiparticle cannot be less than the lattice spacing, which leads to the Mott-Ioffe-Regel limit as a lower bound on the diffusion constant [159, 160]. The strong interactions thus seem to lead to a breakdown of Fermi liquid theory in this regime and a destruction of the quasiparticle picture.

In a cold atom realization of the Fermi-Hubbard model, the diffusion constant of the charge has been measured by observing the relaxation of an imposed density modulation at a fixed doping value of 18% [77]. From the diffusion constant, a value for the resistivity can be obtained. This resistivity exhibits a linear temperature dependence and exceeds the Mott-Ioffe-Regel limit mentioned above.

3.3.4 Stripes

In the cuprate phase diagram at low temperatures and intermediate doping values, superconductivity and stripe order appear to be competing phases. Most generally speaking, stripes are an inhomogeneous spin and charge ordering. First experimental evidence for stripes was found for materials in which some of the original La atoms had been replaced by Nd, thus distorting the crystal structure [161, 162]. This distortion causes spin fluctuations to condense into a static spin density wave. Neutron scattering experiments on such materials then showed that the Bragg peak at the antiferromagnetic ordering vector $\mathbf{Q} = (\pi, \pi)$ splits up into four peaks, which are displaced by $\pm p$, where p is the doping [161, 162]. In the charge sector, the Bragg peaks are displaced from the fundamental lattice reflections by $2p$. In real space, the picture here is that the holes sit in charged stripes, which are quarter (half of half) filled and occur at a distance of $1/2p$ (lattice spacing $a = 1$). These charged stripes correspond to antiphase boundaries for the spins, such that the spin period is twice the value of the charge period, $1/p$. This property leads to the corresponding differences in the positions of the Bragg peaks.

One particular case for static stripes is the formation of a pair density wave, where the charged stripes are internally superconducting, while the phase reverses from stripe to stripe [163]. Without replacing some of the La atoms with Nd, i.e. looking at the origincal compounds, the same general picture holds. However, the spin density wave order is not static, but instead fluctuating, leading to *fluctuating stripes* [164].

Another experimental probe used in this context is scanning tunneling microscopy. Experiments on several different underdoped cuprates have shown charge modulations [133]. Not all charge modulations are however accompanied by spin density wave modulations, thus rendering them distinct from the stripes discussed above.

Numerically, the situation for the Fermi-Hubbard model is still heavily debated. DMRG studies found evidence for stripes in the ground state of the Fermi-Hubbard model on small cylinder geometries [134, 165]. Up to today, the question which state – stripe or superconducting order, some combination thereof or even more complex order – has the lowest energy in a given parameter regime is debated and the close competition between the different states has been shown also for the $t - J$ model, for example with iPEPS (infinite projected-entangled pair states) simulations [166].

The situation for numerical simulations is additionally complicated by the fact that modifying the model slightly, e.g. by adding a t'-term, can change which state is lowest in energy [167]. Moreover, one has to take care not to influence the observed physics by the geometry most suitable for a given numerical method. A lot of DMRG studies for example have been performed on cylinders of width four or six, where this method is capable of resolving the competing phases to a very high accuracy [168].

3.3.5 Superconductivity

Early experiments on the magnetic flux threading through a ring of a cuprate material showed strong evidence for Cooper pairing [169]. In the following years, the pairing symmetry itself was tested, for example through quantum interference effects in a SQUID (superconducting quantum interference device) [170], and the general agreement today is that the cuprates exhibit predominantly d-wave pairing symmetry. For an extensive review on the early experiments we recommend Ref. [171]. ARPES measurements have revealed the concrete form of the gap to be [172, 173]

$$\Delta(k) \propto \Delta_0 \left[\cos(k_x a) - \cos(k_y a)\right] \tag{3.13}$$

The unconventional pairing observed in the cuprates is associated with gapless quasiparticle excitations at the lowest temperatures, leading to different thermodynamic properties than in the conventional superconductors [112].

It has been found that the critical temperature for superconductivity T_c is proportional to the zero-temperature superfluid density, or phase stiffness, $\rho_s(T = 0)$ for many underdoped materials; this is called the Uemura relation [174]. The phase stiffness is a measure for the ability of the superconducting state to carry a supercurrent [130]. In conventional superconductors, the gap is much smaller than the phase stiffness. As the temperature is increased, superconductivity is destroyed because electrons do not pair anymore. In the underdoped cuprates, the two energy scales are more balanced and as the temperature is increased, the ability of the state to carry a supercurrent is destroyed.

Analytical studies, for example a slave-boson mean field theory for the $t-J$ model, showed that a potential superconducting state in this model has d-wave symmetry [127]. Studies by Trugman and Scalapino showed that on a 2×2 plaquette with antiferromagnetic correlations, a paired state has $d_{x^2-y^2}$ symmetry [175]. Numerical results, for example from dynamic cluster approximation techniques, on the d-wave pair-field susceptibility suggest that the two-dimensional Fermi-Hubbard model has a d-wave pairing phase at $U = 4t$ [176]. One has to note however that these studies are limited to some degree by the size of the cluster. Moreover, the interaction strength relevant for the cuprate materials is typically rather $U = 8 \ldots 12t$. A very recent study using DMRG and

auxiliary field quantum Monte Carlo probed pairing in the ground state at $U = 6...8t$ and dopings $0.1 < p < 0.2$ and concluded that in this parameter regime in the pure Fermi-Hubbard model (i.e. without t' term), only short-range pairing occurs and the system is not superconducting [168].

3.3.6 Fermi-liquid at high doping

At high doping, beyond the superconducting dome, the cuprates can be described by Landau's Fermi-liquid theory. As opposed to the neighboring strange metal regime, the resistivity scales as $\rho \propto T^2$ for $T \to 0$ [133]. ARPES measurements in the Fermi-liquid regime have revealed that the Fermi surface is a single large cylinder.

4

One Dimension

One dimensional systems are special, as interactions between particles have more drastic effects here compared to higher dimensions. The restricted dimensionality enhances the interactions between particles and effectively destroys the quasi-particle picture. The excitations of the system are always collective excitations [177]. This collective nature of the excitations can lead to the emergence of new quasiparticles. The low energy behavior of a one dimensional system is universally captured by the Luttinger liquid description, independently of the quantum statistics of the original particles [178, 179]. In the case of spinful fermions, a single fermionic excitation carrying charge ± 1 and spin $\pm 1/2$ can split up into a collective charge excitation and a collective spin excitation. These collective spin and charge excitations are then fundamentally different from free electrons. In general, spin and charge excitation, in the following called spinon and chargon, do not have the same velocity. The spatial separation of a single excitation through the independent dynamics of spinon and chargon is an example of fractionalization.

One dimensional systems are theoretically comparably well understood. Luttinger liquid theory and the bosonization formalism for example predict many properties correctly, such as independent velocities for the different collective excitations and the behavior of correlation functions. Moreover, some one dimensional systems can be solved exactly with the Bethe ansatz [180, 181]. Due to their entanglement structure, one dimensional systems can be studied particularly well nu-

merically with matrix product state methods.

In traditional condensed matter materials, the physics of one dimensional systems can be observed if the couplings in one spatial direction are significantly stronger than in the other two directions. The coupling in one spatial dimension is often strongly reduced due to spacer layers, which physically separate two dimensional planes [182]. One dimensional chains with only weak couplings to the neighboring chains can be realized through anisotropic overlaps of orbitals, for example due to the Jahn-Teller effect [183]. Angle-resolved photoemission spectroscopy (ARPES) experiments on the quasi-one dimensional material $SrCuO_2$ have shown direct signatures of independent spinon and holon branches at low energies [184, 185]. Other one dimensional experimental platforms include carbon-nanotubes, experiments which have shown the expected power law behavior in conductance measurements [186]. In quantum wires in semiconductors, tunneling experiments have shown the singular nature of the spectral function, which is associated with spin-charge separation [187].

Quantum gas microscopy experiments open a new perspective on spin charge separation, as the direct observation in real space and time is possible. In a recent experiment in equilibrium [75], the two-point spin correlations in a Fermi-Hubbard chain were measured. Without doping, antiferromagnetic correlations extend over long distances. As soon as holes are introduced, the spin correlations at distances larger than $d = 1$ are strongly suppressed, seemingly contradicting spin-charge separation. The explanation for this phenomenon is that the antiferromagnetic spin correlations are not truly reduced, but merely hidden. In Ref. [75], these hidden correlations were revealed by going to *squeezed space*. In the squeezed space, the sites occupied by holes are completely removed from the system, leaving behind a spin chain. Within this spin chain, the antiferromagnetic correlations are restored to their undoped values [75].

In this chapter, we first put the squeezed space representation on a more formal footing. We then continue by studying spin-charge separation in the spectral function as well as in a non-equilibrium experiment. In section 4.2 we propose a measurement scheme for the spectral function in quantum gas microscopes, where the finite system sizes allow us to observe spin-charge separation at all energies. In ARPES experiments on traditional materials, the fractionalization manifests itself through a continuum in the spectrum. In a finite size system however, this continuum is replaced by discrete lines, which can be associated with the quantized momenta of the quasi-particles. In section 4.3, we study dynamical spin-charge separation after the creation of a hole in collaboration with a quantum gas microscopy experiment. We observe the emergence of two independent excitations propagating at different velocities through observables in the spin and charge sector, respectively. The corresponding velocities are in agreement with theoretical predictions for the spinon and chargon velocity.

4.1 Squeezed space representation

This section is partly based on the publication

- Annabelle Bohrdt, Daniel Greif, Eugene Demler, Michael Knap, Fabian Grusdt: "Angle-resolved photoemission spectroscopy with quantum gas microscopes." – Phys. Rev. B 97, 125117 (2018) [arXiv:1710.08925]

Structure and text have been rearranged and adapted here.

In the squeezed space representation, empty sites are effectively removed from the system. We independently keep track of the hole positions and spin configurations. While the squeezed space appears to be more of a theoretical construct and is not accessible in traditional condensed matter experiments, it can be directly used in snapshots from a quantum gas microscope. For each snapshot, we can obtain its squeezed space representation by removing the holes from the system and saving their former positions independently. The exact diagonalization implementation of the $t-J$ model with a single hole discussed in section A.1 is inspired by the squeezed space construction: instead of allowing for three states on each site, we construct a spin $1/2$ Hilbert space for $L-1$ sites. For each of the L possible hole positions, the Hamiltonian is then simply constructed by turning off the corresponding spin couplings.
We derive an effective Hamiltonian describing a single hole inside a one-dimensional spin chain. For concreteness we discuss the $t-J^*$ Hamiltonian from Eq. (3.9), but generalizations to other couplings are straightforward. The hole can be described by a bosonic representation where the spins are mapped to constrained fermions $\hat{f}_{j,\sigma}$ and the holons to bosonic operators $\hat{h}_j^\dagger$. In this case

$$\hat{c}_{j,\sigma} = \hat{h}_j^\dagger \hat{f}_{j,\sigma}. \tag{4.1}$$

We can simplify the holon degree of freedom by effectively removing it from the spin chain. This can be achieved by defining a basis of the Hilbert space of a spin chain with a single hole, with basis states $\hat{h}_j^\dagger|0\rangle \otimes |\tilde{\sigma}_1, \ldots, \tilde{\sigma}_{L-1}\rangle$, where

$$|\tilde{\sigma}_1, \ldots, \tilde{\sigma}_{L-1}\rangle \equiv \hat{\tilde{f}}^\dagger_{1,\tilde{\sigma}_1} \ldots \hat{\tilde{f}}^\dagger_{L-1,\tilde{\sigma}_{L-1}}|0\rangle. \tag{4.2}$$

Here, $\tilde{\sigma}_i = \uparrow, \downarrow$. The index i labels spins in the chain from left to right, independent of the holon position. Note that only $L-1$ spins appear in Eq. (4.2) because there is no spin on the physical site occupied by the holon, and we used the spinon operators $\hat{\tilde{f}}$ to define a constrained fermion representation of spins in squeezed space.
Next we need to express the original Hamiltonian, Eq. (3.9), formulated using operators $\hat{c}_{j,\sigma}$, in the

new basis. Without doping, the Hamiltonian

$$\hat{\mathcal{H}} = J \sum_j \hat{\mathbf{S}}_{j+1} \cdot \hat{\mathbf{S}}_j, \qquad \hat{\mathbf{S}}_i = \frac{1}{2} \hat{f}^\dagger_{i,\alpha} \sigma_{\alpha,\beta} \hat{f}_{i,\beta} \tag{4.3}$$

corresponds to a Heisenberg spin chain. In the case with doping, there exist no exchange interactions between the two spins adjacent to the hole. For a single holon we can thus write the Hamiltonian in Eq. (3.9) as $\hat{\mathcal{H}}_{t-J^*} = \hat{\mathcal{H}}_t + \hat{\mathcal{H}}_J + \hat{\mathcal{H}}_{\mathrm{NNN}}$ with

$$\hat{\mathcal{H}}_J = J \sum_j \hat{\tilde{\mathbf{S}}}_{j+1} \cdot \hat{\tilde{\mathbf{S}}}_j \left(1 - \hat{h}^\dagger_j \hat{h}_j\right), \quad \hat{\tilde{\mathbf{S}}}_i = \frac{1}{2} \hat{\tilde{f}}^\dagger_{i,\alpha} \sigma_{\alpha,\beta} \hat{\tilde{f}}_{i,\beta}. \tag{4.4}$$

The hopping term

$$\hat{\mathcal{H}}_t = -t\, \mathcal{P} \sum_{\langle ij \rangle, \sigma} \hat{c}^\dagger_{i,\sigma} \hat{c}_{j,\sigma} \mathcal{P}, \tag{4.5}$$

moves the holon by one site while the order of fermions $\hat{\tilde{f}}$ in squeezed space is not modified. One can write $\hat{\mathcal{H}}_t$ most conveniently as

$$\hat{\mathcal{H}}_t = -t \sum_{\langle ij \rangle} \hat{h}^\dagger_j \hat{h}_i = -2t \sum_k \cos(k) \hat{h}^\dagger_k \hat{h}_k. \tag{4.6}$$

For the next-nearest neighbor tunnelings, the situation is more complicated. They are of a general form

$$\hat{\mathcal{H}}_{\mathrm{NNN}} = \sum_{\sigma,\sigma',\tau,\tau'} g_{\sigma,\sigma',\tau,\tau'} \sum_i \hat{c}^\dagger_{i+2,\sigma} \hat{c}^\dagger_{i+1,\tau} \hat{c}_{i+1,\tau'} \hat{c}_{i,\sigma'} + \mathrm{h.c.}, \tag{4.7}$$

where the coefficients g can be read off from Eq. (3.9). The term in Eq. (4.7) modifies the order of spins because it moves a fermion from site i to $i+2$. This involves an exchange of the fermions at sites i and $i+1$, which introduces an additional minus sign. We can see this by calculating the action of $\hat{\mathcal{H}}_{\mathrm{NNN}}$ on a basis state:

$$\hat{\mathcal{H}}_{\mathrm{NNN}} \hat{h}^\dagger_{i+2} |0\rangle \otimes |\ldots, \tilde{\sigma}_i, \tilde{\sigma}_{i+1}, \ldots\rangle. \tag{4.8}$$

To lighten the notation, we consider the action of a single term in the sum in Eq. (4.7). Representing the basis state in terms of the original $\hat{c}^\dagger_{i,\sigma}$ operators yields

$$\begin{aligned} &\hat{c}^\dagger_{i+2,\sigma} \hat{c}^\dagger_{i+1,\tau} \hat{c}_{i+1,\tau'} \hat{c}_{i,\sigma'} \hat{c}^\dagger_{1,\tilde{\sigma}_1} \ldots \hat{c}^\dagger_{i,\tilde{\sigma}_i} \hat{c}^\dagger_{i+1,\tilde{\sigma}_{i+1}} \ldots |0\rangle \\ &\qquad = \hat{c}^\dagger_{1,\tilde{\sigma}_1} \ldots \hat{c}^\dagger_{i-1,\tilde{\sigma}_{i-1}} (-1)^{i-1} \delta_{\sigma',\tilde{\sigma}_i} \delta_{\tau',\tilde{\sigma}_{i+1}} \times \hat{c}^\dagger_{i+1,\tau} (-1)^i \hat{c}^\dagger_{i+2,\sigma} \ldots |0\rangle. \end{aligned} \tag{4.9}$$

In the notation introduced above, this state can be identified with

$$-\delta_{\sigma',\tilde{\sigma}_i}\delta_{\tau',\tilde{\sigma}_{i+1}}\hat{h}^\dagger_{i+2} \otimes |..., \tilde{\sigma}_{i-1}, \tau, \sigma, \tilde{\sigma}_{i+2}, ...\rangle. \tag{4.10}$$

The next-nearest neighbor term leads to an exchange of the spins on sites i and $i+1$ in squeezed space which can be described by a term of the form $4\tilde{\mathbf{S}}_i \cdot \tilde{\mathbf{S}}_{i+1} - 1$, see e.g. supplementary material in Ref. [75]. By taking into account the minus sign from the fermion exchange above, we arrive at the following expression,

$$\hat{\mathcal{H}}_{\mathrm{NNN}} = \frac{J}{2}\sum_j \hat{h}^\dagger_{j+2}\hat{h}_j \left(\hat{\tilde{\mathbf{S}}}_{j+1} \cdot \hat{\tilde{\mathbf{S}}}_j - \frac{1}{4}\right) + \mathrm{h.c.}. \tag{4.11}$$

From the second term in the brackets, we derive the corresponding term $-\frac{1}{4}J\cos(2k_h)$ in the holon dispersion, Eq. (4.23).
In summary, the $t-J^*$ Hamiltonian for a single hole can be written in squeezed space as

$$\begin{aligned}\hat{\mathcal{H}}_{t-J^*} = -\sum_{k_h}\hat{h}^\dagger_{k_h}\hat{h}_{k_h}\left(2t\cos(k_h) + \frac{1}{4}J\cos(2k_h)\right) + \frac{J}{2}\sum_j\left[\hat{h}^\dagger_{j+2}\hat{h}_j\hat{\tilde{\mathbf{S}}}_{j+1}\cdot\hat{\tilde{\mathbf{S}}}_j + \mathrm{h.c.}\right] \\ + J\sum_j \hat{\tilde{\mathbf{S}}}_{j+1}\cdot\hat{\tilde{\mathbf{S}}}_j\left(1-\hat{h}^\dagger_j\hat{h}_j\right).\end{aligned} \tag{4.12}$$

In section 4.3, we label the coordinates in squeezed space with $\tilde{i}$ and distances in squeezed space as $\tilde{x}$ for clarity.

4.2 Angle-resolved photoemission spectroscopy with quantum gas microscopes

This section is based on the publication

- Annabelle Bohrdt, Daniel Greif, Eugene Demler, Michael Knap, Fabian Grusdt: "Angle-resolved photoemission spectroscopy with quantum gas microscopes." – Phys. Rev. B 97, 125117 (2018) [arXiv:1710.08925]

Structure, text and figures have been rearranged and adapted here.

Quantum gas microscopes are a promising tool to study interacting quantum many-body systems and bridge the gap between theoretical models and real materials. So far, they were limited to measurements of instantaneous correlation functions of the form $\langle \hat{O}(t) \rangle$, even though extensions to frequency-resolved response functions $\langle \hat{O}(t)\hat{O}(0) \rangle$ would provide important information about the elementary excitations in a many-body system. For example, single-particle spectral functions, which are usually measured using photoemission experiments in electron systems, contain direct information about fractionalization and the quasiparticle excitation spectrum.
Traditional solid state experiments rely on measurements of time-dependent response functions of the form $\langle \hat{O}(t)\hat{O}(0) \rangle$ in the frequency domain [1]. Examples include inelastic neutron scattering, x-ray spectroscopy, scanning tunneling microscopy, angle-resolved photoemission spectroscopy (ARPES), or purely optical probes. In contrast, quantum gas microscopes are used to perform destructive measurements accompanied by a collapse of the many-body wave function. In order to relate cold atom experiments to their solid state counterparts and facilitate direct comparisons, it is desirable to measure similar physical observables in both systems [74, 188–193].
One of the most powerful tools for studying strongly correlated electrons in solids is angle resolved photoemission spectroscopy. In this technique, electrons are ejected from the surface of a sample through the photoelectric effect. By counting the number of photoelectrons and measuring their energy ω and momentum k, the single-particle excitation spectrum $A(k, \omega)$ is obtained. The spectral function reveals fundamental properties of the system and its excitations [128, 129], and important insights about high-T_c cuprate superconductors have been obtained from ARPES measurements, see also chapter 3. One of the most puzzling observations in this context is the appearance of Fermi arcs in the spectrum below optimal doping in the pseudogap phase [129]. A microscopic understanding of this phenomenon is currently lacking, and it is expected that experiments with ultracold atoms can shed new light on this long-standing problem.

[1] More precisely, one measures retarded correlation functions, i.e. in the case of bosonic operators $\hat{\varphi}$, $D^R(t) = i\Theta(t)\langle \hat{\varphi}(t)\hat{\varphi}(0) - \hat{\varphi}(0)\hat{\varphi}(t) \rangle$ and for fermionic operators $\hat{\psi}$, $G^R(t) = i\Theta(t)\langle \hat{\psi}(t)\hat{\psi}^\dagger(0) + \hat{\psi}^\dagger(0)\hat{\psi}(t) \rangle$.

Spectral functions have already been measured in fermionic quantum gas experiments for instance by radio-frequency spectroscopy [188] and its momentum resolved extension [194], Bragg spectroscopy [195] and lattice modulation spectroscopy [70, 196]. Although these techniques have been very successful in characterizing strongly correlated systems, acquiring a sufficiently strong signal has always required creating multiple excitations. In addition, final-state interactions often complicate the interpretation of the obtained spectra.

Here, we propose a scheme for the measurement of momentum-resolved single-particle excitation spectra without final-state interactions, similarly to ARPES, using a quantum gas microscope, see Fig. 4.2.1. To demonstrate our scheme, we consider variations of the $t - J$ model with isotropic and anisotropic spin interactions, see section 3.1.

The ground state of the 1D $t - J$ model with isotropic spin interactions does not possess long-range order and is described by Luttinger liquid theory instead [177]. The spin-liquid nature of this ground state leads to an intriguing signature in the spectral function already for a single hole [197]: at low energies, most of the spectral weight is found for momenta $0 \leq |k| \leq \pi/2$, with lattice constant $a = 1$, whereas between $\pi/2 < |k| \leq \pi$ the spectral weight is suppressed by several orders of magnitude, see Fig. 4.2.1 b). This phenomenon is to some extent reminiscent of the Fermi arcs observed by ARPES in the pseudogap phase of cuprates [129].

4.2.1 Measuring spectral functions in a quantum gas microscope

In the following we outline our proposal to experimentally measure the spectral function of a single hole with simultaneous momentum and energy resolution in a quantum gas microscope. The basic idea is to excite a single particle from a filled 1D system S by lattice modulation into an adjacent 1D "detection" system S^{det}. The latter consists of empty sites and is offset in energy by $\Delta \gg t_y$ where t_y is the bare tunneling amplitude between S and S^{det}, see Fig. 4.2.1 a). The lattice modulation can be described by a perturbation term

$$\hat{\mathcal{H}}_{\text{pert}}(\tau) = \delta t_y \sin(\omega_{\text{shake}}\tau)\hat{T}_y \tag{4.13}$$

in the Hamiltonian. Here τ denotes time, δt_y is the modulation amplitude of the hopping between S and S^{det} described by the operator $\hat{T}_y$, and ω_{shake} is the modulation frequency.

Implementation in the $t - J^*$ model A balanced two-component spin mixture of ultracold fermionic atoms in an optical lattice allows for a clean implementation of the $t - J^*$ model introduced in Eq. (3.9) in the limit of large $U/t \gg 1$. To create the optical lattice configuration nec-

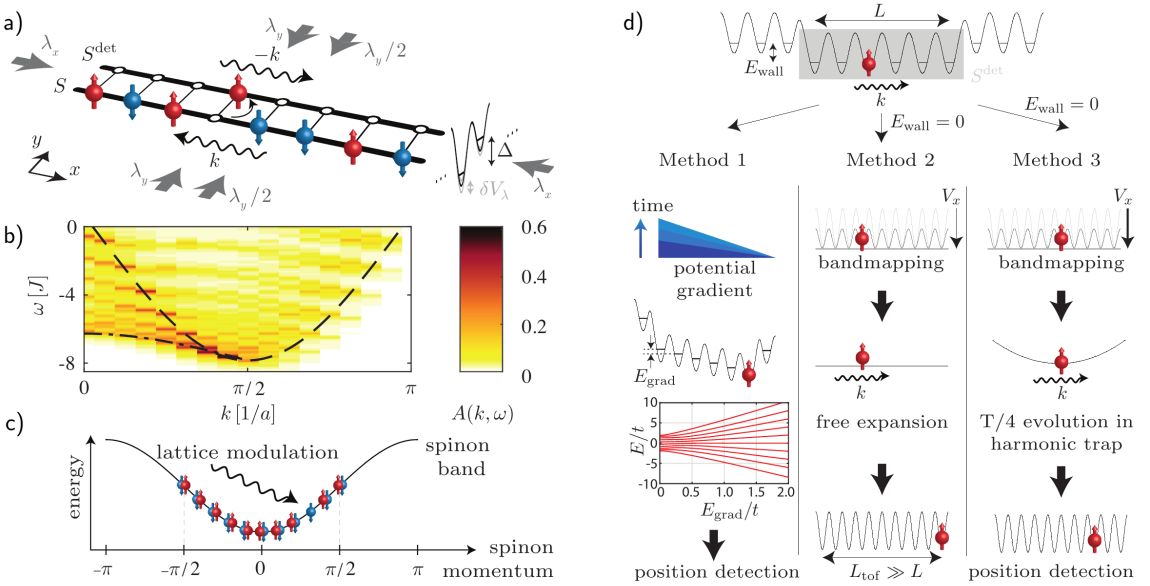

Figure 4.2.1: ARPES in a quantum gas microscope measurement scheme. a) Proposed experimental setup. A lattice modulation along the y-direction creates a hole in the physical system S by transferring a single particle into the neighboring, thermodynamically disconnected detection system S^{det}, which is offset in energy by Δ. A subsequent momentum space mapping technique enables the determination of the momentum k of the excitation. The rate of the transferred atoms is proportional to the spectral function $A(k,\omega)$. b) Exemplary calculated spectral function of the $t-J$ model with next-nearest neighbor interactions and isotropic spin couplings for $L = 16$ sites, tunneling $t/J = 4$, temperature $T/J = 0.2$ and open boundary conditions. The spectral weight in units of $1/J$ is color coded. Individual holon and spinon branches in the spectrum are clearly visible, as indicated by the dashed and dashed-dotted lines. c) In a mean field approach, the ground state of the effective spin degrees of freedom, which is a Luttinger spin liquid, is described as a half-filled Fermi sea of spinons. In the measurement process, a holon is created and a spinon is removed, such that the accessible momenta are restricted to $k \lesssim \pi/2$ at low energies, which explains the asymmetry in b). d) Measuring the momentum of the excitation. The momentum of the hole-excitation in S is measured from the momentum of the excited particle in S^{det}, which has a finite size of L sites determined by the energy offset E_{wall} at the edges. E_{wall} is chosen to be larger than all relevant energy scales in S. The three methods discussed in the main text are illustrated. The exemplary diagram shown in the first column illustrates that the eigenenergies in S^{det} are smoothly connected when introducing a potential gradient E_{grad} (here $L = 10$). For $E_{\mathrm{grad}} \gg t$ the eigenstates are localized on individual lattice sites. For the first method we keep E_{wall} unchanged, whereas we set $E_{\mathrm{wall}} = 0$ for the other two methods before the bandmapping.

essary for the detection scheme we propose a standard retro-reflecting laser configuration along the x-direction with a lattice depth of V_x and tunneling t, and a superlattice configuration in the y-direction that creates several copies of decoupled double-well systems, see Fig. 4.2.1 a). This has the advantage of obtaining several measurements per experimental cycle. However, a standard lattice along the y-direction could also be used and the energy offset Δ could be created with a digital micro-mirror device.

The superlattice potential can be created for example by two retro-reflected laser beams at wavelengths $\lambda_y/2$ and λ_y [198], which create a short and long wavelength lattice of depth V_y^l and V_y^s. By setting their phase difference ϕ close to $\pi/2$ a controlled energy offset between the two sites of the double well can be introduced with bare tunneling t_y. The total optical potential is given by

$$V(x,y) = V_x \cos^2\left(2\pi x/\lambda_x\right) + V_y^l \cos^2\left(2\pi y/\lambda_y\right) + V_y^s \cos^2\left(4\pi y/\lambda_y - \phi\right). \tag{4.14}$$

The lattice depths along the y-direction can be chosen sufficiently deep, such that the tunneling between different double wells is negligible. In addition, the energy offset is much larger than all other energy scales $\Delta \gg U, t$ (but smaller than the energy gap to the next band) to make direct tunneling processes off resonant. This also ensures that there are no atoms in S^{det} when loading the fermionic spin mixture from the initial harmonic trap into the lattice.

To implement the detection scheme for the spectral function, we propose to periodically modulate the depth of the long wavelength lattice according to

$$V_y^l(t) = V_y^l + \delta V_y^l \sin(\omega_{\mathrm{shake}}\tau). \tag{4.15}$$

This leads to an induced oscillatory tunnel coupling δt_y along the y-direction between the spin system S and the detection system S^{det}. Thereby the perturbation described in Eq. (4.17) can be realized. The strength of the induced tunneling is given by

$$\delta t_y = \delta V_\lambda \int w_{\mathrm{L}}^*(y) \cos^2(2\pi y/\lambda) w_{\mathrm{R}}(y) dy, \tag{4.16}$$

where $w_{\mathrm{L}}(y)$ and $w_{\mathrm{R}}(y)$ denote the Wannier functions of the left and right lattice sites of the double-well system created by the lattices along the y-direction [199].

4.2.2 Single-particle transfer

A successful excitation transfers a single particle from S to S^{det}. As the modulation is only along the y-axis (i.e. perpendicular to the 1D system), the total momentum is conserved and the excitation couples simultaneously to all individual momenta k. This can be seen by rewriting the perturbation

(4.13) in momentum space,

$$\hat{T}_y = -\sum_{i,\sigma}\left(\hat{d}^\dagger_{i,\sigma}\hat{c}_{i,\sigma} + \text{h.c.}\right) = -\sum_{k,\sigma}\left(\hat{d}^\dagger_{k,\sigma}\hat{c}_{k,\sigma} + \text{h.c.}\right). \tag{4.17}$$

Here $\hat{c}_{i(k),\sigma}$ denotes the annihilation operator at site i (momentum k) in S and $\hat{d}^\dagger_{i(k),\sigma}$ denotes the respective creation operator in S^{det}. The spin-index is $\sigma = \uparrow, \downarrow$. The energy change of the system with one hole as compared to the initial state without a hole is $\hbar\omega = E^{N-1} - E^N$. For a lattice modulation frequency ω_{shake} this is determined by energy conservation,

$$\hbar\omega = \hbar\omega_{\text{shake}} - E^s(k) - \Delta, \tag{4.18}$$

where Δ is the energy offset and $E^s(k) = -2t\cos(ka)$ is the energy of the particle in the detection system, with t the hopping amplitude of the particle in S^{det}. As explained in Sec. 4.2.3, a subsequent momentum-space mapping technique of the single particle in S^{det} allows one to determine the momentum k of the transferred atom. Thus, both full momentum and energy resolution are achieved. By measuring the final position of the transferred atom and repeating the same measurement for various lattice modulation times, the excitation rate $\Gamma(k,\omega)$ can be determined. This rate quantifies the probability for creating a hole with momentum k and energy $\hbar\omega$ in S, normalized by the modulation time. Up to constant pre-factors, it is identical to the hole spectral function,

$$\Gamma(k,\omega) = \frac{2\pi}{\hbar}|\delta t_y|^2 A(k,\omega), \tag{4.19}$$

as obtained by Fermi's golden rule.
The spectral function of the hole $A(k,\omega)$ is defined as

$$A(k,\omega) = \frac{1}{Z_0}\sum_{n,m}\sum_{\sigma} e^{-\beta E^N_n}|\langle\psi^{N-1}_m|\hat{c}_{k,\sigma}|\psi^N_n\rangle|^2 \times \delta(\hbar\omega - E^{N-1}_m + E^N_n), \tag{4.20}$$

with $|\psi^N_n\rangle, E^N_n$ denoting the eigenstates and -energies of the system S with N particles. Furthermore, $\beta = 1/k_B T$ is the inverse temperature and $Z_0 = \sum_n e^{-\beta E^N_n}$ denotes the partition function before the perturbation Eq. (4.13) is switched on.
For small system sizes it is important to choose a sufficiently small excitation amplitude $\delta t_y/t_y$, such that at most a single particle is transferred, in order to avoid multiple excitations as well as final state interactions. The latter can also be avoided by implementing a spin-changing Raman transfer to a non-interacting spin state instead of a lattice modulation. For large systems, we expect multiple excitations to not alter the spectral function as long as the average fraction of excited particles remains sufficiently small.

4.2.3 Momentum Resolution

A crucial step for measuring the spectral function is the momentum detection in the probe system S^{det}. This can be achieved by combining the capabilities of a quantum gas microscope with a digital micromirror device (DMD), which gives control over the optical potential of the atoms on a site-resolved level. This precise control has already been demonstrated with bosonic and fermionic atoms with single-site resolution [200, 201]. By illuminating the DMD with blue-detuned light, a box-like potential with hard walls at the two ends of the 1D systems can be created. This limits the size of both systems S and S^{det} to L sites. By adding a parabolic potential, any harmonic confinement in the 1D system caused by the underlying Gaussian beam shape of the lattice beams can additionally be cancelled over the region of interest. The box geometry ensures that the absolute value of the momentum $|k|$ of the transferred particle remains unchanged after the action of the perturbation $\hat{\mathcal{H}}_{\mathrm{pert}}(\tau)$, while still confining the particle within S^{det}.
The perturbation is followed by a bandmapping step, which converts momentum space into position space. Subsequent site-resolved imaging then allows one to reconstruct the particle's momentum. We now discuss three possibilities how such a mapping procedure can be implemented and give an estimate for the achievable momentum resolution in typical experimental setups. The momentum resolution κ is quantified by the inverse number N_k of different momentum states in the lowest band with $|k| < \pi/a$ that are detectable,

$$\kappa = 1/N_k. \tag{4.21}$$

Wannier-Stark mapping The first method for mapping momentum space into position space is to smoothly introduce a potential gradient along the x-direction, which causes an energy shift of E_{grad} per lattice site. Such a potential gradient can be implemented for example by applying a magnetic field gradient exploiting the atomic Zeeman shift or by using the DMD. In the limit of a vanishing gradient $E_{\mathrm{grad}} \ll t$ the single-particle energy eigenstates in S^{det} are quasi-momentum states $E^s(k_n)$ with discrete momenta $k_n = n\pi/L$ owing to the finite size of the box. For very large gradients $E_{\mathrm{grad}} \gg t$ the eigenstates are Wannier-Stark states localized on single lattice sites and separated in energy by E_{grad}. As shown in the left column of Fig. 4.2.1 d), these eigenstates are smoothly connected for an increasing potential gradient E_{grad}.
The momentum resolution of this method is determined by the initial number of lattice sites in S^{det} and is given by $1/L$. Adiabatic mapping requires the gradient ramp time to be much slower than the smallest energy splitting δE^s, which in this case is given by the energy spacing between adjacent quasi-momentum states at $E_{\mathrm{grad}} = 0$. The finite lifetime of atomic quantum gases sets an upper limit for the gradient ramp time and thus a lower limit to δE^s. This limits the maximum box size and hence the momentum resolution of this method. Experimentally, ramp timescales of

hundreds of tunneling times are routinely used in lattice loading protocols, corresponding to an energy of about $0.01t$ [63]. Assuming a tenfold slower gradient ramp time to ensure adiabaticity ($\delta E^s = 0.1t$), we find $L = 20$. This demonstrates that already this simple scheme gives a very good momentum resolution of about $\kappa \approx 1/20$. Furthermore, the ramp velocity can be increased at later times in the protocol, since the energy spacings become larger with growing E_{grad}, thus enhancing the momentum resolution.

TIME-OF-FLIGHT MAPPING An alternative method of determining the momentum is to perform a time-of-flight expansion along the x-direction in S^{det} after exciting the single particle. This can be done by suddenly turning off the DMD light which creates the box potential and applying a bandmapping of the lattice in the x-direction, see Eq. 4.14. This maps quasi-momentum states into momentum states [202] of S^{det}. Ballistic expansion of the single particle along the x-direction for a duration of τ_{tof} and subsequent detection of the displaced atomic position x_{tof} using the quantum gas microscope then allows one to determine the atomic momentum via $k = \pi m \lambda_x^2 x_{\mathrm{tof}}/(2h\tau_{\mathrm{tof}})$, where m is the atomic mass, h is the Planck constant and x_{tof} and k are normalized to the lattice spacing.

This procedure requires a sufficiently long time-of-flight expansion such that the initial system size is negligible, i.e. $2h\tau_{\mathrm{tof}}/(m\lambda_x^2) \gg L$. During the detection procedure the lattice depths along the y-direction remain unchanged to ensure that the particle remains trapped inside the 1D tube. The largest achievable value of τ_{tof} is determined by the largest spatial separation L_{tof} under the microscope where site-resolved imaging can still be reliably performed. As the particles are initially located in a box of L sites, there are also L momentum states. After free expansion to a size of L_{tof}, a particle initially in a momentum state will then be detected within a spatial region that approaches L_{tof}/L sites for long time-of-flight times. Corrections due to a finite time-of-flight are therefore negligible if this size exceeds the initial system size L. From this we obtain an upper bound for the initial system size of $L = \sqrt{L_{\mathrm{tof}}}$. In addition, clean mapping requires a flat system along the x-direction after the bandmapping. The harmonic confinement along that direction caused by the y-lattice beams can be cancelled by a blue detuned anti-confinement beam created by a DMD or Gaussian beam with a suitable beam waist.

In bosonic quantum gas microscopy a related variant of the proposed technique has already been implemented, where atoms in a small system of a few sites were expanded in 1D tubes to a width of about $L_{\mathrm{tof}} = 100$ sites and successfully detected with single-site resolution [93]. For these parameters we estimate a momentum resolution of $\kappa \approx 1/10$ for our scheme.

$T/4$-MAPPING A third technique for mapping momentum-space into real space that does not rely on a long expansion distance is based on a quarter period rotation in phase-space in the pres-

ence of a harmonic trap [203]. After suddenly introducing an underlying harmonic confinement with period T into the probe system S^{det}, the real-space distribution after a time evolution of $T/4$ will precisely correspond to the initial momentum distribution of the transferred particle (and vice versa).

To achieve this, we propose to first suddenly turn off the DMD light for the box potential and apply a bandmapping of the V_x lattice, as before. Then a strong harmonic confinement can be introduced by rapidly increasing the lattice depth along the y-direction. This leads to an increased harmonic confinement along the x-direction owing to the Gaussian beam shape of the laser beam. Alternatively, a DMD with red-detuned light could be used. After letting the single particle in S^{det} evolve for a quarter period, its position can be measured with the quantum gas microscope. The advantage of this method compared to the previous one is that it does not require imaging over large distances for good momentum resolution. By adjusting the frequency ω of the strong harmonic trap, the largest displacement of the single particle relative to the center of the box can be controlled. It can be chosen to be comparable to the initial system size L. Assuming a maximum imaging width of 100 sites (as before), this method would allow a momentum resolution of about $\kappa \approx 1/100$.

Current typical sizes of fermionic lattice systems at low temperatures with single-site resolution are on the order of 10 sites [75, 201]. The highest desirable momentum resolution is therefore $\kappa = 1/10$, which would be provided by all three proposed methods. In the future, when larger system sizes become available experimentally, the Wannier-Stark mapping and the quarter-period rotation scheme promise the highest momentum resolution.

4.2.4 Spectral building principle

In one dimension, spin-charge separation takes place and thus the holon propagates on a timescale set by the hopping amplitude t and is largely decoupled from the dynamics of the spinon, which moves on a timescale set by the exchange energy J. In order to determine where spectral weight is expected, spinon and holon are treated as independent particles. This constitutes the so-called spectral building principle [204, 205].

The dispersion relation of a free spinon is known from Bethe ansatz calculations for the isotropic spin chain [177]

$$\varepsilon_s(k_s) = J\frac{\pi}{2}|\cos(k_s)|, \qquad -\pi/2 \leq k_s \leq \pi/2. \tag{4.22}$$

The holon dispersion

$$\varepsilon_h(k_h) = -2t\cos(k_h) - \frac{1}{4}J\cos(2k_h) \tag{4.23}$$

corresponds to the one of a free particle and can be derived from the $t-J^*$ Hamiltonian itself. The second term stems from the next nearest neighbor hopping of the hole, see Eq. (3.9). The spectral

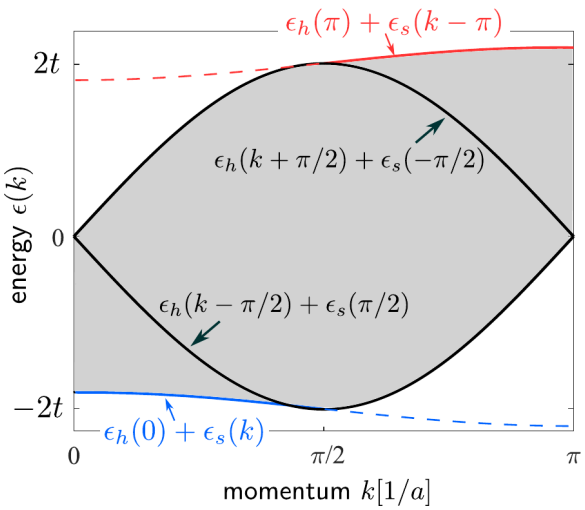

Figure 4.2.2: Spectral building principle. The combined dispersion relation of spinon and holon, Eq. (4.24), can be constructed by fixing the spinon or holon momentum, k_s or k_h, and varying the other momentum, respectively. Because the spinon dispersion is only defined from $k_s = -\pi/2 ... \pi/2$ for zero temperature the spectrum is strongly asymmetric around $k = \pi/2$ at low and high energies (blue and red boundaries). In this case spectral weight can only be found in the shaded areas. The dashed blue and red lines indicate the lower and upper boundaries obtained when the spinon dispersion is extended to $k_s = -\pi ... \pi$ assuming $\varepsilon_s(k_s) = \cos(k_s)J\pi/2$. This case is relevant for high temperatures.

building principle allows us to predict the positions of the peaks in the spectral function by making use of momentum conservation, $k = k_s + k_h$, and energy conservation

$$\varepsilon(k) = \varepsilon_h(k_h) + \varepsilon_s(k_s) = -2t\cos(k_h) - \frac{1}{4}J\cos(2k_h) + J\frac{\pi}{2}|\cos(k_s)|. \tag{4.24}$$

The energy $\varepsilon(k) = E_m^{N-1} - E_n^N$ in Eq. (4.24) enters the δ-function in the Lehmann representation of $A(k,\omega)$, Eq. (4.20) We set $k_s = k - k_h$ in Eq. (4.24) and for a given k regard the holon momentum k_h as a free parameter. In an infinite system, Eq. 4.24 provides an upper and lower bound for the region in which spectral weight exists at zero temperature, see Fig. 4.2.2. For a finite system with L sites, the quantization of the holon momentum leads to L distinct lines instead of a continuum. Each branch in the spectrum shown in Fig. 4.2.1 can be associated with a quantized holon momentum k_h by changing the spinon momentum k_s.

4.2.5 Numerical results for the one dimensional $t-J$ model

The spectral function of a single hole in a one-dimensional, antiferromagnetic spin chain with periodic boundary conditions and at zero temperatures has been studied in the past [197, 204–206]. Here we extend those results to the experimentally relevant case of systems with open boundary conditions, Fig. 4.2.1, and finite temperatures, Fig. 4.2.3. Several ARPES measurements have been

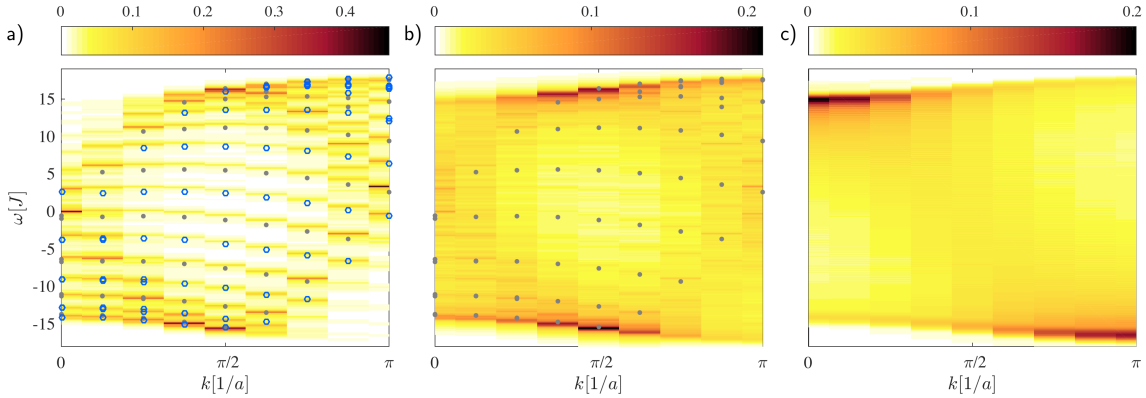

Figure 4.2.3: Temperature dependence of the spectral function. We consider the $t - J^*$ model with periodic boundary conditions and $L = 16$ sites for $t = 8J$ at temperatures a) $T = 0.4J$, b) $T = 0.75J$ and c) $T = 5J$. In a) and b), a comparison with peak positions expected from the spectral building principle due to holon and spinon dispersions, Eq. (4.24), is provided (gray dots). Additionally, in a) open blue circles denote peaks expected from the spectral building principal due to low energy excitations in the spin chain relevant at finite temperatures, see text.

performed in quasi-one dimensional materials, see e.g. Refs. [184, 206], and direct signatures of independent spinon and holon branches have been found at low energies [185].
The spectral function considered here is related to the Green's function of the hole as

$$A(k, \omega) = -(1/\pi)\Im G(k, \omega) \tag{4.25}$$

and can be calculated using standard Lanczos techniques [197, 207], see section A.1.5. The δ-peaks obtained by this means are slightly broadened to obtain a smoother spectral function.

FINITE TEMPERATURE In Fig. 4.2.3, the spectral function is shown for temperatures $T/J = 0.4$, $T/J = 0.75$ and $T/J = 5$. Here, gray dots denote the peak positions predicted by the spectral building principle including shifts in both spinon and holon momentum due to their different quantization conditions, see section B.1.
At sufficiently low temperatures, the peaks of the spectral function as calculated with exact diagonalization methods coincide with the peak positions predicted by the spectral building principle, indicating that spinon and chargon can indeed be treated independently. In particular, this agreement is not restricted to low energies, but holds across the entire spectrum. The peaks are broadened by thermal fluctuations in energy and momentum.
In the case of finite temperature and periodic boundary conditions, additional peaks appear between the lines predicted by the spectral building principle. These peaks, marked by blue circles

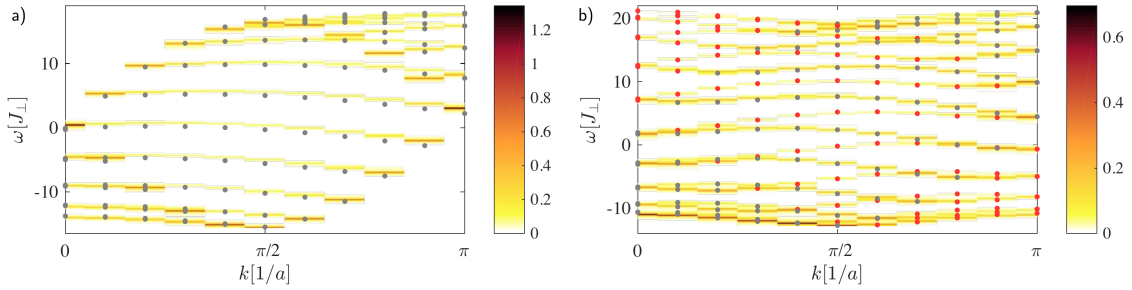

Figure 4.2.4: Spectral function for the t-XXZ Hamiltonian, Eq (3.11), for a system with 20 sites, periodic boundary conditions, with hopping $t = 8J_\perp$ and a) $J_z = J_\perp$, b) $J_z = 4J_\perp$. Gray dots correspond to spinon and holon dispersion, see Eq. (4.24) and Eq. (4.26), respectively, with the spinon momentum restricted to half the Brillouin zone, $-\pi/2 \leq k_s \leq \pi/2$. Red dots in b) denote spinon momenta in the remaining half of the Brillouin zone, where no spectral weight appears in the isotropic case $J_z = J_\perp$.

in Fig. 4.2.3, are caused by the low-lying thermal excitations of the spin chain: the lowest energy states carry momentum close to zero and π. An excitation in the spin chain with momentum π introduces a twisted periodic boundary effect for the chargon, thus causing additional lines in the spectrum; see also section B.1.

Upon increasing the temperature to values $T \gtrsim J$, low-energy excitations start to appear for $\pi/2 \leq k \leq \pi$ and the spectral building principle starts to break down. As the temperature approaches and exceeds J, a single well-defined spinon no longer exists and therefore the distinct lines visible at low temperatures are replaced by a continuum. For high temperatures $T \gg J$, the distribution of spectral weight is mostly determined by the density of states and spectral weight is shifted from $k = \pi/2$ to $k = 0$ and $k = \pi$, respectively.

Anisotropy In Fig. 4.2.4, the spectral function at zero temperature is shown for the $t - XXZ$ model with a) $J_z = J_\perp$ and b) $J_z = 4J_\perp$ for a system with periodic boundary conditions. In the latter case, the additional red dots indicate the peak positions predicted by the spectral building principle for values of the momentum $|k - k_h| > \pi/2$, which are excluded by the spinon dispersion in the isotropic case. The spinon dispersion is given by $\varepsilon_s^{\mathrm{Is}}(k_s) = J_\perp \cos(2k_s) + J_\perp + J_z$ in first order perturbation theory in $J_\perp/J_z$. The spectral building then leads to

$$\varepsilon(k) = -2t\cos(k_h) + J_\perp \cos\left(2(k - k_h)\right) + J_\perp + J_z. \tag{4.26}$$

Fig. 4.2.4 b) shows an almost symmetrical distribution of spectral weight around $|k - k_h| = \pi/2$ in the anistotropic case as compared to the isotropic case in Fig. 4.2.4 a), where no spectral weight

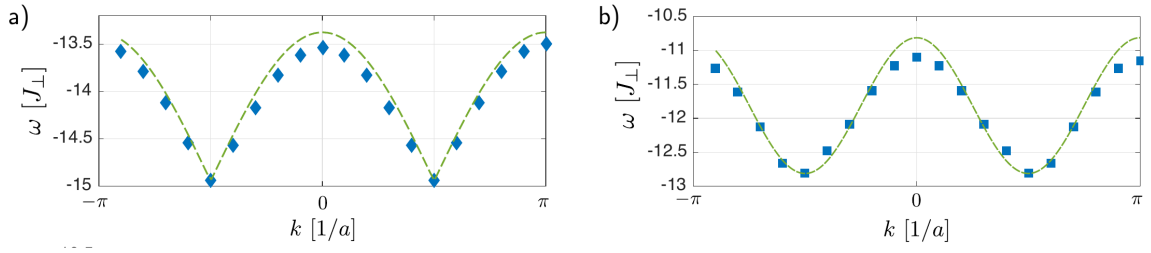

Figure 4.2.5: Ground state energies in the t-XXZ Hamiltonian as a function of the total momentum k for a single hole in a spin chain (full symbols). We used the same parameters as in Fig. 4.2.4 a) and b) respectively. The dashed line corresponds to the free spinon dispersion a) in the Heisenberg model with $J_z = J_\perp$ and b) in the XXZ model with $J_z = 4J_\perp$.

appears for spinon momenta $|k - k_h| \geq \pi/2$.

"Missing" spectral weight The question arises, why in the isotropic case, there is no spectral weight at low energies for $|k - k_h| \geq \pi/2$. In Fig. 4.2.5, we demonstrate that at the corresponding energies and momenta eigenstates of the Hamiltonian exist by calculating the ground state energy of the $t - J$ model with a single hole as a function of total momentum k with exact diagonalization. As can be seen in Fig. 4.2.5, the corresponding low-energy eigenstates exist for all k and their energies are approximately symmetric around $k = \pi/2$.

A possible explanation for the missing spectral weight is a selection rule: since the ground state of the Heisenberg model is a singlet, only states with total spin $S = 1/2$ and one hole can have finite weight in the spectrum at zero temperature. In Ref. [197], it has been shown with exact numerics that the ground state of the $t - J$ model with a single hole at momenta $|k| > \pi/2$ has $S = 3/2$ and thus yields an overlap of zero. However, numerically we find eigenstates with $S = 1/2$ for $|k| > \pi/2$ at energies only slightly higher. In particular, these states give rise to a non-zero spectral weight at low energies for $|k| > \pi/2$. This spectral weight is not visible in Fig. 4.2.4 a) since it is suppressed by about three orders of magnitude compared to the spectral weight at low energies and momentum $|k| < \pi/2$. In contrast to what has been suggested in Ref. [197], a selection rule seems not to be sufficient to explain the asymmetry of the spectral weight observed for a hole created in a Heisenberg chain. In contrast to the Ising case, the Heisenberg spin chain has singlet character and can be understood as a resonating valence-bond state [117]. The ground state of the Majumdar-Gosh model [208, 209] can be represented exactly using resonating valence-bond states. We thus calculate the spectral function of a single hole in the Majumdar-Gosh model to address the question whether the valence-bond character of the ground state wavefunction already leads to a sharp drop of the spectral weight as the spinon momentum crosses $k = \pi/2$.

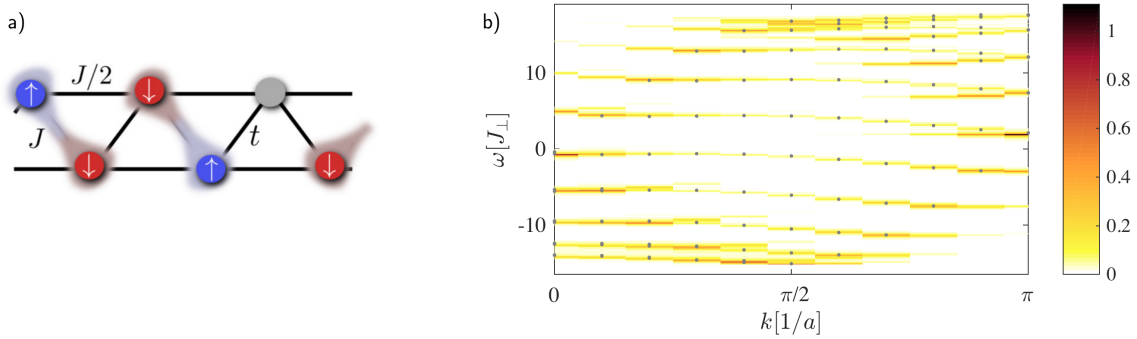

Figure 4.2.6: The Majumdar-Ghosh spin chain. a) Visualization of the model realized on a zig-zag chain. Next-nearest neighbor hopping terms for the hole are not included here. In b), the spectrum of a Majumdar-Ghosh spin chain with 20 sites and periodic boundary conditions with hopping $t = 8J$ and at temperature $T = 0$ is shown. Gray dots correspond to spinon and holon dispersion, see Eq. (4.28).

By adding next-nearest neighbor couplings for the spins to Eq. (3.11), we arrive at the Hamiltonian of the Majumdar-Ghosh model [117, 208, 209] interacting with a hole-like impurity described by $\hat{h}_j$,

$$\hat{\mathcal{H}}_{\mathrm{MG}} = t\sum_j \left(\hat{h}^\dagger_{j+1}\hat{h}_j + \mathrm{h.c.}\right) + J\sum_i \hat{\mathbf{S}}_i \cdot \hat{\mathbf{S}}_{i+1} + \frac{J}{2}\sum_i \hat{\mathbf{S}}_i \cdot \hat{\mathbf{S}}_{i+2} - J\sum_j \hat{h}^\dagger_j \hat{h}_j \hat{\mathbf{S}}_j \cdot \hat{\mathbf{S}}_{j+1}. \quad (4.27)$$

Note that the impurity is only switching off nearest neighbor interactions in our toy model. We defined the spectral function as usual, by removing a spin and creating the hole-like impurity at the same site. Without the hole, the Majumdar-Ghosh model describes certain materials, where the atoms form a zig-zag chain [210], see Fig. 4.2.6 a), and constitutes an example of an exactly solvable, frustrated spin system. Its degenerate ground states are exactly known, for a pedagogical discussion see e.g. Ref. [117]. They spontaneously break the translational symmetry and consist of states in which neighboring spins form a singlet. The two lowest energy states with this property, which are related to each other by a shift by one lattice site, are degenerate in the thermodynamic limit and are separated from the excitation spectrum by a gap.

In Fig. 4.2.6 b), the spectral function of a single hole in a Majumdar-Ghosh spin chain is shown. Gray dots correspond to the combined dispersion relation of the holon and the spinon, $\varepsilon(k) = \varepsilon_h(k_h) + \varepsilon_s(k - k_h)$ with $\varepsilon_h(k_h) = -2t\cos k_h$ and the Majumdar-Ghosh dispersion relation [211]

$$\varepsilon_s(k_s) = J\frac{5}{4} + \frac{J}{2}\cos(2k_s), \quad (4.28)$$

where k_s is restricted to half of the Brillouin zone. The distinct lines in the spectrum are remarkably well described by Eq. (4.28), demonstrating spin-charge separation.

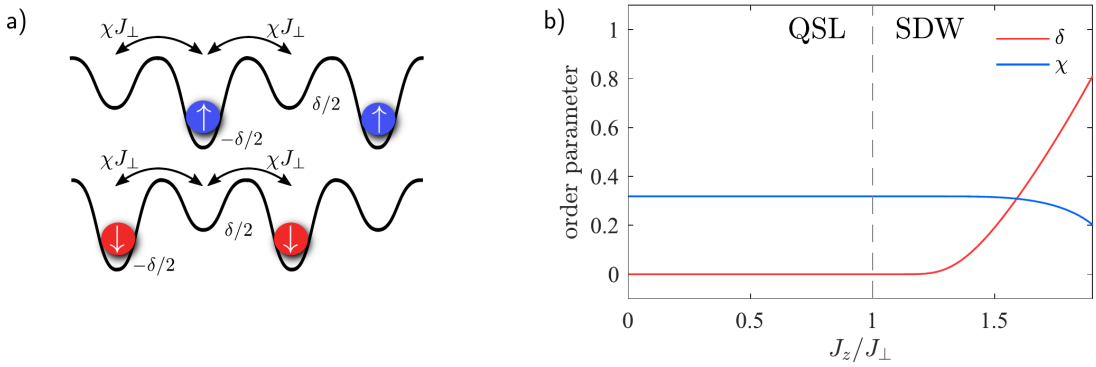

Figure 4.2.7: Mean-field theory for the spin chain. a) Slave-fermion description of the anisotropic spin chain. In the anisotropic XXZ spin chain, the sub-lattice symmetry can be spontaneously broken when $J_z > J_\perp$. In this case the effective hopping Hamiltonian of spinons corresponds to a tight-binding model with alternating on-site potentials. The mean field solutions for different spins are related by a translation of one lattice site. b) Numerical solution of the self-consistency equations for the order parameters χ and δ, Eqs. (4.45), (4.46). For $0 \leq J_z \leq J_\perp$ the ground state is a gapless quantum spin liquid (QSL). For $J_z \gtrsim J_\perp$ the two order parameters δ and χ are both non-vanishing and the ground state is a spin-density wave (SDW).

The comparison to the isotropic Heisenberg spin chain without frustration highlights an interesting feature. An asymmetry in the distribution of spectral weight around $|k - k_h| = \pi/2$ is clearly visible. However, the spectral weight is not as clearly restricted to half of the Brillouin zone as in the spectrum of the Heisenberg chain. Thus, a valence bond solid nature of the ground state is not sufficient to explain the sharp decrease of spectral weight observed for the anisotropic spin chain in Fig. 4.2.4.

Below, we argue that this sharp decrease of spectral weight for a single hole in the one-dimensional $t - J$ model can be understood as a direct signature for the presence of a Fermi sea of spinons. This is characteristic for a quantum spin-liquid, where slave fermions are introduced in a mean field description [28]. Note that this Fermi sea is *not* formed by Jordan-Wigner fermions, obtained by fermionizing the spins, as suggested in Ref. [206]. These Jordan-Wigner fermions are strongly interacting and the non-interacting Fermi sea is thus not a good approximation.

4.2.6 Mean field theory

We use a slave-fermion mean field theory to describe the spin chain [28, 212, 213], which contains a non-trivial order parameter, that is finite even in one dimension. For simplicity we consider situations with zero total magnetization here. Our starting point is the t-XXZ model Eq. (3.11) with zero or one hole. We introduce slave boson operators $\hat{h}_j$ to describe the holons, and constrained fermions $\hat{f}_{j,a}$ describing the spins [117]. The index $a = \uparrow, \downarrow$ corresponds to the two spin states and

it holds

$$\hat{\mathbf{S}}_i = \frac{1}{2}\sum_{\alpha,\beta}\hat{f}^\dagger_{i,\alpha}\sigma_{\alpha,\beta}\hat{f}_{i,\beta}. \tag{4.29}$$

The slave particles satisfy the condition

$$\sum_\alpha \hat{f}^\dagger_{j,\alpha}\hat{f}_{j,\alpha} + \hat{h}^\dagger_j\hat{h}_j = 1. \tag{4.30}$$

The original fermionic operators can be expressed as

$$\hat{c}_{j,\alpha} = \hat{h}^\dagger_j\hat{f}_{j,\alpha}. \tag{4.31}$$

With the new operators, a spin state $|\sigma_1, \ldots, \sigma_L\rangle$ with $\sigma_j = \uparrow, \downarrow$ is expressed as

$$|\sigma_1, \ldots, \sigma_L\rangle \equiv \hat{f}^\dagger_{1,\sigma_1}\ldots\hat{f}^\dagger_{L,\sigma_L}|0\rangle. \tag{4.32}$$

States with holes are created by applying $\hat{h}^\dagger_j\hat{f}_{j,\alpha}$ from Eq. (4.31). Note that the ordering of operators in Eq. (4.32) is important due to their fermionic anti-commutation relations. The hopping term in Eq. (3.11) yields a difficult quartic expression $-t\sum_{\langle \mathbf{i},\mathbf{j}\rangle}\sum_\sigma \hat{h}^\dagger_j\hat{h}_i\hat{f}^\dagger_{i,\sigma}\hat{f}_{j,\sigma}$. In the following, we consider the problem in squeezed space introduced in section 4.1, which is obtained by removing all holes from the chain. The chargons now occupy bonds between the lattice sites $\tilde{j}$ of the squeezed space [75, 214, 215]. In this framework, only operators $\hat{f}_{j,\alpha}$ on sites $\tilde{j}$ are included, thus yielding new operators $\hat{\tilde{f}}_{j,\alpha} = \hat{f}_{\tilde{j},\alpha}$ with $\tilde{j} = j + \sum_{i\le j}\hat{h}^\dagger_i\hat{h}_i$. In terms of the squeezed space operators, the hopping term in Eq. (3.11) yields a quadratic term involving only holons, $-t\sum_{\langle \mathbf{i},\mathbf{j}\rangle}\hat{h}^\dagger_j\hat{h}_i$, see section 4.1. This term contributes the dominating part of the free holon dispersion relation Eq. (4.23), $-2t\cos(k_h)$. The last two terms of Eq. (3.11) do not change in squeezed space and correspond to a spin chain without doping.

The Hamiltonian of the spin chain, Eq. (3.11) at half filling, can be expressed in terms of the spinon operators [28],

$$\hat{\mathcal{H}}_{\mathrm{XXZ}} = -\frac{1}{2}\sum_{i,\alpha}\hat{\tilde{f}}^\dagger_{i,\alpha}\hat{\tilde{f}}_{i+1,\alpha}\left[J_\perp\hat{\tilde{f}}^\dagger_{i+1,\bar{\alpha}}\hat{\tilde{f}}_{i,\bar{\alpha}} + J_z\hat{\tilde{f}}^\dagger_{i+1,\alpha}\hat{\tilde{f}}_{i,\alpha}\right] + \frac{J_z}{2}\sum_{i,\alpha}\hat{\tilde{f}}^\dagger_{i,\alpha}\hat{\tilde{f}}_{i,\alpha} - \frac{J_z}{4}\sum_{i,\alpha,\beta}\hat{\tilde{f}}^\dagger_{i,\alpha}\hat{\tilde{f}}_{i,\alpha}\hat{\tilde{f}}^\dagger_{i+1,\beta}\hat{\tilde{f}}_{i+1,\beta}, \tag{4.33}$$

where, $\bar{\uparrow} = \downarrow$ and $\bar{\downarrow} = \uparrow$. This expression is exact within the subspace defined by the constraint $\sum_\alpha\hat{\tilde{f}}^\dagger_{i,\alpha}\hat{\tilde{f}}_{i,\alpha} = 1$. In the mean field approximation applied below, this constraint is replaced by its ground state expectation value

$$\sum_\alpha\left\langle\hat{\tilde{f}}^\dagger_{i,\alpha}\hat{\tilde{f}}_{i,\alpha}\right\rangle = 1. \tag{4.34}$$

At the isotropic point, $J_z = J_\perp$, Eq. (4.33) corresponds to the $SU(2)$ invariant Heisenberg Hamiltonian $\hat{\mathcal{H}}_{\mathrm{H}}$. In this case the term $\hat{\tilde{f}}^\dagger_{i,a}\hat{\tilde{f}}_{i+1,a}$ is replaced by its ground state expectation value

$$\chi_{i,a} = \left\langle \hat{\tilde{f}}^\dagger_{i,a}\hat{\tilde{f}}_{i+1,a} \right\rangle . \tag{4.35}$$

When $\chi_{i,a} = \chi$ is independent of the spin index a, the resulting mean-field Hamiltonian is also $SU(2)$ invariant. By diagonalizing the latter we obtain a self-consistency equation for χ which will be solved numerically below.

Away from the $SU(2)$ invariant Heisenberg point, i.e. when $J_z \neq J_\perp$, we can write the original Hamiltonian as a sum of the Heisenberg term $\hat{\mathcal{H}}_{\mathrm{H}}$ plus additional Ising couplings,

$$\hat{\mathcal{H}}_{\mathrm{XXZ}} = \hat{\mathcal{H}}_{\mathrm{H}} + \underbrace{(J_z - J_\perp)}_{=\Delta J_z} \frac{1}{4} \sum_i \hat{\delta}_i \hat{\delta}_{i+1}, \tag{4.36}$$

where $\hat{\delta}_i = 2\hat{S}^z_i$ is the local magnetization,

$$\hat{\delta}_i = \sum_a (-1)^a \hat{\tilde{f}}^\dagger_{i,a}\hat{\tilde{f}}_{i,a}, \qquad (-1)^\uparrow = 1, (-1)^\downarrow = -1. \tag{4.37}$$

We allow for a finite expectation value of the magnetization in the mean-field description. Assuming that the discrete symmetry $\hat{T}^x\hat{S}^x$, which flips the spins and translates the system by one lattice site, is unbroken, we obtain

$$\langle \hat{\delta}_i \rangle = (-1)^i \delta. \tag{4.38}$$

This leads to a second self-consistency equation for the staggered magnetization δ. The effective mean-field Hamiltonian is obtained from Eq. (4.36) by introducing the order parameters δ and χ and keeping terms up to quadratic order. It has a two-site unit cell because the magnetization is opposite for different sub-lattices. This corresponds to a tight-binding Hamiltonian with nearest-neighbor tunneling of strength $J_\perp\chi$ and on-site potentials $(-1)^i(-1)^a\delta/2$, as illustrated in Fig. 4.2.7 a). For spinons of type a it can be written as

$$\hat{\mathcal{H}}_a = \int_{-\frac{\pi}{2}}^{\frac{\pi}{2}} dk \left(\hat{\tilde{f}}^\dagger_{k,A,a} \hat{\tilde{f}}^\dagger_{k,B,a} \right) \underline{\underline{h_a}}(k) \begin{pmatrix} \hat{\tilde{f}}_{k,A,a} \\ \hat{\tilde{f}}_{k,B,a} \end{pmatrix}, \tag{4.39}$$

where we defined the Fourier transformed spinon operators $\hat{\tilde{f}}_k$ by the relations

$$\begin{aligned}\hat{\tilde{f}}_{2n,a} &= \sqrt{\frac{L}{2\pi}} \int_{-\frac{\pi}{2}}^{\frac{\pi}{2}} dk\, e^{-2ikn} \hat{\tilde{f}}_{k,A,a} \\ \hat{\tilde{f}}_{2n+1,a} &= \sqrt{\frac{L}{2\pi}} \int_{-\frac{\pi}{2}}^{\frac{\pi}{2}} dk\, e^{-2ikn} e^{-ik} \hat{\tilde{f}}_{k,B,a}.\end{aligned} \tag{4.40}$$

For $a = \uparrow$ spinons it holds

$$\underline{\underline{h}}_{\uparrow}(k) = \begin{pmatrix} -\delta/2 \Delta J_z & -2\chi J_\perp \cos(k_x) \\ -2\chi J_\perp \cos(k_x) & \delta/2 \Delta J_z \end{pmatrix}, \tag{4.41}$$

and a similar expression is obtained for $a = \downarrow$ by changing $\delta \to -\delta$. In addition, there is a constant energy contribution of $J_\perp(1/4 + 2\chi) + 1/4 \Delta J_z \delta^2$ per particle which is not included in Eq. (4.39).
We diagonalize the mean-field Hamiltonian in order to derive the coupled self-consistency equations for δ and χ. A new set of spinon operators $\hat{F}_{k,\mu,a}$, with band index $\mu = \pm$, can be defined, for which

$$\hat{\mathcal{H}}_a = \sum_{\mu=\pm 1} \mu \int_{-\frac{\pi}{2}}^{\frac{\pi}{2}} dk\, \varepsilon_k \hat{F}^\dagger_{k,\mu,a} \hat{F}_{k,\mu,a}. \tag{4.42}$$

The mean-field dispersion relation is given by

$$\varepsilon_k = \sqrt{(2\chi J_\perp \cos(k))^2 + (\Delta J_z \delta/2)^2}, \tag{4.43}$$

which gives rise to a band-gap to collective excitations of

$$\Delta_{\mathrm{MF}} = |\Delta J_z \delta|. \tag{4.44}$$

Thus a non-vanishing staggered magnetization $\Delta J_z \delta \neq 0$ opens a gap in the spectrum. Because of the mean-field constraint in Eq. (4.34) we obtain $\left\langle \hat{\tilde{f}}^\dagger_{i,a} \hat{\tilde{f}}_{i,a} \right\rangle = 1/2$, i.e. we describe spinons at half filling. When $\Delta J_z \delta \neq 0$ the ground state is a band insulator, whereas $\Delta J_z \delta = 0$ corresponds to a gapless spinon Fermi sea.
Using the new spinon operators $\hat{F}_{k,\mu,a}$ we can calculate the order parameters δ and χ self-consistently,

$$\chi = \frac{1}{\pi} \int_{-\frac{\pi}{2}}^{\frac{\pi}{2}} dk\, \cos^2(k) \frac{\chi J_\perp}{\varepsilon_k}, \tag{4.45}$$

$$\delta = \frac{1}{2\pi} \int_{-\frac{\pi}{2}}^{\frac{\pi}{2}} dk\, \frac{\Delta J_z \delta}{\varepsilon_k}. \tag{4.46}$$

The numerical solutions for δ and χ to Eqs. (4.45), (4.46) are shown in Fig. 4.2.7 b). For $0 \leq J_z \leq J_\perp$, the only solution is the symmetric one with $\delta = 0$ and $\chi = 1/\pi$ and energy $E_{\mathrm{MF}}(\delta = 0, \chi = 1/\pi)$. This state has no magnetic order and corresponds to a quantum spin liquid (QSL). At the isotropic Heisenberg point where $J_z = J_\perp = J$ it predicts the following dispersion of spinon excitations,

$$\varepsilon_k = J\frac{2}{\pi}|\cos k|. \tag{4.47}$$

The analytical form of the spinon dispersion $\sim |\cos(k)|$ is correctly described by the mean-field theory. Compared to the exact result from Bethe ansatz calculations, Eq. (4.22), this expression is too small by a factor of $\pi^2/4 \approx 2.47$. Deviations from the exact solution are a result of the mean field approximation, i.e. our neglecting of gauge fluctuations ensuring the constraint of single-occupancy [28].

For $J_z > J_\perp$, two additional solutions $\pm\delta \neq 0$ with an energy below $E_{\mathrm{MF}}(\delta = 0, \chi = 1/\pi)$ appear. Note that in Fig. 4.2.7 b), only the solution with $\delta > 0$ is shown. In this regime, the translational symmetry of the original Hamiltonian Eq. (4.33) is spontaneously broken. Because there exists a non-zero staggered magnetization $\delta \neq 0$, this phase can be identified with a spin density wave (SDW). At large couplings, $J_z \geq 2J_\perp$, we find that the mean-field order parameter χ vanishes and the system is fully ordered with $\delta = \pm 1$ as expected in the classical Néel state. This second transition is an artifact of the mean-field theory: From exact Bethe ansatz calculations it is known that the staggered magnetization approaches the classical value $\delta = \pm 1$ monotonically until it is asymptotically reached for $J_z/J_\perp \to \infty$.

As can be seen from Fig. 4.2.7 b), the order parameter δ only takes a significant value for $J_z \simeq 1.2J_\perp$. By solving the elliptic integral in Eq. (4.46) perturbatively in the limit $\delta \ll 1$, we find that the staggered magnetization depends non-analytically on $J_z - J_\perp$, with all derivatives $d^n\delta/d\Delta J_z^n = 0$ vanishing at the Heisenberg point:

$$\delta \simeq \frac{4}{\pi}\frac{J_\perp}{J_z - J_\perp}e^{-2\frac{J_\perp}{J_z - J_\perp}}. \tag{4.48}$$

From Eq. (4.44) it follows that the excitation gap has the asymptotic form

$$\Delta_{\mathrm{MF}} \simeq \frac{4}{\pi}J_\perp \exp\left[-2\frac{J_\perp}{J_z - J_\perp}\right]. \tag{4.49}$$

Close to the transition point from QSL to SDW Δ_{MF} can be compared to exact results Δ_{B} obtained from Bethe ansatz methods for the XXZ chain. From the exact expressions derived in Ref. [216]

we obtain the following asymptotic behavior,

$$\Delta_B \simeq 4\pi J_\perp \exp\left[-\frac{\pi^2}{2\sqrt{2}}\left(\frac{J_\perp}{J_z - J_\perp}\right)^{1/2}\right]. \tag{4.50}$$

The non-analyticity is correctly predicted by the mean-field theory, and only the power-law exponent appearing in the exponential function is not captured correctly.
We conclude that the slave-fermion mean field theory provides a rather accurate description of the one-dimensional spin chain near the critical Heisenberg point. This is possible because a non-trivial order parameter (χ) is introduced that does not vanish even in one dimension. The theory provides quantitatively reasonable results and describes correctly the qualitative behavior at the singular phase transition from QSL to the conventional symmetry broken SDW phase.

Spectral weight of spinon excitations We proceed by calculating the matrix elements that determine the weight in the single-hole spectra based on the slave-fermion mean field theory. The relevant matrix elements, which describe the creation of a hole in the ground state of the spinon system, are of the form

$$\lambda^n_{k_s} = |\langle\psi_n|\hat{\tilde{f}}_{k_s,\sigma}|\psi_0\rangle|^2 \qquad -\pi \le k_s \le \pi, \tag{4.51}$$

with the ground state of the undoped spin chain

$$|\psi_0\rangle = \prod_{k=-\pi/2}^{\pi/2}\prod_\sigma \hat{F}^\dagger_{k,-,\sigma}|0\rangle. \tag{4.52}$$

The full spectral function $A(k,\omega)$ is a convolution of the spinon part and the holon part,

$$A(k,\omega) = \sum_{k_h,k_s=-\pi}^{\pi}\int d\omega_h d\omega_s\, \delta\left(\omega - \omega_s - \omega_h\right) \times \delta_{k,k_h+k_s} A_s\left(k_s,\omega_s\right) A_h(k_h,\omega_h). \tag{4.53}$$

Neglecting the coupling of the holon to collective excitations of the spin chain, see Ref. [2], the holon spectrum is determined by $A_h(k_h,\omega_h) = \delta(\omega_h - \varepsilon_h(k_h))$. The spinon part is given by $A_s(k_s,\omega_s) = \sum_n \delta(\omega_s - \omega_n)\lambda^n_{k_s}$, where the eigenstate $|\psi_n\rangle$ has energy ω_n.
For every k_s there exists one unique state $|\psi_n\rangle$ with $\lambda^n_{k_s} \neq 0$. The corresponding $\lambda_{k_s} := \lambda^n_{k_s}$ can be calculated by mapping the original spinon operators $\hat{\tilde{f}}_{k_s,\sigma}$ onto the transformed operators $\hat{F}_{k_s,\pm,\sigma}$.

This leads to

$$\lambda_{k_s} = \begin{cases} \cos^2\left(\frac{\theta_{k_s}}{2}\right) & |k_s| \leq \pi/2 \\ \sin^2\left(\frac{\theta_{k_s}}{2}\right) & |k_s| > \pi/2, \end{cases} \tag{4.54}$$

where the mixing angle is determined by

$$\tan\theta_{k_s} = \frac{\delta(J_z - J_\perp)}{4\chi J_\perp \cos(k_s)} \tag{4.55}$$

In the isotropic Heisenberg case, $J_\perp = J_z = J$, the only solution to the self-conistency equation is $\delta = 0$, leading to $\theta_{k_s} = 0$ and thus

$$\lambda_{k_s} = \begin{cases} 1 & |k_s| \leq \pi/2 \\ 0 & |k_s| > \pi/2. \end{cases} \tag{4.56}$$

This discontinuity in λ_{k_s} gives rise to the sharp drop of spectral weight observed in Figs. 4.2.1, 4.2.3, and 4.2.4 when k_s is varied across the value $\pi/2$. It is a direct signature for the spinon Fermi sea, which in turn is a key signature of a quantum spin liquid.
In the Ising limit $J_\perp = 0$ we obtain the classical Néel state with $\delta = \pm 1$ and $\chi = 0$. This yields $\theta_{k_s} = \pi/2$, i.e.

$$\lambda_{k_s} = 1/2. \tag{4.57}$$

In this case, discrete translational symmetry is broken, which leads to a mixing of momenta k_s and $k_s + \pi$ and a homogeneous re-distribution of spectral weight across all k_s. There is therefore no discontinuity in the distribution spectral weight at the zone boundary $k_s = \pm\pi/2$, as observed in Fig. 4.2.4 b).

Spin-imbalanced systems In the slave-particle mean field picture, the slave fermions form two spinon Fermi seas. For a spin-imbalanced system, we thus expect to see two different Fermi momenta. Our scheme to measure the spectral function in experiments with cold atoms is particularly well suited to access the spectral function of a single hole in a system with finite magnetization. Moreover, by detecting the spin of the removed particle [217], the spin-resolved version of the spectral function can be measured. In Fig. 4.2.8 a), the spectral function of a single hole in a spin imbalanced system is shown for a removed particle with spin up and down, respectively. As in Fig. 4.2.4, gray dots denote the positions of expected peaks due to holon and spinon dispersions,

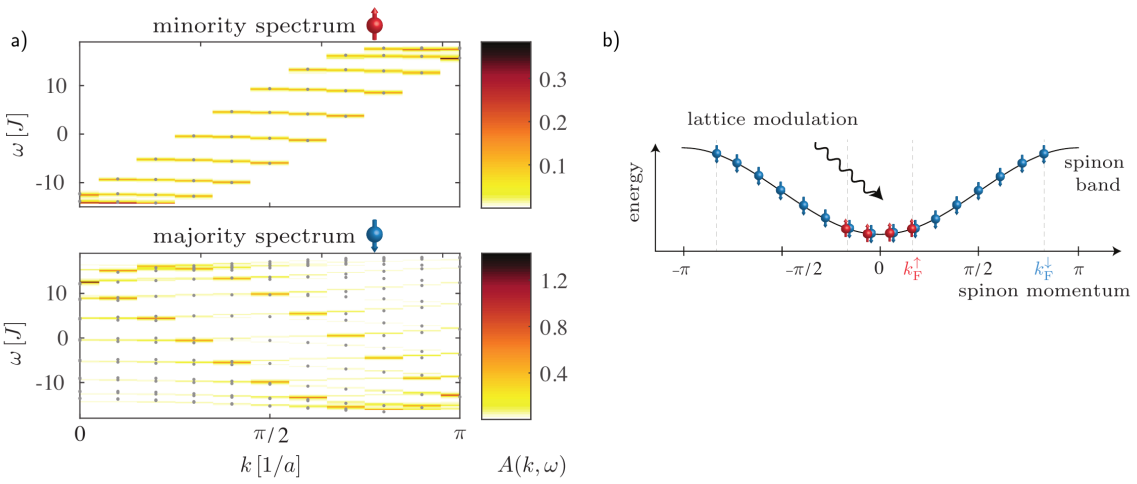

Figure 4.2.8: Spectral function in a spin-imbalanced system with 20 sites and $N_\uparrow = 4$, $N_\downarrow = 16$ at zero temperature and with periodic boundary conditions. a) shows the minority (top) and majority (bottom) spectrum, resolved after the spin of the removed particle. b) depicts the spinon Fermi seas for the two different species, which are filled correspondingly.

Eq. (4.24) for $-k_F^{\uparrow/\downarrow} \leq k \leq k_F^{\uparrow/\downarrow}$ with $k_F^{\uparrow/\downarrow} = \pi N_{\uparrow/\downarrow}/L$. In the slave-fermion mean field theory, the spinons form two Fermi seas, which are filled corresponding to the spin imbalance in the system. Accordingly, in Fig. 4.2.8, the sharp decrease in spectral weight occurs at different momenta for the removed particle belonging to the majority or minority species.

4.3 Time-Resolved Observation of Spin-Charge Deconfinement

This section is based on the publication

- Jayadev Vijayan, Pimonpan Sompet, Guillaume Salomon, Joannis Koepsell, Sarah Hirthe, Annabelle Bohrdt, Fabian Grusdt, Immanuel Bloch, Christian Gross: "Time-Resolved Observation of Spin-Charge Deconfinement in Fermionic Hubbard Chains." – Science 367, 186 (2020) [arXiv:1905.13638]

Structure, text and figures have been rearranged and adapted here.

Quantum gas microscopes are optimally suited to observe dynamics in real space. Recently, equilibrium signatures of spin-charge separation have been observed by Immanuel Bloch's Lithium quantum gas microscope [75]. Here, we probe the dynamical deconfinement of spin and charge excitations in real space and time, where initially a particle is removed from a half-filled Fermi-Hubbard chain. We start from a spin-balanced mixture of Lithium atoms in the lowest two hyperfine states, which is loaded into several one-dimensional tubes. The total atom number is fixed,

such that the chains are close to half-filling in the center of the harmonically confined cloud. In each experimental run there are at least three one-dimensional chains of mean length 13 atoms, each with a unity filled region of about 9 sites and short-range antiferromagnetic spin correlations [84, 85, 217, 218]. The local quench is realized by the high fidelity removal of one atom from a single site in the center of each chain using an elliptically shaped near-resonant laser beam.

The main part of the experimental analysis below is done at $t = h \times 250\text{Hz}$ and $U/t = 15$, corresponding to an exchange interaction of $J = h \times 65\text{Hz}$. We define a hopping time $\tau_t = h \times (4\pi t)^{-1} = 0.32$ ms as the time it takes for a hole to move by one site if it propagates at the theoretically expected maximum group velocity of $v_t^{\max} = a_x/\tau_t$, where a_x is the lattice spacing in the direction of the chain. Correspondingly, we define $\tau_J = h \times (\pi^2 J)^{-1} = 1.56$ ms, which is the time it takes a spinon to move by one site, if it propagates by the theoretically expected maximum group velocity of $v_J^{\max} = a_x/\tau_J$.

4.3.1 Spinon and Chargon Velocity

After the removal of a single particle from the Fermi-Hubbard chain of ultra-cold atoms, the evolution of the system is tracked in real space and time with a quantum gas microscope. In particular, we study the holon dynamics by monitoring the local hole density as well as the spinon dynamics by evaluating nearest neighbor spin correlations in squeezed space, Fig. 4.3.1. The spreading of both types of excitations is approximately ballistic, but with different propagation velocities.
In Ref. [179], the authors study spin charge separation following a quench with time dependent DMRG methods for the one dimensional Hubbard model. The system is in the ground state of the Fermi Hubbard Hamiltonian with an additional spin dependent potential in the chain center. In the beginning of their protocol, this potential is switched off and in the following dynamics, charge and spin location are tracked. Even though the simulation starts from the ground state of the system, the observable signal is comparably small. In the quantum gas microscope experiment, all measurements are based on snapshots, and usually not more than a few thousand snapshots are taken for each time step. Therefore, in order to be able to faithfully measure an observable, the expectation value cannot be too small.
While tracking the hole position in each snapshot is straightforward, monitoring the spinon dynamics requires more specific observables, which are adapted to the experimental capabilities. At the experimental temperatures of $T = 0.7J$, the connected nearest neighbor spin correlation function at half filling is still comparably big. Upon doping, the hole motion washes out the spin correlation functions. However, as has been shown in recent equilibrium experiments [75], the nearest

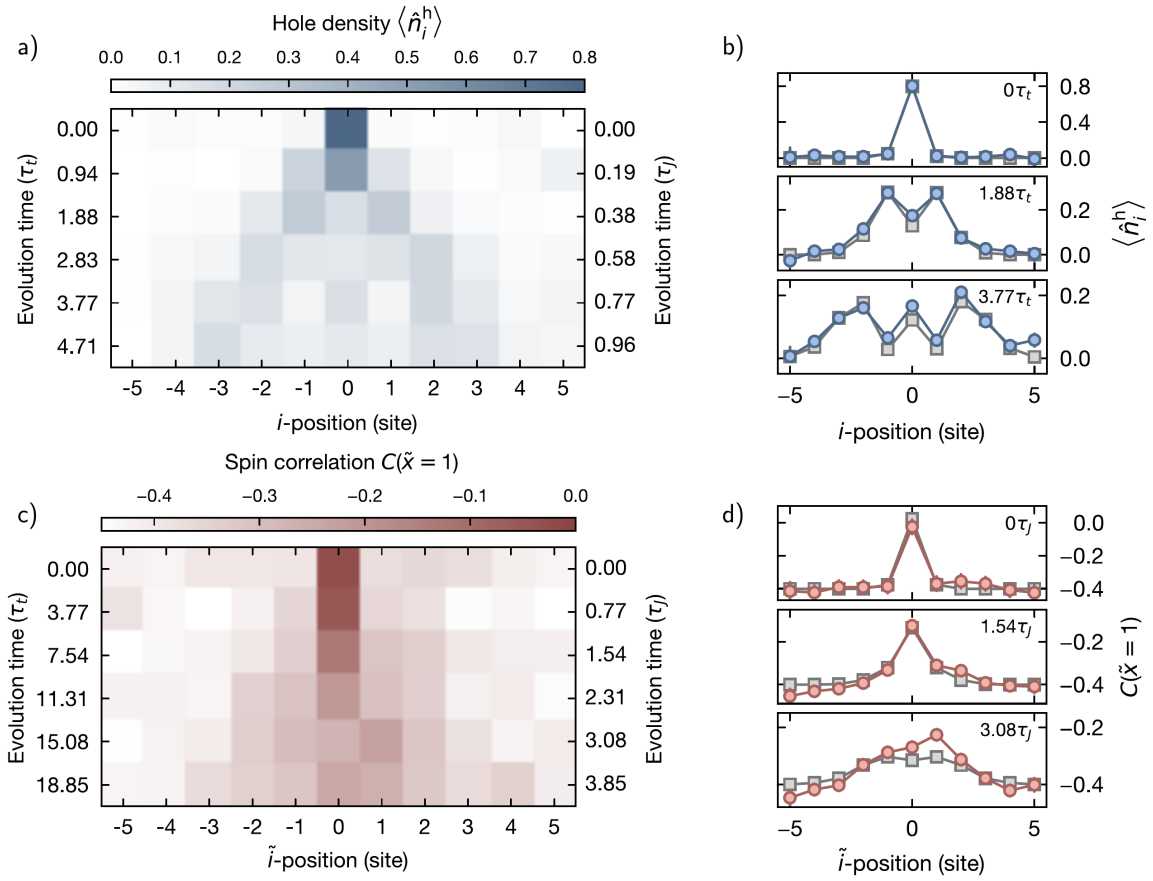

Figure 4.3.1: Experimentally observed spreading of spinon and chargon after the creation of a hole in the center of a Fermi-Hubbard chain at half-filling, with $t = h \times 250$Hz and $U/t = 15$, corresponding to an exchange interaction of $J = h \times 65$Hz. a) Hole density distribution $\langle \hat{n}_i^h \rangle$ as a function of time after the quench. The wavefront of the distribution starts at the center of the chain and expands outward linearly with time. Interference peaks and dips are visible throughout the dynamics, indicating the coherent evolution of the charge excitation. b) 1D cuts of the experimental hole density distributions at times $0\tau_t$, $1.88\tau_t$, and $3.77\tau_t$ (blue circles) are compared with simulations of a single-particle quantum walk (gray squares). c) Nearest-neighbor squeezed-space spin correlation $C(\tilde{x} = 1)$ distribution as a function of time after the quench. d) 1D cuts of the experimental $C(\tilde{x} = 1)$ distributions at times $0\tau_J$, $1.54\tau_J$, and $3.08\tau_J$ (red circles) along with exact diagonalization simulations of the Heisenberg model (gray squares). Error bars denote one standard error of the mean.

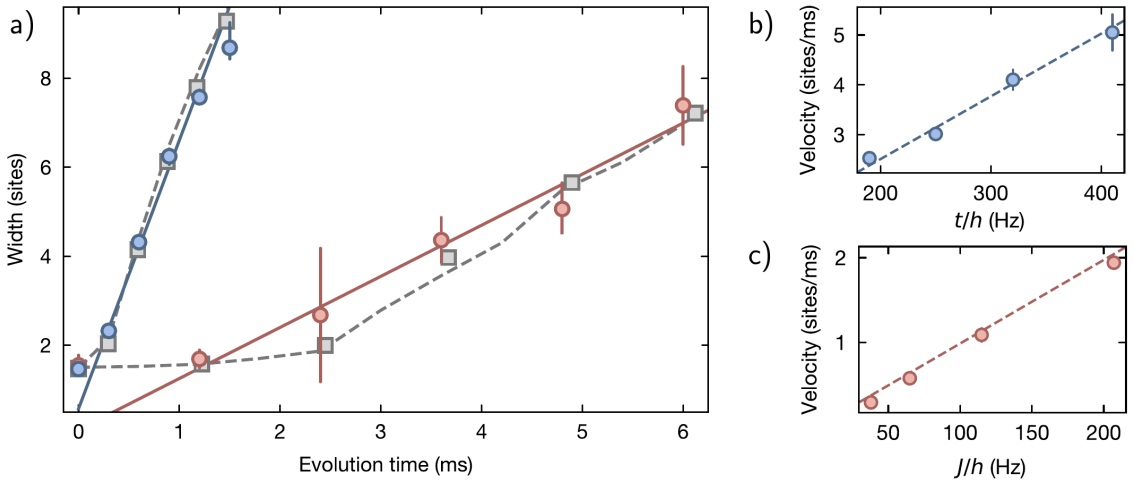

Figure 4.3.2: Spinon and chargon velocity in one dimension. a) Time evolution of the widths of the hole density distributions (blue circles) and nearest-neighbor spin correlation distributions (red circles) after the quench. The measured widths are defined as the full width at 30% of maxima of the distributions (see inset). Density and spin excitations reach the edge of the unity-filled region of the chain (central nine sites) after different evolution times. Their dynamics are in quantitative agreement with both a single-particle quantum walk for the hole and exact diagonalization calculations of the Heisenberg model for the spin (gray squares). They are also found to reproduce the predictions of the extended $t-J$ model at our temperature (gray dashed lines). The velocities of the spin (0.58 ± 0.04 sites/ms) and the charge (3.08 ± 0.09 sites/ms) excitations are obtained as half the slope of a linear fit to the data (solid blue and red lines), ignoring the width immediately after the quench. b) Holon velocities as a function of t/h. The velocities of the holon (blue circles) increase linearly with the tunneling rate in the chain, consistent with $v^t_{\max} = 4\pi t a_x/h$ sites/ms (blue dashed line). c) Spin-excitation velocities as a function of J/h. The velocities of the spin excitation (red circles) increase linearly with the spin-exchange coupling in the chain, consistent with $v^J_{\max} = \pi^2 J a_x/h$ sites/ms (red dashed line). Error bars denote one standard error of the mean.

neighbor spin correlations in squeezed space,

$$C_{\tilde{i}}(\tilde{x}=1) = 4(\left\langle \hat{\tilde{S}}^z_{\tilde{i}} \hat{\tilde{S}}^z_{\tilde{i}+1} \right\rangle - \left\langle \hat{\tilde{S}}^z_{\tilde{i}} \right\rangle \left\langle \hat{\tilde{S}}^z_{\tilde{i}+1} \right\rangle), \tag{4.58}$$

stay sizeable.

Directly after the quench, a strong local reduction of the antiferromagnetic correlations takes place. The spin correlation across the hole corresponds to the equilibrium next nearest neighbor correlation – there is an enhanced probability to find ferromagnetic correlations here. This constitutes the creation of a spinon by the local quench. Note that this next nearest neighbor correlator across the hole corresponds to a nearest neighbor correlator in squeezed space. In the following dynamics, the region with reduced local anti-ferromagnetic correlation spreads with a light-cone like propagation of the wavefront. In order to extract a velocity from the observed light-cone spreading,

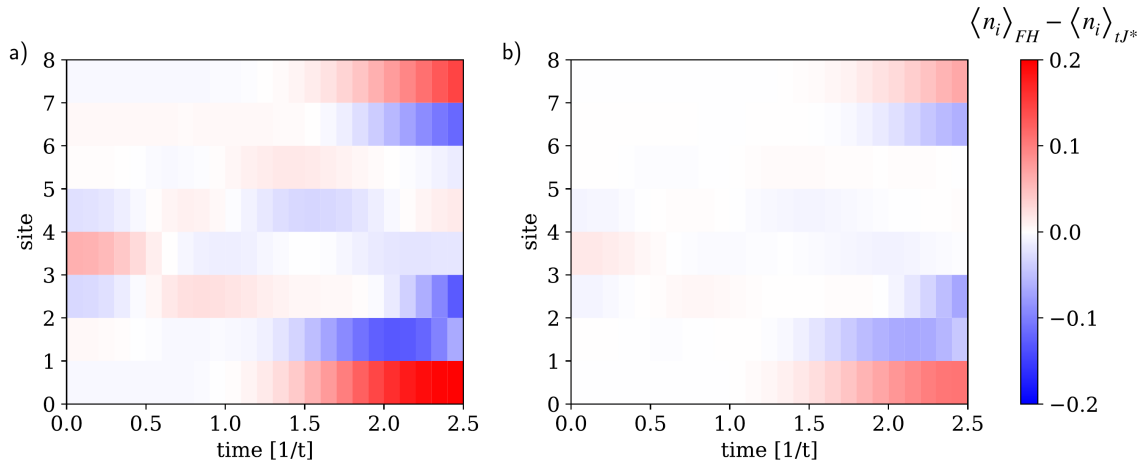

Figure 4.3.3: Dynamics in the Fermi-Hubbard and $t-J^*$ model for a system with 8 sites at a) $U/t = 8$ and b) $U/t = 15$ and t/J correspondingly. The plots show the difference in the local occupation $\langle \hat{n}_i \rangle$ after the removal of a particle in the center of the system. Differences at time zero are due to the fact that the corresponding site can be either empty or occupied by a doublon in the Fermi-Hubbard model, whereas in the $t-J$ model initially each site is occupied by exactly one particle.

we monitor the full width of the distributions. Specifically, we consider the full width at 30% of the maximum of the distribution, see inset of Fig. 4.3.2 c). The velocities are then defined as half the slope of a linear fit to the width as a function of time, Fig. 4.3.2. As expected, the hole density distribution reaches the edge of the system considerably faster than the squeezed space spin correlation function and correspondingly the extracted holon velocity is considerably larger than the spinon velocity. For all different values of U/t probed in the experiment, the extracted velocity is consistent with the theoretically expected maximum group velocity determined by the dispersion of a free particle and the spinon dispersion, respectively, Fig. 4.3.2 b), c).

Comparison to numerics The experimentally observed distributions are furthermore in excellent agreement with exact diagonalization simulations of the $t-J^*$ model, Eq. (3.9), at finite temperature with a harmonic potential. For small system sizes, we also compared exact diagonalization results for the $t-J^*$ and Fermi-Hubbard models and found good agreement up to small differences at the boundaries, Fig. 4.3.3. Increasing the ratio of U/t – and simultaneously t/J for the $t-J^*$ model – reduces these differences further, as can be seen by comparing Fig. 4.3.3 a) $U/t = 8$ and b) $U/t = 15$.

Since the velocities of spinon and chargon differ, we additionally performed separate numerical simulations of their dynamics. To this end, the chargon dynamics is compared to exact diagonalization results of a free particle in a trap. For the spinon dynamics, we consider a Heisenberg spin

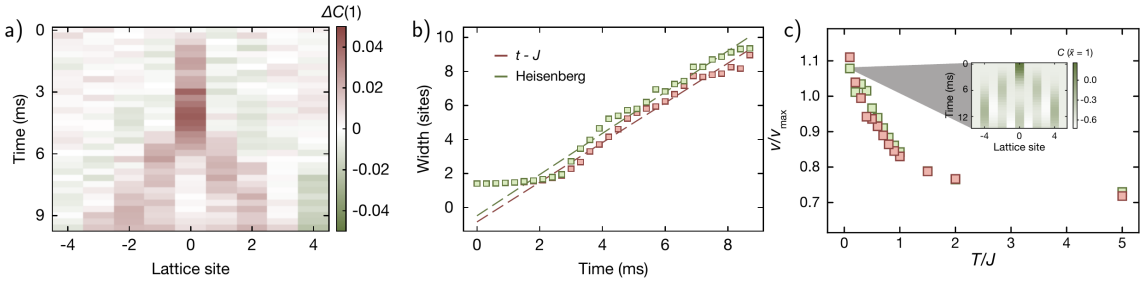

Figure 4.3.4: Dynamics in the $t - J^*$ and Heisenberg model for $t/J = 3.8$, $T/J = 0.7$ and $V/J = 0.456$ from exact diagonalization. a) Difference between the squeezed space nearest neighbour correlator distribution in the $t - J^*$ model and the Heisenberg model $\Delta C(1)$. b) Velocity extraction for the spinon in the simulation of the extended $t - J$ model ($t - J^*$ model) (red squares) and the Heisenberg model (green squares). The extracted velocities of 0.58 ± 0.04 sites/ms for the $t - J^*$ model and 0.61 ± 0.05 sites/ms for the Heisenberg model are obtained by fitting a straight line to the points (dashed lines). c) Temperature dependence of the spinon velocity. The ratio of the numerically extracted velocity and the maximum group velocity $v^J_{\text{max}} = \pi^2 J a_x/h$ for $t/J = 3.8$, $V/J = 0.456$ and periodic (open) boundary conditions for the spins (hole) as calculated for the $t - J^*$ model (red squares) and the Heisenberg model (green squares). At low temperatures, the coherent motion of the spinon which moves by two sites every step (see inset), makes the extraction of the velocity from a linear fit challenging.

chain with L sites, from which one site in the center is removed initially. The remainder of the chain is then squeezed together and the ensuing dynamics is simulated for a spin chain with $L - 1$ sites. Importantly, there is no empty site in the system and as a consequence also no hole dynamics.
Both the spinon and the chargon dynamics show excellent agreement with the corresponding numerical simulations, see Fig. 4.3.2 a). As shown in Fig. 4.3.4, the spin dynamics is very similar for the $t - J^*$ and the Heisenberg model.
Since in the latter case no hole is involved, the comparison between the two simulations yields insights into the effect of the hole on the spin dynamics. In Fig. 4.3.4 a), the relative difference between the squeezed space $C(\tilde{x} = 1)$ correlations for the $t - J^*$ and Heisenberg model are shown. Apart from the initial dynamics on the central bond, the relative difference is below 8% during the entire time evolution, showing how similar the correlations under consideration are in the two models. As shown in Fig. 4.3.4 c), the extracted spinon velocity decreases with increasing temperature. We attribute this effect to the probability to create a spinon, which exhibits a similar temperature dependence, see Fig. 4.3.7 c).
For the chargon, the coherent evolution is visible in the interference pattern of its dynamics. For the spinon on the other hand, the temperatures are much higher in comparison and thus there are no visible interference effects. In numerical simulations, lowering the temperature has an effect on the time evolution of the squeezed space spin correlation function. In the inset of Fig. 4.3.4 c), the corresponding distribution function is shown at a temperature of $T = 0.1J$. In this case, the spinon

excitation moves by two bonds at a time and the bonds in between remain largely untouched by the quench. From the numerical simulations we can again extract a spinon velocity as described above. In Fig. 4.3.4 c), the velocity is shown to decrease as a function of temperature, where the steepest decline happens for temperatures $T \leq J$.

Note that for temperatures $T \lesssim J$, the open boundary conditions have a strong effect on the squeezed space nearest neighbor correlator: the spin at the boundary is only coupled to one other spin, such that the correlations are stronger on every second bond in the vicinity of the edge. This boundary effect is visible throughout the spin chain in squeezed space and renders the extraction of a spinon velocity with the method described above challenging. We therefore simulate periodic boundary conditions for the spins, while the hole is still subject to open boundary conditions and the harmonic potential. This leads to a smooth behavior of the squeezed space correlator $C(\tilde{x} = 1)$ and thus enables the extraction of the spinon velocity, which is used in Fig. 4.3.2

We probe the dynamics of the spin excitation beyond nearest neighbor correlations by considering $\left\langle \hat{\tilde{S}}_i^z \hat{\tilde{S}}_j^z \right\rangle$ at different points in the time evolution after the quench in Fig. 4.3.5. The background signal $\left\langle \hat{\tilde{S}}_i^z \hat{\tilde{S}}_j^z \right\rangle_{\text{bg}}$, defined as the spin correlations in thermal equilibrium at the same temperature, is subtracted here, such that

$$4 \cdot \left\langle \hat{\tilde{S}}_i^z \hat{\tilde{S}}_j^z \right\rangle_{\text{diff}} = 4 \cdot \left\langle \hat{\tilde{S}}_i^z \hat{\tilde{S}}_j^z \right\rangle - 4 \cdot \left\langle \hat{\tilde{S}}_i^z \hat{\tilde{S}}_j^z \right\rangle_{\text{bg}} \tag{4.59}$$

is shown. Note that the spin correlations are reversed beyond nearest neighboring sites, indicating the extent of the spin excitation. The different behavior at the three different time steps shows the spread of the spin excitation throughout the system. In Fig. 4.3.5 b) and c), the excitation starts to reach the boundary at the latest considered time.

So far, we studied the creation of a hole in a spin (or half-filled Fermi-Hubbard) chain. Another possible scenario starts from a pinned hole, which is released at time zero. A pinned hole effectively cuts the chain into two disconnected pieces. The dynamics of the hole itself is very similar to the situation studied before, where the hole was created instead of released, Fig. 4.3.6 a). The spin sector, however, behaves differently: initially, there are no spin correlations between the left and the right half of the chain. As soon as the hole is released and moves through the system, the two disconnected spin chains become connected and correlations start to build up. In Fig. 4.3.6, this scenario is studied with time-dependent matrix product states, starting from the ground state of the system with a pinned hole. Fig. 4.3.6 b) shows the sign-corrected spin correlation function $(-1)^i \left\langle \hat{S}_o^z \hat{S}_i^z \right\rangle$.

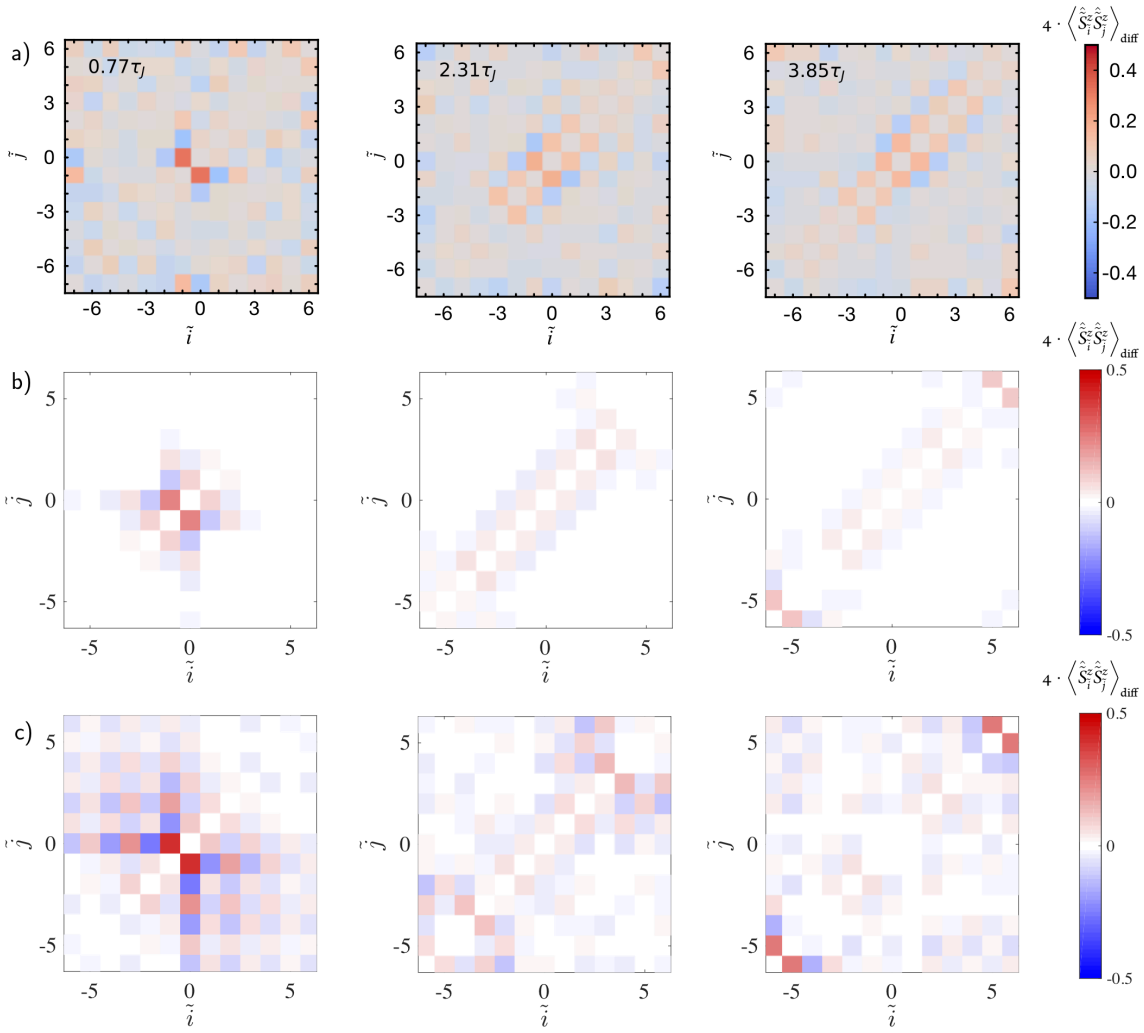

Figure 4.3.5: Long-range squeezed space spin correlations in a spin chain after the sudden creation of a hole at time zero for three different evolution times, Eq. 4.59. Here, the background contribution, i.e. the equilibrium long-range spin correlations in a spin chain with one site less, is subtracted to better visualize the dynamics due to the quench. a) Experimental data. b), c) Exact diagonalization simulation for a Heisenberg spin chain at temperature b) $T = 0.75J$ and c) $T = 0.3J$ with open boundary conditions with $L = 14$ sites, where site 7 is removed initially. The remainder of the chain is squeezed together, there is no hole dynamics.

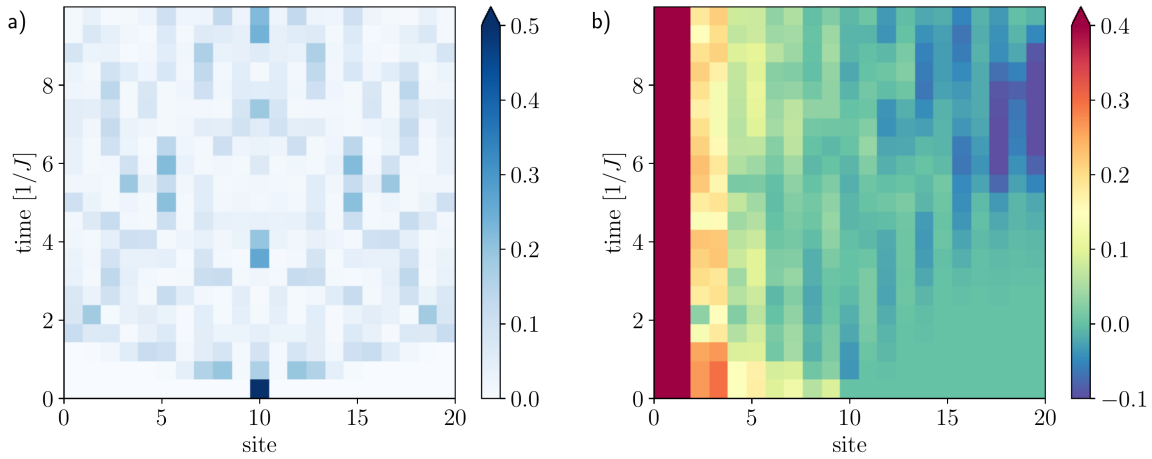

Figure 4.3.6: Releasing a hole in a spin chain. The simulation starts from the ground state of the one-dimensional $t-J$ model with a hole pinned at site 10. At time zero, the hole is released and can move with a hopping amplitude of $t/J = 3.5$ through the system. a) The hole spreads rapidly and reaches the edge of the system at times $\propto 2/J$. The plot shows the hole density, where the colorbar is clipped at 0.5 to make more features visible. b) The spin correlations $(-1)^i \langle \hat{S}^z_0 \hat{S}^z_i \rangle$ between site 0 and site i are zero for $i \geq 10$ initially. The pinned hole cuts the spin chain into two disconnected parts. During the dynamics, spin correlations between the left and the right half of the system build up.

4.3.2 Spatial separation of quasi-particles

Apart from the spreading of the quasi-particles with different velocities, we can use the capabilities of the quantum gas microscope to further probe their spatial separation. In particular, the spin correlation across the hole,

$$C_{SHS}(2) = 4 \sum_i \left\langle \hat{S}^z_i \hat{n}^h_{i+1} \hat{S}^z_{i+2} \right\rangle , \tag{4.60}$$

can be extracted from the snapshots. Initially, this correlation correspond to the equilibrium next nearest neighbor spin correlation, which is positive, Fig. 4.3.7. After a few tunneling times of the chargon, the spin-hole-spin correlation C_{SHS} is negative with a large absolute value. In principle, in an unbound state, the spinon and chargon would spatially separate over arbitrary large distances. However, in the finite size system considered here, the chargon and spinon distributions overlap again after their initial separation. At longer times, C_{SHS} therefore saturates at a value of about -0.25, which is slightly smaller in absolute value than the equilibrium nearest neighbor spin correlation.

In order to analyze the influence of the charge on the spin sector beyond the immediate vicinity of the hole, we compare the nearest neighbor spin correlation as a function of distance from the hole

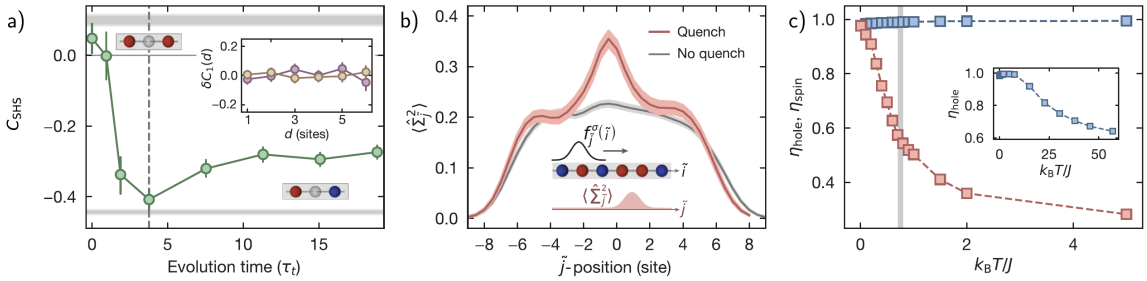

Figure 4.3.7: Deconfinement of the quasi-particles. a) Spin-hole-spin correlations (C_{SHS}) averaged over the entire chain as a function of time after the quench. The correlator starts with a positive value consistent with the next-nearest neighbour spin correlations in the absence of the quench (top grey shaded region) and turns negative, approaching the nearest neighbour spin correlations without the quench (bottom grey shaded region) by $4\tau_t$. At longer evolution times, the correlator shows reduced antiferromagnetic correlations due to the oscillating dynamics of the hole in our finite size system. The inset shows the lack of dependence of the normalized deviation from the mean nearest neighbour correlations δC_1 on the distance d from the hole at times $4\tau_t$ (purple) and $19\tau_t$ (yellow). Error bars denote 1 standard error of the mean (s.e.m.). b) Spatially resolved magnetization fluctuations $\left\langle \Sigma^2_{\tilde{j}} \right\rangle_{(BG)}$ in sub-regions of the chain with (red) and without (grey) the quench at $3.77\tau_t$. The background fluctuations $\left\langle \Sigma^2_{\tilde{j}} \right\rangle_{BG}$ are due to quantum and thermal fluctuations in the system. The peak in the difference signal $\left\langle \Sigma^2_{\tilde{j}} \right\rangle - \left\langle \Sigma^2_{\tilde{j}} \right\rangle_{BG}$ indicates the location of the spin excitation. Grey and red shades denote 1 s.e.m without and after the quench respectively. c) Efficiency of initially creating a single local spinon η_{spin} (orange) and hole η_{hole} (blue) at the central site, as defined in Eqs. (4.63) and (4.64), after an ideal quench as a function of temperature as predicted from exact diagonalization of the Heisenberg model (for the spinon) and the Hubbard model (for the hole). With increasing temperature, η_{spin} (η_{hole}, inset) decreases due to the increase of thermal spin (density) excitations, preventing the creation of a localized spinon (chargon) by the quench. Taking into account our quench efficiency, the measured amplitude is consistent with the prediction at a temperature of $k_BT/J = 0.75$ (grey shaded region).

to the spatially averaged nearest neighbor correlations,

$$\delta C_1(d) = \left\langle \hat{S}^z_i \hat{S}^z_{i+1} \right\rangle_{\bullet_i \bullet_{i+1} \circ_{i+1+d} \vee i-d} / \left\langle \hat{S}^z_i \hat{S}^z_{i+1} \right\rangle - 1. \tag{4.61}$$

Here, d is the distance of the hole from the closest of sites i and $i+1$. In the inset of Fig. 4.3.7 a), δC_1 is shown for two different evolution times. In both cases, there is no dependence on the distance d, indicating the lack of influence of the chargon on the spin excitation.
In order to further characterize the dynamics of the quasi-particles, we locate the excess spin in the system with an envelope function analysis. We define an operator quantifying the local spin fluctuations in squeezed space as

$$\hat{\Sigma}^2_{\tilde{j}} = \left(\sum_{\tilde{i}} \hat{\tilde{S}}^z_{\tilde{i}} \cdot f^{\sigma}_{\tilde{j}}(\tilde{i}) \right)^2 \qquad \text{with} \qquad f^{\sigma}_{\tilde{j}}(\tilde{i}) = \exp(-(\tilde{i}-\tilde{j})^2/(2\sigma^2)) \tag{4.62}$$

a smooth window function centered at lattice site $\tilde{j}$ with a characteristic size σ. At zero temperature, this operator is expected to capture local fractional quantum numbers [219]. Assuming the mean distance between thermal spin fluctuations is larger than the size of the envelope function σ, a single spinon – carrying spin 1/2 – at site $\tilde{j}$ would increase $\left\langle \hat{\Sigma}^2_{\tilde{j}} \right\rangle$ by 1/4.
In Fig. 4.3.7 b), we consider $\left\langle \hat{\Sigma}^2_{\tilde{j}} \right\rangle$ for $\sigma = 1.5$ at time $3.77\tau_t$. At this time, the highest probability to detect the hole is at sites ± 2. We post-select on chains with a single hole in the central nine sites, but outside the central three sites. We compare $\left\langle \hat{\Sigma}^2_{\tilde{j}} \right\rangle$ to $\left\langle \hat{\Sigma}^2_{\tilde{j}} \right\rangle_{BG}$, which is the same quantity, but without the creation of a hole at time zero, and thus provides a background value. We observe a well localized signal extending over the central three sites, which is consistent with Fig. 4.3.1 c) and distinct from the position of the chargon. The maximum deviation $\left\langle \hat{\Sigma}^2_{\tilde{j}} \right\rangle - \left\langle \hat{\Sigma}^2_{\tilde{j}} \right\rangle_{BG}$ reaches 0.13 ± 0.01, which is about half of the value expected at zero temperature. We attribute this difference mainly to the finite temperature in our experimental system leading to a background density of thermal spin excitations. Therefore, even an ideal quench does not create an initially localized spinon with unity probability. In Fig. 4.3.7 c), the probability to create a single local spinon,

$$\eta_{\text{spin}} = 4 \left(\left\langle \hat{\Sigma}^2_{\tilde{j}=0} \right\rangle - \left\langle \hat{\Sigma}^2_{\tilde{j}=0} \right\rangle_{BG} \right), \tag{4.63}$$

and the probability to create a hole,

$$\eta_{\text{hole}} = 1 - \left\langle (\hat{n}_{i=0} - 1)^2 \right\rangle, \tag{4.64}$$

obtained from exact diagonalization calculations is shown. For the spinon, we use the Heisenberg model and for the chargon, the Hubbard model. In the latter case, doublon-hole excitations can

decrease the probability η_{hole}, but comparably high temperatures in units of J are necessary for a sizeable effect. The gray shaded region indicates the experimental temperatures. The experimentally measured value of η_{spin} in Fig. 4.3.7 b) is consistent with this prediction, taking into account the imperfect quench in the experiment.

4.4 Cyclic ring-exchange on a ladder

This section is based on the publication

- Annabelle Bohrdt, Ahmed Omran, Eugene Demler, Snir Gazit, Fabian Grusdt: "Multiparticle interactions for ultracold atoms in optical tweezers: Cyclic ring-exchange terms" – Phys. Rev. Lett. 124, 073601 (2020) [arXiv:1910.00023]

Structure, text and figures have been rearranged and adapted here.

In most of the numerical simulations presented in this work, the Fermi Hubbard model is approximated by the $t-J$ model. However, upon further expanding the Hubbard Hamiltonian in t/U, higher order spin interactions arise. Specifically, cyclic ring exchange terms on the plaquettes of the square lattice appear with a coupling $K = 20t^4/U^3$. Theoretical studies by Roger and Delrieu based on the three band Hubbard model [220] as well as experimental results [221, 222] suggest that these four-spin exchange terms may be important for the physics of the cuprates, however their effect on the phase diagram is still debated. Moreover, experiments show that ring-exchange terms can also be present in copper-based spin-ladder materials [223, 224].
Here we propose a scheme to experimentally realize and probe multi-particle interactions for ultracold atoms with optical tweezers and study a chiral cylic ring exchange (CCR) term with a complex phase on a ladder numerically. Usually, the ring exchange term is considered as a small correction to the two spin exchange coupling J. We instead study a model with only the ring exchange term present, described by the Hamiltonian,

$$\hat{H}_{\mathrm{CCR}}(\varphi) = K\sum_{p}(e^{i\varphi}\hat{P}_p + e^{-i\varphi}\hat{P}_p^\dagger), \tag{4.65}$$

and tune the complex phase φ, which leads to different ground state phases. Here, the sum is over all plaquettes p of the underlying lattice and the operator $\hat{P}_p^\dagger(\hat{P}_p)$ cyclically permutes the spin configuration on plaquette p in the (counter-)clockwise direction. A generalization to finite hole doping, with zero or one particle per lattice site, is straightforward.

4.4.1 Multiparticle interactions for ultracold atoms in optical tweezers

The general idea of the scheme is to use the capabilities of optical tweezers [41, 225–228] in combination with strong Rydberg interactions to quickly change the spatial configuration of atoms in order to realize exchange processes. In the following, the concrete implementation of the Hamiltonian (4.65) on a single plaquette with four sites and SU(2) symmetry is discussed. Note that the

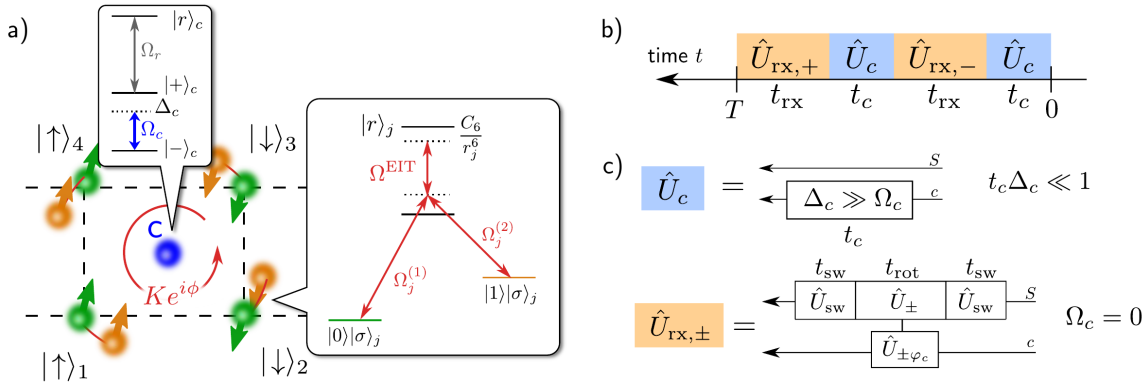

Figure 4.4.1: Realizing chiral cyclic ring exchange. a) Proposed setup: SU(2)-invariant chiral cyclic ring-exchange interactions can be realized by combining state-dependent lattices generated by optical tweezer arrays and strong Rydberg interactions with a central Rydberg-dressed control qubit (C). The auxiliary states $|\tau = 1\rangle|\sigma\rangle$ with $\sigma = \uparrow, \downarrow$ (orange) of the atoms on the sites of the plaquette are subject to a state-dependent tweezer potential, which allows us to permute them coherently around the center. Our protocol makes use of stroboscopic π pulses between the physical states $\tau = 0$ (green) and the auxiliary states $\tau = 1$, which only take place collectively on all sites and are conditioned on the absence of a Rydberg excitation in the control atom. b), c) Proposed protocol: The sequence in b) is repeated periodically with period $T = 2(t_c + t_{\mathrm{rx}})$. When $t_c \ll 2\pi/\Delta_c, 1/\Omega_c$, it implements a Trotterized time evolution of the effective Hamiltonian (4.65), which realizes CCR couplings when $\Delta_c \gg \Omega_c$. The individual time steps are illustrated in c).

scheme can be directly generalized to SU(N) symmetry, to a ladder or two dimensional geometry as well as plaquettes with a different number of sites and moreover to other types of multiparticle interactions.

PERMUTATIONS We consider a plaquette with four sites, where on each site a static optical tweezer traps one atom. Throughout the entire sequence, these atoms remain in the vibrational ground state of the microtraps. Two internal states $\sigma = \uparrow, \downarrow$, for example hyperfine states, are used to implement an effective spin 1/2 on each lattice site. As a specific configuration, we suggest to use ^{133}Cs atoms and utilize their $F = 3$, $m_F = 2, 3$ hyperfine states to represent the two spins. Optical pumping with site-resolved addressing can then be employed to prepare arbitrary initial spin patterns [229] and study their dynamics under H_{CCR}. We then propose to physically rotate the tweezer array around the center of the plaquette in order to realize the permutation

$$\hat{\mathcal{P}}|\sigma_1\sigma_2\sigma_3\sigma_4\rangle = |\sigma_4\sigma_1\sigma_2\sigma_3\rangle \tag{4.66}$$

and its counter-clockwise counterpart. Importantly, the motional and spin states of the atoms are not changed during the rotation. Optimized trajectories can be chosen to cancel heating effects from the motion [230]. These require a timescale set by the quantum speed limit that scales as the inverse energy gap of each trap $t_{\text{rot}} \sim 1/\Delta\varepsilon$. For deep trapping potentials where $\Delta\varepsilon \approx 150\,\text{kHz}$, rotation times of $t_{\text{rot}} < 10\,\mu\text{s}$ are achievable.

SUPERPOSITION Applying the time evolution operator,

$$e^{-i\hat{\mathcal{H}}_{CCR}\Delta t} = 1 - i\hat{\mathcal{H}}_{CCR}\Delta t, \tag{4.67}$$

to a state leads to a superposition of the permuted and non-permuted state. In order to create such a superposition, we assume that each atom has an additional internal degree of freedom $\tau = 0, 1$ and we can employ two sets of optical tweezer arrays, one of which strongly confines the $\tau = 1$ state, but has almost no effect on atoms in the $\tau = 0$ state. We can then permute the atoms if and only if they are in the $\tau = 1$ state, by only rotating the latter set of tweezers, effectively realizing

$$\hat{U}_+ = \prod_j |1\rangle_j\langle 1| \otimes \hat{\mathcal{P}} + \prod_j |0\rangle_j\langle 0| \otimes \hat{1}, \tag{4.68}$$

where $\hat{\mathcal{P}}$ and $\hat{1}$ are applied to the spin 1/2 degree of freedom σ. We denote $\hat{U}_- = \hat{U}_+^\dagger$. The superposition of permuted and non-permuted state is then realized by applying $\hat{U}_+$ to a superposition of all atoms in $|\tau = 1\rangle$ and $|\tau = 0\rangle$. Concretely we propose to realize the new states $|\tau = 1\rangle|\sigma\rangle$ in ^{133}Cs atoms by $F = 4$, $m_F = 3, 4$ hyperfine levels, where $m_F = 3$ ($m_F = 4$) corresponds to $\sigma = \downarrow$ ($\sigma = \uparrow$). These additional levels will be used as auxiliary states, whereas the states $|\tau = 0\rangle|\sigma\rangle$ introduced before – implemented as $F = 3$, $m_F = 2, 3$ levels in ^{133}Cs– realize the physical spin states. The evolution above can then be realized by using the near-magic wavelength $\lambda_{\text{magic}} \approx 871.6\,\text{nm}$ in ^{133}Cs, which strongly confines atoms in the state $\tau = 1$ but almost does not affect atoms in $\tau = 0$.

CONTROL ATOM In order to realize this superposition of all atoms in the $\tau = 1$ and all atoms in the $\tau = 0$ state, we propose to use a control qubit trapped in the center of the plaquette, which can be in the states $|\pm\rangle_c$, Fig. 4.4.1 a). If it is in the state $|+\rangle_c$, a transfer to the Rydberg state $|r\rangle_c$ can occur with a resonant π pulse and Rabi frequency Ω_r. If on the other hand the control atom is in the state $|-\rangle_c$, Ω_r is off-resonant and no excitation to the Rydberg state is possible. The idea is now to use the Rydberg blockade mechanism to collectively transfer or not transfer all atoms on the plaquette from $|0\rangle_j$ to $|1\rangle_j$. To this end, a Raman transition by lasers $\Omega^{(1)}$, $\Omega^{(2)}$ through an intermediate Rydberg state $|r\rangle_j$ is used, where a coupling field Ω^{EIT} established a two photon resonance to the Rydberg state with both of the Raman lasers. Electromagnetically induced transparency (EIT)

[231] then suppresses the transition $|0\rangle_j \leftrightarrow |1\rangle_j$. The EIT is however lifted by the Rydberg blockade if the control atom is in the Rydberg state $|r\rangle_c$ [232], thus enabling the transfer between the τ states of all atoms simultaneously. This part of the sequence corresponds to the switching

$$\hat{U}_{sw} = |+\rangle_c\langle+| \otimes \left(\prod_j |1\rangle_j\langle 0| + \text{h.c.}\right) \otimes \hat{1}_\sigma + |-\rangle_c\langle-| \otimes \hat{1}_\tau \otimes \hat{1}_\sigma \tag{4.69}$$

over a time t_{sw}. After the transfer another π pulse is applied to the control atom in order to ensure that the atom remains trapped, since the Rydberg state might not be trapped by an optical tweezer. The actual superposition between permuted and non-permuted states of the atoms can now be realized by driving a transition between the states $|\pm\rangle_c$ of the control qubit with a dressing laser Ω_c at detuning Δ_c over a time t_c,

$$\hat{\mathcal{H}}_c = \Delta_c|+\rangle_c\langle+| + \Omega_c\left(|+\rangle_c\langle-| + \text{h.c.}\right). \tag{4.70}$$

During the rest of the protocol, $\Omega_c = 0$ and the control atom picks up a phase $\pm\varphi_c$ if it is in the state $|+\rangle_c$. This phase φ_c corresponds to the complex phase in the Hamiltonian (4.65) and can be controlled by adjusting Δ_c and the times of the different steps fo the protocol.

Effective Hamiltonian The complete protocol consists of a periodic repitition of the different steps as shown in Fig. 4.4.1 b). At all discrete time steps nT, where $T = 2(t_c + t_{rx})$ and $t_{rx} = 2t_{sw} + t_{rot}$, the unitary evolution is described by an effective Hamiltonian

$$e^{-inT\hat{\mathcal{H}}_{eff}} = \left(\hat{U}_T\right)^n = \left(\hat{U}_{rx,+}\hat{U}_c\hat{U}_{rx,-}\hat{U}_c\right)^n \tag{4.71}$$

with

$$\hat{U}_{rx,\pm} = \hat{U}_{sw}\left(\hat{U}_{\pm\varphi_c} \otimes \hat{U}_\pm\right)\hat{U}_{sw} \tag{4.72}$$

and

$$\hat{U}_{\pm\varphi_c} = e^{\mp i\varphi_c}|+\rangle_c\langle+| + |-\rangle_c\langle-|. \tag{4.73}$$

For $t_c \ll \frac{2\pi}{\Delta_c}, \frac{2\pi}{\Omega_c}$, the effective Hamiltonian is to leading order in t_c

$$\hat{\mathcal{H}}_{eff} = \frac{t_c}{T}\left(2\Delta_c|+\rangle_c\langle+| \otimes \hat{1} + \Omega_c\left(|-\rangle_c\langle+| \otimes \left(\hat{1} + e^{i\varphi_c}\hat{\mathcal{P}}^\dagger\right) + \text{h.c.}\right)\right). \tag{4.74}$$

For $\Omega_c \ll \Delta_c$, the state $|+\rangle_c$ can be eliminated because it is only virtually excited, yielding

$$\hat{\mathcal{H}}_{eff} = K\left(2 + e^{-i\varphi_c}\hat{\mathcal{P}} + e^{i\varphi_c}\hat{\mathcal{P}}^\dagger\right) \tag{4.75}$$

with

$$K = -\frac{1}{2T} t_c \Delta_c \left(\frac{\Omega_c}{\Delta_c}\right)^2 . \tag{4.76}$$

For realistic parameter values of $\Omega_c = 0.2\Delta_c$, $t_c\Delta_c = 0.4$, $t_{rot} = 10\mu$s and $t_{sw}, t_c \ll t_{rot}$, a strength of $K/\hbar = 2\pi \cdot 50$Hz can be achieved. This requires $\Omega_c/2\pi \gg 1.3$kHz, which can be easily realized; the condition $t_{sw} \ll 10\mu$s can also be met, as the Rydberg π-pulses on the control atom can be executed in $\sim$ 100 ns each and the Raman transfer between the states $|0\rangle_j$ and $|1\rangle_j$ can be driven with coupling strengths above 1 MHz.
The result can be extended to multiple plaquettes by implementing the trotterized time step T interchangeably on inequivalent plaquettes.

Extension to the $J-Q$ model

Our proposed protocol is versatile enough to implement larger classes of models with multi-spin interactions. In our derivation of Eq. (4.75) above we only used the fact that $\hat{P}^\dagger\hat{P} = 1$ and the cyclic ring-exchange operator $\hat{P}$ can be replaced by an arbitrary permutation $\mathcal{P}$ of spins. Moreover, introducing more than one control qubit per plaquette allows to implement multiple such terms $\mathcal{P}_p^{(n)}$ per plaquette p: For every control atom n associated with plaquette p a coupling term

$$\propto \Omega_c^{(n)} \left[|-,n\rangle_c\langle +,n| \left(1 + e^{-i\phi_c^{(n)}} \hat{\mathcal{P}}_p^{(n)}\right) + \text{h.c.}\right]$$

can be implemented. By integrating out the n-th control atom, with detuning $\Delta_c^{(n)} \gg \Omega_c^{(n)}$, an effective Hamiltonian of the form

$$\hat{\mathcal{H}}_{\text{eff}} \propto \sum_{p,n} \frac{(\Omega_c^{(n)})^2}{\Delta_c^{(n)}} \left(e^{-i\phi_c} \hat{\mathcal{P}}_p^{(n)} + \text{h.c.}\right) \tag{4.77}$$

is obtained. We envision that control atoms can be stored in a register and moved into the center of the plaquette individually when they are needed for the protocol.
As a specific example, we discuss an implementation of the $J-Q$ model [233] on a ladder. The conventional way to write the $J-Q$ Hamiltonian [233] is in terms of spin operators $\hat{\mathbf{S}}_\mathbf{j}$ on the sites $\mathbf{j}$ of the lattice,

$$\hat{\mathcal{H}}_{JQ} = J \sum_{\langle \mathbf{i},\mathbf{j}\rangle} \hat{\mathbf{S}}_\mathbf{i} \cdot \hat{\mathbf{S}}_\mathbf{j} - Q \sum_{\langle \mathbf{ijkl}\rangle} \hat{\mathbb{P}}_{\mathbf{i},\mathbf{j}} \hat{\mathbb{P}}_{\mathbf{k},\mathbf{l}}, \tag{4.78}$$

where $\langle \mathbf{ijkl}\rangle$ denotes a sequence of corners of a plaquette. The second term describes projectors on singlets,

$$\hat{\mathbb{P}}_{\mathbf{i},\mathbf{j}} = \hat{\mathbf{S}}_\mathbf{i} \cdot \hat{\mathbf{S}}_\mathbf{j} - \frac{1}{4}. \tag{4.79}$$

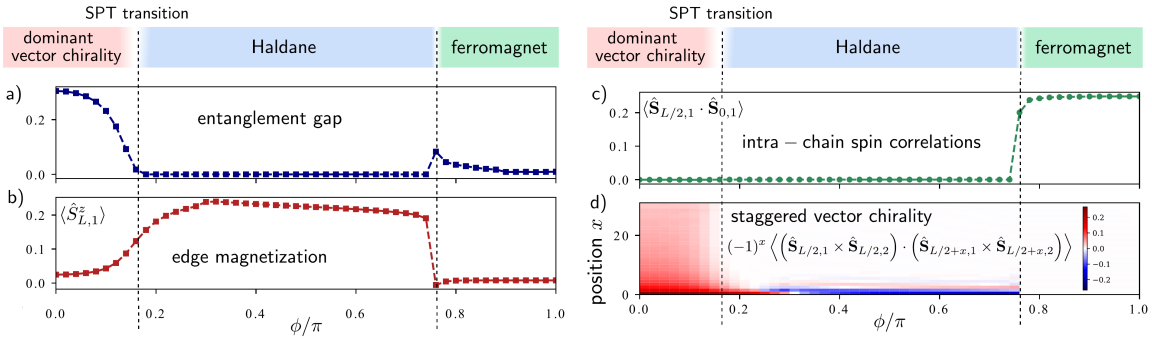

Figure 4.4.2: Ground state phase diagram of the chiral cyclic ring exchange Hamiltonian on a ladder, obtained from DMRG in a system with 64 sites: different observables are evaluated in the ground state of the Hamiltonian (4.65) to characterize the phases. Upon varying φ, three different phases can be identified: A topological Haldane phase featuring a vanishing gap in the entanglement spectrum a) and edge states with a non-zero local magnetization for $S^z_{\text{tot}} = 1$ b); A symmetry-broken phase around $\varphi = \pi$ with long-range ferromagnetic correlations c); And a symmetric phase for small φ, where the staggered vector chirality remains non-vanishing over long distances d).

We use a representation in terms of pairwise permutation operators $\hat{\mathcal{P}}_{\mathbf{i},\mathbf{j}} = 2\left(\hat{\mathbf{S}}_{\mathbf{i}} \cdot \hat{\mathbf{S}}_{\mathbf{j}} + \frac{1}{4}\right)$, for which

$$\hat{\mathcal{H}}_{JQ} = \frac{2Q+J}{2} \sum_{\langle \mathbf{i},\mathbf{j} \rangle \in R} \hat{\mathcal{P}}_{\mathbf{i},\mathbf{j}} + \frac{Q+J}{2} \sum_{\langle \mathbf{i},\mathbf{j} \rangle \in L} \hat{\mathcal{P}}_{\mathbf{i},\mathbf{j}} - \frac{Q}{4} \sum_{\langle \mathbf{ijkl} \rangle} \hat{\mathcal{P}}_{\mathbf{i},\mathbf{j}} \hat{\mathcal{P}}_{\mathbf{k},\mathbf{l}} \tag{4.80}$$

up to an overall energy shift, which depends on the boundary conditions. Here $\sum_{\langle \mathbf{i},\mathbf{j} \rangle \in R}$ ($\sum_{\langle \mathbf{i},\mathbf{j} \rangle \in L}$) denotes a sum over all links on the rungs (legs) of the ladder and the last term contains a sum over sequences of corners $\langle \mathbf{ijkl} \rangle$ of the plaquettes.

To implement Eq. (4.80), we propose to use one control atom per link $\langle \mathbf{i}, \mathbf{j} \rangle$, to realize the first and second terms $\propto \hat{\mathcal{P}}_{\mathbf{i},\mathbf{j}}$. In addition, two control atoms per plaquette are required to realize $\hat{\mathcal{P}}_{12}\hat{\mathcal{P}}_{34}$ and $\hat{\mathcal{P}}_{14}\hat{\mathcal{P}}_{23}$ respectively; here the sites of the plaquette are labeled by integers 1, 2, 3, 4 in anti-clockwise direction around the plaquette.

Similar extensions can be envisioned for implementing the $J - Q$ model in two dimensions. This model features a phase transition around $J/Q \approx 0.04$ between an antiferromagnet and a valence-bond solid, which has been proposed as a candidate for a deconfined quantum critical point [233].

4.4.2 Ground state phase diagram on a ladder

We study the ground state of the Hamiltonian (4.65) using DMRG – in particular, using the iTensor package – and to this end, rewrite the Hamiltonian for a spin 1/2 system in terms of spin operators.

As a starting point, we express $\hat{P}_p$ in terms of pairwise spin-permutation operators,

$$\hat{\mathcal{P}}_{ij} = \hat{\mathcal{P}}_{ji} = 2\left(\hat{\mathbf{S}}_i \cdot \hat{\mathbf{S}}_j + \frac{1}{4}\right), \tag{4.81}$$

for which $\hat{\mathcal{P}}_{ij}|\sigma_i\sigma_j\rangle = |\sigma_j\sigma_i\rangle$. Hence

$$\hat{P}_p = \hat{\mathcal{P}}_{43}\hat{\mathcal{P}}_{32}\hat{\mathcal{P}}_{21}. \tag{4.82}$$

Using standard identities for spin operators, we obtain

$$\begin{aligned} e^{i\varphi}\hat{P}_p + e^{-i\varphi}\hat{P}_p^\dagger = \cos(\varphi)\Big[&\frac{1}{4} + \hat{\mathbf{S}}_1\cdot\hat{\mathbf{S}}_2 + \hat{\mathbf{S}}_2\cdot\hat{\mathbf{S}}_3 + \hat{\mathbf{S}}_3\cdot\hat{\mathbf{S}}_4 + \hat{\mathbf{S}}_4\cdot\hat{\mathbf{S}}_1 + \hat{\mathbf{S}}_2\cdot\hat{\mathbf{S}}_4 + \hat{\mathbf{S}}_1\cdot\hat{\mathbf{S}}_3 \\ &+ 4(\hat{\mathbf{S}}_1\cdot\hat{\mathbf{S}}_2)(\hat{\mathbf{S}}_3\cdot\hat{\mathbf{S}}_4) + 4(\hat{\mathbf{S}}_1\cdot\hat{\mathbf{S}}_4)(\hat{\mathbf{S}}_2\cdot\hat{\mathbf{S}}_3) - 4(\hat{\mathbf{S}}_1\cdot\hat{\mathbf{S}}_3)(\hat{\mathbf{S}}_2\cdot\hat{\mathbf{S}}_4)\Big] \\ &+ 2\sin(\varphi)\Big[\hat{\mathbf{S}}_1\cdot(\hat{\mathbf{S}}_2\times\hat{\mathbf{S}}_3) + \hat{\mathbf{S}}_1\cdot(\hat{\mathbf{S}}_3\times\hat{\mathbf{S}}_4) + \hat{\mathbf{S}}_1\cdot(\hat{\mathbf{S}}_2\times\hat{\mathbf{S}}_4) + \hat{\mathbf{S}}_2\cdot(\hat{\mathbf{S}}_3\times\hat{\mathbf{S}}_4)\Big]. \end{aligned} \tag{4.83}$$

The ground state of the Hamiltonian (4.65) is characterized by different corrrelations as the complex phase φ is varied, Fig. 4.4.2. The limiting cases of $\varphi = 0$ and $\varphi = \pi$ have been studied in Ref. [234]. As predicted there, we find a dominant vector chirality and a ferromagnet, respectively. The latter case can be understood from the variational energy $\langle\hat{\mathcal{H}}_{\mathrm{CCR}}(\pi)\rangle$, which is minimized for ferromagnetic configurations. In the sector $S^z_{\mathrm{tot}} = 0$ used in our DMRG in Fig. 4.4.2 c), we find phase separation with two ferromagnetic domains of opposite magnetization.

At intermediate φ we find an emergent Haldane phase, with two-fold degenerate states in the entanglement spectrum, see Fig. 4.4.2 a). For a finite $S^z_{\mathrm{tot}} = 1$ the expectation value $\langle\hat{S}^z_{L,1}\rangle$ at the edge is non-zero, see Fig. 4.4.2 b). The spin gap $\Delta E_S = E_{0,S=1} - E_{0,S=0}$, defined as the difference between the ground state energy with and without finite total magnetization, is zero in this phase, since the additional spin can be placed in the spin-1/2 topological edge states of the system without increasing the total energy. We corroborate this picture further by considering the $K - K'$ model with alternating strengths K, K' of the CCR interactions on adjacent plaquettes. In subsection 4.4.2 we provide an explicitly derivation of a spin-1 model with a gapped Haldane ground state [235, 236] for $\varphi = \pi/2$ and $K' \ll K$.

For small $\varphi \lesssim \pi/4$, the system is dominated by vector chirality correlations, as discussed in Ref. [234]. This phase is characterized by correlations of the form $\hat{\mathbf{S}}_{x,y}\times\hat{\mathbf{S}}_{x',y'}$ in a staggered arrangement around each plaquette. We find that the staggered correlation between different rungs, measured

from the center $L/2$ of the chain,

$$(-1)^x \left\langle \left(\hat{\mathbf{S}}_{L/2,1} \times \hat{\mathbf{S}}_{L/2,2}\right) \cdot \left(\hat{\mathbf{S}}_{L/2+x,1} \times \hat{\mathbf{S}}_{L/2+x,2}\right) \right\rangle , \tag{4.84}$$

decays slowly as a function of the distance x and retains significant non-zero values over the considered system sizes, see Fig. 4.4.2 d). The transition between the dominant vector chirality and Haldane phases is a symmetry-protected topological (SPT) phase transition.
Using the global SU(2) symmetry, the staggered vector chirality becomes

$$6\left\langle \hat{S}^x_{L/2,1}\hat{S}^y_{L/2,2}\left(\hat{S}^x_{L/2+x,1}\hat{S}^y_{L/2+x,2} - \hat{S}^y_{L/2+x,1}\hat{S}^x_{L/2+x,2}\right)\right\rangle (-1)^x. \tag{4.85}$$

Measuring it requires access to two four-point functions of the form $\langle \hat{S}^\mu_{\mathbf{i}} \hat{S}^\nu_{\mathbf{j}} \hat{S}^\lambda_{\mathbf{k}} \hat{S}^\rho_{\mathbf{l}} \rangle$ which can be detected by making use of local addressing techniques, see e.g. [237]. To detect the Haldane phase experimentally, we propose to study weakly magnetized systems and image the topological edge states. Alternatively, one could work in the plaquette basis and measure the Haldane string order parameter. An interesting future extension would be to use machine learning techniques to retrieve non-local order parameters from a series of quantum projective measurements.

The spin-1 Haldane phase

To obtain a better understanding of the Haldane phase observed in our DMRG simulations, we perform a rigorous analytical analysis of a simplified model with CCR couplings of strength K, K' on alternating plaquettes,

$$\hat{\mathcal{H}}_{\mathrm{CCR}}(K') = K \sum_{p\in \mathsf{P}} (e^{i\varphi}\hat{P}_p + e^{-i\varphi}\hat{P}_p^\dagger) + K' \sum_{p\in \overline{\mathsf{P}}} (e^{i\varphi}\hat{P}_p + e^{-i\varphi}\hat{P}_p^\dagger), \tag{4.86}$$

where P denotes the set including every second plaquette and $\overline{\mathsf{P}}$ its complement.
The $K - K'$ model (4.86) can be solved exactly in the limit $K'/K = 0$, where its ground state is a product of decoupled plaquettes P. The eigenstates of a single plaquette $p \in \mathsf{P}$ can be labeled by the total spin $\hat{\mathbf{S}}_p = \sum_{j=1}^4 \hat{\mathbf{S}}_j$ where $j = 1\ldots4$ denotes the four sites of the plaquette (labeled in anti-clockwise direction).
The two states with $S^z_p = \pm 2$ have an energy $\varepsilon_2(\varphi) = 2K\cos\varphi$. In the sector with $S^z_p = \pm 1$ there exist four states corresponding to the four positions j of the minority spin. The eigenstates are plane wave superpositions of different $j = 1\ldots4$ with discrete momenta $p_n = n\pi/2$ for $n = 0, 1, 2, 3$ and corresponding energy $\varepsilon_1^n(\varphi) = 2K\cos(\varphi + p_n)$. Finally there exist six states with $S^z_p = 0$. Four of them correspond to plane-wave superpositions of domain wall configurations, including $\uparrow\uparrow\downarrow\downarrow$ and all cyclic permutations. They have discrete momenta $p_n = n\pi/2$ for $n = 0, 1, 2, 3$ and the

same energy $\varepsilon_2^n(\varphi) = 2K\cos(\varphi + p_n)$ as states in the sector $S_p^z = \pm 1$. Two additional states $|\pm\rangle$ correspond to symmetric and anti-symmetric superpositions of Néel states $|\uparrow\downarrow\uparrow\downarrow\rangle \pm |\downarrow\uparrow\downarrow\uparrow\rangle$ on the plaquette, with eigenenergies $\varepsilon_2^{\pm}(\varphi) = 2K\cos(\varphi + q_{\pm})$ where $q_+ = 0$ and $q_- = \pi$.
In the following we focus on the case when $\varphi = \pi/2$. The ground state of every plaquette is three-fold degenerate with energy $\varepsilon(\pi/2) = -2K$, and the states are

$$|\uparrow\rangle = \frac{1}{2}\sum_{j=1}^{4} e^{-ij\pi/2}\hat{S}_j^-|\uparrow\uparrow\uparrow\uparrow\rangle \tag{4.87}$$

$$|0\rangle = \frac{1}{2}\sum_{j=1}^{4} e^{-ij\pi/2}\hat{S}_j^+\hat{S}_{j-1}^+|\downarrow\downarrow\downarrow\downarrow\rangle \tag{4.88}$$

$$|\downarrow\rangle = \frac{1}{2}\sum_{j=1}^{4} e^{-ij\pi/2}\hat{S}_j^+|\downarrow\downarrow\downarrow\downarrow\rangle \tag{4.89}$$

Since the single plaquette is SU(2) invariant, this triplet of states corresponds to the sector $S_p = 1$ where the total spin on the plaquette is $\hat{\mathbf{S}}_p = S_p(S_p+1)$.
The three states $|\uparrow\rangle_p$, $|0\rangle_p$, $|\downarrow\rangle_p$ define a system of spin-1 operators $\hat{\mathbf{J}}_p$ on every plaquette $p \in \mathsf{P}$. When $|K'| \ll K$, and without loss of generality $K > 0$, they are protected by a gap $\Delta \approx K$ from further state and K' only introduces coupling between neighboring plaquettes $\langle p, q\rangle$. Making use of SU(2) invariance, we calculated the resulting matrix elements of the term $K'\sum_{p\in\overline{\mathsf{P}}}(e^{i\varphi}\hat{P}_p + e^{-i\varphi}\hat{P}_p^\dagger)$ analytically. This leads to the following effective Hamiltonian,

$$\hat{\mathcal{H}}_{\text{eff}} = \sum_{\langle p,q\rangle}\left(\varepsilon_0 + \lambda\left[\cos(\theta)\left(\hat{\mathbf{J}}_p\cdot\hat{\mathbf{J}}_q\right) + \sin(\theta)\left(\hat{\mathbf{J}}_p\cdot\hat{\mathbf{J}}_q\right)^2\right]\right) \tag{4.90}$$

where $\varepsilon_0 = -2K + \frac{31}{72}K'$. The remaining two coupling constants are given by

$$\lambda\cos(\theta) = \frac{K'}{16}, \qquad \lambda\sin(\theta) = \frac{K'}{144}, \tag{4.91}$$

i.e. $\lambda = 0.0629K'$ and $\theta = 0.035\pi$. For these parameters, the effective Hamiltonian is very close to a Heisenberg spin-1 chain. Because of the small second term $\propto \lambda\sin(\theta) \ll \lambda\cos(\theta)$, the model interpolates between the exactly solvable AKLT model [238] and the simple Heisenberg spin-1 chain. Hence the ground state of the effective Hamiltonian (4.90) is gapped [239] and has spin-1/2 edge states [236] reflecting the symmetry protected topological order [240, 241].
We checked numerically by exact diagonalization of numerically accessible system sizes that the system remains gapped at $\varphi = \pi/2$ when the ratio K'/K is continuously tuned from 0 to 1. Since the system remains inversion symmetric around the central bond of the ladder, and this symmetry is sufficient to protect the topological character of the topological Haldane phase [241], this estab-

lishes that the homogeneous ladder with $K = K'$ is in a non-trivial symmetry-protected phase at $\varphi = \pi/2$. The SU(2) symmetry of the system is also sufficient to protect the topological Haldane phase [241].

Everything should be made as simple as possible, but not simpler.

Albert Einstein

5

One Hole in Two Dimensions

At the heart of high-temperature superconductivity is the quest to describe a single hole in a two dimensional antiferromagnet. In the Fermi-Hubbard model, strong local anti-ferromagnetic correlations persist even at finite doping. Understanding the interplay of spin and charge degrees of freedom is thus a relevant first step to study the phase diagram of the Fermi-Hubbard model in the vicinity of half-filling. In the past decades, a tremendous amount of progress has been made theoretically. However, a unifying yet simple description is still lacking. Moreover, numerical simulations are challenging in the most relevant regime of $U \gg t$.

When a single dopant is introduced into a spin background, it can be considered as a mobile impurity which becomes dressed by magnetic fluctuations and forms a new quasi-particle: a magnetic polaron. In the case of a hole doped into a Heisenberg anti-ferromagnet, as described by the $t - J$ model, this dressing leads to strongly renormalized quasi-particle properties [242–244].

The magnetic polaron problem of a single hole moving in an AFM background is often considered to be essentially solved. Various semi-analytical and numerical techniques have been applied, and many of the key properties of magnetic polarons have been numerically established [207, 242–258]. Nevertheless, there is no agreement on the correct physical interpretation of the obtained results. Partly, this can be attributed to conflicting numerical findings, and disconnected theoretical interpretations of the different features.

Previously, the following theoretical scenarios have been discussed:

(a) *String picture*: Early on, it has been proposed that strings of over-turned spins are attached to mobile dopants in a Néel state [257, 259–265]. This predicts the scaling of the ground state energy $E_0 \simeq -2\sqrt{3}t + c_0 t^{1/3} J^{2/3}$ of a single hole at $t \gg J$, as discussed in section 5.1.1 below. The string picture also predicts the existence of vibrationally excited states, whose energies should scale as $E_n = -2\sqrt{3}t + c_n t^{1/3} J^{2/3}$ – in accordance with numerical observations [253, 254]. Recent ultracold atom experiments measured spin-spin correlation functions [5, 266], as discussed in chapter 6, and spin-charge correlations [267], see also section 5.3, which also support the string picture.

(b) *Parton picture*: Based on phenomenological grounds and numerical evidence, Béran et al. [268] proposed the parton picture, in which mobile dopants are described by fractionalized (heavy) spinons, carrying the spin quantum number, and (light) chargons, carrying its charge. In a subsequent work [269], Laughlin drew an analogy with the 1D Fermi-Hubbard model and suggested that the low-energy ARPES spectrum in cuprates can also be interpreted in terms of point-like spinons and chargons, possibly interacting through a weakly attractive force. Scenarios with spin-charge separation as envisioned by Anderson [30], with a quasi-particle weight $Z = 0$ and as found in 1D, can be ruled out numerically [254] at infinitesimal doping. In principle, the partons could be confined, or form a molecular bound state in a deconfined fractionalized Fermi liquid [270, 271]). Here, we consider the case where spinons and chargons form a bound state. In the parton picture, the dispersion relation of the one-hole ground state is determined by the spinon dispersion, which must have a bandwidth $W_s = \mathcal{O}(J)$ dominated by spin-exchange. In order to make quantitative predictions, detailed knowledge about the parton dispersions and their microscopic interactions is required; this is typically beyond the scope of phenomenological descriptions.

(c) *Polaron picture*: The most widely used microscopic picture so far, has been the polaron scenario [242–244, 246–250]. As the mobile dopant moves through the AFM, one assumes that it interacts with collective magnon excitations. This picture should not be considered to be separate from (a) and (b): For example, strong interactions with magnons can describe strings of over-turned spins attached to the dopant. The strong renormalization of the bandwidth of the dopant from $\mathcal{O}(t)$ to the observed $\mathcal{O}(J)$ is for example predicted in the magnetic polaron picture, although without identifying a clear physical mechanism. This is a general disadvantage of the polaron picture: when $t > J$ the system is so strongly coupled that all predictions require advanced numerics or uncontrolled approximations. While the polaron picture per se is certainly correct, it is of little help in the identification of simpler constituents of these polarons.

Here, we establish a unifying physical picture, which is able to explain the rich phenomenology in the ground state, as well as the spectrum and dynamics at strong couplings $t \gg J$. We combine the parton and string pictures of magnetic polarons, by arguing that the latter are composed of spinons and chargons connected by universal (geometric) strings, as introduced below in section 5.1. Importantly, we provide quantitative descriptions of both ingredients, including a microscopic trial wavefunction [4, 272], see section 5.1.

We go beyond earlier phenomenological studies of partons and demonstrate that *quantitative* predictions of the spinon properties are possible. Our starting point is a parton theory of the *undoped* Heisenberg AFM. Specifically, we focus on fermionic $U(1)$ Dirac spinons: These have previously lead to accurate variational predictions [273, 274] (building upon Anderson's resonating valence bond paradigm [30, 212]), and they have recently been proposed to provide a universal description of a larger class of quantum AFMs [275]. For example, the shape of the magnetic polaron dispersion, with its minimum at the nodal point, is inherited from the optimized spinon mean-field state of the Heisenberg AFM [4]. Similar observations were made in Refs. [276, 277], but without including geometric strings.

Note that for many of the results in the subsequent sections and in chapter 6, we do not need any insights about the spinon properties, but instead apply the frozen spin approximation (see below) to snapshots of the un-doped parent state.

In this chapter, we describe various approaches we took to tackle the problem. We numerically calculate the ground state of the $t-J$ model with a single hole using DMRG, and investigate different spin-charge correlations. We simulate the dynamics after the creation of a hole in the ground state of the Heisenberg model using a matrix product operator based method. In both cases, the numerical results can be understood in the framework of the geometric string theory. We start here by explaining the geometric string theory (GST) and the frozen spin approximation (FSA), which constitute a simple and illustrative picture to interprete our findings. Inspired by the geometric string theory, we introduce an algorithm to search for string patterns in snapshots of the quantum state. In the case of the $t-J_z$ model, these string patterns can be retrieved almost exactly. We present numerical as well as semi-analytical results for the ground state properties and the dynamics after the creation of a hole in terms of hole position, spin and spin-charge correlation functions. We discuss the spectral function, a common observable in conventional solid state experiments.

5.1 Geometric String Theory and Frozen Spin Approximation

This section is based on the publications

- Fabian Grusdt, Marton Kanasz-Nagy, Annabelle Bohrdt, Christie S. Chiu, Geoffrey Ji, Markus Greiner, Daniel Greif, Eugene Demler: "Parton theory of magnetic polarons: Mesonic res-

onances and signatures in dynamics" – Phys. Rev. X 8, 011046 (2018) [arXiv:1712.01874]

- Fabian Grusdt, Annabelle Bohrdt, and Eugene Demler:"Microscopic spinon-chargon theory of magnetic polarons in the t-J model" – Phys. Rev. B 99, 224422 (2019) [arXiv:1901.01113]
- Annabelle Bohrdt, Eugene Demler, Frank Pollmann, Michael Knap, and Fabian Grusdt:"Parton theory of ARPES spectra in anti-ferromagnetic Mott insulators" – Phys. Rev. B 102, 035139 [arXiv:2001.05509]

Structure, text and figures have been rearranged and adapted here.

The geometric string theory is based on earlier work by Beran and others [257, 259–263, 268]. Most importantly, the geometric string theory establishes a connection between the undoped system, here the antiferromagnetic parent state, and the strongly correlated quantum states at finite doping. In this section we consider a single hole and its properties. In section 6, we apply the same approach at finite doping and treat all holes independently of each other and achieve remarkable agreement for all spin-based quantities considered. Without taking into account any correlations between different holes, the geometric string theory allows us to predict the doping dependence of observables like the staggered magnetization, spin correlations as well as the more involved patterns dicussed below.

A single dopant introduced into a spin background can be considered as a mobile impurity, or a polaron. The dressing cloud of the polaron is due to magnetic fluctuations and the new quasi-particle is therefore also called magnetic or spin polaron. Here, we mainly consider a hole doped into an antiferromagnet, where the dressing by magnon fluctuations results in a strong renormalization of the quasi-particle properties [197, 243]. Beran et al. [268] were the first to propose a parton picture of the magnetic polaron, which describes the magnetic polaron as a composite similar to mesons formed by quark-antiquark pairs in high-energy physics. In the case of a hole in an antiferromagnet, the meson-like bound state is formed by a heavy spinon carrying the spin quantum number and a light chargon carrying the charge. The partons are connected by so-called geometric strings of displaced spins. The parton construction is a refinement of the commonly used magnetic polaron picture, which is particularly useful to describe and understand the microscopic structure of the magnetic polaron in real space. These real space properties can often be directly probed by state-of-the art quantum gas microscope experiments.

Within the geometric string theory considered in this thesis, we use the frozen spin approximation (FSA): the motion of the hole merely displaces the spins on its trajectory without changing their quantum states or their entanglement with each other or the remaining spins. As the chargon moves along a given trajectory starting from the spinon, a string of displaced spins is left behind. This means that the spins along the strings change their positions in the lattice while remain-

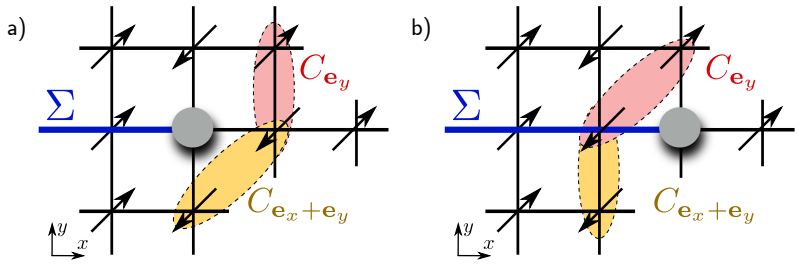

Figure 5.1.1: Frozen spin approximation. In the approximate FSA basis we only allow processes where the motion of the chargon displaces the surrounding spins without changing their quantum states. As a result, nearest neighbor correlations $C_{\mathbf{e}_y}$ – red – (next-nearest neighbor correlations $C_{\mathbf{e}_x+\mathbf{e}_y}$ – yellow – respectively) in the frozen spin background a) contribute to next-nearest neighbor correlators (nearest neighbor correlators respectively) measured in states with longer string lengths b).

ing in the same quantum state. The geometric string theory thus provides a generalization of the squeezed space used in the description of one dimensional systems in chapter 4 to two dimensions: the squeezed space labels of the spins correspond to their original lattice sites before the chargon is introduced. The motion of the chargon along a string Σ then changes the lattice geometry and thus the squeezed space labels no longer correspond to the actual lattice sites occupied by the spins. The connectivity of the lattice is therefore changed by the chargon motion and spins which are nearest neighbors in squeezed space can become next nearest neighbors in the actual lattice. Consequently, nearest neighbor correlations in the frozen spin background contribute to next nearest neighbor correlations measured in the physical lattice and vice versa, see Fig. 5.1.1. For example, in Fig. 5.1.1, the spin operator located at site $\tilde{\mathbf{j}}$ initially, becomes $\tilde{\mathbf{S}}_{\tilde{\mathbf{j}}} = \hat{\mathbf{S}}_{\tilde{\mathbf{j}}-\mathbf{e}_x}$ when the chargon moves from $\tilde{\mathbf{j}} - \mathbf{e}_x$ to $\tilde{\mathbf{j}}$ along the string Σ. Due to the opposite sign and different magnitude of these spin correlations, the next nearest neighbor correlators close to the dopant are strongly suppressed and can even change their sign as discussed in sections 5.3 and 6.

Most theories for the $t-J$ model start from the weak coupling regime, where the hole tunneling t is small compared to the spin exchange coupling J. We consider the opposite limit: for $t \gg J$, but before the Nagaoka regime is reached at $t \approx 20J$, there is not sufficient time for the spins in squeezed space to adjust to the fluctuating lattice geometry introduced by the chargon motion. The frozen spin approximation can be understood as an analogon to the Born Oppenheimer approximation: we first obtain the background of the slow spin system and then solve the problem of the fast chargon on top of this background, where we assume that the spin system cannot react to this fast motion.

The shape and orientation of the geometric string are strongly fluctuating – the string is in a superposition of many different possible configurations, the total number of which grows exponentially

with the average length of the string. This can be seen in the Bethe lattice picture in Fig. 5.1.2: with increasing depth in the Bethe lattice, the number of nodes at this depth increases. As a consequence, after averaging over all different string configurations, the actual effect of the string on a given spin in squeezed space is strongly reduced. This provides an additional justification for the frozen spin approximation.

5.1.1 Formal description

To make the single-occupancy condition built into the $t-J$ model explicit, we use a parton representation, see also section 4.2.6,

$$\hat{c}_{\mathbf{j},\sigma} = \hat{h}^{\dagger}_{\mathbf{j}} \hat{f}_{\mathbf{j},\sigma}. \tag{5.1}$$

Here $\hat{h}_{\mathbf{j}}$ is a bosonic chargon operator and $\hat{f}_{\mathbf{j},\sigma}$ is a $S = 1/2$ fermionic spinon operator [28, 117]. The physical Hilbert space is defined by all states satisfying

$$\sum_{\sigma} \hat{f}^{\dagger}_{\mathbf{j},\sigma} \hat{f}_{\mathbf{j},\sigma} + \hat{h}^{\dagger}_{\mathbf{j}} \hat{h}_{\mathbf{j}} = 1, \quad \forall \mathbf{j}. \tag{5.2}$$

We start from the half-filling ground state $|\Psi_0\rangle$ of the undoped spin Hamiltonian $\hat{\mathcal{H}}_J$, Eq. (3.10), and consider cases where $|\Psi_0\rangle$ has strong AFM correlations. The ground state of the Heisenberg model Eq. (3.10) has long-range AFM order, but the presence of strong and short-ranged AFM correlations would be sufficient to justify the approximations made below.
The simplest state doped with a single hole is obtained by applying $\hat{c}_{\mathbf{j}^s,\bar{\sigma}}$ to $|\Psi_0\rangle$, where $\bar{\cdot}$ reverses the spin: $\overline{\uparrow} = \downarrow, \overline{\downarrow} = \uparrow$. This state,

$$|\mathbf{j}^s, \sigma, 0\rangle = \hat{c}_{\mathbf{j}^s,\bar{\sigma}} |\Psi_0\rangle = \hat{h}^{\dagger}_{\mathbf{j}^s} \hat{f}_{\mathbf{j}^s,\bar{\sigma}} |\Psi_0\rangle, \tag{5.3}$$

with a spinon and a chargon occupying the same lattice site $\mathbf{j}^s$, defines the starting point for our analysis of the parton bound state constituting the magnetic polaron. In the following we assume that $t \gg J$, which justifies a Born-Oppenheimer ansatz: first the initially created valence spinon at site $\mathbf{j}^s$ will be fixed and we determine the fast chargon fluctuations. Similar to nuclear physics, these fluctuations can involve virtual spinon anti-spinon pairs.
The main assumption in the geometric string theory is that we can approximate the Hilbert space of a single hole in a spin system as a tensor product

$$\mathcal{H} = \mathcal{H}_{spinon} \otimes \mathcal{H}_{\Sigma}, \tag{5.4}$$

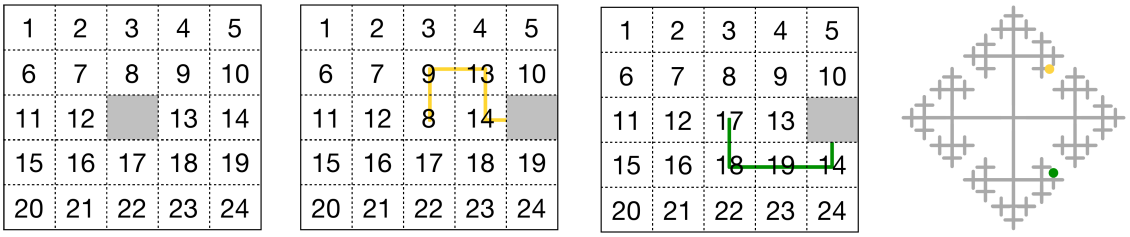

Figure 5.1.2: Bethe lattice description. The spins are labeled according to their initial lattice sites. The motion of the hole then re-arranges the spins, leading to a different spin configuration for different paths taken. We map the different strings to sites on the Bethe lattice. The sites on the Bethe lattice correspond to different arrangements of the spins labeled by their initial lattice sites.

where $\mathcal{H}_{spinon}$ is spanned by all one spinon states and $\mathcal{H}_\Sigma$ is the Hilbert space of geometric strings. Every string state can be represented by a site on the Bethe lattice with coordination number $z = 4$, Fig. 5.1.2. Crucially, even though the hole might end up on the same position, different paths taken lead to different spin configurations and thus different sites on the Bethe lattice. In particular, within the frozen spin approximation, the spins keep their quantum state and their entanglement with each other, but are displaced along the trajectory. Therefore, $\mathcal{H}_\Sigma$ is equivalent to a free particle hopping on a Bethe lattice. A state $|\mathbf{j}^s, \sigma\rangle|\Sigma\rangle$ in the approximate Hilbertspace is – up to normalization – associated with a state in the Hilbertspace of the $t-J$ model as

$$|\mathbf{j}^s, \sigma, \Sigma\rangle \sim |\Psi(\Sigma, \mathbf{j}^s, \sigma)\rangle = \hat{G}_\Sigma \hat{h}^\dagger_{\mathbf{j}^s} \hat{f}_{\mathbf{j}^s,\bar{\sigma}} |\Psi_0\rangle. \tag{5.5}$$

Here the string operator, defined by

$$\hat{G}_\Sigma = \prod_{\langle \mathbf{i},\mathbf{j}\rangle \in \Sigma} \left(\hat{h}^\dagger_{\mathbf{i}} \hat{h}_{\mathbf{j}} \sum_{\tau=\uparrow,\downarrow} \hat{f}^\dagger_{\mathbf{j},\tau} \hat{f}_{\mathbf{i},\tau} \right), \tag{5.6}$$

creates the geometric string by displacing the spin states along Σ. The product $\prod_{\langle \mathbf{i},\mathbf{j}\rangle \in \Sigma}$ is taken over all links $\langle \mathbf{i}, \mathbf{j}\rangle$ which are part of the string Σ, starting from the valence spinon position $\mathbf{j}^s$.
In a 2D classical Néel state, $|\Psi_0^N\rangle = |\ldots \uparrow\downarrow\uparrow \ldots\rangle$, most string states $|\mathbf{j}^s, \sigma, \Sigma\rangle$ are mutually orthonormal. Specific configurations, so-called Trugman loops [261], constitute an exception, but within an effective tight-binding theory it has been shown that this only causes a weak renormalization of the spinon dispersion [3]. Since the ground state $|\Psi_0\rangle$ of the infinite 2D Heisenberg model has strong AFM correlations, similar to a classical Néel state, we expect that the assumption that string states form an orthonormal basis remains justified. To check this, we calculated all such states with string lengths up to $\ell \leq 4$ and arbitrary spinon positions $\mathbf{j}^s$ using exact diagonalization (ED) in a

4×4 system. We found that $|\langle \mathbf{j}^{s'}, \sigma, \Sigma' | \mathbf{j}^{s}, \sigma, \Sigma \rangle|^2 < 0.06$ unless $\Sigma = \Sigma'$ or Σ and Σ' are related by a Trugman loop.

Now we will follow the example of Rokhsar and Kivelson: They introduced their celebrated dimer model [278] by defining a new basis which reflects the structure of the low-energy many-body Hilbert space in a class of microscopic spin systems. Similarly, we will postulate in the context of the FSA that all string states are mutually orthonormal. This defines the new basis of string states $|\mathbf{j}^{s}, \sigma, \Sigma\rangle$ which is at the heart of the FSA. Note, however, that we will return to the full physical Hilbert space of the original $t-J$ model later.

In order to construct the Hamiltonian in the approximate Hilbert space, we need to calculate the matrix elements

$$\langle \psi\left(\Sigma_2, \mathbf{j}_2^{s}, \sigma_2\right) | \hat{H}_{t-J} | \psi\left(\Sigma_1, \mathbf{j}_1^{s}, \sigma_1\right) \rangle. \tag{5.7}$$

This leads to a direct hopping with amplitude t between neighboring sites of the Bethe lattice,

$$\hat{H}_{\Sigma} = -t \sum_{\langle \Sigma_1, \Sigma_2 \rangle} \left(|\Sigma_2\rangle\langle\Sigma_1| + \text{h.c.} \right), \tag{5.8}$$

a potential energy term

$$\hat{H}_{pot} = \sum_{\Sigma} V_J\left(\Sigma\right) |\Sigma\rangle\langle\Sigma| \tag{5.9}$$

with

$$V_J\left(\Sigma\right) = \langle \psi\left(\Sigma, \mathbf{j}_2^{s}, \sigma\right) | \hat{H}_J | \psi\left(\Sigma, \mathbf{j}_2^{s}, \sigma\right) \rangle, \tag{5.10}$$

and a tight-binding Hamiltonian

$$\hat{H}_{sp} = \sum_{\sigma} \sum_{\mathbf{i},\mathbf{j}} J_{\mathbf{i},\mathbf{j}} \left(\hat{s}^{\dagger}_{\mathbf{j},\sigma} \hat{s}_{\mathbf{i},\sigma} + \text{h.c.} \right) = \sum_{\sigma} \sum_{\mathbf{k}} \omega_{sp}(\mathbf{k}) \hat{s}^{\dagger}_{\mathbf{k},\sigma} \hat{s}_{\mathbf{k},\sigma}. \tag{5.11}$$

In the approximation considered in this thesis, other matrix elements are neglected. The effective Hamiltonian in the approximate Hilbert space is thus

$$\hat{H}_{eff} = \hat{H}_{\Sigma} + \hat{H}_{pot} + \hat{H}_{sp}. \tag{5.12}$$

Linear string theory

In the linear string theory, we approximate the potential energy $V_{pot}(\Sigma)$ by its expression for straight strings

$$V_{pot}(\Sigma) \approx \frac{dE}{dl} l_\Sigma + g_0 \delta_{l_\Sigma,0} + \mu_h, \tag{5.13}$$

with the linear string tension

$$\frac{dE}{dl} = 2J\left(C_{\mathbf{e}_x+\mathbf{e}_y} - C_{\mathbf{e}_x}\right), \tag{5.14}$$

where

$$C_{\mathbf{d}} = \langle \psi_0 | \hat{\mathbf{S}}_{\mathbf{d}} \cdot \hat{\mathbf{S}}_0 | \psi_0 \rangle \tag{5.15}$$

are spin-spin correlation functions in the undoped ground state. The second term in Eq. 5.13 contributes only for string lengths $l_\Sigma = 0$ and describes a weak spinon-chargon attraction $g_0 = -J(C_{2\mathbf{e}_x} - C_{\mathbf{e}_x})$. The last term is an overall energy offset, $\mu_h = J(1 + C_{2\mathbf{e}_x} - 5C_{\mathbf{e}_x})$. Here, we assume fourfold rotational symmetry of $|\psi_0\rangle$, which implies that $C_{\mathbf{e}_x} = C_{\mathbf{e}_y}$.
We can then obtain the ground or thermal state of the system by solving the hopping problem on the Bethe lattice in the presence of the linear string potential 5.13. As in Refs. [3, 259, 260, 262], we obtain approximations to the spinon-chargon binding energy $E_{\mathrm{sc}}^{\mathrm{FSA}}$ and the bound state wavefunction,

$$|\psi_{\mathrm{sc}}^{\mathrm{FSA}}(\mathbf{j}^s, \sigma)\rangle = \sum_\Sigma \psi_\Sigma^{\mathrm{FSA}} |\mathbf{j}^s, \sigma, \Sigma\rangle. \tag{5.16}$$

The depth in the Bethe lattice corresponds to the string length. Later we will use the probabilities for different depths in the Bethe lattice for example in the ground state to obtain a string length distribution. When we compare the string theory to numerical or experimental data, we simulate strings by sampling string lengths from this distribution.

Mapping to one dimension

The Schrödinger equation for the holon moving between the sites of the Bethe lattice can be written in compact form as

$$t \sum_s \psi_{\ell+1,s} + t\psi_{\ell-1} + V_\ell \psi_\ell = E\psi_\ell. \tag{5.17}$$

Here the linear string potential is given by $V_\ell = V_{pot}(\Sigma)$, with $V_{pot}(\Sigma)$ from Eq. 5.13 and $\ell = l_\Sigma$. In general the wave function $\psi(\Sigma)$ depends on the index $\Sigma \in \mathrm{BL}$ corresponding to a site on the Bethe lattice, or equivalently a string Σ. A useful parameterization of $\Sigma \in \mathrm{BL}$ is provided by specifying the length ℓ of the string as well as ℓ angular coordinates $\mathbf{s} = s_1, \ldots, s_\ell$ with values $s_1 = 1 \ldots z$ and $s_j = 1 \ldots z-1$ for $j > 1$. This formalism is used in Eq. (5.17). In Eq. (5.17) only the dependence on

$s = s_\ell$ is shown explicitly. Because we started from the LST, the potential V_ℓ is independent of $\mathbf{s}$. The normalization condition is given by

$$\sum_{\Sigma \in \mathrm{BL}} |\psi(\Sigma)|^2 = \sum_{\ell,\mathbf{s}} |\psi_{\ell,\mathbf{s}}|^2 = 1 \tag{5.18}$$

where the sum includes all sites of the Bethe lattice.

The simplest symmetric wave functions $\psi(\Sigma)$ only depend on ℓ and are independent of $\mathbf{s}$. We here only consider this case, which realizes the rotational ground state of the magnetic polaron. It is useful to re-parametrize the wave function ψ_ℓ by writing

$$\psi_{\ell,s} = \underbrace{\frac{(-1)^\ell}{2}(z-1)^{(1-\ell)/2}}_{=\lambda_\ell}\, \varphi_\ell, \qquad \ell \geq 1, \tag{5.19}$$

$$\psi_0 = \varphi_0. \tag{5.20}$$

The normalization for the new wave function φ_ℓ is given by the usual condition, $\sum_{\ell=0}^{\infty} |\varphi_\ell|^2 = 1$, corresponding to a single particle in a semi-infinite one-dimensional system with lattice sites labeled by ℓ.

The Schrödinger equation (5.17) for the 1D holon wave function φ_ℓ becomes [259],

$$-t^* \frac{2}{\sqrt{z-1}} \varphi_1 + V_0 \varphi_0 = E\varphi_0, \tag{5.21}$$

$$-t^* \left(\varphi_2 + \frac{2}{\sqrt{z-1}} \varphi_0 \right) + V_1 \varphi_1 = E\varphi_1, \tag{5.22}$$

$$-t^* \left(\varphi_{\ell+1} + \varphi_{\ell-1} \right) + V_\ell \varphi_\ell = E\varphi_\ell, \qquad \ell \geq 2. \tag{5.23}$$

Away from the origin $\ell = 0$, the effective hopping constant t^* in the 1D model is given by [259, 260]

$$t^* = t\sqrt{z-1}. \tag{5.24}$$

The tunneling rate between $\ell = 0$ and 1, on the other hand, is given by $2t^*/\sqrt{z-1} = 2t$.

We consider the continuum limit of the effective 1D model where $\varphi_\ell \to \varphi(x)$ and $x \geq 0$ becomes a continuous variable, see Ref. [259]. This is a valid description in the strong coupling limit, where $t \gg J$. For simplicity we will ignore deviations of V_ℓ from the purely linear form at $\ell = 0$, as well as the renormalization of the tunneling $t^* \to 2t$ from site $\ell = 0$ to 1. As a result one obtains the Schrödinger equation [259]

$$\left(-\frac{\partial_x^2}{2m^*} + V(x) \right) \varphi(x) = E\varphi(x), \tag{5.25}$$

where the effective mass is $m^* = 1/2t^*$, and the confining potential is given by $V(x) = -2t^* + 4JS^2x$.

By simultaneous rescaling of lengths, $x \to \lambda^{1/3}x$, and the potential $J \to \lambda J$, one can show that the eigen-energies E in the continuum limit are given by [243, 259, 262]

$$E_n(t/J) = -2t\sqrt{z-1} + ta_n(t/J)^{-2/3}, \tag{5.26}$$

for some numerical coefficients a_n.

The scaling of the magnetic polaron energy like $t^{1/3}J^{2/3}$ is considered a key indicator for the string picture. It has been confirmed in different numerical works for a wide range of couplings [207, 246, 248, 254, 279], both in the $t-J$ and the $t-J_z$ models. In section 5.3, we show that the average string pattern length scales with $(t/J)^{1/3}$, as expected from these considerations. Diagrammatic Monte Carlo calculations by Mishchenko et al. [254] have moreover confirmed for the $t-J$ model that the energy $-2\sqrt{3}t$ is asymptotically approached when $J \to 0$. However, for extremely small J/t on the order of 0.03 it is expected [255] that the ground state forms a ferromagnetic polaron [110] with ferromagnetic correlations developing inside a finite disc around the hole. In this regime Eq. (5.26) is no longer valid.

Using ultracold atoms in a quantum gas microscope the universal scaling of the polaron energy can be directly probed, e.g. in the $t-J_z$ model, when J_z/t is varied and for temperatures $T < J_z$. To this end the spin part of the Hamiltonian $\langle\hat{\mathcal{H}}_{J_z}\rangle$ can be directly measured by imaging the spins around the hole. Note that $\langle\hat{\mathcal{H}}_{J_z}\rangle$ has the same universal scaling with $t^{1/3}J_z^{2/3}$ as the ground state energy at strong couplings.

The excited states of the effective 1D Schrödinger equation (5.25) correspond to vibrational resonances of the meson formed by the spinon-holon pair, labeled by the vibrational quantum number n. In a semi-classical picture, they can be understood as states where the string length is oscillating in time. In section 5.4, we find evidence for these vibrational excitations in the spectral function.

Within LST the entire spectrum of the magnetic polaron can easily be derived by making use of the symmetries of the holon Hamiltonian on the Bethe lattice. Around the central site, where $\ell = 0$, we obtain a C_4 symmetry. The C_4-rotation operator has eigenvalues $e^{i\pi m_4/2}$ with $m_4 = 0, 1, 2, 3$ and the eigenfunctions depend on the first angular variable s_1 in the following way: $e^{i\pi m_4 s_1/2}$. So far we assumed that the wave function ψ_ℓ only depends on the length of the string ℓ, which corresponds to an eigenvalue of C_4 which is $m_4 = 0$.

In addition, every node of the Bethe lattice at $\ell > 0$ is associated with a P_3 permutation symmetry. The P_3-permutation operator has eigenvalues $e^{i2\pi m_3/3}$ with $m_3 = 0, 1, 2$ and the eigenfunctions depend on the j-th angular variable s_j, $j > 1$, in the following way: $e^{i2\pi m_3 s_j/3}$. The symmetric wave function ψ_ℓ discussed so far had $m_3 = 0$ for all nodes.

In section 5.2.2, we compare the string length distributions in the ground state and the first excited rotational state and retrieve the corresponding string patterns from snapshots.

Non-linear string theory

Instead of the approximation for the potential energy presented above, we can also obtain the exact value of $V_{pot}(\Sigma)$ for each Σ. In this case, we start from the Heisenberg ground or thermal state. For the numerical results on a cylinder presented below, we use the Heisenberg ground state for the same system size and boundary conditions. From this *parent* state, we calculate the spin correlation functions for all possible distances. Every possible string corresponds to a new configuration of the spins, which are labeled by their intitial position, see Fig. 5.1.2. For each string, we can obtain the corresponding potential energy $V_{pot}(\Sigma)$ by calculating the difference between the initial and final values of $\langle \mathbf{S_i} \cdot \mathbf{S_j} \rangle$ on neighboring sites $\mathbf{i}, \mathbf{j}$. For the latter, we possibly need correlation functions at arbitrary distances, which we calculated before.
While this approach is in principle slightly more exact than the approximation made in the linear string theory, we are here limited to string lengths of $l \leq 11$. Even though we only have to consider a single particle moving in a potential, the number of sites in the Bethe lattice and thus the dimension of the Hilbert space grow as $4 \cdot 3^{l-1}$.

Fermionic spinon representation

We consider the 2D Heisenberg Hamiltonian $\hat{\mathcal{H}}_J$ in Eq. (3.10) at half filling. Its ground state spontaneously breaks the SU(2) spin symmetry and has long-range Néel order [280]. The corresponding low-energy excitations – spin-1 magnons constituting the required Goldstone mode – are most commonly described by a bosonic representation of spins, using e.g. Schwinger- or Holstein-Primakoff bosons. Recently it has been argued that the high-energy excitations of the AFM ground state can be captured more accurately by a fermionic spinon representation [274] however.
The fermionic spinon representation which we use in Eq. (5.1) is partly motivated by analogy with the 1D $t-J$ model, where spinons can be understood as forming a weakly interacting Fermi sea [2, 212, 213], see section 4.2. On the other hand, Marston and Affleck [281] have shown in 2D that the ground state of the Heisenberg model in the large-N limit corresponds to the fermionic π-flux, or d-wave [212], state of spinons. For our case of interest, $N = 2$, the π-flux state is not exact, but it can be used as a starting point for constructing more accurate variational wavefunctions. To this end we consider a general class of fermionic spinon mean-field states $|\Psi_{\mathrm{MF}}(B_{\mathrm{st}}, \Phi)\rangle$, defined as the

ground state at half filling of the following Hamiltonian,

$$\hat{\mathcal{H}}_{f,\mathrm{MF}} = -J_{\mathrm{eff}} \sum_{\langle \mathbf{i},\mathbf{j}\rangle,\sigma} \left(e^{i\theta^{\Phi}_{\mathbf{i},\mathbf{j}}} \hat{f}^{\dagger}_{\mathbf{j},\sigma} \hat{f}_{\mathbf{i},\sigma} + \mathrm{h.c.} \right) + \frac{B_{\mathrm{st}}}{2} \sum_{\mathbf{j},\sigma} (-1)^{j_x+j_y} \hat{f}^{\dagger}_{\mathbf{j},\sigma} (-1)^{\sigma} \hat{f}_{\mathbf{j},\sigma}, \tag{5.27}$$

with Peierls phases $\theta^{\Phi}_{\mathbf{i},\mathbf{j}} = (-1)^{j_x+j_y+i_x+i_y}\Phi/4$ corresponding to a staggered magnetic flux $\pm\Phi$ per plaquette and a staggered Zeeman splitting $\sim B_{\mathrm{st}}$ which can be used to explicitly break the $SU(2)$ symmetry.

A trial wavefunction for the $SU(2)$ symmetric π-flux state is obtained by applying the Gutzwiller projection [30, 212] to the mean-field state with $\Phi = \pi$ and $B_{\mathrm{st}} = 0$, i.e. $|\Psi_{\pi}\rangle = \hat{\mathcal{P}}_{\mathrm{GW}}|\Psi_{\mathrm{MF}}(0,\pi)\rangle$. Although it features no long-range AFM order, this trial state leads to a very low variational energy at half filling and it is also often considered as a candidate state at finite doping [282]. In chapter 6, we sample snapshots from the Gutzwiller-projected thermal density matrix of the mean-field Hamiltonian (5.27) with these parameters and refer to it as π-flux state. Another extreme is the $\Phi = 0$ uniform RVB state with $B_{\mathrm{st}} = 0$, i.e. $|\Psi_0\rangle = \hat{\mathcal{P}}_{\mathrm{GW}}|\Psi_{\mathrm{MF}}(0,0)\rangle$, which also yields a reasonable variational energy at half filling.

The best variational wavefunction of the general type $\hat{\mathcal{P}}_{\mathrm{GW}}|\Psi_{\mathrm{MF}}(B_{\mathrm{st}},\Phi)\rangle$ has been found to have a non-zero staggered field $B_{\mathrm{st}} \neq 0$, consistent with the broken $SU(2)$ symmetry of the true ground state, and staggered flux $0 < \Phi < \pi$ [273]. More recent calculations determined the optimal variational parameters of this "staggered-flux + Néel" (SF+N) trial state

$$|\Psi_{\mathrm{SF+N}}\rangle = \hat{\mathcal{P}}_{\mathrm{GW}}|\Psi_{\mathrm{MF}}(B^{\mathrm{opt}}_{\mathrm{st}},\Phi^{\mathrm{opt}})\rangle \tag{5.28}$$

to be $\Phi^{\mathrm{opt}} \approx 0.4\pi$ and $B^{\mathrm{opt}}_{\mathrm{st}}/J_{\mathrm{eff}} \approx 0.44$ [274]. The corresponding variational energy per particle $E^{\mathrm{SF+N}}_0/L^2 = -0.664J$ is very close to the true ground state energy $E_0/L^2 = -0.669J$ known from first-principle Monte-Carlo simulations [283].

The main shortcoming of mean-field spinon theories as in Eq. (5.27) is that they neglect gauge fluctuations. These lead to spinon confinement in the ground state of the 2D Heisenberg model [28] and, hence, free spinon excitations as described by Eq. (5.27) cannot exist individually. Indeed, if the Gutzwiller projection method is used to define a variational wavefunction, the underlying mean-field spinon dispersion is usually not considered to have a concrete physical meaning. We emphasize, however, that a single spinon can exist in combination with a chargon if they form a meson. In this case, which is of primary interest to us, we argue that the spinon dispersion (5.29) has a concrete physical meaning.

The main difference between spinon models with different values of the staggered flux Φ is their

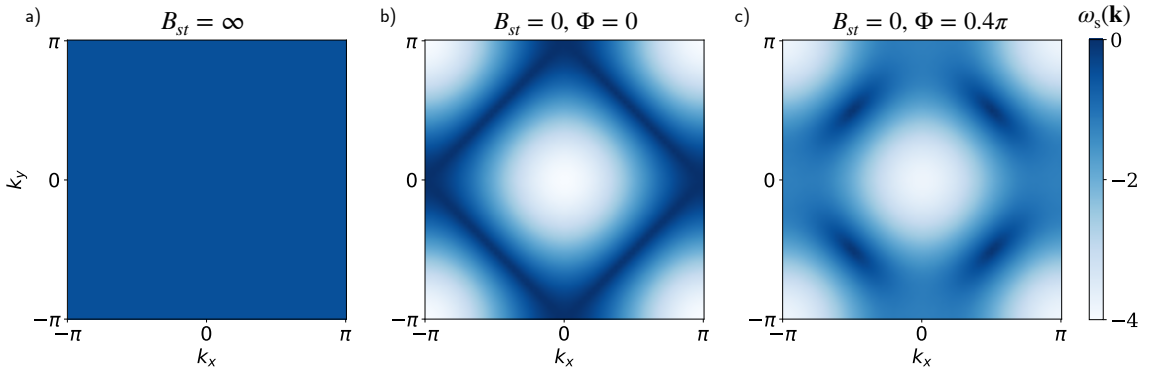

Figure 5.1.3: Mean-field spinon dispersion. $\omega_s(\mathbf{k})$ from Eq. (5.29) is shown in the following limiting cases: a) $B_{st}/J_{eff} \to \infty$, b) $B_{st} = \Phi = 0$, c) $B_{st} = 0$ and $\Phi = 0.4\pi$. The color bar is indicated on the right.

dispersion relation. From the Hamiltonian Eq. (5.27) we obtain the mean-field spinon dispersion

$$\omega_s(\mathbf{k}) = -\sqrt{4J_{eff}^2 \left|\cos(k_x)e^{-i\frac{\Phi}{4}} + \cos(k_y)e^{i\frac{\Phi}{4}}\right|^2 + \frac{B_{st}^2}{4}}. \tag{5.29}$$

For $B_{st} = 0$ and $\Phi \neq 0$ it has Dirac points at the nodal point $\mathbf{k} = (\pi/2, \pi/2)$. A finite staggered magnetic field B_{st} opens a gap everywhere. In this case the dispersion has a minimum at $\mathbf{k} = (\pi/2, \pi/2)$, unless $\Phi = 0$ when the dispersion is degenerate along the edge of the magnetic zone boundary. The energy difference between the anti-nodal point $(0, \pi)$ and the nodal point $(\pi/2, \pi/2)$ is zero for $\Phi = 0$, see Fig. 5.1.3, and maximal when $\Phi = \pi$.

For the optimal variational parameters Φ^{opt} and B_{st}^{opt}, the shape of the mean-field spinon dispersion relation (5.29) closely resembles the known dispersion of a single hole moving inside an AFM: It is weakly dispersive on the edge of the MBZ, has its minimum at $(\pi/2, \pi/2)$ and a pronounced maximum at $(0, 0)$.This is consistent with our conjecture from the spinon-chargon theory that the magnetic polaron dispersion is dominated by the spinon at strong couplings, $t \gg J$.

Trial wavefunction

We propose a trial wave function for the magnetic polaron formed by a single hole, which goes beyond Anderson's RVB paradigm by explicitly including short-range hidden string order. As in the RVB approach, we use Gutzwiller projected mean-field states of spinons as key ingredients in our trial wave function. By adding geometric strings we include short-range hidden order and take Anderson's ansatz in a new direction. Our method is not based on spin-charge separation but instead describes meson-like bound states of spinons and chargons. To obtain a complete description of the meson-like bound state constituting a hole in an AFM, we combine geometric

strings with the fermionic spinon representation. Starting from Eq. (5.5) with $|\Psi_0\rangle = |\Psi_{\mathrm{MF}}^{\mathrm{SF+N}}\rangle \equiv |\Psi_{\mathrm{MF}}(B_{\mathrm{st}}^{\mathrm{opt}}, \Phi^{\mathrm{opt}})\rangle$ we construct a translationally invariant trial wavefunction,

$$|\Psi_{\mathrm{sc}}(\mathbf{k})\rangle = \sum_{\mathbf{j}^s} \frac{(u_{\mathbf{k},\sigma,-}^{(\mathbf{j}^s)})^* e^{i\mathbf{k}\cdot\mathbf{j}^s}}{L/\sqrt{2}} \times \sum_{\Sigma} \psi_{\Sigma}\, \hat{G}_{\Sigma}\, \hat{\mathcal{P}}_{\mathrm{GW}} \hat{f}_{\mathbf{j}^s,\sigma} |\Psi_{\mathrm{MF}}^{\mathrm{SF+N}}\rangle. \tag{5.30}$$

Here $\mathbf{k}$ denotes the total lattice momentum of the spinon-chargon magnetic polaron state, and L denotes the linear system size. We dropped $\hat{h}_{\mathbf{j}}^{\dagger}$ because the state of the single chargon is fully determined by the Gutzwiller projection; $u_{\mathbf{k},\sigma,-}^{(\mathbf{j}^s)}$ denotes the cell-periodic part of a Bloch wavefunction. This ansatz is based on a mean-field model of the Heisenberg AFM with fermionic $U(1)$ Dirac spinons $\hat{f}_{\mathbf{j}^s,\sigma}$, which has attracted renewed interest recently [275]. The mean-field state

$$|\Psi_{\mathrm{MF}}^{\mathrm{SF+N}}\rangle = \prod_{\mathbf{k}\in\mathrm{MBZ}} \prod_{\sigma} \hat{f}_{\mathbf{k},\sigma,-}^{\dagger} |0\rangle \tag{5.31}$$

is a fermionic band insulator [212], where $\hat{f}_{\mathbf{k},\sigma,\mu}^{\dagger}$ creates a spinon with band index $\mu = \pm$.
In general, the values of the string wavefunction $\psi_{\Sigma} \in \mathbb{C}$ can be treated as variational parameters in Eq. (5.30), but in practice we use the result obtained explicitly from the FSA calculation in Eq. (5.16): I.e. we set ψ_{Σ} in Eq. (5.30) equal to $\psi_{\Sigma}^{\mathrm{FSA}}$ determined in Eq. (5.16). The undoped parent state $|\Psi_{\mathrm{MF}}^{\mathrm{SF+N}}\rangle$ in Eq. (5.30) can be replaced by any fermionic spinon mean-field wavefunction $|\Psi_{\mathrm{MF}}^{f}\rangle$. In particular, this allows to use Eq. (5.30) to describe spinon-chargon bound states even in phases with deconfined spinon excitations.
We recapitulate the physics of Eq. (5.30): First, the valence spinon is created in the mean-field state. At strong couplings it carries the total momentum $\mathbf{k}_{\mathrm{MP}}$ of the meson-like bound state, $\hat{f}_{\mathbf{k}_{\mathrm{MP}},\bar{\sigma}} = L^{-1}\sum_{\mathbf{j}} e^{i\mathbf{k}_{\mathrm{MP}}\cdot\mathbf{j}} \hat{f}_{\mathbf{j},\bar{\sigma}}$. The Gutzwiller projection subsequently yields a state in the physical Hilbert space,

$$\hat{\mathcal{P}}_{\mathrm{GW}} \hat{f}_{\mathbf{k}_{\mathrm{MP}},\bar{\sigma}} |\Psi_{\mathrm{MF}}^{\mathrm{SF+N}}\rangle = \sum_{\mathbf{j}^s} \sum_{a} \Phi(\mathbf{j}^s, a) \hat{h}_{\mathbf{j}^s}^{\dagger} \hat{f}_{\mathbf{j}^s,\bar{\sigma}} |a\rangle \tag{5.32}$$

where $\sum_a$ denotes a sum over all half-filled Fock states $|a\rangle$. In this new state the spinon and chargon positions $\mathbf{j}^s$ coincide. In the last step we apply the string operators $\hat{G}_{\Sigma}$ to this state and create a superposition of fluctuating geometric strings in Eq. (5.30), which captures the internal structure of the meson-like bound state. The $\mathbf{k}$-dependent physical properties of the trial wavefunction can be calculated using variational Monte Carlo sampling [4, 113].

5.2 Searching for patterns - the analysis of single snapshots

One of the most fascinating properties of quantum systems is their ability to be in a superposition state. In particular, in a quantum gas microscope, if one repeats the exact same preparation procedure and then takes a measurement, the outcome will most likely be different from realization to realization. The reason is that a quantum gas microscope measures Fock space snapshots, and each Fock space configuration is obtained with a probability given by the square of the absolute value of its amplitude in the wavefunction or density matrix. Intriguingly, in correlated quantum systems, the superposition principle can lead to hidden order: while in every single configuration, a single pattern is present, the specific patterns vary from configuration to configuration and upon averaging, the system simply appears to be less ordered.

When evaluating conventional observables, like the density or two-point correlation functions, one typically averages over many snapshots. However, assuming that the underlying patterns appear in Fock space, the projective measurements performed in quantum gas microscopes can not only restore the hidden order, but also reveal those patterns. In particular, the data provided by a quantum gas microscope contains much more information than just one- or two-point correlation functions and our goal is to make use of this information to learn something about the underlying physics. In the one dimensional case considered in section 4.3, the spin order is hidden by the hole motion. Individual snapshots show antiferromagnetic ordering with the hole at different positions. Averaging over many snapshots yields strongly suppressed two-point spin correlations. We were able to restore the antiferromagnetic order by evaluating the spin correlations in squeezed space, thus taking into account the hole position in each individual snapshot. Similar work has been done in equilibrium in Ref. [75], where the difference between real and squeezed space correlations is studied.

In the remainder of this chapter we aim to reveal underlying patterns in single snapshots of the two dimensional $t-J$ and Fermi-Hubbard model. In particular, we search for string patterns as evidence for the geometric string theory presented in section 5.1. As discussed in detail in section 5.1, the system is usually in a superposition of many different string lengths, positions and configurations. Introducing a hole in an antiferromagnet therefore leads on average to a reduction of the spin ordering. However, in individual snapshots, we can search for patterns of a string attached to the hole.

5.2.1 String pattern finding algorithms

In the following, we will outline three different algorithms to find string patterns in snapshots.

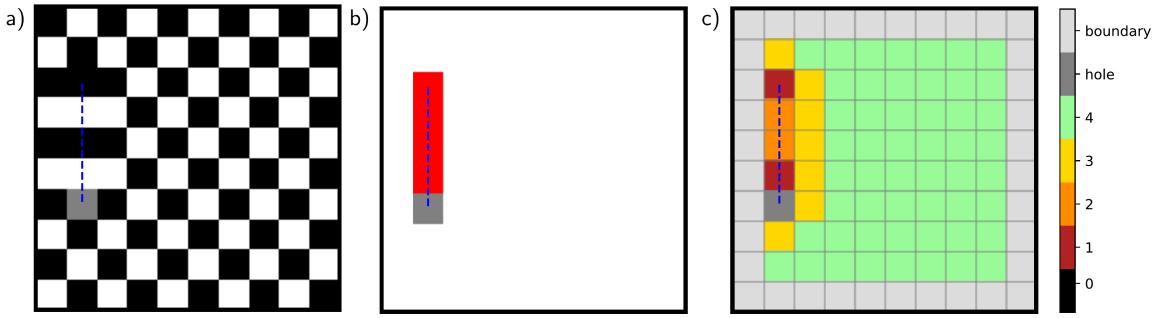

Figure 5.2.1: Different string pattern finding algorithms illustrated for a single straight string in the $t - J_z$ model. a) Exemplary snapshot, showing the spin pattern with spin ups (white), spin downs (black) and hole (gray). b) Red area method: the perfect Néel state with the same sublattice magnetization is subtracted, revealing the string as the difference, here shown in red. The gray site is the position of the hole. c) Happiness method: for each site, the happiness is the number of antiferromagnetic bonds. Starting from the hole, we identify the hole by following a certain happiness pattern as described in the main text.

Red area method

The algorithm used in most of this work is the red area method. The procedure is in principle motivated by the $t - J_z$ model, but can be applied to the isotropic $t - J$ model as well. In the latter case, there will be a background signal. In this algorithm, we consider the difference between the snapshot under consideration and the perfect Néel state with the same sublattice magnetization. This yields a set of sites which differ between the two images. We call these sites *red sites* and a connected set of such sites *red area*. A string pattern is extracted by finding the longest **non-branching** path within the red area connected to the hole.

In the experimental data analyzed in chapter 6, the positions of the holes are not known. We can therefore not straightforwardly follow this algorithm. Instead, we go through all red areas and for each of them, extract the longest non-branching path contained. The set of sites is counted as a string pattern if one end of the non-branching path is consistent with having a hole there, i.e. if the site is detected as empty. Once such a string pattern is identified and added to the list of found strings, we correct the corresponding deviation from the Néel state. This removes the sites belonging to the string pattern from the corresponding red area. If the red area had branches, red sites will remain after this removal. We continue with this algorithm until no red sites remain. The details and results of this method are discussed in section 6.4 and A.4.

In the simplified version of the red area method, we consider the number of sites in the red area connected to the hole, and do not restrict the string patterns to non-branching objects. The results from this method are compared to the original red area method and the happiness method in section A.4.

Happiness method

A different approach to find string patterns is based on analyzing the four bonds of each site. Nearby order is characterized by labeling each site with the number of anti-aligned bonds it has with its nearest neighbors, termed the *happiness* of that site. For example, sites in a classical AFM would all be labelled with happiness 4, while a ferromagnet would have sites with happiness 0. As a hole moves through an AFM, sites which previously had happiness 4 will exhibit reduced happiness, see Fig. 5.2.1 c). Depending on the length of the string, sites within a string can be characterized by specific happiness patterns. Based on this, the algorithm begins by storing all sites which could be the beginning of a string. For each candidate string beginning, it checks if there is a neighboring site which could be the next site in the string, given the happiness and spin occupation of that site. This process continues until the string cannot be propagated any further, at which point the algorithm searches for a neighboring site which could be the end of the string.
For a hole in the $t - J_z$ model, the following reasoning holds: Since the AFM spin order is maintained along a string without loops, the bonds within the string that do not include the holon position are anti-aligned. Since spins on the string are displaced with respect to the surrounding AFM, the bond between site i and j is aligned if site i is occupied by a spin and belongs to the string and site j is not part of the string. Therefore, the happiness θ_i on sites i belonging to the string corresponds to the number of neighboring spins that are also part of the string. For sites j outside of the string, $\theta_j = 4 - N_i^s$, where N_i^s is the number of neighboring sites that belong to the string. By analyzing the happiness according to these rules, we can start from the holon position and reconstruct the attached string. Sites at the boundary have only two or three instead of four neighbors. We can therefore not obtain a reliable value for their happiness. Strings which contain sites at the boundary are thus potentially not identified correctly.
This algorithm has been used in Ref. [3] and as a comparison to the red area method in section 6.4.

Neural network method

A neural network can be used to trace back string patterns in snapshots. One approach is to interpret the process of tracing back the string pattern as a 'time' trace, where in each 'time step' a hole can be placed, moved, or deactivated. For each original snapshot, this leads to a series of snapshots, each of which with a label indicating the required action. We use this series of snapshots then as input for a recurrent neural network, which is a specific type of network taylored for time series [284]. In particular, we use a TensorFlow [285] implementation of a recurrent neural network with an LSTM (long short-term memory) cell [286, 287] and train it to retrace strings. In order to avoid ambiguities during the training process, we always start from the hole which is furthest

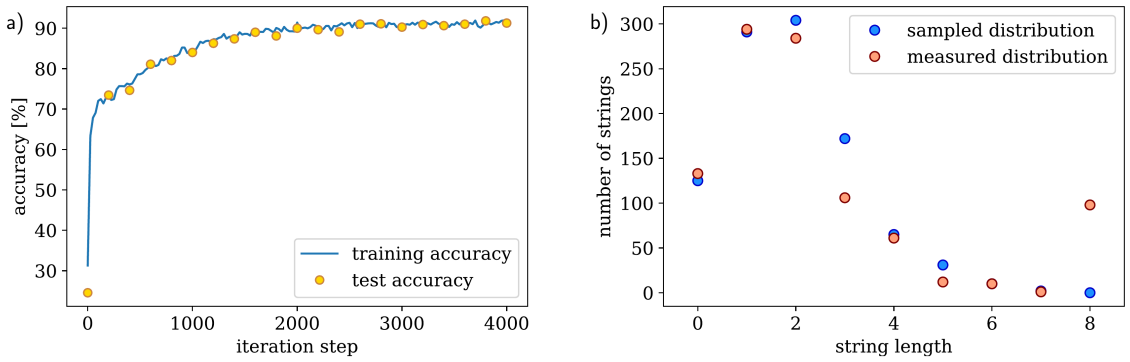

Figure 5.2.2: String pattern finding with a recurrent neural network. A recurrent neural network is used to trace back string patterns in a perfect Néel state in a 6×6 system. a) Training and test accuracy during the training of the neural network. The test accuracy is obtained from a separate data set not used during training. Values of more than 90% are obtained. b) Sampled and retrieved string length distribution.

left and up in the image when we create the labels and snapshot series. Additionally, if the situation is ambigous, we always choose the string to be longer and, if necessary, switch the direction, such that the hole starts further left and/or up. Avoiding any kind of ambiguity in the labeling and correspondingly in the snapshot series generated is important to enable an efficient training of the neural network.

For a system of size $L_x \times L_y$, there are $L_x \times L_y + 5$ possible labels: the first $L_x \times L_y$ labels correspond to the position where a new hole should be initiated. Note that we assume here that we do not know where the holes are, but instead only have knowledge of the position of one spin species as in the experimental data used in chapter 6. To be consistent, the hole can only be placed on an empty site. If a hole is currently active, the label of a new hole position indicates that the old hole is deactivated, and the new hole is initiated at the given position. The next four labels provide the direction of the next move of the currently active hole, namely up, down, left, or right. The last label finishes up the current series of snapshots.

After training, we provide the network with one snapshot at a time. Initially, for each snapshot, the remainder of the series, apart from the first actual snapshot, is filled up with dummy snapshots, e.g. a perfect Néel state. Once this series is used as an input, the network provides a label, which tells us what to do next. Once this action is performed, the new snapshot replaces the first dummy snapshot and the updated snapshot series is used as input. This procedure is repeated until a maximum number of steps is reached, or the network outputs the 'finish'-label.

In Fig. 5.2.2 a) the resulting accuracy is shown. Here, we train the network to find a single string in a perfect Néel state in a 6×6 system. Arbitrary perturbations to the Néel state, as discussed in section 5.2.2, are in principle possible here, too. Note that as opposed to e.g. Fig. 5.2.3, the hole position is

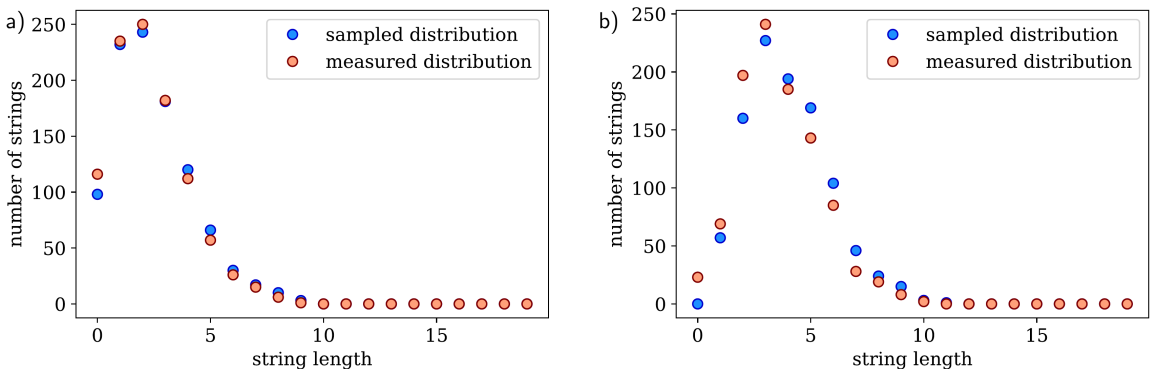

Figure 5.2.3: Finding string patterns in the Néel state. We sample 1000 string lengths according to the string length distribution of a) the ground state and b) the first rotational excitation of the $t - J_z$ model with $t/J_z = 10$. A hole is placed into a perfect Néel state and moved in random directions without self-retracing for a number of bonds given by the sampled string length. The resulting snapshots are analyzed for string patterns with the happiness method. Differences between sampled and measured distributions are due to loops and boundary effects. Loops lead to strings being detected as shorter string patterns.

not known here, such that the network has to find the correct position first. In Fig. 5.2.2 b), the obtained length distribution is compared to the sampled distribution. The main error occurs because the network does not finish a string correctly, but instead oscillates between two configurations, leading to a high count in the longest possible string length.

5.2.2 Finding string patterns in the Néel state and beyond

The algorithms introduced in section 5.2.1 are all motivated by the picture of a Néel state. In this case, the path a single hole has taken can be found with a very high fidelity. The only strings that cannot be retraced exactly are those containing loops and, if working with the happiness method, strings that touch on the boundary. Note that in both cases, the found string pattern will be shorter than the actual string. The most common cases of loops reduce a string of length $l = 4$ to a string pattern of length $l = 0$ (bonds) and $l = 6$ to $l = 2$.

In Fig. 5.2.3 the sampled and measured string length distribution is shown for strings introduced by hand into a Néel state. Here, we use a lattice with 100×100 sites to avoid boundary effects. The discrepancy between sampled and measured distribution is therefore mostly due to loops. In the histogram, more strings are found than sampled for lengths $l \leq 3$. These additional short string patterns are due to loops formed by longer strings. Accordingly, there are less strings with length $l \geq 4$ measured than sampled. Note that only strings of length $l = 4$ and longer can form loops.

Fig. 5.2.3 a) and b) compare the result for the ground state string length distribution with the string length distribution of the first rotational excitation of the string. In the latter case, there are no

strings of length zero and the distribution is shifted to longer string lengths. As a result, there are on average more loops for the first rotational excitation distribution and the measured string length distribution is in this case less accurate compared to the ground state. We do not take into account the probabilities of different string configurations here, i.e. for a string of length $l = 4$, all $4 \cdot 3^3 = 108$ string configurations are equally likely to be put into the Néel pattern by hand, even though the non-linear geometric string theory would predict slightly different weights for different configurations.

Perturbations to the Néel state

In the numerical and experimental results in the remainder of this chapter and chapter 6, we consider the $t - J$ and the Fermi-Hubbard model in the ground state, at finite temperature and out of equilibrium. As compared to the Néel state snapshots analyzed above, there are several perturbations that complicate the search for string patterns. The most relevant of these perturbations are

1. the exchange of the two spins on a bond, as this corresponds to the $\mathbf{S_i} \cdot \mathbf{S_j}$ term in the Hamiltonian.

2. the direction of the Néel order parameter is not necessarily aligned with the measurement axis. Measuring in the wrong basis leads to seamingly random spin flips in the snapshots. In chapter 6, we post-select on a high staggered magnetization to preferably analyze snapshots in which the Néel order parameter is algined with the measurement axis.

3. doublon-hole pairs in the Fermi-Hubbard model: if the two spins on a bond are anti-aligned, they can form a virtual doublon-hole pair, which appears as two empty sites in the snapshots taken in the experiment in chapter 6.

We can mimick these perturbations on top of the Néel state. In particular, we can go through all bonds and exchange the two neighboring spins with a given probability p_{ex}. The direction of the Néel order can be taken into account to some extent by flipping each spin with a probability given by the tilt angle θ. Finally, a doublon-hole pair is created on a bond with a probability p_{dh} if the two spins are anti-aligned.
In Fig. 5.2.4, we study the different perturbations separately as well as combined. In particular,we consider a tilt of $\theta = 0.1, 0.3\pi$ without other disturbances, Fig. 5.2.4 a) and b). The latter tilt angle leads to significant deviations in the measured string length distribution. This indicates that such a strong misalignment between the ordering and measurement axis hinders a faithful retrieval of

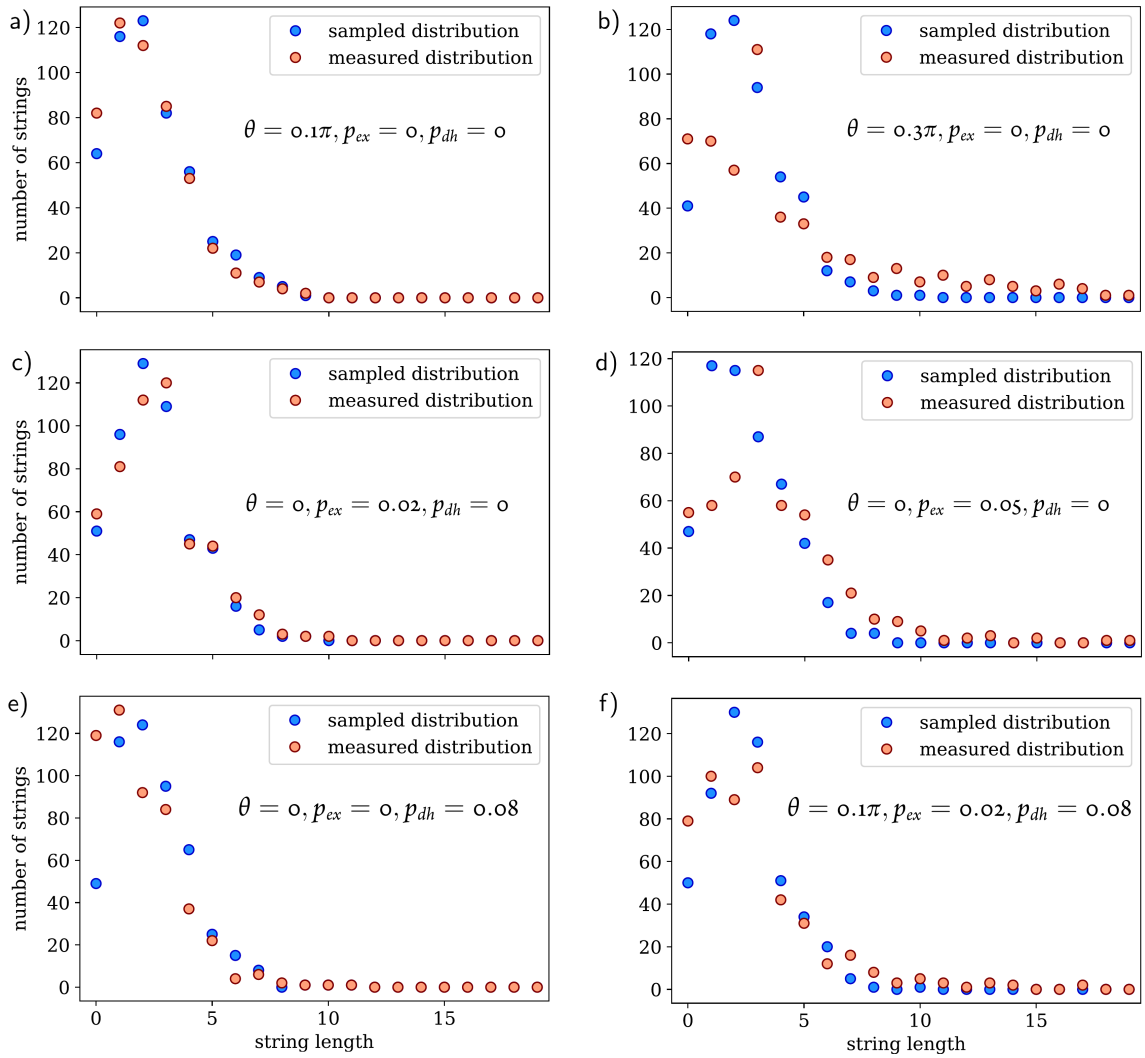

Figure 5.2.4: Finding string patterns in a perturbed Néel state. The Néel order parameter is tilted by an angle θ with respect to the measurement axis. On each bond, spin exchanges are introduced with a probability given by p_{ex}. We sample string lengths according to the string length distribution of the ground state of the $t - J_z$ model with $t/J_z = 10$. A hole is placed into a snapshot after tilting and adding spin exchanges. The hole is then moved in random directions without retracing its own path for a number of bonds given by the sampled string length. Finally, doublon-hole pairs are introduced on bonds with anti-aligned spins with a probability given by p_{dh}. Doublon-hole pairs are here simulated as spin downs, resembling the experimental measurements in chapter 6. The resulting snapshots are analyzed for string patterns with the happiness method. We consider 500 snapshots for each set of parameters. The system size is 100×100 to avoid boundary effects of the happiness method.

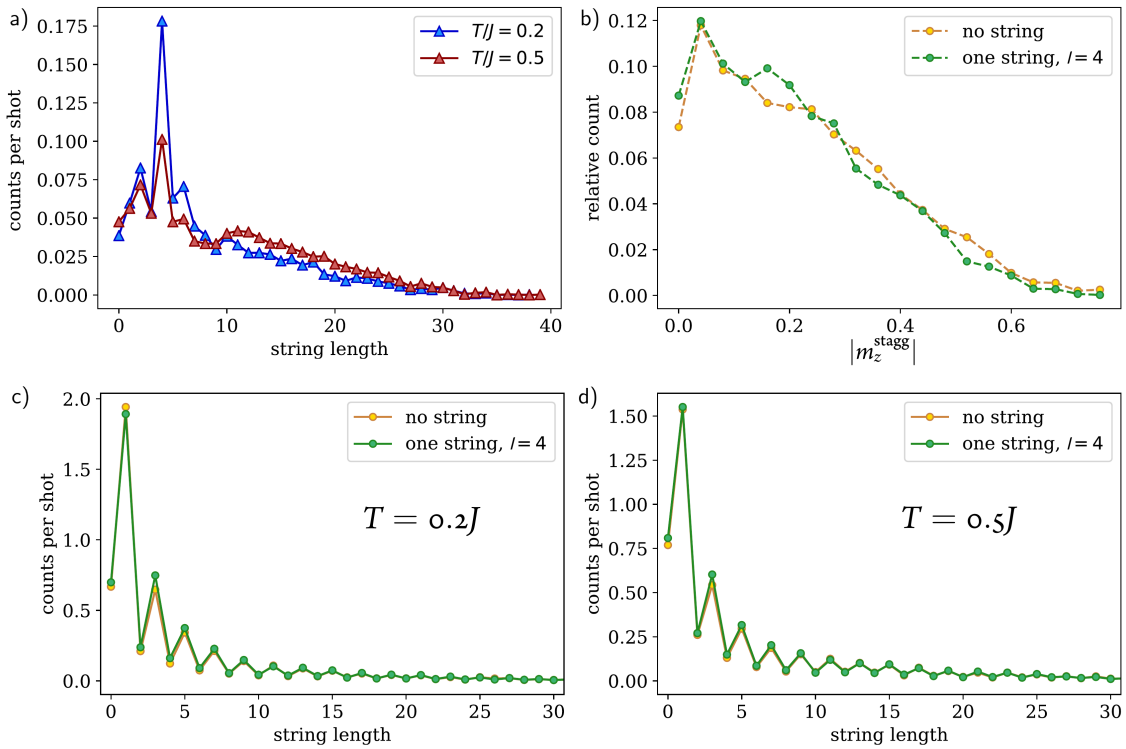

Figure 5.2.5: Finding string patterns in Heisenberg snapshots. a) A string of length four is simulated in Heisenberg quantum Monte Carlo (qMC) snapshots at temperature $T/J = 0.2$ and $T/J = 0.5$. If the hole positions are known, exactly one string is found per snapshot. The length distribution of the found string patterns is peaked at $l = 4$, but has a finite width and a very broad tail for long string lengths. b) The full counting statistics of the absolute value of the staggered magnetization for the Heisenberg data with and without a string of length $l = 4$ at temperature $T/J = 0.5$. c), d) The measured string length distribution for $T/J = 0.2, 0.5$ without knowledge of the hole position.

the string patterns. In Fig. 5.2.4c) and d) the case without a tilt and doublon-hole pairs, but with a probability of $p_{ex} = 0.2, 0.5$ for an exchange process on each bond is studied. While the general form of the distribution is captured roughly in both cases, the snapshots with $p_{ex} = 0.05$ lead again to strong deviations in the retrieved string length distribution. Adding doublon hole pairs with a probability of $p_{dh} = 0.08$ (corresponding to $U/t = 7$) without any other perturbations does not significantly alter the retrieved string length distribution, Fig. 5.2.4e). The main effect is a strongly enhanced signal for $l = 0$ strings, which is most likely due to the fact that the perturbation caused by the doublon hole pair cuts the string off. The combination of all three perturbations leads to a modified measured string length distribution, which however still closely resembles the sampled distribution as long as the perturbations are not too strong, Fig. 5.2.4f).

5.2.3 Retrieving string patterns in Heisenberg quantum Monte Carlo snapshots

Most of the perturbations to a Néel state discussed in section 5.2.2 appear in the Heisenberg model. Here, we analyze snapshots obtained from quantum Monte Carlo (qMC) for the Heisenberg model at finite temperatures $T/J = 0.2$ and 0.5 [288]. The snapshots are obtained for a system of size 40×40 with periodic boundary conditions. We analyze a window of size 10×10 in each snapshot. We study the signatures of a single string of length $l = 4$ against the background of the finite temperature Heisenberg state. In Fig. 5.2.5 a), the string length distribution obtained with the red area method with knowledge of the hole position is shown. While the distribution is peaked at $l = 4$, it is very broad and very long string lengths appear with a sizeable probability. The large amount of very long string patterns found is related to the full counting statistics of the staggered magnetization shown in Fig. 5.2.5 b): since the Néel ordering vector can point in any direction, many of the snapshots taken contain seemingly random patterns. In chapter 6, we post-select on a high staggered magnetization to avoid this effect. The background signal for string patterns in the Heisenberg model is analyzed in Fig. 5.2.5c) and d). Here we compare the pure Heisenberg data to Heisenberg snapshots with a single string of length $l = 4$ added at temperature $T/J = 0.2, 0.5$, respectively. While the signal indeed increases for string patterns of length $l = 4$, the difference is extremely small, rendering a faithful detection of single strings without post-selection difficult. The measured string length distribution is in all cases peaked at odd string lengths. This corresponds to a perturbation of two sites, which occurs frequently in the Heisenberg model due to the $\mathbf{S_i} \cdot \mathbf{S_j}$ term in the Hamiltonian.
In section A.4, we compare the experimental data at half-filling and finite doping to Heisenberg qMC data with and without artificial doublon-hole pairs to study the additional background signal.

5.2.4 Comparisons with geometric string theory snapshots

Given the clear prescription provided by the geometric string theory, we can also generate a new set of snapshots with the predictions of the analytical theory based on data from the Heisenberg model. In each snapshot, we first determine the spinon position either in the center of the system or by sampling from a given distribution. As a next step, we find the length l of the new string by sampling from the analytical string length distribution. Finally, we create a hole at the spinon position and then move it l times by one site, where the direction in each step is random without allowing a self-retracing of the string. Moving the hole through the spin background displaces the spins and introduces a local suppression of the antiferromagnetic ordering present in the system.
While we are aware that the algorithms outlined in section 5.2.1 are not capable of reliably finding the exact path taken by a hole in the $t - J$ or Fermi-Hubbard model, we will show in the following

sections strong evidence that they are sensitive to traces of strings. Most importantly, for the comparison between the actual numerical simulation of the $t - J$ model and the semi-analytically generated geometric string theory snapshots, we apply the same algorithm to both sets of snapshots. Therefore, even though the algorithm might not be perfect, the same types of problems occur in both cases and a straightforward comparison of the results allows to draw conclusions about the similarity of the datasets.

For the MPS simulations discussed in the following, we employ standard Metropolis Monte Carlo sampling techniques to obtain snapshots. There, we start from a random Fock space configuration and propose updates given by exchanges between two sites. Note that the total magnetization $\hat{S}^z_{tot}$ is fixed for all proposed configurations. The probability for a given snapshot is determined by its overlap with the matrix product state of interest.

5.3 A single hole in the ground state of the $t - J$ model

This section is based on the publication

- Fabian Grusdt, Annabelle Bohrdt, and Eugene Demler: "Microscopic spinon-chargon theory of magnetic polarons in the t-J model"
  – Phys. Rev. B 99, 224422 (2019) [arXiv:1901.01113]

Structure, text and figures have been rearranged and adapted here.

The algorithm introduced in 5.2 enables the search for evidence for the hidden string order in the ground state discussed in 5.1 in terms of string patterns. In this section, we present numerical results from matrix product state simulations on a cylinder with a length of eight sites and a circumference of six sites. First, the algorithm is applied to snapshots sampled from the ground state of the Heisenberg model, where a hole was deterministically placed in the origin. As opposed to the $t - J_z$ model discussed in 5.2, the Néel order parameter in the ground state of the Heisenberg model can point in any direction and in particular is not necessarily aligned with the measurement axis, see also section 5.2.3. This leads to a background signal of finite string pattern lengths even for an immobile hole, see Fig 5.3.1 b). The even-odd effect can be explained by quantum fluctuations: a single spin exchange leads to a connected deviation of length two sites from the perfect checkerboard. If the hole is placed next to such a deviation, our algorithm detects it as a string of length two. Note that it is more likely that the hole is placed next to than on top of the two site deviation, because there are three times more possible configurations for the former case. For the ground state of the $t - J$ model with a mobile hole, the distribution of string pattern lengths changes. In the case of a small $t/J = 0.4$, mainly string patterns of length one and three appear, while the count for string patterns of length zero decreases. For $t/J = 3$, the length distribution becomes much broader and the count for longer lengths increases significantly. Since the string pattern algorithm is sensitive to quantum fluctuations in the spin background, the string length distribution predicted by the geometric string theory shown in Fig. 5.3.1 a) differs quantitatively from the extracted string pattern lengths in Fig. 5.3.1 b). However, the broadening of the string pattern length distribution with increasing t/J is correctly predicted and can be understood intuitively from the geometric string theory. Moreover, the string patterns detected in the geometric string theory simulations, bands in Fig. 5.3.1, match the matrix product state simulations. Since we directly use the string length distribution shown in Fig. 5.3.1 a) as input for the GST simulations, this indicates that the difference between the expected and extracted distribution of string lengths is mostly due to the background, which cannot be entirely separated from the signal.
From the string pattern length distribution, an average length can be obtained. As shown in Fig. 5.3.1 c), this average length scales approximately linear with $(t/J)^{1/3}$. This scaling behavior is expected

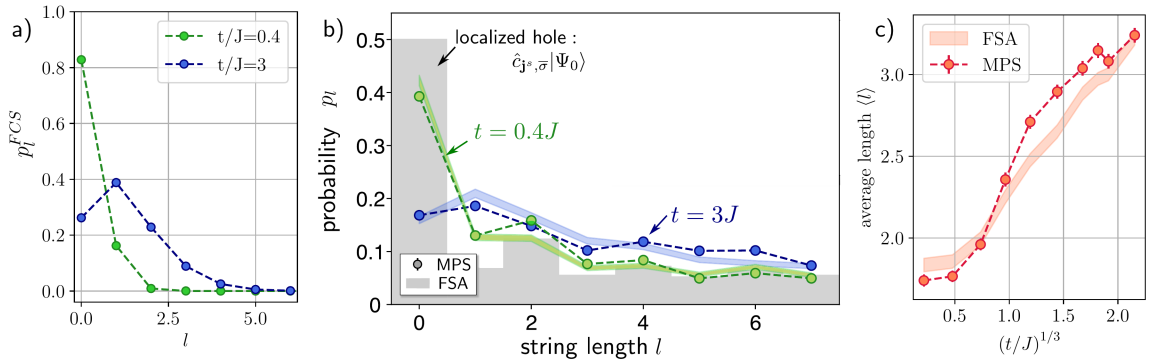

Figure 5.3.1: String pattern lengths extracted from snapshots of the ground state. a) The geometric string theory string length distribution used in the frozen spin approximation for $t/J = 0.4$ and $t/J = 3$. b) The distribution function of the length ℓ of string-like patterns emanating from the hole. A striking difference is observed between a localized and a mobile hole (MPS, indicated by symbols connected with dashed lines). Mobile holes are described quantitatively by the geometric string theory (FSA, shaded ribbons). c) The size of the magnetic polaron as a function of t/J by determining the average length $\langle \ell \rangle$ of the string-like objects revealed in individual snapshots. The scaling behavior with $(t/J)^{1/3}$ is expected from linear string tension in the strong coupling regime, but before the Nagaoka polaron is realized at $t/J \leq 20$.

from the linear string theory in the strong coupling regime before the hole forms a Nagaoka polaron at $t/J \geq 20$, as discussed in section 5.1.

The average string pattern length is a measure for the size of the region around the hole in which the spin background is altered by the hole motion. In each snapshot, one string pattern configuration and length are observed. While a single string like object easily extends over two to three sites away from the hole, averaging over many of those lengths and configurations, and thus directions of the string object, will lead to a much smaller sphere of influence of the chargon. In the language of the commonly used magnetic polaron theory, this sphere of influence is the dressing cloud of the magnetic polaron and its size is given by the magnetic polaron radius. Apart from the average string length, we can estimate the magnetic polaron radius by considering local spin correlations as a function of their bond-center distance to the hole, Fig. 5.3.2 a). The nearest and next nearest neighbor spin correlations shown in Fig. 5.3.2 b) depend strongly on t/J for small bond center distances. Especially the diagonal next nearest neighbor spin correlations close to the hole are strongly suppressed. This can be directly understood from the geometric string theory: the chargon is located at one end of a fluctuating geometric string, along which all spins are displaced by one site. Upon averaging over all string configurations, the next nearest neighbor correlations close to the hole therefore contain a significant contribution of nearest neighbor correlations, which have the

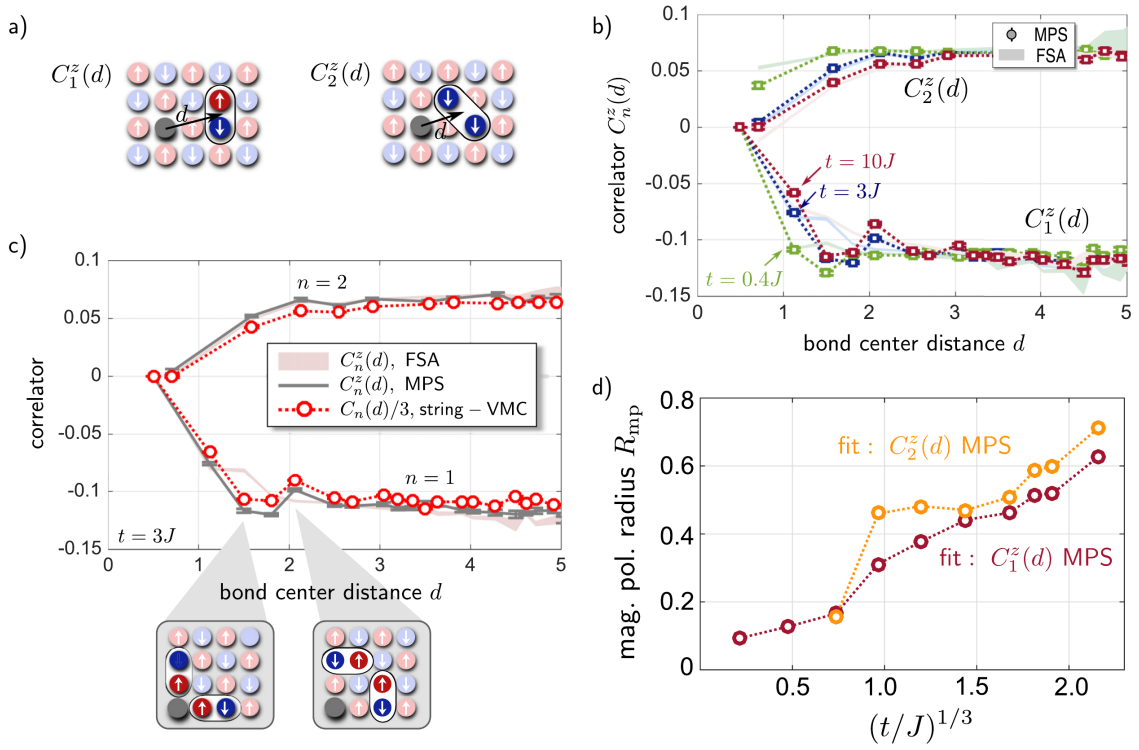

Figure 5.3.2: Magnetic polaron radius extracted from local spin correlations. a) Nearest and next nearest neighbor spin correlation functions are evaluated as a function of their bond center distance from the hole. b) For increasing t/J, the effect on spin correlations near the hole grows. The frozen spin approximation, based on snapshots from the undoped Heisenberg AFM, captures the general behavior, but misses details, like significantly enhanced nearest neighbor correlations at bond-center distances of 1.5 and 2.06. c) Using the trial wave function (string-VMC) introduced in section 5.1 we calculate the local spin correlations as a function of their bond-center distance from the hole. We compare our string-VMC result $C_n(d)/3$ to $C_n^z(d)$ for $t/J = 3$ obtained from the same DMRG simulations as part b). d) The local spin correlations shown in b) are fitted by a function of the form $C_n^\infty + ae^{-d/R_{mp}}$. The fit parameter R_{mp} is interpreted as the magnetic polaron radius.

opposite sign. Directly next to the dopant, the geometric string theory predicts

$$C_2\left(1/\sqrt{2}\right)_{GST} \approx \left(p_0^{GST} + \frac{1 - p_0^{GST}}{2}\right) C_2 + \frac{1 - p_0^{GST}}{2} C_1, \tag{5.33}$$

where p_l^{GST} is the string length distribution and C_1, C_2 are the nearest neighbor and diagonal next nearest neighbor spin correlations in the undoped system. In other words, the diagonal next nearest neighbor correlation directly next to the hole is approximately determined by the weighed sum of C_1 and C_2. The relative contribution of C_1 is given by the probability to have a string of length $l > 0$, which will change two out of four of the diagonal spin correlations to C_1.

Further away from the hole, at bond center distances larger than three sites, there is no visible t/J dependence. After fitting a function of the form $C_n^\infty + ae^{-d/R_{mp}}$ to the spin correlations as a function of the bond center distance d, we extract the fit parameter R_{mp} as the radius of the magnetic polaron, Fig. 5.3.2 c). Similar to the average string pattern length shown in Fig. 5.3.1 c), the radius of the magnetic polaron obtained this way also scales linearly with $(t/J)^{1/3}$. However, the magnetic polaron radius is less than a site for all values of t/J considered, whereas the average string pattern length varies between 2 and 3 sites with increasing t/J. This can be explained by the large number of possible string configurations with a given length l, $N_\Sigma(l) = 4 \times 3^{l-1}$ for $l > 0$. Every single string configuration has a strong effect on those spin correlations, where one of the spins is part of the string and the other is not. Averaging over all those string states yields a significant reduction of the effect of the string on a given spin correlation relative to the dopant. The correlations between the mobile hole and the surrounding spins are thus liquid-like.

Apart from the overall reduction of the spin correlations close to the hole, additional spatial structure in the nearest neighbor spin correlations is observed. At a bond center distance of $d = 1.5$, the correlations are enhanced, whereas at $d = 2.06$, a reduction of the nearest neighbor correlations takes place, which gets stronger with increasing t/J. The frozen spin approximation does not capture this additional spatial structure.

The fact that this feature is present in the trial wave function when $t \ll J$, see Fig. 5.3.2 b), indicates that it is caused by the microscopic correlations of the spinon position with its spin environment. The emergence of a second length scale, in addition to the string length $l \propto (t/J)^{1/3}$ captured by the FSA, can be considered as an indirect indication of fermionic spinon statistics: the Fermi momentum k_F defines a second intrinsic length scale in this case.

In the meantime, this feature has moreover been observed in quantum Monte-Carlo simulations of a single hole in the $t - J$ model at low finite temperatures [289].

5.3.1 Dominant higher-order correlation functions

This section is based on the publications

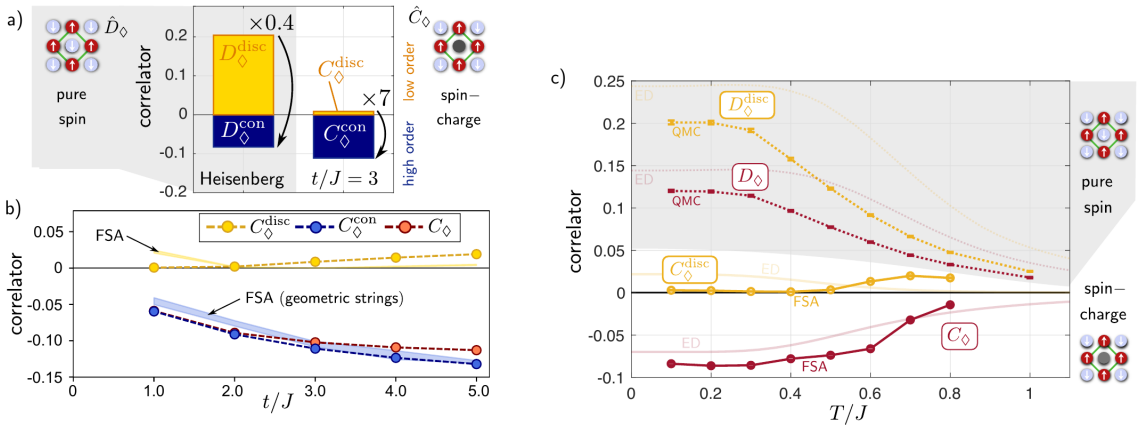

Figure 5.3.3: Higher order correlations in the two-dimensional $t-J$ model. Fifth-order spin-charge correlations around a mobile dopant in the $t-J$ model are compared to the corresponding fourth-order spin correlators in the undoped Heisenberg model. We consider spin-balanced ensembles with $\langle \hat{S}^z \rangle = 0$. a), b)The results are based on DMRG calculations for the ground state on a 6×12 cylinder, where the correlations are evaluated in the center of the cylinder and we average over all legs. a) For the ground state of one mobile dopant in the $t-J$ model, the connected fifth-order correlations $C_\diamondsuit^{\text{con}}$ (blue) are significantly larger than the lower-order disconnected terms $C_\diamondsuit^{\text{disc}} = C_\diamondsuit - C_\diamondsuit^{\text{con}}$ (yellow). In the undoped Heisenberg model, the opposite is true: lower order correlations are dominant, while the connected higher-order correlations are smaller. b) Fifth-order spin-charge correlations in the ground state of the $t-J$ model with a single dopant as a function of t/J. Our numerical results (data points, bare correlations $C_\diamondsuit$ in red) are explained by the frozen-spin approximation ansatz (ribbons, width indicates statistical errors). c) Temperature dependence of the higher-order correlations $C_\diamondsuit$ (red) and the disconnected $C_\diamondsuit^{\text{disc}}$ (yellow) parts. We compare the corresponding correlators $D_\diamondsuit$ in the undoped Heisenberg model (top) to predictions for a mobile dopant with $t/J = 2$ using the FSA based on Heisenberg quantum Monte Carlo snapshots. We moreover show results from exact diagonalization (faint lines).

- Annabelle Bohrdt, Yao Wang, Joannis Koepsell, Marton Kanasz-Nagy, Eugene Demler, and Fabian Grusdt:"Dominant fifth-order correlations in doped quantum anti-ferromagnets" – Phys. Rev. Lett. 126, 026401 (2021) [arXiv:2007.07249]

- Yao Wang, Annabelle Bohrdt, Joannis Koepsell, Eugene Demler, and Fabian Grusdt: "Higher-Order Spin-Hole Correlations around a Localized Charge Impurity" – arXiv:2101.00721

Structure, text and figures have been rearranged and adapted here.

Motivated by the string picture introduced above, we now evaluate higher order correlations. In particular, we consider the correlation function of the four spins surrounding the hole,

$$C_\diamondsuit(\mathbf{r}) = \frac{2^4}{\langle \hat{n}^{\text{h}}_{\mathbf{r}} \rangle} \langle \hat{n}^{\text{h}}_{\mathbf{r}} \hat{S}^z_{\mathbf{r}+\mathbf{e}_x} \hat{S}^z_{\mathbf{r}+\mathbf{e}_y} \hat{S}^z_{\mathbf{r}-\mathbf{e}_x} \hat{S}^z_{\mathbf{r}-\mathbf{e}_y} \rangle, \tag{5.34}$$

see also Fig. 5.3.3. The correlation we consider here is a direct generalization of the three-point spin-charge correlators $\langle \hat{S}^z_{j-1} \hat{n}^h_j \hat{S}^z_{j+1} \rangle$ underlying hidden AFM correlations in the 1D doped Hubbard model [75, 215]. To witness the presence of genuine higher-order correlations, we calculate the connected correlator in the co-moving frame with the hole,

$$C^{\mathrm{con}}_{\diamondsuit}(\mathbf{r}) = C_{\diamondsuit}(\mathbf{r}) - 2^4 \Bigg[\sum_{\mathbf{l} \notin (\mathbf{i},\mathbf{j},\mathbf{k})} \frac{\langle \hat{n}^h_{\mathbf{r}} \hat{S}^z_{\mathbf{r}+\mathbf{i}} \hat{S}^z_{\mathbf{r}+\mathbf{j}} \hat{S}^z_{\mathbf{r}+\mathbf{k}} \rangle_c}{\langle \hat{n}^h_{\mathbf{r}} \rangle} \frac{\langle \hat{n}^h_{\mathbf{r}} \hat{S}^z_{\mathbf{r}+\mathbf{l}} \rangle}{\langle \hat{n}^h_{\mathbf{r}} \rangle} + \sum_{(\mathbf{i},\mathbf{j}) \notin (\mathbf{k},\mathbf{l})} \frac{\langle \hat{n}^h_{\mathbf{r}} \hat{S}^z_{\mathbf{r}+\mathbf{i}} \hat{S}^z_{\mathbf{r}+\mathbf{j}} \rangle_c}{\langle \hat{n}^h_{\mathbf{r}} \rangle} \frac{\langle \hat{n}^h_{\mathbf{r}} \hat{S}^z_{\mathbf{r}+\mathbf{k}} \hat{S}^z_{\mathbf{r}+\mathbf{l}} \rangle_c}{\langle \hat{n}^h_{\mathbf{r}} \rangle}$$
$$+ \sum_{\mathbf{i} \neq \mathbf{j} \notin (\mathbf{k},\mathbf{l})} \frac{\langle \hat{n}^h_{\mathbf{r}} \hat{S}^z_{\mathbf{r}+\mathbf{i}} \rangle}{\langle \hat{n}^h_{\mathbf{r}} \rangle} \frac{\langle \hat{n}^h_{\mathbf{r}} \hat{S}^z_{\mathbf{r}+\mathbf{j}} \rangle}{\langle \hat{n}^h_{\mathbf{r}} \rangle} \frac{\langle \hat{n}^h_{\mathbf{r}} \hat{S}^z_{\mathbf{r}+\mathbf{k}} \hat{S}^z_{\mathbf{r}+\mathbf{l}} \rangle_c}{\langle \hat{n}^h_{\mathbf{r}} \rangle} + \frac{\langle \hat{n}^h_{\mathbf{r}} \hat{S}^z_{\mathbf{r}+\mathbf{e}_x} \rangle}{\langle \hat{n}^h_{\mathbf{r}} \rangle} \frac{\langle \hat{n}^h_{\mathbf{r}} \hat{S}^z_{\mathbf{r}+\mathbf{e}_y} \rangle}{\langle \hat{n}^h_{\mathbf{r}} \rangle} \frac{\langle \hat{n}^h_{\mathbf{r}} \hat{S}^z_{\mathbf{r}-\mathbf{e}_x} \rangle}{\langle \hat{n}^h_{\mathbf{r}} \rangle} \frac{\langle \hat{n}^h_{\mathbf{r}} \hat{S}^z_{\mathbf{r}-\mathbf{e}_y} \rangle}{\langle \hat{n}^h_{\mathbf{r}} \rangle} \Bigg], \quad (5.35)$$

where the sums are over disjoint sets of lower-order connected correlators (defined equivalently) involving sites $\mathbf{i}, \mathbf{j}, \mathbf{k}, \mathbf{l} = \pm \mathbf{e}_{x,y}$ measured relative to the hole. In a spin-balanced ensemble, the expectation values $\langle \hat{n}^h_{\mathbf{r}} \hat{S}^z_{\mathbf{r}+\mathbf{l}} \rangle = 0$ and the only relevant lower-order correlators are

$$C^{\mathrm{disc}}_{\diamondsuit}(\mathbf{r}) = C_{\diamondsuit}(\mathbf{r}) - C^{\mathrm{con}}_{\diamondsuit}(\mathbf{r}) = \sum_{(\mathbf{i},\mathbf{j}) \notin (\mathbf{k},\mathbf{l})} \frac{\langle \hat{n}^h_{\mathbf{r}} \hat{S}^z_{\mathbf{r}+\mathbf{i}} \hat{S}^z_{\mathbf{r}+\mathbf{j}} \rangle_c}{\langle \hat{n}^h_{\mathbf{r}} \rangle} \frac{\langle \hat{n}^h_{\mathbf{r}} \hat{S}^z_{\mathbf{r}+\mathbf{k}} \hat{S}^z_{\mathbf{r}+\mathbf{l}} \rangle_c}{\langle \hat{n}^h_{\mathbf{r}} \rangle}. \quad (5.36)$$

Usually the values of high-order correlation functions are dictated by more fundamental lower-order correlators. Moreover, numerical studies of the Fermi-Hubbard and $t-J$ model have often focused on the analysis of two-point correlation functions with the goal of characterizing different types of broken symmetries. Two-point correlation functions can furthermore be naturally accessed in solid state systems using scattering experiments[290–292] and they play a central role in the development of effective mean-field theories. Recently, with the advent of quantum simulators and especially quantum gas microscopes, the analysis of higher-order correlation functions has become a new experimental tool in the study of quantum many-body states [35, 36, 217, 267, 293, 294]. They have rarely been studied so far, even though they contain a wealth of information about the underlying quantum states and are expected to become relevant when mean-field theories characterized by Gaussian correlations are no longer sufficient to capture the physics.

Intriguingly, for a magnetic polaron, formed when a single mobile hole is doped into an AFM, the lower-order correlators are significantly smaller than the higher-order correlators $C_{\diamondsuit}(\mathbf{r})$ and $C^c_{\diamondsuit}(\mathbf{r})$. In Fig. 5.3.3 we show DMRG results for the ground state of a single hole in the $t-J$ model and compare to the undoped Heisenberg model, where lower-order spin correlations dominate. Our data demonstrates that the mobility of the hole plays an important role for observing sizable higher-order spin-charge correlations. As t/J is increased from $t/J = 1$ to $t/J = 5$, the absolute value of $C^c_{\diamondsuit}$ doubles. Importantly, the product of the two-point correlation functions is an order of magnitude smaller.

We define related fourth-order correlators in the absence of doping as

$$D_{\diamondsuit}(\mathbf{r}) = 2^4 \langle \hat{S}^z_{\mathbf{r}+\mathbf{e}_x} \hat{S}^z_{\mathbf{r}+\mathbf{e}_y} \hat{S}^z_{\mathbf{r}-\mathbf{e}_x} \hat{S}^z_{\mathbf{r}-\mathbf{e}_y} \rangle. \tag{5.37}$$

A corresponding expression is obtained for the connected part $D^{\mathrm{con}}_{\diamondsuit}(\mathbf{r})$. In the Ising AFM, $D_{\diamondsuit} = 1$ and $D^{\mathrm{con}}_{\diamondsuit} = 0$. We performed DMRG simulations for the 2D Heisenberg model on a 6×12 cylinder and obtain $D_{\diamondsuit} = 0.12$ and $D^{\mathrm{con}}_{\diamondsuit} = -0.083$ in the ground state, see Fig. 5.3.3 a). The connected 4th-order correlator only becomes negative because we subtract the significantly larger and positive two-point correlators, $D_{\diamondsuit} - D^{\mathrm{con}}_{\diamondsuit} = 0.20$. As expected for a weakly correlated quantum system, and different from the ground state with a mobile hole in the $t-J$ model, the lower-order correlators dominate in the two-dimensional Heisenberg model: They are more than twice as large as the genuine fourth order correlations.

The order of magnitude of $D^{(\mathrm{con})}_{\diamondsuit}$ can be understood from a simplistic model of spontaneous symmetry breaking. Consider an ensemble of classical Néel states with AFM order parameters pointing in random directions. Because $D^{(\mathrm{con})}_{\diamondsuit}$ is always measured in the z-basis, averaging over the entire ensemble yields

$$D_{\diamondsuit}|_{\mathrm{cl}} = 0.2, \qquad D^{\mathrm{con}}_{\diamondsuit}|_{\mathrm{cl}} = -0.133. \tag{5.38}$$

These correlations are purely classical. Quantum fluctuations are expected to further reduce these values in the $SU(2)$ invariant Heisenberg model, as confirmed by our DMRG calculations. Nonzero fifth-order ring-correlations $C^{\mathrm{con}}_{\diamondsuit}(\mathbf{r}) < 0$ provide a signature of AFM correlations hidden by the motion of the dopants. To gain some intuition, we consider a toy model of a single hole inside an Ising AFM. In this case, $C_{\diamondsuit}$ measures the probability $p_>$ for the hole to be attached to an S^z-string Σ of length $\ell_\Sigma > 0$, $C_{\diamondsuit} \approx p_< - p_> = 1 - 2p_>$. The approximate sign in this equation indicates that we neglected string configurations affecting more than one spin in the direct vicinity of the hole.

Assuming that the system is in an equal superposition of all string configurations, we can estimate various correlation functions. Because the hole is equally likely to occupy either sublattice, $\langle \hat{n}^{\mathrm{h}}_{\mathbf{r}} \hat{S}^z_{\mathbf{r}\pm\mathbf{e}_{x,y}} \rangle = 0$. Three-point correlations $\langle \hat{n}^{\mathrm{h}}_{\mathbf{r}} \hat{S}^z_{\mathbf{r}\pm\mathbf{e}_{x,y}} \hat{S}^z_{\mathbf{r}\pm\mathbf{e}_{x,y}} \rangle \approx 0$ vanish, as can be seen by averaging over the four possible orientations of the first string segment, counting from the hole, and neglecting string configurations which affect more than one spin in the immediate vicinity of the hole, see Fig. 5.3.4 a). Hence, Eq. (5.35) implies $C^c_{\diamondsuit}(\mathbf{r}) \approx C_{\diamondsuit}(\mathbf{r}) \approx -1$.

In this setting, relevant to the $t-J_z$ model [3, 295], $C_{\diamondsuit}$ takes the role of a $\mathbb{Z}_2$ Gauss law: the mobile dopants represent $\mathbb{Z}_2$ charges and the $\mathbb{Z}_2$ electric field lines correspond to S^z-strings of flipped spins. Similarly, in the $SU(2)$ invariant $t-J$ or Fermi-Hubbard models the higher-order correlator $C_{\diamondsuit}$ serves as an indicator for geometric strings [3, 4] of displaced – rather than overturned –

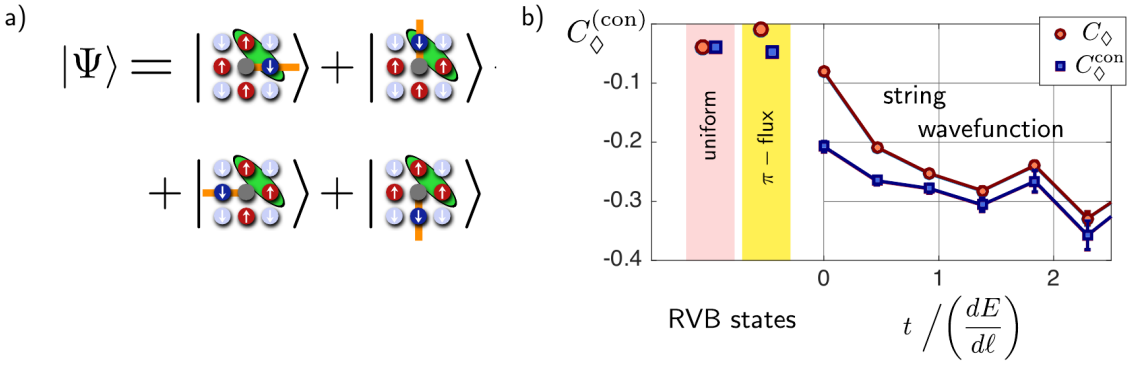

Figure 5.3.4: Higher order correlations: RVB and geometric string trial states. a) The three-point spin-charge correlator diagonally next to the hole, $\left\langle \hat{n}^h_{\mathbf{j}} \hat{S}^z_{\mathbf{j}+\mathbf{e}_x} \hat{S}^z_{\mathbf{j}+\mathbf{e}_y} \right\rangle$ (green bubble) vanishes for a mobile hole moving through a classical Néel state at the end of an infinitely long S^z-string. The fifth-order correlation $C_\Diamond$ remains sizeable and negative. b) Comparison of RVB and geometric string trial states in a 14×14 system with $S^z_{\mathrm{tot}} = 1/2$. For the 'plain vanilla' uniform and π-flux RVB states doped with a single hole (left), $C_\Diamond^{(\mathrm{con})}$ is small. The string wave-function (right) with a weak $SU(2)$ breaking staggered magnetization along S^z exhibits larger values of the spin-charge correlator and shows a strong dependence on the ratio of t and the string tension $\mathrm{d}E/\mathrm{d}l = 1.09J$ [4] which determines the average length of geometric strings in the trial state. Note that the doped RVB states have no t/J dependence.

spins. Note that we observed the reduction of the two-point spin correlations close to the hole in the ground state of the $t-J$ model in Fig. 5.3.2.

The t/J dependence observed in Fig. 5.3.3 b) can be explained by the geometric string ansatz [3, 4], see section 5.1. We compare to this theory by generating a new set of snapshots as discussed in section 5.2.4: we start from snapshots of the Heisenberg ground state in the Fock basis and create a hole by randomly removing one spin. This dopant is subsequently moved through the system in random directions, re-ordering the surrounding spins; the string length distribution is calculated from a linear string model with string tension $dE/d\ell = 2J(C_2 - C_1)$ [3], where $C_{1(2)}$ are nearest (next-nearest) neighbor spin correlations in the undoped system. This way, new sets of snapshots are generated for every value of t/J, from which the higher-order correlators can be obtained.

The interpretation of $C_\Diamond$ as a signature detecting the presence of S^z- or geometric strings suggests that $C_\Diamond < 0$, whereas the corresponding correlator around a particle

$$D_\Diamond(\mathbf{r}) - \langle \hat{n}^h_{\mathbf{r}} \rangle C_\Diamond(\mathbf{r}) = \langle (1 - \hat{n}^h_{\mathbf{r}}) \hat{S}^z_{\mathbf{r}+\mathbf{e}_x} \hat{S}^z_{\mathbf{r}+\mathbf{e}_y} \hat{S}^z_{\mathbf{r}-\mathbf{e}_x} \hat{S}^z_{\mathbf{r}-\mathbf{e}_y} \rangle > 0; \tag{5.39}$$

i.e. negative correlations are only expected around the mobile dopant. In Fig. 5.3.3 a) we confirm this picture by calculating four-spin correlations around a particle instead of a hole.

An important class of microscopic variational wavefunctions that can be used to model problems at finite doping values, is constituted by Anderson's RVB paradigm [30, 212]. Being able to resolve

properties of the many-body wavefunction on microscopic scales, ultracold atom experiments provide an opportunity to put the RVB theory to a rigorous experimental test in a clean system.

Here we calculate the higher-order spin charge correlations $C_{\Diamond}^{(\mathrm{con})}$ for two paradigmatic doped RVB trial states. The uniform RVB state starts from an unpolarized Fermi sea of free spin-up and spin-down spinons, $|\mathrm{FS}\rangle$. To describe a free hole excitation moving through the system, one spinon with momentum $\mathbf{k}$ and spin σ is removed. A meaningful trial state for the $t-J$ model, without double occupancies, is obtained by applying the Gutzwiller projection: $|\Psi_{\mathrm{uRVB}}\rangle = \hat{\mathcal{P}}_{\mathrm{GW}}\hat{f}_{\mathbf{k},\sigma}|\mathrm{FS}\rangle$. We use standard Metropolis Monte Carlo sampling to evaluate $C_{\Diamond}^{(\mathrm{con})}$ in the trial state $|\Psi_{\mathrm{uRVB}}\rangle$, and show our result in Fig. 5.3.4. We find $C_{\Diamond}^{(c)} = -0.040(4)$ with significantly smaller magnitude than found by DMRG, cf. Fig. 5.3.3.

We find a similar result for the doped π-flux RVB state, for which decent agreement with experimental data has recently been reported in ultracold atoms at finite doping [5, 266], see also chapter 6. The π-flux state with a single hole has the same form as the uRVB state above, except that the Fermi sea $|\mathrm{FS}\rangle$ is replaced by a Dirac metal of spinons obtained when introducing π magnetic flux per plaquette in the effective spinon Hamiltonian [277]. In this case $C_{\Diamond}^{\mathrm{con}} = -0.049(3)$ slightly increases and $C_{\Diamond} = -0.008(3)$ decreases in magnitude. Both are significantly weaker than numerically expected from DMRG when $t \gtrsim J$.

As discussed in section 5.1, geometric strings can be included in the trial wavefunction [4]. Now we demonstrate that the presence of such geometric strings increases the expected higher-order correlators. We start from the optimized RVB wavefunction for half filling (no doping) [273, 274], which includes a weak spontaneously formed staggered magnetization along z-direction. A spinon is removed in the usual way and after the Gutzwiller projection a geometric string is added to the hole, thus re-arranging the spins surrounding the dopant; see Ref. [4] for details.

In Fig. 5.3.4 b) (right panel) we show how $C_{\Diamond}^{(\mathrm{con})}$ evaluated for this string wavefunction depends on the ratio of hole tunneling t and the linear string tension $dE/d\ell$ underlying the model. When $t/J = 0$ the length of geometric strings is zero and the observed increase of the higher-order correlator is due to the staggered magnetization along z included in the trial wavefunction. For increasing tunneling t the string length grows and another significant increase of $C_{\Diamond}^{(\mathrm{con})}$ is observed. We also checked that including strings in the $SU(2)$ invariant π-flux RVB state leads to such an increase of higher-order correlations. This supports our picture that the mobility of dopants leads to long geometric strings, which in turn underly strong higher-order spin charge correlations.

We turn to a discussion of the limitations and requirements to observe higher-order correlations experimentally. Fig. 5.3.3 b) demonstrates how thermal fluctuations suppress higher-order correlations. We show the lower-order disconnected terms $C_{\Diamond}^{\mathrm{disc}}$ and compare them to the higher-order correlators $C_{\Diamond}$, in two cases: For the undoped Heisenberg model we use quantum Monte Carlo simulations. For a single mobile dopant our predictions are based on the frozen-spin approxima-

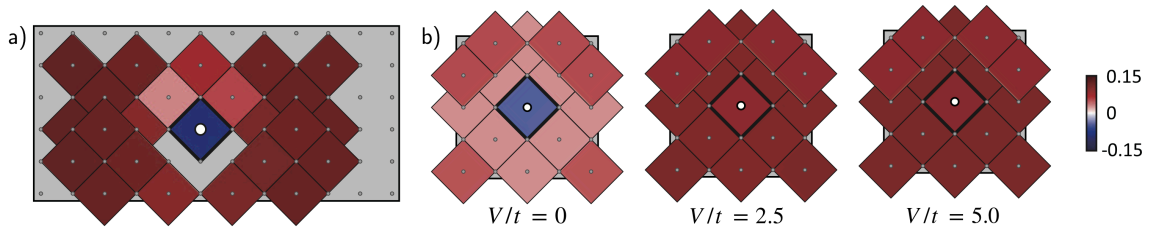

Figure 5.3.5: Higher order correlations and hole mobility $C_\diamondsuit(\mathbf{r}, \mathbf{d})$ as a function of distance $\mathbf{d}$ from the hole. a) DMRG simulation for the ground state on a 6×12 cylinder, where the hole is on site 6. The different distances to the boundaries of the cylinder lead to a small asymmetry in the correlation. b) Exact diagonalization calculations for the ground state of the Fermi-Hubbard model on a 4×4 system with periodic boundary conditions in both directions. The hole is pinned in the origin with a pinning potential V of varying strength, $V/t = 0, 2.5, 5$, and the correlation is shown for $\mathbf{r} = 0$.

tion with the spin background given by Heisenberg quantum Monte Carlo data, see section 5.2.4. The correlators are evaluated from 10^4 snapshots for each temperature. We also compare to exact diagonalization (ED) calculations in a 4×4 system and find good agreement. In the geometric string theory, $C_\diamondsuit^{\text{disc}}$ is approximately zero up to temperatures $T \lesssim 0.5J$, while the higher-order correlator $C_\diamondsuit$ is of the order of -0.1. Without a hole, the disconnected part $D_\diamondsuit^{\text{disc}}$ is significantly larger than $D_\diamondsuit$ for these small temperatures. For $T \gtrsim 0.6J$ the correlations decay quickly. The relevant temperature range has already been accessed experimentally [76], and we expect that more quantum gas microscopy experiments operating in this regime will follow in the near future [65, 83, 85, 217, 296]. In Fig. 5.3.3 b), the proposed higher-order correlations are extracted from snapshots as in a quantum gas microscopy experiment. We expect the main challenge will be to collect sufficient amounts of data to obtain acceptable errorbars. Current experiments offering simultaneous spin- and charge resolution [297] are very close to the temperature regime required for observing the higher-order correlations proposed here.

Our numerical studies for a single doped hole reveal the importance of the hole mobility for establishing higher-order correlations and making them become the dominant spin-charge correlations in the system. In Fig. 5.3.5, we demonstrate this explicitly by considering the effect of a localized pinning potential for the hole. Similar to Eq. (5.34), we define the same correlation function with an additional dependence on the distance $\mathbf{d}$ to the hole as

$$C_\diamondsuit(\mathbf{r}, \mathbf{d}) = \frac{2^4}{\langle \hat{n}^{\text{h}}_{\mathbf{r}} \rangle} \langle \hat{n}^{\text{h}}_{\mathbf{r}} \hat{S}^z_{\mathbf{r}+\mathbf{d}+\mathbf{e}_x} \hat{S}^z_{\mathbf{r}+\mathbf{d}+\mathbf{e}_y} \hat{S}^z_{\mathbf{r}+\mathbf{d}-\mathbf{e}_x} \hat{S}^z_{\mathbf{r}+\mathbf{d}-\mathbf{e}_y} \rangle. \tag{5.40}$$

In Fig. 5.3.5 a), the distance dependent correlation is shown for the ground state of the $t-J$ model on a 6×12 cylinder. While the correlation around the hole is strongly negative, there is only a weak

effect around neighboring sites and no change in $C_\diamondsuit(\mathbf{r}, \mathbf{d})$ for large distances. In Fig. 5.3.5 b), the same correlations are shown for a single dopant in the ground state of the Fermi-Hubbard model on a 4×4 torus simulated with exact diagonalization. Here, a pinning potential V on the origin is included, which restricts the mobility of the dopant. Already for $V/t = 2.5$, $C_\diamondsuit$ around the hole becomes positive and is almost indistinguishable from the background value.
An interesting question concerns the behavior of the higher-order correlations when doping is increased and numerical studies of the Fermi-Hubbard model become more challenging [298]. In this regime we propose to measure the higher-order correlators by state-of-the-art ultracold atom experiments. Such studies can shed new light on the nature of charge carriers in the pseudogap and strange-metal [77] regimes or the pairing mechanism between dopants. They also provide a new experimental route to distinguish theoretical trial states, e.g. in the RVB class. While our machine-learning analysis in section 6.5 suggests that up to $\simeq 15\%$ doping a model based on geometric strings may be favorable compared to doped π-flux RVB states, further refined experiments as proposed here will be required to establish where and how the nature of charge carriers changes upon doping. In a recent work, we implemented a neural network that allows for interpretability of the results and found that similar higher-order (up to fourth order) correlations play a significant role in distinguishing geometric string theory from the π-flux RVB state [16].

5.4 The Spectral Function

This section is based on the publication

- Annabelle Bohrdt, Eugene Demler, Frank Pollmann, Michael Knap, and Fabian Grusdt: "Parton theory of ARPES spectra in anti-ferromagnetic Mott insulators" – Phys. Rev. B 102, 035139 [arXiv:2001.05509]

Structure, text and figures have been rearranged and adapted here.

In Section 4.2, we discussed a measurement scheme for the spectral function in a quantum gas microscope and its application to one dimensional systems. The same scheme can in principle also be applied in a two dimensional system. The spectral function of the two dimensional *attractive* Fermi Hubbard model has moreover been measured with a slightly different protocol in a cold atom experiment at comparably high temperatures across the BCS-BEC crossover [79]. In this work, the authors use a radiofrequency pulse to excite atoms from the interacting system to a non-interacting final state. Afterwards, the $T/4$-mapping discussed in section 4.2.3 is applied in the two-dimensional system to obtain momentum resolution.
Here, we present numerical results for the spectral function of a single hole in the two dimensional

$t-J$ model obtained with TeNPy. The numerical findings can be explained qualitatively with a parton construction based on the geometric string theory.

In the one dimensional case discussed in Section 4.2, the fractionalization of the excitation leads to a continuum – or in the case of a finite system to several distinct lines – in the spectrum. However, in two dimensions, a discrete quasiparticle peak is found, which corresponds to a long-lived magnetic polaron excitation[4, 207, 242–258, 267]. For reconciling the experimental observations with numerical calculations in the clean $t-J$ or Hubbard models, inclusion of electron-phonon interactions has been an important issue [299, 300]. At finite doping, but before the system becomes superconducting, a pseudogap is observed [282]. Instead of a closed Fermi surface, as might be expected from a Fermi-liquid state, Fermi-arcs have been found at low energies around the nodal points $(\pm\pi/2, \pm\pi/2)$ [153] (we use units where the lattice constant $a = 1$ and $\hbar = 1$). These arcs of high spectral weight appear like a part of a small Fermi surface, but the backside of the putative Fermi surface is invisible. The microscopic origin of Fermi arcs in the pseudogap phase of cuprates is not understood today, but their existence has been argued to imply exotic underlying physics and topological order [154–157].

Theoretically predicting ARPES spectra of real solids is challenging. Microscopic models are hard to solve because they involve non-trivial band structures, electron-phonon and electron-electron interactions; Moreover, model parameters are not exactly known. This has lead to a long-standing debate about the explanation of ARPES spectra in the undoped AFM insulator and the origin of Fermi arcs.

Here we focus on ARPES spectra in clean toy models for doped AFMs. Even in such idealized scenarios, the theoretical challenges are significant enough that many open questions remain and a universally accepted understanding is lacking. Our work contributes two significant advances: (i) we improve state-of-the-art numerical simulations of ARPES spectra and (ii) we combine our results with recent insights into the microscopic structure of charge carriers in doped AFMs obtained from numerical simulations and cold atom experiments with quantum gas microscopes, see sections 5.1, 5.3, chapter 6 and Refs. [6, 267]. As a result, we reach a detailed understanding of one-hole ARPES spectra in the paradigmatic $t-J$ model.

Our findings have important consequences, both theoretically and experimentally. Ultracold atom experiments enable clean studies of the Fermi-Hubbard model with tunable parameters [73, 74, 76, 217, 218, 266, 267], in 1D or 2D, as discussed in section 2.1 and 4.2. One can also study continuous dimensional cross-overs which are relevant to solids as well [301, 302]. ARPES spectra can be accessed in optical lattices [2, 79, 189, 194, 196, 303], allowing to experimentally test our theoretical predictions in the near future. On the theoretical side, our work verifies that one-hole ARPES spectra in the AFM can be understood from more fundamental constituents (partons), whose properties we can describe on a quantitative and microscopic level, see also sections 5.1 and

5.3. Moreover, this leads to new insights to the current puzzles of cuprates, in particular the microscopic origin of Fermi arcs.
The main results of this section are as follows.

1. We argue that state-of-the-art numerical calculations of the spectral function conclusively demonstrate that magnetic polarons in the clean $t-J$ model are composed of partons: they form meson-like bound states of spinons and chargons.

2. The spin-charge correlations present in this model at strong coupling can be efficiently described by a Born-Oppenheimer product wavefunction, *if* one works in the so-called geometric string basis [3, 4], see also sections 5.1 and 5.3. As an important consequence of this second result, we demonstrate that all characteristic low-energy features in the spectrum at strong coupling can be attributed to either spinon or chargon properties.

3. We have a simple analytic understanding of the microscopic chargon properties. This leads us to the conjecture that *a one-to-one relation exists, valid at strong coupling, between the observed one-hole spectral function and the spectrum of a constituting spinon in the undoped parent AFM*. This result has consequences well beyond the present work, suggesting ARPES spectroscopy at strong coupling as the most direct tool yet to probe the properties of constituting spinons in quantum AFMs. Possible applications include studies of quantum spin liquids.

For low energies, no more than $\approx 2t$ above the one-hole ground state, the main spectral features of a single hole in the 2D $t-J$ model, assuming $t > J$ are summarized below.

(i) At the lowest energies, a dispersive quasiparticle peak – the magnetic polaron – is observed. Its bandwidth is on the order of the super-exchange coupling J – rather than hole tunneling t – and the shape of the dispersion relation differs significantly from that of a free hole. This is confirmed by our td-MPS studies, see Fig. 5.4.1.

(ii) The quasiparticle residue $Z_{(\pi/2,\pi/2)}$ around the dispersion minimum at the nodal point depends strongly on t/J. All numerical methods have conclusively shown that $Z_{(\pi/2,\pi/2)} > 0$, despite conflicting theoretical proposals [304]. This is also confirmed by our td-MPS simulations, see Fig. 5.4.3.

(iii) Above the magnetic polaron ground state, at excitation energies $\Delta E < t$, a second peak has been observed. The most reliable signatures were obtained by Monte-Carlo calculations [253, 254], while large-scale exact diagonalization studies yielded conflicting results for increasing system sizes [207, 251]. Like the ground state energy E_0 itself, the energy of the first peak E_0 has been shown to be consistent with a scaling of the form $E_n = -2\sqrt{3}t + c_n t^{1/3} J^{2/3}$, asymptotically for $t \gg J$. This is confirmed by our td-MPS studies, see Fig. 5.4.2.

(iv) The quasiparticle residue $Z(\mathbf{k})$ has strong, and non-monotonic momentum dependence. Our td-MPS simulations confirm this feature, see Fig. 5.4.1.

We numerically establish the following additional features, see Fig. 5.4.1:

(v) Around $\mathbf{k} = (\pi, \pi)$ the spectral weight is suppressed in a wide window up to energies of order $\mathcal{O}(2t)$ above the ground state.

(vi) The first excited peak – see (iii) – can be observed for all momenta, provided the ground state residue $Z(\mathbf{k})$ is non-negligible. The dispersion relation of the first excited peak is qualitatively identical to the ground state – i.e. the excitation gap $\Delta_{\mathbf{k}}$ has only weak $\mathbf{k}$-dependence.

Comparing to the different theoretical scenarios discussed in the introduction, some of these features can be explained as follows:

(a) *String picture*: The picture of strings of over-turned spins in a Néel state [257, 259–265] explains (iii), the scaling of the ground state energy $E_0 \simeq -2\sqrt{3}t + c_0 t^{1/3} J^{2/3}$ of a single hole at $t \gg J$; The string picture also predicts the existence of vibrationally excited states, with the same dependence on t and J. Feature (ii) is also expected from the string picture, owing to the finite length of the strings. Features (i) and (iv) - (vi) require explanations beyond the string picture.

(b) *Parton picture*: Here, the mobile dopants are described by fractionalized spinons and chargons. The parton picture explains (i): the dispersion relation of the one-hole ground state is determined by the spinon dispersion, which must have a bandwidth $W_s = \mathcal{O}(J)$ dominated by spin-exchange. The conjectured chargon dispersion, with bandwidth $W_c = \mathcal{O}(t)$, is expected to lead to additional features at higher energies in the spectrum. Features (ii) and (iii) are only consistent with the parton picture, if spinons and chargons form a bound state. To make quantitative predictions and fully explain features (ii) - (vi), detailed knowledge about the parton dispersions and their microscopic interactions is required; this is typically beyond the scope of phenomenological descriptions. An experimental work [305] has also led to an interpretation of the pronounced high-energy features in the spectrum as signatures of spinon and chargon branches.

(c) *Polaron picture*: The mobile dopant is dressed by the collective magnon excitations [242–244, 246–250]. Spin-wave calculations of the spectral function [246, 248] have revealed several vibrational peaks with the expected scaling $\simeq t^{1/3} J^{2/3}$ of their energies [248], thus explaining (iii). The strong renormalization of the bandwidth of the dopant (i), from $\mathcal{O}(t)$ to the observed $\mathcal{O}(J)$ is also predicted, although without identifying a clear physical mechanism.

In section 5.1, we combined the parton and string pictures of magnetic polarons and provide quantitative descriptions of both ingredients. Here we argue why – at strong coupling – any feature of the spectrum is determined by *either* the spinon *or* the chargon / string properties: Essentially, a Born-Oppenheimer product ansatz in the geometric string basis [3, 4], see also section 5.1, allows us to factorize spinon and chargon contributions.
The mean-field theory we use to describe spinons naturally predicts a strongly momentum dependent contribution $Z_s(\mathbf{k})$ to the quasiparticle weight, see Fig. 5.4.4. Already on the mean-field level, a strong suppression of spectral weight around (π, π) is predicted. Since the low-energy excited states of the magnetic polaron correspond to string excitations, sharing the same spinon contribution $Z_s(\mathbf{k})$ to the quasiparticle weight as the ground state, the suppression of spectral weight around (π, π) over a wide energy window is thus explained [feature (v)]. We furthermore go beyond the mean-field theory, by including a Gutzwiller projection in our trial wavefunction, see section 5.1. As a result, we find non-monotonic $\mathbf{k}$-dependence of $Z(\mathbf{k})$ for $t \gtrsim J$ – explaining feature (iv), and in excellent agreement with unbiased numerical results.

5.4.1 Parton theory of ARPES spectra

Similar to the 1D case, we introduce the parton representation

$$\hat{c}_{\mathbf{j},\sigma} = \hat{h}^{\dagger}_{\mathbf{j}} \hat{f}_{\mathbf{j},\sigma} \tag{5.41}$$

with the chargon operator $\hat{h}_{\mathbf{j}}$ and the $S = 1/2$ spinon operator $\hat{f}_{\mathbf{j},\sigma}$, see section 5.1. The physical Hilbert space is spanned by all states satisfying

$$\sum_{\sigma} \hat{f}^{\dagger}_{\mathbf{j},\sigma} \hat{f}_{\mathbf{j},\sigma} + \hat{h}^{\dagger}_{\mathbf{j}} \hat{h}_{\mathbf{j}} = 1 \tag{5.42}$$

for all positions $\mathbf{j}$. As before, we focus on the strong coupling limit $t \gg J$ where the fast motion of the hole can approximately be factorized in the geometric string basis. In this approximation, the spinon-chargon bound state with center-of-mass momentum $\mathbf{k}$ can be described as

$$|\Psi^{\mathrm{FSA}}_{\mathrm{sc}}(\mathbf{k})\rangle = \frac{1}{L} \sum_{\mathbf{j}^s} e^{i\mathbf{k}\cdot\mathbf{j}^s} \sum_{\Sigma} \psi^{\mathrm{FSA}}_{\Sigma} |\mathbf{j}^s\rangle |\Sigma\rangle, \tag{5.43}$$

where the heavy spinon carries the momentum $\mathbf{k}$ and is bound to the lighter chargon, which is delocalized over many different string configurations.
For a parent state $|\psi_0\rangle$ with strong antiferromagnetic correlations, we can assume that the basis

states are mutually orthonormal,

$$\langle \mathbf{j}^{s\prime}|\mathbf{j}^{s}\rangle\langle\Sigma'|\Sigma\rangle \approx \delta_{\mathbf{j}^{s\prime},\mathbf{j}^{s}}\delta_{\Sigma',\Sigma}, \tag{5.44}$$

as discussed in section 5.1. The spectral function can be written as

$$A(\omega,\mathbf{k}) = \mathrm{Re}\frac{1}{\pi}\int_0^\infty dt\, e^{i\omega t} \times \langle\Psi_0|e^{i\hat{\mathcal{H}}t}\left(\sum_\sigma \hat{c}^\dagger_{\mathbf{k},\sigma}\right)e^{-i\hat{\mathcal{H}}t}\left(\sum_\sigma \hat{c}_{\mathbf{k},\sigma}\right)|\Psi_0\rangle. \tag{5.45}$$

The state on the right hand side is

$$\left(\sum_\sigma \hat{c}_{\mathbf{k},\sigma}\right)|\Psi_0\rangle = |\mathbf{k}^{s}\rangle|\Sigma=0\rangle, \tag{5.46}$$

with the plane-wave spinon state

$$|\mathbf{k}^{s}\rangle = L^{-1}\sum_{\mathbf{j}^{s}} e^{i\mathbf{k}^{s}\cdot\mathbf{j}^{s}}|\mathbf{j}^{s}\rangle. \tag{5.47}$$

On the left hand side, $\langle\Psi_0|e^{i\hat{\mathcal{H}}t} = e^{i\omega_0 t}\langle\Psi_0|$. Here, we measure frequencies relative to the energy of the parent state, $\omega_0 = 0$. Based on the assumption that spinon-chargon states are eigenstates, we approximate

$$e^{-i\hat{\mathcal{H}}t}|\mathbf{k}^{s}\rangle|0\rangle \approx e^{-i\hat{\mathcal{H}}_s t}|\mathbf{k}^{s}\rangle e^{-i\hat{\mathcal{H}}_\Sigma t}|0\rangle, \tag{5.48}$$

with $\hat{\mathcal{H}}_s$ and $\hat{\mathcal{H}}_\Sigma$ effective Hamiltonians of the spinon and string (chargon) introduced in section 5.1, respectively. Since the eigenstates factorize into spinon-chargon bound states, the spectral function becomes a convolution of the spinon and chargon contribution,

$$A(\omega,\mathbf{k})|_{\mathrm{bound}} = \int dv\, A_s(\omega-v,\mathbf{k})A_c(v). \tag{5.49}$$

The spinon contribution

$$A_s(\omega,\mathbf{k}^{s}) = \mathrm{Re}\frac{1}{\pi}\int_0^\infty dt\, e^{i\omega t} \times \langle\mathbf{k}^{s}|e^{-i\hat{\mathcal{H}}_s t}|\mathbf{k}^{s}\rangle \tag{5.50}$$

depends on the momentum $\mathbf{k}_s$, whereas the chargon contribution

$$A_c(v) = \mathrm{Re}\frac{1}{\pi}\int_0^\infty dt\, e^{ivt}\langle\Sigma=0|e^{-i\hat{\mathcal{H}}_\Sigma t}|\Sigma=0\rangle \tag{5.51}$$

does not depend on the momentum. We assume the spinon to be static, as in earlier sections, to derive the main features of $A_c(v)$. Due to the approximately linear string tension, a discrete set of vibrational and rotational states is predicted, as discussed in section 5.1. The rotational states have a node in the center, $|\psi_{\Sigma=0}|^2 = 0$, and are thus invisible in the spectral function. In earlier numerical studies, there have however been indications for the lowest vibrational states [248]. We extract the position of the first vibrational peak from the spectral function as discussed in appendix B.2, see also Fig. 5.4.2 a). As shown in Fig. 5.4.2 b), the energy gap to the first vibrational string excitation scales as $\Delta_c \simeq t^{1/3}J^{2/3}$ as expected. The low-frequency regime of the spectrum is thus mainly determined by the spinon spectrum of width $\simeq J \ll \Delta_c$:

$$A(\omega, \mathbf{k}) = A_s(\omega - v_c, \mathbf{k}) Z_c \quad \text{for } \omega \ll \Delta_c, \tag{5.52}$$

where v_c is the ground state energy of the chargon and Z_c is the chargon contribution to the quasiparticle weight. The entire momentum dependence of the spectral function at low energies is thus determined by the spinon contribution, which we expect to exhibit a quasiparticle structure

$$A_s(\omega, \mathbf{k}) = Z_s(\mathbf{k}) \delta\left(\omega - \omega_s(\mathbf{k})\right). \tag{5.53}$$

Here, $Z_s(\mathbf{k})$ is the spinon contribution to the quasiparticle residue and $\omega_s(\mathbf{k})$ is the spinon dispersion.

The chargon contribution to the quasiparticle residue Z_c is determined by the probability of string length zero,

$$Z_c = |\psi_{\Sigma=0}|^2, \tag{5.54}$$

determined from the geometric string theory. As we have seen in section 5.3, the string length distribution and thus Z_c depends strongly on t/J. At low energies, the spectral function is therefore expected to take the form

$$A(\omega, \mathbf{k}) = Z_c Z_s(\mathbf{k}) \, \delta\left(\omega - v_c - \omega_s(\mathbf{k})\right), \;\; \omega \ll \Delta_c. \tag{5.55}$$

While the chargon properties Z_c and v_c are universally determined by the geometric string theory, the spinon properties $Z_s(\mathbf{k})$ and $\omega_s(\mathbf{k})$ depend on specific properties of the parton model. As a consequence, the one-hole spectral function reveals direct information about the properties of constituting spinons in the underlying spin model. The above considerations hold in any system with sufficiently strong local anti-ferromagnetic correlations and strong couplings $t \gg J$. Usually, information about spinons is extracted from the dynamical spin structure factor [274, 306, 307], in which case one can only study pairs of (interacting) spinons.

A comment is in order about our notion of *constituting spinons*. If the spin system is in a confining

phase, as in the case of the 2D Heisenberg AFM with long-range order, isolated spinon excitations cannot exist: there is no spin-charge fractionalization. The strong coupling parton theory above explicitly assumes, however, that the spinon is bound to the chargon. Such mesonic bound states can exist even in a confining phase. In this case the ARPES spectrum is expected to reveal the properties of the constituting spinon, without the strong renormalization effects present e.g. in the spin structure factor due to spinon-spinon interactions. In a possible deconfined phase, free spinon excitations can exist: the constituting spinons are identical to the free spinons in this case. At strong couplings we still expect that spinon-chargon bound states, as described above, will form at low energies. This scenario is realized e.g. in fractionalized Fermi liquids [270, 271], and in this case the ARPES spectrum of the form in Eq. (5.55) is expected to directly reveal the properties of free spinons.

Unbound spinon-chargon pairs

Spin systems in a deconfined phase can also support unbound spinon-chargon pairs. In this case the spectral function also becomes a convolution of a spinon and a chargon (or holon) part, as discussed in detail in section 4.2. Because the center-of-mass momentum can be distributed arbitrarily between the two partons, the convolution includes both frequency and momentum integrals,

$$A(\omega, \mathbf{k})|_{\text{unbound}} = \int d\nu d\boldsymbol{\kappa}\, A_{\text{s}}(\omega - \nu, \mathbf{k} - \boldsymbol{\kappa}) A_{\text{c}}(\nu, \boldsymbol{\kappa}). \tag{5.56}$$

In the absence of a bound state the quasiparticle residue $Z = 0$ vanishes, a hallmark of spin-charge separation [308].

The deconfined scenario is realized for example in the 1D $t-J$ model at strong coupling [177, 205, 213, 309]. There, a similar wavefunction as in Eq. (5.43) can be used to describe the eigenstates of a single hole [215, 310], but the string wavefunctions are extended: $\psi_{\Sigma}^{\text{FSA}}(k_{\text{c}}) = e^{-ik_{\text{c}}\Sigma}/\sqrt{L}$ where $\Sigma \in \mathbb{Z}$ denotes linear string configurations of length $\ell_{\Sigma} = |\Sigma|$ and k_{c} is the chargon momentum. The spinon wavefunction in 1D can be accurately modeled by a slave-particle mean-field ansatz for spinons forming a Fermi sea [2, 213], see section 4.2. Magnon corrections in 1D have also been calculated and shown to be small [2].

5.4.2 Numerical Results

Employing the matrix product state techniques discussed in Section 5.5 and Appendix A.2, we calculate the time-dependent Green's function

$$C_{\uparrow}(x, y, t) = \langle \Psi_{\text{o}} | e^{i\hat{\mathcal{H}}t} \hat{c}^{\dagger}_{x,y,\uparrow} e^{-i\hat{\mathcal{H}}t} \hat{c}_{\text{o,o},\uparrow} | \Psi_{\text{o}} \rangle \tag{5.57}$$

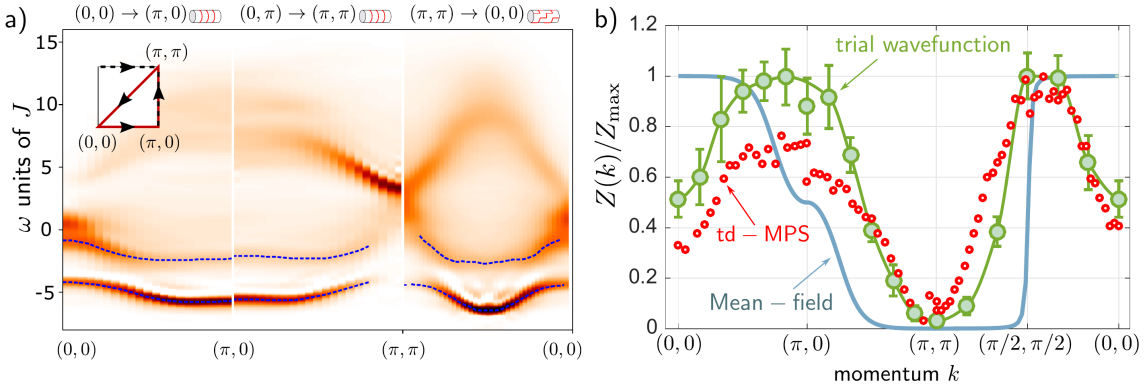

Figure 5.4.1: Spectral function in the 2D $t-J$ model. a) We perform td-MPS simulations of single-hole spectra in the $t-J$ model on 4×40 cylinders of different geometry. At strong couplings $t \gg J$, here $t = 3J$, a strong suppression of spectral weight is observed at (π,π) at low-to-intermediate energies. Details of the td-MPS calculations are provided in Appendix B. The spectrum is obtained along cuts in the Brillouin zone, calculated for different coverings of the cylinder by MPSs (both indicated in the top row). The dashed lines indicate the dispersion relations of the lowest two peaks (determined as local maxima of the spectrum), which we interpret as the ground and first vibrational states of the magnetic polaron. b) Momentum dependence of the quasiparticle weight. We calculate the quasiparticle residue $Z(\mathbf{k})$, normalized by $Z_{\max} = \max_{\mathbf{k}} Z(\mathbf{k})$, from the trial wavefunction (5.30) along a cut $(0,0) - (\pi,0) - (\pi,\pi) - (0,0)$ in a periodic 12×12 system. Parameters are $t = 3J$ and we used the optimized mean-field parameters $B_{\mathrm{st}}/J_{\mathrm{eff}} = 0.44$ and $\Phi = 0.4\pi$. The solid green line is a guide to the eye. We compare our results to the bare mean-field prediction (solid blue line) and results from our td-MPS calculations (red dots). See section B.2 on how $Z(\mathbf{k})$ is numerically extracted from td-MPS.

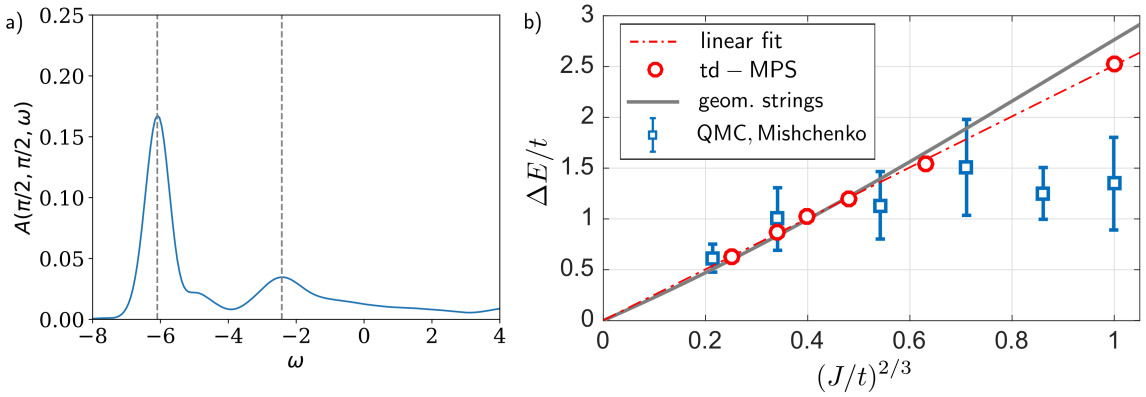

Figure 5.4.2: Vibrational excitations in the spectral function in the 2D $t-J$ model. a) We show the frequency cut of the one-hole spectral function at the nodal point $\mathbf{k} = (\pi/2, \pi/2)$, for the same parameters as in Fig. 5.4.1 a). The extracted positions of the ground state (first peak) and vibrationally excited (second peak) magnetic polaron are indicated by dashed lines. b) We analyze the energy ΔE between the lowest two pronounced peaks in the spectrum. Our td-MPS results (red) on $4 \times L_x$ cylinders are compared to quantum Monte Carlo calculations by Mishchenko et al. (blue, data extracted from Ref. [254]) and the effective geometric string approach (gray). A fit $\Delta E/t = a(J/t)^{2/3} + b$ to our td-MPS data yields $a = 2.51$ and $b = 2 \times 10^{-3}$. All data is for the ground state at the nodal point, $\mathbf{k} = (\pi/2, \pi/2)$. Finite size effects in our td-MPS calculations are expected to be weak, but quantitative estimates of their size are difficult.

for the $t-J$ model on a cylinder, where $|\Psi_0\rangle$ is the ground state at half-filling. We then Fourier transform $C_\uparrow(x, y, t)$ to obtain

$$A(k_x, k_y, t) = \frac{1}{\sqrt{L_x L_y}} \sum_x \sum_y e^{-ik_x x} e^{-ik_y y} C_\uparrow(x, y, t). \tag{5.58}$$

In order to smoothen the spectral function we perform a linear prediction in real time before Fourier transforming to frequency space, see section B.2.

$$A(\omega, \mathbf{k}) = \frac{1}{\sqrt{2\pi}} \sum_t e^{i\omega t} \tilde{A}(k_x, k_y, t). \tag{5.59}$$

The resulting spectral function is shown in Fig. 5.4.1 for $t/J = 3$ and a cylinder with 4 legs. Consistent with earlier spin-wave [248], exact diagonalization [207, 251], truncated basis [257], cluster-perturbation [311] and quantum Monte-Carlo calculations [253, 254], we find a well-defined quasiparticle peak at low energies. The momentum dependence of the peak position corresponds to the spinon dispersion as expected. The vibrational peaks discussed above are extracted from the frequency dependent spectral function $A(\omega, \pi/2, \pi/2)$ as shown in Fig. 5.4.2 a). As can be seen from the cuts at momenta $\mathbf{k} = (0, 0), (\pi/2, \pi/2)$ and (π, π), there is no spectral weight at low energies

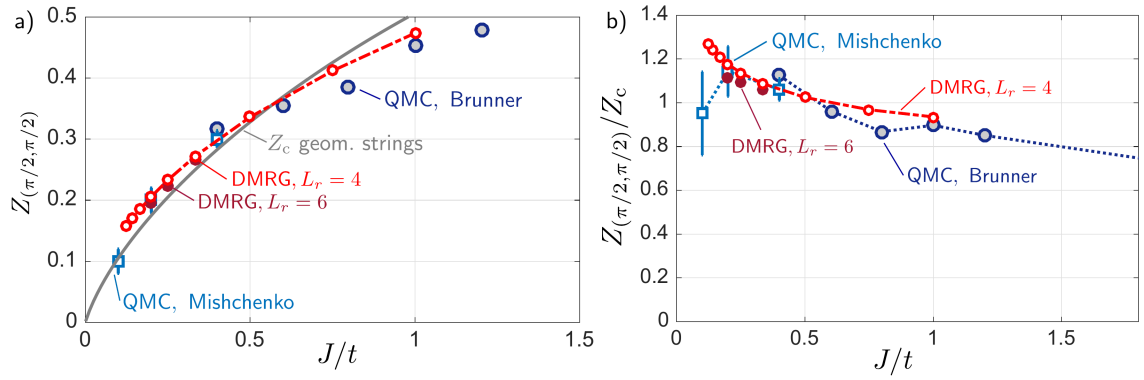

Figure 5.4.3: Quasiparticle residue $Z(\pi/2,\pi,2)$ in the 2D $t-J$ model. a) The quasiparticle weight $Z(\pi/2,\pi/2)$ at the nodal point is shown as a function of J/t. We find that earlier numerical Monte Carlo studies by Brunner et al. [253] and Mishchenko et al. [254] predict values close to the bare chargon, or string, contribution $Z_c = |\psi^{\mathrm{FSA}}_{\Sigma=0}|^2$ expected from the geometric string approach (solid gray line). This is confirmed by our DMRG simulations on cylinders with L_r legs – we used bond dimensions $\chi = 500$ ($\chi = 600$) for $L_r = 4$ ($L_r = 6$). b) We plot $Z_{(\pi/2,\pi/2)}/Z_c$ as a function of J/t. The data shows only weak dependence on J/t, indicating that $Z_c(J/t)$ captures the main J/t-dependence of the quasiparticle weight; note that for $J/t \lesssim 0.2$ ($t/J \gtrsim 5$) finite-size effects start to become more sizable in the DMRG. The insets show the same data plotted over t/J.

in the latter case but instead a high energy feature. Note that this feature appears at a different frequency and exhibits a sharper form than the broad peak observed at $\mathbf{k} = (0,0)$ around $\omega = 0$, indicating that different mechanisms are at play [311]. In order to obtain the ground state quasiparticle weight, we use the ground state of a single hole in the $t-J$ model $|\Psi^{1h}_0\rangle$ to directly calculate

$$Z(\pi/2,\pi/2) = 2 \cdot \sum_{\mathbf{i}} |\left\langle \Psi^{1h}_0 \right| \hat{c}_{\mathbf{i},\uparrow} |\Psi_0\rangle|^2. \tag{5.60}$$

Since the ground state of the $t-J$ model with a single hole is at $\mathbf{k} = (\pi/2,\pi/2)$, only contributions at this momentum are unequal zero and an additional Fourier transform is not necessary. In Fig. 5.4.3, the resulting quasiparticle weights are compared to data from quantum Monte Carlo calculations.

From the parton theory, we expect that the quasiparticle weight factorizes into a spinon and a chargon, or string, contribution, Eq. (5.55). While the momentum dependence is contained in the spinon contribution, only the chargon contribution depends on t/J for $t \gg J$. The gray line in Fig. 5.4.3 directly corresponds to the chargon contribution $Z_c(J/t) = |\psi^{\mathrm{FSA}}_{\Sigma=0}(J/t)|^2$ without any free parameters. This geometric string theory results agrees quantitatively well with the numerics, indicating that the spinon contribution is $Z_s(\pi/2,\pi/2) \approx 1$. In Fig. 5.4.3 b), we further investigate the J/t dependence by normalizing the quasiparticle weight by the chargon contribution, which

yields an approximately flat function. Finite-size effects play an increasing role at smaller values of J/t for the DMRG. We find that the behavior of $Z_{(\pi/2,\pi/2)}/Z_c$ is consistent with approaching 1 when $t \gg J$.

Overall, the parton theory provides a good qualitative and even quantitative understanding of the numerical results for the spectral function at low and intermediate energies. The high energy feature at $\mathbf{k} = (\pi, \pi)$ is not captured by our considerations here.

5.4.3 Trial wavefunction and mean field approximation

We apply variational Monte Carlo sampling [113] to calculate the quasiparticle weight based on the trial wavefunction introduced in section 5.1,

$$Z(\mathbf{k}) = \frac{\sum_\sigma |\langle \Psi_{sc}(\mathbf{k}) | \hat{f}_{\mathbf{k},\sigma} \hat{\mathcal{P}}_{GW} | \Psi_{MF}^{SF+N} \rangle|^2}{|\langle \Psi_{MF}^{SF+N} | \hat{\mathcal{P}}_{GW} | \Psi_{MF}^{SF+N} \rangle \langle \Psi_{sc}(\mathbf{k}) | \Psi_{sc}(\mathbf{k}) \rangle|}. \tag{5.61}$$

Here, the denominator guarantees proper normalization.

A mean-field description of spinons is obtained by dropping the Gutzwiller projection in Eqs. (5.30), (5.61) and working directly with the mean-field Hamiltonian from Eq. (5.27). In principle bosonic or fermionic spinons can both be considered. However, the bosonic theory would require strong interactions to explain the observed spinon quasiparticle weight $Z_s(\mathbf{k}) \approx Z(\mathbf{k})/Z_c$. We will argue that non-interacting fermionic spinons readily predict the qualitative features of $Z_s(\mathbf{k})$.

We calculate $Z^{MF}(\mathbf{k})$ by applying the FSA and mean-field approximations in Eq. (5.61). Note that $\mathbf{k}$ is an arbitrary vector from the full Brillouin zone (BZ); spinon operators $\hat{f}_{\mathbf{k},\sigma}$ are defined in the BZ, whereas for spinons $\hat{f}_{\mathbf{k},\sigma,\nu}$ with band indices ν the cases $\mathbf{k} \in$ MBZ and $\mathbf{k} \notin$ MBZ have to be distinguished.

In the FSA we assume that only the trivial string state $\Sigma = 0$ contributes, since non-trivial string states are approximately orthogonal to the background AFM. Using Eq. (5.30), we obtain

$$\begin{aligned}\langle \Psi_{sc}(\mathbf{k}) | \hat{f}_{\mathbf{k},\sigma} \hat{\mathcal{P}}_{GW} | \Psi_{MF}^{SF+N} \rangle &\approx \psi^*_{\Sigma=0} \sum_{\mathbf{j}^s} \frac{u^{(\mathbf{j}^s)}_{\mathbf{k},\sigma,-} e^{-i\mathbf{k}\cdot\mathbf{j}^s}}{L/\sqrt{2}} \times \langle \Psi_{MF}^{SF+N} | \hat{f}^\dagger_{\mathbf{j}^s,\sigma} \hat{\mathcal{P}}_{GW} \hat{f}_{\mathbf{k},\sigma} \hat{\mathcal{P}}_{GW} | \Psi_{MF}^{SF+N} \rangle \\ &= \psi^*_{\Sigma=0} \langle \Psi_{MF}^{SF+N} | \hat{f}^\dagger_{\mathbf{k},\sigma,-} \hat{\mathcal{P}}_{GW} \hat{f}_{\mathbf{k},\sigma} \hat{\mathcal{P}}_{GW} | \Psi_{MF}^{SF+N} \rangle. \end{aligned} \tag{5.62}$$

In the second step, we used

$$\hat{f}^\dagger_{\mathbf{k},\sigma,\mu} = \sum_{\mathbf{j}} \frac{e^{-i\mathbf{k}\cdot\mathbf{j}}}{L/\sqrt{2}} u^{(\mathbf{j})}_{\mathbf{k},\sigma,\mu} \hat{f}^\dagger_{\mathbf{j},\sigma}. \tag{5.63}$$

Then, dropping the Gutzwiller projectors yields

$$Z^{\mathrm{MF}}(\mathbf{k}) = Z_{\mathrm{c}} \sum_{\sigma} |\langle \Psi_{\mathrm{MF}}^{\mathrm{SF+N}} | \hat{f}^{\dagger}_{\mathbf{k},\sigma,-} \hat{f}_{\mathbf{k},\sigma} | \Psi_{\mathrm{MF}}^{\mathrm{SF+N}} \rangle|^2. \tag{5.64}$$

This expression is of the general form expected from the parton theory, see Eq. (5.55). Note that $\hat{f}_{\mathbf{k}+\mathbf{K},\sigma,-} \equiv \hat{f}_{\mathbf{k},\sigma,-}$, where $\mathbf{K}$ is the reciprocal lattice vector, but $\hat{f}_{\mathbf{k}+\mathbf{K},\sigma} \neq \hat{f}_{\mathbf{k},\sigma}$. We then use the following identities

$$\hat{f}^{\dagger}_{\mathbf{k},\sigma} = \lambda^{+}_{\mathbf{k}} \hat{f}^{\dagger}_{\mathbf{k},\sigma,+} + \lambda^{-}_{\mathbf{k}} \hat{f}^{\dagger}_{\mathbf{k},\sigma,-}, \tag{5.65}$$

$$\hat{f}^{\dagger}_{\mathbf{k}+\mathbf{K},\sigma} = \lambda^{+}_{\mathbf{k}+\mathbf{K}} \hat{f}^{\dagger}_{\mathbf{k},\sigma,+} + \lambda^{-}_{\mathbf{k}+\mathbf{K}} \hat{f}^{\dagger}_{\mathbf{k},\sigma,-}, \tag{5.66}$$

where $\mathbf{k} \in \mathrm{MBZ}$ and the factors $\lambda^{\pm}$ are given by

$$\lambda^{\mu}_{\mathbf{k}} = \frac{1}{\sqrt{2}} \left(u^{(A)}_{\mathbf{k},\sigma,\mu} + u^{(B)}_{\mathbf{k},\sigma,\mu} \right)^{*} \tag{5.67}$$

$$\lambda^{\mu}_{\mathbf{k}+\mathbf{K}} = \frac{1}{\sqrt{2}} \left(u^{(A)}_{\mathbf{k},\sigma,\mu} - u^{(B)}_{\mathbf{k},\sigma,\mu} \right)^{*}; \tag{5.68}$$

A and B denote sites $\mathbf{j}$ from the A and B sublattice, respectively, and $\mu = \pm$ is the band index. The spinon contribution on the right hand side of Eq. (5.64) is thus related to the mean-field Bloch wavefunction $u^{(A,B)}_{\mathbf{k},\sigma,-}$ for sites $\mathbf{j}$ from the A, B sublattice respectively,

$$Z_{\mathrm{s}}^{\mathrm{MF}}(\mathbf{k}) = \frac{1}{2} \sum_{\sigma} \begin{cases} |u^{(A)}_{\mathbf{k},\sigma,-} + u^{(B)}_{\mathbf{k},\sigma,-}|^2, & \mathbf{k} \in \mathrm{MBZ} \\ |u^{(A)}_{\mathbf{k},\sigma,-} - u^{(B)}_{\mathbf{k},\sigma,-}|^2, & \text{else.} \end{cases} \tag{5.69}$$

One important conclusion is that $Z_{\mathrm{s}}^{\mathrm{MF}}(\mathbf{k})$ generally reflects the $\mathbf{k}$-dependence of the Bloch wavefunctions, which is determined by the parameters $B_{\mathrm{st}}/J_{\mathrm{eff}}$ and Φ in the mean-field Hamiltonian Eq. (5.27). Moreover, momenta within the MBZ and outside of it are treated separately, causing constructive and destructive interference of the Bloch wavefunctions respectively. In the following limiting cases the mean-field spinon contribution $Z_{\mathrm{s}}^{\mathrm{MF}}(\mathbf{k})$ shows interesting behavior. In a classical Néel state, when $B_{\mathrm{st}}/J_{\mathrm{eff}} \to \infty$, it holds $(u^{(A)}_{\mathbf{k},\sigma,-}, u^{(B)}_{\mathbf{k},\sigma,-}) = (1, 0)$ or $(0, 1)$. This leads to a featureless spinon spectrum, $Z_{\mathrm{s}}^{\mathrm{MF}}(\mathbf{k}) = 1$ everywhere, see Fig. 5.4.4 a). For the uniform resonating valence bond state, $\Phi = 0$ and $B_{\mathrm{st}} = 0$, it holds $u^{(A)}_{\mathbf{k},\sigma,-} = u^{(B)}_{\mathbf{k},\sigma,-} = 1/\sqrt{2}$. The spinons form a Fermi sea occupying the MBZ, which is directly reflected by the strongly asymmetric spectral weight: $Z_{\mathrm{s}}^{\mathrm{MF}}(\mathbf{k}) = 2$ for $\mathbf{k}$ within MBZ, and $Z_{\mathrm{s}}^{\mathrm{MF}} = 0$ otherwise, see Fig. 5.4.4 b). When $B_{\mathrm{st}} = 0$ but the staggered magnetic flux $\Phi \neq 0$, the mean-field dispersion has a Dirac cone around the nodal point $\mathbf{k} = (\pi/2, \pi/2)$. This leads to a shard drop of spectral weight along the diagonal from $(0, 0)$ to

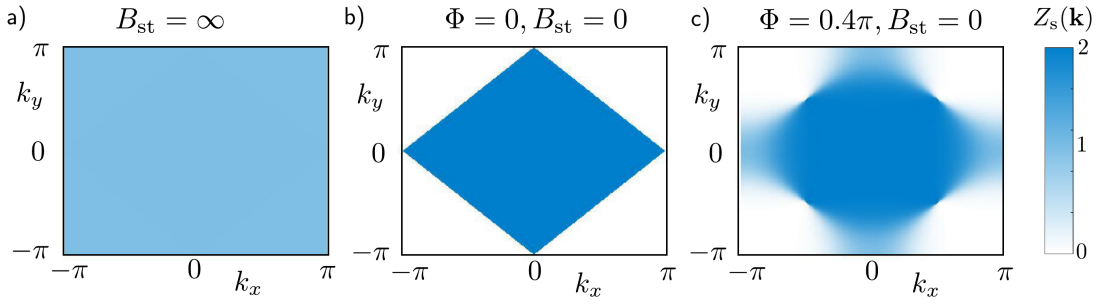

Figure 5.4.4: Mean-field spinon contribution to the quasiparticle residue. $Z_{\mathrm{s}}^{\mathrm{MF}}(\mathbf{k})$ from Eq. (5.69) is shown in the following limiting cases: a) $B_{\mathrm{st}}/J_{\mathrm{eff}} \to \infty$, b) $B_{\mathrm{st}} = \Phi = 0$, c) $B_{\mathrm{st}} = 0$ and $\Phi = 0.4\pi$. The color bar is indicated on the right.

(π, π) crossing the Dirac point, see Fig. 5.4.4 c).

5.4.4 Momentum dependence of quasiparticle weight

In Fig. 5.4.1 b) we plot the $\mathbf{k}$-dependence of the quasiparticle weight Z for $t/J = 3$ obtained from MPS simulations, the trial wavefunction and the mean field approximation. For the MPS simulations, we assume a Gaussian form of the lowest energy peak and extract Z correspondingly from the height and the full width at half maximum of the peak. For the trial wavefunction, we use the string wavefunction $\psi_\Sigma = \psi_\Sigma^{\mathrm{FSA}}$ obtained from the FSA in Eq. (5.30). For the mean-field theory, we use the parameters $B_{\mathrm{st}}/J_{\mathrm{eff}}$ and Φ optimized for the half-filled Heisenberg AFM [274].
The result from the trial wavefunction is in very good agreement with our numerical td-MPS and previous Monte-Carlo results [253]. In the center of the MBZ, around $(0, 0)$, we observe a dip of the spectral weight. The maximum is found at the edge of the MBZ, including at the high-symmetry points $(0, \pi)$ and $(\pi/2, \pi/2)$. Outside the MBZ, the Z-factor is strongly suppressed, dropping to below 10^{-2} at (π, π). Overall we observe a strong momentum dependence of the Z-factor, which is qualitatively captured by the trial wavefunction. The latter includes strong $\mathbf{k}$-dependence as a consequence of the Fermi statistics that determine the spinon properties in the trial state.
In the mean field theory, we observe a sharp drop of $Z_{\mathrm{s}}^{\mathrm{MF}}(\mathbf{k})$ around the nodal point, although the weak staggered field leads to some broadening. Around $(0, \pi)$ and $(\pi, 0)$, the decrease of the spectral weight is smoother, which we attribute to the larger distance in $\mathbf{k}$-space from the Dirac cone found at the nodal point for $B_{\mathrm{st}} = 0$.
Overall, the $\mathbf{k}$-dependence of the quasiparticle weight from the mean-field parton theory, $Z^{\mathrm{MF}}(\mathbf{k}) = Z_{\mathrm{c}} Z_{\mathrm{s}}^{\mathrm{MF}}(\mathbf{k})$, captures the numerical observations. In particular, it explains the strong suppression of spectral weight around (π, π), extending up to high energies, as a direct signature of fermionic spinon statistics. Other features observed numerically, such as the more pronounced broadening of spectral weight around the edge of the MBZ and the suppressed quasiparticle residue at $(0, 0)$

can be attributed to the Gutzwiller projection and effects beyond FSA. As shown above, these features are correctly predicted by the trial wavefunction Eq. (5.30).

The sudden drop of the quasiparticle weight around the nodal point is reminiscent of the missing spectral weight on the backside of the Fermi arcs observed in the pseudogap phase of cuprates [153]. A similar effect has been observed in a doped spin liquid on the Kagomé lattice, believed to exhibit spin-charge separation [312]. Within our microscopic approach, the strong suppression of the quasiparticle residue in the vicinity of the nodal point, but outside the MBZ, is explained by the underlying structure of constituting fermionic spinons.

5.4.5 Dimensional crossover

We subject the parton theory to another test and study ARPES spectra in the dimensional crossover. We tune the ratio

$$a = t_y/t_x \tag{5.70}$$

of tunneling amplitudes along x and y directions, which leads to spin-exchange couplings $J_y = a^2 J_x$. In ultracold atom experiments with optical lattices, the value of a can be easily tuned, see section 3.1.

Our main motivation for considering the dimensional crossover is that the parton theory with fermionic spinons correctly describes the ARPES spectrum in the 1D $t-J$ model [2, 213], as we have seen in section 4.2. For non-zero $a > 0$ we expect a non-vanishing string tension $\propto aJ_x$ which should lead to spinon-chargon binding. At $a = 1$ we have established above that the parton theory can explain the numerically observed spectra.

In the 1D case, spinons and chargons are deconfined and unbound for $t \gg J$. Because the spectrum is a convolution of spinon and chargon contributions both in momentum and frequency domains, see Eq. (5.56), a coherent quasiparticle peak is absent. Nevertheless, the integrated spectral weight $Z_\omega(k) = \int_0^{\Delta\omega} dv\, A(v_0(k)+v, k)$ in a low-energy region of width $\Delta\omega = \mathcal{O}(J)$ around the ground state at $v_0(k)$ reveals the structure of the spinon Fermi sea. Because $t \gg J$, only chargon states from a narrow range of momenta Δk_c around the minimum at $k_c = 0$ of the chargon dispersion $v_c(k_c) = -2t\cos(k_c)$ contribute to $Z_\omega(k)$ [1]; hence $Z_\omega(k) \propto Z_s(k)$. In one dimension, the mean-field parton theory for the optimized parameter $B_{st} = 0$ in Eq. (5.27) predicts a step function, see Eq. (5.69),

$$Z_s^{MF}(k) = \begin{cases} 2, & |k| \leq \pi/2 \\ 0, & \text{else}, \end{cases} \tag{5.71}$$

[1] The chargon and spinon dispersions are only defined up to an overall gauge choice shifting their momenta in opposite directions.

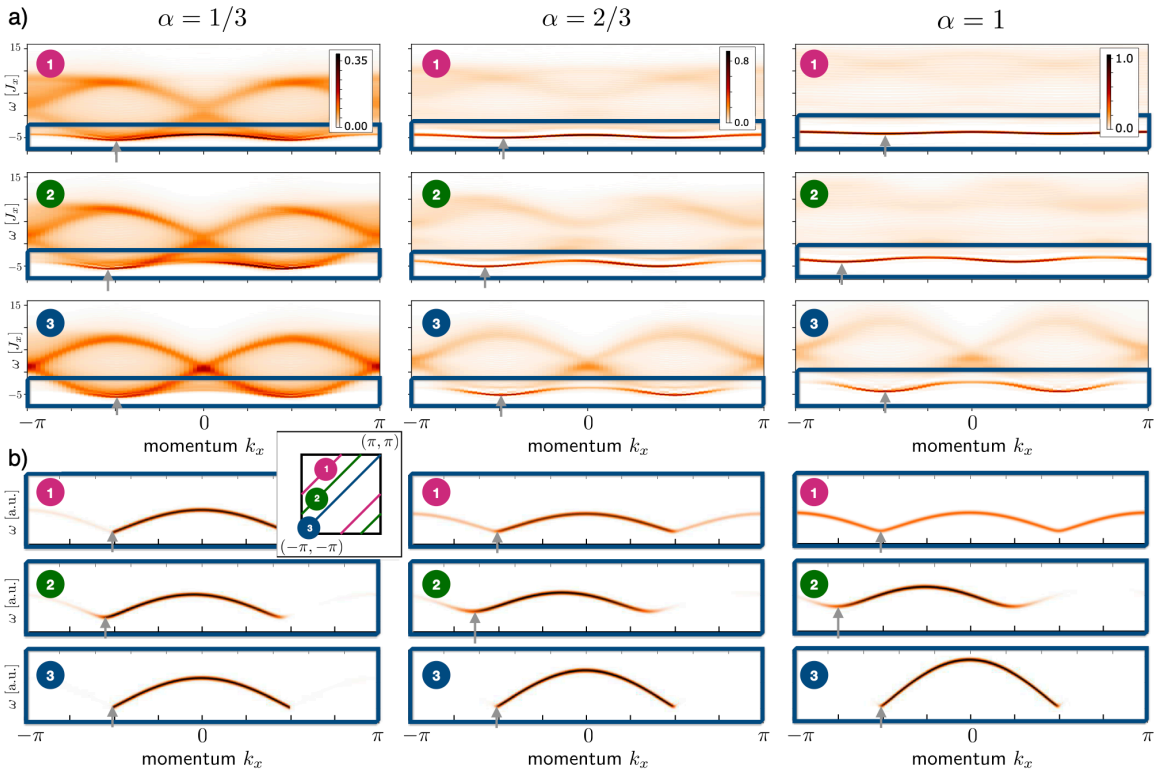

Figure 5.4.5: Dimensional crossover for the spectral function. a) For varying anisotropy $a = t_y/t_x$ (indicated in top row) of the hopping elements, and $a^2 = J_y/J_x$ of the super-exchange couplings, we use td-MPS to calculate the spectral function. We consider cylinders of length $L_x = 40$ along x, with circumference $L_y = 4$ along the periodic y direction; $t_x/J_x = 3$ is fixed. The MPS is wrapped around the cylinder along diagonals, which allows us to calculate diagonal cuts: $k_y = k_x + k_y^{(o)}$ with $k_y^{(o)} = \pi, \pi/2, 0$ (cuts $1, 2, 3$ – see inset below left panel). b) Predictions for the spinon contribution Z_s to the spectral weight (color map) and dispersion from fermionic mean-field theory of spinons, as described in the text. Mean-field parameters are taken from Ref. [272]. The delta-function peaks are represented by broadened lines with integrated weight equal to $Z_s(\mathbf{k})$. In a) and b) the location of dispersion minima in the low-energy region (blue boxes) are indicated by gray arrows.

which directly reflects the Fermi-Dirac distribution of spinons in the ground state [2, 213].
In 1D, the above argument predicts a strong suppression of spectral weight up to energies of order $\mathcal{O}(2t) \gg J$ around $k = \pi$, which has been observed numerically [2, 197, 205], see section 4.2. As discussed earlier, we find the same phenomenology around $\mathbf{k} = (\pi, \pi)$ in two dimensions, where we also attributed the effect to the underlying fermionic spinon statistics in the mean-field parton theory. To further support our argument that the 1D and 2D cases are due to the same physical principle, now we demonstrate that they continuously evolve into each other in a dimensional cross-over.
In Fig. 5.4.5 a) we show our numerical td-MPS results for values of $a = 1/3, 2/3$ and 1. We consider three cuts along diagonals, $k_y = k_x + k_y^{(0)}$ with $k_y^{(0)} = \pi, \pi/2$ and 0. For $a = 1/3$ the spectrum still closely resembles the 1D case, and only a weak dependence on k_y is observed: The minima of the ground state dispersion in the second cut, corresponding to $k_y^{(0)} = \pi/2$, are slightly displaced to the left of $k_x = \pm\pi/2$, as expected from the mean-field spinon dispersion shown in Fig. 5.4.5 b). While some spectral weight appears at $\mathbf{k} = (\pi, 0)$ (first cut with $k_y^{(0)} = \pi$), it remains absent over a broad energy range at $\mathbf{k} = (\pi, \pi)$ (third cut with $k_y^{(0)} = 0$). In general, the high-energy features can still be understood from a theory of quasi-free spinons and chargons as in 1D.
For $a = 2/3$ a well-defined quasiparticle peak is visible at low energies. This is expected from the parton theory, which predicts the formation of a spinon-chargon bound state as soon as the string tension $\propto J_y$ becomes sizable. Around $\mathbf{k} = (\pi, \pi)$ we still observe a strong suppression of spectral weight over a wide energy range of order $\mathcal{O}(2t_x)$. The dispersive features at high energies, reminiscent of a free chargon branch, become increasingly less pronounced as a approaches 1.
In Fig. 5.4.5 b) we plot the mean-field spinon dispersion expected for the dimensional cross-over. While the overall scale is difficult to predict, the shape of the spinon dispersion resembles the numerically observed quasiparticle dispersion [the low-energy onset of the spectrum in Fig. 5.4.5 a)] for all considered values of a. The variational mean-field parameters $B_{\mathrm{st}}(a)$ and $\Phi(a)$ have been taken from Ref. [272]. The color-scale in Fig. 5.4.5 b) indicates the spinon quasiparticle weight $Z_{\mathrm{s}}^{\mathrm{MF}}(\mathbf{k})$. Around the nodal point $\mathbf{k} = (\pi/2, \pi/2)$ the numerically obtained spectrum, as a function of momentum, evolves significantly more smoothly than expected from the mean-field theory. We attribute this to the effect of the Gutzwiller projection neglected in the mean-field calculation, as discussed earlier for the 2D case. Around $\mathbf{k} = (\pi, \pi)$ the mean-field theory correctly predicts the strongly suppressed quasiparticle weight at all values of a. We conclude that the parton theory correctly predicts the observed qualitative features of the ARPES spectrum in the dimensional cross-over.

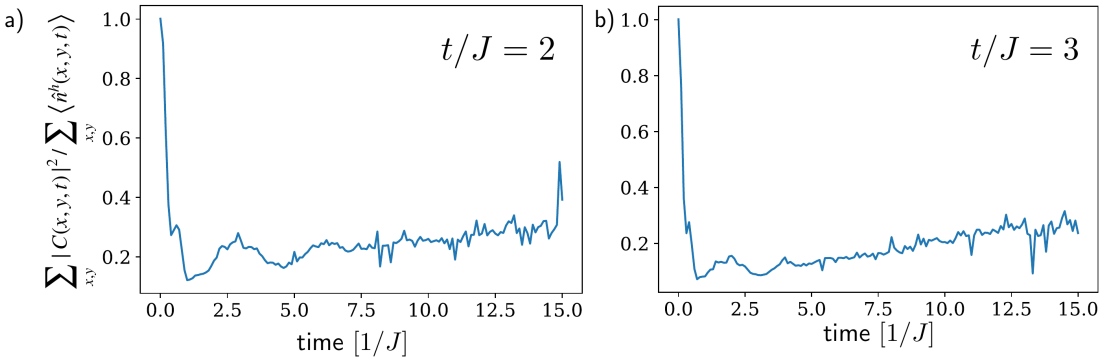

Figure 5.5.1: Spectral function compared to local density. We calculate the ratio of the sum over all positions of the spectral function squared and compare it to total number of holes, which is fixed at one. At short times, the ratio quickly drops to small values, indicating that the time- and site-resolved charge density cannot be captured directly by the spectral function but contains additional information.

5.5 Dynamics of a Hole in two dimensions

This section is based on the publications

- Annabelle Bohrdt, Fabian Grusdt, Michael Knap: "Dynamical formation of a magnetic polaron in a two-dimensional quantum antiferromagnet" – New J. Phys. 22 123023 (2020) [arXiv:1907.08214]

- Geoffrey Ji, Muqing Xu, Lev Haldar Kendrick, Christie S. Chiu, Justus Brüggenjürgen, Daniel Greif, Annabelle Bohrdt, Fabian Grusdt, Eugene Demler, Martin Lebrat, and Markus Greiner: "Dynamical interplay between a single hole and a Hubbard antiferromagnet" – arXiv:2006.06672

Structure, text and figures have been rearranged and adapted here.

The correlation function $C_\sigma(x, y, t)$ defined in Eq. (5.57) can be used to obtain an estimate on the local hole density after the creation of a hole. In particular, the absolute value squared of $C_\sigma(x, y, t)$, summed over both spin indices σ, is

$$|\sum_\sigma C_\sigma(x, y, t)|^2 = \langle \Psi_0 | \hat{c}^\dagger_{0,0} e^{i\hat{\mathcal{H}}t} \hat{c}_{x,y} | \Psi_0 \rangle \langle \Psi_0 | \hat{c}^\dagger_{x,y} e^{-i\hat{\mathcal{H}}t} \hat{c}_{0,0} | \Psi_0 \rangle, \tag{5.72}$$

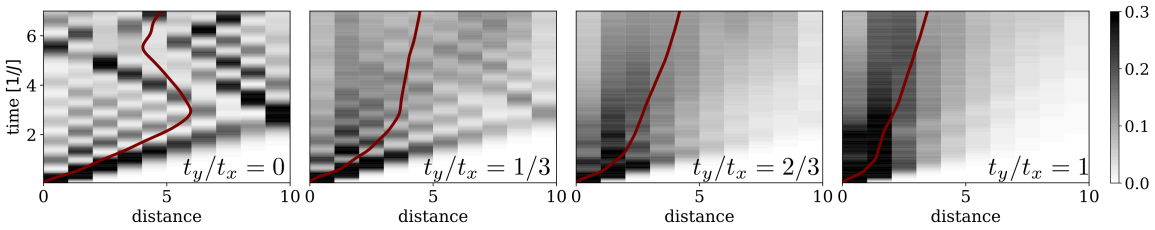

Figure 5.5.2: Hole dynamics in the dimensional crossover from one dimensional spin chains to a two dimensional system. The color plots show the hole density as a function of the distance to the origin in cylinder direction. The red lines are the mean value of the hole density. From left to right, the plots correspond to $t_y/t_x = 0, 1/3, 2/3, 1$.

and the local hole density after the creation of a hole at the origin at time $t = 0$ is

$$\begin{aligned}\langle \hat{n}^h(x,y,t)\rangle &= \langle \Psi_0|\hat{c}^\dagger_{0,0} e^{i\hat{\mathcal{H}}t}\hat{n}^h_{x,y}e^{-i\hat{\mathcal{H}}t}\hat{c}_{0,0}|\Psi_0\rangle \\ &= \langle \Psi_0|\hat{c}^\dagger_{0,0} e^{i\hat{\mathcal{H}}t}(1-\hat{c}^\dagger_{x,y}\hat{c}_{x,y})e^{-i\hat{\mathcal{H}}t}\hat{c}_{0,0}|\Psi_0\rangle \\ &= \langle \Psi_0|\hat{c}^\dagger_{0,0} e^{i\hat{\mathcal{H}}t}\hat{c}_{x,y}\hat{c}^\dagger_{x,y}e^{-i\hat{\mathcal{H}}t}\hat{c}_{0,0}|\Psi_0\rangle.\end{aligned} \tag{5.73}$$

Note that we used the operators $\hat{c}^{(\dagger)}_{x,y} = \hat{c}^{(\dagger)}_{x,y,\uparrow} + \hat{c}^{(\dagger)}_{x,y,\downarrow}$ and particle number conservation in both the spin-up and the spin-down sector in Eq. (5.72). The difference between the hole density after a local quench and the absolute value squared of the real-space and time correlation function $C(x,y,t)$ is thus given by the projection onto the ground state $|\Psi_0\rangle$ in Eq. (5.72). We can obtain the following inequality:

$$|\sum_\sigma C_\sigma(x,y,t)|^2 \leq \langle \Psi_0|\hat{c}^\dagger_{0,0}e^{i\hat{\mathcal{H}}t}\hat{c}_{x,y}\sum_n |\Psi_n\rangle\langle\Psi_n|\hat{c}^\dagger_{x,y}e^{-i\hat{\mathcal{H}}t}\hat{c}_{0,0}|\Psi_0\rangle = \langle \hat{n}^h(x,y,t)\rangle \tag{5.74}$$

In Fig. 5.5.1, we compare the sum over all positions of the absolute value squared of the real-time and -space spectral function to the total hole density, which is fixed to be one. The ratio of the two quantities is significantly below one for the values of $t/J = 2, 3$ considered in Fig. 5.5.1 a), b), respectively, thus indicating that the spectral function does not provide the same information as the local hole density. Note that within the geometric string theory picture, the sum over all positions of $|\sum_\sigma C_\sigma(x,y,t)|^2$ gives the probability to have a string of length zero at time t. In the following, we investigate the dynamics of a hole after its creation (or release) from an antiferromagnet and study its impact on the spin background in terms of string patterns as well as spin correlation functions.

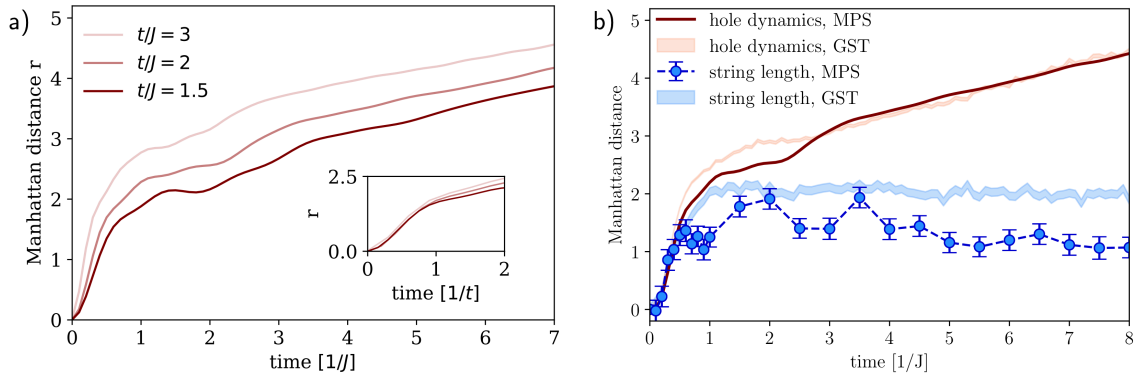

Figure 5.5.3: Hole dynamics in the two dimensional $t-J$ model on a square lattice for $t/J = 1.5, 2, 3$ with cylinder length $L_x = 18$ and circumference $L_y = 4$. a) The initial spreading with velocity proportional to the hole hopping t coincides for all values of the hopping for times in units of $1/t$ (inset). For longer times, the Manhattan distance increases with a slower rate determined by the spin exchange J and is independent of the hopping t. b) Manhattan distance of the hole to the origin and average string pattern length obtained from matrix product state (MPS) snapshots are compared to geometric string theory (GST) predictions at $t/J = 2$. The latter are obtained based on snapshots from the ground state of the Heisenberg model.

5.5.1 IN A QUANTUM ANTIFERROMAGNET

In order to gain insights into the system away from the ground state, we studied the properties of a hole created into the ground state of the Heisenberg model using matrix product operator based techniques [313]. The creation of a hole in the $t-J$ model corresponds to a local high energy excitation. In the one dimensional case discussed in section 4.3, spin-charge separation occurs and spinon and chargon spread independently of one another. Once couplings between several one dimensional chains are turned on, the situation changes. The interplay between spin and charge degrees of freedom introduces an emergent length scale, which depends on the ratio of $t_a/J_{\bar{a}}$, where $a = x, y$, $\bar{x} = y$ and vice versa. In a cold atom experiment, the dimensional crossover can be realized by tuning the lattice depth in one dimension. This leaves the interaction U constant while the ratio of t_y/t_x is changed. As the Fermi-Hubbard Hamiltonian is approximated by the $t-J$ model, the spin exchange couplings are then $J_y/J_x = t_y^2/t_x^2$. For $t_y/t_x = 1/3$, the ratio of spin exchange couplings is thus $J_y/J_x = 1/9$. As a consequence, the chargon can propagate freely for a comparably long distance. For the system sizes considered here, the hole dynamics therefore closely resemble the one dimensional case, see Fig. 5.5.2. As the couplings t_y and J_y are further increased, the hole slows down considerably. The emergent length scale can be read off approximately as the value at which the mean distance starts to bend over (red lines). In the isotropic case, two different timescales are observed. Initially, the hole spreads ballistically with a velocity proportional to t. At

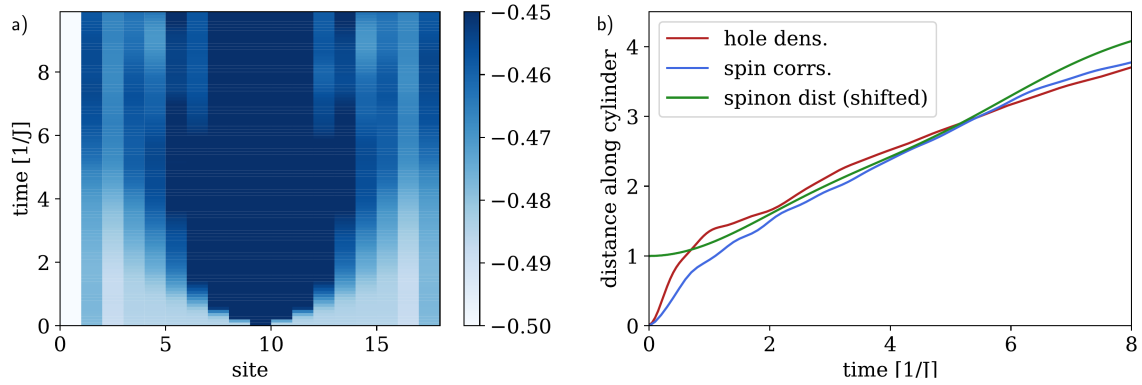

Figure 5.5.4: Time evolution of nearest neighbor spin correlations after creating a hole in the ground state of the $t-J$ model for $t/J = 2$. a) The nearest neighbor spin correlator as a function of position and time. b) Interpreting the deviation of the nearest neighbor spin correlator from its equilibrium value as the spinon distribution, we can compare the spreading of the spinon the hole dynamics. The spinon distance is shown as comparison, but shifted up by one.

long times, the hole again propagates ballistically, but with a velocity given by the spin exchange coupling J. This dependence on t and J is shown in Fig. 5.5.3 a) by considering different values of t/J: the initial dynamics is identical if the time is plotted in units of $1/t$, see inset. However, for later times, the Manhattan distance, defined as

$$r = \sum_x \sum_y (|x| + |y|) \cdot \left\langle \hat{n}^h(x,y) \right\rangle , \tag{5.75}$$

increases with the same slope if the time is shown in units of $1/J$. These numerical findings can be understood in terms of the parton construction described in section 5.1: the excitation created in the system is decomposed into a spinon, carrying the spin quantum number, and a chargon, carrying the charge. Spinon and chargon are bound to each other by a string of displaced spins. The properties of this string can be derived with the help of the geometric string theory. Since chargon and spinon are bound together after the initial short time dynamics, the propagation of the hole at intermediate and long times is determined by the slower spinon dynamics.

We model the spinon dynamics with the help of the tight-binding Hamiltonian (5.11). The spinon dispersion $\omega_{sp}(\mathbf{k})$, and thereby the spinon tunneling matrix elements $J_{\mathbf{j},\mathbf{i}}$ in the effective Hamiltonian (5.11), is determined by fitting it to the magnetic polaron dispersion:

$$\omega_{sp}(\mathbf{k}) = A\left[\cos(2k_x) + \cos(2k_y)\right] + B\left[\cos(k_x + k_y) + \cos(k_x - k_y)\right] . \tag{5.76}$$

The fit parameters A and B depend weakly on t/J, and we take them from Ref. [246]. For $t/J = 2$ this yields: $A = 0.25J$ and $B = 0.36J$.

Further evidence for the string theory is provided by analyzing Fock space snapshots sampled from the time evolved matrix product state. We search for the string pattern connected to the hole in each snapshot by applying the algorithm described in section 5.2. Since the ground state of the Heisenberg model is not a perfect checkerboard pattern, the average length directly after the creation of the hole is already larger than zero. Thus, the difference to this initial length is shown in Fig. 5.5.3. At short times, the average length of the string pattern grows exactly as the Manhattan distance of the hole to the origin. After a time proportional to $1/J$, the string pattern length saturates, while the hole distance increases further with a smaller velocity. At long times, the string length decays slightly, an effect that is not captured by the geometric string theory. Note that the sum over all positions of $|\sum_\sigma C_\sigma(x, y, t)|^2$ considered in Fig. 5.5.1, simultaneously increases. This is consistent with a decrease of the string length, as this quantity corresponds to the probability to have a string of length zero.

The predictions of the geometric string theory combined with the dynamics of the spinon can be compared to the numerical results by placing and moving the hole by hand in snapshots of the Heisenberg ground state, as discussed in section 5.2.4. In particular, the dynamics of the chargon relative to the spinon is in this picture described by the motion of a single particle in a potential, see section 5.1, for which the dynamics can be easily solved. We solve the single spinon problem on a cylinder with the same circumference as used in the exact numerics as described above. As shown in Fig. 5.5.3 b), this leads to a remarkable agreement with the numerical data. Note that there is no free fitting parameter in the theory here.

In Fig. 5.5.4, the dynamics of the spin excitation is directly compared to the spinon dynamics according to Eqs. (5.11) and (5.76). Fig. 5.5.4 a) shows the time evolution of the nearest neighbor spin correlations along the cylinder. We can interpret this as a probability distribution by considering the value of the nearest neighbor spin correlations relative to their equilibrium value and normalizing the resulting distribution in each time step to one. From this numerically observed probability distribution, we obtain the spreading of the spinon shown in Fig. 5.5.4 b) (blue) and compare it to the spinon dynamics discussed above (green). Apart from the short-time dynamics, the time evolution of the spinon spreading, obtained from the spin correlations as well as from the tight-binding model, matches the spreading of the hole itself.

In section 5.1, we discussed the non-linear as well as the linear string theory. The linear string theory assumes the same potential energy for each string of a given length, irrespective of its configuration. In this approximation, the potential energy cost of the spin system is given by the same string tension for each site the hole moves. In the non-linear string theory, the different energies of

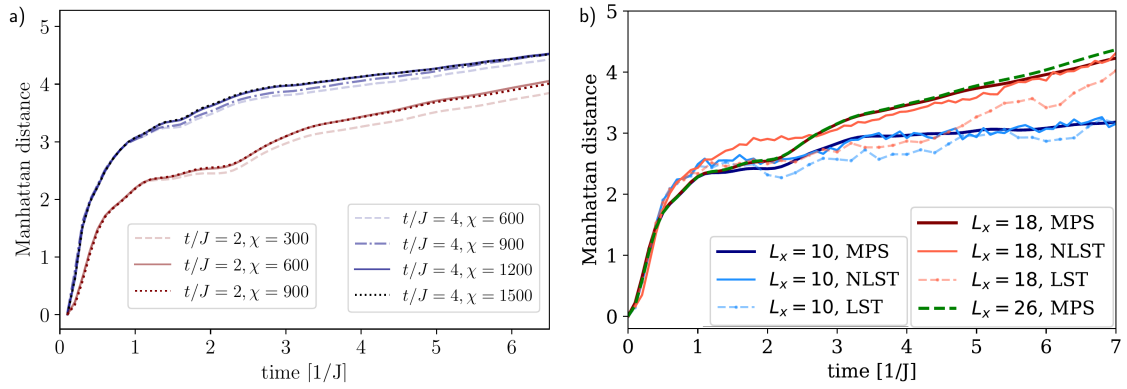

Figure 5.5.5: Convergence of hole dynamics with bond dimension and system size. a) Manhattan distance of the hole to the origin for $t/J = 2, 4$ and values of the bond dimension $\chi = 300, 600, 900, 1200, 1500$. For the times used here, the differences between simulations with different bond dimensions are small. b) System size dependence of the Manhattan distance of the hole for $t/J = 2$. For a cylinder of length 10 sites, finite size effects become visible at an earlier time. The dynamics of the observed quantities is very similar for cylinders of length 18 and 26 sites up to longer times. Dashed versus straight lines compare the two theoretical approximations (NLST and LST) to the numerical results for the Manhattan distance of the hole. Non-linear string theory results are limited to a string length of 10 bonds.

the spin background for different configurations of the string are taken into account. In Fig. 5.5.5 b), the Manhattan distance of the hole to the origin is compared to linear as well as non-linear string theory predictions. There is a visible difference between the two approximations and the non-linear string theory agrees significantly better with the numerical results.

The dynamics considered so far took place on a cylinder of length 18 or 19 sites. At long times, a significant fraction of the hole density has reached the edge, as can be seen in Fig. 5.5.2. We therefore also evaluated the dynamics on cylinders of length 10 and 26 sites, Fig. 5.5.5 b). In the case of a short cylinder, the Manhattan distance of the hole to the origin already saturates at early times, before the second velocity is observable. The value at which the distance saturates is the same for $t/J = 2$ and $t/J = 4$, the only difference being that it is reached at earlier times in the latter case. For longer cylinders, $L_{cyl} = 18, 26$, the Manhattan distance of the hole to the origin coincides on the timescales considered here. The results presented above are therefore not subject to sizeable finite size effects regarding the cylinder direction.

So far, we studied the dynamics after a hole was created in the ground state of the Heisenberg model. A slightly different scenario takes place if we start from the ground state with an immobile hole in the origin, which is then released. In Fig. 5.5.6, the time evolution of different spin observables after releasing the hole is shown. The magnitude of the next nearest neighbor spin correlations, both across the origin and across the hole, Fig. 5.5.6 a), decays quickly and then saturates

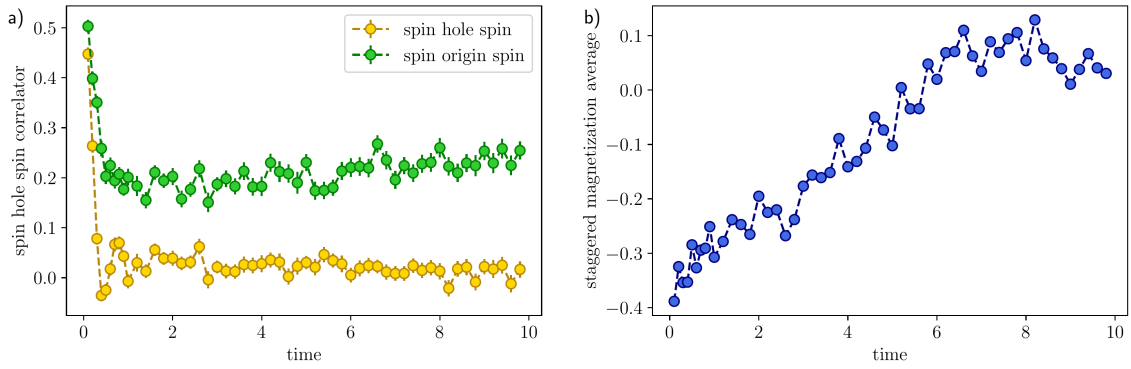

Figure 5.5.6: Time evolution of spin observables after releasing a hole from the ground state of the $t-J$ model. a) The next nearest neighbor spin correlator next to the hole (yellow) and the origin (green) exhibits fast initial dynamics and reaches a constant value on the time scale of $1/J$. b) The global staggered magnetization oscillates slowly with a period determined by the system size.

at a finite value. Note that the diagonal spin correlations across the hole (averaged over all four bonds) is close to zero, which can be understood from the geometric string theory picture, see also Eq. (5.33).

The global staggered magnetization, Fig. 5.5.6 b), however exhibits slow oscillations with a period determined by the system size. Since the total spin is conserved, there is a minority spin species, which favors the sublattice on which the hole is pinned initially. The localized hole has therefore a similar effect as a staggered field. After the hole is released and is approximately equally likely on both sublattices, no sublattice is favored anymore by the minority spin species – the effective staggered field is turned off. Note that the situation in 2D is different to the case of a pinned hole in a one-dimensional system studied in Fig. 4.3.6. In the latter case, the two halfs of the system are previously disconnected and therefore no correlations exist at time zero. For a two-dimensional system, the effect of a pinned hole is not as strong, but still has a significant influence on the spin surroundings, see also Fig. 5.3.5 and Ref. [18].

5.5.2 in a Quantum Antiferromagnet at Finite Temperature

The dynamics of a single hole in a two-dimensional system can be explored in a quantum gas microscope, as introduced in section 2.1 and discussed in section 4.3 for a one-dimensional system. Here, I collaborated with the group of Markus Greiner at Harvard to study the dynamics of a single dopant. The initial system is a half-filled two-dimensional square lattice of fermionic Lithium-6 atoms at $U/t = 8.72(28)$, corresponding to $t/J = 2.18(7)$ and a temperature of $T/t = 0.340(19)$, with a single hole pinned at a fixed site with the help of a digital micromirror device (DMD). In particular, the DMD is used to project a repulsive potential locally on a single lattice site. During

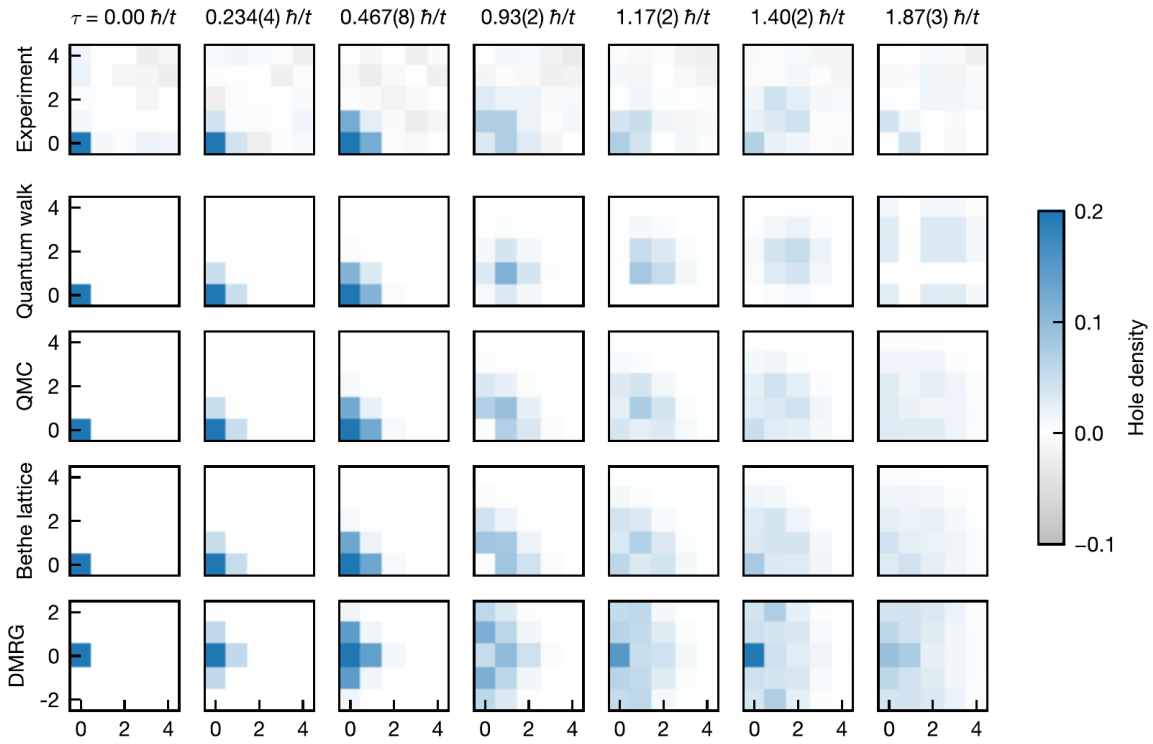

Figure 5.5.7: Short-time dynamics of a hole after a quench clipped to 5×5 quadrants. The experimental data is averaged over horizontal, vertical and diagonal reflections. We compare the experimental data to a non-interacting quantum walk, a non-interacting spin-$1/2$ QMC simulation at $T = \infty$, a free particle on a Bethe lattice, and time-dependent MPS simulations of the $t - J$ model at $t/J = 2$. For the MPS simulation, the rows at $d_y = \pm 2$ are equivalent and are duplicated for clarity.

the adiabatic loading process, atoms will preferentially not populate a site with such a repulsive potential, thus leading to pinned holes. After adiabatic loading, the pinned holes are released by rapidly shutting off the light illuminating the DMD and thus the pinning potential within $0.03\hbar/t$. In this particular experiment, spin-resolved imaging is not possible. After a variable evolution time τ, the dynamics can be frozen by rapidly increasing the lattice depth, and either the parity projected density or the density of one of the two spin states can be imaged. Due to charge fluctuations in the form of doublon-hole pairs, it is not possible to exactly track the holes in each experimental realization. Instead, we compute the average density distribution of singly occupied sites and subtract it from the background density of singles obtained from experimental realizations without any holes.

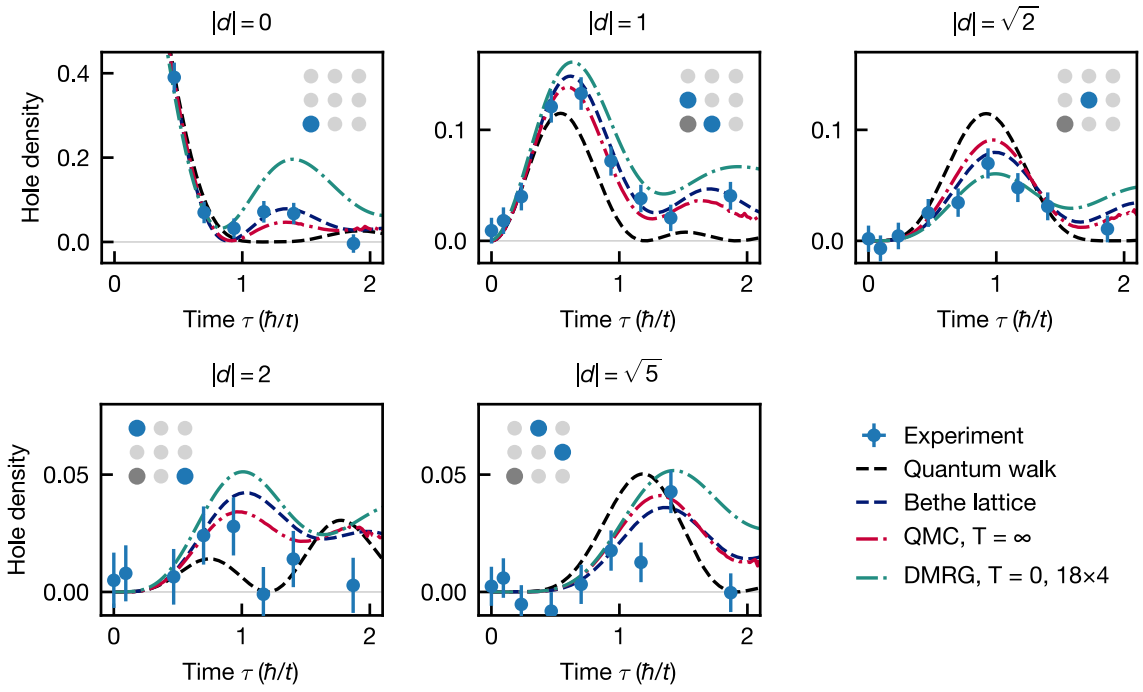

Figure 5.5.8: Short-time evolution of the hole density at the central and adjacent sites. The experimental data is compared to a non-interacting quantum walk, a non-interacting spin-1/2 QMC simulation at $T = \infty$, and time-dependent MPS simulations of the $t - J$ model at $t/J = 2$ and $T = 0$.

Short-time dynamics of the hole

In order to collect more data for the short-time dynamics of the system, four holes are pinned simultaneously in a seven site wide square pattern. The average hole density on these four sites is initially $0.81(2)$, without significantly affecting the adjacent sites. In Fig. 5.5.7, the background subtracted density distribution is shown for selected times, averaged across all four holes and the dihedral symmetries of the square lattice. Within half a tunneling period, the hole tunnels to the four neighboring sites, Fig. 5.5.7. The short-time dynamics retains clear coherent features, such as the loss and revival of the hole density at the origin, or return probability, that sets it apart from a classical diffusion process. We compare the experimental data to different theoretical approaches:

(i) A free quantum walk, corresponding to the motion of a hole in a ferromagnetic environment. The data is based on the analytic formula in [314], scaled to a two-dimensional system:

$$\rho_{i,j}(\tau) = |\mathcal{J}_i(2\tau t)\mathcal{J}_j(2\tau t)|^2, \tag{5.77}$$

where $\mathcal{J}$ is the Bessel function of the first kind and i, j are the site coordinates relative to the

initial location.

(ii) The motion of a hole in a paramagnetic spin-1/2 environment, simulated with a quantum Monte Carlo algorithm in a 40×40 system, using the code provided at https://github.com/MartonKN/Dynamical-spin-correlations-at-infinite-temperature.

(iii) The propagation of a hole on a Bethe lattice, motivated by the general discussion in section 5.1, but at $J = 0$. The calculation here is based on [315]. The path-distinguishability effects due to the spin background are modeled by incoherently summing probabilities on node of the graph leading to the same hole location.

(iv) Time-dependent matrix product state simulations of the dynamics of a single hole created in the ground state of the $t - J$ model at $t/J = 2$, as discussed in section 5.5.1.

In Fig. 5.5.8, we compare the experimental hole densities on the central site and its neighbors at $\mathbf{d} = (1,0), (0,1)$, $\mathbf{d} = (1,1)$, $\mathbf{d} = (2,0), (0,2)$, and $\mathbf{d} = (2,1), (1,2)$ to the different theoretical predictions. Up to times $\tau \approx 0.5\hbar/t$, all shown theoretical models describe the experimental results quantitatively correct. For intermediate times, the td-MPS simulation correctly predicts the revival time of the density at the central site at $\tau = 1.2\hbar/t$, but the actual value of the density is magnified due to finite size effects.
The amplitude of the oscillations in the density on the nearest neighbor sites is directly related to the indistinguishability of spin backgrounds after two tunneling events ending at the same site. Quantum interference is maximal in a ferromagnet (free quantum walk), reduced in an antiferromagnet (ground-state td-MPS simulation) and between these two extremes in a paramagnet (infinite temperature QMC). In the experiment, we observe a suppressed density at the nearest neighboring site at $\tau = 1\hbar/t$, indicating that the antiferromagnetic background plays a role for the hole motion.

Long-time dynamics of the hole

For later times, the density distributions of the four holes overlap. For times later than $\tau = 1\hbar/t$, we therefore prepare a single hole in the center of the system. In this case, the hole density on the initial site before release is $0.867(12)$. In order to study the hole propagation at later times, we want to calculate the root-mean-squared (RMS) hole distance from its initial site. In principle, the RMS distance could be calculated directly from the experimental data as

$$\mathbf{d}_{\mathrm{RMS}} = \sqrt{\sum_{d_x,d_y} (d_x^2 + d_y^2)\rho_{\mathbf{d}} \Big/ \sum_{d_x,d_y} \rho_{\mathbf{d}}}, \tag{5.78}$$

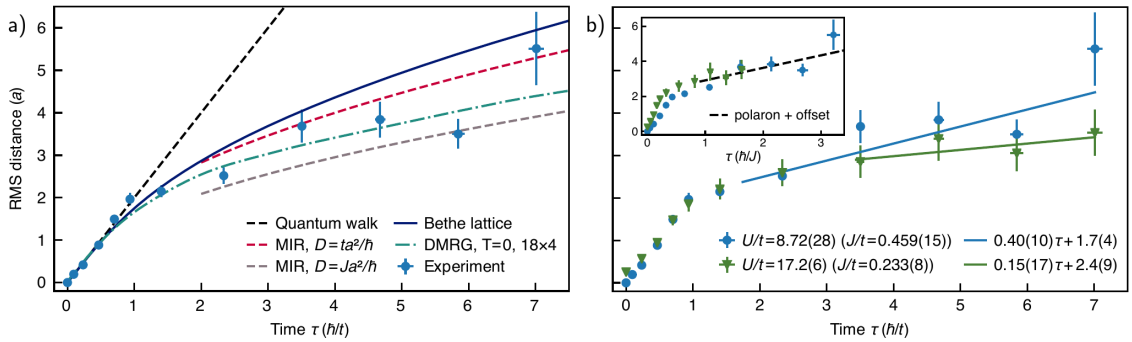

Figure 5.5.9: Long-time evolution of the hole density in terms of the root mean square (RMS) distance. a) Experimental data compared to a non-interacting quantum walk, dynamics on a Bethe lattice, the Mott-Ioffe-Regel (MIR) limit, and time-dependent MPS simulations of the $t-J$ model at $t/J=2$ and $T=0$. b) Experimental RMS distance for $U/t=8.72(28)$ and $U/t=17.2(6)$.

where $\rho_{\mathbf{d}}$ is the hole density at coordinate $\mathbf{d}=(d_x,d_y)$ relative to the initial hole position. However, statistical fluctuations in the hole density at large distances lead to large uncertainties in the hole position. Therefore, we fit the experimental data to a Gaussian density distribution in an analysis region, which contains most of the hole density [14]. In Fig. 5.5.9 a), the RMS distance of the hole in the experiment is compared to the theoretical approaches described above, as well as a diffusive square-root law $d_{RMS}=\sqrt{4D\tau}$ with diffusion constants $D=t^2a/\hbar$ and $D=J^2a/\hbar$. At short times, the RMS distance exhibits the same ballistical growth observed in Fig. 5.5.3. This behavior is captured by all theories. After times $\tau=1\hbar/t$, the RMS distance shows a clear bend, similar to the time-dependence discussed in section 5.5.1. For a free quantum walk, the RMS distance is given by $d_{RMS}=(2t/\hbar)\tau$, which does not capture the experimentally observed dynamics. The Bethe lattice dynamics (iii) predicts a crossover to diffusive hole motion at times consistent with the bend in the RMS distance. This confirms that quantum interference effects start to play a role at timescales comparable with the tunneling time. The Mott-Ioffe-Regel (MIR) limit sets the diffusion constant $D=t^2a/\hbar$ in the diffusive square-root law $d_{RMS}=\sqrt{4D\tau}$ shown in Fig. 5.5.9 a). This limit classically corresponds to Brownian motion with a mean-free-path of one lattice constant. The hole velocity in this picture is set by the tunneling energy t. Experiments in the group of Waseem Bakr have shown that the MIR limit provides a lower bound for diffusion at large doping values [77]. For the quench considered here, this lower bound is violated. However, a similar lower bound is satisfied, with the hole hopping t replaced by the spin exchange J, indicating that the long-time velocity is determined by the superexchange instead of the bare tunneling. In order to compare the td-MPS simulations on the four-leg cylinder to the experimental data in the full two-dimensional system, we calculate the one-dimensional RMS distance in the td-MPS data and scale

it to a two-dimensional Euclidian norm. Over the observable time-scales, the td-MPS simulation agrees well with the experiment. It should be noted, however, that the anisotropy of the td-MPS simulation could in principle favour faster ballistic motion, whereas the increased magnetic order in the ground state (as compared to the finite temperature state in the experiment) could enhance the slow-down of the hole.

In the ground state simulations in Fig. 5.5.3, we changed the ratio of t/J and observed that the long time dynamics only depends on J. In the experiment, we can equivalently tune U/t and thus t/J using a Feshbach resonance, as discussed in section 2.1, and compare the resulting RMS distance as shown in Fig. 5.5.9 b) for $U/t = 8.72(28)$ and $U/t = 17.2(6)$. The temperature in units of t is slightly decreased for the larger value of U/t to $T/t = 0.241(18)$. Similar as in the numerical simulations in Fig. 5.5.3, the short-time dynamics agrees almost exactly, confirming the ballistic growth with t, independent of J. Small initial deviations are due to a larger hole preparation infidelity. At times larger than $\tau = 1\hbar/t$, the RMS distance bends over for both values of U/t, but the velocity for the larger U/t (i.e. smaller J/t) is significantly reduced, indicating again that the spin exchange J plays a role in this dynamics. In the inset, the same data is shown with time in units of $1/J$ instead of $1/t$, confirming that J is determining the time evolution in the long-time limit. The dashed black line corresponds to the RMS distance of a magnetic polaron, where the overall scale is shifted for better comparison. These results suggest the formation of a magnetic polaron at short times, which then continues to spread ballistically, as discussed in section 5.5.1. A linear fit to the RMS distance for times $\tau \geq 0.8\hbar/J$ yields a velocity of $0.15(17)a/(\hbar/t)$ for $U/t = 17.2(6)$ and a velocity of $0.40(10)a/(\hbar/t)$ for $U/t = 8.72(28)$. The ratio of the velocities is consistent with a ballistic spreading with velocity proportional to J.

Spin recovery dynamics

In section 5.5.1, we obtained the average length of the string pattern attached to the hole as a function of time. In this experimental setup, it is not possible to resolve hole and both spin species simultaneously, and thus the string pattern attached to the hole cannot be determined. However, through the separate imaging of both spin components, the spin correlations can be measured. It is not possible to track the spin correlations relative to the hole, but we can study the recovery of the spin correlations at the origin, where the hole was originally pinned. In Fig. 5.5.10 a), the spin correlations from the initial hole location are shown for select times. Initially, these correlations vanish due to the presence of the hole. As the hole hops to one of the neighboring sites, the correlations from the initial hole site correspond to those of the exchanged neighboring spin. The antiferromagnetic correlation pattern is thus reversed, which can be seen by the red color in Fig. 5.5.10 a).

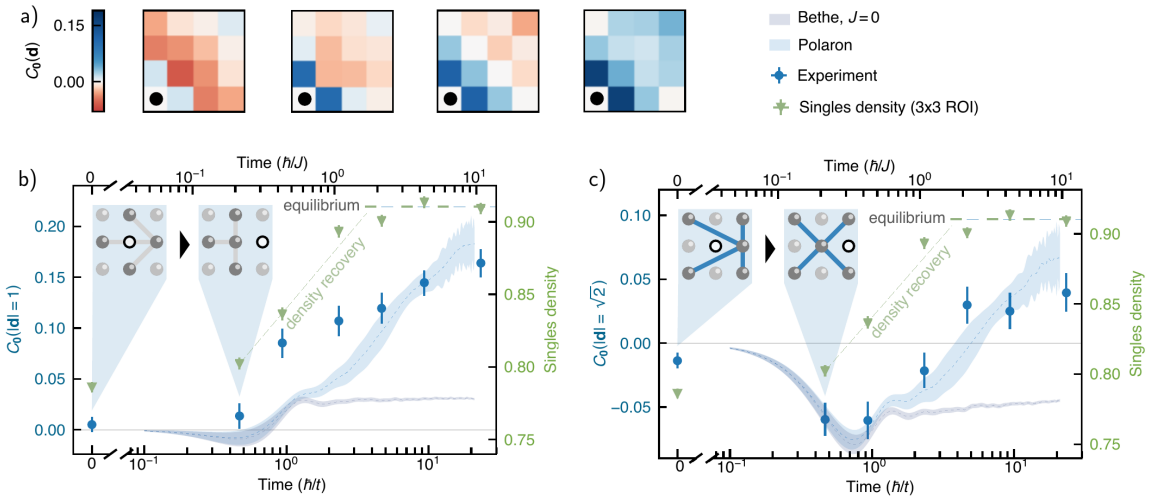

Figure 5.5.10: Dynamics of spin correlations after a quench. a) Sign-corrected spin correlations from the initial hole location at select times, symmetrised across reflections. The correct AFM pattern (blue) is slowly restored, but does not fully equilibrate during the experimentally observed times. b), c) Sign-corrected nearest and next nearest spin correlations from the initial hole as a function of time. A Bethe-lattice model (purple band) describes the short-time dynamics, but does not capture the slow dynamics at long times. The same spinon dynamics described in section 5.5.1 quantitatively captures this long-time behavior of the experimental spin correlations. The green triangulars show the recovery of the singles density at the initial site.

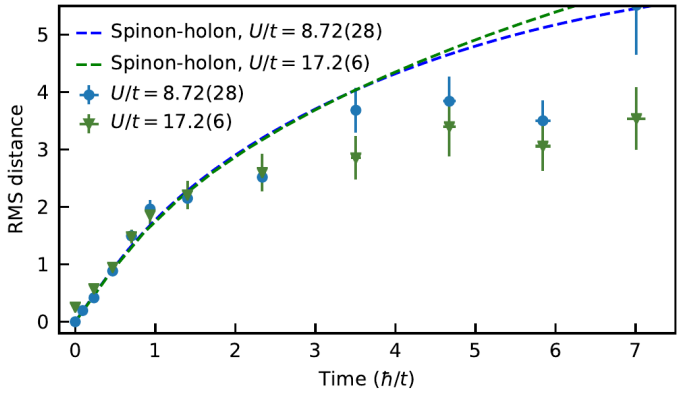

Figure 5.5.11: Comparing experiment to linear string theory. Root mean square (RMS) hole distance as measured in experiment (points) and predicted by spinon-holon model (dashed curves).

Note that the nearest neighbor spin correlation does not turn ferromagnetic at short times, since it results from a mixture of diagonal correlations weakened by the presence of the pinned hole. This reversal of the antiferromagnetic pattern is the dynamical analogue to the polaronic behavior in equilibrium observed in [267].

The nearest and next nearest spin correlations from the initial hole site shown in Fig. 5.5.10 b) and c) clearly show the slow dynamics at long times. The swapping of the spin correlations by the hole motion can be modeled and we can quantitatively compare the experimental measurements to the correspondingly swapped spin correlations of the same system without a quench. In particular, we displace spins by hand in the experimental snapshots at time $\tau = 0$ to obtain a new set of snapshots for each time τ. In the simplest picture, the hole trajectories are predicted by the Bethe lattice model, which does not include any exchange coupling J. As shown in Fig. 5.5.10 b) and c), this model correctly describes the spin correlations at short times, but cannot capture the relaxation at long times. We can include the spinon dynamics discussed in section 5.5.1 by shifting the experimental snapshots, and thus the effective hole origin, according to the time-dependent spinon distribution. This picture corresponds to the formation of a magnetic polaron, in our discussion here a spinon-holon-string, which then spreads with the spinon velocity. Including the spinon dynamics results in an accurate prediction of the long-time behavior of the spin correlations, capturing their slow return to equilibrium. The discrepancy between the spinon-holon-string and the experimental data around $\tau = 1 - 2\hbar/t$ in the nearest neighbor spin correlation is potentially caused by spin relaxation mechanisms beyond this model, such as magnon emission. We furthermore note that the string model in this case overestimates the RMS distance of the hole compared to the experimental measurements, Fig. 5.5.11.

To compute the RMS hole distance, we here first convert the string-hole wave function to a proba-

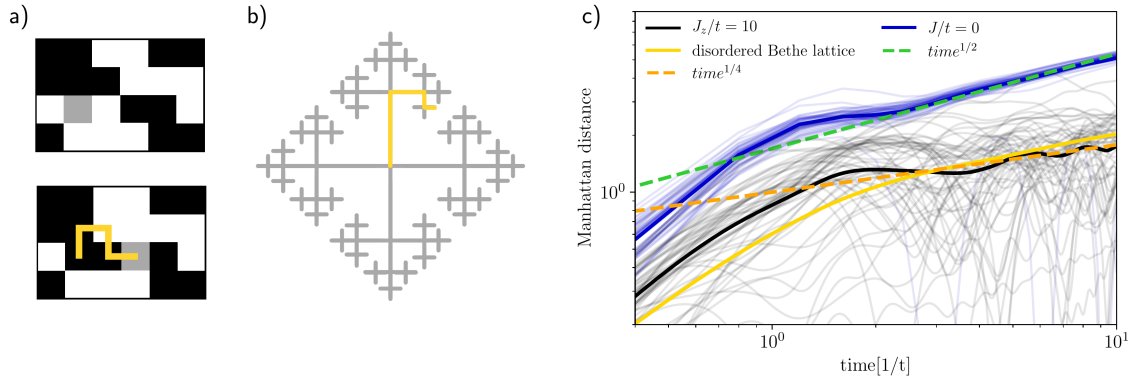

Figure 5.5.12: Dynamics in an infinite temperature background. a) A hole is created in the center of a cylinder with a random configuration of spins. As the hole moves through the system, it rearranges the spins and thereby leaves a memory. b) Its dynamics can therefore be approximated as a quantum random walk on the Bethe lattice. c) For no spin couplings, $J = 0$, the hole spreads diffusively at intermediate times. In the case of strong Ising interactions, $J_z = 10t$, the spreading is limited to comparably short distances. The faint lines are the results for individual inital product states. Fluctuations strongly increase for finite J_z. The yellow line corresponds to the dynamics of a single particle on the Bethe lattice with a disorder potential.

bility distribution $p_{h,\mathrm{rel}}$ for $\mathbf{r}_h - \mathbf{r}_s$, where $\mathbf{r}_h$ is the hole position. This is possible because every string Σ can be mapped (by following the path Σ takes on the square lattice) to a relative position $\mathbf{r}_h - \mathbf{r}_s$, so that converting $p_h(\ell, \tau)$ to $p_{h,\mathrm{rel}}(\mathbf{r}_h - \mathbf{r}_s, \tau)$ only requires solving the combinatorial problem of how many paths at each layer ℓ of the Bethe lattice arrive at each relative position $\mathbf{r}_h - \mathbf{r}_s$. The RMS distance of the hole is then given by

$$d_{\mathrm{RMS}}(\tau)^2 = \sum_{\mathbf{r}_h, \mathbf{r}_s} p_s(\mathbf{r}_s, \tau) p_{h,\mathrm{rel}}(\mathbf{r}_h - \mathbf{r}_s, t) \mathbf{r}_h^2, \tag{5.79}$$

which can be computed either directly or by summing the RMS distances of $p_{h,\mathrm{rel}}$ and p_s in quadrature.

5.5.3 In a Random Initial State

So far, we considered the dynamics of the hole starting from the ground state and a low temperature equilibrium state of the system. However, we can also create a hole in a product state. Sampling over a random ensemble of such product states constitutes an effective infinite temperature state of the spin system as initial state. We expect the chargon dynamics to be well described by the geometric string theory at finite but small temperatures, such that the spin correlations are still non-vanishing. At infinite temperature on the other hand, all spin correlations are zero and thus no

string tension exists. As shown in Refs. [315, 316], the chargon dynamics is nevertheless and even for $J/t = 0$ still associated with a memory effect in the spin system.

As the hole moves through the system, different paths taken lead to different spin configurations. The hole dynamics for $J/t = 0$ can therefore be approximated by a quantum random walk on the Bethe lattice [315], where we assume that all paths are distinguishable. Mapping back to the square lattice, the ballistic motion on the Bethe lattice translates to diffusive behavior. The dynamics observed in our numerical simulations is consistent with this diffusive motion, Fig. 5.5.12. For the spin 1/2 system considered here, different paths of the hole can lead to the same spin configuration, rendering those paths effectively indistinguishable. Especially since aligned neighboring spins occur more often, finding string patterns relative to the initial Fock space configuration is considerably harder compared to the case where the hole is created in the ground state of the Heisenberg model. Moreover, this indistinguishability of different paths can in principle lead to a slight modification of the diffusive behavior.

Introducing spin couplings effectively creates a disorder potential on the Bethe lattice. In order to simplify our theoretical picture, we here consider only Ising interactions. The disorder potential can be understood as follows: in each Fock space configuration, the motion of the hole by one site from i to j changes the energy of the spin system by $\Delta\varepsilon_{\langle ij\rangle} = 0.25J^z\left(\Delta N_{\sigma\bar{\sigma}} - \Delta N_{\sigma\sigma}\right)$, where $\Delta N_{\sigma(\bar{\sigma})\sigma}$ is the change in the number of (anti-)aligned spins on neighboring sites. The energy difference $\Delta\varepsilon_{\langle ij\rangle}$ is therefore a random number between $\pm 0.5(\tilde{z}-1)J^z$ with $\tilde{z}$ the coordination number of the lattice. The hole motion can then be approximated by a quantum random walk on the Bethe lattice with a disorder potential $W_l = \sum_{\langle ij\rangle\in\Sigma}\Delta\varepsilon_{\langle ij\rangle}$, where the sum runs over all bonds $\langle ij\rangle$ along the string Σ. For the spin configuration depicted in Fig. 5.5.12 a), the potential of the different hole position along the considered path is $W_l/J^z = 0, -1.5, 0, 0.5, 0.5$ for $l = 0, \ldots, 4$ for example. Note that for sites further apart on the Bethe lattice, the range of possible energy differences scales with the distance between the sites.

In Fig. 5.5.12 c), we consider the case of strong Ising interactions, $J^z = 10t$, which could for example be realized with Rydberg interactions. Strong spin interactions lead to a strong disorder potential and thus the spreading of the hole is significantly reduced and consistent with subdiffusive spreading.

For the $t-J$ model with $J^\perp = J^z = 0.5t$, the spin interactions are similarily expected to constitute a disorder potential on the Bethe lattice. The additional spin dynamics however limit our numerical simulations for the $t-J$ model with $J^\perp = J^z = 0.5t$ to short times. On the time scales accessible, a fast initial growth of the root mean squared distance to the origin is observed as in the cases shown in Fig. 5.5.12.

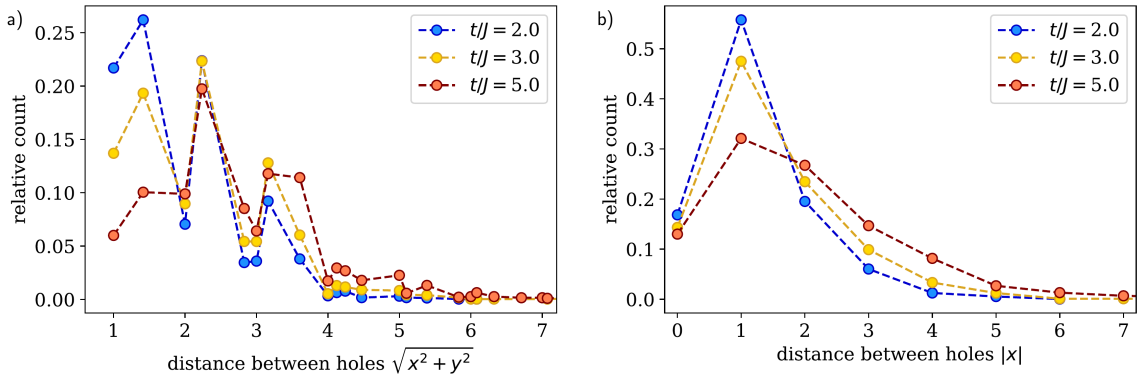

Figure 5.6.1: Distance between two holes in the ground state. For two holes in the ground state of the $t-J$ model on a 6×18 cylinder, a) the root mean square distance and b) the distance along the cylinder (x-direction) between the holes is shown for $t/J = 2, 3, 5$, evaluated from 2000 snapshots for each value of t/J. With increasing t/J, the distance distribution gets broader. For the considered parameters, the two holes are mostly within a distance of ~ 5 sites of each other.

5.6 Two Holes in Two Dimensions

So far, we considered the properties of a single hole in the two-dimensional $t-J$ model in the ground state as well as out-of-equilibrium. Many of the observed phenomena can be explained not only qualitatively, but also quantitatively with the geometric string theory introduced in section 5.1, where the charge excitation is bound to a spin excitation through a string of displaced spins. For the case of two holes, different scenarios are possible and we cannot straightforwardly generalize the description used for a single hole. Here we present numerical results for the ground state of two holes in the $t-J$ model on a cylinder obtained with TeNPy.

The most obvious quantity to consider in this case is the distance between the two holes. In Fig. 5.6.1, the root mean square distance between the holes is shown. Since the finite circumference of the cylinder limits the distance in y-direction to $y = 3$, we also show the distance along the cylinder separately. The data shown here is evaluated from 2000 snapshots for each value of t/J. For the smallest ratio of hopping amplitude to spin exchange considered, $t/J = 2$, the two holes are on nearest or next nearest neighboring sites in almost half of the snapshots. With increasing t/J, the distance distribution gets broader, but the holes tend to stay within approximately 5 sites of each other even for $t/J = 5$.

In section 5.3, we analyzed how a single hole changes the surrounding spin correlations. In the case of two holes considered here, we can evaluate the spin correlations for any given configuration of the holes. If we for example consider holes on nearest or next nearest neighboring sites, which

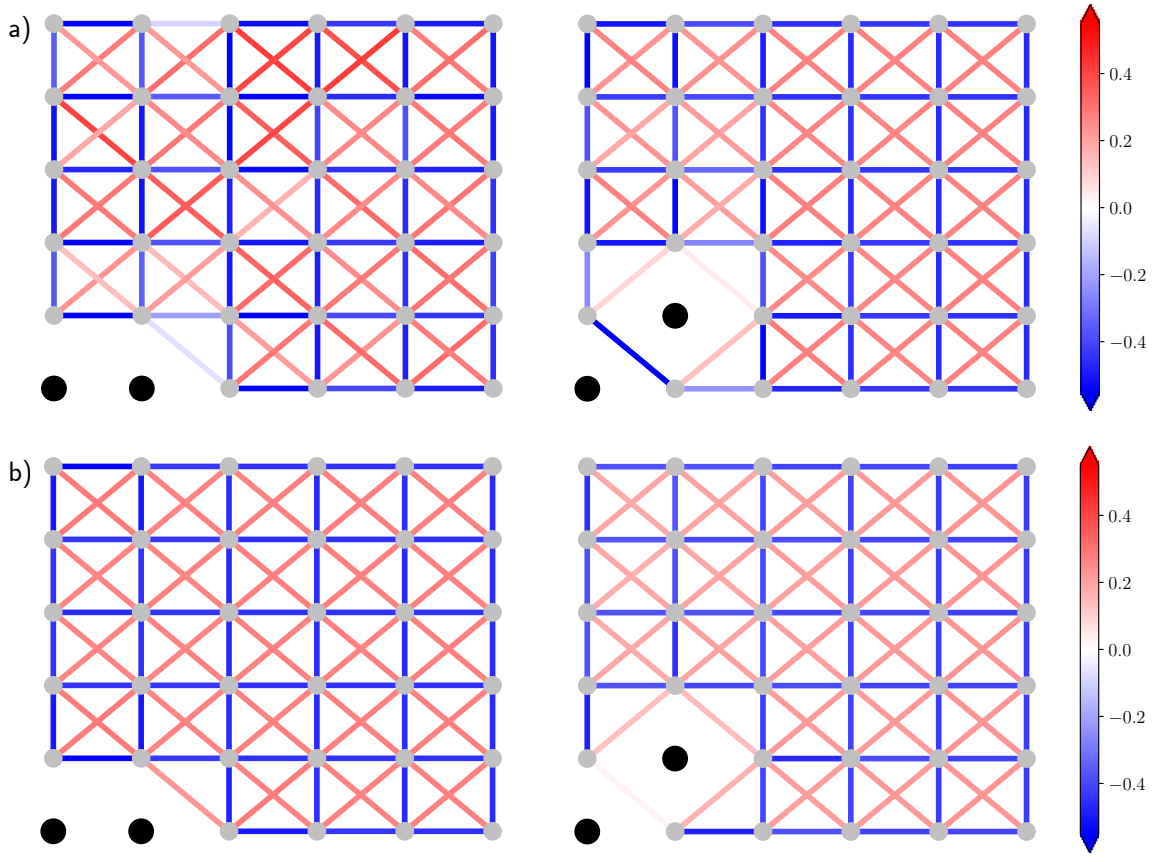

Figure 5.6.2: Spin correlations relative to two holes in the ground state of the $t-J$ model on a 6×18 cylinder for holes at a distance $\mathbf{d} = (1, 0)$ (left) and $\mathbf{d} = (1, 1)$ (right), marked as black circles. a) $t/J = 3$, evaluated from 2000 snapshots (left) and directly from the matrix product state (right). b) The holes are pinned in the center of the cylinder at the corresponding relative distance and the spin correlations are directly evaluated from the matrix product state. The colorscale is clipped from -0.55 to $+0.55$ in all cases.

are among the most common configurations for $t/J = 3$, the spin correlations far away from the holes should be unaffected and close to the corresponding value in the Heisenberg model, similar to the case for one hole. In the immediate vicinity of the holes, the spin correlations can however be heavily influenced, as shown in Fig. 5.6.2 a) for $t/J = 3$. For two holes on a nearest neighbor bond, Fig. 5.6.2 a) left, the diagonal spin correlation next to the pair is strongly reduced, while the other bonds remain unaffected. The case of two holes on the diagonal next nearest neighbor bond is even more striking: the diagonal spin correlation between the holes is reversed and becomes strongly antiferromagnetic instead of ferromagnetic.

We confirm that this effect is not purely geometric in Fig. 5.6.2 b) by considering the case of two holes located in the center of the cylinder at the corresponding relative position to each other with the help of a strong pinning potential $V/t = 20$. While the corresponding corelations are also reduced, there is no sign reversal and the overall effect is much weaker.

Similar correlations were evaluated for mobile holes in the ground state of the $t - J$ model in Ref. [317] and interpreted as a signature of hole pairing. In Ref. [15], we evaluate the connected counterpart of the four-point spin-hole correlation considered here at finite temperature and finite doping in a quantum gas microscope. Considering the connected part means that all lower order contributions are subtracted and we thus directly analyze signatures in the spin correlations due to the interaction of the two holes with each other. While there is no signature of pairing in the hole-hole correlations, the connected higher-order spin-hole correlations, in particular for the $\mathbf{d} = (1, 0)$ configuration of the two holes, shows the same behavior as observed in the ground state $t - J$ model numerics.

In Fig. 5.6.3, we evaluate spin correlations relative to holes further apart. Correlations further away from the holes remain unaffected, while all correlations between the holes are either strongly reduced, or sign reversed. Note that the statistical noise increases here, since the correlations are evaluated from snapshots and the corresponding hole configurations appear less frequently, as shown in Fig. 5.6.1. In both cases considered here, the diagonal spin correlations between the holes are strongly antiferromagnetic instead of ferromagnetic. In a simple picture similar to the geometric string theory discussed for the case of a single hole, this can be intuitively understood by the different possible paths connecting the two holes, yielding the same mechanism that leads to sign changes in the diagonal next nearest neighbor spin correlation closest to a single hole discussed in section 5.3.

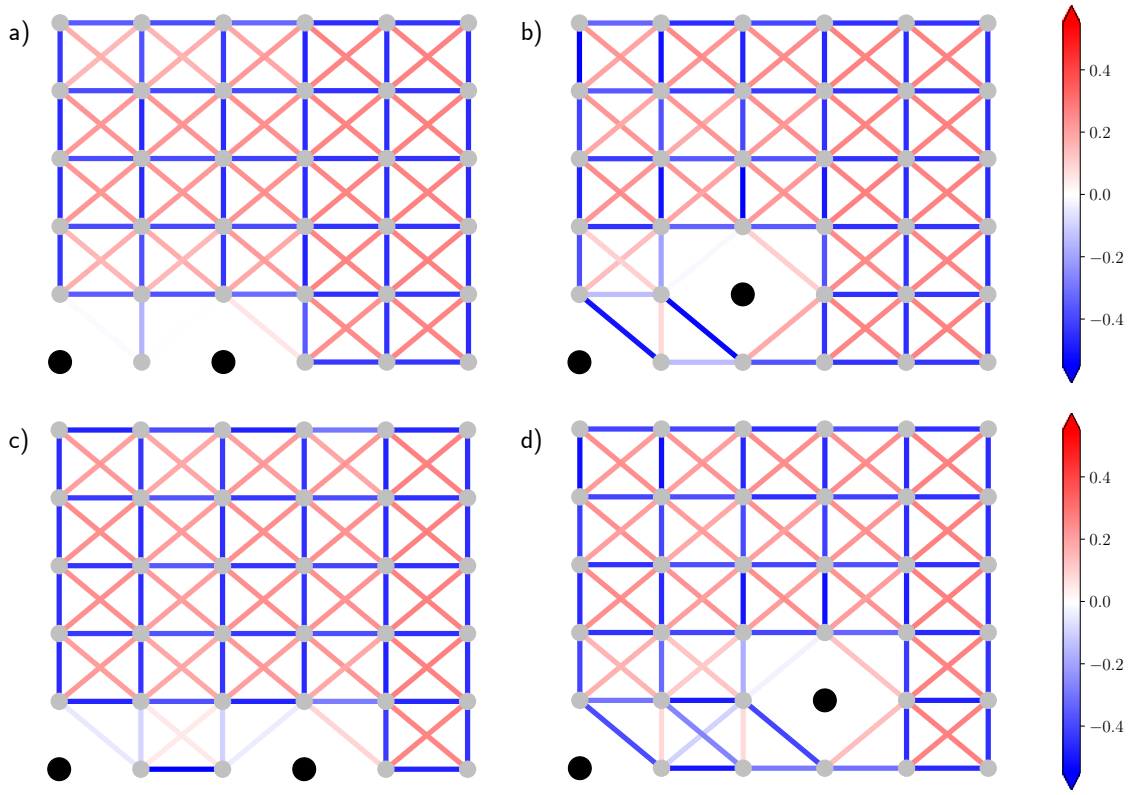

Figure 5.6.3: Spin correlations relative to two holes at increasing distance in the ground state of the $t - J$ model with $t/J = 3$ on a 6×18 cylinder for holes at a distance a) $\mathbf{d} = (2, 0)$, b) $\mathbf{d} = (2, 1)$, c) $\mathbf{d} = (3, 0)$, d) $\mathbf{d} = (3, 1)$ marked as black circles. The correlations are evaluated in the center of the cylinder. The colorscale is clipped from -0.55 to $+0.55$ in all cases.

6

Many Holes in Two Dimensions

This chapter is based on the publications

- Annabelle Bohrdt, Christie S. Chiu, Geoffrey Ji, Muqing Xu, Daniel Greif, Markus Greiner, Eugene Demler, Fabian Grusdt, Michael Knap: "Classifying Snapshots of the Doped Hubbard Model with Machine Learning"
  – Nature Physics Vol. 15, pp. 921–924 (2019) [arXiv:1811.12425]

- Christie S. Chiu, Geoffrey Ji, Annabelle Bohrdt, Muqing Xu, Michael Knap, Eugene Demler, Fabian Grusdt, Markus Greiner, Daniel Greif: "String patterns in the doped Hubbard model" – Science Vol. 365, Issue 6450, pp. 251-256 (2019) [arXiv:1810.03584]

Structure, text and figures have been rearranged and adapted here.

Can we understand the behavior of many holes with a theoretical description based on a single hole? While we certainly do not describe all properties correctly, we present convincing evidence in this chapter that a lot of the physics seen at finite doping is already captured if each hole is considered independently. Apart from the geometric string theory introduced earlier, we also compare the experimental results to a resonating valence bond theory ansatz. For the results in this chapter, I collaborated closely with the team from professor Markus Greiner's Lithium experiment. In the

following, we first describe the specifics of the experimental setup, which was already introduced in section 2.1. Next, conventional observables like spin correlation functions are discussed. In the remainder of the section, the ability of the quantum gas microscope to measure snapshots of the quantum many-body state is put to use. A modified version of the string pattern finding algorithm discussed earlier is applied to the experimental as well as theoretical snapshots. Finally, we present our machine learning approach to the problem, where a neural network is trained to distinguish the two theories and then has to decide which one describes the experiment best.

6.1 The Experiment

Understanding the phase diagram of the Fermi-Hubbard model remains one of the key challenges in condensed matter theory. Experiments on cuprate materials have shed some light on the underlying mechanisms, but have at the same time opened up new questions for theorists. In the past, phenomenological and numerical approaches have provided important insights. Quantum gas microscopy is naturally suited to assess microscopic theoretical approaches. Here, we study the Fermi-Hubbard model realized with cold atoms in a quantum gas microscope as introduced in chapter 2.

The experimental setup used here consists of a balanced two-component gas of fermionic Lithium in the lowest band of a square optical lattice with $U/t = 8.1(2)$, see also Refs. [76, 84]. Entropy redistribution with a digital micro-mirror device enables a disk-shaped homogeneous system of approximately 80 sites with temperatures as low as $T/J = 0.50(4)$ [6, 296]. The local chemical potential can be altered, thus doping the system, while the temperature is independently controlled [6]. We use the nearest-neighbor spin correlator to determine the temperature by comparing to numerical data.

The quantum gas microscope provides projective measurements of the quantum state of the system in the parity-projected Fock basis. In the case of the doped Fermi-Hubbard model, parity-projection means that a double occupancy cannot be distinguished from a hole. In the current state of the experiment, the measurements of the microscope moreover only tell us whether there is an atom or not, but does not reveal the hyperfine state, which encodes the spin. We can however selectively image one of the spin states by removing the other spin state before imaging, as discussed in section 2.1. For each doping value considered below, we usually have three sets of snapshots: one where only spin ups are imaged, one where only spin downs are imaged and one where both spin up and spin down are imaged. Note however that this does not allow us to infer the occupation of a given empty site in any one of the snapshots, as each image corresponds to a separate run of the experiment.

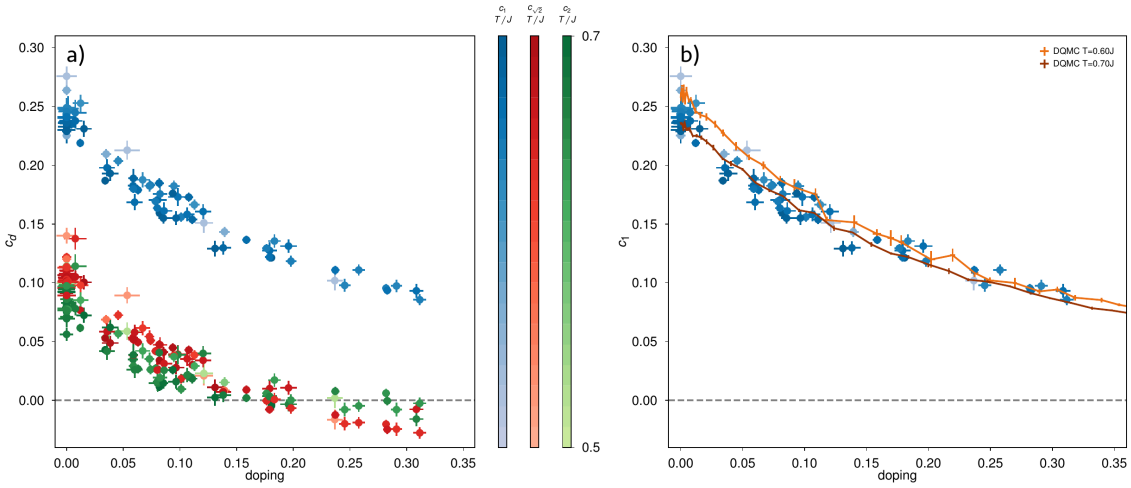

Figure 6.1.1: Spin correlations as function of doping and temperature. a) prior to grouping by doping shows additional spread from statistical fluctuation and temperature. The temperature of each dataset is indicated by the colorbars; the average temperature of all datasets, weighted by dataset size, is $T = 0.65(4)J$. b) Comparison of the measured nearest-neighbor spin correlator to determinantal quantum Monte Carlo simulation shows that as we dope the system, its temperature does not increase.

Due to the fact that only one spin species is imaged in each snapshot, the spin-spin correlations

$$C_s(\mathbf{d}) = (-1)^{||\mathbf{d}||} \sum_{\mathbf{i}} \langle S^z_{\mathbf{i}} S^z_{\mathbf{i}+\mathbf{d}} \rangle - \langle S^z_{\mathbf{i}} \rangle \cdot \langle S^z_{\mathbf{i}+\mathbf{d}} \rangle. \tag{6.1}$$

need to be evaluated through particle correlations. In Ref. [63] it was found that the spin-spin correlations can be expressed as

$$C_s(\mathbf{d}) = \frac{1}{2} \sum_{\sigma \in \{\uparrow,\downarrow\}} (\langle pp \rangle_{R\sigma} + \langle hh \rangle_{R\sigma} - \langle ph \rangle_{R\sigma} - \langle hp \rangle_{R\sigma}) - \langle hh \rangle_{NR} - (\langle p \rangle_{R\uparrow} - \langle p \rangle_{R\downarrow})^2, \tag{6.2}$$

where the indices for the two different sites have been droped and the subscripts refer to no removal (NR), removal of spin up ($R\uparrow$) or removal of spin down ($R\downarrow$) atoms. The correlations $\langle pp \rangle$, $\langle ph \rangle$ etc. are then the particle particle, particle hole and hole hole correlations averaged over the snapshots after the corresponding removal for the distance $\mathbf{d}$. For a more detailed discussion, see Ref. [63]

The data presented in section 6.3 includes samples with temperatures between $0.5J$ and $0.7J$, binned by doping values with 2% resolution. In Fig. 6.1.1 a) we plot $C_s(1)$, $C_s(\sqrt{2})$, and $C_s(2)$ versus doping for each individual experimental dataset, where colorbars for each quantity denote temperature. While it is clear that colder temperatures are accompanied by stronger correlations, crucially one can see that the zero crossing of $C_s(\sqrt{2})$ persists across the entire temperature range included.

We can also compare the experimentally measured doping dependence of the nearest neighbor spin correlator $C_s(1)$ to determinantal quantum Monte Carlo calculation of the Hubbard model on an 8×8 homogeneous square lattice using the Quantum Electron Simulation Toolbox, see Fig. 6.1.1 b) [79, 318]. Agreement between the two indicate that our experimental approach to doping the system does not change the temperature of the sample beyond experimental uncertainty.

The doping itself is determined from the single-particle occupation density (singles density). As discussed in chapter 3, there are doublon-hole fluctuations in the Fermi-Hubbard model, which are mostly restricted to nearest neighboring sites. Due to the parity projected measurements in the experiment, doublons appear as empty sites. The doping can therefore not simply be determined by counting the number of singly occupied sites in the snapshots. Instead, we obtain the doping as a function of the singles density from independent numerical simulations. For data between $T = 0.6J$ and $T = 0.8J$ we use data obtained from a determinantal quantum Monte Carlo algorithm [79, 318], and for all larger temperatures we use data obtained from a numerical linked-cluster expansion algorithm [150]. For $T < 0.6J$, the sign problem becomes significant. As a result, in this regime we use data at $T = 0.6J$, as the density sector of the equation of state is relatively insensitive to temperature here. We account for an imaging fidelity of 98.5%. When statistical fluctuations cause the singles density to exceed the numerically-obtained singles density at half-filling, we treat those samples as at half-filling. As discussed in section 2.1, the ramp protocol in the experiment can influence the number of doublon-hole pairs as well as the distance between doublon and hole in the snapshots.

When determining the standard error of doping values for each experimental dataset, we assume that the particle density is linearly dependent on singles density. We apply a linear fit to doping versus singles density from the numerical simulation mentioned above, yielding approximately $\delta = 1.22 \times (0.905 - n_s)$, where δ is doping and n_s is the singles density. We then calculate the standard error of the singles density and use the linear fit result to get the standard error of the mean doping value.

Since the actual doping value varies across datasets, we group datasets by their mean doping values within windows of width 2%. This yields a single mean doping value $\bar{d}$ for the entire group. The associated uncertainty Δ is determined by assuming each dataset k within the group was taken at a different doping value d_k with a corresponding uncertainty δd_k. Then Δ can be calculated as:

$$\Delta = \sqrt{\frac{1}{\sum_k n_k} \sum_k ((d_k - \bar{d})^2 + \delta {d_k}^2) n_k} \tag{6.3}$$

For datasets which are sufficiently close to half-filling, fluctuations of additional holes or particles will both result in a decrease of the singles density. This single-sided cut-off of statistical fluctuations will lead to a systematic offset in the mean. To estimate this offset, we assume that the statis-

tical fluctuations in total density follow a normal distribution centered at half filling with standard deviation σ. Then the resulting distribution in the singles density follows a half-normal distribution, characterized by an offset in the mean of $\sigma\sqrt{2/\pi}$ and standard deviation of $\sigma\sqrt{1-2/\pi}$. Note that this provides an upper bound of the systematic offset, because in reality our datasets are not all centered exactly at half filling. If we consider all datasets which are within one standard deviation of half filling, this results in an estimated systematic offset in the mean doping of the grouped dataset of about 0.25%. This systematic uncertainty is included in the errorbar for half-filling doping values. We note that a higher-order correction to the dependence of the singles density on the total density makes the singles density less sensitive and therefore would only decrease the magnitude of this systematic error.

Based on the experimental snapshots at half-filling, we can generate a dataset of geometric string theory snapshots for each desired doping value, as outlined in section 5.2.4. Using the effective geometric string Hamiltonian $\hat{\mathcal{H}}^{\Sigma}$ introduced in section 5.1, we can calculate the expected string length distribution. We consider a thermal state $\hat{\rho}^{\Sigma} = e^{\beta\hat{\mathcal{H}}^{\Sigma}}/Z_{\Sigma}$ for the string part. The overall state $\hat{\rho} = \hat{\rho}_{1/2} \otimes \hat{\rho}_{\Sigma}$ factorizes and we use the experimental temperature $T = 0.6J$ throughout. This fixes the string tension $(dE/dl) = 0.85J$, which we obtain by calculating the finite-temperature spin correlations $C_s(1)$, $C_s(\sqrt{2})$ in the undoped Heisenberg model using a standard quantum Monte Carlo code from the ALPS package. We keep track of the exponentially large string Hilbert space by making use of the discrete rotational symmetries of the Bethe lattice which are present when the string potential depends only on the length l_{Σ} of the string. Note that in this section, we show string lengths in units of sites rather than the bond count: the length of a string l (in sites) is related to the length l_{Σ} (in bonds) as $l = l_{\Sigma} + 1$. We fix the quantum numbers σ and $\mathbf{j}$ specifying the beginning of the geometric string. However, spin-exchange processes introduce matrix elements between states with different initial positions, $|\mathbf{j}, \sigma, \Sigma\rangle$ and $|\mathbf{j}', \sigma, \Sigma'\rangle$ with a strength $\propto J$ smaller than the dominant hopping amplitude $t > J$. As a result of such processes, we expect that $\mathbf{j}$ can be chosen randomly. The beginnings of different fluctuating strings are expected to become correlated at sufficiently low temperatures. However, since their dynamics is determined by an energy scale J, and the experimental temperature is of similar order of magnitude, we expect that such correlations between $\mathbf{j}_1$ and $\mathbf{j}_2$ associated with two different holes can be neglected in the current experimental regime.

Additionally, we generate a set of *sprinkled hole* snapshots for each doping value under consideration by placing the corresponding number of holes into the experimental half-filling data at random positions without moving them afterwards, thus effectively realizing a geometric string theory dataset with string length $l_{\Sigma} = 0$ throughout.

6.2 π Flux Theory

Anderson's resonating valence bond (RVB) picture [30] considers trial wavefunctions of free holes moving through a spin liquid comprised of singlet coverings. Originally, Anderson suggested RVB states as possible ground state of the two dimensional Heisenberg model. It can be shown that if the total state of a system is a singlet, the state can be written as a superposition of states, each of which corresponding to some singlet configuration. In particular, in every one of those states, each spin is part of a singlet. Resonating valence bond states describe states which are superpositions of different coverings of the lattice with singlets, typically on nearest neighbor bonds. Note that if the system size goes to infinity, the ground state of the 2D Heisenberg model spontaneously breaks a symmetry and possesses long-range anti-ferromagnetic order, which cannot be described by a quantum spin liquid. After the discovery of high temperature superconductivity, Anderson put RVB states forward as description of the regime at finite doping, where the hole motion introduces frustration.

Here, we want to compare experimental data from the doped Fermi-Hubbard model to an $SU(2)$ invariant quantum spin liquid ansatz. We consider one particular class of RVB wavefunctions which has been studied extensively, called π-flux states [277, 319], see also section 5.1.1. While we can in principle construct many different resonating valence bond wavefunctions, we assume that the details of the RVB theory are not highly relevant, since these are usually probed through long wavelength properties, which we do not consider here. The variational energy of the π-flux state provides a reasonable estimate of the ground state energy at half-filling and also appears at finite temperature and doping in the phase diagram calculated by Wen and Lee [277]. At half-filling, the Gutzwiller projected π-flux state is equivalent to the Gutzwiller projected d-wave superconducting ground state [277]. Sampling snapshots from the d-wave superconducting ground state is somewhat involved, since the number of fermions is not conserved and one therefore needs to consider arbitrary particle number sectors simultaneously. In order to understand how well a quantum spin liquid state can describe the Fermi-Hubbard model at finite doping, we here consider the reasonable yet comparably simple π-flux state.

The resonating valence bond states can be obtained from a Gutzwiller projected mean field state. In order to obtain a mean field description of a spin liquid, we use the same description as in section 4.2 and express the spin operators as

$$\hat{\mathbf{S}}_{\mathbf{i}} = \frac{1}{2} \sum_{\alpha,\beta} \hat{f}^{\dagger}_{\mathbf{i},\alpha} \sigma_{\alpha,\beta} \hat{f}_{\mathbf{i},\beta}, \tag{6.4}$$

see Eq. 4.29. We proceed as before and replace the operator $\hat{f}^{\dagger}_{\mathbf{i},a}\hat{f}_{\mathbf{j},a}$ by its expectation value $\chi_{\mathbf{ij}}$. The π-flux state is now given by the ansatz [28]

$$\chi_{\mathbf{i},\mathbf{i}+\mathbf{x}} = i\chi_1, \qquad \chi_{\mathbf{i},\mathbf{i}+\mathbf{y}} = i\chi_1(-1)^{i_x}. \tag{6.5}$$

The mean field Hamiltonian is then equivalent to free fermions hopping on a square lattice with π flux per plaquette. We obtain the snapshots for the π-flux state by sampling from the thermal density matrix of the mean field Hamiltonian as described in detail in section A.3. In the sampling process, each site in real space can only be empty or occupied by one of the two fermion species. We thus avoid double occupancies and directly perform a Gutzwiller projection. Without the Gutzwiller projection, double occupancies are not penalized in the mean field theory and thus appear more frequently than expected from the original problem.
Note that already in the description of a single hole in the ground state in sections 5.3 and 5.4, we used a similar construction to obtain a trial wavefunction for the spin background at half-filling.

6.3 Conventional Observables

For each doping value, we now have four sets of snapshots: the experiment, π flux theory, the geometric string theory, and sprinkled holes. These datasets can be analyzed for a variety of observables. Conventionally, one- and two-point correlation functions are studied.

6.3.1 Spin Correlations

In order to determine how far the antiferromagnetic ordering of the system spreads, we consider two point spin correlation functions, Eq.6.1. Evaluating these correlations as a function of the distance, we obtain the correlation length. According to the Mermin-Wagner-Hohenberg theorem, the continuous $SU(2)$ symmetry cannot be spontaneously broken in two spatial dimensions in the thermodynamic limit at finite temperature, and thus there is no long-range spin order. However, in this experiment, the system sizes are finite with a linear system size of about ten sites. For sufficiently low temperatures $T < J$, the correlation length can become comparable to the system size. The antiferromagnetic correlations extend then across the entire system. Given that we later want to apply an algorithm similar to the string pattern finding algorithm introduced in section 5.2.1, the correlation should span a distance comparable to the linear size of the system. In Fig. 6.3.1, we study the sign corrected spin correlations as a function of distance for low temperatures, $T \leq 0.7J$ and high temperatures, $T > 1.2J$. Note that the data at half-filling is the same data shown in Fig. 6.1.1 grouped for a range of temperatures. For the experimental temperatures of $T = 0.6J$, the spin

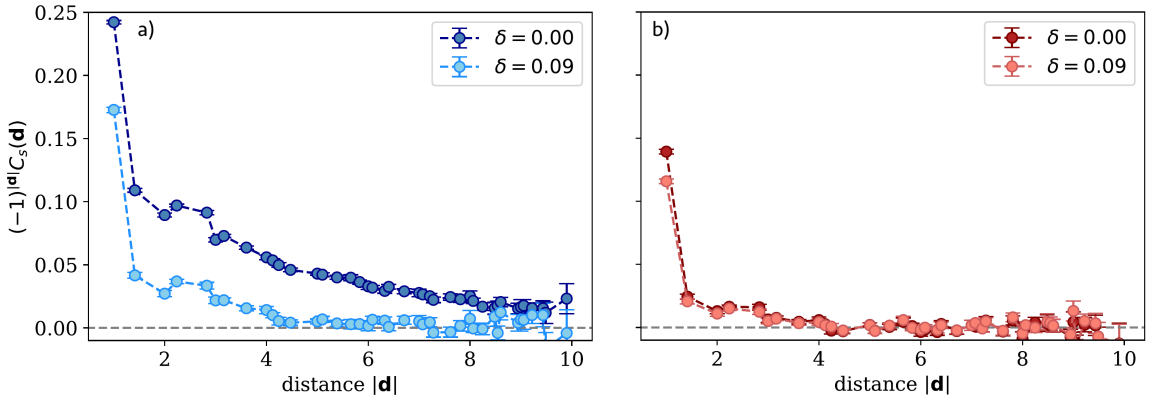

Figure 6.3.1: Spin correlations as function of distance for doping $\delta = 0$ and $\delta = 0.09$ and a) cold and b) hot temperatures. The spin correlations are obtained from the particle particle, particle hole and hole hole correlations in snapshots without removal and after removal of spin up or spin down atoms, Eq. 6.1.

correlations at large distances are still finite, but small. Upon doping, these correlations decrease further, as shown in Fig. 6.3.1. We therefore primarily analyze local correlation functions and compare the two theories to the experiment at different doping values. In Fig. 6.3.2, the spin correlations for $d = 1$, $d = \sqrt{2}$, and $d = 2$ are shown as a function of doping. As more and more holes are introduced into the system, the spin correlations get smaller. This qualitative behavior is captured by both theories and to some extend even by the sprinkled holes dataset. However, at a doping value of about 20%, the diagonal next-nearest neighbor spin correlations change sign and become negative, see Fig. 6.3.2 b). While the π-flux theory predicts a slow further decay towards zero, the geometric string theory correctly predicts the sign change.

This effect can be understood directly in the string picture: as the holes move through the system, the spins are re-arranged and spins which used to be nearest neighbors, are suddenly next-nearest neighbors. The – formerly positive – next-nearest neighbor spin correlator therefore now contains an admixture of the nearest neighbor spin correlator, which is negative and bigger. Once the doping is high enough, the diagonal next-nearest neighbor spin correlator averaged over the entire system therefore turns negative. We observed the same effect in section 5.3, where in the ground state of the $t - J$ model with a single hole, the diagonal next-nearest neighbor spin correlation function closest to the hole was strongly suppressed, see Fig. 5.3.2. While the three point correlation function between two spins and a hole cannot be evaluated in this experimental setting, it has been extracted in two recent works from Immanuel Bloch's group [15, 267]. In Ref. [15], we compare the corresponding connected correlations to the geometric string theory as well as a uniform and π-flux RVB state. The latter does not capture the experimentally observed behavior of the connected three point correlation functions.

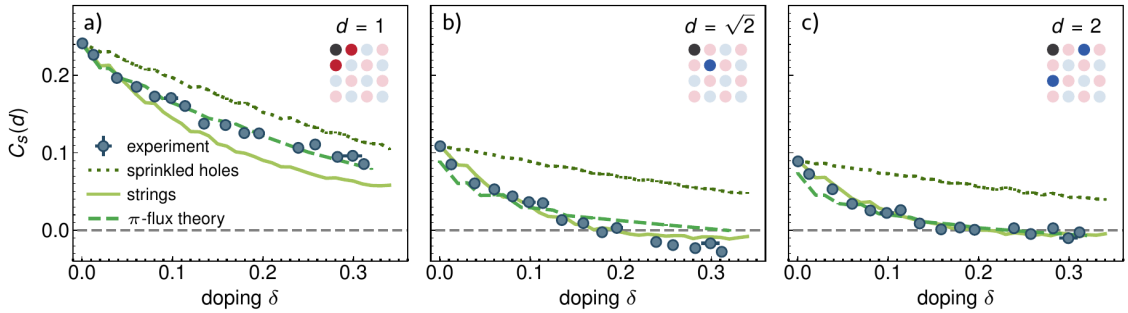

Figure 6.3.2: Spin correlations as function of doping. Decay of a) nearest-neighbor, b) diagonal next-nearest-neighbor, and c) straight next-nearest-neighbor spin-spin correlation functions upon doping. While the π-flux theory most quantitatively explains $C_s(1)$, only the string model captures the sign change of $C_s(\sqrt{2})$ and more quantitatively explains the two longer-distance correlators. In all three cases, sprinkled holes overestimate the spin correlations.

The same reasoning holds in principle for the straight next-nearest neighbor correlator. In this case, the absolute values of the correlation function are even smaller, thus rendering a statement about the sign change harder. The nearest neighbor spin correlator decays as a function of doping, but stays negative up to the largest doping values considered. The quantitative behavior is extremely well described by the π-flux theory, where the free fitting parameter was used to optimally match the experimental half-filling $C_s(d = 1)$. The geometric string theory captures the qualitative behavior, but does not match the experiment as well as the π-flux theory does. One possible reason is the existence of doublon hole pairs: we do not know the location of doublon hole pairs in the experimental half-filling snapshots on which the geometric string theory is based. Upon introducing and moving holes by hand in those snapshots, doublon hole pairs will get split up, which can lead to a smaller nearest neighbor correlator. This is an artifact of the way the geometric string theory snapshots are generated and the lack of full information about hole and doublon positions in the experimental data. Another possible explanation are back actions of the spin system, which starts to heal the string. Such a healing process would presumably first affect the nearest neighbor spin correlations, since those directly appear in the Hamiltonian. In Fig. 6.3.3, we study sign-corrected spin-spin correlations up to distance $d = 3$ for experimental data, geometric string theory and π-flux theory. The longer-distance spin correlations have however very small absolute values at increased doping, such that a clear statement about a possible sign-change in the experimental data is difficult.

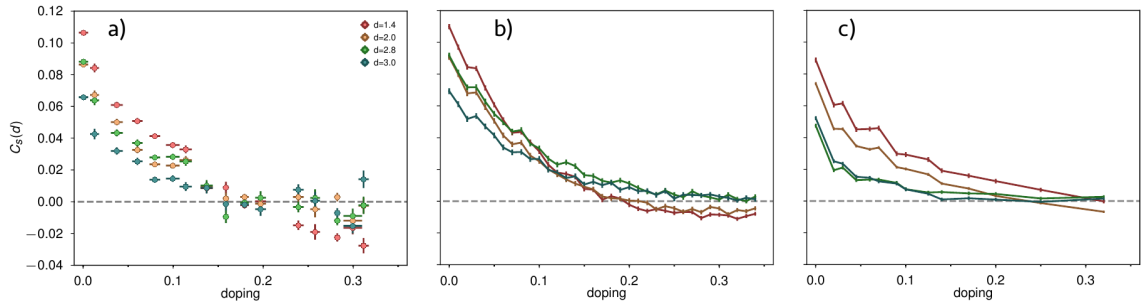

Figure 6.3.3: Spin correlations up to distances of three sites as function of doping from experiment (left), geometric string theory (middle), and π-flux states (right). Geometric string theory seems to explain the experimental data more closely than π-flux states.

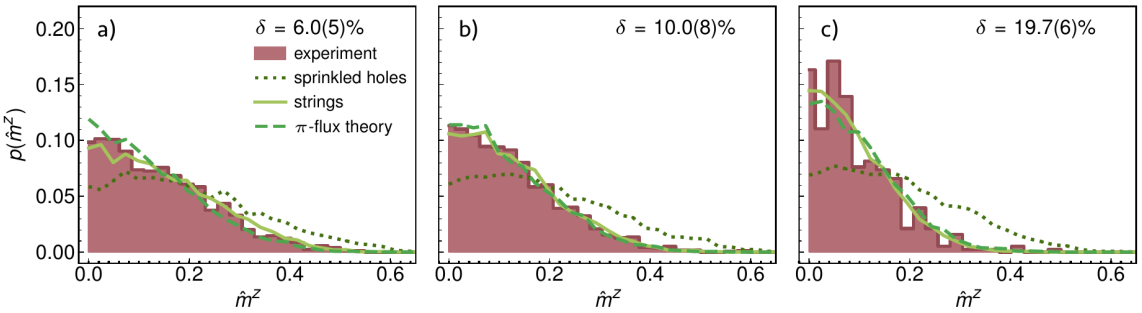

Figure 6.3.4: Full counting statistics of the staggered magnetization for doping values of $6.0(5)\%$ (left), $10.0(8)\%$ (center), and $19.7(6)\%$ (right). Both π-flux states and geometric string theory show reasonable agreement, whereas sprinkled holes do not. The figure is based on more than $29,900$ experimental realizations at an average temperature of $T = 0.65(4)J$.

6.3.2 Staggered Magnetization

The spin correlations analyzed above were averaged over the entire ensemble of snapshots. As a first step in making full use of the capabilities of the quantum gas microscope, full counting statistics of quantities are considered. In particular, we calculate the staggered magnetization for each snapshot and study histograms showing how often which value of the staggered magnetization occurs in the entire set of snapshots. In Fig. 6.3.4, the staggered magnetization full counting statistics is shown for three different doping values. With increasing doping, the distribution gets narrower. This can be understood as a loss of antiferromagnetic ordering due to the motion of more and more holes in the system. The snapshots where holes are sprinkled into the experimental half filling images do not capture this effect at all. Both the π-flux as well as the geometric string theory predict the behavior seen in the experimental data and show very good quantitative agreement. For small dopings, Fig. 6.3.4 a), the geometric string theory describes the experimental results more accurate than the π-flux theory, which underestimates the antiferromagnetic ordering in the system a bit.

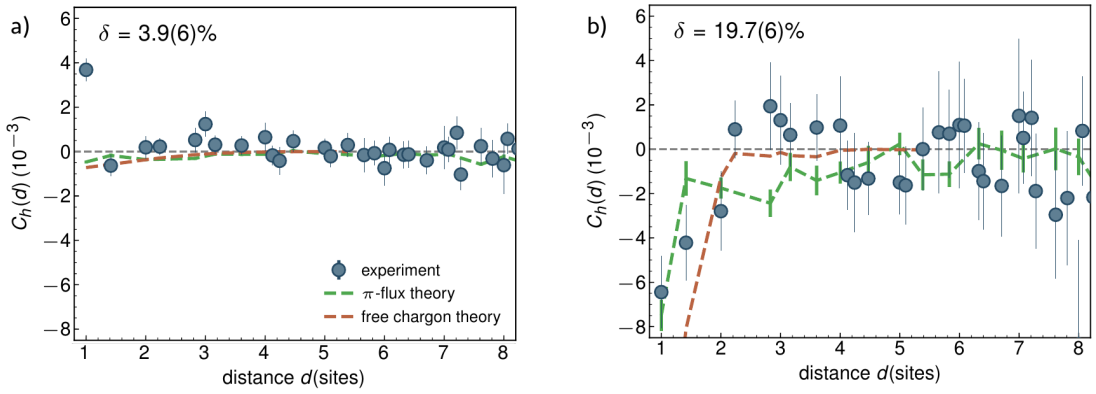

Figure 6.3.5: Distance dependence of anti-moment correlations for a) low and b) high doping values. The correlation functions are in stark contrast up to distances of $d = \sqrt{5}$.

6.3.3 Anti-moment Correlations

The observables studied so far contain only information about the spin sector and in the geometric string theory we even assume that the holes are uncorrelated. Experimentally, we can access anti-moment correlation functions in the entire parameter regime studied so far. Based on previous theoretical investigations and solid state experiments, signatures of hole pairing, stripe phases and even hole anti-bunching are expected in different regions of the phase diagram, see chapter 3.
Since in the snapshots obtained from this experiment, doublons and holons are indistinguishable, we consider anti-moment correlations

$$C_h(|\mathbf{d}|) = \langle (1 - \hat{n}_{s,\mathbf{i}})\,(1 - \hat{n}_{s,\mathbf{i}+\mathbf{d}})\rangle - \langle (1 - \hat{n}_{s,\mathbf{i}})\rangle\,\langle (1 - \hat{n}_{s,\mathbf{i}+\mathbf{d}})\rangle\,, \tag{6.6}$$

where $\hat{n}_{s,\mathbf{i}}$ is the single particle occupation on site $\mathbf{i}$. The anti-moment correspond to the moment correlations, since on every site in the experimental images there is either a particle or no particle. At half-filling, numerical simulations predict an increased nearest neighbor anti-moment correlator due to doublon hole pairs. In the experiment, this effect is observed qualitatively but with a smaller amplitude than predicted theoretically. This quantitative disagreement is most likely based on imperfect imaging fidelity and does not change the qualitative results presented here. In order to avoid signatures based on doublon hole pairs, we focus on anti-moment correlations between sites further apart than nearest neighbors.
In Fig. 6.3.5, the distance dependence of the anti-moment correlations for 3% and 19% doping is shown. Close to half filling, the nearest neighbor anti-moment correlation is positive due to doublon hole pairs and for further distances, the correlations are approximately zero. However, upon increasing doping, all anti-moment correlations up do distances $d = 2$ are statistically significantly

negative, indicating a hole-hole repulsion in this regime. The negative anti-moment correlations at distance $d = 1$ correspond to correlations between sites of different sub-lattices and indicate that holes do not tunnel preferentially between sites of one sub-lattice, as was predicted by theories of point-like magnetic polarons with a dispersion minimum at $(\pi/2, \pi/2)$ in the Brillouin zone [243, 244, 246, 248]. At larger distances, even though there appear to be some oscillations in the anti-moment correlations, within error bars the holes are uncorrelated.

The anti-moment correlations in Fig. 6.3.5 are compared to π-flux theory data. Within error bars, π flux theory shows good qualitative agreement with the experimental data for the anti-moment correlations.

As a reference, we additionally consider a phenomenological theory of free fermionic chargons described by an effective Hamiltonian

$$\hat{H}_{ch} = t \sum_{\langle ij \rangle} \left(\hat{h}_j^\dagger \hat{h}_i + \text{h.c.} \right) \tag{6.7}$$

on a square lattice. The chargon-chargon correlations in this theory are calculated from the corresponding thermal density matrix $\hat{\rho}_{ch} = e^{-\beta \hat{H}_{ch}}$ with $\beta = 1/k_B T$ the inverse temperature and $T = 0.3t$ as in the experiment. The free chargon theory is motivated by considering magnetic polarons with a finite extent due to the spinon-chargon bound state predicted by the geometric string theory. At sufficiently large doping, the geometric strings are expected to overlap substantially, yielding a chargon dispersion relation independent of the spinons. As a consequence, a deconfined phase of spinless chargons may be realized. Here, we consider free fermions for simplicity, but qualitatively similar anti-correlations are expected for a gas of bosonic chargons with hard-core repulsion. Apart from an overestimation of the $d = 1$ anti-moment correlation, the free chargon theory shows good agreement with the experimental results, Fig. 6.3.5.

We further characterize the observed anti-correlations by studying the doping dependence of the diagonal and straight next-nearest neighbor anti-moment correlations in Fig. 6.3.6 a). Starting from doping values of approximately 10%, the anti-moment correlations are consistently negative outside of the error bars and continue to decrease as more holes are introduced into the system. The anti-moment correlation function considered so far contains trivial contributions from doublon hole pairs present in the system. In Fig. 6.3.6, we study the anti-moment correlation function normalized by the amount of holes doped into the system δ:

$$\tilde{g}^{(2)}(|\mathbf{d}|) = \frac{C_h(|\mathbf{d}|)}{\delta^2} + 1. \tag{6.8}$$

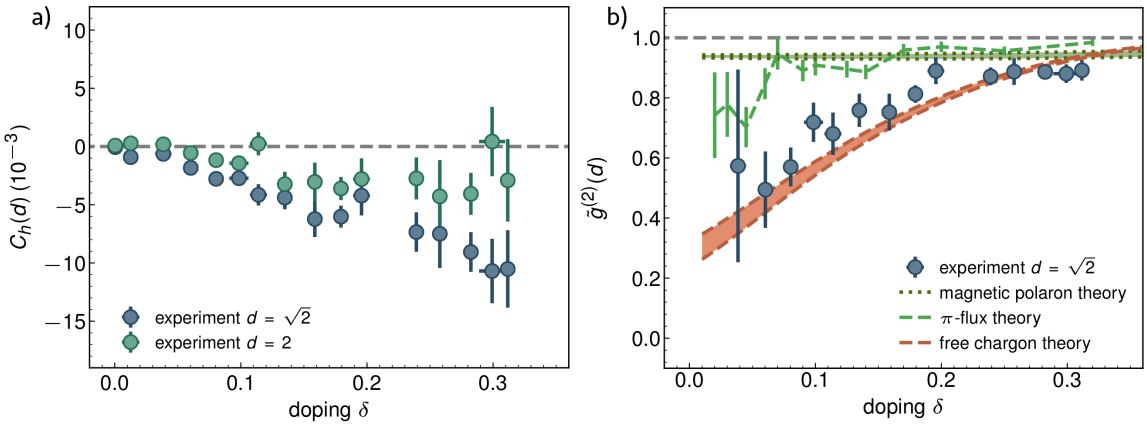

Figure 6.3.6: Doping dependence of anti-moment correlations. a) Diagonal next-nearest neighbor and straight next-nearest neighbor antimoment correlators versus doping. At both distances negative correlations grow with doping. b) Normalized antimoment correlator at $d = \sqrt{2}$ versus doping. The experimental result cannot be explained by the π-flux or a point-like magnetic polaron theory (see text), but instead matches a free fermionic chargon theory. Error bars on the doping are calculated as described in section 6.1. All other error bars represent one s.e.m.. The figure is based on more than 9900 experimental realizations at an average temperature of $T = 0.65(4)J$.

The rescaled correlation function can now be directly compared to theoretical approaches without doublon hole pairs. In particular, we here compare to π flux theory data without artificially introduced doublon hole pairs in order to avoid any artifacts due to the chosen procedure.

Given the small number of introduced holes below 5% doping, no statement can be made about the correlations in the experimental data in this regime. As mentioned above, in the geometric string theory data used so far, we assumed that the chargons are completely uncorrelated with each other. In Fig. 6.3.5, we compared the experimental data to a free chargon theory motivated by a picture of strongly overlapping strings. The comparison for the normalized $g^{(2)}(d = \sqrt{2})$ function, Fig. 6.3.6 b), shows consistency of this theoretical approach with the experiment.

We additionally compare the experimental results to a description of the chargons as point-like magnetic polarons in terms of the tight-binding Hamiltonian

$$\hat{\mathcal{H}}_{mp} = \sum_k \varepsilon_{mp}(k)\hat{m}_k^\dagger \hat{m}_k \tag{6.9}$$

with the known dispersion relation of the dressed hole [246, 248]

$$\varepsilon_{mp}(k) = \left[4\chi^2 J^2 |\cos(k_x)e^{-i\Phi/4} + \cos(k_y)e^{i\Phi/4}|^2 + B_{st}^2/4\right]^{1/2}. \tag{6.10}$$

This model is motivated by the mean-field description of the Néel state with staggered flux, where the parameters $\chi = 0.8$, $B_{st} = 0.35J$, and $\Phi = 0.4\pi$ are chosen such that the quantum Monte Carlo results at $J = 0.4t$ are correctly captured [253]. The comparison in Fig. 6.3.6 b) shows that this approach is incompatible with the experimental data, since the former predicts significantly weaker hole-hole anti-correlations. In the π-flux theory, the doped holes are similarily modeled as point-like objects moving in a quantum spin liquid of singlets. As can be seen in Fig. 6.3.6 b), this theory underestimates the magnitude of the anti-correlations as well.
Note that we do not compare directly to the geometric string theory and sprinkled hole snapshots, as the holes in both datasets are placed at random positions and there are thus no correlations between them.

6.4 String Patterns

Measurements performed in quantum gas microscopes contain more information than the observables discussed so far. As explained in detail in section 5.2, a set of several hundreds or thousands of snapshots can be analyzed for different patterns and thereby we can aim to take more – if not all – available information into consideration. For the sets of snapshots considered here, the algorithm outlined in section 5.2 has to be slightly modified for two main reasons. First, we consider finite doping here, so for most datasets there is more than one hole in each snapshots and different string patterns can overlap. Second, the positions of the holes are not known and we can therefore not take the longest string-like object attached to a hole as string pattern as we did before. We tackle these problems by hard-coding a procedure to extract string patterns. As before, we take as a reference the checkerboard pattern where the sublattice magnetization is chosen according to the snapshot under consideration. Analyzing the sites which deviate from the checkerboard pattern, we extract string patterns according to the following rules [6]:

1. every string pattern is a connected subset of sites forming a path without branching points,
2. each site can only be part of one string pattern,
3. longer string patterns are favored,
4. every string pattern must have at one end a site which is detected as empty, and therefore consistent with having a hole on that site.

A more detailed version of this algorithm as well as two modifications and the corresponding results are discussed in section A.4. Since the hole positions are not known here, almost every deviation from a Néel state will be counted as a string pattern. Therefore, already at half filling a large number

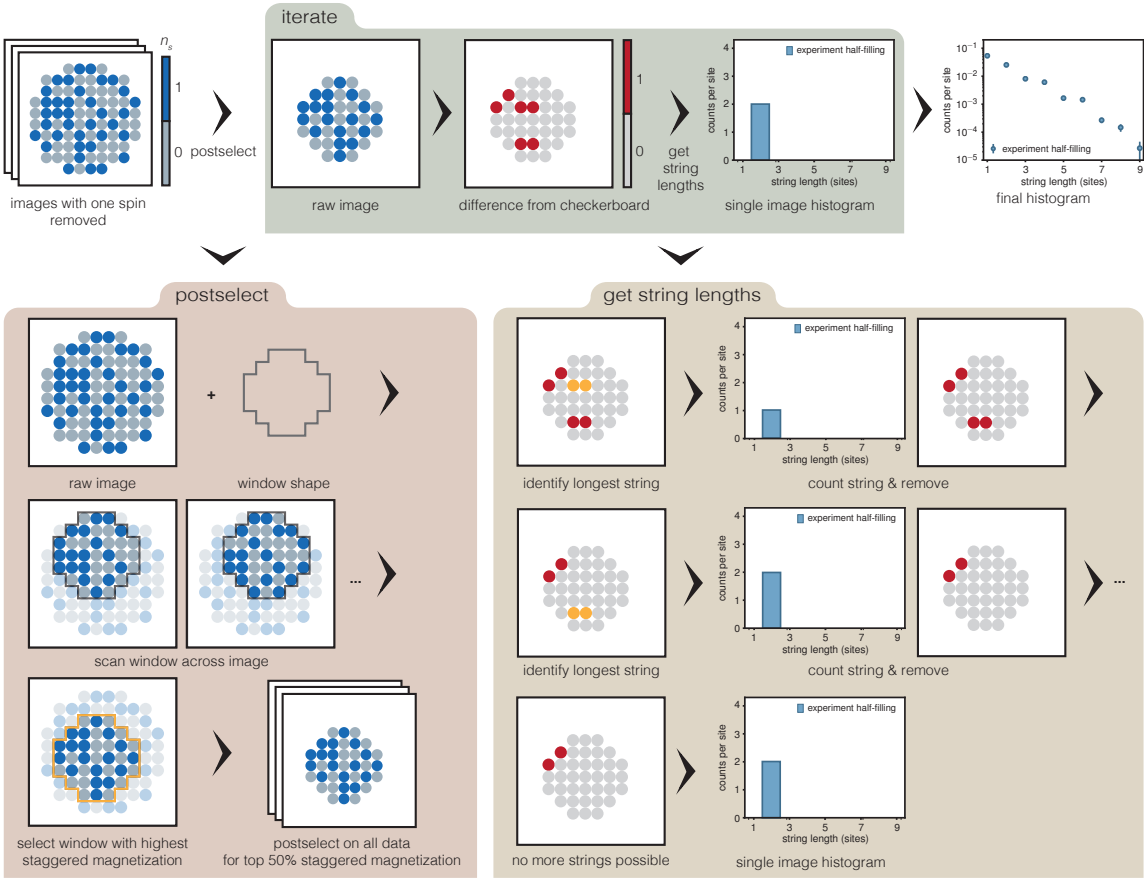

Figure 6.4.1: String pattern finding algorithm for the experimental data at finite temperature and doping and unknown hole positions. The algorithm only uses images with one spin species removed. After postselection, the deviation from a reference checkerboard pattern is used to identify string patterns.

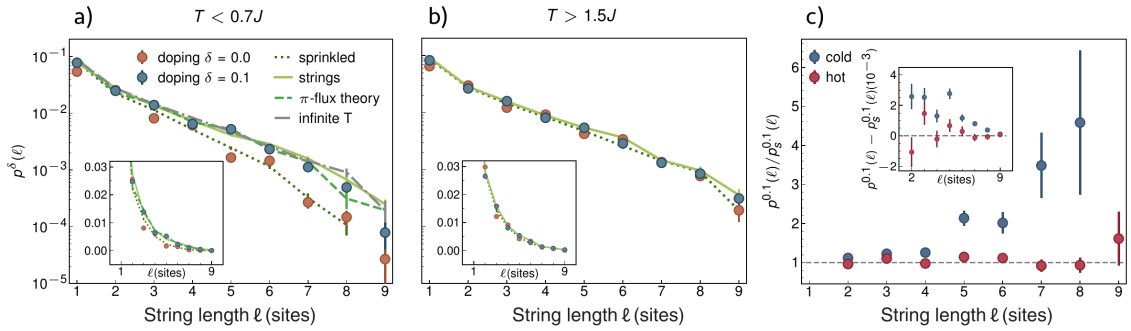

Figure 6.4.2: String patterns for different temperatures at half filling and 10% doping and comparison with simulated models, for temperatures below a) and above b) the superexchange energy J. The observable is only sensitive to doping in the colder dataset, and simulated strings seem to fit the doped experimental result best. Points have been slightly offset horizontally for readability and insets plot the same data on linear-linear axes. c) Relative and absolute (inset) difference between doped and undoped pattern-length histograms, highlighting temperature-dependent sensitivity. The sprinkled-hole result is used for the undoped case as it accounts for the change in density.

of string patterns is extracted, yielding a considerable background signal, Fig. 6.4.2 a). In order to be able to observe a change with finite doping, we consider only string patterns which are longer than two sites in the total string pattern counts discussed later, thus omitting the signal from the most common spin fluctuations.

Moreover, as opposed to sections 5.3 and 5.5, the spin background does not correspond to the ground state of the system, but a finite temperature state with additional thermal excitations, which lead to additional deviations from the Néel state. In particular, for the temperatures realized in the experiment, the correlation length of the spin system is smaller than the system size. In each snapshot, we therefore consider a smaller window with a linear size of seven sites, Fig. 6.4.1. This window is moved through the snapshot and the position with the highest staggered magnetization is taken, assuming that in this area, the measurement axis is aligned with the direction of the Néel order parameter. Additionally, we post-select the new set of smaller snapshots to be analyzed for string patterns and consider only the 50% with the highest value of the staggered magnetization for each doping value. Note that we choose a fraction of available snapshots instead of a fixed threshold. Based on the assumption that the hole motion reduces the antiferromagnetic order in the snapshots, we do not want to only use snapshots above a fixed staggered magnetization threshold, but also capture those with lower staggered magnetization due to the motion of the holes. In Fig. 6.4.2 a), the string length distribution $p^{\delta}(l)$ is shown for the lowest experimentally achieved temperatures, $T < 0.7J$, and doping $\delta = 0.0$ (red), as well as $\delta = 0.1$ (blue). For all string pattern lengths except for $l = 2$ and $l = 4$, a clear difference between half filling and finite doping is visible. The comparably high values of $p^{0.0}(l = 2)$ and $p^{0.0}(l = 4)$ stem from the same effect as discussed

in section 5.3 – spin exchange processes leading to a deviation of two sites from the Néel state.
The finite doping $\delta = 0.1$ case is compared to the string length distributions obtained from the corresponding snapshots for the geometric string theory, π flux theory, sprinkled holes as well as an infinite temperature state. The sprinkled holes scenario shows almost no difference to the half filling case, suggesting that the mere existence of additional holes is not sufficient to account for the increase in string patterns found in the snapshots. The π flux ansatz as well as the geometric string theory show good agreement with the experimental data for a doping of $\delta = 0.1$. It should be noted, however, that both theories as well as the experiment almost coincide with the infinite temperature limit for $\delta = 0.1$, suggesting that a form of saturation, where no additional string patterns can be found, is reached here.
For high temperatures, $T > 1.5J$, there is almost no difference between half filling and finite doping anymore, both closely resemble the infinite temperature case, Fig. 6.4.2 b). In particular, the experimentally found number of string patterns $p^{0.1}(l)$ at $\delta = 0.1$ relative to the sprinkled holes case $p_s^{0.1}(l)$ is significantly enhanced at long string lengths for the cold data, whereas no increase in the number of string patterns is found in the hot data, Fig. 6.4.2 c). Considering the absolute instead of the relative difference in the string length distributions shows an increase in the number of extracted string patterns across all lengths for the cold experimental data at a doping of $\delta = 0.1$. By summing over the number of found strings of all lengths, we obtain a total string count. Here, we neglect strings of length two sites and shorter to avoid an overly large background signal. In Fig. 6.4.2 d), we systematically study the difference in the string count between the experimental data at 10% doping and the sprinkled holes snapshots at the corresponding doping value. With increasing temperature, the difference in the string count decreases and for temperatures $T > J$, no significant signal is measurable. As can be seen in the inset, this effect is mainly due to the fact that the background signal measured in the sprinkled holes data increases considerably with increasing temperature, thus making it hard to see any effects due to the actual doping.
In Fig. 6.4.3 a) we evaluate the same quantity, the total string count, for the lowest temperatures achieved in this experiment as a function of doping. For doping values up to about 10%, the string count per site increases approximately linearly with the doping. For doping values bigger than 15%, the string count saturates. This is most likely an effect of the string pattern finding algorithm, which is limited to finding a certain number, depending on the specific length distribution, of strings in a snapshot. As expected from the previous results, the sprinkled holes do not capture the increase seen in the experimental data, and instead only show a small growth as a function of doping. The geometric string theory, on the other hand, captures the experimental result remarkably well over all doping values. As shown in section A.4, the input string length distribution used to generate the geometric string theory snapshots is crucial to obtain this agreement – considering input distribu-

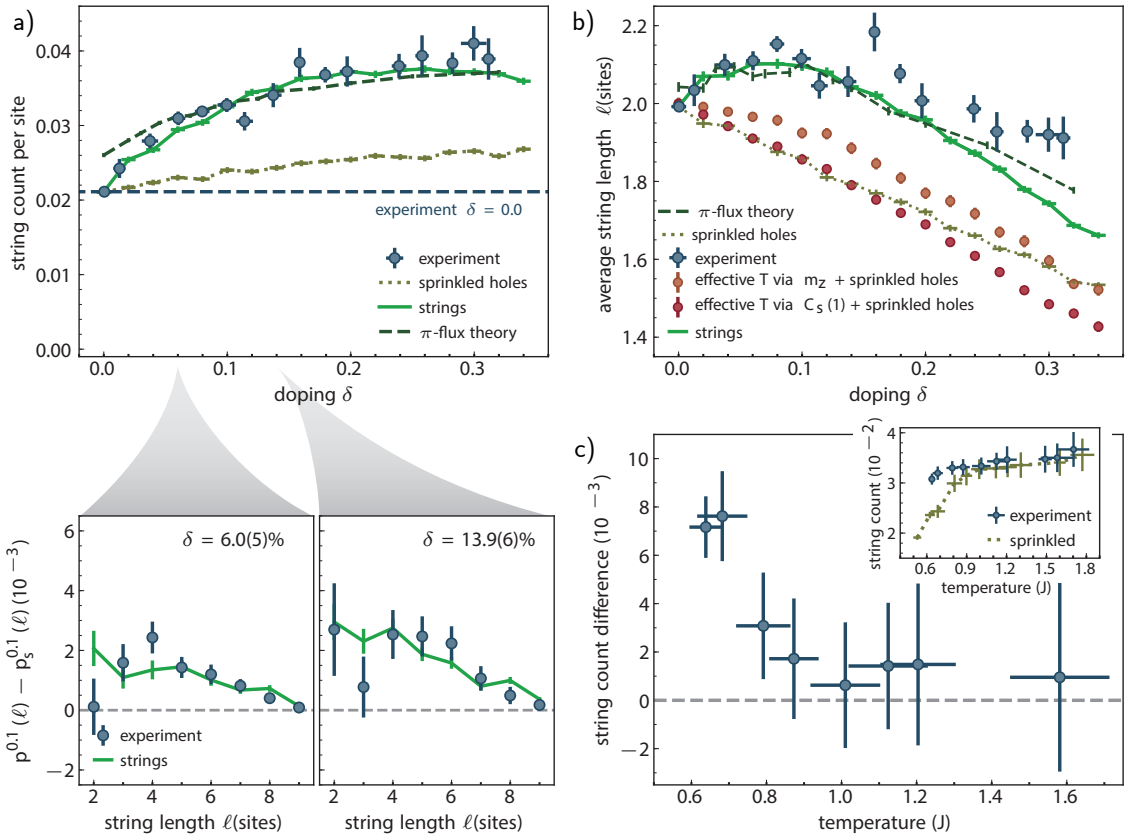

Figure 6.4.3: String pattern count and average length for different doping values at the lowest achieved temperatures $T < 0.7J$. a) (Top) Total number of string patterns exceeding length 2, normalized by the system size, as a function of doping. Although the string model and sprinkled-hole simulation both agree with experiment at half-filling by construction, already at low doping the string model performs significantly better than sprinkled holes. The string model is quantitatively accurate across a larger doping range than for π-flux states, but both are in better agreement with experiment than the sprinkled-hole simulation. (Bottom) Although the absolute difference between doped and sprinkled-hole pattern-length histograms increases with doping, the shape remains roughly invariant. b) Average string-pattern length versus doping. Doped AFMs exhibit longer-length string patterns compared to heated AFMs, even when the staggered magnetization or nearest-neighbor spin correlator is equal and holes are sprinkled in to equate doping levels (see text). c) Total string count at 10% doping as a function of temperature, with corresponding sprinkled-hole string count subtracted. Sensitivity to strings decreases with temperature owing to decreased order in the parent AFM as seen in the sprinkled string count (inset). In a) and b), error bars on the doping are calculated as described in section 6.1. All other error bars represent 1 s.e.m.. The figure is based on more than $24,800$ experimental realizations.

tions given by different temperatures leads to bigger deviations from the experimental results. In comparison to the geometric string theory, the π flux theory captures the qualitative behavior but overestimates the string count at small dopings and underestimates it at large values of the doping, thus yielding a slightly worse quantitative agreement with the experimental data.
From the string length distribution $p^{\delta}(l)$ we can furtermore obtain an average string length given by the weighted average

$$\langle l \rangle_{\delta} = \sum_{l} p^{\delta}(l) l. \tag{6.11}$$

In the geometric string theory picture, where we treat each hole independently of all the other holes, the string length should stay constant. With small modifications, this is what we observe up to doping values of almost 20% for both the experimental data as well as the geometric string theory snapshots. For larger dopings, the string patterns start to overlap substantially, which leads to overall shorter strings as different string patterns cut each other into smaller pieces.
In order to ensure that we defined new observables and not merely complicated measures for the magnetic ordering, we compare these results to experimental data at higher temperatures, where the magnetic ordering is lost due to the increased temperature instead of the finite doping. To this end, we use experimental data at temperatures between $T = 0.7J$ and $T = 1.6J$. From each temperature dataset, we obtain a number of new datasets with holes sprinkled in according to all doping values under consideration. We thus obtain a set of snapshots for each temperature and doping value. From the experimental data at finite doping, we determine the average staggered magnetization m_z as well as the nearest neighor spin correlations C_1. For a given doping value, we then compare m_z as well as C_1 to the finite temperature data with the corresponding number of holes sprinkled in. It is necessary to compare to the hole sprinkled data since the string pattern observables are constructed to be to some extent sensitive to the total number of holes present in the snapshots. For each doping value, the corresponding set of snapshots with the same m_z (orange) or C_1 (red) is selected and the average string pattern length is shown. As can be seen in Fig. 6.4.2 c), both approaches lead to a different qualitative behavior than the actual experimental doping. At half filling, the same dataset is analyzed for the experimental doping, both high temperature approaches and the geometric string theory. As soon as the doping is increased, the average string pattern length obtained from both high temperature approaches decreases almost linearly and is significantly smaller than the results from experimental doping. We are thus confident that the string pattern observables measure qualitatively new physics as compared to conventional observables.

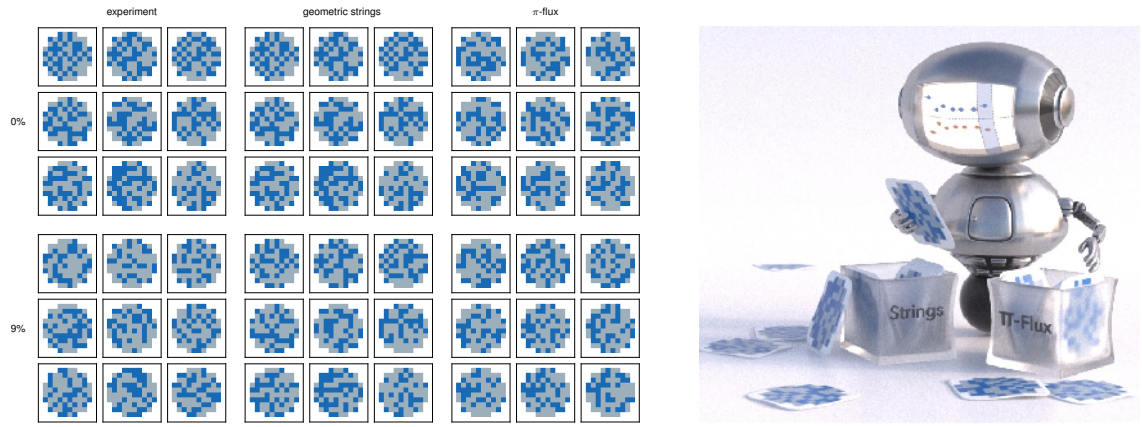

Figure 6.5.1: Machine Learning snapshots from the Fermi-Hubbard model. Exemplary snapshots from the experiment, geometric string theory and π-flux theory at half-filling and 9% doping (left). A neural network is trained to distinguish geometric string from π-flux theory. After training, the network is shown experimental snapshots and has to assign one of the theory labels (right), see text. Image by C. Hohmann.

6.5 Classifying Snapshots with Machine Learning

So far, we compared the experimental data to π-flux and geometric string theory with respect to specific observables, namely conventional quantities like the staggered magnetization and two point correlation functions as well as string patterns. The latter were specifically taylored for the geometric string theory and it is not straightforward to find a comparable observable for the π-flux theory – or any other theory one might want to compare the experimental data to.

In order to decide which theory fits the experiment best, taking into account all available data, we now choose an approach without any bias towards one theory by employing machine learning methods. In the past few years, machine learning has become a valuable tool in condensed matter physics.

Its main applications so far include representing the wave functions of correlated many-body states [320–323], the determination and characterization of a phase transition [324–333], quantum state tomography [334, 335], hypothesis testing for experimental scanning tunneling microscopy data [336], and to support quantum simulation experiments, for example in optical readout in quantum gas microscopes [337] or optimized quantum circuits in digital quantum simulation [338]. For a recent review, see Ref. [339]. Here, we take an alternative route and use a convolutional neural network (CNN) to classify experimental data at finite doping into different theoretical categories in order to determine which theory describes the system best on the microscopic level, see also section A.5. This approach provides insights into the underlying microscopic structures of the state, which may be inaccessible to conventional observables but can be essential for gaining a

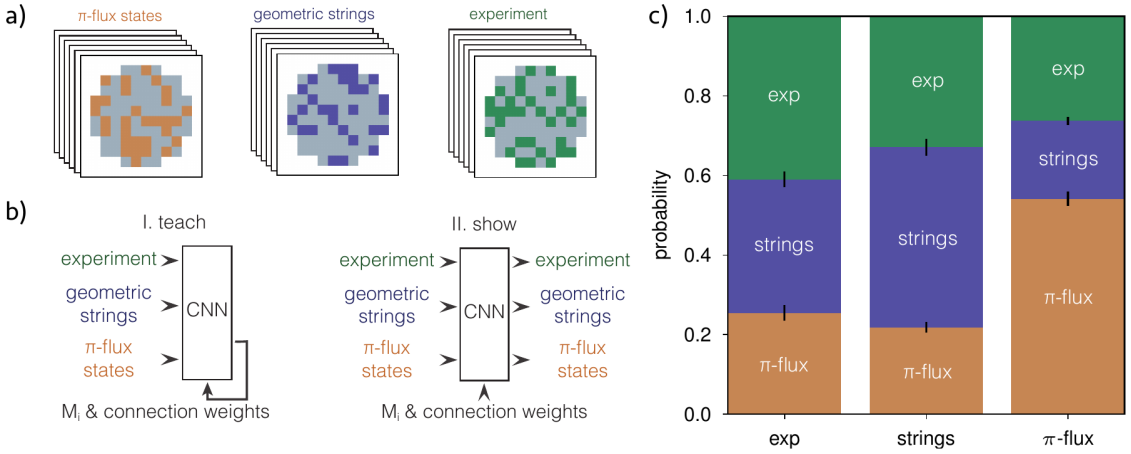

Figure 6.5.2: Classifying single snapshots of the many-body density matrix. a) Randomly chosen snapshots from the experiment and the two theories. Colored sites are occupied by one spin species, gray sites represent the other spin species, holes and doublons. b) The convolutional neural network is trained to identify to which dataset category any given snapshot belongs. Here, we consider experimental data, geometric strings and snapshots from π-flux theory, all at 9% doping. The probabilities in c) show how a sample of 400 snapshots which have not been used during training is classified. While the π-flux theory is recognized comparably well, a clear separation between experimental data and geometric strings is not possible. The standard errors of the mean over ten repetitions of the process are shown by the errorbars, see text for details.

deeper understanding of the emergent physics. First, we train a convolutional neural network to distinguish snapshots from the following three categories: experiment, π flux theory, and geometric string theory, all at 9% doping. The resulting classification of a test set of data not used during training is shown in Fig. 6.5.2. Here, the x axis displays the actual class of a snapshot, while the y axis corresponds to the probability with which the network sorts it into the different categories. The overall accuracy achieved for this task is 47%, which is a comparably low value. Notably, the network manages to distinguish π-flux from geometric string theory data with a higher accuracy. In particular, the experimental snapshots are classified as such in less than half of the cases. This indicates that it is in principle meaningful to classify the experimental images as one of the two theories, because otherwise experimental images would be classified correctly most of the time.

Next, we make use of one of the most powerful features of neural networks: their ability to generalize to new data not encountered during training. We train the neural network to distinguish π-flux from geometric string theory snapshots at each doping value and subsequently input experimental images into the network, which then has to assign one of the two theory labels. This classification shows how similar the experimental data is to the theoretically simulated data. In Fig. 6.5.3 b), the resulting classification is shown. Up to doping values of about 15%, significantly more experi-

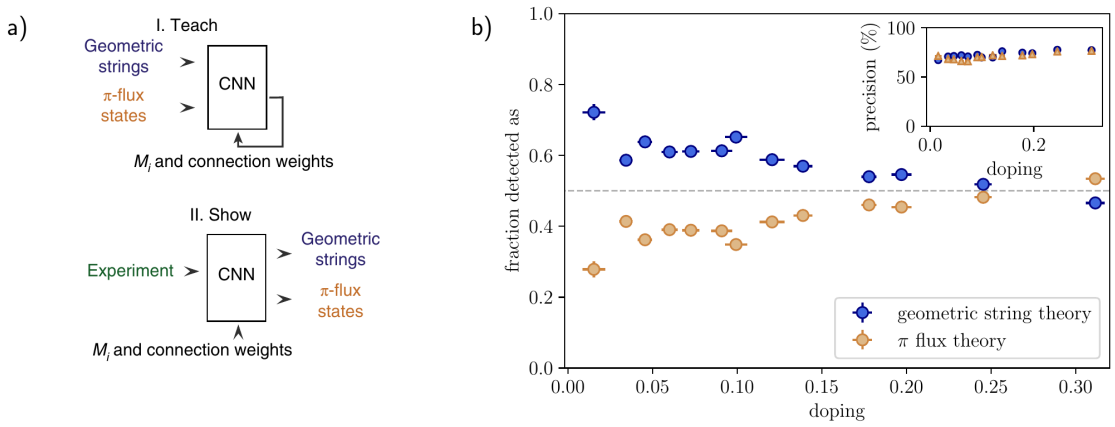

Figure 6.5.3: Training to distinguish theories. a) The network is trained to distinguish snapshots from geometric string theory (blue) and π-flux theory (orange) at each doping value. After the training sequence, experimental images at the same doping are shown to the network. b) The average of the resulting classification of the experimental data at the corresponding doping value. The inset shows the precision for the trained classes on a subset of data not used for training. The vertical errorbars show the standard errors of the mean over ten repetitions of the process and are smaller than the plot markers. The horizontal errorbars for the doping are obtained as described in section 6.1.

mental snapshots are classified as geometric string theory than as π flux theory. For higher doping values, roughly the same number of snapshots are classified as either theory.

The ability of the neural network to distinguish π-flux from geometric string theory on the level of individual images indicates that the physical structure of these states is different. We can further improve the accuracy of our classification by taking into account the information that an entire set of measurements belongs to the same physical state. When the CNN sorts each snapshot into one of the two categories with probabilities p and $1 - p$, the entire sample is classified by the category in which the majority is sorted. As the number of shots in each category follows a binomial distribution, the probability to make a wrong classification of the entire sample decays exponentially with the number of snapshots. Therefore, the entire experimental dataset at any doping value below 15% would be classified as geometric string theory data with almost 100% probability

In Fig. 6.5.4 a), we combine four snapshots at a time to a single image. As shown in the inset, the precision increases to values higher than 80%. Moreover, experimental snapshots are classified as geometric string theory with a much higher probability up to intermediate doping values of 12%. For higher doping values, where no signicifant distinction was possible in the case of the classification of a single snapshot at a time, Fig. 6.5.3 b), the experimental data is now labeled as π flux theory.

Before training the neural network, we randomly select 250 snapshots from the full data for testing. These snapshots are not used during training, but only to test the performance of the network and

determine the accuracy. In order to average out fluctuations in the results, we repeat the training with a different choice of the test data set and sorting of experimental data ten times. The error bars for the different accuracies as well as the percentage of experimental snapshots detect as one of the two theories shown in the figures represent the standard deviation over the different runs,

$$\Delta x = \frac{\sqrt{\sum_{i=1}^{\mathcal{N}} (x_i - \bar{x})^2}}{\mathcal{N} - 1}, \tag{6.12}$$

where $\mathcal{N}$ is the number of runs, x_i is the quantity under consideration in the i-th run and $\bar{x}$ is the average value of the said quantity over all $\mathcal{N}$ runs.

So far, the geometric string theory snapshots were based on experimental data at half filling. In order to avoid any potential bias, we also generated geometric string theory data based on Heisenberg Quantum Monte Carlo (QMC) snapshots instead of experimental data. In this case, we additionally have to add doublon-hole pairs, similar to the π flux theory snapshots. Since we are not restricted by the number of available experimental snapshots, we increase our data sets here to 6800 snapshots per theory for each doping value. Similar as before, for each doping value, we train the network to distinguish the two theories and subsequently input experimental snapshots, which are then labeled as one of the two theories. The obtained classification is qualitatively equivalent to the results shown before, see Fig. 6.5.4 b). We can thus conclude that the reason the string theory is favored by the neural network is not the fact that it is based on experimental data.

On a test set not used during training, the network achieves a precision above 70% for the classification of snapshots from the two theories for all doping values considered. The precision is defined as the percentage of snapshots classified as a theory, which in fact stem from that theory. For basic applications of machine learning, such as the recognition of handwritten digits, much higher values are commonly achieved for the precision. However, as exemplified in Fig. 6.5.1, single snapshots from the two theories look extremely similar - far more so than different handwritten digits. Moreover, we have shown in section 6.3 that commonly evaluated observables, such as spin correlation functions and the staggered magnetization are very similar in both cases. Increasing the system size, and thus providing more information in each image, can enhance the precision. Other ways to improve the performance include larger data sets as well as full information about both spin species and doublon and hole positions. In Fig. 6.5.4 d), the network is trained to distinguish the two theories based on snapshots where simultaneously the positions of the holes and both spin species are known. The geometric string theory in this case is based on Heisenberg Quantum Monte Carlo data, because in the experimental half filling data, doublon hole pairs are present with unknown positions. While we cannot sort experimental data as one of the two theories in this case, since not all information is available in this case, Fig. 6.5.4 d) shows a significantly increased precision in the

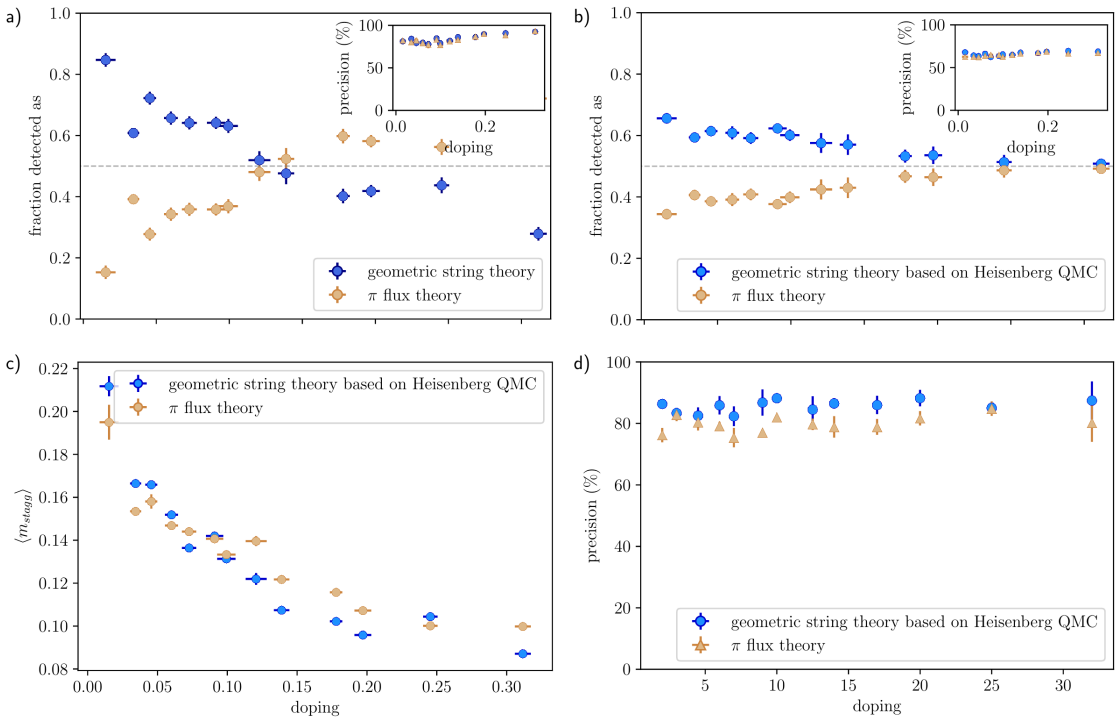

Figure 6.5.4: Distinguishing π flux and geometric string theory. The network is trained to distinguish snapshots from geometric string theory (blue) and π-flux theory (orange) at each doping value, a) four snapshots at a time. Each input corresponds to four randomly chosen images from one theory. After training, experimental images at the same doping are shown to the network. Again, we show the network four images at a time and the network has to classify them into the same category. The plot shows the average of the resulting classification over all available experimental data at the corresponding doping value. The inset shows the precision that is achieved for the trained classes on a subset of data not used for training. b), c), d) As opposed to Fig. 6.5.3 and a), the geometric string theory data is based on Heisenberg quantum Monte Carlo simulations to avoid a potential bias by using experimental half-filling data. After training, experimental images at the same doping are shown to the network. b) shows the average of the resulting classification over all available experimental data at the corresponding doping value. The inset shows the precision that is achieved for the trained classes on a subset of data not used for training. c) Staggered magnetization of the two classes after sorting. After training the CNN to distinguish geometric string theory and π-flux theory, we show experimental data to it, which is then classified by the network as one of the two theories. As a result, we obtain a subset of experimental data sorted into the string theory class and accordingly a second complementary subset classified as π-flux theory. For these two new datasets, we now determine the average value of the staggered magnetization. d) No doublon-hole pairs are added and the information about the positions of the holes is kept in the snapshots. Since both datasets stem only from theoretical data, we are not restricted in the number of snapshots and use 6800 snapshots from each category. The performance of the network improves as compared to the inset of part b).

classification of a test set of the two theories.

In order to obtain some insights on what quantity the network uses to make its decisions, we analyzed the experimental datasets after the classification. For each doping value, we obtain two subsets of experimental images: the snapshots which are classified as π flux theory, and those labeled as geometric string theory. In Fig. 6.5.4 c) we show the average staggered magnetization separately in those two datasets. Across all doping values, the obtained staggered magnetization is similar for the sets of data classified as the two theories, indicating that this observable is not employed for the classification by the neural network. In Ref. [16] we develop a modification of the network architecture, the Correlator Convolutional Neural Networks (CCNN), with which an interpretation of the patterns used by the neural network is possible. We employ this architecture to again distinguish geometric string from π-flux theory with full information and without doublon hole pairs and find that the dominating signature of geometric string theory at finite doping are four-point correlators with two neighboring aligned spins next to a hole. This correlation function is expected due to the string re-arranging the spins. In particular, we observed similar correlation functions in the ground state in section 5.3 and experimentally, these signatures have been observed in Ref. [267] and at finite doping in Ref. [15].

One way to simplify the pattern recognition is to post-select the snapshots to a high value of the staggered magnetization. In all snapshots, the underlying SU(2) symmetry of the Fermi-Hubbard Hamiltonian leads to fluctuations of the Néel ordering vector. The post-selection is a way to avoid confusion due to images with Néel ordering vector that is not aligned with the measurement axis, in which case it can be harder to find certain patterns in a single snapshot. In Fig. 6.5.5, we perform the following post-selection procedure: for experimental as well as theory data, we calculate the absolute value of the staggered magnetization $|m_z|$ for every snapshot and use only the 30% of all snapshots with the highest value of $|m_z|$ in each dataset. Importantly, this still corresponds to a large number of snapshots, which can be considered as a representative sample of the quantum state.

Fig. 6.5.5 a) is qualitatively the same as the corresponding result in Fig. 6.5.3 b). However, the post-selection seems to improve the precision achieved by the CNN to some degree, even though less snapshots are available for training here.

Starting at half-filling and cold temperatures around $0.6J$ the AFM correlations vanish both with increasing doping or increasing temperature [6]. We approach the question of how similar these regimes are on the microscopic level. At each doping value we train the CNN to distinguish geometric string theory data and experimental data at high temperature and half-filling. We randomly add holes to the hot data according to the respective doping level to prevent the network from distinguishing the two theories trivially by the density. In order to obtain a sufficiently large training

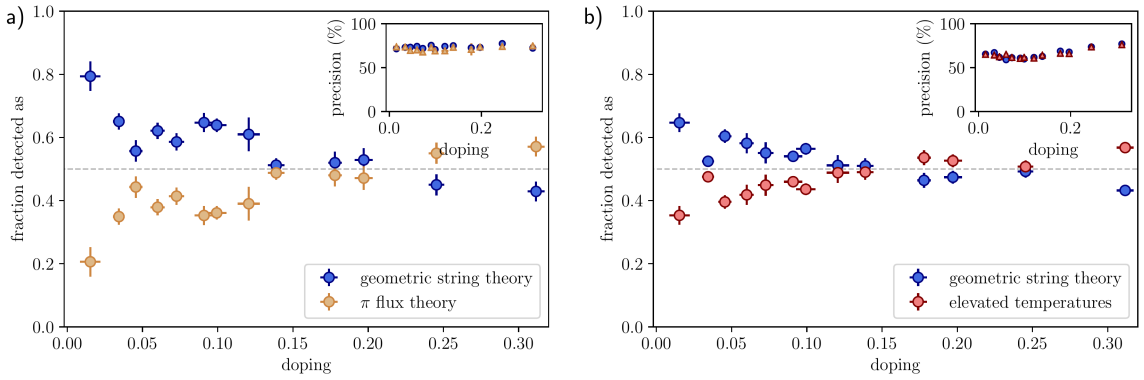

Figure 6.5.5: Machine learning post-selected snapshots. a) The network is trained to distinguish snapshots from geometric string theory (blue) and π-flux theory (orange) at each doping value. All datasets are post-selected to high absolute values of the staggered magnetization. After training, experimental images at the same doping are shown to the network. The plot shows the average of the resulting classification over all available experimental data at the corresponding doping value. The inset shows the precision that is achieved for the trained classes on a subset of data not used for training. The vertical errorbars show the standard errors of the mean over five repetitions of the process and the horizontal errorbars for the doping are obtained as described in section 6.1. b) The CNN is trained to distinguish geometric string theory at a given doping value from experimental images at half-filling and temperatures $T \geq 0.9J$ with the corresponding number of holes randomly sprinkled into the pictures to prevent a distinction based on the filling. After training, experimental images at low temperatures, $T \approx 0.6J$, and the corresponding doping value are shown to the network. The plot shows the average of the resulting classification. The inset shows the precision that is achieved for the trained classes on a subset of data not used for training. The vertical errorbars show the standard errors of the mean over ten repetitions of the process and the horizontal errorbars for the doping are obtained as described in section 6.1.

set, we use half-filling data for temperatures between $T = 0.9J$ and $1.8J$ for the high temperature class. As in Fig. 6.5.5 a), we apply post-selection based on high values of the staggered magnetization here. For doping below $\sim 15\%$, the network classifies the experimental data as geometric string theory, see Fig. 6.5.5 b). However, the precision decreases with increased doping, see inset of Fig. 6.5.5 b). This shows that it is difficult for the CNN to distinguish the theories, indicating that the classification of experimental pictures around 15% doping is challenging.

6.5.1 Confusion Learning

The precision or accuracy achieved on a test set not used during training can itself be used as a probe of the system. The confusion learning scheme introduced in [325] provides a method to investigate the question how the system changes as a parameter – such as the temperature – is varied. Given snapshots of the Heisenberg model, obtained from QMC, at temperatures between $0.1J$ and $1.6J$, we assign the label A to all snapshots at temperatures $T < T_i$ and the label B to all data at $T \geq T_i$ for some cutoff temperature T_i. We then train a CNN to assign these labels correctly to single snapshots. If $T_i = 0.1J$, all data will be labeled as B and therefore the accuracy of the network will be optimal, because it can simply learn to always choose the label B. Similarily, if $T_i = 1.7J$, all labels will be A and again the accuracy will be 100%.

If there is a detectable change in the snapshots at a temperature T^* in the considered range, the network should also be able to classify snapshots with an elevated accuracy if $T_i = T^*$. For other values of T_i, the performance should be worse. A W-shaped accuracy as a function of T_i is therefore the signature of such a detectable change. Furthermore, if no temperature exists at which a significant change in the snapshot occurs, the accuracy as a function of T_i will be in the shape of a V instead.

In Fig. 6.5.6 a), we demonstrate this scheme for the case of a qualitative change in the data at an intermediate temperature T^*. For a threshold value $0.1J < T_i < T^*$, the network has to learn to assign label B to a mixture of snapshots for $T < T^*$ and $T > T^*$, i.e. snapshots that differ qualitatively. It is thus impossible to learn the correct labeling, and instead the network will learn to assign the label B to whichever category has more snapshot for the given threshold T_i. The accuracy for category B, shown for the case of a strong qualitative change at $T/J = 0.8$ as faint orange line in Fig. 6.5.6 c), therefore stays constant at 100% for the lowest few values of the temperature. The same is true for category A, coming from high temperatures.

In Fig. 6.5.6 b), the performance of the network is shown for different values of T_i. Even though the accuracy does not increase up to 100% at any intermediate value, a peak around $T = 0.8J$ arises. This is in agreement with quantum Monte Carlo calculations where the uniform spin susceptibility has a peak at roughly the same value [150, 340, 341]. This behavior of the spin susceptiblity

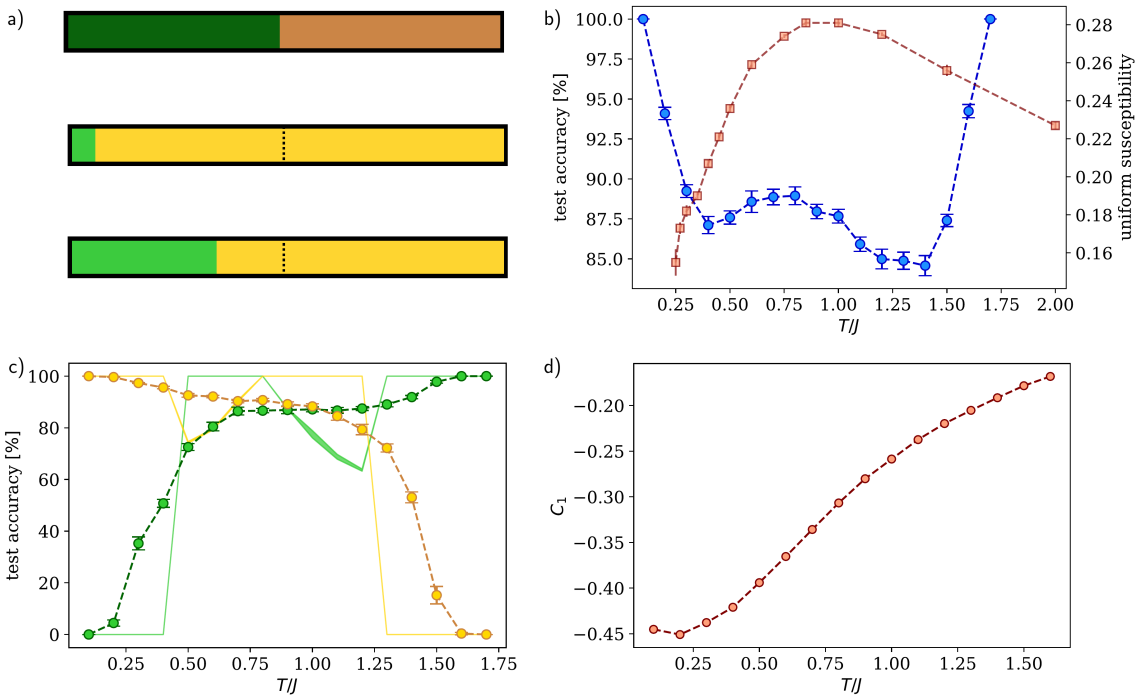

Figure 6.5.6: Confusion Learning in the Heisenberg model. In the confusion learning scheme, the existence and value of a parameter at which a qualitative change in the data occurs is investigated on the basis of the accuracy of the neural network. Here, we label Heisenberg Quantum Monte Carlo snapshots from a 16×16 system at temperatures below a cutoff T_i with label A and correspondingly data at $T > T_i$ with label B. a) If there is a qualitative change in the data, e.g. in the middle of the temperature range, the network learns the 'wrong' label for the minority label within each half. b) The plot shows the accuracy achieved for a test set of 500 images not used during training. If the network can find a qualitative change in the data at some intermediate value of the temperature, a peak appears between the lower and upper bound of available data. This yields the characteristic W-shape. The shaded squares show the uniform susceptibility $\chi(\mathbf{q} = 0, T)$ obtained from Quantum Monte Carlo calculations for the Heisenberg model [340]. c) Accuracies for the subsets labeled as A and B for different threshold values. Shaded lines correspond to artificial data, where all snapshots below $T/J = 0.8$ are all ones, whereas snapshots for temperatures $T/J > 0.8$ are zeros. d) Averaged nearest-neighbor spin correlation C_1 as a function of temperature, obtained from the snapshots.

is a signature of the pseudogap phase observed in the cuprates materials. The fact that the neural network finds a qualitative change in the snapshots at the same temperature indicates that the phenomenology can be observed in this type of data. It will be an exciting future direction to study the observables on which the neural network bases its decision, for example with the method developed in Ref. [16]. Note that the most obvious quantities that can be extracted from the snapshots, such as the nearest neighbor spin correlation function, do not exhibit a drastic change at $T/J = 0.8$, but instead decrease continously as a function of temperature.

7

Summary and Outlook

In this part of my thesis, we studied the Fermi-Hubbard model in one and two spatial dimensions. We observed spin-charge separation in the dynamics of a cold atom experiment and proposed a measurement scheme for the spectral function in a quantum gas microscope. In the spectral function of a single hole in a spin chain, spin charge separation can be observed across all energy scales, even at the finite temperatures realized in cold atom experiments. An interesting future direction is thus the experimental realization of our proposal. In principle, the measurement can even be performed for a two dimensional system with the help of a second layer as probe system. We calculated the spectral function for a single hole in the two-dimensional $t - J$ model with matrix product state techniques. From the spectral function, the quasi-particle weight and the magnetic polaron dispersion can be extracted. In future work, the properties of the Fermi-Hubbard model on a ladder could be studied in more detail. Here, we proposed a scheme to realize chiral ring exchange interactions with optical tweezers. It remains an open question how doping modifies the phase diagram obtained here. The interplay between multi-body interactions and higher order correlation functions, in particular in the presence of dopants, is an interesting future direction. The ladder itself is on the one hand a natural interpolation between one dimensional chains and a two dimensional system, but on the other hand has properties distinct from both the 1D and the 2D case. Further investigation into ladders could also include the study of two independent spin

chains only coupled through the motion of holes.

In our work on the two-dimensional Fermi-Hubbard model and its descendants, we compare numerical and experimental results to predictions from the geometric string theory. This analytical theory provides an intuitive understanding for the motion of a hole in a spin background with strong local anti-ferromagnetic correlations. For the spectral function, we obtain excellent quantitative agreement for the dependence of the quasiparticle weight on the ratio t/J without any free fitting parameter. The geometric string theory moreover describes the qualitative momentum dependence of the quasiparticle weight correctly. The string itself has excited states, such as vibrational and rotational excitations. In the conventional spectral function, rotational excitations are not visible, since the creation of a local hole realizes the symmetry of the lowest rotational state $m = 0$. Higher rotational states can however be observed if the excitation is chosen correspondingly. In future work, we want to numerically calculate the spectral function for a corresponding initial excitation of a hole hopping to its neighboring sites with a hopping element modified by a complex phase. We additionally want to work on schemes to experimentally realize such an excitation in a quantum gas microscope and conventional ARPES experiments. In our numerical work we were able to observe a peak which is fully consistent with the first vibrational excitation in terms of its momentum dependence as well as the t/J dependence of the gap to the ground state.

We simulated the ground state of a single hole in the $t-J$ model numerically and compared different observables to predictions from the geometric string theory. To obtain these predictions, we used two different methods: we described the ground state of the Heisenberg model by a trial state obtained from the best available RVB state and then added strings on top of the spin background. Alternatively, we sampled snapshots from an MPS representing the ground state of the Heisenberg model and then put one string with a length given by the geometric string theory into each snapshot by hand. One exciting future direction would be to implement a matrix product state representation of the string theory prediction by adding the strings not in the sampled snapshots, but directly to the MPS. With this kind of representation, our predictions could be tested more directly and observables not accessible with snapshots could be evaluated. Furthermore, the combination of geometric string theory and matrix product states could be extended to finite doping, allowing also for comparisons in this regime. For our calculations of a single hole in the ground state, we considered higher-order spin-charge correlations, such as the spin-spin correlations as a function of distance to the hole or the ring-type correlation around the hole. While some of these correlations have already been observed in equilibrium experiments [15, 267], we hope to be also able to observe higher order ring-type correlations in a quantum gas microscope in the future.

One of the central parts of my PhD has been the development of methods to gain more information from snapshots as generated by a quantum gas microscope. Firstly, we modified a set of snapshots by hand to obtain a GST prediction. Secondly, we search for specific patterns in those snapshots.

Finally, we used machine learning techniques to analyze the snapshots. In the ground state of a single hole in the $t-J$ model, we searched for string patterns and compared the found string pattern length distribution to predicitions from geometric string theory. A natural extension of this work is to consider the same system at finite temperature. The geometric string theory predicts a transition at some finite temperature, as the free energy can be minimized by increasing the entropy through a large number of possible configurations. With finite temperature matrix product state methods, we are in principle able to again sample snapshots and search for string patterns.

We studied the dynamics of a single hole created in the ground state of the Heisenberg model on a cylinder. After a fast initial dynamics, the hole motion slows down significantly, but still spreads ballistically with a velocity now given by the spinon velocity. This, combined with the saturation of the average string pattern length found in snapshots, provides convincing evidence for the formation of a magnetic polaron as a chargon and spinon bound together by a string. Extensions of this work include the study of the dynamics of a hole in a harmonic confining potential, which is directly realized in cold atoms experiments. We furthermore studied the dynamics of a hole in a finite temperature spin background experimentally and found behavior consistent with the theoretical description in the ground state. At the currently realized temperatures of $T \approx 0.7J$, the spin correlations decay comparably fast with distance and the string tension is already somewhat smaller as compared to the ground state. The dynamics of the spinon is not as straightforward in the case of finite temperature, and diffusvie behavior is expected at long times. Further theoretical investigations are needed here.

Within the geometric string theory, we assume that the motion of the hole introduces anti-ferromagtonetic, thus frustrating, J_2 couplings between next nearest neighboring spins. The study of a single hole in the J_1-J_2-model would therefore be a first step towards simulating the spin background at finite doping. Another approach would be to study the properties of a spin model with randomly chosen regions with J_2-couplings, since this is how we assume independent holes to introduce the frustration. The J_1-J_2 model and modifications thereof can be readily studied with MPS methods.

A natural next step is the study of two holes, where a wealth of open questions remain. We studied the properties of the ground state of two holes in the $t-J$ model and in particular their relative distance and the microscopic *potential landscape* between the two holes by calculating the corresponding multi-point spin-hole correlation functions. In future research, following our analysis so far, one can search for string patterns, possibly connecting the two holes and study how their binding energy behaves as a function of t/J. Additionally, a deeper understanding in terms of a simple theory, for example by extension of the GST, is needed. Understanding the properties of two holes in a system with bosonic particles could provide additional insights.

In the last chapter of this part, we studied the Fermi-Hubbard model at finite doping and compared conventional observables, such as spin correlation functions, as well as string patterns to

an RVB state and the geometric string theory. We showed that both theories capture the behavior of the experimental data to a large extent with one or even without any fitting parameter. At the same time, many open questions and opportunities for refinement exist. The geometric string theory used here is based on the assumption that each hole can be treated independently, which is almost certainly no longer true for intermediate to high doping values. Interaction effects between different holes should be included in the theoretical description and a first step towards this could be taken by studying two holes, as mentioned above. In the experimental data, we observed strong anti-correlations between holes at finite doping, which the GST did not include. These anti-correlations were also not captured by the π-flux state. In future work, the theoretical approaches should be modified to be able to describe this behavior. With the π-flux state, we chose one particular RVB state, while in principle many different possibilities exist. One could compare different RVB states in terms of conventional observables, string patterns and also with our machine learning approach. Here, we trained a neural network to distinguish GST from π-flux snapshots. After training, we input experimental data, which was then assigned one of the two theory labels. The same approach can be used to compare the many different existing theories, for example in terms of RVB states with different parameters. Potentially different results will be obtained in different regions of the phase diagram, enabling an understanding of the physical mechanisms at play. We developed a new network architecture, the correlator convolutional neural network, which directly determines which correlation function is most important to distinguish two theories, or experiment from theory. An exciting question for future research is which particular correlations are most important when distinguishing other theories, or theory from experiment.

The experimental data used in this study suffered from the drawback that the two different spin species could not be resolved simultaneously. In the coming months and years, updates to the experiments are expected which will allow for full resolution and hopefully also lower temperatures. Data with information of the hole positions, obtained either from new experimental studies or numerical simulations, such as MPS or QMC data, enable a more detailed study. In particular, the above proposed studies for two holes could also be done for many holes by analyzing the spin correlations between holes as well as string patterns connecting several holes, maybe even allowing for something akin to a percolation transition. With the knowledge of the hole positions in snapshots at finite doping, we can also analyse the data for pattern-pattern correlations and possible nematicity.

New numerical and experimental tools, such as neural network quantum states or silicon donor arrays provide a new opportunity to gain insights into the doped Fermi-Hubbard model and at the same time come with the challenge to ask the right questions and to find suitable observables. On the other hand, an exciting next step is to go back to the actual cuprate materials we aimed to describe with the Fermi-Hubbard model. In solid state experiments, such as ARPES or STM, these

materials are probed and we hope to be able to draw some closer connections between these results and our theoretical approaches. In particular, our numerical and analytical results for the spectral function could be extended to include for example the effect of phonons.

In conclusion, we were able to gain many interesting insights from quantum simulation experiments, numerical simulations and theoretical considerations. A comparably simple theory can explain a lot of the physics we observed in the Fermi-Hubbard model in and out of equilibrium, in the ground state and at finite temperature and close to half filling as well as at finite doping. At the same time, many exciting open questions remain for future research.

Part II

The Bose-Hubbard Model

The paradigmatic model to study interacting bosons is the Bose Hubbard model, described by the Hamiltonian

$$\hat{H} = -J \sum_i (\hat{a}_i^\dagger \hat{a}_{i+1} + \text{h.c.}) + \frac{U}{2} \sum_i \hat{n}_i(\hat{n}_i - 1) - \sum_i \mu \hat{n}_i. \tag{7.1}$$

Here, $\hat{a}_i^{(\dagger)}$ is the annihilation (creation) operator of a boson at site i and $\hat{n}_i = \hat{a}_i^\dagger \hat{a}_i$ is the local particle number operator. The Bose-Hubbard model was introduced by Fisher et al. in 1989 in order to describe the destruction of superfluidity in the presence of strong interactions [342]. Jaksch et al. suggested in 1998 to realize the Bose-Hubbard model with cold atoms in optical lattices [343]. In an experiment with cold atoms, the ratio U/J can be easily tuned by varying the depth of the lattice. The kinetic energy, given by J, favors delocalization of the particles over lattice sites. The interaction energy U disfavors having more than one particle at any given site. If the ratio of atoms to lattice sites is an integer and U/J is larger than a critical value, the ground state of the system is no longer a compressible superfluid with power-law correlations but a gapped Mott insulator with short range correlations. The transition from a superfluid to a Mott insulating phase has been observed in a Bose-Einstein condensate in a three-dimensional optical lattice upon tuning the lattice depth in the famous experiment by Greiner et al. [68]. At finite temperatures and in one dimension, the system is a correlated, normal fluid.

In this part, we study the one dimensional Bose-Hubbard model and its thermalization properties with and without disorder. In a thermalizing system, the expectation value of any local, non-conserved operator reaches its thermal value after sufficiently long time. If the time evolution starts from a product state, this expectation value corresponds to the thermal equilibrium expectation value at a temperature given by the energy density in the system. Thermalization itself – either starting from an arbitrary state, such as a product state, or after the local perturbation of an equilibrium state – is a process that can have many fascets. For example, operators that commute with the Hamiltonian are conserved under the time-evolution and their expectation value cannot change. Globally conserved quantities can slow down the thermalization process. However, local observables can reach their thermal equilibrium value much earlier in the time-evolution and thus *look* thermal. Depending on which quantity one studies, the system can appear thermalized, even though it is not yet. Introducing disorder can slow down and even inhibit thermalization completely. Here, we study different aspects of thermalization and the lack there-of in a variety of observables.

In chapter 8, we propose a measurement protocol to experimentally access time-ordered as well as out-of-time ordered (OTO) correlation functions. The latter are related to the scrambling of information in correlated quantum systems and we numerically study their behavior in the non-integrable, one-dimensional Bose-Hubbard model in the incoherent high-temperature regime. While

information scrambling happens ballistically even in this regime, other correlation functions, which are related to globally conserved quantities, exhibit much slower diffusive behavior.
In chapter 9, we study many body localization. The presence of strong disorder in the one-dimensional Bose-Hubbard model leads to localization. In section 9.2 we probe the effects of interactions between the particles with an interferometric protocol and extract the non-local couplings in the many-body localized phase. We use two different echo protocols – where similar to the out-of-time ordered correlation functions the effect of reversing the time-evolution is used – to further investigate interaction effects. With superconducting qubits, the reduced density matrix of a subsystem is directly accessible and we extract the entanglement of formation and the distillable entanglement from the two qubit density matrix. In section 9.3 we study the transition from a thermalizing to a many-body localized (MBL) phase in a quantum gas microscope. We use machine learning techniques to study the dynamics of the system after a global quench in snapshots of the quantum many-body state.
We summarize our findings and provide an outlook for interesting future research questions in chapter 10.

8

Scrambling and Thermalization

This chapter is based on the publication

- A. Bohrdt, C. B. Mendl, M. Endres, M. Knap: "Scrambling and thermalization in a diffusive quantum many-body system." – New J. Phys. 19, 063001 (2017) [arXiv:1612.02434]

Structure, text and figures have been rearranged and adapted here.

The dynamical response of a many-body system to a local perturbation is obtained from a time ordered correlation function, $\langle \hat{W}(t)\hat{V}(0)\rangle$, which describes the *relaxation* of the many-body system following the initial excitation by the operator $\hat{V}$ that is then probed at later times by $\hat{W}$. However, in general such time-ordered correlation functions cannot capture the spread of information across a quantum system, especially in a regime where quasiparticles are not well-defined. Recently, it has been proposed that spreading or "*scrambling*" of quantum information across all the system's degrees of freedom can be characterized by out-of-time ordered (OTO) correlation functions: $\langle \hat{W}^\dagger(t)\hat{V}^\dagger(0)\hat{W}(t)\hat{V}(0)\rangle$ [344–349]. The OTO correlation in a state $|\psi\rangle$ can be understood as overlap between two states $|\psi_1(t)\rangle$, $|\psi_2(t)\rangle$, which differ in the order in which the operators are

applied,

$$|\psi_1(t)\rangle = e^{i\hat{H}t}\hat{W}e^{-i\hat{H}t}\hat{V}|\psi\rangle \tag{8.1}$$

$$|\psi_2(t)\rangle = \hat{V}e^{i\hat{H}t}\hat{W}e^{-i\hat{H}t}|\psi\rangle. \tag{8.2}$$

The out-of-time ordered correlation thus probes how the operators $\hat{W}$ and $\hat{V}$ inhibit the cancelation between the time evolution forward and backward [350], similar to the echo protocols discussed in section 9.2.

The OTO correlation functions appear as the out-of-time ordered part of $C(t) = \langle|[\hat{W}(t), \hat{V}(0)]|^2\rangle$ and hence predict the growth of the squared commutator between $\hat{W}(t)$ and $\hat{V}(0)$. OTO correlators could thus be capable of describing a quantum analogue of the butterfly effect in classical chaotic systems, which characterizes the spread of local excitations over the whole system. At short times, OTO correlators are expected to grow exponentially with a rate characterized by the Lyapunov exponent λ_L. The Lyapunov exponent has been conjectured to be bounded by $0 \leq \lambda_L \leq 2\pi T$ [348]. This bound is saturated in strongly coupled field theories with a gravity dual [345] and in disordered models describing a strange metal [346, 351, 352]. By contrast, λ_L does not fully saturate the bound for a critical Fermi surface [353] and is parametrically smaller in Fermi liquids or other weakly coupled states [352, 354, 355].

Here, we study both time-ordered and OTO correlators in a diffusive many-body system by considering the concrete example of the non-integrable, one-dimensional Bose-Hubbard model. Thus far, it is a largely open question, how OTO correlators spread in diffusive systems with a few globally conserved quantities [349, 353, 355, 356]. In our work, we study this question by performing matrix-product operator (MPO) based simulations of the Bose-Hubbard model at high temperatures, at which well defined quasi-particles cease to exist. We demonstrate that in this regime the time-ordered one-particle correlation functions are strongly incoherent and feature rapidly decaying excitations, whereas the OTO correlators indeed describe the *ballistic* spreading of information across the quantum system (see Fig. 8.1.1). In contrast to the linear light-cone spreading of quantum information, the eventual *global* thermalization of the closed system takes parametrically longer, due to hydrodynamic power-laws resulting from globally conserved quantities. For example, we show that the local density correlation function decays as $\sim 1/\sqrt{Dt}$, describing diffusion in one dimension with the corresponding diffusion constant D. Thus, the time scales associated with the spread of information and with global thermalization are different.

We compute the dynamical correlation functions at finite-temperature for systems up to $L = 50$ sites using MPO techniques. The presented results are evaluated for virtual bond dimension 200 to 400 and the local bosonic Hilbert space is truncated to three states, which is sufficient to render the system nonintegrable. The presented results are checked for convergence with respect to the

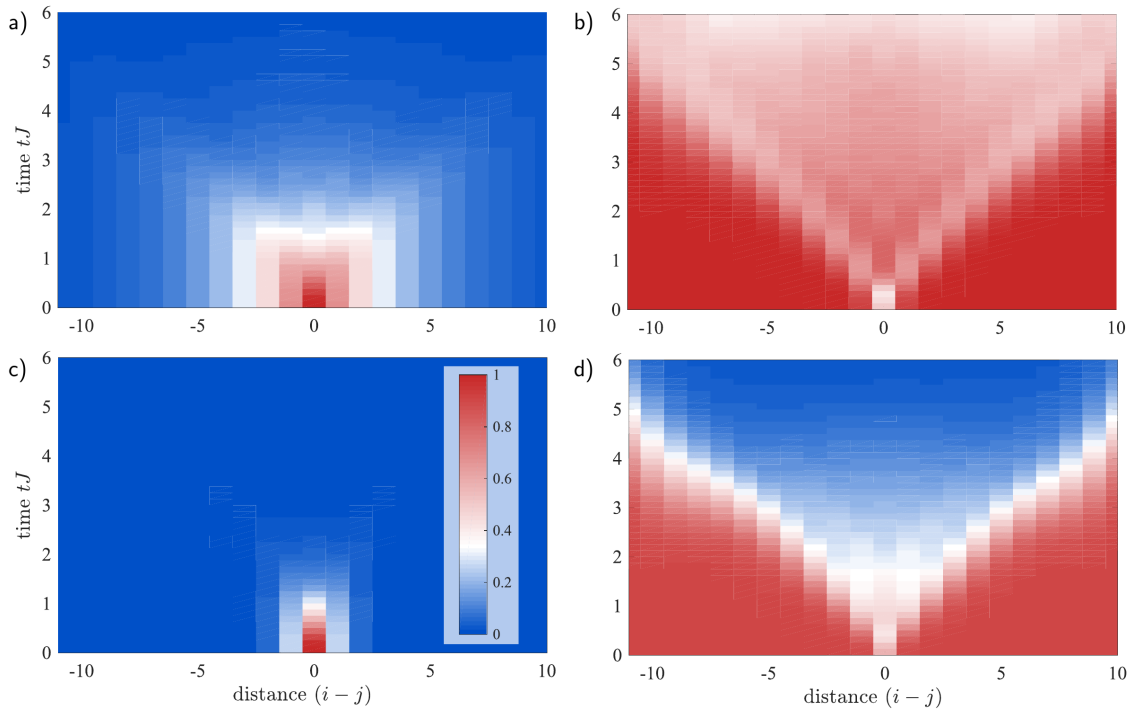

Figure 8.1.1: Green's function and OTO correlation for the one-dimensional Bose-Hubbard model at $U/J = 1$, $\mu = 0$ and a), b) $T/J = 1$ and c), d) $T/J = 4$ for $L = 24$ sites, calculated at a maximum bond dimension of 200. At the lower temperature of $T/J = 1$, a faint light-cone can be observed in the Green's function a). A light-cone with the same velocity is exhibited by the OTO correlator b). c) In the high temperature regime, well-defined quasi-particles cease to exist. The breakdown of well-defined quasiparticles is demonstrated by the one-particle Green's function $\mathcal{G}_{ij}(t) = \langle c_j^\dagger(t) c_i \rangle$, which quickly decays to zero within $\tau J \sim 0.6$. The lifetime is thus shorter than the hopping rate, indicating a regime of incoherent transport. d) However, the OTO correlator $\mathcal{F}_{ij}$ exhibits a light-cone spreading of information.

MPO bond dimension and system size; see section C.1 for details on the numerical simulations.

8.1 Spread of Quantum Information

We numerically simulate the Bose Hubbard model in a parameter regime $(U = J, \mu = 0, T = 4J)$, where the time-ordered single-particle Green's function

$$\mathcal{G}_{ij}(t) = \langle c_j^\dagger(t) c_i \rangle, \tag{8.3}$$

rapidly decays in time, Fig. 8.1.1 c). We extract a quasiparticle lifetime of approximately $\tau J \sim 0.6$, shorter than the microscopic hopping rate, which indicates incoherent transport. In sections 4.2 and 5.4, we saw how much information about the quantum state of the system is contained in time-

ordered correlation functions. However, in general, time-ordered correlation functions are not capable of capturing the spread of information and entanglement. This holds especially in the case where no well-defined quasiparticles exist and the single particle Green's function is almost featureless. The spread of quantum information is generically not linked to the transport of quasiparticles [357] and thus a need for different probes arises. Recently, out-of-time ordered correlators (OTOCs) were proposed as a measure of the spread of quantum information and entanglement across all degrees of freedom of the system [344–349].
OTO correlators describe the growth of the commutator between two local operators $\hat{W}$ and $\hat{V}$ in time

$$C(t) = -\langle |[\hat{W}(t), \hat{V}(0)]|^2 \rangle. \tag{8.4}$$

The time-dependent operator $\hat{W}(t) = e^{i\hat{H}t}\hat{W}e^{-i\hat{H}t}$ can be expanded as

$$\hat{W}(t) = \sum_{l=0}^{\infty} \frac{(it)^l}{l!}[\hat{H}, ...[\hat{H}, \hat{W}], ...]. \tag{8.5}$$

In the following, we will consider local operators $\hat{W}$, which act on a single site. The Hamiltonian $\hat{H}$ typically couples two neighboring sites. As time increases, and therefore the higher order terms in Eq. (8.5) become important, the time-dependent operator $\hat{W}(t)$ affects more and more sites. This expansion in real space is captured by the OTO correlation. The commutator $C(t)$ defined above will be zero initially for spatially separated operators $\hat{W}$, $\hat{V}$. Once the operator $\hat{W}(t)$ has spread to the location of $\hat{V}$, the commutator will become sizable.
In classical chaotic systems, the sensitivity of the time evolution on the initial conditions is characterized by the Lyapunov exponent, $(\partial q(t)/\partial q(0))^2 \sim \exp[\lambda_L t]$. In a quantum system, the time evolution is unitary, and therefore quantities like the fidelity are preserved during the dynamics. In a semiclassical picture, the commutator in (8.4) can be replaced by Poisson brackets. Then, for the choice of $\hat{W} = q_j$ and $\hat{V} = p_i$, this quantity reduces to

$$C(t) \sim \langle (\partial q_j(t)/\partial q_i(0))^2 \rangle. \tag{8.6}$$

Therefore, the correlation function $C(t)$ describes the sensitivity of the time evolution and is expected to grow exponentially at short times $\sim \exp[\lambda_L t]$, with a rate λ_L that resembles the Lyapunov exponent in classical chaotic dynamics. Rewriting the momenta and coordinates as combinations of creation and annihilation operators, (8.4) generically consists of OTO correlators of the form

$$\mathcal{F}_{ij}(t) = \langle c_j^\dagger(t) c_i^\dagger c_j(t) c_i \rangle. \tag{8.7}$$

In a chaotic system, information spreads ballistically [350], with a velocity given by the butterfly velocity v_B. In other cases, such as in a system that exhibits many-body localization as discussed in chapter 9, operators spread logarithmically and the out-of-time ordered correlation function thus exhibits power law rather than exponential time dependence [350, 358, 359].

Here, we are interested in the high temperature regime of a thermalizing system and thus consider the quantum statistical average $\langle \ldots \rangle = \mathrm{tr}[\hat{\rho} \ldots]$ over an initial thermal state with weights distributed according to the Gibbs ensemble $\hat{\rho} = e^{-\hat{H}/T}/Z$. Z is the partition function and the Boltzmann constant k_B is set to one. Alternatively, the average can also be performed with respect to an arbitrary initial state, for example a pure state $\hat{\rho} = |\psi_0\rangle\langle\psi_0|$. For thermalizing systems, it is then expected that an effective temperature is approached at late times which depends on the energy density imprinted on the system by the initial state [360–362]. Once the system is thermalized, the expectation value of a local, non-conserved operator will correspond to the thermal expectation value at this effective temperature. Regarding this quantity, the information about the initial state is lost.

In Fig. 8.1.1 d), OTO correlators $\mathcal{F}_{ij}$ evaluated at comparatively high temperatures $T = 4J$, interactions $U = J$, and chemical potential $\mu = 0$ are shown as a function of time t and distance $(i - j)$. For OTO correlators in the coherent Luttinger Liquid regime, see Ref. [363]. Despite the high temperature and in sharp contrast to the single particle Green's function, the OTO correlator $\mathcal{F}_{ij}$ exhibits a pronounced light-cone spreading of the information across the quantum state for $|i - j| \lesssim 7$. For larger distances the light cone seems to exhibit a plateau, which we attribute to the finite MPO bond dimension used in the numerical simulations. OTO correlators are somewhat challenging to simulate with MPO techniques, because they directly reflect the fast spreading of entanglement.

8.1.1 Lyapunov exponent, butterfly and light-cone velocity

We now characterize the OTO correlators $\mathcal{F}_{ij}(t)$ in detail. To this end, we subtract $\langle \hat{n}_i \hat{n}_j \rangle$ from the $\mathcal{F}_{ij}(t)$ and consider its relative change: $\mathcal{F}^r_{ij}(t) = |\mathcal{F}_{ij}(t) - \langle \hat{n}_i \hat{n}_j \rangle| / \langle \hat{n}_i \hat{n}_j \rangle$. Examples for the reduced OTO correlator $\mathcal{F}^r_{ij}(t)$ are shown in Fig. 8.1.2 for interaction $U = J$ and different temperatures T. The reduced OTO correlator $\mathcal{F}^r_{ij}(t)$ starts off at zero, forms the light-cone plateau, and approaches the steady-state value as an exponential.

From the light-cone spread of the OTO correlator, we extract two velocities:

1. The light-cone velocity v_{lc}, which we define by the space-time region where the reduced OTO correlators $\mathcal{F}^r_{ij}(t)$ surpasses a small threshold of 0.05% of its final value.

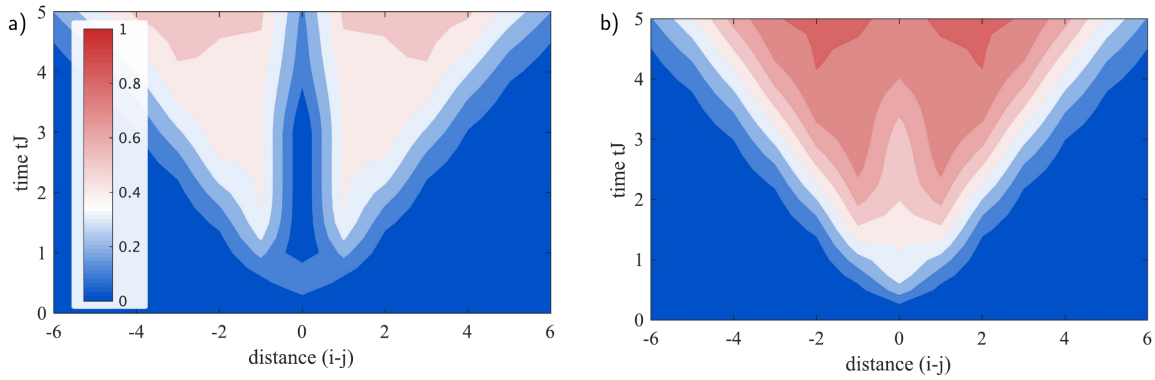

Figure 8.1.2: Light-cone spreading of quantum information. Contour plots of the reduced OTO correlator $\mathcal{F}^r_{ij}(t) \sim |\mathcal{F}_{ij}(t) - \langle \hat{n}_i \hat{n}_j \rangle| / \langle \hat{n}_i \hat{n}_j \rangle$ as a function of time and distance for interaction strength $U = J$, chemical potential $\mu = 0$, and temperature a) $T = 2J$ and b) $T = 16J$, respectively. The spreading of quantum information forms a light-cone pattern. The contour lines indicate changes of $\mathcal{F}^r_{ij}(t)$ by 0.1.

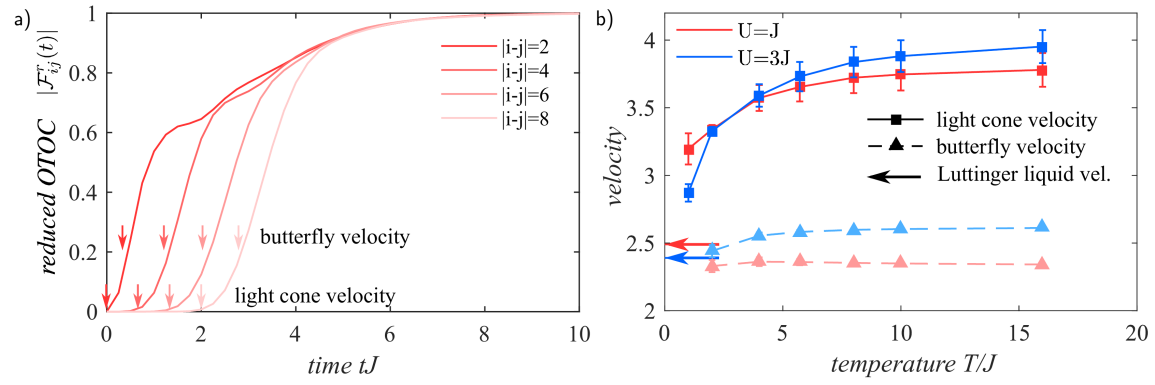

Figure 8.1.3: Butterfly and light-cone velocity a) Reduced OTO correlators $\mathcal{F}^r_{ij}(t)$ are shown as a function of time for different distances $|i - j|$, interaction strength $U = J$, and temperature $T = 4J$. We introduce the light-cone velocity v_{lc} by the space-time region, where $\mathcal{F}^r$ surpasses a small threshold and the butterfly velocity v_b where it attains a large fraction of order one. b) The light-cone velocity v_{lc} grows with temperature and is bounded from below by the zero temperature Luttinger liquid velocity (colored arrows). By contrast, the butterfly velocity v_b is systematically smaller than v_{lc} and approximately independent of temperature T. The data is shown for two values of the interaction strength $U = J$ and $U = 3J$.

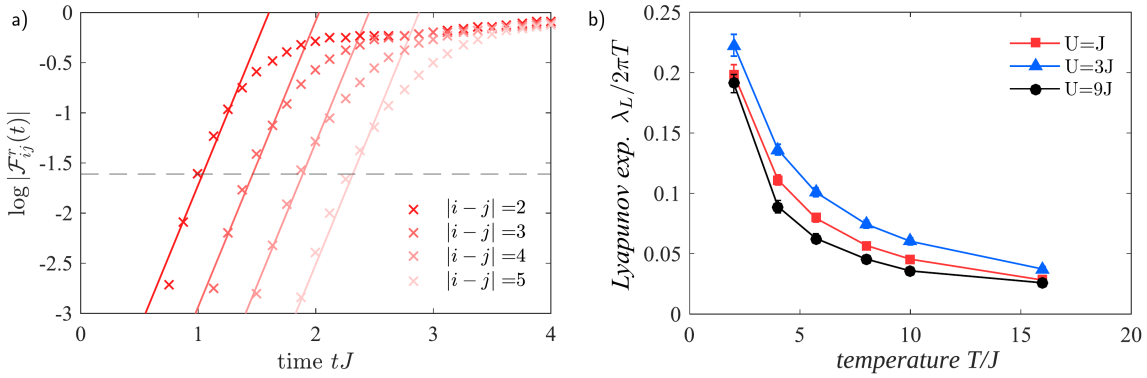

Figure 8.1.4: Lyapunov exponent. The reduced OTO correlator $\mathcal{F}^r_{ij}(t)$ is expected to grow exponentially on a timescale set by the butterfly velocity v_b with a rate that defines the Lyapunov exponent λ_L. a) In our system, the regime of exponential growth is restricted to a rather small time range, see also section C.1. b) Our data suggests that the Lyapunov exponent λ_L is parametrically smaller than the conjectured upper bound $2\pi T$ and increases slowly as the temperature T is lowered. The data is shown for interaction strength $U = \{1, 3, 9\}J$.

2. The butterfly velocity v_b, which we define by the space-time region where the OTO correlator attains a large fraction (20%) of its final value. We find that v_b does not significantly depend on this cutoff, as long as it is chosen to a sizeable fraction; see section C.1.

The light cone velocity v_{lc} increases with temperature T and is bounded from below by the zero temperature Luttinger liquid velocity; see Fig. 8.1.3. The butterfly velocity v_b is systematically lower than v_{lc} and is almost independent of temperature. The butterfly velocity determines the time scale t_{scr} for scrambling information across the many-body quantum state which is linear in system size $t_{scr} \sim L/v_b$. Based on results from holography, it has been argued in Ref. [356] that the light-cone and the butterfly velocity should be quite generally the same. This should be contrasted to our results for the Bose-Hubbard model and to a study of non-relativistic non-Fermi liquids [353]. In both cases the butterfly velocity has been found to be smaller than the light-cone velocity.

Previous studies of strongly coupled field theories [348] or disordered SYK models [346] predict an exponential growth in the initial dynamics of the reduced OTO correlator of the form $\mathcal{F}^r_x(t) \sim \exp[\lambda_L(t - x/v_b)]$ with butterfly velocity v_b and a growth rate λ_L, which is refered to as Lyapunov exponent. Both systems display a clear separation between the collision time τ and the scrambling time t_{scr}, at which the OTO correlator assumes an appreciably large value. Hence, in these systems the exponential growth occurs up to parametrically late times determined by a large parameter N, which controls the approach to a semiclassical limit. We tested the results of our numerical simulations against this prediction and find that they are incompatible with an exponential growth in time inasmuch as there appears to be no parametrically large regime of exponential growth in our model, see Fig. 8.1.4 a) and section C.1. This is a consequence of the average particle

density, which is controlled by the chemical potential, being typically on the order of one for the chosen parameters. This effectively restricts the accessed local Hilbert space dimension and hence there is no large separation between collision and scrambling time [364]. Therefore, we cannot unambiguously define a Lyapunov exponent. Finding the analytic form for the initial growth in our system remains an outstanding challenge.

Nonetheless, one can estimate a growth rate λ_L by linearizing the OTO correlator around the space-time region set by the butterfly velocity, which is shown as a function of temperature for different values of the interaction strength U and chemical potential $\mu = 0$ in Fig. 8.1.4 b). We note however that the concrete values for the Lyapunov exponent depend on the space-time region, around which we linearize, see Fig. 8.1.4 a) and section C.1. It has been conjectured that the Lyapunov exponent is bounded by $2\pi T$, which is the value it assumes in a strongly coupled field theory with a gravity dual [348]. In our system, λ_L is parametrically lower than this bound and increases slowly when lowering the temperature. Moreover, we find that the dependence of the Lyapunov exponent on the interaction strength U is small with slightly larger values of λ_L for intermediate interaction strength, $U = 3J$, which is in the vicinity of the quantum critical point.

8.2 Thermalization

Conserved quantities restrict how a closed quantum system can approach global equilibrium: while local equilibrium is approached after a few scattering events, attaining global equilibrium is restricted due to the relaxation of conserved quantities, which have to be transported over long distances. Since observables that overlap with conserved quantities evolve slowly, global thermalization becomes a slow process. In the Bose-Hubbard model, energy, lattice momentum and the total particle number are conserved. From hydrodynamics we infer that, for example, the conserved particle number leads to a diffusion equation of the density [365, 366]

$$\partial_t n - D\nabla^2 n = 0, \tag{8.8}$$

where D is the diffusion constant. The connected density correlation function $C_n(x - x', t - t') = \mathrm{Re}[\langle n(x,t)n(x',t')\rangle - \langle n(x)\rangle\langle n(x')\rangle]$ relates the density at space-time (x,t) to the density at (x',t') via

$$n(x,t) \sim \int dt'dx' C_n(x - x', t - t')n(x',t') \tag{8.9}$$

and itself satisfies the diffusion equation for times $t > 0$ in a hydrodynamic regime. From the solution of this equation, together with the boundary condition $C_n(x, t = 0) = \delta(x - x')$, $C_n(x,t)$

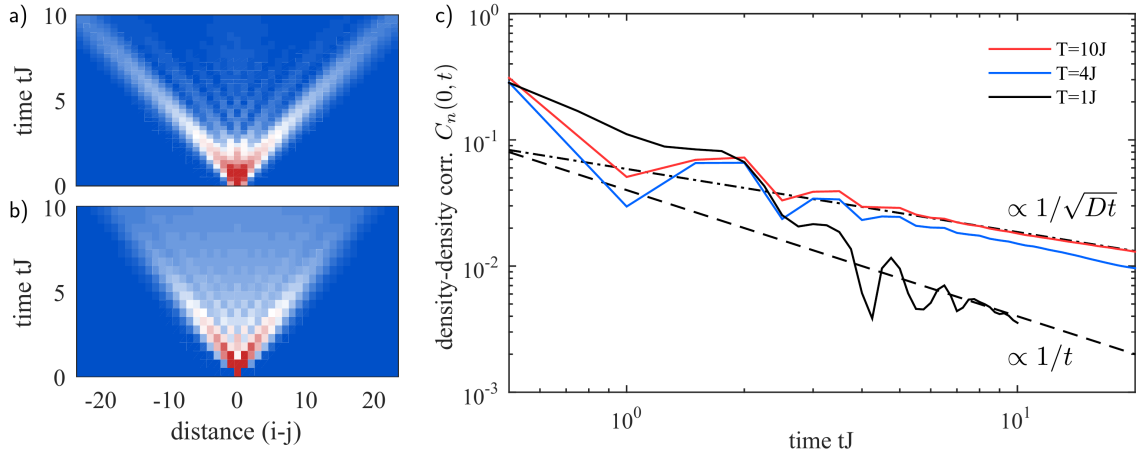

Figure 8.2.1: Density correlations in the Bose Hubbard model. Conserved quantities restrict the approach of a closed quantum system to global equilibrium, thus, rendering global thermalization a slow process. In the Bose-Hubbard model the total particle number is conserved leading to diffusive power-law tails in the connected density correlator $C_n(x,t) = \mathrm{Re}[\langle \hat{n}_x(t)\hat{n}_0\rangle - \langle \hat{n}_x\rangle\langle \hat{n}_0\rangle]$. a) At low temperatures ($T = J$), where quasiparticles are reasonably well defined, the density correlator does not reach the diffusive regime within the accessible simulation time but is dominated by ballistic sound peaks. b) By contrast, for high temperatures ($T = 10J$) the crossover to diffusion becomes apparent. c) For temperatures $T \gtrsim 4J$ the local density correlator $C_n(0,t) \sim 1/\sqrt{Dt}$, where D is the diffusion constant. By contrast, at low temperature $T = J$ the diffusive regime has not yet been reached within the numerically accessible times and the correlations rather decay ballistically $C_n(0,t) \sim 1/t$. The slow relaxation of the hydrodynamic modes leads to the global thermalization time scale $t_{\mathrm{th}} \sim L^2/D$ that is parametrically larger than the scrambling time scale $t_{\mathrm{scr}} \sim L/v_{\mathrm{b}}$ of quantum information.

is expected to be of the form [365]

$$C_n(x,t) \cong \frac{\tilde{C}}{\sqrt{4\pi D|t|}} e^{-\frac{x^2}{4D|t|}}, \tag{8.10}$$

with $\tilde{C} = \int dx\, C_n(x,0)$. At sufficiently low temperatures $T = J$, Fig. 8.2.1 a), quasiparticles are reasonably well defined and the ballistic spread of sound modes dominates the dynamics of the connected density correlator in the numerically accessible time regime. For high temperatures $T = 10J$, the density correlator displays diffusive behavior after a few hopping times and attains a finite value in the region between the sound mode peaks. The local $x - x' = 0$ density correlation function shown in Fig. 8.2.1 c) exhibits diffusive power-law decay $C_n(0,t) \sim 1/\sqrt{Dt}$ for temperatures $T \gtrsim 4J$. Here, D is a diffusion constant, which is extracted for temperatures $T \geq 4J$ in 8.2.1. The decrease of the diffusion constant with increasing temperature observed here is somewhat counterintuitive. We attribute this behavior to the fact that the calculations are performed in

T/J	$D/(a^2J)$	$D\lambda_L/v_b^2$
4	14.29(27)	7.2(6)
6	11.69(10)	6.0(4)
8	10.42(04)	5.4(3)
10	9.79(01)	5.1(3)

Table 8.2.1: Diffusion constant D and the ratio $D\lambda_L/v_B^2$ for different temperatures T. The errors as indicated in the parentheses are errors from the fits.

the grand-canonical ensemble, where the particle density depends on the temperature and, in particular, increases with temperature in the chosen parameter regime.

The slow relaxation of the hydrodynamic modes leads to the global thermalization time scale $t_{\text{th}} \sim L^2/D$ that is parametrically larger than the scrambling time scale $t_{\text{scr}} \sim L/v_{\text{b}}$ of quantum information.

We note that the connected density correlator does not exhibit pronounced hydrodynamic long time tails, which could result from higher order gradient corrections to the diffusion equation and mask the $1/\sqrt{Dt}$ decay. This seems to be a particular property of the density correlator, as we find at high-temperatures pronounced $t^{-3/4}$ corrections in the energy-density correlation function (not shown), in agreement with Ref. [366].

It has been proposed that the diffusion constant is related to the butterfly velocity v_{b} and the Lyapunov exponent λ_L via $D \sim v_{\text{b}}^2/\lambda_L$ [367–370], where $1/\lambda_L$ is a bound for the local thermalization time in which the system is able to attain local equilibrium characterized by a local temperature and local chemical potential that varies between different regions in space. From our simulations, we obtain coefficients of the order $D\lambda_L/v_{\text{b}}^2 \sim 5.5$ for temperatures $T \gtrsim 6J$; see Tab. 8.2.1, which seems to suggest a connection between the spread of information and *local* thermalization, as suggested by calculations for holographic matter. However, clearly *global* thermalization is a parametrically slower process than information scrambling and takes for systems of size L times of the order $t_{\text{th}} \sim L^2/D$. Experimentally measuring OTO correlators and density correlators will make it possible to further check these holographic predictions.

8.3 Measuring Dynamical Correlators

Despite their usefulness to characterize interacting many-body systems, it remains challenging to experimentally access dynamical correlation functions in *real* space and time [192, 371], see also the discussions in section 4.2 and 5.4. In the following, we present two different protocols to measure dynamical correlation functions, including the special case of out of time ordered correlators. While a sign reversal of the Hamiltonian is needed to measure the out of time ordered correlators,

our protocols do not rely on an ancilla spin to switch between different Hamiltonians, as many other proposals do [372–374]. Both protocols discussed below are general and can be applied to bosons as well as fermions and require no specific form of the Hamiltonian.

8.3.1 Global Protocol

The global protocol is based on the interference of the entire many body state, as first pioneered in quantum gas microscopy experiments studying the second Renyi entropy [93, 94], and results in the measurement of the exact correlation function under consideration. The drawbacks of this protocol are that it does not work for thermal initial states and it is not scalable to large system sizes, since it is based on the measurement of a many-body wave function overlap. This requires a high fidelity of the beam splitter operations, since the number of necessary beam splitter operations is extensive.
For the measurement of both the Green's function and the OTO correlators, the initial state $|\psi\rangle$ can be an arbitrary pure state, such as the ground state, or a simple product state. An effective finite temperature state can be obtained for quenches from initial pure states to some final Hamiltonian. In a thermalizing system [360–362], the effective temperature is then determined by the energy-density produced by the quantum quench, as discussed in detail in section 9.3.

Single particle Green's function

1. Prepare two identical copies of a pure state $|\psi\rangle \otimes |\psi\rangle$. Remove a particle on site i in the left system by locally transferring the atom to a hyperfine state that is decoupled from the rest of the system or by transferring it to a higher band of the optical lattice, yielding $c_i |\psi\rangle \otimes |\psi\rangle$.

2. Evolve the system in time for a period t, $\exp[-i\hat{H}t]c_i |\psi\rangle \otimes \exp[-i\hat{H}t]|\psi\rangle$.

3. Create a hole on site j of the right system

$$|\psi_l(t)\rangle \otimes |\psi_r(t)\rangle \equiv e^{-i\hat{H}t}c_i |\psi\rangle \otimes c_j e^{-i\hat{H}t}|\psi\rangle. \tag{8.11}$$

4. Measure the swap operator $\hat{\mathcal{V}}$, which interchanges the particles between the left and the right subsystem

$$\begin{aligned}\langle\hat{\mathcal{V}}\rangle &= \mathrm{tr}[|\psi_r(t)\rangle\langle\psi_l(t)| \otimes |\psi_l(t)\rangle\langle\psi_r(t)|] \\ &= |\langle\psi_r(t)|\psi_l(t)\rangle|^2 = |\langle c_j^\dagger(t)c_i\rangle|^2 = \mathcal{G}_{ij}^{\mathrm{gl}}(t).\end{aligned} \tag{8.12}$$

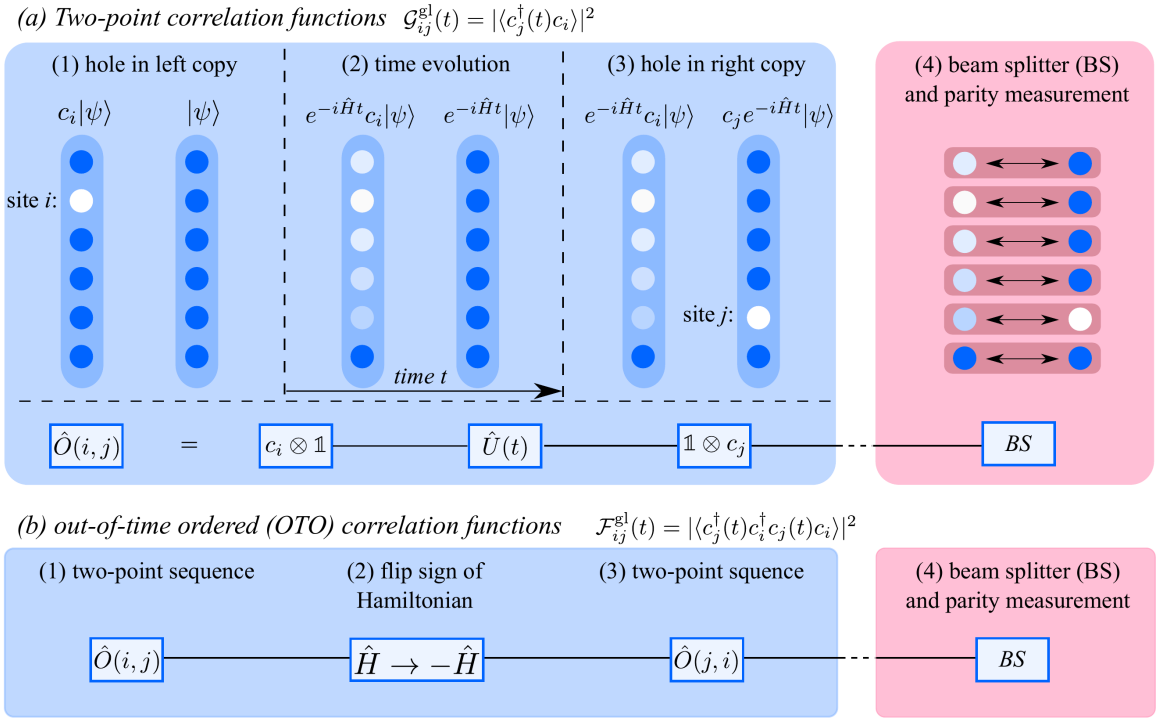

Figure 8.3.1: Global scheme to measure dynamical correlation functions. Schematic illustration of the experimental protocol to determine the a) time-ordered Green's function $\mathcal{G}_{ij}^{\mathrm{gl}}(t) = |\langle\psi|c_j^\dagger(t)c_i|\psi\rangle|^2$ as well as b) OTO correlation functions $\mathcal{F}_{ij}^{\mathrm{gl}}(t) = |\langle\psi|c_j^\dagger(t)c_i^\dagger c_j(t)c_i|\psi\rangle|^2$. Details of the protocol are described in the text.

The expectation value of the swap operator is experimentally determined by a global 50%-50% beam splitter operation, which is realized by tunnel-coupling the left and the right system, followed by a measurement of the parity-projected particle number [93, 375, 376]. We abbreviate the sequence of the operations (1–3) as $\hat{O}(i,j)$.

Out of time ordered correlations The OTOCs can be measured using the same basic steps as the single particle Green's function, where additionally the sign of the Hamiltonian has to be reversed in the middle of the protocol.

1. Apply $\hat{O}(i,j)$ (see above).

2. Globally invert the sign of the Hamiltonian. For the interaction term, this can be achieved by ramping the magnetic field across a Feshbach resonance, as demonstrated experimentally, for instance, in the realization of negative temperature states [377]. The sign of the hopping matrix element can be inversed by appropriately tuning the drive frequency of a modulated optical lattice [378].

3. Apply $\hat{O}(j,i)$ again, yielding

$$|\psi_l(t)\rangle \otimes |\psi_r(t)\rangle \equiv e^{i\hat{H}t} c_j e^{-i\hat{H}t} c_i |\psi\rangle \otimes c_i e^{i\hat{H}t} c_j e^{-i\hat{H}t} |\psi\rangle. \tag{8.13}$$

4. Measure the wavefunction overlap of the two systems using beam splitter operations in order to obtain the square modulus of the OTOC.

Thermal initial states In the case of a thermal initial state, after the first three steps of our protocol, Fig. 8.3.1 a), the system is prepared in the state $\rho_l(t) \otimes \rho_r(t)$, where $\rho_a(t)$ is a generic density matrix. The measurement of the swap operator $\hat{\mathcal{V}}$ yields [376]

$$\begin{aligned}
\langle \hat{\mathcal{V}} \rangle &= \operatorname{tr} \hat{\mathcal{V}} \rho_l(t) \otimes \rho_r(t) \\
&= \operatorname{tr} \hat{\mathcal{V}} \sum_{\mu\nu} \rho_{l,\mu}(t) \rho_{r,\nu}(t) |\mu\rangle\langle\mu| \otimes |\nu\rangle\langle\nu| \\
&= \operatorname{tr} \sum_{\mu\nu} \rho_{l,\mu}(t) \rho_{r,\nu}(t) |\nu\rangle\langle\mu| \otimes |\mu\rangle\langle\nu| \\
&= \sum_{\mu} \rho_{l,\mu}(t) \rho_{r,\mu}(t) = \operatorname{tr} \rho_l(t) \rho_r(t).
\end{aligned} \tag{8.14}$$

For pure states, $\rho_{l,r}(t) = |\psi_{l,r}(t)\rangle\langle\psi_{l,r}(t)|$, we directly obtain (8.12). However, at finite temperature, the measurement does not directly yield the square of the correlation function. In particular,

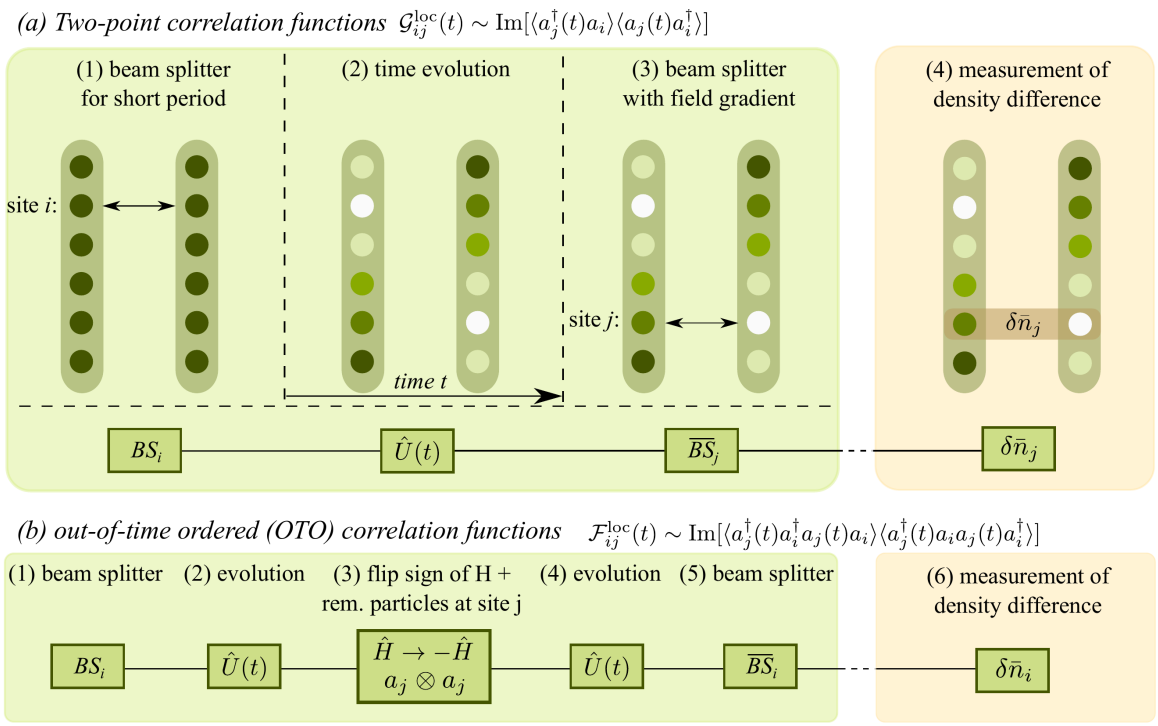

Figure 8.3.2: Local scheme to measure dynamical correlation functions. Using local beam-splitter operations only, our protocol measures a) time ordered correlator $\mathcal{G}_{ij}^{\mathrm{loc}}(t) \sim \mathrm{Im}[\langle a_j^\dagger(t) a_i \rangle \langle a_j(t) a_i^\dagger \rangle]$ as well as b) the OTO correlator $\mathcal{F}_{ij}^{\mathrm{loc}}(t) \sim \mathrm{Im}[\langle a_j^\dagger(t) a_i^\dagger a_j(t) a_i \rangle \langle a_j^\dagger(t) a_i a_j(t) a_i^\dagger \rangle]$. A detailed description of the protocol is given in the text.

we obtain for the Green's function protocol

$$\langle \hat{\mathcal{V}} \rangle = \sum_{\mu\nu} \rho_\mu \rho_\nu \langle \mu | c_i^\dagger c_j(t) | \nu \rangle \langle \nu | c_j^\dagger(t) c_i | \mu \rangle . \tag{8.15}$$

By contrast, the desired modulus square of the thermal Green's function would be

$$|\langle c_i(t)^\dagger c_j \rangle|^2 = \sum_{\mu\nu} \rho_\mu \rho_\nu \langle \mu | c_i^\dagger c_j(t) | \mu \rangle \langle \nu | c_j^\dagger(t) c_i | \nu \rangle . \tag{8.16}$$

Hence, at high temperatures, (8.15) is suppressed by a factor $1/Z$, where Z is the partition sum, and thus vanishes in the thermodynamic limit. A similar reasoning applies in the case of OTO correlators.

8.3.2 Local Protocol

Here, we introduce an alternative local protocol that is scalable to large system sizes since it only requires two beam splitter operations irrespective of the system size.

Local beam splitter operation A local beam splitter operation on site l is realized by coupling the left and the right copy of the quantum system by a tunneling Hamiltonian

$$\hat{H}_l^{\mathrm{BS}} = -J_{\mathrm{BS}}(a_l^\dagger b_l + b_l^\dagger a_l), \tag{8.17}$$

where $a_l^\dagger$ ($b_l^\dagger$) creates a particle in the left (right) system. The unitary evolution under (8.17), $\mathrm{BS}_l(\tau) = \exp[-i\hat{H}_l^{\mathrm{BS}}\tau]$, for time $\tau_{\mathrm{BS}} = \pi/4J_{\mathrm{BS}}$ defines a 50%-50% beam splitter operation

$$\begin{pmatrix} \bar{a}_l \\ \bar{b}_l \end{pmatrix} = \underbrace{\frac{1}{\sqrt{2}}\begin{pmatrix} 1 & -i \\ -i & 1 \end{pmatrix}}_{=\mathrm{BS}_l} \begin{pmatrix} a_l \\ b_l \end{pmatrix}. \tag{8.18}$$

Furthermore, the phase of the beam splitter can be adjusted by applying a field gradient between the left and the right system $\hat{H}_l^{\mathrm{F}} = \frac{h}{2}(b_l^\dagger b_l - a_l^\dagger a_l)$ for a duration τ_f, $R(\tau_f) = \exp[-i\hat{H}_l^{\mathrm{F}}\tau_f]$:

$$\overline{\mathrm{BS}}_l = R^\dagger(\varphi)\,\mathrm{BS}_l\,R(\varphi) = \frac{1}{\sqrt{2}}\begin{pmatrix} 1 & -ie^{-i\varphi} \\ -ie^{i\varphi} & 1 \end{pmatrix}, \tag{8.19}$$

where $\varphi = h\tau_f$.

Single particle Green's function

1. Apply a beam splitter operation on site i for a duration τJ_{BS}. In the limit of small $\tau J_{\mathrm{BS}} \ll 1$, the unitary evolution can be linearized $\mathrm{BS}_l(\tau) = 1 - i\hat{H}_l^{\mathrm{BS}}\tau + O(J_{\mathrm{BS}}^2\tau^2)$.
2. Evolve the two copies for the physical time t.
3. Apply a 50%-50% beam splitter operation on site j with a phase that is detuned from the first one by $\varphi = \pi/2$.
4. Measure the density difference $\delta\bar{n}_j$ between the right and the left subsystem. The densities after the beam splitter operation $\overline{\mathrm{BS}}_j$ are

$$\bar{n}_{l,j} = \bar{a}_j^\dagger \bar{a}_j = \frac{1}{2}(a_j^\dagger - b_j^\dagger)(a_j - b_j) \tag{8.20a}$$

$$\bar{n}_{r,j} = \bar{b}_j^\dagger \bar{b}_j = \frac{1}{2}(a_j^\dagger + b_j^\dagger)(a_j + b_j), \tag{8.20b}$$

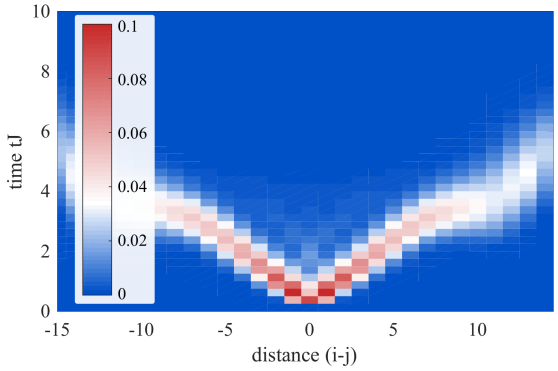

Figure 8.3.3: Correlation functions obtained from the local interference of two quantum states. OTO correlation functions $\mathcal{F}_{ij}^{\text{loc}}(t)$ as measured by the protocol based on local beam splitter operations contain similar information as the originally introduced correlators. The data is shown for temperature $T = 4J$, interactions $U = J$, chemical potential $\mu = 0$, and systems of size $L = 30$. The comparison with Fig. 8.1.1 d) shows the same light-cone spreading.

such that the density difference between the right and left system is

$$\delta\bar{n}_j = \bar{n}_{l,j} - \bar{n}_{r,j} = -(b_j^\dagger a_j + a_j^\dagger b_j). \tag{8.21}$$

The measurement outcome is thus

$$\begin{aligned}\mathcal{G}_{ij}^{\text{loc}}(t) &= \langle \text{BS}_i^\dagger(\tau) e^{i\hat{H}t} \overline{\text{BS}}_j^\dagger \delta\bar{n}_j \overline{\text{BS}}_j e^{-i\hat{H}t} \text{BS}_i(\tau)\rangle \\ &= 4J_{\text{BS}}\tau \,\text{Im}\{\langle a_j^\dagger(t) a_i\rangle \langle a_j(t) a_i^\dagger\rangle\} + O(J_{\text{BS}}^3\tau^3),\end{aligned} \tag{8.22}$$

where in the second line particle number conservation and the fact that the duration of the first beam splitter operation on site i is short was used.

The conventional time ordered one-body correlation function is defined as $\mathcal{G}_{ij}(t) = \langle a_j^\dagger(t) a_i\rangle$. In our protocol, the imaginary part of the product of a particle and a hole correlation function is measured. However, we argue below that this observable carries related information as the time-ordered correlation function $\mathcal{G}_{ij}(t)$. Since we measure the imaginary part of the correlation function, $\mathcal{G}_{ij}^{\text{loc}}(t)$ is initially zero but then develops a peak that quickly decays. We determine the quasiparticle lifetime $\tau J \sim 0.32$, which corresponds roughly to half the lifetime obtained for the Green's function $\mathcal{G}_{ij}(t)$. This factor can be attributed to the fact that here the product of two correlation functions is measured.

OUT OF TIME ORDERED CORRELATIONS can be measured in the same way:

1. Apply a beam splitter operation for a short duration $\tau J_{\text{BS}} \ll 1$ at site i.

2. Evolve the system for a duration t.

3. Remove a particle on site j in both copies using single-site addressing.

4. Flip the sign of the Hamiltonian $\hat{H} \to -\hat{H}$, as discussed in the global protocol.

5. Time evolve the system for a duration t.

6. Apply the 50%-50% beam splitter operation $\overline{\mathrm{BS}}_i$ on site i, yielding

$$\begin{aligned}\mathcal{F}_{ij}^{\mathrm{loc}}(t) &= \langle \mathrm{BS}_i^\dagger(\tau) e^{i\hat{H}t} a_j^\dagger b_j^\dagger e^{-i\hat{H}t} \overline{\mathrm{BS}}_i^\dagger \delta\bar{n}_i \\ &\qquad \times \overline{\mathrm{BS}}_i e^{i\hat{H}t} a_j b_j e^{-i\hat{H}t} \mathrm{BS}_i(\tau)\rangle \\ &= 4J_{\mathrm{BS}}\tau \,\mathrm{Im}\{\langle a_j^\dagger(t) a_i^\dagger a_j\,(t) a_i\,\rangle \langle a_j^\dagger(t) a_i\, a_j\,(t) a_i^\dagger\rangle\} + O(J_{\mathrm{BS}}^3\tau^3). \end{aligned} \tag{8.23}$$

The OTO correlator $\mathcal{F}_{ij}^{\mathrm{loc}}(t)$ obtained from local interference corresponds to the product of two OTO correlation function. At the temperatures considered here, it contains essentially the same information as the one originally introduced as shown in Fig. 8.3.3. Since the protocol measures the imaginary part of a product of two OTO correlators, its initial value is zero. The scrambling of information across the quantum state manifests itself in the linear propagation of a wave-packet in $\mathcal{F}_{ij}^{\mathrm{loc}}(t)$ from which light-cone and butterfly velocities can be extracted. In Fig. 8.3.3, we once again attribute the plateau in the light-cone, which starts at $|i-j| \gtrsim 7$, to the finite MPO bond dimension of 400.

8.3.3 Static correlation functions and full state tomography

With both the global and the local protocol, static one-body correlation functions can be straightforwardly measured by setting the physical time $t = 0$. A generalization of the local protocol makes it possible to measure static correlations functions of *arbitrary* order. Above, we used correlators of $\delta\bar{n}_i$ to determine one-body correlation functions of the original many-body state:

$$\langle \delta\bar{n}_i \delta\bar{n}_j\rangle = 2\langle a_i^\dagger a_j\,\rangle\langle a_i\, a_j^\dagger\rangle. \tag{8.24}$$

Correspondingly, higher order correlators in $\delta\bar{n}_i$ yield higher order static correlation functions in the creation $a_i^\dagger$ and annihilation operators a_i. This protocol scales favorable with system size. Moreover, correlators between arbitrary sites and of arbitrary order can be evaluated in a single shot by performing the beam splitter operations on the full system.
With the knowledge of arbitrary static correlation functions, a full state tomography can be per-

formed. The density matrix describing the quantum state of a system can be expressed as

$$\hat{\rho} = \mathcal{N} \sum_{i_1,\dots i_N} r_{i_1,\dots i_N} \hat{\sigma}_{i_1} \otimes \dots \otimes \hat{\sigma}_{i_N}, \tag{8.25}$$

where $\mathcal{N}$ is a normalization constant and the $\hat{\sigma}_{i_j}$ constitute a suitable basis [379]. For fermions or hard-core bosons, the Pauli matrices provide a possible basis. Using correlators up to sufficient order, it is possible to determine the Stokes parameters $r_{i_1,\dots i_N}$ and thereby to reconstruct the density matrix, which paves the way for the full state tomography of quantum states with massive particles.

8.3.4 Dynamical density correlation functions

The protocols discussed so far are suitable to measure the single particle Green's function as well as the OTO correlator. In order to observe the diffusive behavior of the dynamical density correlation functions discussed in section 8.2, we discuss two different schemes to access them experimentally. The dynamic structure factor $S(k, \omega)$, which is the spatial and temporal Fourier transform of the density correlator $C_n(x, t)$, can be measured with Bragg spectroscopy [380, 381]. In Bragg spectroscopy, the detuning of the two laser beams sets the frequency ω and the angle between the beams the transferred momentum k. A measurement of the absorption of the system as a function of k and ω directly maps out the dynamic structure factor $S(k, \omega)$. Diffusion manifests itself in the wavevector and frequency resolved structure factor $S(k, \omega)$ as Lorentzian peaks with half-width-half-maximum that scales as Dq^2.

It is furthermore possible to measure the dissipative response $\langle [n_i(t), n_j] \rangle$ to a local perturbation of the system in a quantum gas microscope. To this end, a local potential $\delta H = n_j \delta\mu$ is created at site j by applying a laser for a short time τ, yielding the time evolution $\exp[-i\delta H\tau] \sim 1 - i\delta H\tau + O(\delta\mu^2\tau^2)$. Measuring the density at site i after the unitary time evolution for duration t we obtain

$$\chi_{ij}^{\mathrm{loc}}(t) = \langle n_i(t) \rangle + i\delta\mu\tau \langle [n_i(t), n_j] \rangle + O(\delta\mu^2\tau^2). \tag{8.26}$$

In equilibrium, the fluctuation-dissipation theorem provides an exact relation between $\langle [n_i(t), n_j] \rangle$ and $\langle n_i(t) n_j \rangle$. The accurate measurement of the former therefore enables the observation of diffusive response in the dynamical density correlator.

9

Many-Body Localization

9.1 Introduction

Most of the systems discussed so far thermalize in the sense that the different degrees of freedom of the system exchange energy and information efficiently. While the system itself has to remain in a pure quantum state under the unitary time evolution, it can act as a thermal bath for its subsystems. The subsystems then appear thermal after a comparably short time and information about the initial state is mostly lost in the time evolution. This evolution of a far-from-equilibrium state to a state that appears to be in thermal equilibrium is described by the eigenstate thermalization hypothesis (ETH) [360–362]. This behavior is the most common in the dynamics of quantum systems and the properties of such systems are usually described using quantum statistical mechanics. In chapter 8, we discussed how conserved quantities, such as the density, can lead to slow diffusion. In a thermalizing system, the local physical observables a long time after a quench are only determined by the values of these conserved quantities.

Some systems, however, avoid thermalization. In these cases, information encoded in the initial state can remain accessible even long times after the quench. A famous example is Anderson localization in non-interacting systems with disorder [382], where single-particle eigenstates become exponentially localized. Anderson himself already posed the question how interactions between

the particles change this scenario. In the past two decades, localization in an interacting system at finite energy density, called *many body localization* (MBL) has been investigated extensively [383–388].

A lot of numerical studies have been performed for the *XXZ* spin chain with a random magnetic field $h_i^z \in [-W, W]$ at each site. This model realizes Anderson localization in the limit of $J_z \to 0$. In this case, an arbitrary small disorder strength W is sufficient to localize all single particle states. In the interacting system, disorder strengths smaller than a critical value, $W < W_c$, lead to delocalized eigenstates in the middle of the spectrum, introducing a *many-body mobility edge* [389], which may however cease to exist in the thermodynamic limit [390]. Even in one dimension, there is therefore a transition between the many-body localized and the thermal phase [92]. One way to determine the critical disorder strength is to study the average ratio of adjacent level spacings. In the ergodic phase, the level statistics of the energy spectrum correspond to a Gaussian-orthogonal ensemble, whereas in the localized phase, the level statistics are Poisson [385].

9.1.1 Entanglement properties

In a system for which ETH holds, a sufficiently small subsystem A of an eigenstate $|\alpha\rangle$ will have thermal expectation values. The corresponding reduced density matrix $\hat{\rho}_A = \mathrm{tr}_B\, |\alpha\rangle\langle\alpha|$ is thermal. The entanglement entropy then corresponds to the thermodynamic entropy $S_{ent}(A) = \mathrm{tr}\, \hat{\rho}_A \log \hat{\rho}_A = S_{th}(A)$. The thermodynamic entropy, however, is extensive. For eigenstates $|\alpha\rangle$ at finite energy density, the entanglement entropy thus has a volume-law scaling.

In the many-body localized case, the entanglement entropy follows an area-law. This behavior is typical for the ground state of a gapped system. In MBL systems, even highly excited states obey this area-law scaling. Intuitively, this can be understood from the fact that within the MBL phase, a local perturbation can only affect the degrees of freedom within the localization length ξ, which we will introduce below. The effect on spins far away from the local perturbation is expected to decay exponentially with distance. In particular, a Hamiltonian $\hat{H} = \hat{H}_A \otimes \hat{H}_B$ has no entanglement between subsystems A and B. We now introduce a term coupling the subsystems A and B locally. The eigenstates of the new Hamiltonian can be obtained from the eigenstates of the old Hamiltonian by entangling spins in A with spins in B over a distance $\propto \xi$ around the boundary of A and B. The entanglement entropy then scales with the size of the boundary between the subsystems.

9.1.2 Integrals of motion: the τ-bit picture

Eigenstates of a (topologically trivial) MBL Hamiltonian can be connected to product states by a finite number of quasi-local unitary transformations, since they exhibit area-law scaling of the entanglement. These unitary transformations accordingly diagonalize the MBL Hamiltonian in

the corresponding product state basis [386].
We consider the *XXZ* spin chain with a disorder field and apply the unitary transformation U with

$$\hat{\tau}_i^z = \hat{U}^\dagger \hat{S}_i^z \hat{U}, \tag{9.1}$$

where the $\hat{\tau}_i^z$ are the integrals of motion of the Hamiltonian, i.e. $[\hat{\tau}_i^z, \hat{H}] = 0$. Since $[\hat{\tau}_i^z, \hat{\tau}_i^{x,y}] \neq 0$, the Hamiltonian expressed in the τ-basis cannot contain any $\hat{\tau}^x$ or $\hat{\tau}^y$ in order to satisfy $[\hat{\tau}_i^z, \hat{H}] = 0$. In other words, any $\hat{\tau}_i^{x,y}$ terms would change $\hat{\tau}_i^z$, which is a conserved quantity. The Hamiltonian therefore takes the general form

$$\hat{H}_\tau = \sum_i \tilde{h}_i \hat{\tau}_i^z + \sum_{i,j} \tilde{J}_{ij} \hat{\tau}_i^z \hat{\tau}_j^z + \sum_{i,j,k} \tilde{J}_{ijk} \hat{\tau}_i^z \hat{\tau}_j^z \hat{\tau}_k^z + \ldots = \sum_i \Delta_i(\{\tau_j^z\}) \tau_i^z. \tag{9.2}$$

In the MBL regime, the unitary operator $\hat{U}$ is quasi-local, and thus the $\hat{\tau}_i^z$ are typically close to the $\hat{S}_i^z$. The τ-bit operator on site i is constructed using $\hat{S}_i^z$ and nearby sites. The weights for contributions from other sites decays exponentially with the distance in the localized regime. The couplings $\tilde{J}_{ij}$, $\tilde{J}_{ijk}$, ... have to decay exponentially with distance because $\hat{H}_\tau$ is obtained from the local Hamiltonian $\hat{H}$ through the quasi-local transformations $\hat{U}$. Note that the $\tilde{J}_{ij}$, $\tilde{J}_{ijk}$, ... terms are what distinguished MBL from an Anderson localized system. In Section 9.2.3, the couplings $\tilde{J}_{ij}$ between two sites are measured experimentally.
This form of the Hamiltonian is particularly convenient to consider dynamics, because it is written in terms of conserved quantities. Thus, if we consider the time evolution of a product state of τ_i^zs, the state cannot change but only acquires a phase. A generic initial state can be written as a superposition of product states of τ_i^z:

$$\left|\psi_0\right\rangle = \sum_a p_a \left|a\right\rangle, \tag{9.3}$$

where $\left|a\right\rangle$ is a product state of τ_i^zs, and the time evolution is

$$\left|\psi_0(t)\right\rangle = \sum_a e^{-iE_a t} p_a \left|a\right\rangle. \tag{9.4}$$

Expressing the Hamiltonian as (9.2) directly gives an intuitive explanation for the breakdown of ergodicity: the initial values of the local integrals of motion cannot change during the dynamics and the MBL system therefore keeps a memory of the initial state during the time evolution.

Intuitive picture for entanglement entropy dynamics

We consider the case of strong disorder and assume that we directly manipulate τ bits in the experiment for simplicity. If we start from the vacuum and apply $\pi/2$ pulses on sites i and j and for now ignore all sites in between, the state is

$$|\psi\rangle = \frac{1}{2}\left(|0\rangle + |1\rangle\right)_i \otimes \left(|0\rangle + |1\rangle\right)_j . \tag{9.5}$$

Time evolution leads to

$$|\psi(t)\rangle = \frac{1}{2} e^{i\tilde{J}_{ij}t}\left(|0\rangle_i \otimes |0\rangle_j + |1\rangle_i \otimes |1\rangle_j\right) + \frac{1}{2} e^{-i\tilde{J}_{ij}t}\left(|0\rangle_i \otimes |1\rangle_j + |1\rangle_i \otimes |0\rangle_j\right), \tag{9.6}$$

where we neglected the fields $\tilde{h}_i$, since they do not contribute to the build-up of entanglement. The reduced density matrix of site i is

$$\rho_i = \mathrm{tr}_j\, \rho = \frac{1}{2}\begin{pmatrix} 1 & \cos(2\tilde{J}_{ij}t) \\ \cos(2\tilde{J}_{ij}t) & 1 \end{pmatrix}. \tag{9.7}$$

The entanglement entropy

$$S = -\,\mathrm{tr}\,\rho_i \log \rho_i \tag{9.8}$$

therefore reaches its maximum value of $\log(2)$ when the off-diagonal entries are zero, i.e. for $\tilde{J}_{ij}t = \pi/4$. For a single value of $\tilde{J}_{ij}$, the entanglement entropy is then given by

$$S = -\cos^2(\tilde{J}_{ij}t)\log\cos^2(\tilde{J}_{ij}t) - \sin^2(\tilde{J}_{ij}t)\log\sin^2(\tilde{J}_{ij}t) \tag{9.9}$$

and thus oscillates in time. Averaging over many disorder realizations, and thus a distribution of $\tilde{J}_{ij}$'s as shown in section 9.2.3, leads to a slow growth, followed by a saturation to a finite value determined by the shape of the distribution.

The same argument can be generalized to the case of many spins. During the time evolution, each spin accumulates a phase given by the effective field created by all the other spins. The couplings $\tilde{J}_{ij}$, ... which determine this effective field, decay exponentially with distance. The effective magnetic field thus also decays exponentially with distance. At the same time, the couplings $\tilde{J}_{ij}$, ... follow a distribution which can become very broad for small distances $|i-j|$, see section 9.2.3. In order for a given spin to acquire a phase of order one, a correspondingly long time needs to pass, leading to the characteristic logarithmic growth of entanglement in the MBL phase. Note that this growth is not observed in the Anderson localized case, as there are no interactions $\tilde{J}_{ij}$, $\tilde{J}_{ijk}$, etc..

In this chapter, we study the interacting Bose-Hubbard model with strong disorder, which exhibits many-body localization. We investigate different aspects of the question how much the time

evolved quantum state differs from the initial state and which role interactions play. In section 9.2, we use an array of superconducting qubits to study many-body localization. We start by proposing a measurement scheme that employs the Jarzynski equality to access the free energy of a system that does not necessarily have to thermalize. As a first experimental step, we measure the local particle number, which provides a first sign of localization, in the one-dimensional as well as small two-dimensional systems. We then proceed by making full use of the preparation and read-out capabilities of the experimental setup and extract the non-local couplings $\tilde{J}_{ij}$. Using interferometric protocols, we provide further evidence for said couplings. Finally, we reconstruct the reduced density matrix of a two-qubit subsystem and extract different entanglement properties from it. In section 9.3, we work with Fock space snapshots of the time-evolved state of the system after a global quench. These snapshots can be directly obtained in a quantum gas microscope. We use machine learning techniques to study the MBL transition. Evaluating experimental data from a quantum gas microscope leads to excellent agreement with numerical simulations. Based on the same type of snapshots, we study the approach to thermal equilibrium with the help of a neural network.

9.2 Probing many-body localization with superconducting qubits

Subsections 9.2.2, 9.2.3, 9.2.4, and 9.2.5 of this section are based on the publication

- B. Chiaro, C. Neill, A. Bohrdt, M. Filippone, et al. [collaboration with the group of J. Martinis] "Direct measurement of non-local interactions in the many-body localized phase" – arXiv:1910.06024

Structure, text and figures have been rearranged and adapted here.

In this section, we use an array of coupled superconducting qubits, as introduced in section 2.2, to study the dynamics of interacting photon excitations in a disordered potential. The system is described by the Bose-Hubbard model, Eq. (7.1), with a random on-site detuning $\mu_i \in [-W, W]$. The qubit frequency, the nearest neighbor coupling, and the nonlinearity set μ_i, J, and U, respectively. We are able to tune μ_i and J independently at a fixed nonlinearity of $U = 160\text{MHz}$. Similar to the Schrieffer-Wolf transformation discussed in chapter 3 for the Fermi-Hubbard model, the Hamiltonian can be approximated by an XXZ spin chain in the case of low occupancies and strong interactions $U \gg J, W$.

The remainder of this section is organized as follows. In subsection 9.2.1, we introduce the Jarzynski equality and discuss a measurement protocol, which is directly accessible with the superconducting qubit setup used in the remainder of this section. We then turn to the experimental part and show results for the local particle number as a first sign of localization. Next, we extract the couplings J_{ij} from the τ-bit picture introduced in section 9.1.2. We use the experimental capabilities

of the superconducting qubit setup to perform interferometric probes of many-body localization, again enabling us to directly observe interaction effects. Finally, we reconstruct the two-qubit reduced density matrix in subsection 9.2.5 and extract different entanglement properties.

9.2.1 The work distribution function and Jarzynski equality

The Jarzynski equality states that the mean work performed on a system during a thermodynamic process and the difference in the free energies of the system before and after the process are connected by the equality [391]

$$\left\langle e^{-\beta w}\right\rangle_w = e^{-\beta \Delta F}. \tag{9.10}$$

Here,

$$\left\langle e^{-\beta w}\right\rangle_w = \int dw p(w) e^{-\beta w} \tag{9.11}$$

is the average with respect to the work distribution function $p(w)$, where the latter is defined as the probability density of having performed the work w during the process. Importantly, the difference in the free energy ΔF enters the equality regardless of whether the system is in equilibrium at the end of the protocol. This means that for the Jarzynski equality to hold it is not necessary that the system actually equilibrates. In particular, one can measure the free energy of a system that does not actually ever reach an equilibrium state, such as a many body localized system [391–395].
We consider a quantum system described by a Hamiltonian H_0. Let us first assume that the system is prepared in a thermal initial state $\rho_0 = \frac{1}{Z_0} e^{-\beta H_0}$. We will see below that this does not have to be realized experimentally. Ramping some parameters, the final system will be described by a different Hamiltonian H_1. We will be interested in the free energy of H_1 as a function of temperature. We define the characteristic function $G(u)$ as

$$G(u) = \int dw e^{-iwu} p(w). \tag{9.12}$$

It can be shown [392] that

$$G(u) = \langle e^{iuH_1} e^{-iuH_0}\rangle_0, \tag{9.13}$$

where the expectation value is with respect to the initial density matrix ρ_0. When setting $u = i\beta$ we obtain the Jarzynski relation

$$G(i\beta) = \langle e^{-\beta w}\rangle_w = e^{-\beta \Delta F}. \tag{9.14}$$

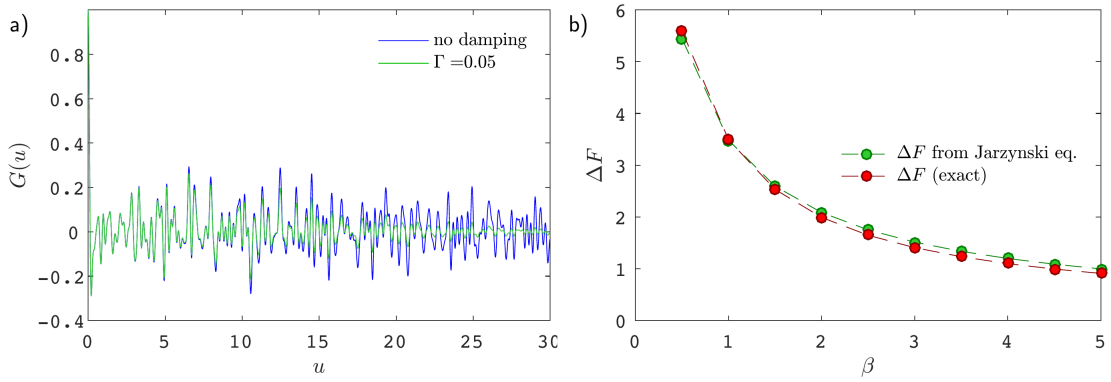

Figure 9.2.1: Free energy from the Jarzynski equality. Numerical simulation for the Jarzynski protocol described in the main text for a one-dimensional system described by the Hamiltonian (7.1) with $L = 6$ sites, $N = 3$ particles, disorder strength $W/J = 5$, and interaction strength $U/J = 3.5$. a) The characteristic function $G(u)$ obtained as described in the main text. In order to calculate the free energy difference ΔF, we multiply $G(u)$ with a damping function. b) Free energy difference ΔF, calculated according to the Jarzynski equality (green) and compared to the exact result (red).

We now assume that the initial Hamiltonian H_0 is in the form

$$H_0 = \sum_i \varepsilon_i |i\rangle\langle i|. \tag{9.15}$$

This allows us in particular to easily simulate the thermal initial state by preparing product states and multiplying the result with the corresponding thermal weight and furthermore to obtain the free energy of the trivial Hamiltonian H_0 directly. The characteristic function $G(u)$ can in this case be obtained by measuring the overlaps

$$r_i(u) = \langle i|e^{iH_1 u}|i\rangle, \tag{9.16}$$

and successively multiplying the r_i with $e^{-i\varepsilon_i u}$. For each temperature, we furthermore weight the overlaps with the corresponding thermal weight, such that

$$G(u) = \frac{1}{Z_0}\sum_i e^{-\beta\varepsilon_i} e^{-i\varepsilon_i u} r_i(u). \tag{9.17}$$

This mimics the thermal state ρ_0. In order to obtain the work distribution function $p(w)$ we have to perform a Fourier transformation. Because $G(u)$ will be damped in the experiment, we use a filter function

$$\mathcal{F}(u) = e^{-(\Gamma u)^2}, \tag{9.18}$$

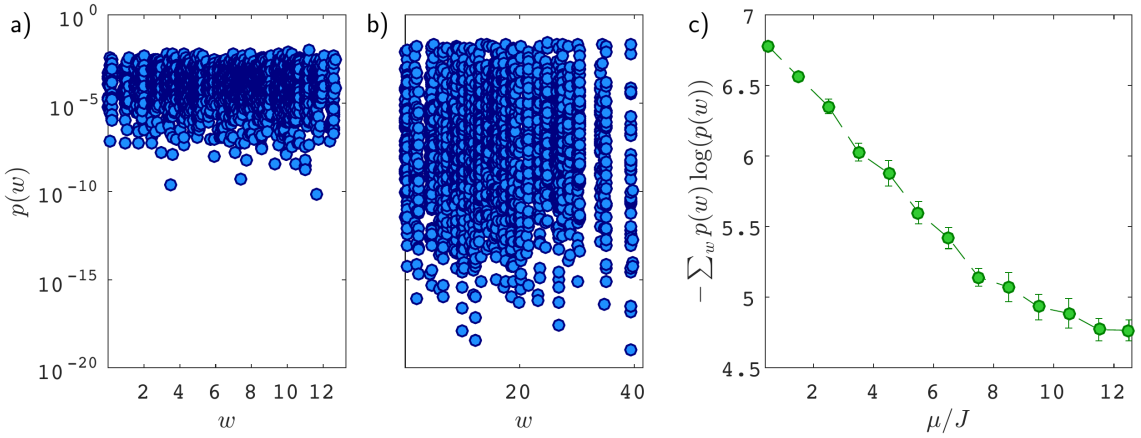

Figure 9.2.2: Work distribution function $p(w)$ in a disordered Bose-Hubbard model as described by Hamiltonian (7.1) with $L = 6$ sites, $N = 3$ particles, disorder strength a) $W/J = 1$, b) $W/J = 10.5$, interaction strength $U/J = 3.5$, and inverse temperature $\beta J = 5$, from exact diagonalization. In the case of strong disorder, b), the work distribution function is dominated by a few peaks, as compared to a rather broad feature for weak disorder. c) This behavior can be quantified by considering for example $-\sum_w p(w)\log p(w)$ for a range of disorder values. For each disorder value in c), we average over 15 disorder realizations. The error bars denote 1 s.e.m.

which gives:

$$p(w) = \int du\ e^{-iwu}\mathcal{F}(u)G(u). \tag{9.19}$$

In other words, the filter function broadens the delta-peaks in the spectrum and thus in $p(w)$. Therefore, Γ has to be chosen smaller than the many-body energy spacings of the Hamiltonians, but still sufficiently large to work as a proper cutoff to the temporal data in $G(u)$. In the experiment, there will anyways be some decoherence rate present, so an artificial broadening is not necessary. With the help of the Jarzynski equality, we can determine the difference in free energy ΔF from the work distribution function $p(w)$,

$$\langle e^{-\beta w}\rangle_w = \int dw e^{-\beta w}p(w) = e^{-\beta\Delta F}. \tag{9.20}$$

This finishes the protocol and we were able to measure the free energy of a closed and interacting many-body system which has not even been at equilibrium.

Measurement protocol summary

1) Measurement

   (i) generate initial product state $|i\rangle$

(ii) time evolve with Hamiltonian of interest $\hat{H}_1$ for a time u

(iii) measure overlap $r_i(u) = \langle i|e^{iH_1 u}|i\rangle$

(iv) repeat (i)-(iii) for a set of initial states $|i\rangle$

2) Postprocessing

(i) calculate $G(u)$ for desired β from the measured $r_i(u)$. All temperatures are obtained simultaneously

(ii) Fourier transform $G(u)$ to obtain $p(w)$

(iii) Use Jarzynski equality to obtain ΔF

Experimentally, one only needs to measure the overlaps $r_i(u)$. For a system of superconducting qubits, this has already been done in the context of the measurement of the energy spectrum of a many-body localized system [108].
Intriguingly, the work distribution $p(w)$ itself, which is directly obtained during the protocol outlined above, shows signatures of many-body localization. In Fig. 9.2.2 a), b), the work distribution $p(w)$ for the Bose-Hubbard model is shown for weak and strong disorder for a fixed disorder realization, indicating the different behavior. We quantify this behavior by calculating

$$-\sum_w p(w)\log p(w) \tag{9.21}$$

for a range of disorder strengths μ, where we average over 15 disorder realizations for each value of μ.
The Jarzynski equality itself has been experimentally tested, for example in a system of trapped ions [395].

9.2.2 First signs of localization – local particle numbers

Evidence for localization can be obtained by measuring the mobility of excitations. The time evolution of the local occupation is a straightforward measure for localization, which has been observed for example in cold atom experiments in one and two dimensions [90–92]. In Fig. 9.2.3, we initialize the system with a number of photon excitations n_{ph}. We measure the population $\overline{N_{q_9}(t)}$ on one of the initially excited qubits, q_9, as the system evolves under Hamiltonian (7.1). Fig. 9.2.3 a) shows $\overline{N_{q_9}(t)}$ for $n_{ph} = 2$. We choose a reference time t_{ref}, in which $\overline{N_{q_9}(t)}$ approaches an asymptotic value after initial transients have been damped, before the dynamics of our system are dominated by relaxation to the environment at large time scales (dashed black line), or delocalization within our closed system driven by extrinsic dephasing [13, 396–400].

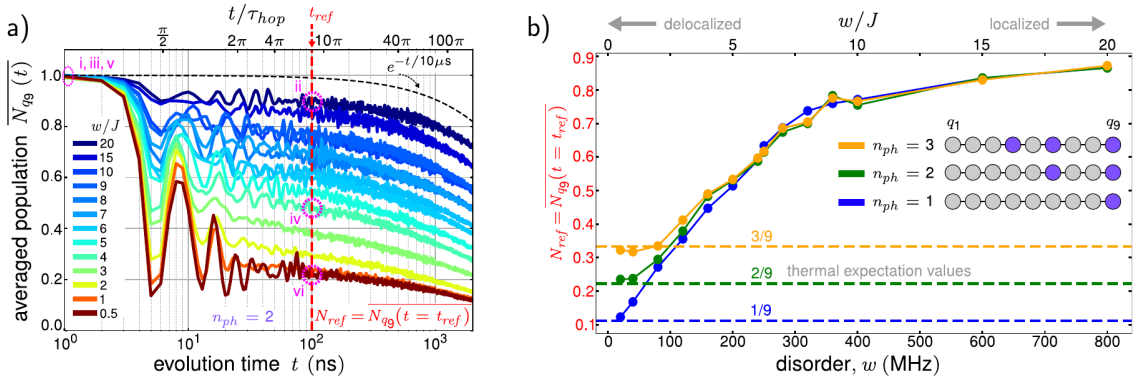

Figure 9.2.3: Time evolution of the local particle number for different disorder strengths w/J. a) In a chain of 9 qubits, two qubits were excited ('q6', 'q9'). The on-site population of 'q9' was measured with resolution of $|0\rangle$, $|1\rangle$, $|2\rangle$ for various magnitudes of disorder w/J, with $J = 40$ MHz. The overline indicates average over disorder realizations, and each data point is the average of 50 realizations. The parameter $\tau_{hop} = (2\pi J)^{-1}$ has been introduced to connect the laboratory time t with the hopping energy. N_{ref} is defined to be the average on-site population across instances of disorder at the reference time $t_{ref} = 100$ ns, after initial transients have been damped. The dashed black line indicates expected photon loss for a single qubit measured in isolation. b) N_{ref} as a function of disorder for $n_{ph} = 1, 2, 3$. Inset shows which qubits were excited at $t = 0$ ns.

Fig. 9.2.3 b) shows the disorder averaged population after $t_{ref} = 100$ ns of evolution as a function of the disorder strength. At low disorder, in the diffusive regime, we expect the dynamics to satisfy the ergodic hypothesis. Here, a uniform averaging over the available phase space implies that the expected occupancy of a given qubit should be n_{ph}/n_Q. For multiple photon excitations our observations are consistent with ergodic dynamics at weak disorder; however, as we increase the disorder strength, significant deviations from the thermal value are observed, which indicates that our system becomes many-body localized. We note that with more photons in the system, the population converges to its thermal expectation value at higher disorders. This is expected because the increased interactions assist with the thermalization process and drive delocalization. In the case of a single excitation our system is non-interacting and hence localized for all disorder magnitudes. The apparent approach of the population to the thermal value at extremely weak disorder indicates the regime where the single-particle localization length exceeds our system size. In Fig. 9.2.4, the onsite population for small 2D geometries is shown for $n_{ph} = 1, 2, 3, 4$. The initial location of the excitations was randomized between runs but the observation site was always one of the initially excited qubits. Similar to the 1D geometry, with sufficient disorder the onsite population takes a non-thermal stationary value and is consistent with many-body localization. In the 2D geometries the onsite population is consistent with thermalization at higher disorders when there are more

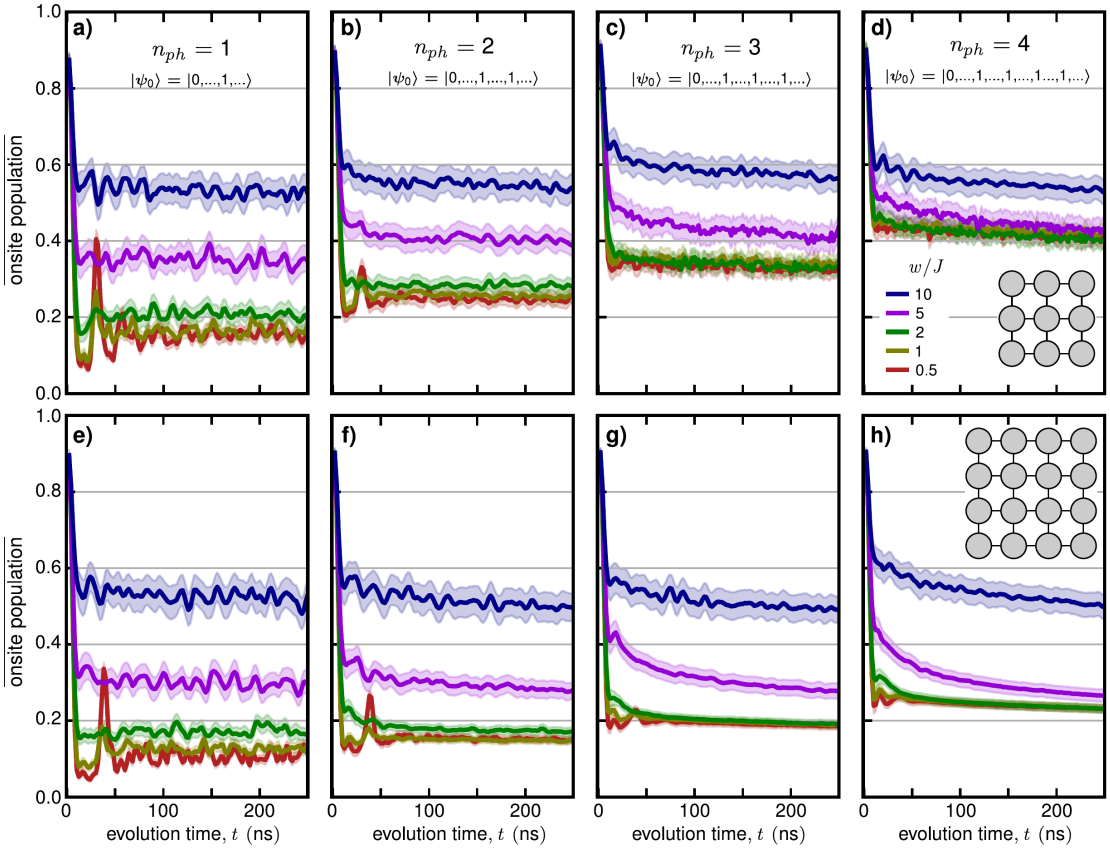

Figure 9.2.4: Time evolution of the local particle number in 2d arrays for different disorder strengths w/J and particle numbers. a)-d) Onsite population for $n_{ph} = 1, 2, 3, 4$ on a 3x3 array of qubits. e)-h) Onsite population for $n_{ph} = 1, 2, 3, 4$ on a 4x4 array of qubits.

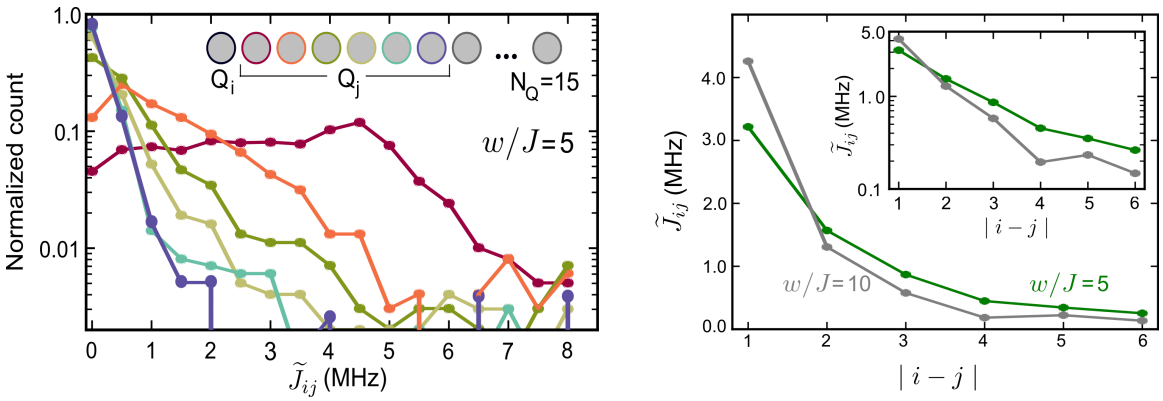

Figure 9.2.5: Distribution of the non-local interactions a) The histogram of $\tilde{J}_{ij}$ values measured for 1000 instances of disorder vs. distance between Q_i and Q_j . b) The disorder-instance-averaged values of $\tilde{J}_{ij}$ in linear (main) and semi-logarithmic scale (inset) for two ratios of disorder $w/J = 5$ (green) and $w/J = 5$ (gray).

photons in the system (greater n_{ph}), as in the 1D case.

9.2.3 Extracting the couplings

A hallmark of the MBL phase are the non-local interactions $\tilde{J}_{ij}$ between τ-bits introduced in Section 9.1.2. To investigate the emergent non-local interactions, we measure the distribution of the couplings $P(\tilde{J}_{ij})$, Fig. 9.2.5 with a conditional phase measurement made possible by our ability to drive on-site rotations. Our protocol consists of preparing the qubit Q_i in a superposition state $(|0\rangle + |1\rangle)/\sqrt{2}$ and then measuring the time evolution of $\langle\sigma_i^x\rangle$ under two conditions: when Q_j is in the $|0\rangle$ state and when it is in the $|1\rangle$ state. The rate of phase accumulation of Q_i is conditioned on the state of Q_j and thereby permits the extraction of the $\tilde{J}_{ij}$. In the τ-bit picture, the protocol can be understood as follows. We start from the initial state

$$|\psi_A\rangle = \frac{1}{\sqrt{2}}(|0\rangle + |1\rangle) \otimes |1\rangle, \tag{9.22}$$

where we only consider the two sites i and j. The system then evolves under the Hamiltonian

$$\hat{H} = h_1\hat{\tau}_1^z + h_2\hat{\tau}_2^z + \tilde{J}_{12}\hat{\tau}_1^z\hat{\tau}_2^z. \tag{9.23}$$

During a time-evolution for time t, a phase accumulation takes place, such that

$$|\psi(t)\rangle = \frac{1}{\sqrt{2}}(e^{-i\varphi_{01}t}|01\rangle + e^{-i\varphi_{11}t}|11\rangle) \tag{9.24}$$

with

$$\varphi_{01} = -h_1 + h_2 - \tilde{J}_{ij} \qquad \text{and} \qquad \varphi_{11} = h_1 + h_2 + \tilde{J}_{ij}. \tag{9.25}$$

Measuring $\langle \sigma_1^x \rangle$ in this case yields $2\cos(\varphi_A t)$ with $\varphi_A = -2h_1 - 2\tilde{J}_{ij}$. If we on the other hand start from the initial state

$$|\psi_B\rangle = \frac{1}{\sqrt{2}}(|0\rangle + |1\rangle) \otimes |0\rangle, \tag{9.26}$$

the measurement of $\langle \sigma_1^x \rangle$ will give $2\cos(\varphi_B t)$ with $\varphi_B = -2h_1 + 2\tilde{J}_{ij}$. The difference between the two phases thus directly yields the coupling $\tilde{J}_{ij}$.

In a system with more than two sites, in principle also higher order interactions $\tilde{J}_{ijk}$, ... should be taken into account. For the measurements presented here, these interactions can be neglected.

We Fourier transform the experimentally measured time evolution and determine the dominant low frequency peak and associate its shift as the $\tilde{J}_{ij}$. Repeating this process several times for different disorder realizations, we obtain the distribution of the couplings $\tilde{J}_{ij}$. We find the $\tilde{J}_{ij}$ to be broadly distributed, Fig. 9.2.5 a) with a mean that is rapidly decaying with increasing distance between the qubits (Fig. 9.2.5 b)). The broad distribution of the couplings has profound consequences. In particular, upon disorder averaging the entanglement entropy between the two qubits grows logarithmically in time and saturates at a finite value, see also section 9.2.5. By contrast, a sharp distribution of the couplings would lead to an oscillatory behavior of the entanglement entropy between two entities[401].

9.2.4 Interferometric Probes

The effect of interactions on the properties of a localized system can be probed by comparing measurements from spin and DEER echo protocols [402]. The main idea is to probe the dephasing of a given spin due to its entanglement with a different, distant spin, see Fig. 9.2.6. While in the experimentally realized Hamiltonian local occupation numbers of 2 and higher are crucial to obtain any interactions, we only consider manipulations and measurements in the 0 and 1 manifold for the protocols discussed here. Local occupations higher than one are unlikely, Fig. 9.2.6 c), and we thus expect that neglecting them does not alter the qualitative outcome of the discussion.

In order to illustrate the protocols, we consider the case of strong disorder, where the τ_i^z are very close to the physical spins S_i^z and assume that we directly manipulate τ bits in the experiment. For simplicity, we start with the initial state $|\psi_0\rangle = |0\rangle \otimes |...0_j...\rangle$. First a $\pi/2$ pulse is applied locally at site i in both protocols,

$$|\psi\rangle = R(\pi/2)\,|\psi_0\rangle = \frac{1}{\sqrt{2}}(|0\rangle + |1\rangle) \otimes |...0_j...\rangle. \tag{9.27}$$

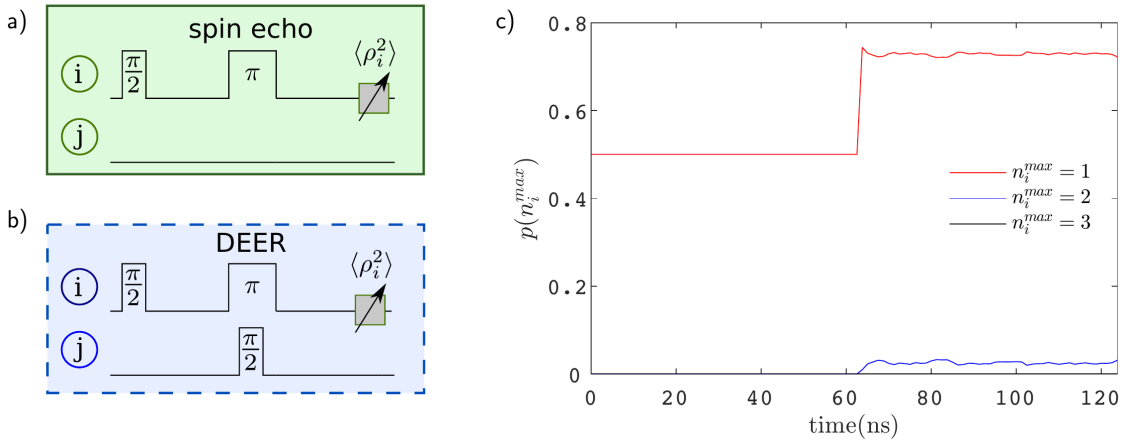

Figure 9.2.6: Spin and DEER echo protocol. a) Spin and b) DEER echo pulse sequences. DEER differs from spin echo by the addition of a remote $\pi/2$-pulse simultaneous with the π-pulse between the free precession intervals. c) Exact diagonalization estimate of the occupation of higher transmon levels during the DEER echo protocol. The probability to have a maximum local occupation of $n_i^{max} = 1, 2, 3$ during the DEER echo protocol is shown.

Next, the system is time evolved for a time t. During this time evolution, the spin at site i experiences a field

$$\Delta_i = \tilde{h}_i + \sum_j J_{ij}\tau_j^z + \sum_{j,k} J_{ijk}\tau_j^z\tau_k^z + \ldots \tag{9.28}$$

given by the state of the surrounding τ bits, such that

$$|\psi\rangle = e^{-i\hat{H}t}R(\pi/2)\,|\psi_0\rangle = \frac{1}{\sqrt{2}}(e^{i\Delta_i t}|0\rangle + e^{-i\Delta_i t}|1\rangle)\otimes|\ldots 0_j\ldots\rangle. \tag{9.29}$$

At the middle of the protocol, a π pulse is applied at site i, such that

$$|\psi\rangle = R(\pi)\,e^{-i\hat{H}t}R(\pi/2)\,|\psi_0\rangle = \frac{1}{\sqrt{2}}(e^{i\Delta_i t}|1\rangle - e^{-i\Delta_i t}|0\rangle)\otimes|\ldots 0_j\ldots\rangle \tag{9.30}$$

In the case of the spin echo protocol, the system is then again time evolved for a time t. The phases picked up during the first and second time evolution cancel in this case

$$|\psi\rangle = e^{-i\hat{H}t}R(\pi)\,e^{-i\hat{H}t}R(\pi/2)\,|\psi_0\rangle = e^{-i\hat{H}t}|\psi_\pi\rangle = \frac{1}{\sqrt{2}}(|1\rangle - |0\rangle)\otimes|\ldots 0_j\ldots\rangle \tag{9.31}$$

and after the final $\pi/2$ pulse, the system is back in its initial state:

$$|\psi\rangle = R(\pi/2)\,e^{-i\hat{H}t}R(\pi)\,e^{-i\hat{H}t}R(\pi/2)\,|\psi_0\rangle = -|0\rangle\otimes|\ldots 0_j\ldots\rangle = -|\psi_0\rangle. \tag{9.32}$$

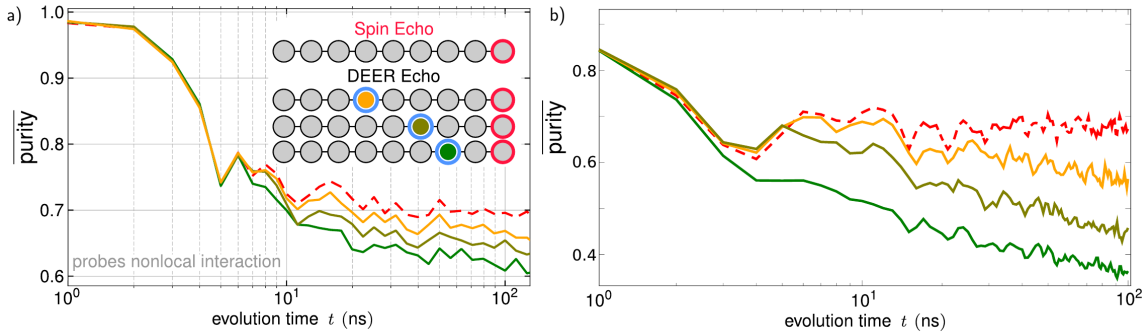

Figure 9.2.7: Spin and DEER echo in the disordered Bose Hubbard model. a) Purity of the single qubit for spin (red dashed) and DEER (solid) echo experiments for $w/J = 5$. The remote DEER pulse induces dephasing, decreasing the purity. The contrast between spin and DEER echo probes the non-local interaction $\widetilde{J}_{ij}$ between the spin and DEER echo lattice sites. b) Same as a) from exact diagonalization simulations.

In the system under consideration, the physical spins do not exactly correspond to the τ bits and therefore the system does not return entirely to its initial state, as other dynamics is also possible during the time evolution.

In the DEER echo sequence, the first time evolution is the same as above, with effective field Δ_i. Then, a $\pi/2$ pulse is applied at site j, putting the τ bit at that site in a superposition of $|0\rangle$ and $|1\rangle$, where for the latter case the effective field experienced by the τ bit at site i changes to $\tilde{\Delta}_i$, which corresponds to Δ_i with all terms that contain τ_j^z modified accordingly. The state after the second time evolution is therefore

$$|\psi\rangle = \frac{1}{2}\Big[|1\rangle \otimes |\ldots 0_j \ldots\rangle + e^{i(\Delta_i - \tilde{\Delta}_i)t - i\Delta_j t}|1\rangle \otimes |\ldots 1_j \ldots\rangle \\ -|0\rangle \otimes |\ldots 0_j \ldots\rangle - e^{-i(\Delta_i - \tilde{\Delta}_i)t - i\Delta_j t}|0\rangle \otimes |\ldots 1_j \ldots\rangle\Big] \quad (9.33)$$

and the final $\pi/2$ pulse gives

$$|\psi\rangle = -\frac{1}{\sqrt{2}}\Big[|0\rangle \otimes |\ldots 0_j \ldots\rangle + ie^{-i\Delta_j t}\sin((\Delta_i - \tilde{\Delta}_i)t)|1\rangle \otimes |\ldots 1_j \ldots\rangle \\ +e^{-i\Delta_j t}\cos((\Delta_i - \tilde{\Delta}_i)t)|0\rangle \otimes |\ldots 1_j \ldots\rangle\Big]. \quad (9.34)$$

Measurement of τ_i^z then yields

$$\langle \tau_i^z \rangle = \frac{1}{2}\Big[1 + \cos(2(\Delta_i - \tilde{\Delta}_i)t)\Big]. \quad (9.35)$$

The final measurement of $\langle \tau_i^z \rangle$ thus probes the effect of the interaction with the – possibly distant

– spin on site j. In particular, the comparison between spin and DEER echo protocols directly shows the effect of the interactions in the system. The difference between spin and DEER echo decreases with increasing distance between the two lattice sites, since the corresponding couplings $\widetilde{J}_{ij}$ decay, see Section 9.2.3. As the DEER echo site is moved closer to the probe site, the signal in terms of difference between the two echo protocols gets stronger, see Fig. 9.2.7. The experimental imperfections caused e.g. by dephasing reduce the contrast between the two echos compared to the exact diagonalization results, Fig. 9.2.7 b), but is still clearly visible. In a thermalizing system, other processes lead to dephasing and change the state during the time evolution, leading to a strong decay of both echos. In an Anderson localized system, the two protocols would also yield the same result, but in this case the final state is close to the initial state and the overlap is thus big.
From Eq. (9.35), the coupling $\tilde{J}_{ij}$ can in principle be extracted for a given disorder realization as the frequency of the cosine.

9.2.5 The two qubit reduced density matrix

In a superconducting qubits experiment, the density matrix can in principle be completely measured, since arbitrary local rotations are possible. In practice, the exponentially growing size of the Hilbert space and the correspondingly growing number of necessary measurements restricts the number of states on which a full state tomography is performed. Here, the reduced density matrix of two separate qubits is reconstructed.
Numerically, the reduced density matrix of a small subsystem can be obtained in two different ways: by tracing out the parts of the full density matrix which belong to spins other than the ones under consideration or by explicitely measuring all possible correlations up to n-th order, where n is the number of spins in the subsystem, see also Section 8.3.3. For the case of two spins, the latter approach is still feasible.

Von Neumann entanglement entropy From the reduced density matrix ρ_{2q} of the qubits on site 1 and 3, we extract the von Neumann entropy

$$S_{vN} = -\mathrm{tr}\, \rho_{2q} \log \rho_{2q} \tag{9.36}$$

as a measure of the entanglement of the subsystem with its environment, Fig. 9.2.8. The fast initial rise of the von Neumann entanglement entropy can be related to a hopping to the neighboring sites. Similarily, the local occupation changes on the same time scales, Fig. 9.2.8 f)-h). The disorder averaged expectation value $\langle \bar{\sigma_z} \rangle$, with $\langle \sigma_z \rangle = 1/2 - \langle \hat{n}_i \rangle$ initially rises because population from the subsystem qubits is transferred to the environment which has a smaller photon density.

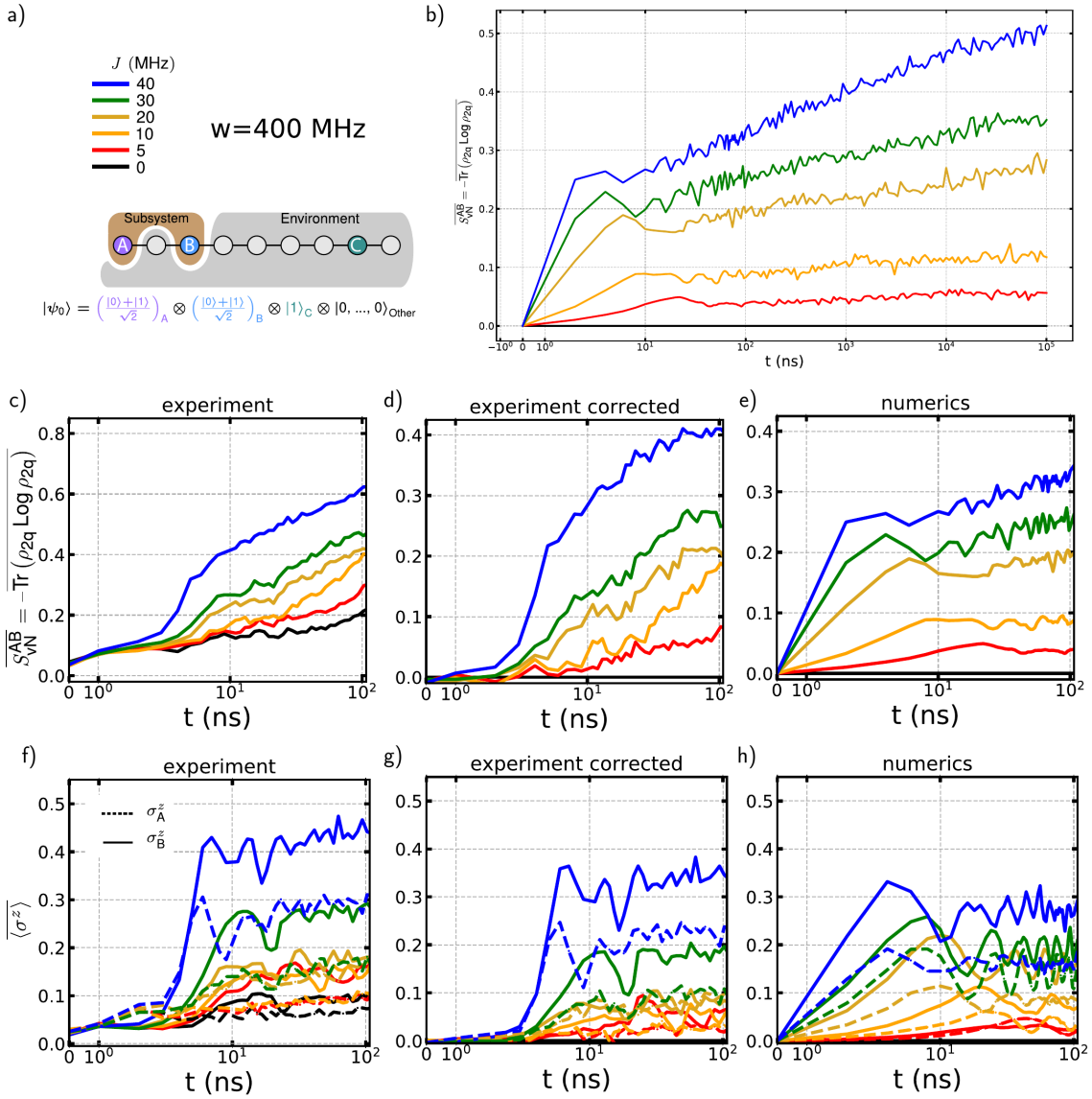

Figure 9.2.8: Von Neumann entanglement entropy of a two qubit subsystem a) Partitioning of the 9-qubit chain into a subsystem and environment. The subsystem qubits (A and B) are initialized into superposition states, and an additional excitation is placed on site C to enhance many-body interactions. b) Numerically calculated von Neumann entanglement entropy for times up to 10^5 ns. The logarithmical growth at long times is clearly visible. c) Von Neumann entanglement entropy extracted from the two qubit reduced density matrix reconstructed tomographically from experimental measurements. The $J = 0$ data acts as a control experiment. We attribute entropy accumulation in the control experiment to open system effects. d) Experimental data after subtracting the baseline entropy measured in the control experiment from each of the data series. e) Result of exact diagonalization numerics. f)-h): same as c)-e) for the disorder averaged expectation value $\langle \sigma^z \rangle$, which does not change significantly after an evolution time of 10 ns.

Note that in the convention used here, a larger value for $\langle \bar{\sigma_z} \rangle$ corresponds to a lower occupation. However, while the local occupation stays approximately constant afterwards, the entanglement entropy continues to rise albeit much slower. The long time behavior is consistent with the logarithmic growth expected from numerical simulations, see Fig. 9.2.8 a), as well as the τ-bit picture discussed in Section 9.1.2. Similar behavior for the entanglement growth has been observed numerically, see e.g. Ref. [403] and experimentally in a quantum gas microscope [35]. The von Neumann entropy quantifies entanglement with all external degrees of freedom and is not able to disambiguate entanglement with the environmental qubits due to unitary dynamics from open system effects. As such, our observed entropy S_{vN} is an upper bound for the entanglement generated under the closed system Hamiltonian time evolution. The $J = 0$ curve (black) in Fig. 9.2.8 c) provides an estimate of the amount of entropy that is due to open system effects, as there are no interactions between the qubits in the system and the observed entropy is thus attributed to extrinsic dephasing and relaxation processes. In Fig. 9.2.8 d) we show the experimentally measured von Neumann entropy after subtracting the baseline provided by the $J = 0$ data, which compares well to the exact diagonalization calculations in e). The disagreement at short times is attributed to the transient response of the control pulses. The time evolution of the von Neumann entanglement entropy depends on the choice of initial state, as illustrated in Fig. 9.2.9. The chosen initial state for the two qubits in subregion A directly creates a superposition state similar to the superposition between two neighboring sites used in Ref. [401]. If the initial state corresponds to product state excitations in region A, only rare resonances between neighboring sites realize superpositions. After a fast initial dynamics, no additional growth of the entanglement entropy can be observed on the time scales considered here.

Operational entanglement measures In order to estimate the entanglement contained in the two qubit subsystem, we make use of operational entanglement measures, since the subsystem is in a mixed state as it is part of a larger system. One such operational entanglement measure is the entanglement of formation (EOF), which is a measure for the entanglement needed to create the observed two-qubit reduced density matrix [404]. With this entanglement measure, we are affirmatively detecting entanglement between sites of the subsystem. The observed EOF cannot be attributed to open system effects which would tend to suppress the entanglement of formation. The EOF is therefore a more conservative entanglement measure than for example the von Neumann entanglement entropy, and a valuable tool for characterizing the experimental system, which is always coupled to environmental degrees of freedom to some extent. The entanglement of formation is defined as

$$E_F(\rho) = \varepsilon(\mathcal{C}(\rho)) \tag{9.37}$$

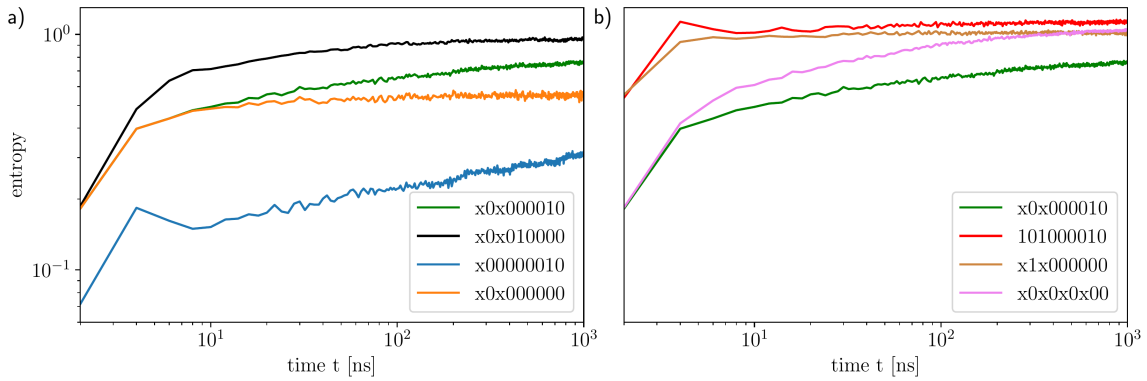

Figure 9.2.9: Von Neumann entanglement entropy of a two qubit subsystem – initial state dependence. We perform a numeric analysis on a nine site chain to show the importance of the initial state in the time evolution of the entanglement entropy. We choose sites 1 and 3 as subregion A and the rest of the system as region B. Choosing the initial state considered in Fig. 9.2.8 (green line) leads to good qualitative agreement with the experimental results shown in Fig. 9.2.8 c)-e). There is a sharp increase in entanglement entropy during the first hopping interval, followed by a growth consistent with a logarithmic time dependence. a) Placing the excitation in subregion B closer to subregion A (black line) leads to a sharper increase for short times. Starting from a state with a superposition on site 1 and an excitation on site 8, but without any occupation on site 3 (blue line) leads to the same growth at long times. However, the initial increase is less pronounced. Without the excitation in subregion B, the entanglement grows only very weakly at long times (orange line). b) Initializing product instead of superposition states locally (red line) leads to a relaxation on short time-scales, after which the two body reduced density matrix does not change much anymore, the entanglement saturates correspondingly. Placing the excitation in subregion B on site 2 (brown line) yields similar results. An initial state with more local superpositions distributed over the entire system (pink line) leads again to a slow growth of the entanglement with time.

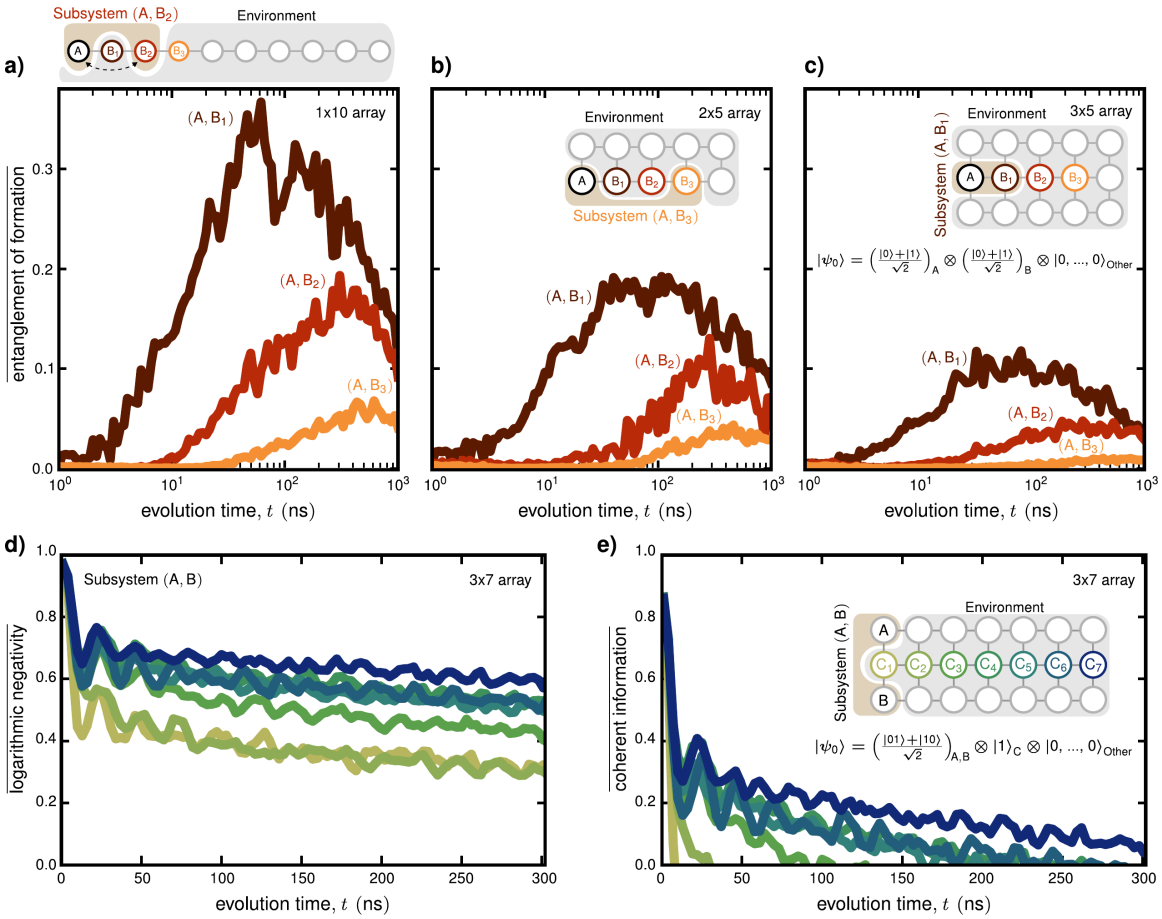

Figure 9.2.10: Operational entanglement measures Entanglement of formation between qubits in various 2-qubit subsystems (A,B$_i$). To observe the development of entanglement between sites A and B the subsystem is initialized in a product of single qubit superposition states and the entanglement of formation of the two qubit density matrix is extracted, for subsystems of a) 1×10, b) 2×5, and c) 3×5 array of qubits with $J = 30$ MHz and $w/J = 10$. In a 2 qubit subsystem (A,B) of a 3 by 7 array of qubits, a Bell pair is created, and the logarithmic negativity d) and coherent information e) are extracted from measurements of the subsystem density matrix and averaged over 80 realizations of disorder for $J = 30$ MHz with $w/J = 12$. We initialize the environment with an excitation at a position C_i which is varied.

with

$$\varepsilon(x) = -h_+(x)\log_2 h_+(x) - h_-(x)\log_2 h_-(x) \tag{9.38}$$

where

$$h_\pm(x) = -\frac{1}{2}\left(1 \pm \sqrt{1-x^2}\right). \tag{9.39}$$

The concurrence $\mathcal{C}(\rho)$ of a mixed state of two qubits is defined as

$$\mathcal{C}(\rho) = \max\left(0, \lambda_1 - \lambda_2 - \lambda_3 - \lambda_4\right), \tag{9.40}$$

where λ_i are the eigenvalues of

$$R = \sqrt{\sqrt{\rho}\tilde{\rho}\sqrt{\rho}} \tag{9.41}$$

and

$$\tilde{\rho} = (\sigma_y \otimes \sigma_y)\rho^*(\sigma_y \otimes \sigma_y). \tag{9.42}$$

In Fig. 9.2.10, the experimentally measured entanglement of formation is shown for a) a one dimensional system, b) a two-leg ladder and c) a three-leg ladder. We initialize the subsystem in a product state of single qubit superpositions and observe the development of entanglement between the subsystem qubits. Regardless of geometry of the qubit array, entanglement grows gradually between the localized, spatially separated sites over several hopping times. The entanglement grows faster when the subsystem qubits are closer to each other. This can be understood by considering two isolated qubits, which are becoming correlated with a rate given by the effective interactions $\widetilde{J}_{ij}$ that increases with decreasing distance, see Fig. 9.2.5. The EOF for a single disorder realization possesses a sinusoidal shape. However, due to the disorder average over the broad distribution of the couplings $\widetilde{J}_{ij}$ the EOF saturates at intermediate times and only decays at late times due to open system effects. The EOF results have to be contrasted with the von Neumann entanglement entropy, which would continuously increase because it includes entanglement with all degrees of freedom external to the subsystem.

Within the τ-bit picture, the different τ^z eigenstates only acquire a phase but do not transform into each other during the time evolution. In particular, the two qubit states $|00\rangle$, $|01\rangle$, $|10\rangle$ and $|11\rangle$ accumulate a phase $\pm J_{AB}t$. Following the calculation above for the entanglement of formation yields

$$E_F(\rho) = \sin(2J_{AB}t) \tag{9.43}$$

for the chosen initial state. For qubits A, B further apart, the coupling J_{AB} is smaller and thus the timescales are longer.

The results thus far illustrate how interaction effects propagate entanglement throughout the system in terms of the von Neumann entropy and the entanglement of formation. However, because

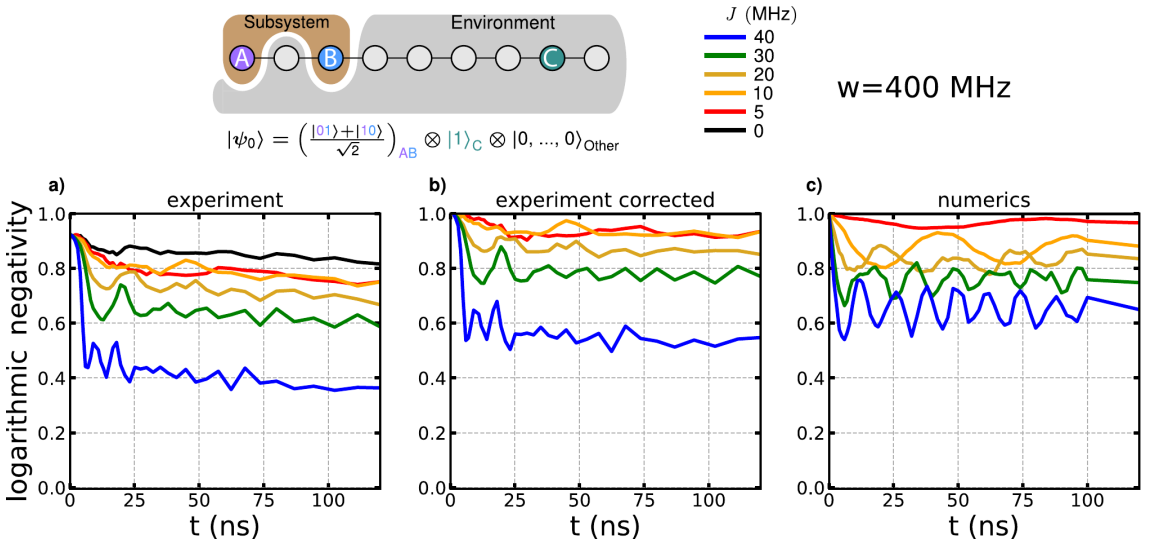

Figure 9.2.11: Logarithmic negativity in the one-dimensional Bose-Hubbard model. In a 2 qubit subsystem (A,B) of a one-dimensional array of nine qubits, a Bell pair is created, and the logarithmic negativity is extracted from a) experimental measurements of the subsystem density matrix. b) Similar to Fig. 9.2.8 b), the experimentally measured time trace for $J = 0$ is subtracted. c) Exact diagonalization simulation.

MBL systems are non-thermal, features of their initial state remain imprinted on them. While stable non-thermal local occupations as shown in Fig. 9.2.3 exemplify this behavior, the extension of this memory to quantum correlations has not been demonstrated experimentally. To probe this aspect, we prepare a maximally entangled Bell state between two subsystem qubits in a 3×7 qubit array and monitor the subsystem density matrix as the pair interacts with a remote photon. We focus on the distillable entanglement (DE), i.e., the entanglement which can be extracted from the mixed density matrix. The upper and lower bounds of the DE are the logarithmic negativity entropy and the coherent information entropy respectively, shown in Fig. 5(d) and (e).

To probe this aspect, we start from a highly entangled state and then study how this entanglement is preserved over time. To this end, we prepared the subsystem of qubits on sites A and B (see Fig. 9.2.10 d)) in a Bell state and let the system time evolve. In the strongly localized phase, the system can be described in the τ bit picture, where dephasing between the different τ bits causes a loss of the quantum information imprinted in the subsystem, but only on exponentially long time scales. Again, we have to make use of operational entanglement measures, since the subsystem is in a mixed state as it is part of a larger system. Specifically, we consider the entanglement that can in principle be extracted from the two qubit subsystem: the distillable entanglement. While it is in general not possible to exactly determine the distillable entanglement, a lower bound is given by the coherent information

$$E_D(\rho_{2q}) \geq S_{vN}(\rho_{1q}) - S_{vN}(\rho_{2q}), \tag{9.44}$$

where $\rho_{1q,2q}$ are the reduced density matrices of one of the two qubits and the two qubit subsystem, respectively, and $S_{vN}(\rho)$ is the von Neumann entanglement entropy. An upper bound to the distillable entanglement is given by the logarithmic negativity[405–409] which is defined as

$$E_N(\rho_{2q}) = \log_2 ||\rho_{2q}^{T_A}||_1. \tag{9.45}$$

Here, $\rho_{2q}^{T_A}$ is the partial transpose of the reduced density matrix with respect to one of the qubits and $||\cdot||_1$ denotes the trace norm.

The initial drop of the distillable entanglement on the single hopping timescale, Fig. 9.2.10 d), e) is attributed to population transfer from the Bell pair into the environmental qubits. Thereafter, interaction with the remote photon induces local dephasing in the subsystem. With the remote photon at larger distances, the distillable entanglement remains finite over several hopping times for high disorder strengths. The distillable entanglement is increasingly reduced as the remote photon is brought closer to the Bell pair and the coherent information that lower bounds the distillable entanglement approaches zero at earlier times. This data illustrates that in the many-body localized phase, a memory of the initial entanglement can persist to late times.

In Fig. 9.2.11, the logarithmic negativity is determined in a one-dimensional system of nine qubits for a fixed disorder strength $w = 400$ MHz and varying couplings $J = 0, 5, 10, 20, 30, 40$ MHz. In the case of weak disorder w/J, the logarithmic negativity decays to a low value on short time scales, since the quantum dynamics entangles the two qubit subsystem with the remainder of the system, Fig. 9.2.11. For increasing disorder strength w/J, the long-time value of the logarithmic negativity increases significantly.

By introducing phase sensitive algorithms and measurement, we have directly probed the nonlocal interactions responsible for entanglement propagation and mapped the spatial structure of the localized orbitals. The techniques introduced here extend easily to the characterization of digital algorithms and also more broadly to other synthetic quantum systems, thus offering a new toolkit to experimentally probe entanglement dynamics in a variety of settings.

9.3 Machine learning dynamics in a disordered system

This section is based on the publication

- A. Bohrdt, S. Kim, A. Lukin, M. Rispoli, R. Schittko, M. Knap, M. Greiner, and J. Léonard: "Analyzing non-equilibrium quantum states through snapshots with artificial neural networks" – arXiv:2012.11586

Structure, text and figures have been rearranged and adapted here.

Quantum simulation experiments can enable the observation of the time-evolution of a quantum many-body system starting from a non-equilibrium state with almost perfect isolation from the environment, as we have for example seen in sections 4.3, 5.5.2, and 9.2. In the past decade, a variety of non-equilibrium phenomena has been observed with examples ranging from exotic phases realized through Floquet driving [410] to time crystals [411, 412] and quantum scars [413].
Depending on the experimental platform, different measurements and observables are accessible. In a quantum gas microscope, Fock space snapshots of the quantum many-body state are measured. While quantities such as the entanglement entropy, as studied with superconducting qubits in section 9.2, are not easily accessible in this setup, Fock space snapshots provide a wealth of information about the quantum many-body state and a variety of different, also non-local and higher-order, correlations can be obtained. In many cases, theory can provide a clear prediction which observables should be studied, such as a given order parameter for a well-known phase transition. For some problems, however, it is not as clear which observable to look at, and by making a choice for one specific quantity, valuable information might be discarded. In section 6.5, we showed that Fock space snapshots of the quantum many-body state provide a natural input for neural networks. Employing these snapshots as training and test data in machine learning applications has, among others, the advantages that usually, many hundreds to thousands of snapshots are routinely taken and moreover, raw data is used, where no analysis for specific quantities based on human interpretations has taken place. Therefore the neural network itself makes the decision which observables to extract from the data and use for the specific task at hand.
In this section we study the dynamics of an interacting quantum many-body system in terms of actual experimental data as well as numerically generated, but experimentally accessible data with the help of neural networks. In particular, we consider the one-dimensional Bose-Hubbard model, Eq. 7.1, for different disorder strengths W and interaction strengths U. In a cold atom setup, the on-site disorder can be created with an incommensurate lattice as

$$h_i = \cos(2\pi\beta i + \varphi). \tag{9.46}$$

In the experiment considered here, the full on-site occupation can be resolved in the snapshots taken with the quantum gas microscope by splitting up the one-dimensional chain in a second spatial direction before imaging.
This system exhibits a many-body localized phase. The transition from an ergodic to a many-body localized phase is fundamentally different from the well-studied case of equilibrium phase transitions, as it describes a non-equilibrium setting. Machine learning approaches to study the MBL phase transition have employed the entanglement spectrum [414–416] or full eigenstates [417] as inputs. Those quantities are experimentally not, or at least not easily, accessible. In Ref. [418], time traces of the local magnetization are used as inputs to a neural network. Here, we go one step further and consider Fock space snapshots. This analysis has two main advantages:

(i) these snapshots are the direct measurement in quantum gas microscopes, whereas the local magnetization or particle number requires averaging over many snapshots, and thus more data taking.

(ii) Averaging over many measurements always means discarding information, which might be valuable. In Ref. [35] it was for example shown that measures for the entanglement entropy can be extracted from Fock space snapshots. Using snapshots as input allows the neural network to find the best observable for the classification task at hand, using all available information without any bias.

We start by characterizing the transition from a thermalizing to a many-body localized system by training a neural network to distinguish the extreme cases, then using data at intermediate values of the disorder strength as input in section 9.3.1. The accuracy achieved by the neural network can itself be used as a probe. This idea is for example employed in the confusion learning scheme introduced in Ref. [325] and used in this section for snapshots in a wide range of disorder values. We start from a uniform density state and apply the confusion learning scheme separately for different points in the time evolution. While the characteristic 'W'-shape, indicative of a qualitative change in the data, emerges for all time steps, the corresponding value of the disorder strength slowly increases with increasing time. Finally, in section 9.3.2, we use the accuracy as a probe to study how the system approaches thermal equilibrium – or fails to do so. In particular, we evaluate the accuracy achieved when the network is trained to distinguish the current time step from a thermal state at an effective temperature determined by the energy density of the initial state. This approach makes optimal use of the capabilities of a neural network, as the network parameters are in each time step optimized to distinguish this time step from thermal equilibrium, thus allowing the neural network to determine the observable most strikingly different in the two datasets.

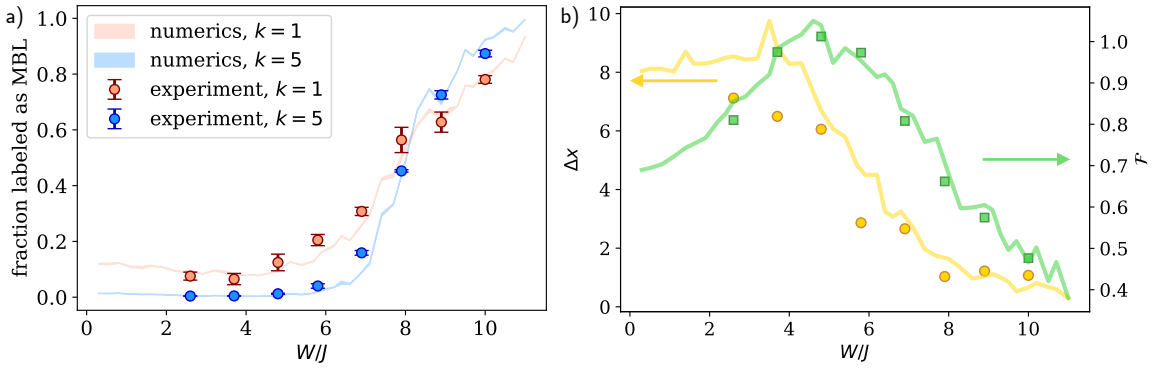

Figure 9.3.1: Learning a phase transition. Snapshots of the many-body quantum state in the long-time limit for various disorder strengths W/J are analyzed with machine learning techniques. a) A neural network is trained to distinguish exact diagonalization snapshots at $W/J = 0.3$ and $W/J = 11$ for $U/J = 2.9$ and a system with 12 sites. After the training process is finished, snapshots at intermediate values of the disorder strength are used as input. The plot shows the resulting classification for numerical data (shaded band) as well as experimental snapshots (symbols). Increasing the number of snapshots grouped together k leads to a sharper signal. We simultaneously evaluate snapshots from ten different disorder realizations in the numerical data. In the experimental data, each snapshot is from a different disorder realization. The accuracies are averaged over two independent runs and the errors denote one s.e.m. b) The transport distance Δx and on-site fluctuations $\mathcal{F}$, see text, are evaluated from the same snapshots. Shaded bands correspond to exact diagonalization snapshots, symbols are based on experimental data.

Among the first applications of machine learning techniques to the study of quantum many-body systems was the investigation of phase transitions, and in particular, the transition from a thermalizing to a many-body localized (MBL) phase. In Refs. [414, 415], for example, the entanglement spectrum was used as an input to the neural network. These works showed that a neural network can in principle be used to locate the transition. Here, we focus on Fock space snapshots of the many-body quantum state as input data, which are the direct output of quantum gas microscopy experiments and thus experimentally readily accessible for the systems of interest.

In Fig. 9.3.1, we first train the network to distinguish snapshots of the many-body quantum state, obtained from exact diagonalization calculations, in the long-time limit after a quench for low ($W/J = 0.3$) and high ($W/J = 11.0$) disorder strength for an interaction strength of $U/J = 2.9$. We consider a one-dimensional system with 12 sites, which is initialized in a uniform density state, $|\psi(t = 0)\rangle = |111111111111\rangle$, and use snapshots in the long-time limit at time $tJ = 100$. Here, we average over ten different disorder realizations, obtained by varying the phase φ in the potential (9.46). After the network has learned to label the extremal cases correctly with sufficiently high

accuracy, we input snapshots for intermediate values of the disorder strength. As output, for each disorder strength we obtain the fraction of snapshots labeled as *many-body localized* and *thermalizing*, see Fig. 9.3.1 a). Based on these results, the phase transition to the many-body localized phase is located between $W/J = 6$ and $W/J = 10$, as expected. One way to determine the exact position of the transition is the analysis of the level statistics, which change from Gaussian-orthogonal ensemble statistics to Poisson statistics as the disorder strength is increased and one enters the MBL phase. As shown in section C.2.2, finite size effects inhibit the determination of the exact position of the transition here. The machine learning method identifies a transition at $W^*/J \approx 8$, which is consistent with the level statistics calculated for smaller systems in section C.2.2. The increase in the fraction of snapshots classified as MBL becomes sharper as more snapshots are grouped together during training and evaluation, as can be seen by comparing the results for different numbers of snapshots grouped together k in Fig. 9.3.1 a). After training and evaluating numerically simulated snapshots, we can also use experimental data at $U/J = 2.9$ and various disorder strengths as input to the neural network. As shown in Fig. 9.3.1 a), the resulting classification agrees well with the neural network output for purely numerically simulated data.
In order to relate to previous work, in particular Ref. [66], we directly evaluate observables from the snapshots and calculate the transport distance Δx, defined as

$$\Delta x = 2 \sum_d |d| \cdot \left\langle G_c^{(2)}(i, i+d) \right\rangle_i \tag{9.47}$$

with

$$G_c^{(2)}(i, i+d) = \langle \hat{n}_i \hat{n}_{i+d} \rangle - \langle \hat{n}_i \rangle \langle \hat{n}_{i+d} \rangle , \tag{9.48}$$

and the on-site fluctuations $\mathcal{F}$, defined as

$$\mathcal{F} = G_c^{(2)}(d = 0), \tag{9.49}$$

in Fig. 9.3.1 b). Comparing the output of the neural network in part a) with the transport distance Δx in b) shows a similar behavior, indicating that the network presumably uses a similar observable to make the distinction.

Confusion Learning In Ref. [325], it was suggested to use the accuracy achieved on a test set to probe whether and where a phase transition exists. The method, called *confusion learning*, is explained in detail in section 6.5. Here, we have a dataset of snapshots for values of the disorder strength $0.3 \leq W/J \leq 11.0$. In order to test for a qualitative change in the data at a given value W^*,

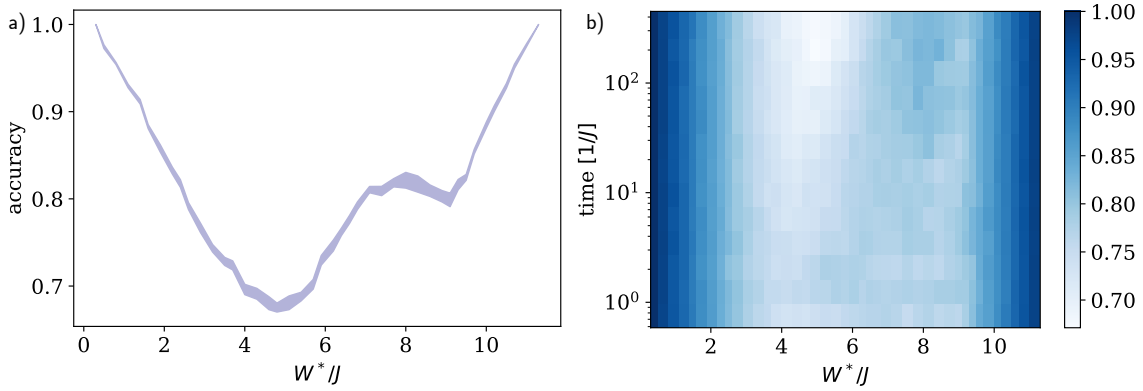

Figure 9.3.2: Confusion learning in a disordered system. Snapshots of the many-body quantum state of a system with 12 sites, $U/J = 2.9$, and various disorder strengths W/J and a single disorder realization are analyzed using confusion learning. A neural network is trained to label all snapshots with $W < W^*$ as *phase A* and the remainder as *phase B*. If a qualitative change in the data occurs, the accuracy will peak at an intermediate value of W^*. a) Resulting accuracy in the long-time limit, $tJ = 250$. b) Accuracies during the time evolution. The results are averaged over 15 independent runs and the width of the band in a) corresponds to one s.e.m.

we label all snapshots for $W \leq W^*$ as *phase A* and correspondingly all snapshots with $W > W^*$ as *phase B*. Assuming the snapshots are qualitatively different for $W \leq W^*$ as compared to $W > W^*$, the network should achieve a high accuracy in assigning the correct labels. However, if there is no qualitative change at the W^* under consideration, there will be confusion about the correct labels and the accuracy will thus be lower. Therefore, if there is a detectable phase transition or qualitative change in the data, the accuracy as a function of W^* will be in the shape of a W, where the central peak occurs at the phase transition, $W^* = W_c$.

As opposed to Fig. 9.3.1, we consider a single disorder realization here. Additionally, we specifically train the network to find differences between the snapshots at all available values of the disorder strength. Before, we trained the network to distinguish the extremal cases of $W/J = 0.3$ and $W/J = 11.0$, thus identifying the observables with the largest difference in their expectation value for these two values of the disorder strength. In the confusion learning scheme, however, the network is trained to distinguish snapshots at a disorder strength smaller and larger than the current limit W^*, and training occurs separately for each available value of W^*. Thus, differences in the snapshots occuring for intermediate values of the disorder strength can be learned here.

In Fig. 9.3.2 a), the resulting accuracy achieved by the network is shown as a function of W^* for training snapshots in the long-time limit at $tJ = 250$. In agreement with Fig. 9.3.1, a peak around $W^*/J = 8$ is clearly visible. After the initial short-time dynamics, a peak at intermediate values of W^*/J appears not only in the long-time limit, but at all times. For each time step shown, we separately apply the confusion learning scheme. As can be seen in Fig. 9.3.2 b), the position of the

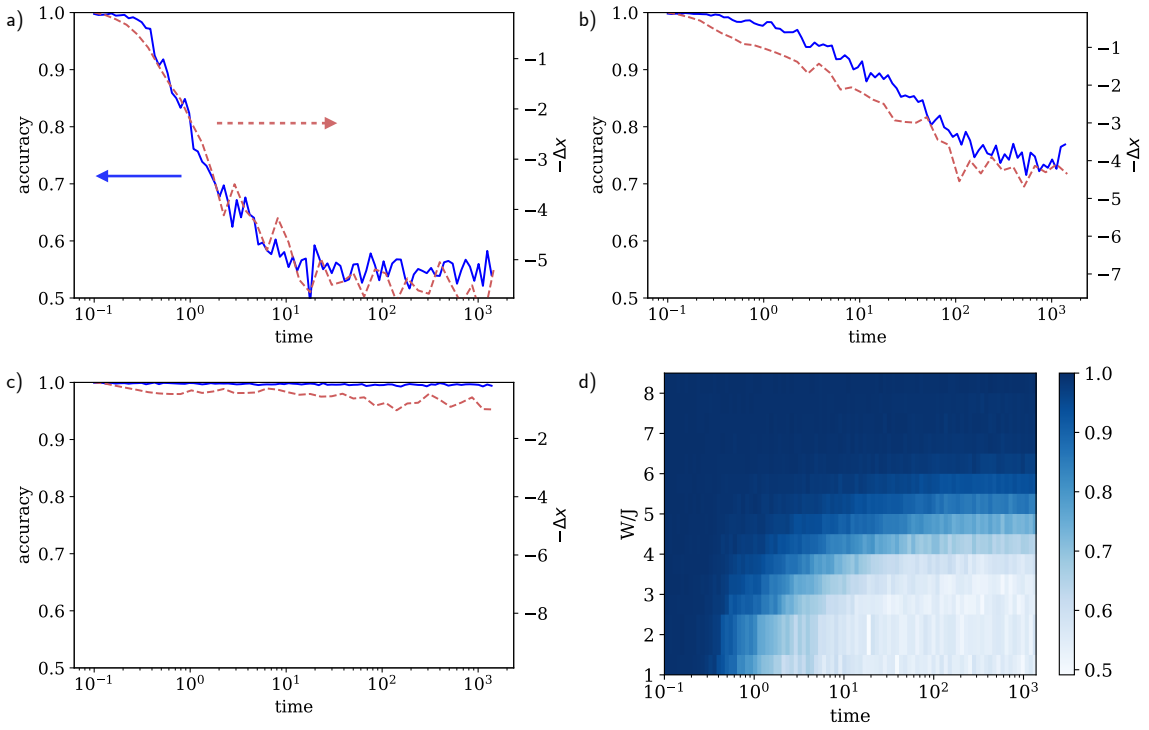

Figure 9.3.3: Learning thermalization in the Bose-Hubbard model with disorder. The system is initialized in a state with uniform density and the ensuing time evolution is investigated. In each time step, the neural network is trained to distinguish snapshots from the current time step from snapshots from a thermal state with the same energy density. The plots show the resulting accuracy, while grouping 5 snapshots together in each input, for a) $W/J = 1.5$, b) $W/J = 4.5$, c) $W/J = 8.0$, and d) a wide range of disorder strengths. A high accuracy indicates that the current time step can be easily distinguished from the thermal state. The upper limit of the plots in a)-c) for both the accuracy and $-\Delta x$ corresponds to the value at time $t = 0$, whereas the lower limit corresponds to the value in thermal equilibrium.

peak slowly moves from $W^*/J \approx 6$ to $W^*/J \approx 8$.

9.3.2 Learning thermalization

Similar to the confusion learning scheme studied above, we now use the accuracy itself as probe. In particular, starting from a product state of the form

$$|\psi(t = 0)\rangle = |11111111\rangle \tag{9.50}$$

we study the approach to thermal equilibrium by comparing the current time step to a thermal state of the same Hamiltonian. In principle, all conserved quantities of the model should be taken into account. Most importantly, the energy density of the initial state can be matched by choosing the

temperature of the thermal state accordingly. In particular, the energy density of the initial state $|\psi_0\rangle$ is given by

$$E_i = \langle\psi_0|\hat{H}|\psi_0\rangle. \tag{9.51}$$

The effective temperature T_{eff} is then determined such that the density matrix of the system,

$$\hat{\rho}_\beta = \frac{1}{Z}\exp\left(-\beta_{eff}\hat{H}\right), \tag{9.52}$$

with the inverse temperature $\beta_{eff} = 1/T_{eff}$ and

$$Z = \mathrm{tr}\left(\exp\left(-\beta_{eff}\hat{H}\right)\right) \tag{9.53}$$

fufills

$$E_i = \mathrm{tr}\left(\hat{H}\hat{\rho}_\beta\right). \tag{9.54}$$

The energy density

$$E(\beta) = \mathrm{tr}\left(\hat{H}\hat{\rho}_\beta\right) \tag{9.55}$$

is calculated for a range of values β until the effective temperature is determined such that Eq. 9.54 is fulfilled. We then sample snapshots for each time step under consideration as well as the effective temperature. Note that in the entire procedure, one has to consider a fixed disorder realization, since the energy density and thus the effective temperature as well as the resulting thermal state varies between different realizations, see section C.2.2.

Additionally to the energy, the total particle number is conserved in the system. The thermal state is calculated within a correspondingly fixed particle number sector to take this conservation into account. As discussed in chapter 8, such conserved quantities can lead to slow diffusive behavior, for example in the corresponding correlation functions.

In Fig. 9.3.3 the accuracy achieved on a test set not used during training is shown as a function of time for different disorder strengths. In each time step, the neural network parameters are optimized to enable the classification of snapshots into the categories *current timestep* versus *thermal*. This procedure has the advantage that the features used to make the classification can vary for different time steps and in particular, the network specifically searches for differences between the current time and thermal equilibrium. It is therefore in principle capable of identifying specific observables that have not yet reached their thermal equilibrium value.

For small W/J, Fig. 9.3.3 a), the system thermalizes comparably fast: for times $tJ \propto 10$, the network basically fails to distinguish snapshots from the time-evolved state after the quench from the corresponding thermal state and only reaches an accuracy of approximately 50%, which corresponds to guessing. The accuracy achieved by the neural network shows a very similar behavior as the trans-

port distance Δx , Eq. 9.47. Note that the lower limit of the plot in Fig. 9.3.3 a)-c) corresponds to the thermal equilibrium value. At intermediate W/J, Fig. 9.3.3 b), where the system is in a critical regime [66], the network is able to distinguish the time-evolved from the thermal state at all available times, up to $tJ \propto 1000$. At short to intermediate times, the accuracy stays close to 100%, even though the transport distance Δx already shows a visible increase. This indicates that the neural network picks up a quantity that thermalizes slower than Δx, which is defined by the connected density-density correlation function. For high values of W/J the system fails to thermalize on the time-scales accessed here, and the network is able to distinguish the current timestep from the thermal equilibrium state with an accuracy of almost 100%, while Δx increases slightly. As shown in Fig. 9.3.3 d), the accuracy is close to 100% at all times considered for disorder strengths $W/J \geq 6$, indicating that the system is very far from reaching a thermal equilibrium state. In Fig. 9.3.1 a), the transition to the MBL phase was located at slightly larger values of W/J. However, in this case, we considered a system with $L = 12$ sites, which is considerably larger than the $L = 8$ site system studied here. The critical disorder strength typically shifts to slightly larger values as the system size is increased.

10

Summary and Outlook

In this part of the thesis, we studied the scrambling of information, thermalization and entanglement properties in the Bose-Hubbard model with and without disorder.

Out-of-time ordered correlators (OTOCs) have been proposed as a measure of the scrambling of information in a quantum many-body system. We calculate OTO and time ordered correlation functions in the one-dimensional Bose-Hubbard model with matrix product state techniques at finite temperature. At sufficiently high temperatures, we saw that quasiparticles cease to exist, as the single particle Green's functions decays rapidly. The out-of-time ordered correlator however exhibits a distinct light-cone spreading. This ballistic spreading is to be contrasted to the density correlations, which show diffusive behavior due to the conserved total particle number. For future work, it would be interesting to develop analytical predictions for the growth of OTOCs, which in our numerics deviates significantly from the simple exponential growth obtained in strongly coupled field theories, or for the bounds that characterize the information propagation and Lyapunov exponents. The numerical study of out-of-time ordered correlators in other interacting many-body systems, such as Fermi-Hubbard or spin models, could be beneficial. Taking such routes could help to advance our fundamental understanding of information scrambling, transport, and thermalization.

We propose measurement protocols to experimentally access OTO and time ordered correlations

in a quantum simulator. An exciting future direction would of course be to measure OTOCs in a diffusive many-body system experimentally. In the past few years, a number of other proposals to measure OTOCs have been published. In Ref. [419], OTOCs of local operators in a small Ising spin chain have been measured in a nuclear magnetic resonance quantum simulator setup. In a trapped ion quantum simulator with seven sites, OTOCs have been measured in a protocol which at the same time verifies that quantum scrambling – as opposed to decoherence – took place [420]. The scheme introduced in Ref. [421], based on the idea to use randomized measurements, has been applied in a trapped ion quantum simulator [422] and could also be used in the superconducting qubit system studied in section 9.2.

Here, we used this experimental setup to study many-body localization in the Bose-Hubbard model with disorder in one dimension as well as ladder and small two-dimensional systems. As a first step, we observed the localization of particles during the time-evolution. The localization in terms of local particle numbers has been observed in large one- and two-dimensional systems in cold atom experiments [90–92]. However, the entanglement properties of the system cannot be directly studied in such a setup, and superconducting qubits provide a promising platform to further investigate the entanglement dynamics in larger two-dimensional systems in the future.

Localization can occur without any interactions between the particles. In the many-body localized phase, the system can be described by the τ-bit picture introduced in section 9.1.2, where distant qubits interact (in lowest order) through non-local interactions $\tilde{J}_{ij}$. We were able to experimentally measure the distribution of these couplings $\tilde{J}_{ij}$. For small distances, many different coupling strengths are measured for different disorder realizations. For larger distances, the measured distribution becomes increasingly narrow. Theoretically, one expects a log-normal distribution for the couplings $\tilde{J}_{ij}$, with a variance that grows linearly with spatial separation [423]. Detecting the corresponding broad tails with small weight remains however an open challenge for experiments. The experimentally measured disorder averaged values for $\tilde{J}_{ij}$ decay for increasing distance and exhibit a broader distribution as function of $|i-j|$ for weaker disorder. The distance and disorder strength dependence of these non-local interactions explain the observed behavior in the remainder of this section. We used the interferometric protocols introduced in Ref. [371] to further probe the interaction effects in the many-body localized phase.

With the measurements possible in a superconducting qubit experiment, full state tomography of a subsystem is feasible. We reconstructed the reduced density matrix of a two qubit subsystem and and directly extracted entanglement properties from it, such as the von Neumann entropy and operational entanglement measures. In the many-body localized regime, we observed growth of the von Neumann entanglement entropy even when the local particle numbers did not change anymore. Operational entanglement measures, such as the entanglement of formation, show a growth of the entanglement over time when the system is initialized in a product state. Finally, we prepared

the system in a Bell state and used the coherent information and logarithmic negativity to estimate how much distillable entanglement remains in the system after a given evolution time. Increasing disorder or reducing the distance between the two qubits involved in the initial Bell state leads to a finite value of the distillable entanglement for the experimentally accessible times.

In future research, it would be interesting to investigate the reduced density matrix of subsystems larger than two qubits. One specific route could be to employ machine learning techniques to efficiently reconstruct the reduced density matrix with an optimized choice of measurements. Another interesting research direction along these lines is machine learning assisted Hamiltonian interference from a given set of measurements, where the Hamiltonian actually realized experimentally – including all possible couplings and imperfections – could be studied.

We used machine learning techniques to study thermalization in the Bose-Hubbard model with disorder, as realized by the Rubidium quantum gas microscopy experiment in Markus Greiner's group at Harvard. Training a neural network to distinguish snapshots of the many-body state at the current time step from a thermal state at the same energy density allows us to use the accuracy as a proxy for how thermal the state looks. In particular, the network is trained to find all possible differences between the time-evolved and the thermal state, such that any possible differences visible in Fock space snapshots will be taken into account. An interesting future direction would be to directly extract (almost) conserved local operators with this approach, which would be in the case of many-body localization a complementary route to the extraction of the couplings $\tilde{J}_{ij}$ performed in the superconducting qubit experiment, section 9.2.3.

Again employing machine learning methods, we studied the transition between the thermalizing and the many-body localized phase in the Fock space snapshots of the one-dimensional Bose-Hubbard model in the long-time limit as well as during the time evolution. We showed that the confusion learning scheme introduced in Ref. [325] is well suited to find the transition. An interesting future direction is to employ different network architectures, such as for example recurrent neural networks, and to use the entire time trace as an input.

We proposed a protocol to use the Jarzynski equality to access the free energy of a system that is not necessarily in thermal equilibrium. With the measurements performed in Ref. [108], the free energy of the corresponding system – the chain of superconducting qubits with disorder studied in section 9.2 – can be directly evaluated. This method provides a valuable tool to further investigate the thermalization properties of a system.

The experimental setups discussed in this part of my thesis are extremely promising platforms to study interesting two-dimensional quantum many-body systems in the future, such as for example fractional quantum Hall physics. Moreover, the superconducting qubit setup with which we worked here is well suited to apply unitary gates, thus enabling digital quantum computing [102] as well as the implementation of random local unitary circuits [424]. From a theorists perspec-

tive, the development of schemes to realize and probe interesting phenomena, while employing the advantages of a given experiment, is an important and exciting task.

Part III

Appendices

A Methods

A.1 Exact diagonalization

The idea of exact diagonalization is to write down the Hamiltonian in some (more or less) convenient basis. This Hamiltonian can then be diagonalized exactly to obtain ground and excited states, finite temperature expectation values and time evolutions. For a Hilbert space dimension exceeding a certain size, the matrix cannot be diagonalized exactly anymore, as for example a dimension of 65536 already requires 34GB to store the full Hamiltonian matrix. As long as the Hamiltonian can still be stored efficiently, Lanczos techniques can be used to study all of the above, see Sec. A.1.5. Even with Lanczos techniques, exact diagonalization can only be used for comparably small system sizes, for example for low-energy properties of systems with 40 sites for a spin-1/2 model with $S^z_{tot} = 0$ or 20 sites for the Fermi-Hubbard model at half-filling, all while employing all possible symmetries [425]. In the following, we discuss the construction of Hilbert space and operators for different physical systems and Lanczos methods.

A.1.1 Spin systems

In a spin 1/2 system, the local Hilbert space dimension is two, spin up and spin down. A convenient representation of a Fock state is thus the binary representation: 0 corresponds to spin down, 1 to spin up. In order to construct a Hilbert space without taking any conserved quantities into account,

we can simply use the numbers between 0 and 2^{L-1}, where L is the number of sites. Each number corresponds then to the state given by its binary representation and all 2^L states are included.
In order to represent the S_i^+ operators for a given site i, we go through the basis states $|a\rangle$ and check whether the entry on position i is 0 or 1. If it is 1, no entry in the matrix for S_i^+ is made for this specific basis state. If the basis state entry on position i is 0, we construct the new state $|\tilde{a}\rangle$ by changing this 0 to a 1. The new state corresponds to a different position in the basis, namely the basis state at the position given by its binary representation. In the matrix for S_i^+ the entry in line $\tilde{a}$, column a is set to 1.
Once the S_i^+ operator is constructed, the remaining spin operators are obtained as $S_i^- = \left(S_i^+\right)^\dagger$ and $S_i^z = S_i^+ S_i^- - 1/2\hat{1}$. The Hamiltonian as well as arbitrary obesrvables are then constructed as sums of products of S_i^+, S_i^- and S_i^z for the different sites i.

S^z_{TOT} CONSERVATION

It often is helpful to make use of conservation laws in the Hamiltonian. In particular, this can mean to arrange the basis states according to a conserved quantity, such that for example states are sorted according to their value of S^z_{tot}. When the Hamiltonian conserves S^z_{tot} and is written in this reorganized basis, it becomes block-diagonal. This can be helpful in diagonalizing the Hamiltonian. Often one is only interested in a certain value of S^z_{tot}, for example because the ground state is in this sector or because a time evolution starting from a product state is considered.
The conservation of S^z_{tot} can be readily implemented using the same general concept as before. In the construction of the basis, we however only take states which are in the S^z_{tot} sector under consideration. This leads to a set of numbers a, given by the binary representation of these basis states, which is smaller than 2^L. These numbers are saved in a list, such that the index $l(a)$ of a given number a in this list corresponds to the number the state $|a\rangle$ takes in this block.
In order to construct the S_i^+ operator, two consecutive blocks of S^z_{tot} must be considered, since by applying S_i^+ we go from one block to the other. The construction of the operators is exactly the same as before, with the only difference that the entry in the matrix is not made at position $(\tilde{a}, a)$, but instead at position $(l_1(\tilde{a}), l_2(a))$. Here, $l_1(\tilde{a})$ corresponds to the index of $\tilde{a}$ in the list corresponding to the block with the higher number of S^z_{tot}.
If only one specific value of S^z_{tot} is considered, the operators S_i^z can be directly obtained in this subsector. The same holds for the product $S_i^+ S_j^-$, which usually appear in the Hamiltonian. Note however that applying the operators $S_i^\pm$ always changes the S^z_{tot} sector. If for example expectation values of the form

$$\langle\psi|S_i^- e^{-i\hat{H}t} S_j^+|\psi\rangle \tag{A.1}$$

are evaluated, the entire calculation, including the state $|\psi\rangle$ and the Hamiltonian $\hat{H}$ have to be considered in the combined subsectors of S^z_{tot}, $S^z_{\text{tot}} + 1$.
Taking the conservation of S^z_{tot} into account, the dimension of the Hilbert space used for practical calculations can be reduced from 2^L to

$$D(L,N) = \sum_{j=0}^{\left\lfloor \frac{N}{2} \right\rfloor} (-1)^j \binom{L+N-1-2j}{L-1} \binom{L}{j} = \binom{L}{N}, \tag{A.2}$$

where N is the number of spin ups in the block under consideration.

Shift operator $\hat{T}$ for spins

It can be useful to have an operator that shifts all spins by one site, for example to make use of translational invariance either in the pure spin system or in a spin system with a single hole, see Sec. A.1.2. In order to construct this operator directly, we can again make use of the binary representation. The shift operator $\hat{T}$ shifts each spin by one site to the right and attaches the right-most spin on the left side again. To explicitly construct $\hat{T}$, we do

- divide out the last site: $\tilde{a} = a - 2^{L-1} \cdot \text{bitget}(a, L)$
- shift everything by one site to the right: $\tilde{a} \to 2 \cdot \tilde{a}$
- preprend last entry of a as first entry of $\tilde{a}$: $\tilde{a} \to \tilde{a} + \text{bitget}(a, L)$.

Here, $\text{bitget}(a, L)$ means the L-th digit of the binary representation of a.

A.1.2 $t - J$ model with a single hole

For a single hole in the $t - J$ model, the Hilbert space can be constructed as L times the Hilbert space of a spin system with $L - 1$ sites, $D_{t-J}(L,N) = L \cdot D_{\text{spin}}(L-1,N)$. The Hamiltonian has a block structure: the blocks on the diagonal correspond to different hole positions, Fig. A.1.1 a). The entries are thus the spin Hamiltonians with dimension $D_{\text{spin}}(L-1,N)$ with the couplings according to the hole position turned off. On the off-diagonal, the hole hopping is implemented by connecting the according diagonal blocks through blocks of the form $t \cdot \hat{1}$.
In order to create a hole in a spin system, we need to construct a hole creation operator that acts in the according Hilbert space. The matrix representing this operator is rectangular, as it takes us from the $D_{\text{spin}}(L, N(+1))$-dimensional Hilbert space of the spin system to the $D_{t-J}(L,N)$-dimensional Hilbert space of the $t - J$ model. We distinguish between the creation of an up and a down hole, i.e. the annihilation of an up or down spin. To construct the up-hole creation operator on site i,

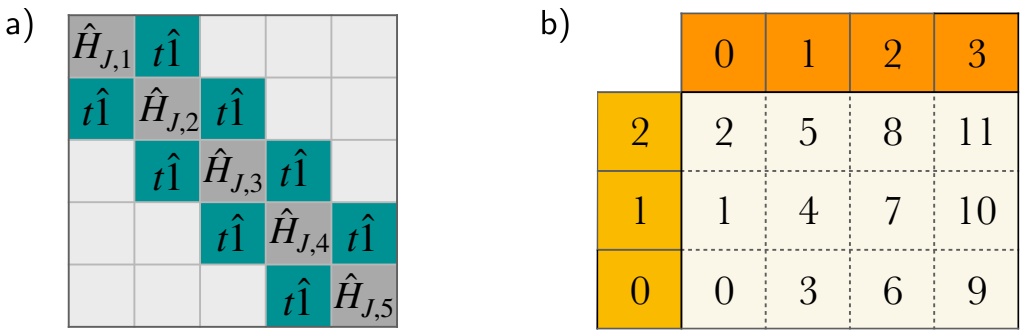

Figure A.1.1: Exact diagonalization methods. a) exemplary construction of the $t-J$ Hamiltonian for a single hole in one dimension. The blocks on the diagonal correspond to the spin part of the Hamiltonian, the off-diagonal terms are the hole hopping. b) Labeling of a two-dimensional lattice for convenient implementation in exact diagonalization.

$\hat{h}^{\dagger}_{i,\uparrow}$, we go through the spin basis for L sites and $N+1$ spin ups and check for each basis state $|a\rangle$ whether there is a spin up on site i. If no, the application of $\hat{h}^{\dagger}_{i,\uparrow}$ annihilates the state. If yes, we remove that site from the basis and thus construct a new state $|\tilde{a}\rangle$ on $L-1$ sites with N instead of $N+1$ spin ups. We find the index of this state in the $(L-1,N)$ basis and make an entry in the column corresponding to $|a\rangle$ and the row corresponding to $|\tilde{a}\rangle$ in the i-th block.
Note that we can further simplify the numerical calculations if the system is translationally invariant. In this case, we can apply a Lee-Low-Pines transformation which brings us in the co-moving frame of the hole. We then obtain a block diagonal Hamiltonian for each momentum value k with the dimension given by $D_{\text{spin}}(L-1,N)$, thus reducing the Hilbert space dimension under consideration by a factor of L.

Labeling a two-dimensional square lattice

So far, we only discussed the creation of operators along a chain of length L. The geometry of the Hamiltonian can in principle be arbitrary. Due to the limited system sizes that can be treated with exact diagonalization, one usually considers one-dimensional or small two-dimensional (2D) systems. In order to easily construct the Hamiltonian one usually labels the sites in a 2D system in a convenient way.
One straightforward example for the labeling of the sites is shown in Fig. A.1.1 b): the sites are sequentially labeled throughout the 2D grid with dimensions m_x, m_y. The index i of a site can be obtained from its 2D coordinates (x,y) as

$$i = x \cdot m_y + y. \tag{A.3}$$

A.1.3 Fermi-Hubbard model

The Hilbert space for spinful fermions corresponds to the product of the Hilbert spaces for two separate spin 1/2 systems, where the number of spin ups in the first spin system corresponds to the number of up fermions in the Fermi-Hubbard system, $N_1 = N_\uparrow$. Accordingly, the number of spin ups in the second spin system is given by the number of down fermions in the Fermi-Hubbard system, $N_2 = N_\downarrow$. We can therefore construct the two spin bases separately according to the description in Sec. A.1.1. The S^z_{tot} conservation for the spin Hilbert space corresponds to the conservation of $N_\uparrow$ and $N_\downarrow$ for the Fermi-Hubbard Hilbert space, thus reducing the dimension from 4^L to $D(L, N_\uparrow) \cdot D(L, N_\downarrow)$. We can further employ the same algorithm to construct the S_i^+ operators for a spin system. These operators can be used directly to obtain the $\hat{c}^\dagger_{i,\sigma}$ operators with $\sigma = \uparrow, \downarrow$, acting on the respective subspace of the Hilbert space, e.g.

$$\hat{c}^\dagger_{i,\uparrow} = \hat{S}_i^+ \otimes \hat{1}, \tag{A.4}$$

where the identity acts on the other spin chain. This construction is possible since nothing changes for the basis states of the down fermions when an up fermion is created/annihilated.
Since the S_i^+ operators are constructed within two subsectors of the total magnetization, it is useful to first obtain the terms $S_i^+ S_j^-$, which will be used in the Hamiltonian. This allows us to use only the block corresponding to the total magnetization or particle number $N_\uparrow$ under consideration in the Fermi-Hubbard Hamiltonian. Note that in the construction of operators, Fermi statistics need to be taken into account. In particular, one given convention for the ordering of the creation and annihilation operators has to be used consistently. For hopping terms this means that we need to include a factor $(-1)^{\Delta n}$, where Δn is the number of (up and down) fermions on intermediate sites. For a nearest neighbor hopping of σ fermions from site i to $i+1$, we need to include a factor of $(-1)^{\hat{n}_{i,\bar{\sigma}}}$, where $\bar{\sigma}$ is the flipped spin.

A.1.4 Bose-Hubbard model

For the Bose-Hubbard model, we cannot simply use the binary representation of numbers or modifications thereof as we did so far. The general strategy however remains the same: find a convenient representation of the basis states and then construct the operators $\hat{b}_i^\dagger$ by going through the basis. In order to get a manageable dimension of the Hilbert space, we use the conservation of the total particle number N and introduce a cut-off $n_{\max}$ to restrict the maximally possible occupation on

each site. The dimension of the Hilbert space of N particles on L sites is

$$D(L,N,n_{\max}) = \sum_{j=0}^{\left\lfloor \frac{N}{n_{\max}+1} \right\rfloor} (-1)^j \binom{L+N-1-j(n_{\max}+1)}{L-1} \binom{L}{j}. \tag{A.5}$$

We follow the algorithm presented in Ref. [426] to construct the basis states but modify it to accomodate the cut-off in the local particle number $n_{\max}$. For a given total particle number N, the basis is obtained as follows:

- start with all particles on the first site as initial state $|\psi_0\rangle$
- if $N > n_{\max}$, we obtain the next state from $|\psi_0\rangle$ with the algorithm given in Ref. [426] until we have a state for which the local occupations n_i all fulfill $n_i \leq n_{\max}$. This is then the initial state $|\psi_0\rangle$.
- we obtain the number of states for N particles on L sites,

$$d = \frac{(N+L-1)!}{N!(L-1)!}, \tag{A.6}$$

  which is an upper limit for the numer of states in the sector under consideration.
- while the count $c \leq d$, we construct a new state from the last state added to the basis. During the construction of the next state, the count c is increased by one for all intermediate states, even if those do not fulfill $n_i \leq n_{\max}$ for all sites i.

Through the construction of the basis states presented below, the states are ordered according to the rule that the state $|n_1, n_2, \ldots, n_L\rangle$ is *superior* to the state $|\tilde{n}_1, \tilde{n}_2, \ldots, \tilde{n}_L\rangle$ if $n_i = \tilde{n}_i$ for $1 \leq i \leq k-1$ and $n_k > \tilde{n}_k$. The construction of the next state, given $|\psi_0\rangle$, is done as follows:

- start with the highest state $|N00\ldots0\rangle$
- suppose $n_k \neq 0$ and $n_i = 0 \forall k+1 \leq i \leq L-1$
- obtain the next (*inferior*) state $|\tilde{n}_1, \tilde{n}_2, \ldots, \tilde{n}_L\rangle$ with
  - $\tilde{n}_i = n_i \forall 1 \leq i \leq k-1$
  - $\tilde{n}_k = n_k - 1$
  - $\tilde{n}_{k+1} = N - \sum_{i=1}^{k} \tilde{n}_i$
  - $\tilde{n}_i = 0$ for $i \geq k+2$.

We now have constructed the basis. The most straightforward way to obtain the operators $\hat{b}_i^\dagger$ is to go through this basis for particle number N and for each state get a new state after the application of the creation operator. Then, the index of this new state in the basis for particle number $N+1$ is searched by going through the entire basis. However, this last step is rather inefficient. Since we know exactly how we constructed the basis, we can infer the index of each basis state directly without having to search through an entire basis.
In particular, to construct the operator $\hat{b}_i^\dagger$ going from N to $N+1$ particles, we go through the basis states $|a\rangle$ and for each state, find the occupation on site i. If that occupation is $n_i \leq n_{\max} - 1$, we obtain a new state $|\tilde{a}\rangle$ in the $N+1$ particle basis by setting $\tilde{n}_i = n_i + 1$. The corresponding entry in the matrix for $\hat{b}_i^\dagger$ will be $\sqrt{n_i+1}$. We then find the position p of $|\tilde{a}\rangle$ in the basis by employing the same algorithm we used to construct the basis:

- initialize the number of remaining particles as $R = N+1$ and the position of $|\tilde{a}\rangle$ in the basis as $p = 1$
- loop through the sites $j = 1 : L-1$
  - for each site j, loop through the possible occupation numbers higher than the one realized in the current state: $n_j^{\text{higher}} = \tilde{n}_j + 1 : \min(N+1, n_{\max})$
    - calculate the number $D(L-j, R, n_{\max})$ of possibilities to distribute R particles on $L-j$ sites with the help of the formula in Eq. A.5
    - increase $p = p + D(L-j, R, n_{\max})$
  - update the number of remaining particles as $R = R - \tilde{n}_j$

As a result, the index p of $|\tilde{a}\rangle$ is obtained and we can make the corresponding entry in the matrix for $\hat{b}_i^\dagger$. Note that it can be beneficial to calculate and save $\binom{N}{k}$ for all needed values of N and k in the beginning of the algorithm and then later access them in a table instead of repeatedly performing the same calculation. The basis for all values of N can be constructed in the same way. Since we know from Eq. A.5 how big each block is, we know the start and end indices of the corresponding blocks in the combined Hilbert space, such that we can easily access the subsector under consideration later. The Bose-Hubbard Hamiltonian as well as arbitrary observables can be directly obtained using the raising and lowering operators.

A.1.5 Lanczos methods

The goal of the Lanczos methods presented here is to obtain some quantity, for which we in principle would need to diagonalize the Hamiltonian. We need to have some initial state $|\psi_0\rangle$ and know the action of the Hamiltonian $\hat{H}$ on any given state. Note that it is not strictly necessary to construct

the Hamiltonian explicitly to apply these algorithms. The main idea of the Lanczos algorithm is to repeatedly apply the Hamiltonian to $|\psi_0\rangle$ to obtain a small set of states which are important for the specific quantity we want to calculate.

Krylov basis

The Krylov basis is the set of states obtained by repeatedly applying the Hamiltonian to some initial state and subsequently orthonormalizing the new state with respect to the existing states. We start with some initial state $|v_0\rangle$, which depends on the problem under consideration. We then obtain a second state as

$$|\tilde{v}_1\rangle = \hat{H}|v_0\rangle - \varepsilon_0|v_0\rangle, \tag{A.7}$$

where $\varepsilon_n = \langle v_n|\hat{H}|v_n\rangle$ is the expectation value of $\hat{H}$. The norm of $|\tilde{v}_1\rangle$ is β_1 and we obtain $|v_1\rangle$ by normalizing $|\tilde{v}_1\rangle$ accordingly. Given the two states $|v_0\rangle$ and $|v_1\rangle$, we obtain the next state $|v_2\rangle$ as

$$|\tilde{v}_{n+1}\rangle = \hat{H}|v_n\rangle - \varepsilon_n|v_n\rangle - \beta_n|v_{n-1}\rangle \tag{A.8}$$

with $\beta_n = \sqrt{\langle\tilde{v}_n|\tilde{v}_n\rangle}$. The state $|v_2\rangle$ is obtained by normalizing $|\tilde{v}_2\rangle$. We continue to construct states $|v_n\rangle$ until $n \geq d_{\text{Krylov}}$ or other conditions for convergence are satisfied.
For most applications, it is not even necessary to save all the basis states $\{|v\rangle\}$ as discussed below. In general, we approximate the Hamiltonian as

$$\hat{H} = \hat{V}\hat{T}\hat{V}^\dagger, \tag{A.9}$$

where $\hat{V}$ is the Krylov basis and $\hat{T}$ is the tridiagonal matrix obtained as

$$\hat{T}_{n,m} = \langle v_n|\hat{H}|v_m\rangle = \langle v_n|\tilde{v}_{m+1}\rangle + \varepsilon_m\langle v_n|v_m\rangle + \beta_m\langle v_n|v_{m-1}\rangle = \beta_n\delta_{n,m+1} + \varepsilon_m\delta_{n,m} + \beta_m\delta_{n,m-1}. \tag{A.10}$$

The dimension of this matrix $\hat{T}$ is given by the number of states in the Krylov basis which can usually be chosen to be much smaller than the dimension of the full Hamiltonian $\hat{H}$.

Dynamics

To calculate the time evolution of some state $|\psi_0\rangle$ under the Hamiltonian $\hat{H}$, we first construct the Krylov basis as described above. Note that we do not need to save all the basis states but in each step n only keep the two preceeding vectors $|v_{n-1}\rangle$ and $|v_n\rangle$. Note that with step n, the constructing of the state $|v_{n+1}\rangle$ is meant as we start from the state $|v_0\rangle$. With all available values β_i, ε_i, $i \leq n$, we

construct the matrix $\hat{T}$, Eq. A.10 and diagonalize it such that

$$\hat{T} = \hat{U}\hat{D}\hat{U}^{\dagger}. \tag{A.11}$$

The contribution to the time-evolved state is then obtained with the help of

$$|\varphi\rangle = \hat{U}e^{-it\hat{D}}\hat{U}^{\dagger}\hat{e}_1, \tag{A.12}$$

where t is the time and $\hat{e}_1 = (1, 0, 0, \ldots, 0)^T$ in Krylov space. If the last entry in $|\varphi\rangle$, φ_n (since we are in the n-th step of constructing the Krylov basis), is smaller than some threshold, we can stop here and do not need to calculate further states in the Krylov basis. The time evolved state is in each step n updated as

$$|\psi(t)\rangle = |\psi(t)\rangle + \varphi_{n-2}|v_{n-1}\rangle, \tag{A.13}$$

where φ_{n-2} is the corresponding entry in $|\varphi\rangle$.
In order to now time evolve a given state $|\psi_0\rangle$ up to time t, we discretize the time steps as $dt = t/N_{\text{steps}}$. We only time evolve by dt to obtain a new state $|\psi(dt)\rangle$, from which we construct a new Krylov basis and again time evolve by dt. This process is then repeated N_{steps} times.

Spectral function

The spectral function can be written as

$$A(\omega) = \frac{1}{\pi}\Im G_A(\omega + i\eta + E_0) \tag{A.14}$$

with the Green's function

$$G_A(z) = \langle\psi_0|\hat{A}^{\dagger}(z - \hat{H})^{-1}\hat{A}|\psi_0\rangle \tag{A.15}$$

for some operator $\hat{A}$. In Krylov space, we can approximate this Green's function as [204, 427]

$$\tilde{G}_A(z) = \langle\psi_c|\frac{1}{z - \hat{T}}|\psi_c\rangle = \sum_{n=0}^{d_{\text{Krylov}}} \frac{1}{z - \tilde{E}_n} \langle\psi_c|\tilde{\psi}_n\rangle \langle\tilde{\psi}_n|\psi_c\rangle . \tag{A.16}$$

Here, $|\psi_c\rangle = A|\psi_0\rangle$ and $\tilde{E}_n$, $|\tilde{\psi}_n\rangle$ are the eigenvalues and corresponding eigenvectors of $\hat{T}$. The Krylov space is constructed with $|\psi_c\rangle$ as initial state.
Upon constructing the basis state, we thus keep the values of ε_n and β_n as before to construct $\hat{T}$. For every basis vector n we moreover need to calculate $\langle\psi_c|\hat{V}|\tilde{\psi}_n\rangle$ where $\hat{V}$ is the Krylov basis. This however corresponds to the first entry in $\hat{V}|\tilde{\psi}_n\rangle$ by construction of $\hat{V}$. We thus save the energies $\tilde{E}_n$ and the corresponding weights $|\langle\psi_c|\hat{V}|\tilde{\psi}_n\rangle|^2$. With this values, we can obtain the Green's function

for arbitrary values of z as

$$G_A(z) = \sum_{n=0}^{d_{\text{Krylov}}} \frac{1}{z - \tilde{E}_n} |\langle \psi_c | \hat{V} | \tilde{\psi}_n \rangle|^2. \tag{A.17}$$

The spectral function is then obtained as

$$A(\omega) = \frac{1}{\pi} \Im \sum_{n=0}^{d_{\text{Krylov}}} \frac{1}{\omega + i\eta + E_0 - \tilde{E}_n} |\langle \psi_c | \hat{V} | \tilde{\psi}_n \rangle|^2. \tag{A.18}$$

Finite temperature

Lanczos techniques can also be used to calculate finite temperature expectation values [428, 429]. In this case, the initial state for the Krylov basis is a random state and we sample over many different random states. The expectation value is then written as

$$\langle \hat{A} \rangle = \frac{D}{R \cdot Z} \sum_{r=1}^{R} \sum_{j=0}^{d_{\text{Krylov}}} e^{-\beta \tilde{E}_j^r} \left\langle r | \tilde{\psi}_j^r \right\rangle \langle \tilde{\psi}_j^r | \hat{A} | r \rangle, \tag{A.19}$$

where R is the number of random states used and D is the dimension of the (subsector of the) Hilbert space under consideration. The partition sum can be calculated as

$$Z = \frac{D}{R} \sum_{r=1}^{R} \langle r | \hat{V} \hat{U} e^{-\beta \hat{D}} \hat{U}^\dagger \hat{V}^\dagger | r \rangle \tag{A.20}$$

and the thermal expectation value of the operator $\hat{A}$ thus becomes

$$\langle \hat{A} \rangle = \frac{\sum_{r=1}^{R} \langle r | \hat{V} \hat{U} e^{-\beta \hat{D}} \hat{U}^\dagger \hat{V}^\dagger \hat{A} | r \rangle}{\sum_{r=1}^{R} \langle r | \hat{V} \hat{U} e^{-\beta \hat{D}} \hat{U}^\dagger \hat{V}^\dagger | r \rangle}. \tag{A.21}$$

Where for each random state $|r\rangle$ a separate Krylov basis $\hat{V}$ and correspondingly matrix $\hat{T}$ and its diagonalization $\hat{D}$, $\hat{U}$ is created.
For very low temperatures, the finite temperature Lanczos method does not converge well and instead the low temperature Lanczos method should be used, see Ref. [430].

Finite temperature spectral function

The methods introduced above can be combined to obtain the spectral function at finite temperatures [428]. Assume we want to calculate

$$A(k,\omega) = \frac{1}{Z_o}\sum_{n,m} e^{-\beta E_n^N} |\langle \psi_m^{N-1}|\hat{c}_k|\psi_n^N\rangle|^2 \delta(\omega - E_m^{N-1} + E_n^N) = \frac{1}{\pi}\Im G(k,\omega) \tag{A.22}$$

with

$$G(k,\omega) = \frac{1}{Z_o}\sum_n e^{-\beta E_n} \langle \psi_n(N-1)|(\omega - \hat{H} - i\eta)^{-1}|\psi_n(N-1)\rangle \tag{A.23}$$

and $|\psi_n(N-1)\rangle = \hat{c}_k|\psi_n^N\rangle$. Without the finite temperature Lanczos method, we could now go through all eigenstates $|\psi_n^N\rangle$ of the Hamiltonian, apply $\hat{c}_k$ to obtain $|\psi_n(N-1)\rangle$ and then generate for each of these D states a Krylov basis $\hat{V}$. The finite temperature spectral function can then be calculated as described in A.1.5 with an additional thermal weight given by $e^{-\beta E_n^N}/Z_o$ for the contribution of the state $|\psi_n^N\rangle$.
Instead, we can also use the finite temperature Lanczos method and sample R random states $|r\rangle$, for each of which we generate a Krylov basis. The Green's function is then calculated as

$$G(k,\omega) = \frac{1}{Z}\sum_r \sum_l \sum_m e^{-\beta\varepsilon_l^{(r)}} \left\langle r|\psi_l^{(r)}\right\rangle \frac{\langle \psi_l^{(r)}|\hat{c}_k^\dagger \hat{V}^{(h)}|\varphi_m^{(h)}\rangle \langle \varphi_m^{(h)}|\hat{V}^{(h)\dagger}\hat{c}_k|r\rangle}{\omega + i\eta + \varepsilon_l^{(r)} - E_m^{(h)}} \tag{A.24}$$

with

$$Z = \sum_r \sum_l |\left\langle r|\psi_l^{(r)}\right\rangle|^2 e^{-\beta\varepsilon_l^{(r)}}. \tag{A.25}$$

For the calculation of A.24, we can use the following:

- for each random vector $|r\rangle$, a Krylov basis $\hat{V}$ is created. The overlap $\left\langle r|\psi_l^{(r)}\right\rangle$ equals the first entry in the l-th eigenstate of the matrix $\hat{T}$, the energy $\varepsilon_l^{(r)}$ is the corresponding eigenvector.
- from the eigenstate $|\varphi_l^{(r)}\rangle$ of $\hat{T}$ we calculate $\hat{c}_k|\psi_l^{(r)}\rangle = \hat{c}_k\hat{V}|\varphi_l^{(r)}\rangle$.
- analogous to Section A.1.5, we use $\hat{c}_k|r\rangle$ as initial state for the Krylov basis $V^{(h)}$ to calculate the spectral function.
- from this, we obtain $\hat{T}^{(h)}$, which is diagonalized to get the eigenstates $|\varphi_m^{(h)}\rangle$ and corresponding eigenvalues $E_m^{(h)}$.
- as in Section A.1.5, we obtain a list of energies and corresponding weights. In this case, the same energy can appear twice. Before the spectral function is calculated from the Green's function, these weights are added up and the second entry is removed from the list.

A.2 Matrix Product States: ground state and dynamics with TeNPy

For small system sizes, the exact diagonalization methods introduced in section A.1 are the technique of choice. However, the Hilbert space of a quantum many-body system grows exponentially with the size of the system, and therefore the limitations of exact diagonalization are typically reached at systems with a few tens of lattice sites. In order to numerically simulate larger system, one needs some way of truncation, since it is impossible to keep all basis states. One of the most successful numerical methods is the density matrix renormalization group (DMRG) introduced by Steven White in 1992 [431]. This method is based on the idea to use the entanglement properties of the system to choose a clever subset of basis states in which to perform the calculation, omitting states which do not play a big role for the properties of the system. In this appendix, we give a brief overview over matrix product states, matrix product operators and the DMRG algorithm. For a comprehensive introduction on the subject and a discussion of all the technical details we recommend the excellent review articles Ref. [432] and Ref. [433].

For a typical state, such as most randomly chosen states from a given Hilbert space, the bipartite entanglement exhibits a volume law. That means that the entanglement between two parts of the system grows with their size. However, the ground states of gapped, local systems follows an area law: the bipartite entanglement scales with the area of the border between the two parts of the system. In a Schmidt decomposition of the states, the Schmidt values decay rapidly in this case. This allows for an efficient truncation by neglecting states with small values in the Schmidt decomposition.

A generic pure quantum state for a system with N sites can be written as

$$|\psi\rangle = \sum_{j_1,j_2,\ldots,j_N} \psi_{j_1 j_2 \ldots j_N} |j_1, j_2, \ldots, j_N\rangle, \tag{A.26}$$

with a local basis j_n on site n with $j_n = 1, \ldots, d$. Here, d is the local Hilbert space dimension, which is e.g. $d = 2$ for a spin-1/2 system, $d = 3$ for the $t - J$ model and $d = 4$ for the Fermi-Hubbard model. The idea of a matrix product state is then to write the coefficients $\psi_{j_1 j_2 \ldots j_N}$ as a product of matrices, with one matrix for each site $i = 1, \ldots, N$ [433]:

$$|\psi\rangle = \sum_{j_1,j_2,\ldots,j_N} M^{[1]j_1} M^{[2]j_2} \ldots M^{[N]j_N} |j_1, j_2, \ldots, j_N\rangle, \tag{A.27}$$

where $M^{[n]j_n}$ is a $\chi_n \times \chi_{n+1}$ dimensional matrix. χ_n is the bond dimension, which determines how many states are kept. Changing the bond dimension in a simulation allows for a convergence check: if the bond dimension is changed significantly, but the physical properties do not change anymore, the simulation is likely to be converged. At the boundary, the matrices are vectors, since the bond

dimensions $\chi_1 = 1$ and $\chi_{N+1} = 1$. For each site, we will have d matrices – one for each physical index – which are typically grouped together into one tensor of order three.
In principle, this representation is exact, if we choose the bond dimension χ sufficiently big. In practice, the dimension of the Hilbert space grows exponentially with the system size, such that a truncation is necessary to be able to tackle the problem with reasonable computational ressources. This truncation is done by limiting the bond dimension and thus the size of the matrices. After some procedures, it is necessary to *compress* the matrix product state, i.e. to reduce the bond dimension due to a prior increase. Such an increase in bond dimension happens for example due to the summation of two matrix product states, or due to the application of a matrix product operator (see below) to the matrix product state. There are two general routes to do so: variational compression and SVD (singular value decomposition) compression. Variational compression is in general computationally cheaper, but relies on a reasonable starting state for the variational procedure. The idea here is to find the best approximation of the given MPS with large bond dimension χ' in the space of matrix product states with smaller bond dimension χ. For SVD compression, one does not need a suitable starting state. Depending on how big χ' is compared to χ, the computational cost for this procedure is however $\mathcal{O}(\chi'^2 d\chi)$ if $\chi' \leq d\chi$ and $\mathcal{O}(\chi' d^2 \chi^2)$ otherwise [432].
Note that the MPS representation in Eq. (A.27) is not unique, since there is some freedom in transforming the matrices. A common choice is the canonical form, where each matrix M (omitting sub- and superscripts) is decomposed into a product of a matrix Γ and a square, diagonal matrix Λ. Bringing an arbitrary MPS into canonical form – usually by a sequence of singular value decompositions – is an operation of $\mathcal{O}(\chi^3)$ [432].

A.2.1 Constructing the Hamiltonian as MPO

Matrix product operators (MPOs) are the natural generalization of matrix product states to operators. Similar to Eq. (A.27), we can represent an operator as

$$O = \sum_{j_1,\dots,j_N,j'_1,\dots,j'_N} v^L W^{[1]j_1 j'_1} W^{[2]j_2 j'_2} \dots W^{[N]j_N j'_N} v^R |j_1, \dots, j_N\rangle \langle j'_1, \dots, j'_N|, \tag{A.28}$$

where each $W^{[n]j_n j'_n}$ is a $D \times D$ matrix with operators as entries [433]. Here, D is determined by the object we are representing and is typically much smaller than the bond dimension χ of the MPS. The left and right vectors v^L, v^R terminate the MPO at the boundaries and are correspondingly given by

$$v^L = (1, 0, \dots, 00) \qquad v^R = (0, 0, \dots, 0, 1)^T \tag{A.29}$$

with a length given by D.
A local Hamiltonian with short-range interactions can be represented exactly using an MPO with a

comparably small dimension D. But also for long-range interactions, a good approximation of the Hamiltonian as MPO is often possible [432]. A typical example for the construction of an MPO is the XXZ Heisenberg spin chain, which is described by the Hamiltonian

$$H = \sum_n \left[J \left(S_n^x S_{n+1}^x + S_n^y S_{n+1}^y + \Delta S_n^z S_{n+1}^z \right) + h_z S_n^z \right] . \tag{A.30}$$

In order to obtain its MPO representation, it is useful to write the Hamiltonian as a tensor product,

$$\begin{aligned} H = & J[S^x \otimes S^x \otimes 1 \otimes 1 \otimes \ldots \otimes 1 + 1 \otimes S^x \otimes S^x \otimes 1 \otimes \ldots \otimes 1 + \ldots \\ & + S^y \otimes S^y \otimes 1 \otimes 1 \otimes \ldots \otimes 1 + 1 \otimes S^y \otimes S^y \otimes 1 \otimes \ldots \otimes 1 + \ldots \\ & + \Delta \left(S^z \otimes S^z \otimes 1 \otimes 1 \otimes \ldots \otimes 1 + 1 \otimes S^z \otimes S^z \otimes 1 \otimes \ldots \otimes 1 + \ldots \right)] \\ & + h_z \left(S^z \otimes 1 \otimes 1 \otimes \ldots \otimes 1 + 1 \otimes S^z \otimes 1 \otimes \ldots \otimes 1 + \ldots \right) . \end{aligned} \tag{A.31}$$

The corresponding matrix product operator for a given site n can then be written as

$$W^{[n]} = \begin{pmatrix} 1 & S^x & S^y & S^z & h_z S^z \\ 0 & 0 & 0 & 0 & J S^x \\ 0 & 0 & 0 & 0 & J S^y \\ 0 & 0 & 0 & 0 & J \Delta S^z \\ 0 & 0 & 0 & 0 & 1. \end{pmatrix} \tag{A.32}$$

Taking the product in Eq. (A.30) yields the correct expression for the Hamiltonian. Constructing the MPO for a given Hamiltonian is typically straightforward, but – depending on the terms in the Hamiltonian – can require a bit of book-keeping. We follow the steps below to construct the MPOs used in this thesis, which are typically for a cylinder geometry. In this geometry, we consider one (or two, depending on the couplings) rings around the cylinder. Within a ring, we treat the first and last site slightly differently.

- Define the local Hilbert space dimension d and the corresponding operators. For example, $d = 3$ for the $t-J$ model. In this case, for example the spin operators used in the MPO need to have dimension $d = 3$ accordingly.
- The entries in the top left and bottom right corner of each matrix $W^{[n]}$ are 1.
- In the first row of each $W^{[n]}$, put all possible operators from which a term in the Hamiltonian can start
- Starting in the second row, in the first column to the right of the last entry in the first row,

put identities on the diagonal until the second to last column. In some cases, we want to change the entries on some of said diagonals from identities to other operators, for example if we need Jordan-Wigner strings connecting the two operators in the first row and the last column. In the example above, this step changes nothing, as the last entry in the first row is already in the second to last column.

- Finalize the term in the Hamiltonian with the corresponding operator in the last column.

- In order to figure out which operator goes where – which can be a bit cumbersome on a cylinder – it is useful to know that the coupling between sites i and $i + r$ in the Hamiltonian corresponds to the entry in the last column at position $N_{op} \cdot (r - 1)$, where N_{op} is the number of operators used in the first row.

A.2.2 DMRG

Here, we very briefly outline the general idea of the DMRG algorithm to obtain the ground state of a Hamiltonian under consideration. For a detailed discussion we strongly recommend the review articles [432] and [433]. The DMRG algorithm is a variational approach to optimize the matrix product state with regards to the energy. In particular, one considers bond after bond and variationally optimizes the tensors of the two neighboring sites on this bond to minimize the ground state energy $\langle\psi|H|\psi\rangle$, all while keeping the rest of the chain fixed. The ground state within the space spanned by the basis set on the bond under consideration can be found for example with a standard Lanczos algorithm. The effective Hamiltonian is a matrix with dimensions $\chi_{max}^2 d^2 \times \chi_{max}^2 d^2$. In the Lanczos algorithm, the most costly operation is the matrix-vector multiplication, which scales as $\mathcal{O}(\chi_{max}^3 D d^2 + \chi_{max}^2 D^2 d^3)$ [433]. Once the ground state in the subspace is found, a singular value decomposition has to be applied to get the MPS back to canonical form. Additionally, if the maximal bond dimension is already reached, one needs to truncate to avoid the growth $\chi \to d\chi$. The same procedure is then repeated for the next bond.
The computational cost can be lowered by making use of conserved quantities, such as the charge or $S^{z,tot}$. In this case, the tensors can be brought into a block-diagonal structure, which can be kept during the entire algorithm. A block diagonal structure lowers the computational cost, for example of the SVD. In TeNPy, conserved quantities are conveniently implemented through a vector, which gives the value of each conserved quantity for each basis state. Correspondingly, the entries in the Hamiltonian have to be zero if the conserved quantities do not match up [433].

A.2.3 MPO based time evolution

This section is based on the supplemenary material of the publication

- Annabelle Bohrdt, Fabian Grusdt, Michael Knap: "Dynamical formation of a magnetic polaron in a two-dimensional quantum antiferromagnet" – New J. Phys. 22 123023 (2020) [arXiv:1907.08214]

Structure and text have been rearranged and adapted here.

In sections 5.4 and 5.5, we consider a cylinder with $L_r = 4$ legs and the matrix product operator representing the Hamiltonian thus contains terms coupling sites at a distance of up to L_r. After creating a hole in the origin by applying $\hat{c}_{0,0}$, we time-evolve the matrix product state with the matrix product operator based technique introduced in Ref. [313]. This method has the advantages that it can be applied to long-ranged Hamiltonians, such as our model on the cylinder, while preserving the symmetries of the problem and that it has a constant error per site.
In the Euler approximation of the operator exponential

$$e^{-i\delta\hat{H}} = 1 - i\delta \sum_j \hat{H}_j + \mathcal{O}(\delta^2), \tag{A.33}$$

where $\hat{H} = \sum_j \hat{H}_j$ and the $\hat{H}_j$ act on a subset of the lattice, the error per site is $L\delta^2$, since L^2 combinations of $\hat{H}_j$ are omitted. In Ref. [313], a local version of the Euler stepper in the next order was introduced,

$$\hat{U}^{\mathrm{II}}(\delta) = 1 - i\delta \sum_j \hat{H}_j - \frac{1}{2}\delta^2 \sum_{j,k}{}'' \hat{H}_j \hat{H}_k + \ldots, \tag{A.34}$$

where the sum $\sum''_{j,k}$ runs over all terms $\hat{H}_j, \hat{H}_k$ with maximally one overlapping site. In this approximation, only $\mathcal{O}(L)$ contributions, namely those that overlap, are omitted and the error per site is therefore constant in the system size. Moreover, contributions with arbitrary powers of single-site terms are treated exactly here. While there is no closed general matrix product operator representation for $\hat{U}^{\mathrm{II}}(\delta)$, there exists an approximation scheme with error $\mathcal{O}(\delta^3)$. Details on this approximation and the algorithm to obtain the corresponding MPO can be found in Ref. [313], see also Refs. [434–436]. For a review on time evolution techniques for matrix product states see Ref. [437].

A.3 Metropolis Monte Carlo sampling

A.3.1 Snapshots from an MPS

Our starting point is a matrix product state $|\psi\rangle$, for example the ground state of the $t-J$ model with a single hole, and we want to sample real space snapshots using a standard Metropolis Monte Carlo sampling algorithm. In the following, we denote such a real space snapshot, or the configuration of spin ups, spin downs and holes, by a. In order to apply the Monte Carlo algorithm, we need to specify allowed steps to obtain a new configuration, e.g. the exchange of the occupation of two neighboring sites. Another option would be to exchange two randomly chosen, possibly distant, sites. Once a protocol to obtain a new configuration is chosen, we can calculate the number of possible updates M_n reachable from a given configuration a_n.
The sampling procedure is as follows:

1. choose a random configuration $a_0 = a$, with the corresponding number of spin ups, spin downs and holes

2. calculate the probability $p(a) = |\langle a|\ \psi\rangle|^2$

3. while $n < n_{\max}$ do

   (a) find the number of possible updates $M(a)$, randomly choose one of them as proposed configuration a'.

   (b) calculate the probability $p(a') = |\langle a'|\ \psi\rangle|^2$

   (c) find the number of possible updates $M(a')$

   (d) the transition probability is given by $A(a'|a) = \min\left(1, \frac{M(a)p(a')}{M(a')p(a)}\right)$

   (e) draw a random number $r \in [0, 1)$

   - if $r < A(a'|a)$, the state is accepted and $a_{n+1} = a'$
   - if not, then the state is rejected and $a_{n+1} = a_n$.

Initially, the probabilities in general increase rapidly and then settle to a more or less constant value for large n. The first snapshot should not be extracted from above procedure while the $p(a_n)$ are still increasing significantly. Then, every l-th snapshot is saved, where l should be sufficiently big to allow for changes all across the system, $l = \mathcal{O}(L_x \cdot L_y)$.
Usually, one repeats the entire process several times, i.e. starts at 1. with different randomly chosen initial states, to ensure that the extracted snapshots are really independent of one another.

A.3.2 π-FLUX STATES

This section is based on the supplemenary material of the publication

- Christie S. Chiu, Geoffrey Ji, Annabelle Bohrdt, Muqing Xu, Michael Knap, Eugene Demler, Fabian Grusdt, Markus Greiner, Daniel Greif: "String patterns in the doped Hubbard model" – Science Vol. 365, Issue 6450, pp. 251-256 (2019) [arXiv:1810.03584]

Structure, text and figures have been rearranged and adapted here.

Shortly after the discovery of high-temperature superconductivity in the cuprate materials, Anderson proposed the resonating valence bond (RVB) states as a possible description of these systems [30]. We simulate such RVB states, for example in section 6.2 and in Ref. [15], by sampling Fock space snapshots from the Gutzwiller projected thermal density matrix of the mean-field Hamiltonian

$$\begin{aligned}\hat{H}_{MF} = &-\frac{1}{2}J^*\sum_{\mathbf{i}\in A}\sum_{\sigma}\left(e^{i\theta_\circ}\hat{c}^\dagger_{\mathbf{i},\sigma}\hat{c}_{\mathbf{i}+\mathbf{x},\sigma} + e^{-i\theta_\circ}\hat{c}^\dagger_{\mathbf{i},\sigma}\hat{c}_{\mathbf{i}+\mathbf{y},\sigma} + h.c.\right)\\ &-\frac{1}{2}J^*\sum_{\mathbf{i}\in B}\sum_{\sigma}\left(e^{-i\theta_\circ}\hat{c}^\dagger_{\mathbf{i},\sigma}\hat{c}_{\mathbf{i}+\mathbf{x},\sigma} + e^{i\theta_\circ}\hat{c}^\dagger_{\mathbf{i},\sigma}\hat{c}_{\mathbf{i}+\mathbf{y},\sigma} + h.c.\right)\end{aligned} \tag{A.35}$$

introduced in section 5.1.1. Here, $\mathbf{i} \in A(B)$ denoting lattice sites $\mathbf{i}$ which are part of the A(B) sublattice and $\hat{c}^{(\dagger)}_{\mathbf{i},\sigma}$ is the annihilation (creation) operator of a fermion with spin σ. The Hamiltonian describes a system with staggered flux $\pm\Phi = \pm 4\theta_\circ$. We choose $\theta_\circ = \frac{\pi}{4}$. Although it features no long-range AFM order, this choice of parameters leads to a very low variational energy for the ground state at half filling and it is also often considered as a candidate state at finite doping [282]. We want to obtain Fock states of fermions described by the Gutzwiller projected thermal density matrix $\hat{\rho} = \mathcal{P}_{GW}e^{-\hat{H}_{MF}/k_BT}\mathcal{P}_{GW}$. In order to do so, we simultaneously sample in real and momentum space. The sampling in real space yields the required snapshots. The Gutzwiller projection is automatically taken into account, as no site can be occupied by more than one particle. We sample in momentum space to describe the finite temperature state correctly. We diagonalize $\hat{H}_{MF}$ to obtain the dispersion relation, which is necessary to determine the thermal weights. The combination of real and momentum space sampling is taken into account through the Slater determinant.
Fourier transforming $\hat{H}_{MF}$ leads to

$$\hat{H}_{MF} = \sum_{\mathbf{k}\in MBZ,\sigma}\begin{pmatrix}\hat{c}^\dagger_{\mathbf{k},\sigma} & \hat{c}^\dagger_{\mathbf{k}+\mathbf{G},\sigma}\end{pmatrix}\hat{h}_{\mathbf{k}}\begin{pmatrix}\hat{c}_{\mathbf{k},\sigma}\\ \hat{c}_{\mathbf{k}+\mathbf{G},\sigma}\end{pmatrix} \tag{A.36}$$

with

$$\hat{h}_{\mathbf{k}} = \mathrm{Re}R(\mathbf{k})\hat{\tau}^z + \mathrm{Im}R(\mathbf{k})\hat{\tau}^y \tag{A.37}$$

and

$$R(\mathbf{k}) = -J^* \left(\cos k_x e^{i\theta_\circ} + \cos k_y e^{-i\theta_\circ} \right), \tag{A.38}$$

with Pauli matrices $\hat{\boldsymbol{\tau}} = (\hat{\tau}^x, \hat{\tau}^y, \hat{\tau}^z)$. Here, $\mathbf{k} \in MBZ$ denotes momenta $\mathbf{k} = \left(k_x, k_y\right)$ in the magnetic Brillouin zone. Diagonalizing $\hat{h}_\mathbf{k}$ leads to two eigenstates $\left|u_{\mathbf{k},\mu}\right\rangle = \left(u^\circ_{\mathbf{k},\mu}, u^1_{\mathbf{k},\mu}\right)^T$ for every momentum $\mathbf{k}$ in the magnetic Brillouin zone. Bloch's theorem yields the wave function

$$\psi_{\mathbf{k},\mu}(\mathbf{r}) = \frac{1}{\sqrt{L^2}} \left(u^\circ_{\mathbf{k},\mu} + u^1_{\mathbf{k},\mu} e^{-i\mathbf{G}\mathbf{r}} \right) e^{-i\mathbf{k}\mathbf{r}} \tag{A.39}$$

with band index $\mu = \pm$. We consider a system of 16 by 16 sites and cut out a circular region of interest of the same size as in the experiment to obtain the same boundary effects in both cases. For a given doping value, we assume a spin balanced system and start from a random occupation of states in momentum space for both up and down fermions as well as a random configuration without double occupancies in real space. The exclusion of states with double occupancies in the sampling corresponds to applying the Gutzwiller projection. From any given state, updates in real space as well as updates in momentum space for up and down fermions are possible. In real space, two neighboring sites can exchange their occupation if they differ. In momentum space, a given fermion can change its momentum to any other unoccupied momentum. Note that in momentum space, we treat up and down fermions separately from each other such that two fermions of opposite spin can have the same momentum. The snapshots are generated by Metropolis Monte Carlo sampling [113] according to the probability distribution

$$p_\beta(a_\mathbf{r}, a_\mathbf{k}) = e^{-\beta E(a_\mathbf{k})} \left| \langle a_\mathbf{r} | a_\mathbf{k} \rangle \right|^2, \tag{A.40}$$

where $\beta = (k_B T)^{-1}$ is the inverse temperature and $\left|a_{\mathbf{r}(\mathbf{k})}\right\rangle$ denote Fock states in configuration (momentum) space. Note that Eq. (A.40) is not normalized. However, the normalization does not matter for the Metropolis sampling, since only ratios of probability distributions are required. In Fig. A.3.1 a), the evolution of the logarithm of the probabilities during sampling is shown. The energy of a state $|a_\mathbf{k}\rangle$ is given by

$$E(a_\mathbf{k}) = \sum_{\mathbf{k}\text{ occ. in } a_\mathbf{k}} \varepsilon(\mathbf{k}) \tag{A.41}$$

with eigenenergies $\varepsilon(\mathbf{k})$ of $\hat{h}_\mathbf{k}$ and $\mathbf{k}$ occ. in $a_\mathbf{k}$ denotes momenta $\mathbf{k}$ which are occupied in the considered Fock state $|a_\mathbf{k}\rangle$.

After generating a sample of several thousand Fock states a_r, doublon-holon pairs are artificially added with a probability given by $4t^2/U^2$ on nearest-neighbor sites with opposite spins for the data

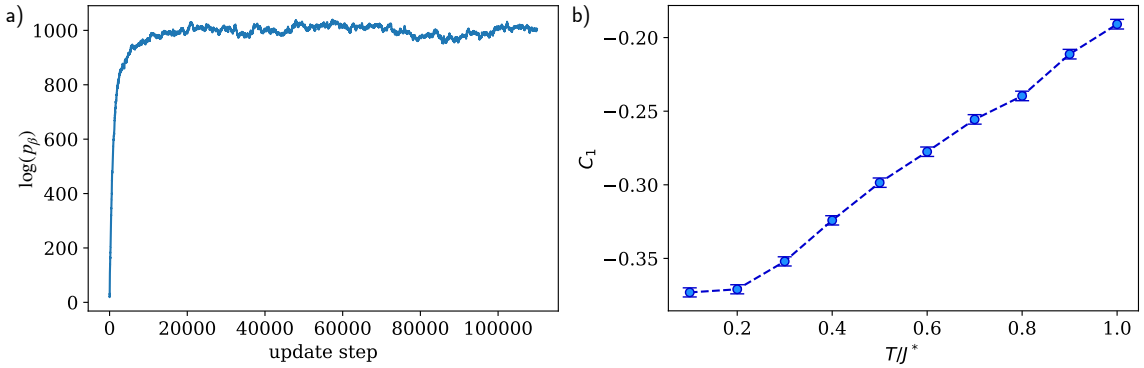

Figure A.3.1: Sampling snapshots for π-flux theory. a) Logarithmic probabilities $\log(p_\beta)$ for the Metropolis Monte Carlo sampling at $T = 0.5J^*$ for one particle per site. After a fast initial increase, the probability saturates at a constant value. Once this plateau is reached, snapshots are taken during the sampling. Between two snapshots that are used in the analysis, we sample 2000 steps. Each set of snapshots consists of several independent Monte Carlo runs starting from randomly chosen initial configurations. b) Temperature dependence of the nearest neighbor spin correlation at half-filling. While the temperature dependence is qualitatively similar to the behavior in the Heisenberg model, see Fig.6.5.6, the absolute values differ.

shown in chapter 6. The experimentally measured anti-moment correlator as shown in Fig. 6.3.6 of the main text, as well as numerics[438], indicate that restricting doublon-hole pairs to nearest neighbors is a valid approximation in this regime, see also Fig.3.1.1. In the following, we consider a region of interest of the same size and shape as in the experiment. Furthermore, we simulate the experimental imaging procedure and keep in every snapshot the knowledge of either the parity-projected density distribution of both spins or with one spin state removed. The coupling $J^* = 3J$ in the mean field Hamiltonian is chosen such that at half filling, the nearest- and next-nearest-neighbor spin correlators obtained from the simulation at the temperature $T = 0.2J^* = 0.6J$ fit the experimental data as closely as possible. Without any other fitting parameter, the doping dependence of the nearest neighbor spin correlator is described correctly. However, the temperature dependence of the spin correlators even at half filling is not captured correctly with these parameters.

In Fig. A.3.1 b), the temperature dependence of the nearest neighbor spin correlation C_1 at half-filling is shown for the π-flux theory snapshots without doublon-hole pairs. While the general trend with temperature is the same as in the Fermi-Hubbard model at half-filling, or the Heisenberg model, see Fig. 6.5.6, the temperature can not be scaled up linearly: while $T/J = 0.6$ in the Heisenberg model roughly corresponds to $T/J^* = 0.2$ for the *pi*-flux theory, doubling the temperature leads to $C_1 = -0.22$ for $T/J = 1.2$ in the Heisenberg model and $C_1 = -0.32$ for $T/J^* = 0.4$ in π-flux theory. Since the temperature enters the density matrix before the Gutzwiller projection, there is no one-to-one correspondence with the actual temperature.

In Ref. [15], we use the same algorithm to sample snapshots for a π-flux as well as a uniform RVB

state and free fermions. In the latter case, we do not constrain ourselves to Fock states $|\tilde{a}_{\mathbf{r}}\rangle$ with maximally one fermion per site. Here, we set the effective coupling $J^* = t$, motivated by the fact that at high dopings, the mean-field Hamiltonian with uniform flux is a good approximation of the actual system.

A.4 Snapshot Analysis

A.4.1 String pattern finding algorithm

This section is based on the publication

- Christie S. Chiu, Geoffrey Ji, Annabelle Bohrdt, Muqing Xu, Michael Knap, Eugene Demler, Fabian Grusdt, Markus Greiner, Daniel Greif: "String patterns in the doped Hubbard model" – Science Vol. 365, Issue 6450, pp. 251-256 (2019) [arXiv:1810.03584]

Structure, text and figures have been rearranged and adapted here.

Postselection and finite-size effects

The size of the postselection region is chosen to be 7 sites in diameter according to the AFM correlation length at half filling. We vary the window to a smaller circular region of 5 sites in diameter, or to a larger circular region of 8 sites in diameter, and find that the qualitative dependence of the string count on doping remains the same, see Fig. A.4.1. The baseline string count at half filling increases for larger postselection regions as the region becomes larger than the correlation length and the deviation from the reference checkerboard increases.
This finite-size variation seems to affect experiment and all theoretical simulation results similarly, which is reasonable given that the pattern detection algorithm is identical in all analyses. However, in Fig. A.4.2g), we simulate strings in the infinite-length limit and detect a greater number of string patterns upon doping. This result suggests that when the system is much smaller than the length of the string patterns, the number of detected strings is biased higher. Indeed, increasing the size of the postselection region results in a slight decrease of the estimated detection efficiency.
We also consider the effect of moving the window to achieve the highest values of the staggered magnetization. We find that fixing the window to the center of the system while keeping a postselection threshold of 60% greatly increases the number of string patterns found at half filling relative to the additional number of patterns found upon doping the system, see Fig. A.4.1 b). This is due to a greater average deviation from the reference checkerboard. In principle, we could achieve a better signal to noise by postselecting more strongly on which images we use, at the cost of increased statistical fluctuation. While the half-filling value changes, the estimated detection efficiency does not change statistically significantly, indicating robustness of the detection algorithm to this effect. Finally, the fraction of images kept in the post-selection process can be varied. We choose to keep the top 60% of images in an effort to capture the tail of the histogram of the staggered magnetization, while maintaining a reasonably high number of images. Upon changing the postselection

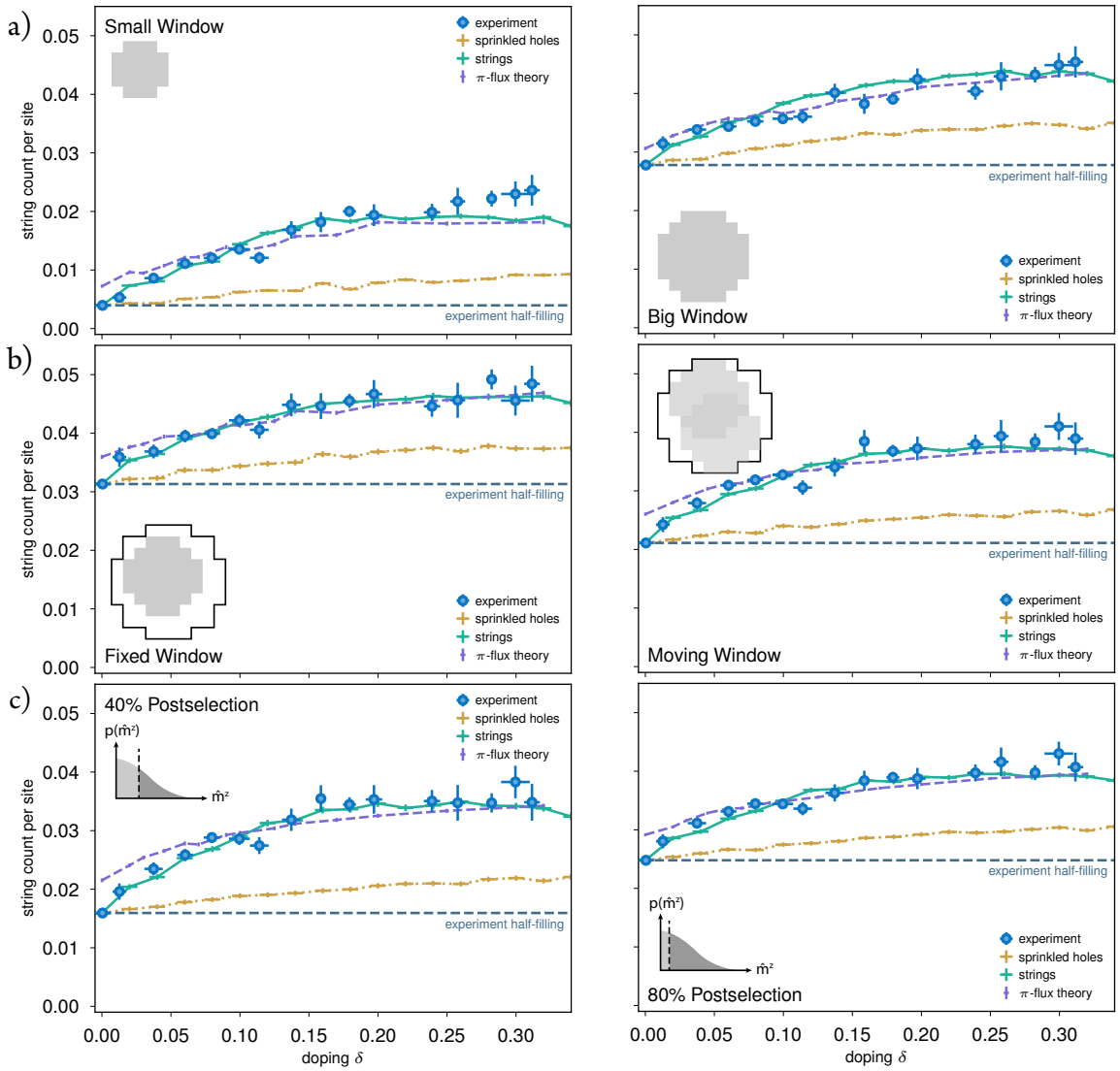

Figure A.4.1: Effect of post-selection on string count. All parameters not mentioned are kept fixed as in the procedure outlined in the main text. In all cases, we see that the qualitative features described in the main text are maintained. a) Using a different-size window for the analysis region, either 5 or 8 sites in diameter. b) Fixing the window position to the center of the system, compared to scanning the window position to maximize the staggered magnetization. c) Varying the percentage of data kept when postselecting on the staggered magnetization, either 40% or 80%.

to 40% or 80%, see Fig. A.4.1c), we find fewer or more string patterns at half-filling, respectively. However, the slope of the string count as a function of doping in the low-doping regime does not change statistically significantly.

Different input distributions

We vary the geometric string theory prediction of the string length distribution to examine how the resulting detected string-pattern length distribution changes, see Fig. A.4.2 b)-g). Changing the temperature for Boltzmann sampling of the string states yields a worse agreement with the experimental result, as does changing the participation ratio of holes in strings by only moving a fraction of the holes which have been randomly placed. We also alternatively select only strings of a given length and find the best agreement for strings of length 4; this is close to the average string length at $T = 0.6J$ of 4.2. From these results we conclude that perturbations to the analytic string length histogram are unlikely to improve agreement with the experimental measurement. We note that the decrease in string count at very high doping for infinite-length strings is likely an artifact from simulation.

Comparison to full readout

In images taken in the experiment, we do not distinguish between holes, doublons, and the removed spin species. In a system with full readout, this distinction is available. In this case, the hole positions are known and the number of detected string patterns must correspond to the number of holes which are not in doublon-hole pairs, i.e. dopants. However, the detected distribution of string lengths can still be modified by overlaps between strings in the same way as in our experiment. In the main text, we discuss the fidelity of the different string pattern detection algorithms in section 5.2. Here, we simulate the experimental situation as closely as possible, but with full spin readout. We simulate full spin readout in quantum Monte Carlo simulations of the Heisenberg model with simulated strings. The simulation is performed on a 40-site by 40-site system with periodic boundary conditions, from which a 10-site-diameter disk is cut out to match the experimental system. Postselection is then done in the same way as in the experimental data analysis. In Fig. A.4.3 a) a comparison of the detected string length distribution with and without full readout is shown, where the distribution obtained without full readout has the half-filling distribution subtracted. While the signal with full readout is a factor of about five higher, the relative distribution of the detected string-pattern lengths remains the same.

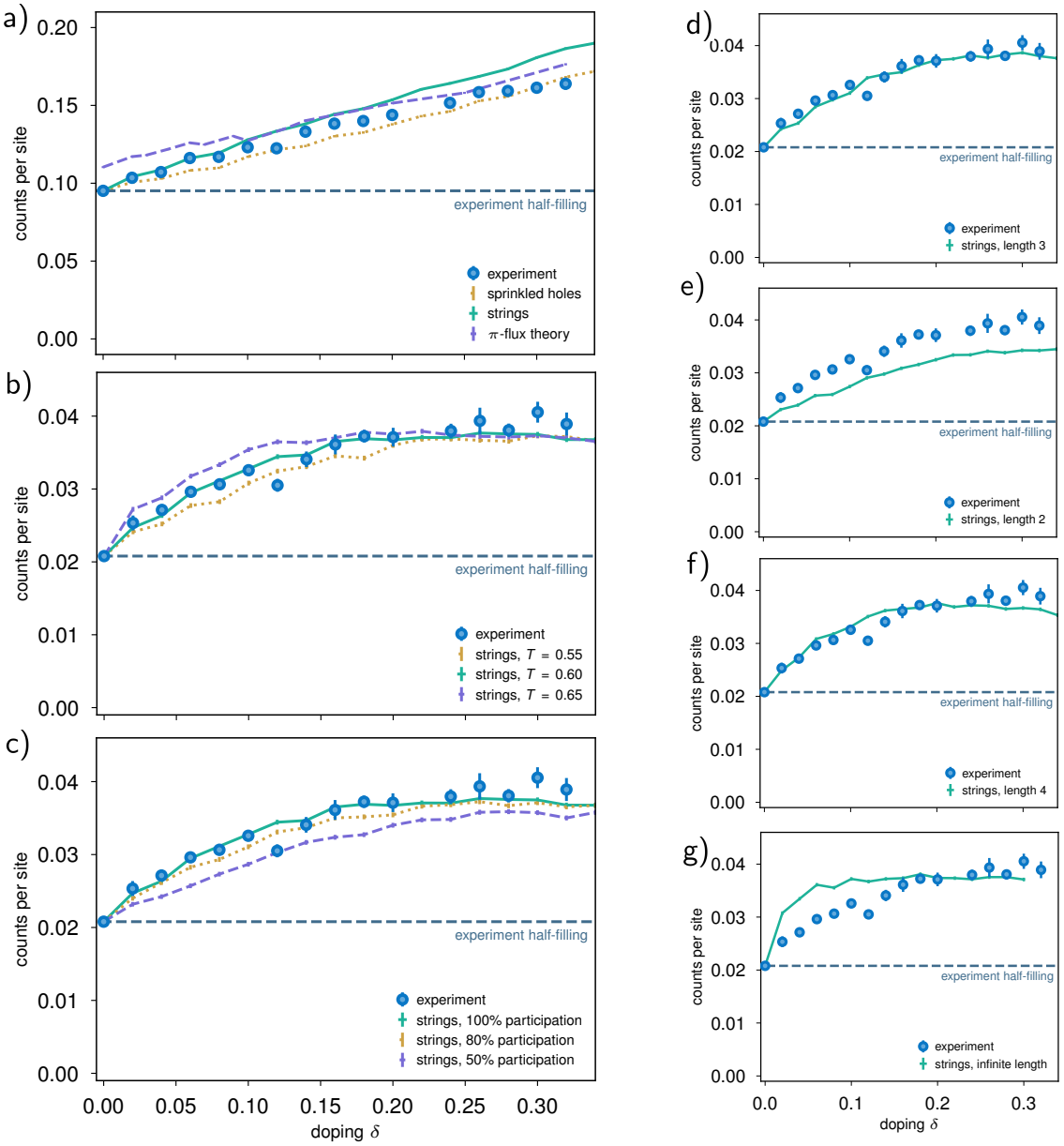

Figure A.4.2: Effect of analytic string length distribution on measured string count. a) String count versus doping, as in Fig. 6.4.3 of the main text, but including all string-pattern lengths in the count. The agreement between all simulations and experiment suggests that this quantity may be trivially dependent on doping. b) Comparison of experimentally measured string count and simulated geometric strings, for analytic string length distributions corresponding to temperatures T/J of 0.55, 0.60 (as in main text), and 0.65. The $T/J = 0.60$ distribution matches experiment best. c) Same, but varying the fraction of simulated holes which are then propagated to simulate strings. The best agreement occurs when all holes are part of strings. d-g) Same, but for simulated strings which are of all of a single length, ranging from 2 sites to the infinite-site limit, instead of sampled from the analytic distribution as described in the main text. In b-g), the experimental result shown is the same.

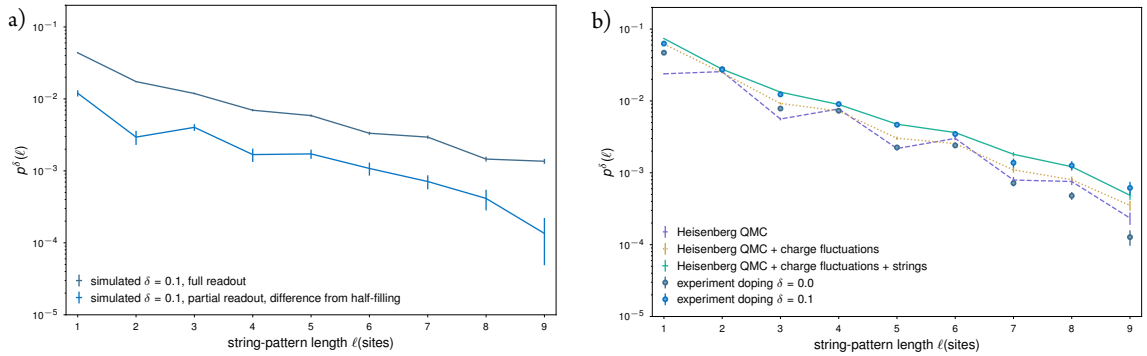

Figure A.4.3: Background signal in string pattern detection. a) String pattern detection with simulated full spin readout and partial readout, the latter with the half-filling signal subtracted, using Heisenberg QMC data with added charge fluctuations and strings. The signals have qualitatively the same shape but are offset due to the lower detection efficiency without full spin readout. b) Measured string pattern distribution for Heisenberg QMC simulation at half-filling and for 10% doping. Without introducing charge fluctuations in the Heisenberg simulation, we see a significant deviation from experiment in the half-filling distribution at low lengths. However, the simulation including charge fluctuations qualitatively matches experimental data, providing evidence that the string patterns detected in the experimental data at half-filling arise from the distinction between snapshots of a quantum antiferromagnet and the reference checkerboard.

Signal at half-filling

Apart from doublon-hole pairs, the Fermi-Hubbard model at half filling for $U \gg t$ can be approximated by the Heisenberg model. We can therefore examine the detected string-pattern length distribution from Heisenberg QMC simulation to better understand our experimental signal at half filling. For consistency, after simulating a 40-site by 40-site system with periodic boundary conditions, we cut out the same sample size and use the same readout and post-selection schemes as in the experiment, and we add doublon-hole pairs into the simulation by converting neighboring sites with opposite spins into doublon-hole pairs with a probability given by $4t^2/U^2$.

Fig. A.4.3 b) shows the string length distribution from the experiment at half filling as well as from QMC simulations of the Heisenberg model at $T = 0.6J$ with and without artificial doublon-hole pairs. The introduction of artificial doublon-hole pairs corrects the significant discrepancy between the QMC data and the experimental data at strings of short lengths. The resulting simulated data agrees reasonably well with experiment, suggesting that the detected string patterns in the experimental data at half filling come from the deviation of a quantum AFM from the checkerboard reference pattern. Slightly more long string patterns are found in Heisenberg QMC snapshots compared to experiment half-filling. This discrepancy may be due to a failure to consider non-adjacent doublon-hole pairs, which are expected at the experimental parameters. Indeed, this effect decreases upon doping as doublon-hole fluctuations become rarer, where the QMC data with

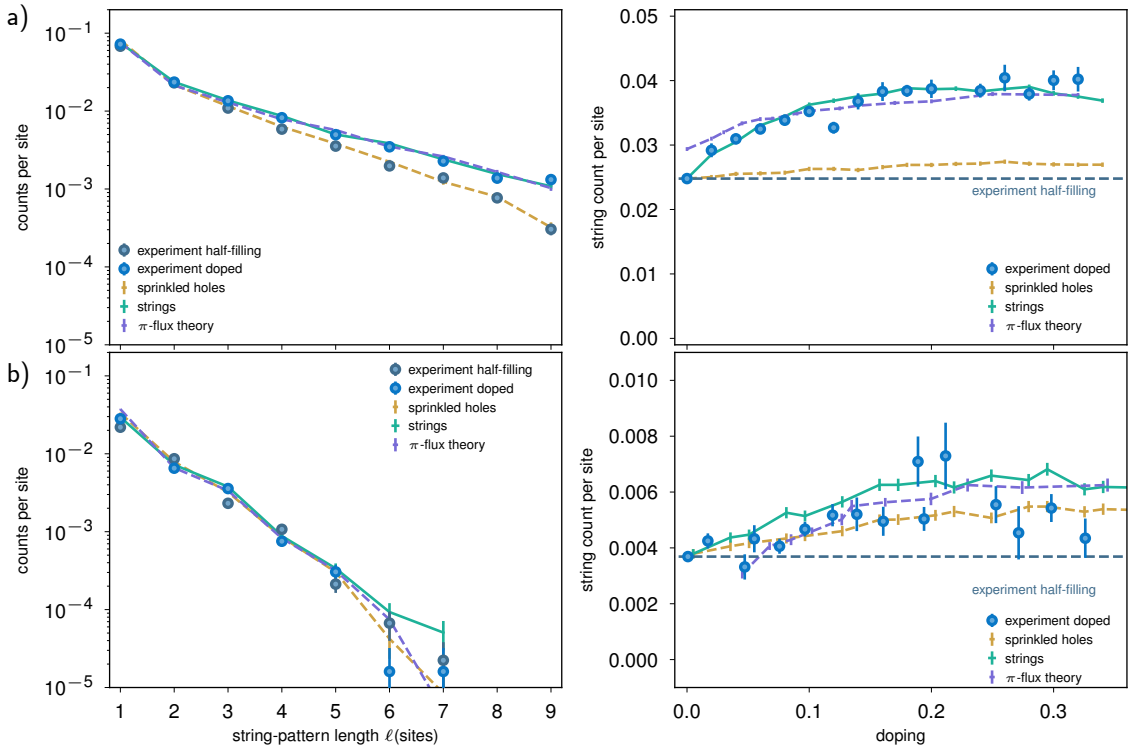

Figure A.4.4: Comparison to other string finding algorithms. a) The string length histogram and total string count produced with the simplified red area algorithm. Apart from an increase in values of the string-pattern-based observables at half-filling, the results are similar to the detection algorithm used in the main text. b) Same quantities, but produced with the happiness method, are also sensitive to doping but may be too noisy to be useful.

simulated strings agrees quite well with the experimental measurements.

Comparison to other string finding algorithms

Figure A.4.4 shows the same quantities plotted in main text Figs. 6.4.2 and 6.4.3, but under a) the simplified red area and b) the happiness string detection algorithm introduced in section 5.2.1. Note that the signal to noise ratio is significantly lower and the absolute signal itself is lower by almost an order of magnitude. This is not surprising, especially given that quantum fluctuations and projection noise do contribute considerably to measurement and reduce the sensitivity of string patterns to string states. Here the experimental result seems to best match the sprinkled holes simulations, however uncertainties are large and this is highly inconsistent with all other results with conventional observables, requiring further investigation.

A.5 Machine learning

In this section, we give a brief introduction into neural networks and an overview over machine learning techniques. For a detailed introduction into the topic we refer to the many excellent ressources, for example Refs. [285, 287, 339, 439]. Here, we discuss supervised learning algorithms and in particular convolutional neural networks.

A.5.1 Neural networks

A neural network is a collection of connected neurons, inspired by the biological neural networks in brains. Each of the neurons typically has several incoming connections and provides an output, which is some non-linear function of the sum of the incoming data. The connections and neurons are associated with weights and biases, which we will call θ here. The weights and biases are adjusted during the learning process. A standard example is the learning of handwritten digits: many images of handwritten digits are input to the network. Each of these images $x^{(i)}$ has as a label $y^{(i)}$ the digit it represents. The neural network is then trained to adjust its weights and biases in such a way that for a given input image, the output $h_\theta(x^{(i)})$ corresponds to the correct label $y^{(i)}$. For an inpuct vector $x^{(i)}$, the values of the neurons in the next layer are calculated as

$$a^{(2)} = g(z^{(2)}) \qquad \text{with} \qquad z^{(2)} = \theta^{(1)} a^{(1)}. \tag{A.42}$$

Note that here, the superscripts refer to the number of the layer as opposed to the number of the sample under consideration. The first layer is the input, $a^{(1)} = x^{(i)}$. The function $g(z)$ can for example be the sigmoid function,

$$g(z) = \frac{1}{1 + e^{-z}}. \tag{A.43}$$

A cost function is defined, which we aim to minimize during the training process. One could for example choose the square distance between the output of the neural network and the correct label, such that the cost function becomes

$$J(\theta) = \frac{1}{2N} \sum_{i=1}^{N} |h_\theta(x^{(i)}) - y^{(i)}|^2. \tag{A.44}$$

The goal is then to minimize $J(\theta)$ as a function of the network paramters θ. A common way to do so is to use gradient descent. Here, one starts with some initial guess for θ and then changes θ in

each step of the process along the direction in which $J(\theta)$ becomes smaller:

$$\theta_j \to \theta_j - a\frac{\partial}{\partial\theta_j}J(\theta) \qquad \forall\theta_j \in \theta. \tag{A.45}$$

Note that all weigths and biases θ_j are updated simultaneously. The parameter a is the learning rate. If it is chosen too small, the gradient descent will be slow. If a is too large, the gradient descent may fail to converge. We decrease the learning rate a over the course of training to obtain fast convergence.
In order to avoid problems when calculating the gradient, the cost function is often chosen as

$$\text{cost}(h_\theta(x^{(i)}), y^{(i)}) = -y_i \log(h_\theta(x^{(i)})) - (1 - y^{(i)}) \log(1 - h_\theta(x^{(i)})) \tag{A.46}$$

with

$$J(\theta) = \frac{1}{N}\sum_{i=1}^{N} \text{cost}(h_\theta(x^{(i)}), y^{(i)}). \tag{A.47}$$

In the case of more than two possible outputs, the labels $y^{(i)}$ are written as vectors of length K, where K is the number of possible outputs. All entries in $y^{(i)}$ are zero except for the k-th entry, which corresponds to the correct label and is set to one. If we for example want to label handwritten digits with labels $1, 2, 3, 4, 5, 6, 7, 8, 9, 0$, the label 2 would be represented by the vector $(0, 1, 0, 0, 0, 0, 0, 0, 0, 0)^T$. The cost function then becomes

$$J(\theta) = \frac{1}{N}\sum_{i=1}^{N}\sum_{k=1}^{K}\left(-y_k^{(i)} \log((h_\theta(x^{(i)}))_k) - (1 - y_k^{(i)}) \log(1 - (h_\theta(x^{(i)}))_k)\right). \tag{A.48}$$

If the number of free parameters in the neural network is too big compared to the sample size, overfitting can become a problem. There are two standard ways to avoid this: one can add the square of the weights to the cost function, such that large weights are punished and the network has to find ways to avoid using all possible weights. Alternatively, one can use dropout, where a randomly chosen subset of neurons is not used in each training step, such that the network cannot rely too much on any given neuron. We chose the latter approach.
In order to calculate the gradient of $J(\theta)$ efficiently, the backpropagation algorithm is commonly used. In this algorithm, a given training example $(x^{(i)}, y^{(i)})$ is first propagated forward through the network, calculating the values of all neurons, including the output value $h_\theta(x^{(i)})$. For each node in each layer, we now want to obtain a measure for the error stemming from this node, given a total error in the output. For an output node, this is straightforward, and the error is simply the difference between the output $h_\theta(x^{(i)})$ and the correct label $y^{(i)}$. For the neurons in the hidden layers, the process is a bit more involved and we have to backtrace the error terms of the nodes in

the following layer (i.e. closer to the output). For a neural network with one hidden layer, we do the following for each sample $x^{(i)}$:

1. the sample $x^{(i)}$ is propagated forward through the network, yielding the values of $z^{(2)}$, $a^{(2)}$ for the hidden layer and $z^{(3)}$, $a^{(3)}$ for the output layer.

2. for each possible label k in the output layer, we get

$$\delta_k^{(3)} = a_k^{(3)} - y_k. \tag{A.49}$$

3. for the hidden layer ($l = 2$), the errors are

$$\delta^{(2)} = \left((\theta^{(2)})^T \delta^{(3)}\right) .* g'(z^{(2)}), \tag{A.50}$$

   where $.*$ is the element-wise multiplication and $g'(z)$ is the gradient of the sigmoid function, which is conveniently

$$g'(z) = g(z)(1 - g(z)). \tag{A.51}$$

4. add the contribution to the gradient from this example as

$$\Delta^{(l)} = \Delta^{(l)} + \delta^{(l+1)}(a^{(l)})^T. \tag{A.52}$$

5. the gradient for the cost function is then

$$\frac{\partial}{\partial \theta_{mn}^{(l)}} J(\theta) = D_{mn}^{(l)} = \frac{1}{N} \Delta_{mn}^{(l)}. \tag{A.53}$$

Convolutional neural network

In a convolutional neural network (CNN), Fig. A.5.1, each neuron of the first hidden layer is only connected to a small subregion in the input data. The input is usually two dimensional, such as an image. In our case, we use subregions of 3×3 and the input are snapshots of the quantum many body state. For further discussion and applications of CNNs in quantum many-body physics see References [326–328, 441] The hidden layer in the CNN is generated as a convolution of a mask M_i with the input. Each neuron in one layer is obtained from the same – in our case 3×3 – mask M_i at different positions of the input. Different masks then lead to several layers instead of only one hidden layer. The fact that one mask is moved across the entire input image to generate one hidden layer makes use of translational invariance: the same feature can appear anywhere in the

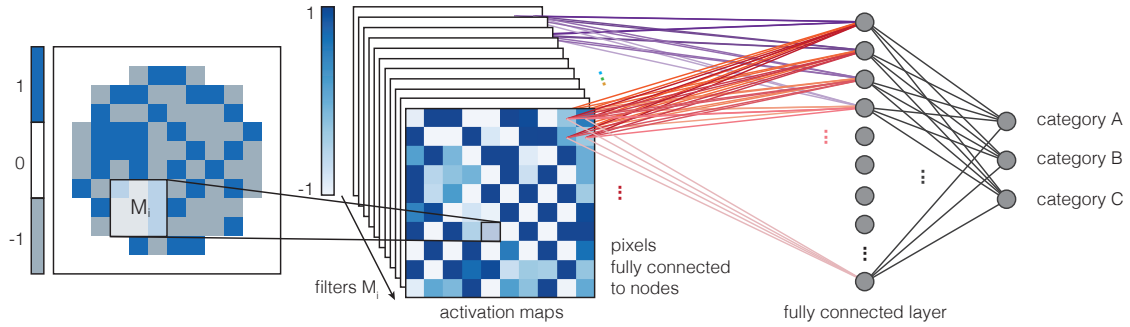

Figure A.5.1: Convolutional Neural Network. The main building block of CNNs, which are conventionally used to analyze visual imagery, is the convolutional layer with a set of learnable filters M_i as parameters [440]. At each possible position of a given filter in the input image, the inner product between the filter and the input data is computed. This yields a two dimensional activation map of the filter. During training, the network learns to set the entries of the filters such that the corresponding value in the activation map is high when specific types of patterns are detected. The convolutional layer is followed by a fully connected layer, which then sorts the data into the different categories [5].

picture and we do not need to encode it with a number of variables of the system size in the neural network. Instead, we encode one feature in one filter, which is then moved to all positions. This way, the number of neural network parameters is reduced significantly as compared to a fully connected neural network which allows for all possible positions of a number of features. We use the tensorflow [285] package to implement a convolutional neural network to analyse snapshots of the doped Fermi-Hubbard model. The network is implemented as shown in the Python example code below.

```
import tensorflow as tf
tf.reset_default_graph()

### saving
path = './network/Doping'+str(doping)+'/'

### tf Graph input
x = tf.placeholder("float", [None, mX*mY])
y_ = tf.placeholder("float", [None, len(cases)])
x_image = tf.reshape(x, [-1, mX, mY, 1])
keep_prob1 = tf.placeholder(tf.float32)
keep_prob2 = tf.placeholder(tf.float32)

### Store layers weight & bias
weights = {
```

```
'Wc1': tf.Variable(tf.truncated_normal([p1, p1, 1, f1], stddev=0.1)),
'Wfc1': tf.Variable(tf.truncated_normal([int(mX*mY*f1),fcSize1], stddev=0.1)),
'out': tf.Variable(tf.truncated_normal([fcSize1, len(cases)], stddev=0.1))
}
biases = {
'bc1': tf.Variable(tf.constant(0.1,shape=[featureSize1])),
'bfc1': tf.Variable(tf.constant(0.1,shape=[fcSize1])),
'out': tf.Variable(tf.constant(0.1,shape=[len(cases)]))
}

### Create model
def neural_net(x_image):
    # First convolutional layer:
    h_conv1=tf.nn.relu(tf.add(tf.nn.conv2d(x_image, weights['Wc1'],
    strides=[1, 1, 1, 1],padding='SAME'), biases['bc1']))
    h_flat = tf.reshape(h_conv1, [-1, int(mX*mY*featureSize1)])
    # dropout
    h_drop = tf.nn.dropout(h_flat, keep_prob1)
    # first fully connected layer
    h_fc1 = tf.nn.relu(tf.add(tf.matmul(h_drop, weights['Wfc1']),

    # dropout
    h_fc2_drop = tf.nn.dropout(h_fc1, keep_prob1)
    # Output fully connected layer with a neuron for each class
    out_layer = tf.matmul(h_fc2_drop, weights['out']) + biases['out']
    return out_layer


y_conv = neural_net(x_image)
outs = tf.nn.softmax(y_conv)
prediction = tf.argmax(tf.nn.softmax(y_conv),1)


cross_entropy = tf.reduce_mean(
    tf.nn.softmax_cross_entropy_with_logits(labels=y_, logits=y_conv))
regularizer = tf.nn.l2_loss(weights['Wfc1']) # optional regularization
loss_fct = tf.reduce_mean(cross_entropy + lambdao * regularizer)

global_step = tf.Variable(0, trainable=False)
learning_rate = tf.train.exponential_decay(starter_learning_rate,
global_step, decay_steps, decay_rate, staircase=True)

train_step = tf.train.AdamOptimizer(learning_rate).minimize(loss_fct)
```

```
correct_prediction = tf.equal(tf.argmax(y_conv, 1), tf.argmax(y_, 1))
accuracy = tf.reduce_mean(tf.cast(correct_prediction, tf.float32))
```

Before training the neural network, we randomly select 250 snapshots from the full data for testing. These snapshots are not used during training, but only to test the performance of the network and determine the accuracy. In order to average out fluctuations in the results, we repeat the training with a different choice of the test data set and sorting of experimental data ten times. The error bars for the different accuracies as well as the percentage of experimental snapshots detect as one of the two theories shown in the figures represent the standard deviation over the different runs,

$$\Delta x = \frac{\sqrt{\sum_{i=1}^{\mathcal{N}} (x_i - \bar{x})^2}}{\mathcal{N} - 1}, \tag{A.54}$$

where $\mathcal{N}$ is the number of runs, x_i is the quantity under consideration in the i-th run and $\bar{x}$ is the average value of the said quantity over all $\mathcal{N}$ runs.

There are many other architectures and applications for neural network. In our search for string patterns, we also applied recurrent neural networks, which are optimally suited for time-traces, to backtrace strings, see section 5.2.1. A different approach would be to implement an unsupervised learning algorithm, such as reinforcement learning, to find strings in snapshots.

B

Details on the spectral function

B.1 1D ARPES

This section is based on the publication

- Annabelle Bohrdt, Daniel Greif, Eugene Demler, Michael Knap, Fabian Grusdt: "Angle-resolved photoemission spectroscopy with quantum gas microscopes." – Phys. Rev. B 97, 125117 (2018) [arXiv:1710.08925]

Structure, text and figures have been rearranged and adapted here.

B.1.1 Extensions of the measurement scheme

The scheme for measuring the spectral function of a single hole can be generalized to implement different spectroscopic probes using ultracold atoms. This appendix illustrates two examples: measuring the dynamical structure factor $S(\omega, k)$ in one-dimensional spin chains and extending the scheme to implement the analog of double photoelectron spectroscopy [442, 443].

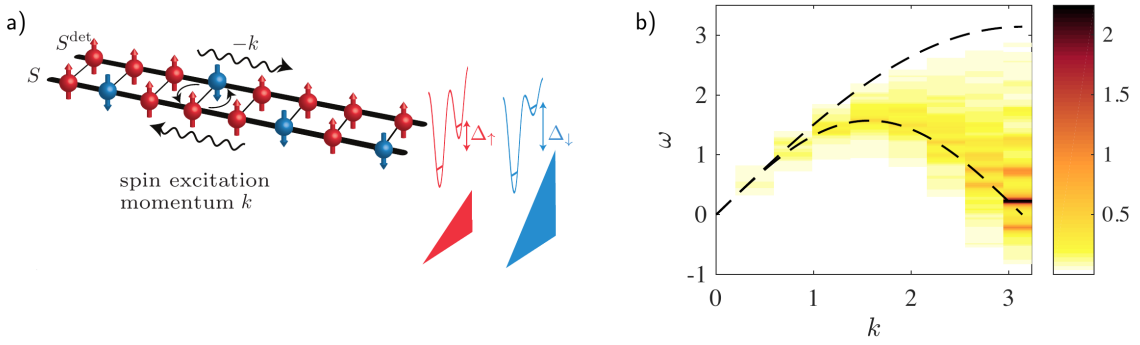

Figure B.1.1: Direct measurement of the dynamical spin structure factor. a) The empty probe system is replaced by a fully polarized spin chain and coupled to the system using superexchange interactions in the y-direction. By detecting a single magnon created in S^{det} and measuring its momentum, the dynamical spin structure factor $S(k,\omega)$ can be measured. In b) we calculate $S(k,\omega)$ for the isotropic Heisenberg model in a finite-size box of length $L = 16$ at a temperature $T = 0.2J$. It shows the expected broad continuum reflecting the fractionalization of a spin-flip excitation into a pair of spinons. The black dashed lines correspond to the theoretically expected upper and lower boundaries at zero temperature.

B.1.2 Dynamical spin structure factor

The spectral function $A(k,\omega)$ probes the properties of a single hole interacting with the surrounding spins. To obtain information about the spin system alone, more direct measurement schemes are required where no charge excitations are generated. The most common example is the dynamical spin structure factor $S(k,\omega)$, where a spin-flip excitation with momentum k is created at an energy ω. Using a Lehmann representation similar to Eq. (4.20) it can be defined by

$$S(k,\omega) = \frac{1}{2Z_0}\sum_{n,m} e^{-\beta E_n^M} |\langle \psi_m^{M+1}|\hat{S}_k^+|\psi_n^M\rangle|^2 \times \delta(\hbar\omega - E_m^{M+1} + E_n^M), \tag{B.1}$$

with $|\psi_n^M\rangle$, E_n^M denoting the eigenstates and -energies of the system S with total magnetization M. In solids, $S(k,\omega)$ can be measured in inelastic neutron scattering experiments [444].

To directly measure the dynamical spin structure factor $S(k,\omega)$ using a quantum gas microscope, we propose to replace the empty probe system S^{det} by a spin chain which is fully polarized along the z-direction, see Fig. B.1.1 a). Instead of the modulated tunnel coupling $\hat{T}_y$ from Eq. (4.17), the system can be coupled to the probe by super-exchange interactions,

$$\hat{J}_y = \sum_i \hat{\mathbf{S}}_i \cdot \hat{\mathbf{S}}_{i,\mathrm{det}}, \tag{B.2}$$

where $\hat{\mathbf{S}}_{i,\mathrm{det}}$ denotes the spin operator on site i in the probe system. By modulating the tunneling amplitude t_y as in the case of the spectral function, the resulting super-exchange coupling j_y

is also modulated with the same frequency ω_{shake}. The time-dependent perturbation thus reads $\hat{\mathcal{H}}_{\text{pert}}(\tau) = \delta j_y \sin(\omega_{\text{shake}}\tau)\hat{J}_y$, cf. Eq. (4.13).

Similar to the case of the spectral function, the perturbation creates an excitation in the probe system S^{det}: here, the excitation is a magnon carrying spin $S^z = -1$ with momentum $-k$ and energy $\omega_m(-k)$, where $\omega_m(k)$ denotes the magnon dispersion relation. In order to measure the momentum of the magnon, we assume that spin up and down states have different magnetic moments. By applying a magnetic field gradient along the x-direction before taking a spin-resolved image [217] one can thus implement the Wannier-Stark mapping discussed in Sec. 4.2.3 for the single magnon in S^{det}. Similarly, a magnetic field gradient along the y-direction can be used to realize spin-dependent energy offsets Δ_σ, analogous to the energy offset Δ considered in the case of the spectral function. Finally, by measuring the position of the magnon after applying the Wannier-Stark mapping, the excitation rate $\Gamma(k, \omega)$ is obtained, which is directly related to the dynamical spin structure factor

$$\Gamma(k, \omega) = \frac{2\pi}{\hbar}|\delta j_y|^2 S(k, \omega), \tag{B.3}$$

as obtained by Fermi's golden rule.

In Fig. B.1.1 b) we show an example for the dynamical spin structure factor $S(k, \omega)$, calculated at finite temperature and for realistic system sizes accessible in current experiments. The spin-flip creates a pair of two fractionalized spinon excitations. As a result, one can observe a broad spinon continuum, which is considered a key indicator for a quantum spin liquid.

B.1.3 Double photoelectron spectroscopy

Further insight into the nature of excitations in the system can be obtained by measuring their spatial correlations. An interesting method which achieves this goal in solids is double photoelectron spectroscopy [442, 443], where a correlated pair of two photoelectrons is emitted and detected. Similarly, processes can be considered where two atoms are transferred into the initially empty probe system S^{det}. To avoid interactions between the two emitted atoms, one could e.g. consider a situation with two probe systems $S^{\text{det}}_{\text{L,R}}$, one to the left and one to the right of the system S, and post-select on cases with one atom per probe system.

The resulting spectrum contains pairs of individual one-particle events as well as two-particle processes which provide additional information about the system. The two-particle contributions can be distinguished from one-particle effects by using coincidence measurements. In this technique one post-selects events where both excitations are created simultaneously. In the quantum gas microscope setups discussed here this can be achieved by extending $S^{\text{det}}_{\text{L,R}}$ in the y-direction. One can use the travelled distance from the system S in y-direction as a measure of the time that passed between the creation and the detection of a particle.

From the coincidence measurements described above, information about the two-hole spectral function $A_{12}(k_1, k_2, k_1', k_2'; \omega)$ can be extracted, see Ref. [443]. It contains information about the correlations between the two created holes in the system. These correlations are expected to be weak in a system with one-dimensional chains with spin-charge separation, where holons form a weakly interacting Fermi sea [177, 310]. On the other hand, in systems that are superconducting, correlations are expected to play an important role and give rise to distinct features of Cooper pairing in the two-hole spectrum [445]. Using ultracold atoms, situations with attractive Hubbard interactions $U < 0$ have been realized [446] which become superconducting at low temperatures. Here the method described above could be applied to directly access the strong two-particle correlations present in this system.

B.1.4 Details on the boundary conditions and momentum shifts

In this Appendix, we discuss the different shifts for holon and spinon momenta that have to be taken into account in the application of the spectral building principle in Eqs. (4.24) and (4.26). Strictly speaking, there is no translational invariance in squeezed space. However, it is a good approximation up to $1/L$. The first momentum shift we discuss is due to these corrections. The holon moves along L lattice sites. Its momentum is therefore quantized in units of $2\pi/L$. By contrast, there are only $L-1$ spins, such that the spinon momentum is $k_s = n_s 2\pi/(L-1)$ with n_s integer. Therefore, we have to shift the momentum to account for the different quantization conditions for spinon and holon. The spinon momentum $k_s = k - k_h$ in Eq. (4.24) is thus replaced by

$$k_s' = k - k_h + \frac{k - k_h}{L-1}. \tag{B.4}$$

This is the smallest possible shift to obtain the correct quantization of k_s' as an integer multiple of $2\pi/(L-1)$.

In a chain with periodic boundary conditions, a further momentum correction arises: the holon shifts the spins by one lattice site every time it moves across the entire system. When the spins are translated by one site, the wavefunction picks up an overall phase e^{iP_s} where P_s is the total momentum of the spin chain after removing the holon. $P_s = P_0 + k_s$ is determined from the spinon momentum k_s up to an additive constant P_0 which is independent of the momentum. Thereby, a *twisted periodic boundary effect* with twist angle given by the spinon momentum P_s is introduced. This corresponds to a shift of all holon momenta k_h by the momentum P_s of the spins divided by the system size L. For periodic boundary conditions, we thus have to replace k_h in Eq. (4.24) with

$$k_h' = k_h - \frac{P_s}{L}. \tag{B.5}$$

In Fig. 4.2.3 a) and b) we included the corrections from Eq. (B.4), (B.5) for the positions of the gray dots and found by comparison to our numerical calculations that $P_0 = \pi$.
At small but finite temperatures, there exist collective excitations which carry momentum π. They contribute to P_s in Eq. (B.5) and thus shift the holon momentum in the case of periodic boundary conditions by an additional amount of π/L,

$$k_h' = k_h - \frac{2\pi + k_s}{L}. \tag{B.6}$$

Correspondingly, additional peaks appear between the ones found at zero temperature, which are marked by blue circles in Fig. 4.2.3 a).

B.2 2D SPECTRAL FUNCTION: DETAILS ON THE NUMERICAL SIMULATIONS

This section is based on the publication

- Annabelle Bohrdt, Eugene Demler, Frank Pollmann, Michael Knap, and Fabian Grusdt: "Parton theory of ARPES spectra in anti-ferromagnetic Mott insulators" – Phys. Rev. B 102, 035139 [arXiv:2001.05509]

Structure, text and figures have been rearranged and adapted here.

The spectral function is calculated as the Fourier transform of the time-dependent correlation function

$$C_{\mathbf{i},\mathbf{j}}(t) = \sum_\sigma \langle \psi_0 | e^{i\hat{H}t} \hat{c}^\dagger_{\mathbf{j},\sigma} e^{-i\hat{H}t} \hat{c}_{\mathbf{i},\sigma} | \psi_0 \rangle, \tag{B.7}$$

where $|\psi_0\rangle$ is the ground state of the $t-J$ model without a hole on a cylinder with four legs. The time evolution of the ground state with the $t-J$ Hamiltonian $e^{i\hat{H}t}|\psi_0\rangle = e^{iE_0 t}|\psi_0\rangle$. We thus calculate

- the ground state without a hole, $|\psi_0\rangle$, using DMRG
- the time evolution of the ground state after a hole was created in the origin, $|\psi(t)\rangle = e^{-i\hat{H}t}\hat{c}_{0,\sigma}|\psi_0\rangle$
- the overlap of $|\psi(t)\rangle$ with the state where a hole was created at a position $\mathbf{j}$, $|\psi_1\rangle = \hat{c}_{\mathbf{j},\sigma}|\psi_0\rangle$.

The time evolution of $\hat{c}_{0,\sigma}|\psi_0\rangle$ is performed using the matrix product operator based time evolution introduced in Ref. [313]. In Fig. B.2.1 a) we compare the correlation function $C_{\mathbf{i},\mathbf{j}}(t)$ for different bond dimensions χ at a time of $t_0 = 8\ (1/J)$, which is the maximal time used for the spectral function shown in the main text. While there are small differences in the absolute numbers, the qualitative behavior is captured correctly already at a bond dimension of $\chi = 600$. For later times,

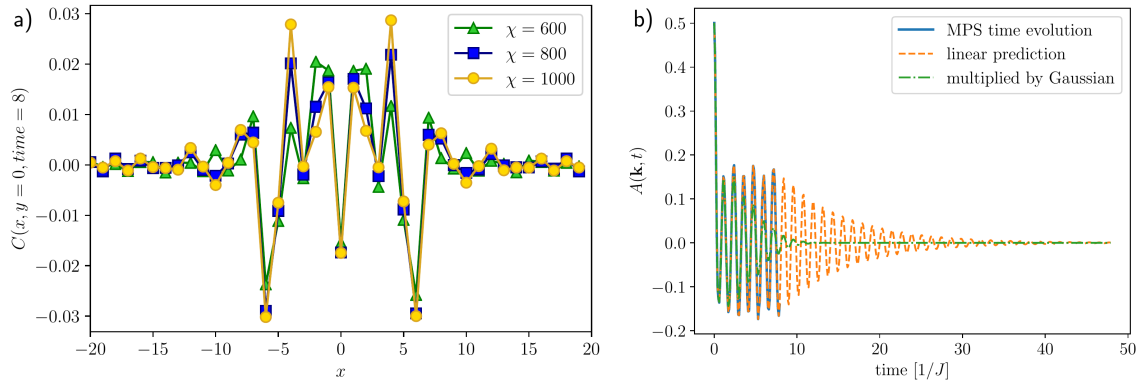

Figure B.2.1: Numerical details for the 2D Spectral function. a) We check the convergence of our td-MPS calculations with the bond dimension χ in the real time and space correlation function $C_{\mathbf{i},\mathbf{j}}(t)$ for the latest time (8 in units of $1/J$) considered for $t/J = 3$. b) Linear prediction and Gaussian envelope. After the spatial Fourier transform, we use linear prediction to enhance the time window (orange dashed). Before Fourier transforming in time, the time dependent data is multiplied with a Gaussian envelope of width $\sigma\omega = 0.25J$ (green dashed-dotted). Here, as an example, we show the corresponding time traces for $k_x = 0$, $k_y = \pi/2$ at $t/J = 3$.

the deviations between different bond dimensions increase further.

We perform a spatial Fourier transform to obtain

$$A(\mathbf{k}, t) = \sum_{\mathbf{j}} e^{-i\mathbf{k}\cdot\mathbf{j}} C_{0,\mathbf{j}}(t). \tag{B.8}$$

As our time evolution is limited to times $0 \leq t \leq t_0 = 8/J$, we use linear prediction to increase the time window. Afterwards, the data is multiplied with a Gaussian envelope $w(t) = \exp[-0.5(t\sigma_\omega)^2]$, where $\sigma_\omega = 2/t_0 = 0.25J$ is chosen in order to minimize the weight of the data generated by linear prediction in the spectrum [436]. An example of a time-trace used for our calculation of the spectral function is shown in Fig. B.2.1 b). We confirmed that the results do not depend on the details of this procedure. Fourier transforming in time yields the spectral function

$$A(\mathbf{k}, \omega) = \frac{1}{2\pi} \int_{-\infty}^{\infty} dt A(\mathbf{k}, t). \tag{B.9}$$

In this signal, the Gaussian envelops introduced in the time domain before lead to Gaussian broadening of the obtained peaks, sufficiently small for our analysis.

The diagonal cut through the Brillouin zone from $(0, 0)$ to (π, π) is obtained by labeling the sites around the cylinder in a *zigzag* fashion as indicated in top of Fig. 5.4.1 a). One ring around the cylinder with this labeling contains $2L_r$ instead of L_r sites. We calculate the ground state as well as the dynamics with the couplings in the Hamiltonian according to the modified lattice geometry.

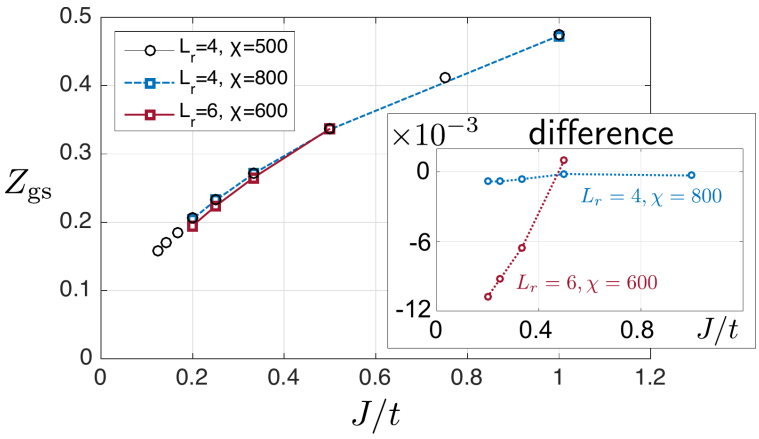

Figure B.2.2: Dependence of DMRG data on parameters. We check how our DMRG calculations of the ground state quasiparticle weight Z change when the bond dimension χ and the circumference L_r of the cylinder are changed. The inset shows the difference $Z_{\mathrm{gs}}(L_r, \chi) - Z_{\mathrm{gs}}(L_r = 4, \chi = 500)$ – note the overall scale 10^{-3}.

For each time step, we obtain an array with $m_x \cdot 2L_r$ entries. This array is reshaped into an $2m_x \cdot L_r$ array and then the Fourier transform is performed, yielding $A(\mathbf{k}, t)$. Due to the relabeling of the sites, the momenta are transformed as

$$\begin{aligned} k_x &\to k_x \\ k_y &\to k_y + k_x. \end{aligned} \tag{B.10}$$

In particular, for $k_y = 0$ we obtain the cut from $(0, 0)$ to $(\pi/2, \pi/2)$ shown in Fig. 5.4.1 a).

It can be shown analytically that the ground state quasiparticle weight $Z(\pi/2, \pi/2)$ shown in Fig. 5.4.3 in the main text corresponds to the integral over the first peak in the spectral function. However, $Z(\pi/2, \pi/2)$ can be expressed more conveniently as the overlap:

$$Z(\pi/2, \pi/2) = \sum_{\sigma} \left| \langle \psi_0^{1\mathrm{h}} | \hat{c}_{(\pi/2,\pi/2),\sigma} | \psi_0^{0\mathrm{h}} \rangle \right|^2 . \tag{B.11}$$

We can thus obtain the quasiparticle weight directly from the ground states of the $t-J$ model without a hole, $|\psi_0^{0\mathrm{h}}\rangle$, and with a single hole, $|\psi_0^{1\mathrm{h}}\rangle$, without the need to calculate any time evolution. The ground state of a single hole in the $t-J$ model has momentum $\mathbf{k} = (\pi/2, \pi/2)$. In a translational invariant system, we can further simplify the calculation by writing:

$$Z(\pi/2, \pi/2) = \sum_{\sigma} \sum_{\mathbf{j}} \left| \langle \psi_0^{1\mathrm{h}} | \hat{c}_{\mathbf{j},\sigma} | \psi_0^{0\mathrm{h}} \rangle \right|^2 . \tag{B.12}$$

Hence we only need to calculate the overlap of the one-hole ground state with a locally created hole at different positions $\mathbf{j}$: $\hat{c}_{\mathbf{j},\sigma}|\psi_o^{oh}\rangle$. In Fig. B.2.2 we show how this procedure changes with the bond dimension χ and circumferences $L_r = 4$ and 6, for different t/J.

A comment is in order concerning the use of Eq. (B.12). To employ it in our finite-size cylinders, we must assume that the ground state $|\psi_o^h\rangle$ does not spontaneously break the translational symmetry in the thermodynamic limit and can be well approximated by a standing wave of nodal point momenta $\pm(\pi/2, \pm\pi/2)$ in the finite-size system. In Refs. [447, 448] Zhu et al. have shown in few-leg ladders with open boundary conditions, that the finite-size ground state $|\psi_o^h\rangle$ can show manifestations of a spontaneously broken translational symmetry in the thermodynamic limit, as indicated by strong charge modulations in the finite-size ground state. In our numerics on four-leg cylinders, we find no indications for this scenario.

To extract $Z(\mathbf{k})$ for $\mathbf{k}$ different from the nodal points, we determine the height of the first peak and its full width at half maximum. We assume a Gaussian form and thus calculate $Z(\mathbf{k})$ as the corresponding integral over the Gaussian function.

C

Details on the Bose-Hubbard model

C.1 Numerical simulations and data analysis for the OTOCs

This section is based on the publication

- A. Bohrdt, C. B. Mendl, M. Endres, M. Knap: "Scrambling and thermalization in a diffusive quantum many-body system." – New J. Phys. 19, 063001 (2017) [arXiv:1612.02434]

Structure, text and figures have been rearranged and adapted here.

C.1.1 Numerical simulations

The numerical simulations are based on finite-temperature, time-dependent matrix product operators (MPO) [432, 449–453], and were implemented by Christian B. Mendl.
For the density correlations, we evaluate [452]

$$\left\langle \hat{n}_\ell(t)\hat{n}_j(0)\right\rangle_\beta \overset{\text{def}}{=} \frac{1}{Z}\operatorname{tr}\left[e^{-\beta\hat{H}}\left(e^{it\hat{H}}\hat{n}_\ell e^{-it\hat{H}}\right)\hat{n}_j\right] = \frac{1}{Z}\operatorname{tr}\left[\left(e^{i\frac{t}{2}\hat{H}}e^{-\beta\hat{H}/2}\hat{n}_\ell e^{-i\frac{t}{2}\hat{H}}\right)\left(e^{-i\frac{t}{2}\hat{H}}\hat{n}_j e^{-\beta\hat{H}/2}e^{i\frac{t}{2}\hat{H}}\right)\right], \tag{C.1}$$

where β is the inverse temperature and Z the partition function. We construct the MPO approximation of the two terms in the parentheses by first computing $e^{-\beta\hat{H}/2}\hat{n}_\ell$ and $\hat{n}_j e^{-\beta\hat{H}/2}$, respectively,

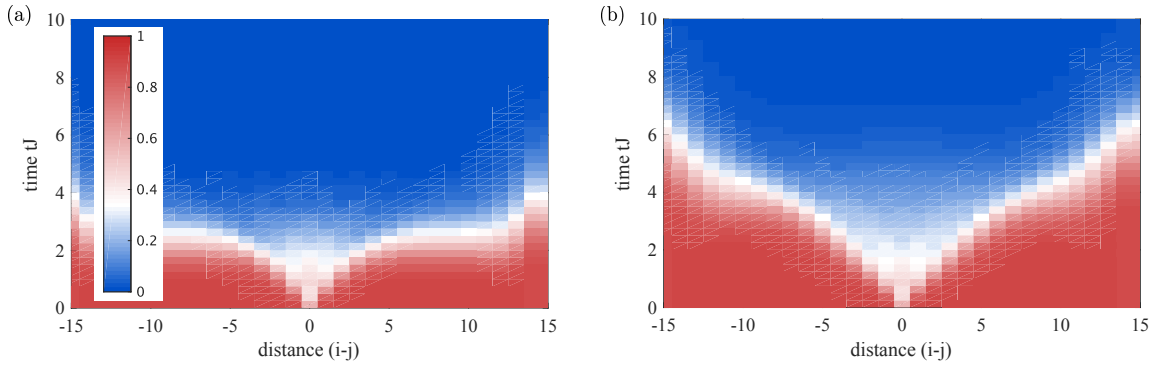

Figure C.1.1: Comparison of numerical data for different bond dimensions. OTO correlators $\mathcal{F}_{ij}(t)$ are shown for $T = 4J$ and $U = J$, and bond dimension a) 20 and b) 400. The plateau emerging around $|i-j| \approx 5$ in a) diminishes and appears only at larger distances for the higher bond dimension shown in b). However, despite the large difference in the bond dimension, deviations from the linear light cone are still apparent.

and then performing a real-time evolution up to $\frac{t}{2}$ and $-\frac{t}{2}$. By exploiting the time translation invariance, $\langle \hat{n}_\ell(t)\hat{n}_j(0)\rangle_\beta = \langle \hat{n}_\ell(t/2)\,\hat{n}_j(-t/2)\rangle_\beta$, the maximum simulated time has effectively been reduced by a factor two, which in turn reduces the required virtual bond dimension of the MPO. To evaluate $e^{-\beta\hat{H}/2}$, we employ a second-order Suzuki-Trotter decomposition with imaginary time step $\Delta\tau$ (typically $\Delta\tau J = 0.025$) after splitting the Hamiltonian into even and odd bonds, as described in Ref. [449]. The real-time evolution proceeds by Liouville steps $\hat{A}(t+\Delta t) = e^{i\Delta t\hat{H}}\hat{A}(t)e^{-i\Delta t\hat{H}}$. For each of the steps we combine a fourth-order partitioned Runge-Kutta method [454] with even-odd bond splitting of the Hamiltonian. As noted in Ref. [452], the Liouville time evolution has the advantage that the virtual bond dimension does not increase outside the space-time cone set by Lieb-Robinson-type bounds. The high order decomposition also allows for relatively large time steps (in our case $\Delta tJ = 0.125$ or 0.25).

For the OTO correlators $\langle c_j^\dagger(t)c_\ell^\dagger c_j(t)c_\ell\rangle_\beta$, a regrouping analogous to Eq. (C.1) would lead to four terms inside the trace, such that a straightforward contraction to evaluate the trace becomes computationally very expensive. Instead, we evaluate

$$\left\langle c_j^\dagger(t)c_\ell^\dagger c_j(t)c_\ell\right\rangle_\beta = \frac{1}{Z}\,\mathrm{tr}\left[\left(e^{it\hat{H}}e^{-\beta\hat{H}}c_j^\dagger e^{-it\hat{H}}c_\ell^\dagger\right)\left(e^{it\hat{H}}c_j e^{-it\hat{H}}c_\ell\right)\right] \tag{C.2}$$

and time-evolve both $e^{-\beta\hat{H}}c_j^\dagger$ and c_j up to time t. Subsequent application of the site-local operators $c_\ell^\dagger$ and c_ℓ does not affect the virtual bond dimension in the MPO representation.

In our simulations, we restrict the local Hilbert space to three states due to computational limitations. Since the average particle number per site is approximately one, this restriction should not qualitatively affect the simulation results. Moreover, truncating the local Hilbert space to three states is sufficient to render the system non-integrable, which is crucial to observe the thermaliza-

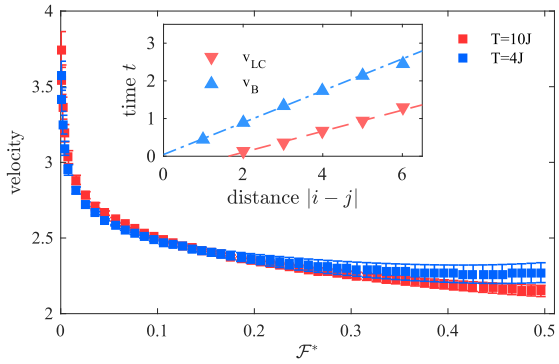

Figure C.1.2: Determining the light-cone v_{lc} and butterfly velocity v_b. The velocities resulting from a linear fit to the times at which $\mathcal{F}^r_{ij}(t)$ reaches the value $\mathcal{F}^*$ are shown for $U = J$ and $T = \{4, 10\}J$. The errorbars are the fitting errors. Inset: The inverse slope of the linear fit to the times as a function of distance $|i-j|$ determines the different velocities (shown for $U = J$ and $T = 4J$).

tion behavior studied in this work.

Since OTO correlators are closely linked to the spreading of entanglement, it is challenging to simulate them using MPO techniques. In Fig. C.1.1 we compare the data obtained for the same simulation parameters but different maximal bond dimensions. The MPO bond dimension of 20 leads to an apparently super-ballistic growth of the light-cone around $|i-j| \approx 5$, see Fig. C.1.1 a). Increasing the bond dimension shifts this numerical artifact to larger distances. It is however exponentially costly to reach full convergence of the OTO correlator. In the analysis of the numerical data we therefore only considered small distances, where we checked that increasing the bond dimension does not alter the correlators.

C.1.2 Data analysis

We describe in detail, how we determine the light-cone velocity v_{lc}, the butterfly velocity v_b, and the Lyapunov exponent λ_L. The light-cone velocity is defined as the ratio of the distance $|i-j|$ and the time at which the reduced OTO correlator $\mathcal{F}^r_{ij}(t)$ reaches a small threshold. The butterfly velocity, however, sets a scale for the time it takes to scramble information over the system and is therefore defined via the time at which $\mathcal{F}^r_{ij}(t)$ attains a large value of order one. The specific threshold one chooses to determine the butterfly velocity is thus somewhat arbitrary. We illustrate the dependence of the velocity v on the chosen threshold $\mathcal{F}^*$ of the reduced OTO correlator $\mathcal{F}^r_{ij}(t)$ in Fig. C.1.2. For large values of $\mathcal{F}^*$, the velocity converges toward a constant. Hence, the butterfly velocity will be largely insensitive to the precise choice of $\mathcal{F}^*$ as long as it is large enough. For the definition of v_b, we consider the specific value of $\mathcal{F}^*_b = 0.2$.

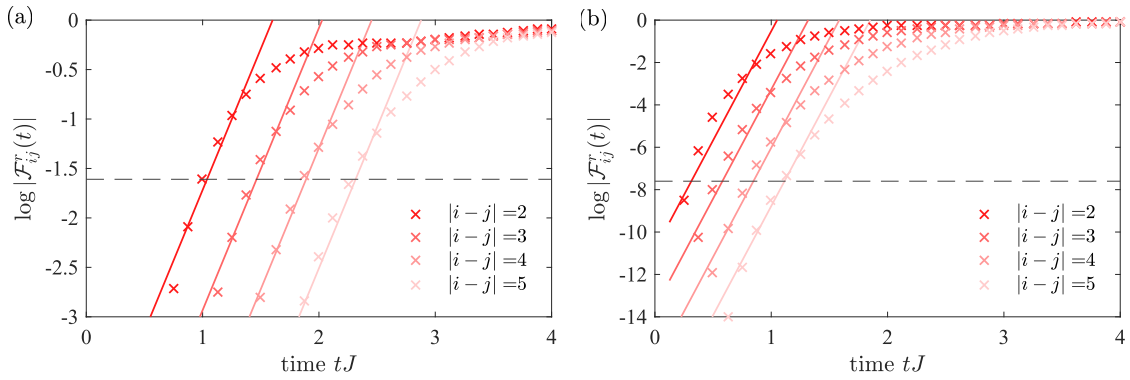

Figure C.1.3: Determining the Lyapunov exponent λ_L. OTO correlators $\mathcal{F}^r_{ij}(t)$ are shown for $T = 10J$ and $U = J$. Solid lines depict the predicted exponential growth from which we determine (a) the Lyapunov exponent $\lambda_L = 2.9(1)$ and (b) the light-cone exponent $\Lambda_{lc} = 10.3(5)$. The dashed gray line denotes the threshold value $\mathcal{F}^*$ used to determine the velocities v_b and v_{lc}, respectively. We obtain the exponents by fitting our data in a restricted regime around the threshold value $\mathcal{F}^*$ to the predicted exponential growth, see text for details. However, we note that in our data the exponential growth is limited to a rather small time range. The errorbars shown in Fig. 8.1.4 correspond to errors obtained from such fits.

In the limit $\mathcal{F}^* \to 0$, there is a strong dependence of v on the choice of the threshold. The light-cone velocity v_{lc} is defined by the fastest spread of information through the system and is determined by the reduced OTO correlator attaining a small value. To fulfill this definition, we fix $\mathcal{F}^*_{lc} = 0.0005$; see inset in Fig. C.1.2.

As described in section 8.1, from the SYK model and strongly coupled field theories one could expect that the OTO correlator grows exponentially on a timescale set approximately by the butterfly velocity. We thus fit the exponential function

$$\mathcal{F}^r_x(t) = a \cdot e^{\lambda_L\left(t-\frac{x}{v_b}\right)} \tag{C.3}$$

to the numerical data simultaneously for distances $1 \leq |i-j| \leq 5$ within the range $-2.5 \leq \log \mathcal{F}^r_{ij}(t) \leq -1$. The butterfly velocity v_b is determined as described above with the threshold $\mathcal{F}^* = 0.2$, which lies well within the interval of the considered data points; see Fig. C.1.3a for an exemplary plot. We note, however, that our data does not support an exponential growth of the OTO correlator over parametrically large times, since the collision time τ is similar to the scrambling time t_{scr} in our system. This is demonstrated by extracting the growth rate Λ_{lc} from linearizing the OTO correlator around the light-cone velocity within the range $-14 \leq \log \mathcal{F}^r_{ij}(t) \leq -4.5$, Fig. C.1.3b, which yields larger rates. In particular, for the parameters shown in Fig. C.1.3, we obtain $\lambda_L = 2.9(1)$ and $\Lambda_{lc} = 10.3(5)$, respectively.

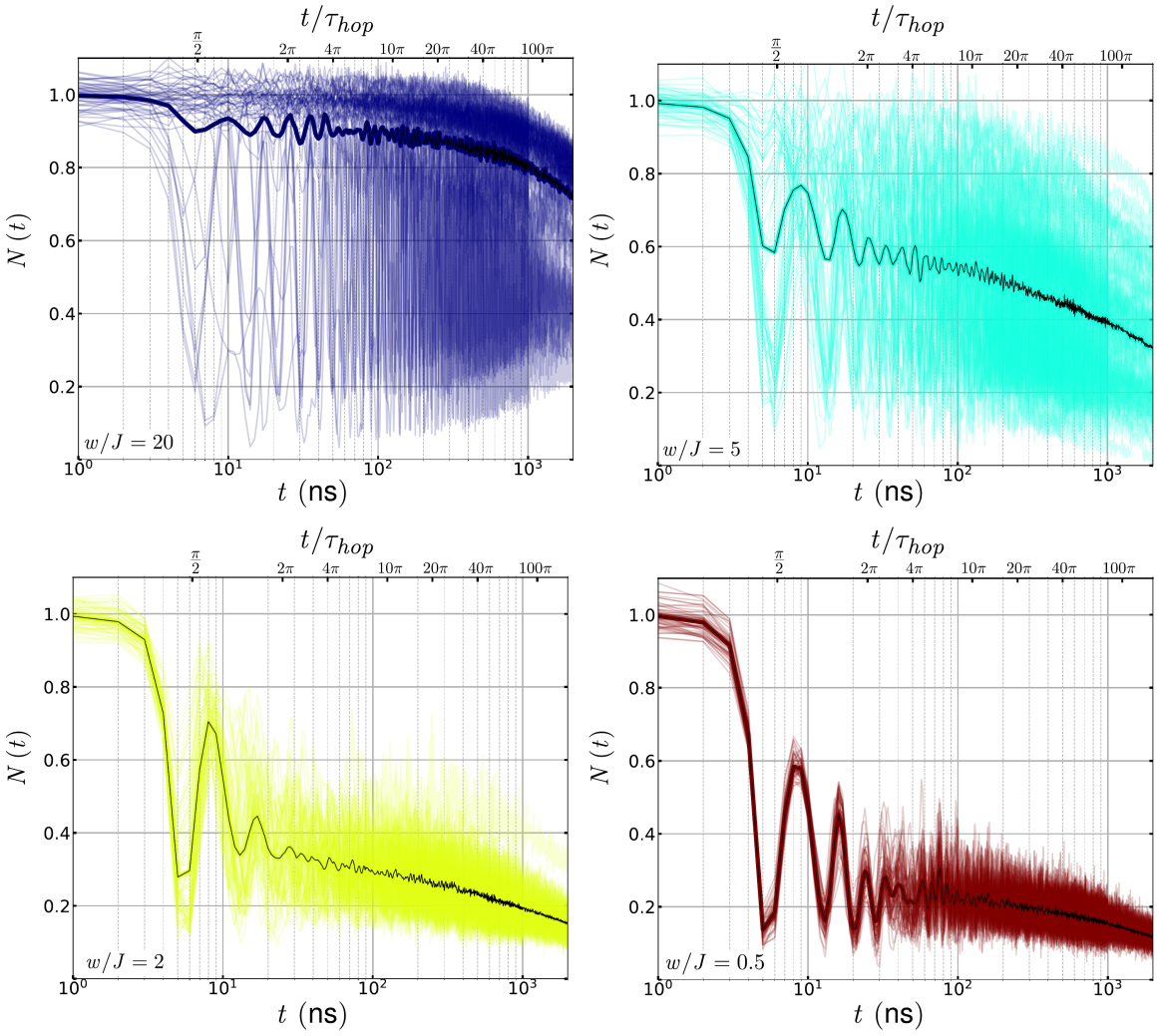

Figure C.2.1: Time evolution of the local particle number for all disorder instances for different disorder strengths w/J. The data shown in Fig. 9.2.3 prior to disorder averaging for disorder strengths a) $w/J = 20$, b) $w/J = 5$, c) $w/J = 2$ and d) $w/J = 0.5$.

C.2 Details on MBL

C.2.1 Characterizing MBL with superconducting qubits: additional data

In Fig. C.2.1, we show the time evoution of the local particle number prior to disorder averaging for $n_{ph} = 2$ and selected values of disorder parameter w for $J = 40$ MHz. The disorder averaged data (black lines) is contained in Fig. 9.2.3 a) of the main text. The spread in values at short time is primarily due to readout error, as state preparation error is small. For stronger disorder, Fig. C.2.1 a), b), the spread between disorder realizations is significantly larger than for small disorder strengths, Fig. C.2.1 c), d).

In the main text, we consider the dynamics up to times of about 100ns, well before the system is dominated by decoherence. The coupling to the environment renders the actual experiment an open system with relaxation – i.e. photon loss – and dephasing. The characteristic relaxation time is $T_1 \sim 10\mu s$, while the characteristic dephasing time is a few μs. The relaxation can be approximately modeled for a single qubit as

$$\overline{N^{\text{corr}}}(t) = \overline{N}(t)/e^{-t/10\mu s}. \tag{C.4}$$

In the case of strong disorder, and thus small localization length, relaxation is the dominant process by which a photon leaves the site on which it was initialized. This can be observed by the bending of the local particle number in Fig. C.2.1 starting at times $\sim 1\mu s$.

In Fig. C.2.2 we show extended data for echo sequence measurements for several values of the disorder strength w with J held fixed at 40MHz. Compared with Fig. 9.2.7 of the main text, the initial state for these measurements had an additional excitation at the indicated position (purple). In these measurements $\overline{\langle \sigma^z \rangle} = \overline{\langle 1 - 2\hat{a}^\dagger \hat{a} \rangle}$ does not depend on the position of the echo pulses. Note that an increase in $\overline{\langle \sigma^z \rangle}$ corresponds to a reduction in the local photon number, e.g. due to tunneling to the neighboring sites. In the case of strong disorder, $\overline{\langle \sigma^z \rangle}$ stays constant for all the observed times. We observe the expected signature of non-local interactions for all disorder strengths in the measurement of the purity. For increasing values of the disorder strength w/J, the purity stays at a higher value as expected from the τ-bit picture.

C.2.2 Machine learning dynamics in a disordered system: additional data

Transition: level statistics

Upon increasing the disorder strength, the level statistics of the Hamiltonian evolve from Gaussian-orthogonal ensemble statistics to Poisson statistics as the system enters the MBL phase [385]. We consider the level spacings

$$\delta_\varphi^{(n)} = |E_\varphi^{(n)} - E_\varphi^{(n-1)}|, \tag{C.5}$$

where $E_\varphi^{(n)}$ is the n-th eigenenergy of Hamiltonian (7.1) with disorder realization given by φ. The ratio of adjacent gaps is then given as

$$r_\varphi^{(n)} = \min\left(\delta_\varphi^{(n)}, \delta_\varphi^{(n+1)}\right) / \max\left(\delta_\varphi^{(n)}, \delta_\varphi^{(n+1)}\right). \tag{C.6}$$

For a given system size L, we fix the particle density to one particle per site and for each disorder strength W/J obtain the average value of this ratio over 30 disorder realizations, i.e. different values of φ. In Fig. C.2.3, the resulting average value of the ratio of adjacent energy gaps $\langle r \rangle$ is shown as a

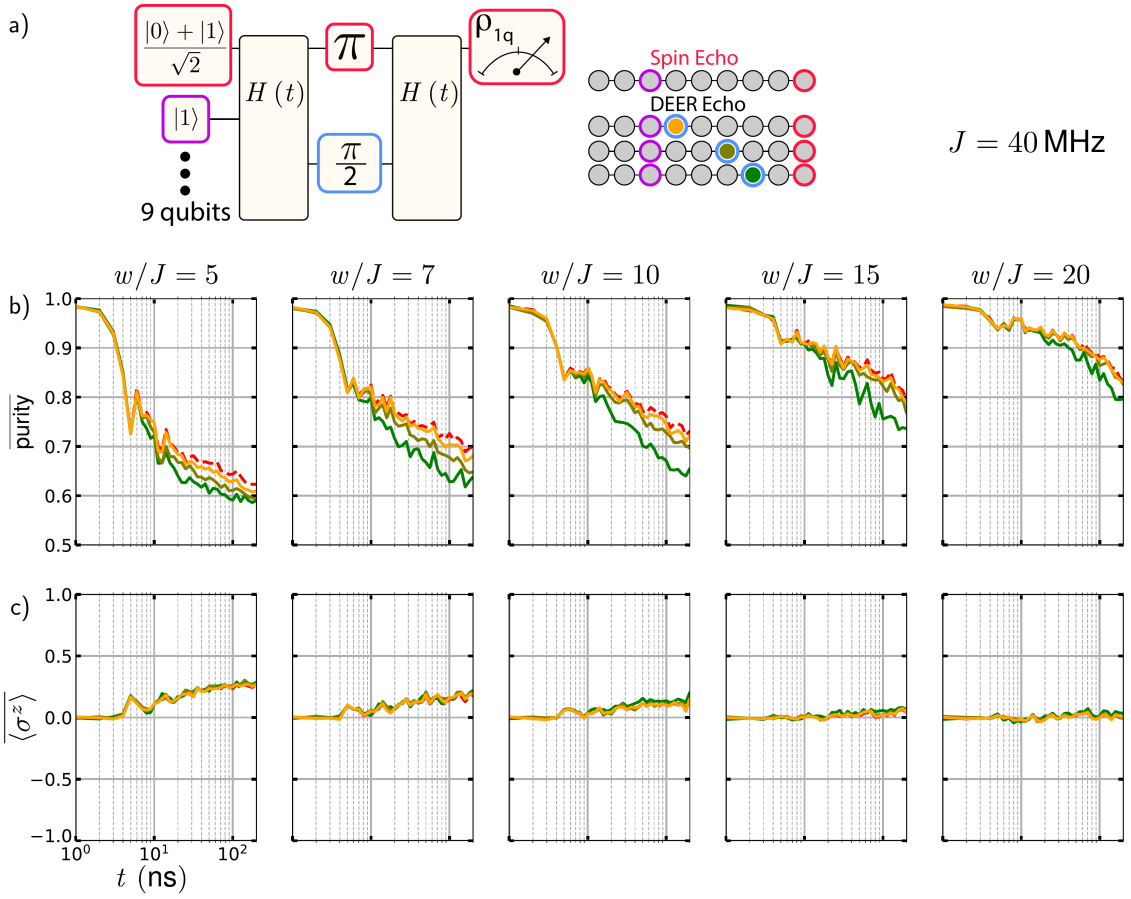

Figure C.2.2: Spin and DEER echo in the disordered Bose Hubbard model for different disorder strengths w/J. a) Spin and DEER echo pulse sequences. The blue outline indicates the position of the DEER echo pulse, and the position of an additional excitation is indicated in purple. b) Purity of the single qubit density matrix after the spin echo (dashed red lines) and DEER echo (solid lines) experiments. c) $\langle\sigma^z\rangle$ monitored over the echo experiments.

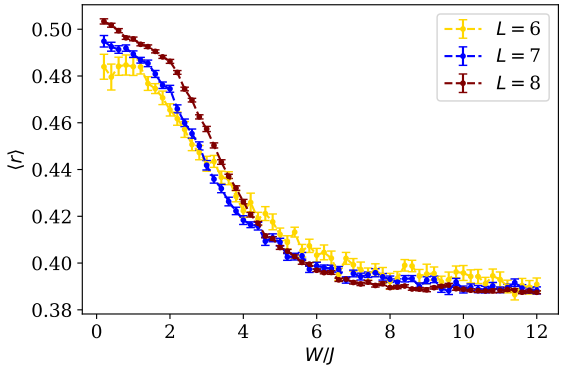

Figure C.2.3: Level statistics. Average value of the ratio of adjacent energy gaps for different system sizes $L = 6, 7, 8$ at a density of one particle per site as a function of disorder strength.

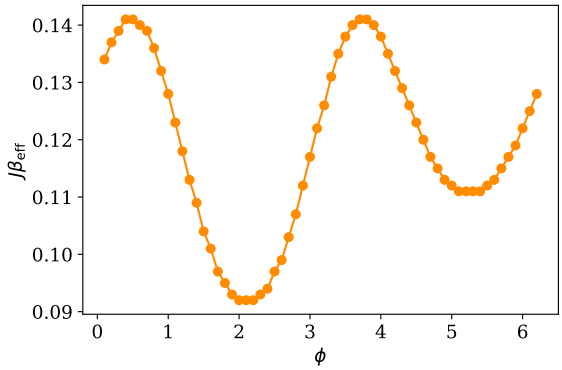

Figure C.2.4: Effective temperatures. Effective inverse temperatures β_{eff} for $U/J = 2.9$, $W/J = 4.5$ as a function of φ for a system with $L = 6$ sites and a density of one particle per site.

function of the disorder strength for system sizes $L = 6, 7, 8$. Comparing the different system sizes shows strong finite size effects, inhibiting the determination of the exact position of the transition.

Thermalization: effective temperatures

In section 9.3.2, we determine the effective temperature corresponding to the energy density of the initial state of the system. Due to the disorder potential, this effective temperature varies for different values of φ, where φ determines the disorder realization, see Eq. (9.46). In Fig. C.2.4, the effective temperature is shown as a function of φ for a system with $L = 6$ sites at unity filling for interaction strength $U/J = 2.9$ and disorder strength $W/J = 4.5$.

References

[1] A Bohrdt, C B Mendl, M Endres, and M Knap. Scrambling and thermalization in a diffusive quantum many-body system. *New Journal of Physics*, 19(6):063001, jun 2017.

[2] A. Bohrdt, D. Greif, E. Demler, M. Knap, and F. Grusdt. Angle-resolved photoemission spectroscopy with quantum gas microscopes. *Phys. Rev. B*, 97:125117, Mar 2018.

[3] F. Grusdt, M. Kánasz-Nagy, A. Bohrdt, C. S. Chiu, G. Ji, M. Greiner, D. Greif, and E. Demler. Parton theory of magnetic polarons: Mesonic resonances and signatures in dynamics. *Phys. Rev. X*, 8:011046, Mar 2018.

[4] Fabian Grusdt, Annabelle Bohrdt, and Eugene Demler. Microscopic spinon-chargon theory of magnetic polarons in the t–j model. *Phys. Rev. B*, 99:224422, Jun 2019.

[5] Annabelle Bohrdt, Christie S. Chiu, Geoffrey Ji, Muqing Xu, Daniel Greif, Markus Greiner, Eugene Demler, Fabian Grusdt, and Michael Knap. Classifying snapshots of the doped hubbard model with machine learning. *Nature Physics*, 15(9):921–924, 2019.

[6] Christie S. Chiu, Geoffrey Ji, Annabelle Bohrdt, Muqing Xu, Michael Knap, Eugene Demler, Fabian Grusdt, Markus Greiner, and Daniel Greif. String patterns in the doped hubbard model. *Science*, 365(6450):251–256, 2019.

[7] Jayadev Vijayan, Pimonpan Sompet, Guillaume Salomon, Joannis Koepsell, Sarah Hirthe, Annabelle Bohrdt, Fabian Grusdt, Immanuel Bloch, and Christian Gross. Time-resolved observation of spin-charge deconfinement in fermionic hubbard chains. *Science*, 367(6474):186–189, 2020.

[8] C. Hubig, A. Bohrdt, M. Knap, F. Grusdt, and J. I. Cirac. Evaluation of time-dependent correlators after a local quench in iPEPS: hole motion in the t-J model. *SciPost Phys.*, 8:21, 2020.

[9] Annabelle Bohrdt, Ahmed Omran, Eugene Demler, Snir Gazit, and Fabian Grusdt. Multiparticle interactions for ultracold atoms in optical tweezers: Cyclic ring-exchange terms. *Phys. Rev. Lett.*, 124:073601, Feb 2020.

[10] Annabelle Bohrdt, Eugene Demler, Frank Pollmann, Michael Knap, and Fabian Grusdt. Parton theory of angle-resolved photoemission spectroscopy spectra in antiferromagnetic mott insulators. *Phys. Rev. B*, 102:035139, Jul 2020.

[11] Annabelle Bohrdt, Fabian Grusdt, and Michael Knap. Dynamical formation of a magnetic polaron in a two-dimensional quantum antiferromagnet. *arXiv e-prints*, page arXiv:1907.08214, July 2019.

[12] A. Bohrdt, Y. Wang, J. Koepsell, M. Kánasz-Nagy, E. Demler, and F. Grusdt. Dominant fifth-order correlations in doped quantum anti-ferromagnets. *arXiv e-prints*, page arXiv:2007.07249, July 2020.

[13] B. Chiaro, C. Neill, A. Bohrdt, M. Filippone, F. Arute, K. Arya, R. Babbush, D. Bacon, J. Bardin, R. Barends, S. Boixo, D. Buell, B. Burkett, Y. Chen, Z. Chen, R. Collins, A. Dunsworth, E. Farhi, A. Fowler, B. Foxen, C. Gidney, M. Giustina, M. Harrigan, T. Huang, S. Isakov, E. Jeffrey, Z. Jiang, D. Kafri, K. Kechedzhi, J. Kelly, P. Klimov, A. Korotkov, F. Kostritsa, D. Landhuis, E. Lucero, J. McClean, X. Mi, A. Megrant, M. Mohseni, J. Mutus, M. McEwen, O. Naaman, M. Neeley, M. Niu, A. Petukhov, C. Quintana, N. Rubin, D. Sank, K. Satzinger, A. Vainsencher, T. White, Z. Yao, P. Yeh, A. Zalcman, V. Smelyanskiy, H. Neven, S. Gopalakrishnan, D. Abanin, M. Knap, J. Martinis, and P. Roushan. Growth and preservation of entanglement in a many-body localized system. *arXiv e-prints*, page arXiv:1910.06024, October 2019.

[14] Geoffrey Ji, Muqing Xu, Lev Haldar Kendrick, Christie S. Chiu, Justus C. Brüggenjürgen, Daniel Greif, Annabelle Bohrdt, Fabian Grusdt, Eugene Demler, Martin Lebrat, and Markus Greiner. Dynamical interplay between a single hole and a Hubbard antiferromagnet. *arXiv e-prints*, page arXiv:2006.06672, June 2020.

[15] Joannis Koepsell, Dominik Bourgund, Pimonpan Sompet, Sarah Hirthe, Annabelle Bohrdt, Yao Wang, Fabian Grusdt, Eugene Demler, Guillaume Salomon, Christian Gross, and Immanuel Bloch. Microscopic evolution of doped mott insulators from polaronic metal to fermi liquid. *arXiv e-prints*, page 2009.04440, September 2020.

[16] Cole Miles, Annabelle Bohrdt, Ruihan Wu, Christie Chiu, Muqing Xu, Geoffrey Ji, Markus Greiner, Kilian Q. Weinberger, Eugene Demler, and Eun-Ah Kim. Correlator convolutional neural networks: An interpretable architecture for image-like quantum matter data. 2020.

[17] A. Bohrdt, S. Kim, A. Lukin, M. Rispoli, R. Schittko, M. Knap, M. Greiner, and J. Léonard. Analyzing non-equilibrium quantum states through snapshots with artificial neural networks. 2020.

[18] Yao Wang, Annabelle Bohrdt, Joannis Koepsell, Eugene Demler, and Fabian Grusdt. Higher-order spin-hole correlations around a localized charge impurity. 2021.

[19] P. W. Anderson. More Is Different. *Science*, 177(4047):393–396, August 1972.

[20] Bose, S. N. Plancks Gesetz und Lichtquantenhypothese. *Zeitschrift fur Physik*, 26(1):178–181, December 1924.

[21] A. Einstein. Quantentheorie des einatomigen idealen gases. *S. B. Preuss. Akad. Wiss. phys.-math. Klasse*, 1924.

[22] M. H. Anderson, J. R. Ensher, M. R. Matthews, C. E. Wieman, and E. A. Cornell. Observation of bose-einstein condensation in a dilute atomic vapor. *Science*, 269(5221):198–201, 1995.

[23] K. B. Davis, M. O. Mewes, M. R. Andrews, N. J. van Druten, D. S. Durfee, D. M. Kurn, and W. Ketterle. Bose-einstein condensation in a gas of sodium atoms. *Phys. Rev. Lett.*, 75:3969–3973, Nov 1995.

[24] David C. Aveline, Jason R. Williams, Ethan R. Elliott, Chelsea Dutenhoffer, James R. Kellogg, James M. Kohel, Norman E. Lay, Kamal Oudrhiri, Robert F. Shotwell, Nan Yu, and Robert J. Thompson. Observation of bose–einstein condensates in an earth-orbiting research lab. *Nature*, 582(7811):193–197, 2020.

[25] T. Giamarchi. *Quantum Physics in One Dimension*. International Series of Monographs on Physics. Clarendon Press, 2003.

[26] K. V. Klitzing, G. Dorda, and M. Pepper. New Method for High-Accuracy Determination of the Fine-Structure Constant Based on Quantized Hall Resistance. *Phys. Rev. Lett.*, 45(6):494–497, August 1980.

[27] D. C. Tsui, H. L. Stormer, and A. C. Gossard. Two-dimensional magnetotransport in the extreme quantum limit. *Phys. Rev. Lett.*, 48:1559–1562, May 1982.

[28] Xiao-Gang Wen. *Quantum Field Theory of Many-body Systems*. Oxford University Press, 2004.

[29] J. G. Bednorz and K. A. Müller. Possible high T_c superconductivity in the Ba-La-Cu-O system. *Zeitschrift fur Physik B Condensed Matter*, 64:189–193, Jun 1986.

[30] Philip Warren Anderson. The Resonating Valence Bond State in La2CuO4 and Superconductivity. *Science*, 235(4793):1196–1198, 1987.

[31] F. C. Zhang and T. M. Rice. Effective hamiltonian for the superconducting cu oxides. *Phys. Rev. B*, 37:3759–3761, Mar 1988.

[32] Richard P. Feynman. Simulating Physics with Computers. *International Journal of Theoretical Physics*, 21(6-7):467–488, June 1982.

[33] Ehud Altman, Kenneth R. Brown, Giuseppe Carleo, Lincoln D. Carr, Eugene Demler, Cheng Chin, Brian DeMarco, Sophia E. Economou, Mark A. Eriksson, Kai-Mei C. Fu, Markus Greiner, Kaden R. A. Hazzard, Randall G. Hulet, Alicia J. Kollar, Benjamin L. Lev, Mikhail D. Lukin, Ruichao Ma, Xiao Mi, Shashank Misra, Christopher Monroe, Kater Murch, Zaira Nazario, Kang-Kuen Ni, Andrew C. Potter, Pedram Roushan, Mark Saffman, Monika Schleier-Smith, Irfan Siddiqi, Raymond Simmonds, Meenakshi Singh, I. B. Spielman, Kristan Temme, David S. Weiss, Jelena Vuckovic, Vladan Vuletic, Jun Ye, and Martin Zwierlein. Quantum Simulators: Architectures and Opportunities. *arXiv e-prints*, page arXiv:1912.06938, December 2019.

[34] Thomas Schweigler, Valentin Kasper, Sebastian Erne, Igor Mazets, Bernhard Rauer, Federica Cataldini, Tim Langen, Thomas Gasenzer, Jürgen Berges, and Jörg Schmiedmayer. Experimental characterization of a quantum many-body system via higher-order correlations. *Nature*, 545(7654):323–326, May 2017.

[35] Alexander Lukin, Matthew Rispoli, Robert Schittko, M. Eric Tai, Adam M. Kaufman, Soonwon Choi, Vedika Khemani, Julian Léonard, and Markus Greiner. Probing entanglement in a many-body–localized system. *Science*, 364(6437):256–260, 2019.

[36] Torsten V. Zache, Thomas Schweigler, Sebastian Erne, Jörg Schmiedmayer, and Jürgen Berges. Extracting the field theory description of a quantum many-body system from experimental data. *Phys. Rev. X*, 10:011020, Jan 2020.

[37] D. Fausti, R. I. Tobey, N. Dean, S. Kaiser, A. Dienst, M. C. Hoffmann, S. Pyon, T. Takayama, H. Takagi, and A. Cavalleri. Light-induced superconductivity in a stripe-ordered cuprate. *Science*, 331(6014):189–191, 2011.

[38] J. Choi, S. Hild, J. Zeiher, P. Schauss, T. Yefsah A. Rubio-Abadal1, V. Khemani, D. A. Huse, I. Bloch, and C. Gross. Exploring the many-body localization transition in two dimensions. *Science*, 352:1547–1552, 2016.

[39] Christian Gross and Immanuel Bloch. Quantum simulations with ultracold atoms in optical lattices. *Science*, 357(6355):995–1001, 2017.

[40] Markus Greiner. Atomic legos: Building and investigating quantum materials one atom at a time. *https://www.youtube.com/watch?v=QQo7oumFly4*, May 2014.

[41] Manuel Endres, Hannes Bernien, Alexander Keesling, Harry Levine, Eric R. Anschuetz, Alexandre Krajenbrink, Crystal Senko, Vladan Vuletic, Markus Greiner, and Mikhail D. Lukin. Atom-by-atom assembly of defect-free one-dimensional cold atom arrays. *Science*, 354(6315):1024–1027, 2016.

[42] John L. Bohn, Ana Maria Rey, and Jun Ye. Cold molecules: Progress in quantum engineering of chemistry and quantum matter. *Science*, 357(6355):1002–1010, 2017.

[43] R. Blatt and C. F. Roos. Quantum simulations with trapped ions. *Nature Physics*, 8(4):277–284, 2012.

[44] G. Kucsko, S. Choi, J. Choi, P. C. Maurer, H. Zhou, R. Landig, H. Sumiya, S. Onoda, J. Isoya, F. Jelezko, E. Demler, N. Y. Yao, and M. D. Lukin. Critical thermalization of a disordered dipolar spin system in diamond. *Phys. Rev. Lett.*, 121:023601, Jul 2018.

[45] Mete Atatüre, Dirk Englund, Nick Vamivakas, Sang-Yun Lee, and Joerg Wrachtrup. Material platforms for spin-based photonic quantum technologies. *Nature Reviews Materials*, 3(5):38–51, 2018.

[46] Hengyun Zhou, Joonhee Choi, Soonwon Choi, Renate Landig, Alexander M. Douglas, Junichi Isoya, Fedor Jelezko, Shinobu Onoda, Hitoshi Sumiya, Paola Cappellaro, and et al. Quantum metrology with strongly interacting spin systems. *Physical Review X*, 10(3), Jul 2020.

[47] J. Salfi, J. A. Mol, R. Rahman, G. Klimeck, M. Y. Simmons, L. C. L. Hollenberg, and S. Rogge. Quantum simulation of the hubbard model with dopant atoms in silicon. *Nature Communications*, 7(1):11342, 2016.

[48] Enrico Prati, Kuninori Kumagai, Masahiro Hori, and Takahiro Shinada. Band transport across a chain of dopant sites in silicon over micron distances and high temperatures. *Scientific Reports*, 6(1):19704, 2016.

[49] U. Mukhopadhyay, J.P. Dehollain, C. Reichl, W. Wegscheider, , and L.M.K. Vandersypen. A 2×2 quantum dot array with controllable inter-dot tunnel couplings. *Appl.Phys.Lett. 112, 183505*, 2018.

[50] T. Hensgens, T. Fujita, L. Janssen, Xiao Li, C. J. Van Diepen, C. Reichl, W. Wegscheider, S. Das Sarma, and L. M. K. Vandersypen. Quantum simulation of a fermi–hubbard model using a semiconductor quantum dot array. *Nature*, 548(7665):70–73, 2017.

[51] Immanuel Bloch, Jean Dalibard, and Wilhelm Zwerger. Many-body physics with ultracold gases. *Rev. Mod. Phys.*, 80:885–964, Jul 2008.

[52] Leticia Tarruell and Laurent Sanchez-Palencia. Quantum simulation of the hubbard model with ultracold fermions in optical lattices. *Comptes Rendus Physique*, 19(6):365 – 393, 2018.

[53] Maxwell Parsons. *Probing the Hubbard Model With Single-Site Resolution*. PhD thesis, Graduate School of Arts and Sciences, Harvard University, 2016.

[54] Anton Mazurenko. *Probing Long Range Antiferromagnetism and Dynamics in the Fermi-Hubbard Model*. PhD thesis, Graduate School of Arts and Sciences, Harvard University, 2017.

[55] Christie S. Chiu. *Quantum simulation of the Hubbard model*. PhD thesis, Graduate School of Arts and Sciences, Harvard University, 2019.

[56] Jayadev Vijayan. *Microscopy of spin-charge dynamics in Fermi-Hubbard chains*. PhD thesis, Februar 2020.

[57] Thomas Hartke, Botond Oreg, Ningyuan Jia, and Martin Zwierlein. Measuring total density correlations in a fermi-hubbard gas via bilayer microscopy. *arXiv e-prints*, page 2003.11669, March 2020.

[58] G. Zürn, T. Lompe, A. N. Wenz, S. Jochim, P. S. Julienne, and J. M. Hutson. Precise characterization of ^{6}Li feshbach resonances using trap-sideband-resolved rf spectroscopy of weakly bound molecules. *Phys. Rev. Lett.*, 110:135301, Mar 2013.

[59] Karl D. Nelson, Xiao Li, and David S. Weiss. Imaging single atoms in a three-dimensional array. *Nature Physics*, 3(8):556–560, 2007.

[60] Waseem S. Bakr, Jonathon I. Gillen, Amy Peng, Simon Foelling, and Markus Greiner. A quantum gas microscope for detecting single atoms in a hubbard-regime optical lattice. *Nature*, 462(7269):74–U80, November 2009.

[61] Jacob F. Sherson, Christof Weitenberg, Manuel Endres, Marc Cheneau, Immanuel Bloch, and Stefan Kuhr. Single-atom-resolved fluorescence imaging of an atomic mott insulator. *Nature*, 467(7311):68–U97, September 2010.

[62] Florian Huber. *Site-Resolved Imaging with the Fermi Gas Microscope*. PhD thesis, Graduate School of Arts and Sciences, Harvard University, 2014.

[63] Maxwell F. Parsons, Anton Mazurenko, Christie S. Chiu, Geoffrey Ji, Daniel Greif, and Markus Greiner. Site-resolved measurement of the spin-correlation function in the Fermi-Hubbard model. *Science*, 323(6305):1253–6, 2016.

[64] Ahmed Omran, Martin Boll, Timon A. Hilker, Katharina Kleinlein, Guillaume Salomon, Immanuel Bloch, and Christian Gross. Microscopic observation of pauli blocking in degenerate fermionic lattice gases. *Phys. Rev. Lett.*, 115:263001, Dec 2015.

[65] Lawrence W. Cheuk, Matthew A. Nichols, Melih Okan, Thomas Gersdorf, Vinay V. Ramasesh, Waseem S. Bakr, Thomas Lompe, and Martin W. Zwierlein. Quantum-gas microscope for fermionic atoms. *Phys. Rev. Lett.*, 114:193001, May 2015.

[66] Matthew Rispoli, Alexander Lukin, Robert Schittko, Sooshin Kim, M. Eric Tai, Julian Léonard, and Markus Greiner. Quantum critical behaviour at the many-body localization transition. *Nature*, 573(7774):385–389, 2019.

[67] Immanuel Bloch, Jean Dalibard, and Sylvain Nascimbène. Quantum simulations with ultracold quantum gases. *Nature Physics*, 8(4):267–276, 2012.

[68] Markus Greiner, Olaf Mandel, Tilman Esslinger, Theodor W. Hänsch, and Immanuel Bloch. Quantum phase transition from a superfluid to a mott insulator in a gas of ultracold atoms. *Nature*, 415(6867):39–44, 2002.

[69] Manuel Endres, Takeshi Fukuhara, David Pekker, Marc Cheneau, Peter Schauβ, Christian Gross, Eugene Demler, Stefan Kuhr, and Immanuel Bloch. The 'higgs'amplitude mode at the two-dimensional superfluid/mott insulator transition. *Nature*, 487(7408):454–458, 2012.

[70] Robert Jordens, Niels Strohmaier, Kenneth Gunter, Henning Moritz, and Tilman Esslinger. A mott insulator of fermionic atoms in an optical lattice. *Nature*, 455(7210):204–207, September 2008.

[71] U. Schneider, L. Hackermüller, S. Will, Th. Best, I. Bloch, T. A. Costi, R. W. Helmes, D. Rasch, and A. Rosch. Metallic and insulating phases of repulsively interacting fermions in a 3d optical lattice. *Science*, 322(5907):1520–1525, 2008.

[72] Pedro M. Duarte, Russell A. Hart, Tsung-Lin Yang, Xinxing Liu, Thereza Paiva, Ehsan Khatami, Richard T. Scalettar, Nandini Trivedi, and Randall G. Hulet. Compressibility of a fermionic mott insulator of ultracold atoms. *Phys. Rev. Lett.*, 114:070403, Feb 2015.

[73] Daniel Greif, Thomas Uehlinger, Gregor Jotzu, Leticia Tarruell, and Tilman Esslinger. Short-range quantum magnetism of ultracold fermions in an optical lattice. *Science*, 340(6138):1307–1310, 2013.

[74] Russell A. Hart, Pedro M. Duarte, Tsung-Lin Yang, Xinxing Liu, Thereza Paiva, Ehsan Khatami, Richard T. Scalettar, Nandini Trivedi, David A. Huse, and Randall G. Hulet. Observation of antiferromagnetic correlations in the hubbard model with ultracold atoms. *Nature*, 519:211––214, 02 2015.

[75] Timon A Hilker, Guillaume Salomon, Fabian Grusdt, Ahmed Omran, Martin Boll, Eugene Demler, Immanuel Bloch, and Christian Gross. Revealing hidden antiferromagnetic correlations in doped Hubbard chains via string correlators. *Science*, 357:484–7, 2017.

[76] Anton Mazurenko, Christie S. Chiu, Geoffrey Ji, Maxwell F. Parsons, Márton Kanász-Nagy, Richard Schmidt, Fabian Grusdt, Eugene Demler, Daniel Greif, and Markus Greiner. A cold-atom Fermi–Hubbard antiferromagnet. *Nature*, 545(7655):462–6, 2017.

[77] Peter T. Brown, Debayan Mitra, Elmer Guardado-Sanchez, Reza Nourafkan, Alexis Reymbaut, Charles-David Hebert, Simon Bergeron, A.-M. S. Tremblay, Jure Kokalj, David A. Huse, Peter Schauß, and Waseem S. Bakr. Bad metallic transport in a cold atom fermi-hubbard system. *Science*, 363(6425):379–, January 2019.

[78] Matthew A. Nichols, Lawrence W. Cheuk, Melih Okan, Thomas R. Hartke, Enrique Mendez, T. Senthil, Ehsan Khatami, Hao Zhang, and Martin W. Zwierlein. Spin transport in a Mott insulator of ultracold fermions. *Science*, 363(6425):383–387, January 2019.

[79] Peter T. Brown, Elmer Guardado-Sanchez, Benjamin M. Spar, Edwin W. Huang, Thomas P. Devereaux, and Waseem S. Bakr. Angle-resolved photoemission spectroscopy of a fermi–hubbard system. *Nature Physics*, 16(1):26–31, Oct 2019.

[80] Martin Miranda, Ryotaro Inoue, Yuki Okuyama, Akimasa Nakamoto, and Mikio Kozuma. Site-resolved imaging of ytterbium atoms in a two-dimensional optical lattice. *Phys. Rev. A*, 91:063414, Jun 2015.

[81] Ryuta Yamamoto, Jun Kobayashi, Takuma Kuno, Kohei Kato, and Yoshiro Takahashi. An ytterbium quantum gas microscope with narrow-line laser cooling. *New Journal of Physics*, 18(2):023016, feb 2016.

[82] Elmar Haller, James Hudson, Andrew Kelly, Dylan A. Cotta, Bruno Peaudecerf, Graham D. Bruce, and Stefan Kuhr. Single-atom imaging of fermions in a quantum-gas microscope. *Nat Phys*, 11(9):738–742, September 2015.

[83] G. J. A. Edge, R. Anderson, D. Jervis, D. C. McKay, R. Day, S. Trotzky, and J. H. Thywissen. Imaging and addressing of individual fermionic atoms in an optical lattice. *Phys. Rev. A*, 92:063406, Dec 2015.

[84] Maxwell F. Parsons, Florian Huber, Anton Mazurenko, Christie S. Chiu, Widagdo Setiawan, Katherine Wooley-Brown, Sebastian Blatt, and Markus Greiner. Site-Resolved Imaging of Fermionic 6 Li in an Optical Lattice. *Physical Review Letters*, 114(21):213002, 2015.

[85] Peter T. Brown, Debayan Mitra, Elmer Guardado-Sanchez, Peter Schauß, Stanimir S. Kondov, Ehsan Khatami, Thereza Paiva, Nandini Trivedi, David A. Huse, and Waseem S. Bakr. Spin-imbalance in a 2d fermi-hubbard system. *Science*, 357(6358):1385–, September 2017.

[86] M. Aidelsburger, M. Atala, S. Nascimbene, S. Trotzky, Y.-. A. Chen, and I. Bloch. Experimental realization of strong effective magnetic fields in an optical lattice. *Physical Review Letters*, 107(25):255301, December 2011.

[87] M. Aidelsburger, M. Atala, M. Lohse, J. T. Barreiro, B. Paredes, and I. Bloch. Realization of the hofstadter hamiltonian with ultracold atoms in optical lattices. *Physical Review Letters*, 111:185301, 2013.

[88] Gregor Jotzu, Michael Messer, Rémi Desbuquois, Martin Lebrat, Thomas Uehlinger, Daniel Greif, and Tilman Esslinger. Experimental realization of the topological haldane model with ultracold fermions. *Nature*, 515(7526):237–240, 2014.

[89] N. Fläschner, B. S. Rem, M. Tarnowski, D. Vogel, D.-S. Lühmann, K. Sengstock, and C. Weitenberg. Experimental reconstruction of the berry curvature in a floquet bloch band. *Science*, 352(6289):1091–1094, 2016.

[90] M. Schreiber, S. S. Hodgman, P. Bordia, H. P. Luschen, M. H. Fischer, R. Vosk, E. Altman, U. Schneider, and I. Bloch. Observation of many-body localization of interacting fermions in a quasirandom optical lattice. *Science*, 349(6250):842–845, Jul 2015.

[91] Pranjal Bordia, Henrik Lüschen, Sebastian Scherg, Sarang Gopalakrishnan, Michael Knap, Ulrich Schneider, and Immanuel Bloch. Probing slow relaxation and many-body localization in two-dimensional quasiperiodic systems. *Phys. Rev. X*, 7(4):041047, 2017.

[92] Thomas Kohlert, Sebastian Scherg, Xiao Li, Henrik P. Lüschen, Sankar Das Sarma, Immanuel Bloch, and Monika Aidelsburger. Observation of many-body localization in a one-dimensional system with a single-particle mobility edge. *Phys. Rev. Lett.*, 122:170403, May 2019.

[93] Rajibul Islam, Ruichao Ma, Philipp M. Preiss, M. Eric Tai, Alexander Lukin, Matthew Rispoli, and Markus Greiner. Measuring entanglement entropy in a quantum many-body system. *Nature*, 528(7580):77–83, December 2015.

[94] A. M. Kaufman, M. E. Tai, A. Lukin, M. Rispoli, R. Schittko, P. M. Preiss, and M. Greiner. Quantum thermalization through entanglement in an isolated many-body system. *Science*, 353:794–800, 2016.

[95] Sebastian Hild, Takeshi Fukuhara, Peter Schauß, Johannes Zeiher, Michael Knap, Eugene Demler, Immanuel Bloch, and Christian Gross. Far-from-equilibrium spin transport in heisenberg quantum magnets. *Phys. Rev. Lett.*, 113:147205, Oct 2014.

[96] Takeshi Fukuhara, Adrian Kantian, Manuel Endres, Marc Cheneau, Peter Schauss, Sebastian Hild, David Bellem, Ulrich Schollwoeck, Thierry Giamarchi, Christian Gross, Immanuel Bloch, and Stefan Kuhr. Quantum dynamics of a mobile spin impurity. *Nature Physics*, 9(4):235–241, April 2013.

[97] M. H. Devoret, A. Wallraff, and J. M. Martinis. Superconducting Qubits: A Short Review. *arXiv e-prints*, pages cond–mat/0411174, Nov 2004.

[98] Charles Neill. *A path towards quantum supremacy with superconducting qubits*. PhD thesis, University of California Santa Barbara, 2017.

[99] Morten Kjaergaard, Mollie E. Schwartz, Jochen Braumüller, Philip Krantz, Joel I.-J. Wang, Simon Gustavsson, and William D. Oliver. Superconducting qubits: Current state of play. *Annual Review of Condensed Matter Physics*, 11(1):369–395, Mar 2020.

[100] Alexander Shnirman, Gerd Schön, and Ziv Hermon. Quantum Manipulations of Small Josephson Junctions. *Physical Review Letters*, 79(12):2371–2374, Sep 1997.

[101] P. Roushan, C. Neill, A. Megrant, Y. Chen, R. Babbush, R. Barends, B. Campbell, Z. Chen, B. Chiaro, A. Dunsworth, and et al. Chiral ground-state currents of interacting photons in a synthetic magnetic field. *Nature Physics*, 13(2):146–151, Oct 2016.

[102] Frank Arute, Kunal Arya, Ryan Babbush, Dave Bacon, Joseph C. Bardin, Rami Barends, Rupak Biswas, Sergio Boixo, Fernando G. S. L. Brandao, David A. Buell, Brian Burkett, Yu Chen, Zijun Chen, Ben Chiaro, Roberto Collins, William Courtney, Andrew Dunsworth, Edward Farhi, Brooks Foxen, Austin Fowler, Craig Gidney, Marissa Giustina, Rob Graff, Keith Guerin, Steve Habegger, Matthew P. Harrigan, Michael J. Hartmann, Alan Ho, Markus Hoffmann, Trent Huang, Travis S. Humble, Sergei V. Isakov, Evan Jeffrey, Zhang Jiang, Dvir Kafri, Kostyantyn Kechedzhi, Julian Kelly, Paul V. Klimov, Sergey Knysh, Alexander Korotkov, Fedor Kostritsa, David Landhuis, Mike Lindmark, Erik Lucero, Dmitry Lyakh, Salvatore Mandrà, Jarrod R. McClean, Matthew McEwen, Anthony Megrant, Xiao Mi, Kristel Michielsen, Masoud Mohseni, Josh Mutus, Ofer Naaman, Matthew Neeley, Charles Neill, Murphy Yuezhen Niu, Eric Ostby, Andre Petukhov, John C. Platt, Chris Quintana, Eleanor G. Rieffel, Pedram Roushan, Nicholas C. Rubin, Daniel Sank, Kevin J. Satzinger, Vadim Smelyanskiy, Kevin J. Sung, Matthew D. Trevithick, Amit Vainsencher, Benjamin Villalonga, Theodore White, Z. Jamie Yao, Ping Yeh, Adam Zalcman, Hartmut Neven, and John M. Martinis. Quantum supremacy using a programmable superconducting processor. *Nature*, 574(7779):505–510, 2019.

[103] Y. Salathé, M. Mondal, M. Oppliger, J. Heinsoo, P. Kurpiers, A. Potočnik, A. Mezzacapo, U. Las Heras, L. Lamata, E. Solano, S. Filipp, and A. Wallraff. Digital quantum simulation of spin models with circuit quantum electrodynamics. *Phys. Rev. X*, 5:021027, Jun 2015.

[104] R. Barends, L. Lamata, J. Kelly, L. García-Álvarez, A. G. Fowler, A. Megrant, E. Jeffrey, T. C. White, D. Sank, J. Y. Mutus, B. Campbell, Yu Chen, Z. Chen, B. Chiaro, A. Dunsworth, I. C. Hoi, C. Neill, P. J. J. O'Malley, C. Quintana, P. Roushan, A. Vainsencher, J. Wenner, E. Solano, and John M. Martinis. Digital quantum simulation of fermionic models with a superconducting circuit. *Nature Communications*, 6(1):7654, 2015.

[105] P. J. J. O'Malley, R. Babbush, I. D. Kivlichan, J. Romero, J. R. McClean, R. Barends, J. Kelly, P. Roushan, A. Tranter, N. Ding, B. Campbell, Y. Chen, Z. Chen, B. Chiaro, A. Dunsworth, A. G. Fowler, E. Jeffrey, E. Lucero, A. Megrant, J. Y. Mutus, M. Neeley, C. Neill, C. Quintana, D. Sank, A. Vainsencher, J. Wenner, T. C. White, P. V. Coveney, P. J. Love, H. Neven,

A. Aspuru-Guzik, and J. M. Martinis. Scalable quantum simulation of molecular energies. *Phys. Rev. X*, 6:031007, Jul 2016.

[106] Zhiguang Yan, Yu-Ran Zhang, Ming Gong, Yulin Wu, Yarui Zheng, Shaowei Li, Can Wang, Futian Liang, Jin Lin, Yu Xu, Cheng Guo, Lihua Sun, Cheng-Zhi Peng, Keyu Xia, Hui Deng, Hao Rong, J. Q. You, Franco Nori, Heng Fan, Xiaobo Zhu, and Jian-Wei Pan. Strongly correlated quantum walks with a 12-qubit superconducting processor. *Science*, 364(6442):753–756, 2019.

[107] Clai Owens, Aman LaChapelle, Brendan Saxberg, Brandon M. Anderson, Ruichao Ma, Jonathan Simon, and David I. Schuster. Quarter-flux hofstadter lattice in a qubit-compatible microwave cavity array. *Phys. Rev. A*, 97:013818, Jan 2018.

[108] P. Roushan, C. Neill, J. Tangpanitanon, V. M. Bastidas, A. Megrant, R. Barends, Y. Chen, Z. Chen, B. Chiaro, A. Dunsworth, A. Fowler, B. Foxen, M. Giustina, E. Jeffrey, J. Kelly, E. Lucero, J. Mutus, M. Neeley, C. Quintana, D. Sank, A. Vainsencher, J. Wenner, T. White, H. Neven, D. G. Angelakis, and J. Martinis. Spectroscopic signatures of localization with interacting photons in superconducting qubits. *Science*, 358(6367):1175–1179, 2017.

[109] Ruichao Ma, Brendan Saxberg, Clai Owens, Nelson Leung, Yao Lu, Jonathan Simon, and David I. Schuster. A dissipatively stabilized mott insulator of photons. *Nature*, 566(7742):51–57, 2019.

[110] Yosuke Nagaoka. Ferromagnetism in a Narrow, Almost Half-Filled s Band. *Physical Review*, 147(1):392–405, 1966.

[111] J. Hubbard. Electron Correlations in Narrow Energy Bands. *Proceedings of the Royal Society of London Series A*, 276(1365):238–257, Nov 1963.

[112] B. Keimer, S. A. Kivelson, M. R. Norman, S. Uchida, and J. Zaanen. From quantum matter to high-temperature superconductivity in copper oxides. *Nature*, 518:179–186, 2015.

[113] Claudius Gros. Physics of Projected Wavefunctions. *Annals of Physics*, 189:53–88, 1989.

[114] Adrian Cho. High tc: The mystery that defies solution. *Science*, 314(5802):1072–1075, 2006.

[115] Philip W. Anderson. Personal history of my engagement with cuprate superconductivity, 1986-2010. *International Journal of Modern Physics B*, 25(01):1–39, 2011.

[116] A. H. MacDonald, S. M. Girvin, and D. Yoshioka. $\frac{t}{U}$ expansion for the hubbard model. *Phys. Rev. B*, 37:9753–9756, Jun 1988.

[117] Assa Auerbach. *Interacting Electrons and Quantum Magnetism*. Springer, Berlin, 1998.

[118] Alexey V. Gorshkov, Salvatore R. Manmana, Gang Chen, Jun Ye, Eugene Demler, Mikhail D. Lukin, and Ana Maria Rey. Tunable superfluidity and quantum magnetism with ultracold polar molecules. *Phys. Rev. Lett.*, 107:115301, Sep 2011.

[119] Johannes Zeiher, Rick van Bijnen, Peter Schausz, Sebastian Hild, Jae-yoon Choi, Thomas Pohl, Immanuel Bloch, and Christian Gross. Many-body interferometry of a rydberg-dressed spin lattice. *Nat Phys*, 12(12):1095–1099, December 2016.

[120] Johannes Zeiher, Jae-yoon Choi, Antonio Rubio-Abadal, Thomas Pohl, Rick van Bijnen, Immanuel Bloch, and Christian Gross. Coherent many-body spin dynamics in a long-range interacting ising chain. *Physical Review X*, 7(4), Dec 2017.

[121] L. M. Duan, E. Demler, and M. D. Lukin. Controlling Spin Exchange Interactions of Ultracold Atoms in Optical Lattices. *Physical Review Letters*, 91(9):090402, Aug 2003.

[122] R. C. Brown, R. Wyllie, S. B. Koller, E. A. Goldschmidt, M. Foss-Feig, and J. V. Porto. Two-dimensional superexchange-mediated magnetization dynamics in an optical lattice. *Science*, 348(6234):540–544, 2015.

[123] Guillaume Salomon, Joannis Koepsell, Jayadev Vijayan, Timon A. Hilker, Jacopo Nespolo, Lode Pollet, Immanuel Bloch, and Christian Gross. Direct Observation of Incommensurate Magnetism in Hubbard Chains. *Nature*, 565:56–60, Jan 2019.

[124] N.E. Bickers, D.J. Scalapino, and R.T. Scalettar. Cdw and sdw mediated pairing interactions. *International Journal of Modern Physics B*, 01(03n04):687–695, 1987.

[125] C. Dong, J. K. Liang, G. C. Che, S. S. Xie, Z. X. Zhao, Q. S. Yang, Y. M. Ni, and G. R. Liu. Superconductivity and crystal structure in the La-Ba-Cu-O system. *Physical Review B*, 37(10):5182–5185, Apr 1988.

[126] C. Gros, D. Poilblanc, T. M. Rice, and F. C. Zhang. Superconductivity in correlated wavefunctions. *Physica C Superconductivity*, 153:543–548, Jun 1988.

[127] Gabriel Kotliar and Jialin Liu. Superexchange mechanism and d-wave superconductivity. *Physical Review B*, 38(7):5142–5145, Sep 1988.

[128] Andrea Damascelli, Zahid Hussain, and Zhi-Xun Shen. Angle-resolved photoemission studies of the cuprate superconductors. *Rev. Mod. Phys.*, 75:473–541, Apr 2003.

[129] Patrick A. Lee, Naoto Nagaosa, and Xiao Gang Wen. Doping a Mott insulator: Physics of high-temperature superconductivity. *Reviews of Modern Physics*, 78(1):17–85, 2006.

[130] J. Orenstein and A. J. Millis. Advances in the physics of high-temperature superconductivity. *Science*, 288(5465):468–474, 2000.

[131] S. Badoux, W. Tabis, F. Laliberté, G. Grissonnanche, B. Vignolle, D. Vignolles, J. Béard, D. A. Bonn, W. N. Hardy, R. Liang, and et al. Change of carrier density at the pseudogap critical point of a cuprate superconductor. *Nature*, 531(7593):210–214, Feb 2016.

[132] Nicolas Doiron-Leyraud, Cyril Proust, David Leboeuf, Julien Levallois, Jean-Baptiste Bonnemaison, Ruixing Liang, D. A. Bonn, W. N. Hardy, and Louis Taillefer. Quantum oscillations and the Fermi surface in an underdoped high-T_c superconductor. *Nature*, 447(7144):565–568, May 2007.

[133] Cyril Proust and Louis Taillefer. The remarkable underlying ground states of cuprate superconductors. *Annual Review of Condensed Matter Physics*, 10(1):409–429, 2019.

[134] D. J. Scalapino. Numerical Studies of the 2D Hubbard Model. *arXiv e-prints*, pages cond–mat/0610710, October 2006.

[135] Thomas Maier, Mark Jarrell, Thomas Pruschke, and Matthias H. Hettler. Quantum cluster theories. *Rev. Mod. Phys.*, 77:1027–1080, Oct 2005.

[136] J. E. Hirsch. Two-dimensional hubbard model: Numerical simulation study. *Phys. Rev. B*, 31:4403–4419, Apr 1985.

[137] D. J. Scalapino. A common thread: The pairing interaction for unconventional superconductors. *Rev. Mod. Phys.*, 84:1383–1417, Oct 2012.

[138] S. A. Kivelson, E. Fradkin, and V. J. Emery. Electronic liquid-crystal phases of a doped mott insulator. *Nature*, 393(6685):550–553, 1998.

[139] Tuomas I. Vanhala and Päivi Törmä. Dynamical mean-field theory study of stripe order and *d*-wave superconductivity in the two-dimensional hubbard model. *Phys. Rev. B*, 97:075112, Feb 2018.

[140] Steven R. White and D. J. Scalapino. Competition between stripes and pairing in a $t - t' - j$ model. *Phys. Rev. B*, 60:R753–R756, July 1999.

[141] A. Himeda, T. Kato, and M. Ogata. Stripe states with spatially oscillating *d*-wave superconductivity in the two-dimensional $t - t^{'} - J$ model. *Phys. Rev. Lett.*, 88:117001, Feb 2002.

[142] D. Vaknin, S. K. Sinha, D. E. Moncton, D. C. Johnston, J. M. Newsam, C. R. Safinya, and H. E. King. Antiferromagnetism in la_2cuo_{4-y}. *Phys. Rev. Lett.*, 58:2802–2805, Jun 1987.

[143] G. Shirane, Y. Endoh, R. J. Birgeneau, M. A. Kastner, Y. Hidaka, M. Oda, M. Suzuki, and T. Murakami. Two-dimensional antiferromagnetic quantum spin-fluid state in la_2cuo_4. *Phys. Rev. Lett.*, 59:1613–1616, Oct 1987.

[144] Y. Endoh, K. Yamada, R. J. Birgeneau, D. R. Gabbe, H. P. Jenssen, M. A. Kastner, C. J. Peters, P. J. Picone, T. R. Thurston, J. M. Tranquada, G. Shirane, Y. Hidaka, M. Oda, Y. Enomoto, M. Suzuki, and T. Murakami. Static and dynamic spin correlations in pure and doped la_2cuo_4. *Phys. Rev. B*, 37:7443–7453, May 1988.

[145] Erich J Mueller. Review of pseudogaps in strongly interacting fermi gases. *Reports on Progress in Physics*, 80(10):104401, Sep 2017.

[146] W. W. Warren, R. E. Walstedt, G. F. Brennert, R. J. Cava, R. Tycko, R. F. Bell, and G. Dabbagh. Cu spin dynamics and superconducting precursor effects in planes above T_c in $yba_2cu_3o_{6.7}$. *Phys. Rev. Lett.*, 62:1193–1196, Mar 1989.

[147] Henri Alloul, Takashi Ohno, and Philippe Mendels. 89y nmr studies of the electronic and magnetic properties of the 123 compounds. *Journal of the Less Common Metals*, 164-165:1022 – 1038, 1990.

[148] A V Puchkov, D N Basov, and T Timusk. The pseudogap state in high- superconductors: an infrared study. *Journal of Physics: Condensed Matter*, 8(48):10049–10082, nov 1996.

[149] Xi Chen, J. P. F. LeBlanc, and Emanuel Gull. Simulation of the nmr response in the pseudogap regime of the cuprates. *Nature Communications*, 8(1):14986, 2017.

[150] Ehsan Khatami and Marcos Rigol. Thermodynamics of strongly interacting fermions in two-dimensional optical lattices. *Physical Review A*, 84(5), Nov 2011.

[151] Thomas A. Maier and Douglas J. Scalapino. Pairfield fluctuations of a 2d hubbard model. *npj Quantum Materials*, 4(1):30, 2019.

[152] R. Preuss, W. Hanke, C. Gröber, and H. G. Evertz. Pseudogaps and their interplay with magnetic excitations in the doped 2d hubbard model. *Phys. Rev. Lett.*, 79:1122–1125, Aug 1997.

[153] Kyle M. Shen, F. Ronning, D. H. Lu, F. Baumberger, N. J. C. Ingle, W. S. Lee, W. Meevasana, Y. Kohsaka, M. Azuma, M. Takano, H. Takagi, and Z.-X. Shen. Nodal quasiparticles and antinodal charge ordering in $ca_{2-x}na_xcuo_2cl$. *Science*, 307(5711):901–904, 2005.

[154] J. M. Luttinger. Fermi surface and some simple equilibrium properties of a system of interacting fermions. *Phys. Rev.*, 119:1153–1163, Aug 1960.

[155] Masaki Oshikawa. Topological approach to luttinger's theorem and the fermi surface of a kondo lattice. *Phys. Rev. Lett.*, 84:3370–3373, Apr 2000.

[156] Debanjan Chowdhury and Subir Sachdev. The enigma of the pseudogap phase of the cuprate superconductors. In *Quantum Criticality in Condensed Matter*, 2015.

[157] Subir Sachdev and Debanjan Chowdhury. The novel metallic states of the cuprates: Topological fermi liquids and strange metals. *Progress of Theoretical and Experimental Physics*, 2016(12):12C102, Nov 2016.

[158] C. Collignon, S. Badoux, S. A. A. Afshar, B. Michon, F. Laliberté, O. Cyr-Choinière, J.-S. Zhou, S. Licciardello, S. Wiedmann, N. Doiron-Leyraud, and Louis Taillefer. Fermi-surface transformation across the pseudogap critical point of the cuprate superconductor $la_{1.6-x}nd_{0.4}sr_xcuo_4$. *Phys. Rev. B*, 95:224517, Jun 2017.

[159] AF Ioffe and AR Regel. Non-crystalline, amorphous and liquid electronic semiconductors. *Prog. Semicond*, 4(89):237–291, 1960.

[160] N. F. Mott. Conduction in non-crystalline systems ix. the minimum metallic conductivity. *The Philosophical Magazine: A Journal of Theoretical Experimental and Applied Physics*, 26(4):1015–1026, 1972.

[161] J. M. Tranquada, B. J. Sternlieb, J. D. Axe, Y. Nakamura, and S. Uchida. Evidence for stripe correlations of spins and holes in copper oxide superconductors. *Nature*, 375(6532):561–563, 1995.

[162] J. M. Tranquada, J. D. Axe, N. Ichikawa, A. R. Moodenbaugh, Y. Nakamura, and S. Uchida. Coexistence of, and competition between, superconductivity and charge-stripe order in $la_{1.6-x}nd_{0.4}sr_xcuo_4$. *Phys. Rev. Lett.*, 78:338–341, Jan 1997.

[163] Eduardo Fradkin, Steven A. Kivelson, and John M. Tranquada. Colloquium: Theory of intertwined orders in high temperature superconductors. *Reviews of Modern Physics*, 87(2):457–482, May 2015.

[164] K. Yamada, C. H. Lee, K. Kurahashi, J. Wada, S. Wakimoto, S. Ueki, H. Kimura, Y. Endoh, S. Hosoya, G. Shirane, R. J. Birgeneau, M. Greven, M. A. Kastner, and Y. J. Kim. Doping dependence of the spatially modulated dynamical spin correlations and the superconducting-transition temperature in $la_{2-x}sr_xcuo_4$. *Phys. Rev. B*, 57:6165–6172, Mar 1998.

[165] Steven R. White and D. J. Scalapino. Stripes on a 6-leg hubbard ladder. *Phys. Rev. Lett.*, 91:136403, Sep 2003.

[166] Philippe Corboz, T. M. Rice, and Matthias Troyer. Competing states in the *t-j* model: Uniform *d*-wave state versus stripe state. *Phys. Rev. Lett.*, 113:046402, Jul 2014.

[167] Hong-Chen Jiang and Thomas P. Devereaux. Superconductivity in the doped hubbard model and its interplay with next-nearest hopping t′. *Science*, 365(6460):1424–1428, Sep 2019.

[168] Mingpu Qin, Chia-Min Chung, Hao Shi, Ettore Vitali, Claudius Hubig, Ulrich Schollwöck, Steven R. White, and Shiwei Zhang. Absence of superconductivity in the pure two-dimensional hubbard model. *arXiv e-prints*, page 1910.08931, 2019.

[169] C. E. Gough, M. S. Colclough, E. M. Forgan, R. G. Jordan, M. Keene, C. M. Muirhead, A. I. M. Rae, N. Thomas, J. S. Abell, and S. Sutton. Flux quantization in a high-tc superconductor. *Nature*, 326(6116):855–855, 1987.

[170] D. A. Wollman, D. J. Van Harlingen, W. C. Lee, D. M. Ginsberg, and A. J. Leggett. Experimental determination of the superconducting pairing state in ybco from the phase coherence of ybco-pb dc squids. *Phys. Rev. Lett.*, 71:2134–2137, Sep 1993.

[171] C. C. Tsuei and J. R. Kirtley. Pairing symmetry in cuprate superconductors. *Rev. Mod. Phys.*, 72:969–1016, Oct 2000.

[172] Z.-X. Shen, D. S. Dessau, B. O. Wells, D. M. King, W. E. Spicer, A. J. Arko, D. Marshall, L. W. Lombardo, A. Kapitulnik, P. Dickinson, S. Doniach, J. DiCarlo, T. Loeser, and C. H. Park. Anomalously large gap anisotropy in the a-b plane of $bi_2sr_2cacu_2o_{8+\delta}$. *Phys. Rev. Lett.*, 70:1553–1556, Mar 1993.

[173] H. Ding, J. C. Campuzano, A. F. Bellman, T. Yokoya, M. R. Norman, M. Randeria, T. Takahashi, H. Katayama-Yoshida, T. Mochiku, K. Kadowaki, and G. Jennings. Momentum dependence of the superconducting gap in $bi_2sr_2cacu_2O_8$. *Phys. Rev. Lett.*, 74:2784–2787, Apr 1995.

[174] Y. J. Uemura, G. M. Luke, B. J. Sternlieb, J. H. Brewer, J. F. Carolan, W. N. Hardy, R. Kadono, J. R. Kempton, R. F. Kiefl, S. R. Kreitzman, P. Mulhern, T. M. Riseman, D. Ll. Williams, B. X. Yang, S. Uchida, H. Takagi, J. Gopalakrishnan, A. W. Sleight, M. A. Subramanian, C. L. Chien, M. Z. Cieplak, Gang Xiao, V. Y. Lee, B. W. Statt, C. E. Stronach, W. J. Kossler, and X. H. Yu. Universal correlations between T_c and $\frac{n_s}{m^*}$ (carrier density over effective mass) in high-T_c cuprate superconductors. *Phys. Rev. Lett.*, 62:2317–2320, May 1989.

[175] D. J. Scalapino and S. A. Trugman. Local antiferromagnetic correlations and dx2-y2 pairing. *Philosophical Magazine B*, 74(5):607–610, Nov 1996.

[176] T. A. Maier, M. Jarrell, T. C. Schulthess, P. R. C. Kent, and J. B. White. Systematic study of *d*-wave superconductivity in the 2d repulsive hubbard model. *Phys. Rev. Lett.*, 95:237001, Nov 2005.

[177] Thierry Giamarchi. *Quantum Physics in One Dimension*. Oxford University Press, 2003.

[178] F D M Haldane. 'luttinger liquid theory' of one-dimensional quantum fluids. i. properties of the luttinger model and their extension to the general 1d interacting spinless fermi gas. *Journal of Physics C: Solid State Physics*, 14(19):2585, 1981.

[179] C. Kollath, U. Schollwöck, and W. Zwerger. Spin-charge separation in cold fermi gases: A real time analysis. *Phys. Rev. Lett.*, 95:176401, Oct 2005.

[180] H. Bethe. Zur theorie der metalle. *Zeitschrift für Physik*, 71(3):205–226.

[181] J.-S. Caux and J. M. Maillet. Computation of Dynamical Correlation Functions of Heisenberg Chains in a Magnetic Field. *Physical Review Letters*, 95(7):077201, August 2005.

[182] I. U. Heilmann, G. Shirane, Y. Endoh, R. J. Birgeneau, and S. L. Holt. Neutron study of the line-shape and field dependence of magnetic excitations in $cucl_2{\cdot}2n(c_5d_5)$. *Phys. Rev. B*, 18:3530–3536, Oct 1978.

[183] Hironobu Ikeda and Kinshiro Hirakawa. Neutron Diffraction Study in One-Dimensional Antiferromagnet $KCuF_3$. *Journal of the Physical Society of Japan*, 35(3):722–728, 1973.

[184] C. Kim, A. Y. Matsuura, Z.-X. Shen, N. Motoyama, H. Eisaki, S. Uchida, T. Tohyama, and S. Maekawa. Observation of spin-charge separation in one-dimensional $srcuo_2$. *Phys. Rev. Lett.*, 77:4054–4057, Nov 1996.

[185] B. J. Kim, H. Koh, E. Rotenberg, S.-J. Oh, H. Eisaki, N. Motoyama, S. Uchida, T. Tohyama, S. Maekawa, Z.-X. Shen, and C. Kim. Distinct spinon and holon dispersions in photoemission spectral functions from one-dimensional srcuo2. *Nat Phys*, 2(6):397–401, June 2006.

[186] Marc Bockrath, David H. Cobden, Jia Lu, Andrew G. Rinzler, Richard E. Smalley, Leon Balents, and Paul L. McEuen. Luttinger-liquid behaviour in carbon nanotubes. *Nature*, 397(6720):598–601, 1999.

[187] O. M. Auslaender, H. Steinberg, A. Yacoby, Y. Tserkovnyak, B. I. Halperin, K. W. Baldwin, L. N. Pfeiffer, and K. W. West. Spin-charge separation and localization in one dimension. *Science*, 308(5718):88–92, 2005.

[188] C. Chin, M. Bartenstein, A. Altmeyer, S. Riedl, S. Jochim, J. Hecker Denschlag, and R. Grimm. Observation of the pairing gap in a strongly interacting fermi gas. *Science*, 305(5687):1128–1130, 2004.

[189] Corinna Kollath, Michael Köhl, and Thierry Giamarchi. Scanning tunneling microscopy for ultracold atoms. *Phys. Rev. A*, 76:063602, Dec 2007.

[190] Tung-Lam Dao, Antoine Georges, Jean Dalibard, Christophe Salomon, and Iacopo Carusotto. Measuring the one-particle excitations of ultracold fermionic atoms by stimulated raman spectroscopy. *Phys. Rev. Lett.*, 98:240402, Jun 2007.

[191] Michael Knap, Aditya Shashi, Yusuke Nishida, Adilet Imambekov, Dmitry A. Abanin, and Eugene Demler. Time-dependent impurity in ultracold fermions: Orthogonality catastrophe and beyond. *Phys. Rev. X*, 2:041020, Dec 2012.

[192] Michael Knap, Adrian Kantian, Thierry Giamarchi, Immanuel Bloch, Mikhail D. Lukin, and Eugene Demler. Probing real-space and time-resolved correlation functions with many-body ramsey interferometry. *Phys. Rev. Lett.*, 111:147205, Oct 2013.

[193] Marko Cetina, Michael Jag, Rianne S. Lous, Isabella Fritsche, Jook T. M. Walraven, Rudolf Grimm, Jesper Levinsen, Meera M. Parish, Richard Schmidt, Michael Knap, and Eugene Demler. Ultrafast many-body interferometry of impurities coupled to a fermi sea. *Science*, 354(6308):96–99, 2016.

[194] J. T. Stewart, J. P. Gaebler, and D. S. Jin. Using photoemission spectroscopy to probe a strongly interacting fermi gas. *Nature*, 454(7205):744–747, August 2008.

[195] G. Veeravalli, E. Kuhnle, P. Dyke, and C. J. Vale. Bragg spectroscopy of a strongly interacting fermi gas. *Phys. Rev. Lett.*, 101:250403, Dec 2008.

[196] Daniel Greif, Leticia Tarruell, Thomas Uehlinger, Robert Jördens, and Tilman Esslinger. Probing nearest-neighbor correlations of ultracold fermions in an optical lattice. *Phys. Rev. Lett.*, 106:145302, Apr 2011.

[197] K. J. von Szczepanski, P. Horsch, W. Stephan, and M. Ziegler. Single-particle excitations in a quantum antiferromagnet. *Phys. Rev. B*, 41:2017–2029, Feb 1990.

[198] S. Foelling, S. Trotzky, P. Cheinet, M. Feld, R. Saers, A. Widera, T. Mueller, and I. Bloch. Direct observation of second-order atom tunnelling. *Nature*, 448(7157):1029–U4, August 2007.

[199] Yu-Ao Chen, Sylvain Nascimbène, Monika Aidelsburger, Marcos Atala, Stefan Trotzky, and Immanuel Bloch. Controlling correlated tunneling and superexchange interactions with ac-driven optical lattices. *Phys. Rev. Lett.*, 107:210405, Nov 2011.

[200] Philip Zupancic, Philipp M. Preiss, Ruichao Ma, Alexander Lukin, M. Eric Tai, Matthew Rispoli, Rajibul Islam, and Markus Greiner. Ultra-precise holographic beam shaping for microscopic quantum control. *Opt. Express*, 24(13):13881–13893, 2016.

[201] Anton Mazurenko, Christie S. Chiu, Geoffrey Ji, Maxwell F. Parsons, Marton Kanasz-Nagy, Richard Schmidt, Fabian Grusdt, Eugene Demler, Daniel Greif, and Markus Greiner. A cold-atom fermi-hubbard antiferromagnet. *Nature*, 545(7655):462–466, May 2017.

[202] Markus Greiner, Immanuel Bloch, Olaf Mandel, Theodor W. Hänsch, and Tilman Esslinger. Exploring phase coherence in a 2d lattice of bose-einstein condensates. *Phys. Rev. Lett.*, 87:160405, Oct 2001.

[203] P. A. Murthy, D. Kedar, T. Lompe, M. Neidig, M. G. Ries, A. N. Wenz, G. Zürn, and S. Jochim. Matter-wave fourier optics with a strongly interacting two-dimensional fermi gas. *Phys. Rev. A*, 90:043611, Oct 2014.

[204] R. Eder and Y. Ohta. Photoemission spectra of the *t-j* model in one and two dimensions: Similarities and differences. *Phys. Rev. B*, 56:2542–2550, Aug 1997.

[205] R. N. Bannister and N. d'Ambrumenil. Spectral functions of half-filled one-dimensional hubbard rings with varying boundary conditions. *Phys. Rev. B*, 61:4651–4658, Feb 2000.

[206] C. Kim, Z.-X. Shen, N. Motoyama, H. Eisaki, S. Uchida, T. Tohyama, and S. Maekawa. Separation of spin and charge excitations in one-dimensional srcuo$_2$. *Phys. Rev. B*, 56:15589–15595, Dec 1997.

[207] Elbio Dagotto, Robert Joynt, Adriana Moreo, Silvia Bacci, and Eduardo Gagliano. Strongly correlated electronic systems with one hole: Dynamical properties. *Phys. Rev. B*, 41:9049–9073, May 1990.

[208] Chanchal K. Majumdar and Dipan K. Ghosh. On next-nearest-neighbor interaction in linear chain. i. *Journal of Mathematical Physics*, 10(8):1388–1398, 1969.

[209] C K Majumdar. Antiferromagnetic model with known ground state. *Journal of Physics C: Solid State Physics*, 3(4):911–, 1970.

[210] Claudine Lacroix, Philippe Mendels, and Frederic Mila, editors. *Introduction to Frustrated Magnetism*. Springer Series in Solid-State Sciences, 2011.

[211] B. Sriram Shastry and Bill Sutherland. Excitation spectrum of a dimerized next-neighbor antiferromagnetic chain. *Phys. Rev. Lett.*, 47:964–967, Sep 1981.

[212] G. Baskaran, Z. Zou, and P.W. Anderson. The resonating valence bond state and high-tc superconductivity - a mean field theory. *Solid State Communications*, 63(11):973–976, 1987.

[213] Z. Y. Weng, D. N. Sheng, and C. S. Ting. Spin-charge separation in the t-j model: Magnetic and transport anomalies. *Phys. Rev. B*, 52:637–664, Jul 1995.

[214] J. Zaanen, O. Y. Osman, H. V. Kruis, Z. Nussinov, and J. Tworzydlo. The geometric order of stripes and luttinger liquids. *Philosophical Magazine B: Physics of Condensed Matter*, 2001.

[215] H. V. Kruis, I. P. McCulloch, Z. Nussinov, and J. Zaanen. Geometry and the hidden order of luttinger liquids: The universality of squeezed space. *Phys. Rev. B*, 70:075109, Aug 2004.

[216] Sutherland. *Beautiful Models, 70 Years of Exactly Solved Quantum Many-Body Problems*. World Scientific Publishing, 2004.

[217] Martin Boll, Timon A. Hilker, Guillaume Salomon, Ahmed Omran, Jacopo Nespolo, Lode Pollet, Immanuel Bloch, and Christian Gross. Spin- and density-resolved microscopy of antiferromagnetic correlations in fermi-hubbard chains. *Science*, 353(6305):1257–1260, 2016.

[218] Lawrence W. Cheuk, Matthew A. Nichols, Katherine R. Lawrence, Melih Okan, Hao Zhang, Ehsan Khatami, Nandini Trivedi, Thereza Paiva, Marcos Rigol, and Martin W. Zwierlein. Observation of spatial charge and spin correlations in the 2d fermi-hubbard model. *Science*, 353(6305):1260–1264, 2016.

[219] S. Kivelson and J. R. Schrieffer. Fractional charge, a sharp quantum observable. *Phys. Rev. B*, 25:6447–6451, May 1982.

[220] M. Roger and J. M. Delrieu. Cyclic four-spin exchange on a two-dimensional square lattice: Possible applications in high-tc superconductors. *Phys. Rev. B*, 39:2299–2303, Feb 1989.

[221] R. Coldea, S. M. Hayden, G. Aeppli, T. G. Perring, C. D. Frost, T. E. Mason, S.-W. Cheong, and Z. Fisk. Spin waves and electronic interactions in la_2cuo_4. *Phys. Rev. Lett.*, 86:5377–5380, Jun 2001.

[222] A. M. Toader, J. P. Goff, M. Roger, N. Shannon, J. R. Stewart, and M. Enderle. Spin correlations in the paramagnetic phase and ring exchange in la_2cuo_4. *Phys. Rev. Lett.*, 94:197202, May 2005.

[223] J. Lorenzana, J. Eroles, and S. Sorella. Does the heisenberg model describe the multimagnon spin dynamics in antiferromagnetic cuo layers? *Phys. Rev. Lett.*, 83:5122–5125, Dec 1999.

[224] S. Brehmer, H.-J. Mikeska, M. Müller, N. Nagaosa, and S. Uchida. Effects of biquadratic exchange on the spectrum of elementary excitations in spin ladders. *Phys. Rev. B*, 60:329–334, Jul 1999.

[225] Daniel Barredo, Sylvain de Leseleuc, Vincent Lienhard, Thierry Lahaye, and Antoine Browaeys. An atom-by-atom assembler of defect-free arbitrary two-dimensional atomic arrays. *Science*, 354(6315):1021–, November 2016.

[226] Hyosub Kim, Woojun Lee, Han-gyeol Lee, Hanlae Jo, Yunheung Song, and Jaewook Ahn. In situ single-atom array synthesis using dynamic holographic optical tweezers. *Nature Communications*, 7(1):13317, 2016.

[227] Carsten Robens, Jonathan Zopes, Wolfgang Alt, Stefan Brakhane, Dieter Meschede, and Andrea Alberti. Low-entropy states of neutral atoms in polarization-synthesized optical lattices. *Phys. Rev. Lett.*, 118:065302, Feb 2017.

[228] Daniel Ohl de Mello, Dominik Schäffner, Jan Werkmann, Tilman Preuschoff, Lars Kohfahl, Malte Schlosser, and Gerhard Birkl. Defect-free assembly of 2d clusters of more than 100 single-atom quantum systems. *Phys. Rev. Lett.*, 122:203601, May 2019.

[229] Han-Ning Dai, Bing Yang, Andreas Reingruber, Hui Sun, Xiao-Fan Xu, Yu-Ao Chen, Zhen-Sheng Yuan, and Jian-Wei Pan. Four-body ring-exchange interactions and anyonic statistics within a minimal toric-code hamiltonian. *Nature Physics*, 13:1195–, August 2017.

[230] M. Murphy, L. Jiang, N. Khaneja, and T. Calarco. High-fidelity fast quantum transport with imperfect controls. *Phys. Rev. A*, 79:020301, Feb 2009.

[231] M. Fleischhauer, A. Imamoglu, and J. P. Marangos. Electromagnetically induced transparency: Optics in coherent media. *Reviews of Modern Physics*, 77(2):633–673, 2005.

[232] M. Müller, I. Lesanovsky, H. Weimer, H. P. Büchler, and P. Zoller. Mesoscopic rydberg gate based on electromagnetically induced transparency. *Phys. Rev. Lett.*, 102:170502, Apr 2009.

[233] Anders W. Sandvik. Evidence for deconfined quantum criticality in a two-dimensional heisenberg model with four-spin interactions. *Phys. Rev. Lett.*, 98:227202, Jun 2007.

[234] A. Läuchli, G. Schmid, and M. Troyer. Phase diagram of a spin ladder with cyclic four-spin exchange. *Phys. Rev. B*, 67:100409, Mar 2003.

[235] F. D. M. Haldane. Non-linear field-theory of large-spin heisenberg anti-ferromagnets - semiclassically quantized solitons of the one-dimensional easy-axis neel state. *Physical Review Letters*, 50(15):1153–1156, 1983.

[236] T Kennedy. Exact diagonalisations of open spin-1 chains. *Journal of Physics: Condensed Matter*, 2(26):5737, 1990.

[237] Christof Weitenberg, Manuel Endres, Jacob F. Sherson, Marc Cheneau, Peter Schauß, Takeshi Fukuhara, Immanuel Bloch, and Stefan Kuhr. Single-spin addressing in an atomic mott insulator. *Nature*, 471(7338):319–324, Mar 2011.

[238] Ian Affleck, Tom Kennedy, Elliott H. Lieb, and Hal Tasaki. Rigorous results on valence-bond ground states in antiferromagnets. *Phys. Rev. Lett.*, 59:799–802, Aug 1987.

[239] F. D. M. Haldane. Continuum dynamics of the 1-d heisenberg anti-ferromagnet - identification with the o(3) non-linear sigma-model. *Physics Letters A*, 93(9):464–468, 1983.

[240] Tom Kennedy and Hal Tasaki. Hidden symmetry breaking and the haldane phase in s=1 quantum spin chains. *Commun. Math. Phys.*, 147:431–484, 1992.

[241] Frank Pollmann, Erez Berg, Ari M. Turner, and Masaki Oshikawa. Symmetry protection of topological phases in one-dimensional quantum spin systems. *Phys. Rev. B*, 85:075125, Feb 2012.

[242] S. Schmitt-Rink, C. M. Varma, and A. E. Ruckenstein. Spectral function of holes in a quantum antiferromagnet. *Phys. Rev. Lett.*, 60:2793–2796, Jun 1988.

[243] C. L. Kane, P. A. Lee, and N. Read. Motion of a single hole in a quantum antiferromagnet. *Physical Review B*, 39(10):6880–6897, 1989.

[244] Subir Sachdev. Hole motion in a quantum Néel state. *Physical Review B*, 39(16):12232–12247, 1989.

[245] Veit Elser, David A. Huse, Boris I. Shraiman, and Eric D. Siggia. Ground state of a mobile vacancy in a quantum antiferromagnet: Small-cluster study. *Phys. Rev. B*, 41:6715–6723, Apr 1990.

[246] Gerardo Martinez and Peter Horsch. Spin polarons in the t-j model. *Phys. Rev. B*, 44:317–331, Jul 1991.

[247] Assa Auerbach and Brond E. Larson. Small-polaron theory of doped antiferromagnets. *Phys. Rev. Lett.*, 66:2262–2265, Apr 1991.

[248] Zhiping Liu and Efstratios Manousakis. Dynamical properties of a hole in a heisenberg antiferromagnet. *Phys. Rev. B*, 45:2425–2437, Feb 1992.

[249] Massimo Boninsegni and Efstratios Manousakis. Green's-function monte carlo study of the t-j model. *Phys. Rev. B*, 46:560–563, Jul 1992.

[250] Massimo Boninsegni and Efstratios Manousakis. Variational description of a quasihole excitation in a quantum antiferromagnet. *Phys. Rev. B*, 45:4877–4884, Mar 1992.

[251] P. W. Leung and R. J. Gooding. Dynamical properties of the single-hole t-j model on a 32-site square lattice. *Phys. Rev. B*, 52:R15711–R15714, Dec 1995.

[252] Oleg A. Starykh, Oziel F. de Alcantara Bonfim, and George F. Reiter. Self-consistent born approximation for the hole motion in the three-band model: A comparison with photoemission experiments. *Phys. Rev. B*, 52:12534–12537, Nov 1995.

[253] Michael Brunner, Fakher F. Assaad, and Alejandro Muramatsu. Single-hole dynamics in the $t - j$ model on a square lattice. *Phys. Rev. B*, 62:15480–15492, Dec 2000.

[254] A. S. Mishchenko, N. V. Prokof'ev, and B. V. Svistunov. Single-hole spectral function and spin-charge separation in the $t - j$ model. *Phys. Rev. B*, 64:033101, Jun 2001.

[255] Steven R. White and Ian Affleck. Density matrix renormalization group analysis of the nagaoka polaron in the two-dimensional $t - j$ model. *Phys. Rev. B*, 64:024411, Jun 2001.

[256] G. Sangiovanni, A. Toschi, E. Koch, K. Held, M. Capone, C. Castellani, O. Gunnarsson, S.-K. Mo, J. W. Allen, H.-D. Kim, A. Sekiyama, A. Yamasaki, S. Suga, and P. Metcalf. Static versus dynamical mean-field theory of mott antiferromagnets. *Phys. Rev. B*, 73:205121, May 2006.

[257] Efstratios Manousakis. String excitations of a hole in a quantum antiferromagnet and photoelectron spectroscopy. *Physical Review B*, 75:035106, 2007.

[258] Fabio Mezzacapo. Variational study of a mobile hole in a two-dimensional quantum antiferromagnet using entangled-plaquette states. *Phys. Rev. B*, 83:115111, Mar 2011.

[259] L. N. Bulaevskii, É. L. Nagaev, and D. I. Khomskii. A new type of auto-localized state of a conduction electron in an antiferromagnetic semiconductor. *Journal of Experimental and Theoretical Physics*, 27(5):836–838, 1968.

[260] W. F. Brinkman and T. M. Rice. Single-Particle Excitations in Magnetic Insulators. *Physical Review B*, 2(5):1324–1338, 1970.

[261] S. A. Trugman. Interaction of holes in a Hubbard antiferromagnet and high-temperature superconductivity. *Physical Review B*, 37(4):1597–1603, 1988.

[262] Boris I. Shraiman and Eric D. Siggia. Two-particle excitations in antiferromagnetic insulators. *Phys. Rev. Lett.*, 60:740–743, Feb 1988.

[263] Oleg A. Starykh and George F. Reiter. Hole motion in the ising antiferromagnet: An application of the recursion method. *Phys. Rev. B*, 53:2517–2522, Feb 1996.

[264] Denis Golež, Janez Bonča, Marcin Mierzejewski, and Lev Vidmar. Mechanism of ultrafast relaxation of a photo-carrier in antiferromagnetic spin background. *Physical Review B*, 89:165118, 2014.

[265] Krzysztof Bieniasz, Piotr Wrzosek, Andrzej M. Oles, and Krzysztof Wohlfeld. From "Weak" to "Strong" Hole Confinement in a Mott Insulator. *SciPost Phys.*, 7:66, 2019.

[266] Christie S. Chiu, Geoffrey Ji, Annabelle Bohrdt, Muqing Xu, Michael Knap, Eugene Demler, Fabian Grusdt, Markus Greiner, and Daniel Greif. String patterns in the doped hubbard model. *Science*, 365(6450):251–256, 2019.

[267] Joannis Koepsell, Jayadev Vijayan, Pimonpan Sompet, Fabian Grusdt, Timon A. Hilker, Eugene Demler, Guillaume Salomon, Immanuel Bloch, and Christian Gross. Imaging magnetic polarons in the doped Fermi–Hubbard model. *Nature*, 572(7769):358–362, August 2019.

[268] P. Béran, D. Poilblanc, and R. B. Laughlin. Evidence for composite nature of quasiparticles in the 2D t-J model. *Nuclear Physics B*, 473:707–720, 1996.

[269] R. B. Laughlin. Evidence for quasiparticle decay in photoemission from underdoped cuprates. *Phys. Rev. Lett.*, 79:1726–1729, Sep 1997.

[270] T. Senthil, Subir Sachdev, and Matthias Vojta. Fractionalized fermi liquids. *Phys. Rev. Lett.*, 90:216403, May 2003.

[271] Matthias Punk, Andrea Allais, and Subir Sachdev. Quantum dimer model for the pseudogap metal. *Proceedings of the National Academy of Sciences*, 112(31):9552–9557, 2015.

[272] Fabian Grusdt, Zheng Zhu, Tao Shi, and Eugene Demler. Meson Formation in Mixed-Dimensional t-J Models. *SciPost Physics*, 5:057, Dec 2018.

[273] T. K. Lee and Shiping Feng. Doping dependence of antiferromagnetism in la_2cuo_4: A numerical study based on a resonating-valence-bond state. *Phys. Rev. B*, 38:11809–11812, Dec 1988.

[274] B. Dalla Piazza, M. Mourigal, N. B. Christensen, G. J. Nilsen, P. Tregenna-Piggott, T. G. Perring, M. Enderle, D. F. McMorrow, D. A. Ivanov, and H. M. Ronnow. Fractional excitations in the square-lattice quantum antiferromagnet. *Nat Phys*, 11(1):62–68, January 2015.

[275] Xue-Yang Song, Chong Wang, Ashvin Vishwanath, and Yin-Chen He. Unifying description of competing orders in two-dimensional quantum magnets. *Nature Communications*, 10(1):4254–, 2019.

[276] T. Giamarchi and C. Lhuillier. Dispersion relation of a single hole in the t-j model determined by a variational monte carlo method. *Phys. Rev. B*, 47:2775–2779, Feb 1993.

[277] Xiao-Gang Wen and Patrick A. Lee. Theory of underdoped cuprates. *Phys. Rev. Lett.*, 76:503–506, Jan 1996.

[278] Daniel S. Rokhsar and Steven A. Kivelson. Superconductivity and the quantum hard-core dimer gas. *Phys. Rev. Lett.*, 61:2376–2379, Nov 1988.

[279] Zhiping Liu and Efstratios Manousakis. Spectral function of a hole in the t-j model. *Phys. Rev. B*, 44:2414–2417, Aug 1991.

[280] J. D. Reger and A. P. Young. Monte carlo simulations of the spin-(1/2 heisenberg antiferromagnet on a square lattice. *Phys. Rev. B*, 37:5978–5981, Apr 1988.

[281] J. Brad Marston and Ian Affleck. Large-*n* limit of the hubbard-heisenberg model. *Phys. Rev. B*, 39:11538–11558, Jun 1989.

[282] Patrick A Lee. From high temperature superconductivity to quantum spin liquid: progress in strong correlation physics. *Reports on Progress in Physics*, 71(1):012501, 2008.

[283] Nandini Trivedi and D. M. Ceperley. Green-function monte carlo study of quantum antiferromagnets. *Phys. Rev. B*, 40:2737–2740, Aug 1989.

[284] Samuel Dupond. A thorough review on the current advance of neural network structures. *Annual Reviews in Control*, 14:200–230, 2019.

[285] Martín Abadi, Ashish Agarwal, Paul Barham, Eugene Brevdo, Zhifeng Chen, Craig Citro, Greg S. Corrado, Andy Davis, Jeffrey Dean, Matthieu Devin, Sanjay Ghemawat, Ian Goodfellow, Andrew Harp, Geoffrey Irving, Michael Isard, Yangqing Jia, Rafal Jozefowicz, Lukasz Kaiser, Manjunath Kudlur, Josh Levenberg, Dandelion Mané, Rajat Monga, Sherry Moore, Derek Murray, Chris Olah, Mike Schuster, Jonathon Shlens, Benoit Steiner, Ilya Sutskever, Kunal Talwar, Paul Tucker, Vincent Vanhoucke, Vijay Vasudevan, Fernanda Viégas, Oriol Vinyals, Pete Warden, Martin Wattenberg, Martin Wicke, Yuan Yu, and Xiaoqiang Zheng. TensorFlow: Large-scale machine learning on heterogeneous systems, 2015. Software available from tensorflow.org.

[286] Sepp Hochreiter and Jürgen Schmidhuber. Long short-term memory. *Neural computation*, 9(8):1735–1780, 1997.

[287] Aurélien Géron. *Hands-On Machine Learning with Scikit-Learn and TensorFlow*. O'Reilly, 2017.

[288] Anders W. Sandvik. Stochastic series expansion method with operator-loop update. *Phys. Rev. B*, 59:R14157–R14160, Jun 1999.

[289] Emil Blomquist and Johan Carlström. Ab initio description of magnetic polarons in a mott insulator. *arXiv e-prints*, page 1912.08825, December 2019.

[290] Robert J. Birgeneau, Chris Stock, John M. Tranquada, and Kazuyoshi Yamada. Magnetic neutron scattering in hole-doped cuprate superconductors. *Journal of the Physical Society of Japan*, 75(11):111003, 2006.

[291] Luuk J. P. Ament, Michel van Veenendaal, Thomas P. Devereaux, John P. Hill, and Jeroen van den Brink. Resonant inelastic x-ray scattering studies of elementary excitations. *Rev. Mod. Phys.*, 83:705–767, Jun 2011.

[292] Sean Vig, Anshul Kogar, Matteo Mitrano, Ali Husain, Luc Venema, Mindy Rak, Vivek Mishra, Peter Johnson, Genda Gu, Eduardo Fradkin, and et al. Measurement of the dynamic charge response of materials using low-energy, momentum-resolved electron energy-loss spectroscopy (m-eels). *SciPost Physics*, 3(4), Oct 2017.

[293] M. Endres, M. Cheneau, T. Fukuhara, C. Weitenberg, P. Schauss, C. Gross, L. Mazza, M. C. Banuls, L. Pollet, I. Bloch, and S. Kuhr. Observation of correlated particle-hole pairs and string order in low-dimensional mott insulators. *Science*, 334(6053):200–203, 2011.

[294] Maximilian Prüfer, Torsten V. Zache, Philipp Kunkel, Stefan Lannig, Alexis Bonnin, Helmut Strobel, Jürgen Berges, and Markus K. Oberthaler. Experimental extraction of the quantum effective action for a non-equilibrium many-body system. *arXiv e-prints*, page 1909.05120, September 2019.

[295] A. L. Chernyshev and P. W. Leung. Holes in the $t - J_z$ model: A diagrammatic study. *Phys. Rev. B*, 60:1592–1606, Jul 1999.

[296] Christie S. Chiu, Geoffrey Ji, Anton Mazurenko, Daniel Greif, and Markus Greiner. Quantum state engineering of a hubbard system with ultracold fermions. *Phys. Rev. Lett.*, 120:243201, Jun 2018.

[297] Joannis Koepsell, Sarah Hirthe, Dominik Bourgund, Pimonpan Sompet, Jayadev Vijayan, Guillaume Salomon, Christian Gross, and Immanuel Bloch. Robust bilayer charge pumping for spin- and density-resolved quantum gas microscopy. *Physical Review Letters*, 125(1), July 2020.

[298] J. P. F. LeBlanc, Andrey E. Antipov, Federico Becca, Ireneusz W. Bulik, Garnet Kin-Lic Chan, Chia-Min Chung, Youjin Deng, Michel Ferrero, Thomas M. Henderson, Carlos A. Jiménez-Hoyos, E. Kozik, Xuan-Wen Liu, Andrew J. Millis, N. V. Prokof'ev, Mingpu Qin,

Gustavo E. Scuseria, Hao Shi, B. V. Svistunov, Luca F. Tocchio, I. S. Tupitsyn, Steven R. White, Shiwei Zhang, Bo-Xiao Zheng, Zhenyue Zhu, and Emanuel Gull. Solutions of the two-dimensional hubbard model: Benchmarks and results from a wide range of numerical algorithms. *Phys. Rev. X*, 5:041041, Dec 2015.

[299] T. Cuk, D. H. Lu, X. J. Zhou, Z.-X. Shen, T. P. Devereaux, and N. Nagaosa. A review of electron–phonon coupling seen in the high-tc superconductors by angle-resolved photoemission studies (arpes). *physica status solidi (b)*, 242(1):3–3, 2005.

[300] Satyaki Kar and Efstratios Manousakis. Finite-temperature spectral function of a hole in a quantum antiferromagnet and the role of phonons. *Phys. Rev. B*, 78:064508, Aug 2008.

[301] Ian Affleck and Bertrand I Halperin. On a renormalization group approach to dimensional crossover. *Journal of Physics A: Mathematical and General*, 29(11):2627–2631, Jun 1996.

[302] F. Kagawa, K. Miyagawa, and K. Kanoda. Unconventional critical behaviour in a quasi-two-dimensional organic conductor. *Nature*, 436(7050):534–537, Jul 2005.

[303] Paivi Torma. Physics of ultracold fermi gases revealed by spectroscopies. *Physica Scripta*, 91(4):043006–, 2016.

[304] D. N. Sheng, Y. C. Chen, and Z. Y. Weng. Phase String Effect in a Doped Antiferromagnet. *Physical Review Letters*, 77(25):5102–5105, 1996.

[305] J. Graf, G.-H. Gweon, K. McElroy, S. Y. Zhou, C. Jozwiak, E. Rotenberg, A. Bill, T. Sasagawa, H. Eisaki, S. Uchida, H. Takagi, D.-H. Lee, and A. Lanzara. Universal high energy anomaly in the angle-resolved photoemission spectra of high temperature superconductors: Possible evidence of spinon and holon branches. *Phys. Rev. Lett.*, 98:067004, Feb 2007.

[306] Ruben Verresen, Frank Pollmann, and Roderich Moessner. Quantum dynamics of the square-lattice heisenberg model. *Phys. Rev. B*, 98:155102, Oct 2018.

[307] Francesco Ferrari and Federico Becca. Spectral signatures of fractionalization in the frustrated heisenberg model on the square lattice. *Phys. Rev. B*, 98:100405, Sep 2018.

[308] Z. Y. Weng, D. N. Sheng, Y.-C. Chen, and C. S. Ting. Phase string effect in the t-j model: General theory. *Phys. Rev. B*, 55:3894–3906, Feb 1997.

[309] Elliott H. Lieb and F. Y. Wu. Absence of mott transition in an exact solution of the short-range, one-band model in one dimension. *Phys. Rev. Lett.*, 20:1445–1448, Jun 1968.

[310] Masao Ogata and Hiroyuki Shiba. Bethe-ansatz wave function, momentum distribution, and spin correlation in the one-dimensional strongly correlated Hubbard model. *Physical Review B*, 41(4):2321–2338, 1990.

[311] Y. Wang, K. Wohlfeld, B. Moritz, C. J. Jia, M. van Veenendaal, K. Wu, C.-C. Chen, and T. P. Devereaux. Origin of strong dispersion in hubbard insulators. *Phys. Rev. B*, 92:075119, Aug 2015.

[312] Andreas Läuchli and Didier Poilblanc. Spin-charge separation in two-dimensional frustrated quantum magnets. *Phys. Rev. Lett.*, 92:236404, Jun 2004.

[313] Michael P. Zaletel, Roger S. K. Mong, Christoph Karrasch, Joel E. Moore, and Frank Pollmann. Time-evolving a matrix product state with long-ranged interactions. *Phys. Rev. B*, 91:165112, Apr 2015.

[314] T Hartmann, F Keck, H J Korsch, and S Mossmann. Dynamics of Bloch oscillations. *New J. Phys.*, 6:2–2, January 2004.

[315] Márton Kanász-Nagy, Izabella Lovas, Fabian Grusdt, Daniel Greif, Markus Greiner, and Eugene A. Demler. Quantum correlations at infinite temperature: The dynamical Nagaoka effect. *Phys. Rev. B*, 96(1):014303, July 2017.

[316] Johan Carlström, Nikolay Prokof'ev, and Boris Svistunov. Quantum walk in degenerate spin environments. *Phys. Rev. Lett.*, 116:247202, Jun 2016.

[317] Steven R. White and D. J. Scalapino. Hole and pair structures in the t-j model. *Phys. Rev. B*, 55:6504–6517, Mar 1997.

[318] C. N. Varney, C.-R. Lee, Z. J. Bai, S. Chiesa, M. Jarrell, and R. T. Scalettar. Quantum monte carlo study of the two-dimensional fermion hubbard model. *Phys. Rev. B*, 80:075116, Aug 2009.

[319] Ian Affleck and J. Brad Marston. Large-n limit of the heisenberg-hubbard model: Implications for high-T_c superconductors. *Phys. Rev. B*, 37:3774–3777, Mar 1988.

[320] Giuseppe Carleo and Matthias Troyer. Solving the quantum many-body problem with artificial neural networks. *Science*, 355(6325):602–606, 2017.

[321] I. Glasser, N. Pancotti, M. August, I. D. Rodriguez, and J. I. Cirac. Neural-Network Quantum States, String-Bond States, and Chiral Topological States. *Physical Review X*, 8(1):011006, January 2018.

[322] Kenny Choo, Giuseppe Carleo, Nicolas Regnault, and Titus Neupert. Symmetries and many-body excitations with neural-network quantum states. *Phys. Rev. Lett.*, 121(16):167204, 2018.

[323] Sirui Lu, Xun Gao, and L.-M. Duan. Efficient representation of topologically ordered states with restricted boltzmann machines. *Phys. Rev. B*, 99:155136, Apr 2019.

[324] Juan Carrasquilla and Roger G. Melko. Machine learning phases of matter. *Nature Physics*, 13:431–434, 02 2017.

[325] Evert P. L. van Nieuwenburg, Ye-Hua Liu, and Sebastian D. Huber. Learning phase transitions by confusion. *Nature Physics*, 13:435–439, 02 2017.

[326] Benno S. Rem, Niklas Käming, Matthias Tarnowski, Luca Asteria, Nick Fläschner, Christoph Becker, Klaus Sengstock, and Christof Weitenberg. Identifying quantum phase transitions using artificial neural networks on experimental data. *Nature Physics*, 15(9):917–920, Jul 2019.

[327] P. Broecker, J. Carrasquilla, R. G. Melko, and S. Trebst. Machine Learning Quantum Phases of Matter beyond the Fermion Sign Problem. *Scientific Reports*, 7:8823, August 2017.

[328] Kelvin Ch'ng, Juan Carrasquilla, Roger G. Melko, and Ehsan Khatami. Machine learning phases of strongly correlated fermions. *Phys. Rev. X*, 7:031038, Aug 2017.

[329] M. J. S. Beach, A. Golubeva, and R. G. Melko. Machine Learning Vortices at the Kosterlitz-Thouless Transition. *Phys. Rev. B*, 97(4):045207, January 2018.

[330] Xiao-Yu Dong, Frank Pollmann, and Xue-Feng Zhang. Machine Learning of Quantum Phase Transitions. *Physical Review B*, 99:121104, Mar 2019.

[331] Jonas Greitemann, Ke Liu, and Lode Pollet. Probing Hidden Spin Order with Interpretable Machine Learning. *Physical Review B*, 99:060404, Feb 2019.

[332] Ke Liu, Jonas Greitemann, and Lode Pollet. Learning Multiple Order Parameters with Interpretable Machines. *Physical Review B*, 99:104410, Mar 2019.

[333] M. Koch-Janusz and Z. Ringel. Mutual Information, Neural Networks and the Renormalization Group. *Nature Physics*, 14:578–582, June 2018.

[334] Giacomo Torlai, Guglielmo Mazzola, Juan Carrasquilla, Matthias Troyer, Roger Melko, and Giuseppe Carleo. Neural-network quantum state tomography. *Nature Physics*, 14(5):447–450, 2018.

[335] Giacomo Torlai, Brian Timar, Evert P. L. van Nieuwenburg, Harry Levine, Ahmed Omran, Alexander Keesling, Hannes Bernien, Markus Greiner, Vladan Vuletić, Mikhail D. Lukin, Roger G. Melko, and Manuel Endres. Integrating neural networks with a quantum simulator for state reconstruction. *Phys. Rev. Lett.*, 123:230504, Dec 2019.

[336] Yi Zhang, A. Mesaros, K. Fujita, S. D. Edkins, M. H. Hamidian, K. Ch'ng, H. Eisaki, S. Uchida, J. C. Séamus Davis, Ehsan Khatami, and et al. Machine learning in electronic-quantum-matter imaging experiments. *Nature*, 570(7762):484–490, Jun 2019.

[337] Lewis R B Picard, Manfred J Mark, Francesca Ferlaino, and Rick van Bijnen. Deep learning-assisted classification of site-resolved quantum gas microscope images. *Measurement Science and Technology*, 31(2):025201, nov 2019.

[338] Adrien Bolens and Markus Heyl. Reinforcement learning for digital quantum simulation, 2020.

[339] Juan Carrasquilla. Machine learning for quantum matter. *Advances in Physics: X*, 5(1):1797528, 2020.

[340] Miloje S. Makivić and Hong-Qiang Ding. Two-dimensional spin-1/2 heisenberg antiferromagnet: A quantum monte carlo study. *Phys. Rev. B*, 43:3562–3574, Feb 1991.

[341] Thereza Paiva, Richard Scalettar, Mohit Randeria, and Nandini Trivedi. Fermions in 2d optical lattices: Temperature and entropy scales for observing antiferromagnetism and superfluidity. *Phys. Rev. Lett.*, 104:066406, Feb 2010.

[342] Matthew P. A. Fisher, Peter B. Weichman, G. Grinstein, and Daniel S. Fisher. Boson localization and the superfluid-insulator transition. *Phys. Rev. B*, 40:546–570, Jul 1989.

[343] D. Jaksch, C. Bruder, J. I. Cirac, C. W. Gardiner, and P. Zoller. Cold bosonic atoms in optical lattices. *Phys. Rev. Lett.*, 81:3108–3111, Oct 1998.

[344] Larkin A.I. and Ovchinnikov Yu. N. Quasiclassical method in the theory of superconductivity. *JETP Lett.*, 28(6):1200, 1969.

[345] Stephen H. Shenker and Douglas Stanford. Black holes and the butterfly effect. *Journal of High Energy Physics*, 2014(3), Mar 2014.

[346] A. Y. Kitaev. A simple model of quantum holography. *KITP Program on Entanglement in Strongly-Correlated Quantum Matter*, 2015.

[347] Daniel A. Roberts, Douglas Stanford, and Leonard Susskind. Localized shocks. *Journal of High Energy Physics*, 2015(3), Mar 2015.

[348] Juan Maldacena, Stephen H. Shenker, and Douglas Stanford. A bound on chaos. *Journal of High Energy Physics*, 2016(8), Aug 2016.

[349] Pavan Hosur, Xiao-Liang Qi, Daniel A. Roberts, and Beni Yoshida. Chaos in quantum channels. *Journal of High Energy Physics*, 2016(2), Feb 2016.

[350] Brian Swingle. Unscrambling the physics of out-of-time-order correlators. *Nature Physics*, 14(10):988–990, 2018.

[351] Subir Sachdev and Jinwu Ye. Gapless spin-fluid ground state in a random quantum Heisenberg magnet. *Phys. Rev. Lett.*, 70(21):3339–3342, 1993.

[352] Sumilan Banerjee and Ehud Altman. Solvable model for a dynamical quantum phase transition from fast to slow scrambling. *Physical Review B*, 95(13), Apr 2017.

[353] Aavishkar A. Patel and Subir Sachdev. Quantum chaos on a critical fermi surface. *Proceedings of the National Academy of Sciences*, 114(8):1844–1849, Feb 2017.

[354] Douglas Stanford. Many-body chaos at weak coupling. *Journal of High Energy Physics*, 2016(10), Oct 2016.

[355] Igor L. Aleiner, Lara Faoro, and Lev B. Ioffe. Microscopic model of quantum butterfly effect: Out-of-time-order correlators and traveling combustion waves. *Annals of Physics*, 375:378–406, Dec 2016.

[356] Márk Mezei and Douglas Stanford. On entanglement spreading in chaotic systems. *Journal of High Energy Physics*, 2017(5), May 2017.

[357] Hyungwon Kim and David A. Huse. Ballistic spreading of entanglement in a diffusive nonintegrable system. *Physical Review Letters*, 111(12), Sep 2013.

[358] Yichen Huang, Yong-Liang Zhang, and Xie Chen. Out-of-time-ordered correlators in many-body localized systems. *Annalen der Physik*, 529(7):1600318, Dec 2016.

[359] Xiao Chen, Tianci Zhou, David A. Huse, and Eduardo Fradkin. Out-of-time-order correlations in many-body localized and thermal phases. *Annalen der Physik*, 529(7):1600332, Dec 2016.

[360] J. M. Deutsch. Quantum statistical mechanics in a closed system. *Phys. Rev. A*, 43:2046–2049, Feb 1991.

[361] Mark Srednicki. Chaos and quantum thermalization. *Physical Review E*, 50(2):888–901, Aug 1994.

[362] Marcos Rigol, Vanja Dunjko, and Maxim Olshanii. Thermalization and its mechanism for generic isolated quantum systems. *Nature*, 452(7189):854–858, Apr 2008.

[363] Balázs Dóra and Roderich Moessner. Out-of-time-ordered density correlators in luttinger liquids. *Physical Review Letters*, 119(2), Jul 2017.

[364] Ivan Kukuljan, Sašo Grozdanov, and Tomaž Prosen. Weak quantum chaos. *Physical Review B*, 96(6), Aug 2017.

[365] P. M. Chaikin and T. C. Lubensky. *Principles of Condensed Matter Physics*. Cambridge University Press, Cambridge; New York, USA, 2000.

[366] Jonathan Lux, Jan Müller, Aditi Mitra, and Achim Rosch. Hydrodynamic long-time tails after a quantum quench. *Physical Review A*, 89(5), May 2014.

[367] Mike Blake. Universal charge diffusion and the butterfly effect in holographic theories. *Physical Review Letters*, 117(9), Aug 2016.

[368] Sean A. Hartnoll. Theory of universal incoherent metallic transport. *Nature Physics*, 11(1):54–61, Dec 2014.

[369] Brian Swingle and Debanjan Chowdhury. Slow scrambling in disordered quantum systems. *Phys. Rev. B*, 95:060201, Feb 2017.

[370] Andrew Lucas and Julia Steinberg. Charge diffusion and the butterfly effect in striped holographic matter. *Journal of High Energy Physics*, 2016(10), Oct 2016.

[371] M. Serbyn, M. Knap, S. Gopalakrishnan, Z. Papic, N. Y. Yao, C. R. Laumann, D. A. Abanin, M. D. Lukin, and E. A. Demler. Interferometric probes of many-body localization. *Phys. Rev. Lett.*, 113:147204, Oct 2014.

[372] Brian Swingle, Gregory Bentsen, Monika Schleier-Smith, and Patrick Hayden. Measuring the scrambling of quantum information. *Phys. Rev. A*, 94:040302, Oct 2016.

[373] Guanyu Zhu, Mohammad Hafezi, and Tarun Grover. Measurement of many-body chaos using a quantum clock. *Phys. Rev. A*, 94:062329, Dec 2016.

[374] Norman Y. Yao, Fabian Grusdt, Brian Swingle, Mikhail D. Lukin, Dan M. Stamper-Kurn, Joel E. Moore, and Eugene A. Demler. Interferometric Approach to Probing Fast Scrambling. *arXiv:1607.01801*, 2016.

[375] C. Moura Alves and D. Jaksch. Multipartite entanglement detection in bosons. *Physical Review Letters*, 93(11), Sep 2004.

[376] A. J. Daley, H. Pichler, J. Schachenmayer, and P. Zoller. Measuring entanglement growth in quench dynamics of bosons in an optical lattice. *Physical Review Letters*, 109(2), Jul 2012.

[377] S. Braun, J. P. Ronzheimer, M. Schreiber, S. S. Hodgman, T. Rom, I. Bloch, and U. Schneider. Negative Absolute Temperature for Motional Degrees of Freedom. *Science*, 339(6115):52–55, 2013.

[378] H. Lignier, C. Sias, D. Ciampini, Y. Singh, A. Zenesini, O. Morsch, and E. Arimondo. Dynamical control of matter-wave tunneling in periodic potentials. *Phys. Rev. Lett.*, 99:220403, Nov 2007.

[379] Daniel F. V. James, Paul G. Kwiat, William J. Munro, and Andrew G. White. Measurement of qubits. *Phys. Rev. A*, 64:052312, Oct 2001.

[380] D. Clément, N. Fabbri, L. Fallani, C. Fort, and M. Inguscio. Exploring correlated 1d bose gases from the superfluid to the mott-insulator state by inelastic light scattering. *Phys. Rev. Lett.*, 102:155301, Apr 2009.

[381] Philipp T. Ernst, Soren Gotze, Jasper S. Krauser, Karsten Pyka, Dirk-Soren Luhmann, Daniela Pfannkuche, and Klaus Sengstock. Probing superfluids in optical lattices by momentum-resolved Bragg spectroscopy. *Nat Phys*, 6(1):56–61, 2010.

[382] P. W. Anderson. Absence of diffusion in certain random lattices. *Phys. Rev.*, 109:1492–1505, Mar 1958.

[383] I. Gornyi, A. Mirlin, and D. Polyakov. Interacting electrons in disordered wires: Anderson localization and low-T transport. *Phys. Rev. Lett.*, 95:206603, Nov 2005.

[384] D.M. Basko, I.L. Aleiner, and B.L. Altshuler. Metal-insulator transition in a weakly interacting many-electron system with localized single-particle states. *Annals of Physics*, 321:1126–1205, 2006.

[385] Arijeet Pal and David A. Huse. Many-body localization phase transition. *Phys. Rev. B*, 82:174411, Nov 2010.

[386] Maksym Serbyn, Z. Papić, and Dmitry A. Abanin. Local conservation laws and the structure of the many-body localized states. *Phys. Rev. Lett.*, 111:127201, Sep 2013.

[387] David A. Huse, Rahul Nandkishore, and Vadim Oganesyan. Phenomenology of fully many-body-localized systems. *Phys. Rev. B*, 90(17):174202, 2014.

[388] Dmitry A. Abanin, Ehud Altman, Immanuel Bloch, and Maksym Serbyn. Colloquium: Many-body localization, thermalization, and entanglement. *Reviews of Modern Physics*, 91(2), May 2019.

[389] Patrick A. Lee and T. V. Ramakrishnan. Disordered electronic systems. *Rev. Mod. Phys.*, 57:287–337, Apr 1985.

[390] Wojciech De Roeck, Francois Huveneers, Markus Müller, and Mauro Schiulaz. Absence of many-body mobility edges. *Physical Review B*, 93(1), Jan 2016.

[391] C. Jarzynski. Nonequilibrium Equality for Free Energy Differences. *Phys. Rev. Lett.*, 78(14):2690–2693, April 1997.

[392] Peter Talkner, Eric Lutz, and Peter Hänggi. Fluctuation theorems: Work is not an observable. *Phys. Rev. E*, 75:050102, May 2007.

[393] Michele Campisi, Peter Hänggi, and Peter Talkner. Colloquium: Quantum fluctuation relations: Foundations and applications. *Rev. Mod. Phys.*, 83:771, 2011.

[394] Tiago Batalhao, Alexandre M. Souza, Laura Mazzola, Ruben Auccaise, Ivan S. Oliveira, John Goold, Gabriele De Chiara, Mauro Paternostro, and Roberto M. Serra. Experimental reconstruction of work distribution and verification of fluctuation relations at the full quantum level. *Phys. Rev. Lett.*, 113:140601, August 2014.

[395] Shuoming An, Jing-Ning Zhang, Mark Um, Dingshun Lv, Yao Lu, Junhua Zhang, Zhang-Qi Yin, H. T. Quan, and Kihwan Kim. Experimental test of the quantum jarzynski equality with a trapped-ion system. *Nat Phys*, 11(2):193–199, February 2015.

[396] Marko Žnidarič. Relaxation times of dissipative many-body quantum systems. *Phys. Rev. E*, 92:042143, Oct 2015.

[397] Emanuele Levi, Markus Heyl, Igor Lesanovsky, and Juan P. Garrahan. Robustness of many-body localization in the presence of dissipation. *Phys. Rev. Lett.*, 116:237203, Jun 2016.

[398] Mark H Fischer, Mykola Maksymenko, and Ehud Altman. Dynamics of a many-body-localized system coupled to a bath. *Phys. Rev. Lett.*, 116:160401, Apr 2016.

[399] Henrik P. Lüschen, Pranjal Bordia, Sean S. Hodgman, Michael Schreiber, Saubhik Sarkar, Andrew J. Daley, Mark H. Fischer, Ehud Altman, Immanuel Bloch, and Ulrich Schneider. Signatures of many-body localization in a controlled open quantum system. *Phys. Rev. X*, 7:011034, Mar 2017.

[400] EPL van Nieuwenburg, J Yago Malo, AJ Daley, and MH Fischer. Dynamics of many-body localization in the presence of particle loss. *Quantum Science and Technology*, 3(1):01LT02, dec 2017.

[401] Maksym Serbyn, Z. Papić, and Dmitry A. Abanin. Universal slow growth of entanglement in interacting strongly disordered systems. *Phys. Rev. Lett.*, 110:260601, Jun 2013.

[402] Maksym Serbyn, Z. Papić, and D. A. Abanin. Quantum quenches in the many-body localized phase. *Phys. Rev. B*, 90:174302, Nov 2014.

[403] Jens H. Bardarson, Frank Pollmann, and Joel E. Moore. Unbounded growth of entanglement in models of many-body localization. *Phys. Rev. Lett.*, 109:017202, Jul 2012.

[404] William K. Wootters. Entanglement of formation of an arbitrary state of two qubits. *Phys. Rev. Lett.*, 80:2245–2248, Mar 1998.

[405] G. Vidal and R. F. Werner. Computable measure of entanglement. *Phys. Rev. A*, 65:032314, Feb 2002.

[406] Karol Zyczkowski, Pawel Horodecki, Anna Sanpera, and Maciej Lewenstein. Volume of the set of separable states. *Phys. Rev. A*, 58:883–892, Aug 1998.

[407] Jinhyoung Lee, M. S. Kim, Y. J. Park, and S. Lee. Partial teleportation of entanglement in a noisy environment. *Journal of Modern Optics*, 47(12):2151–2164, 2000.

[408] Pasquale Calabrese, John Cardy, and Erik Tonni. Entanglement entropy of two disjoint intervals in conformal field theory. *Journal of Statistical Mechanics: Theory and Experiment*, 2009(11):P11001, Nov 2009.

[409] Johnnie Gray, Leonardo Banchi, Abolfazl Bayat, and Sougato Bose. Machine-learning-assisted many-body entanglement measurement. *Phys. Rev. Lett.*, 121:150503, Oct 2018.

[410] M. Aidelsburger, M. Lohse, C. Schweizer, M. Atala, J. T. Barreiro, S. Nascimbene, N. R. Cooper, I. Bloch, and N. Goldman. Measuring the chern number of hofstadter bands with ultracold bosonic atoms. *Nat Phys*, 11(2):162–166, February 2015.

[411] J. Zhang, P. W. Hess, A. Kyprianidis, P. Becker, A. Lee, J. Smith, G. Pagano, I.-D. Potirniche, A. C. Potter, A. Vishwanath, and et al. Observation of a discrete time crystal. *Nature*, 543(7644):217–220, Mar 2017.

[412] Soonwon Choi, Joonhee Choi, Renate Landig, Georg Kucsko, Hengyun Zhou, Junichi Isoya, Fedor Jelezko, Shinobu Onoda, Hitoshi Sumiya, Vedika Khemani, and et al. Observation of discrete time-crystalline order in a disordered dipolar many-body system. *Nature*, 543(7644):221–225, Mar 2017.

[413] Hannes Bernien, Sylvain Schwartz, Alexander Keesling, Harry Levine, Ahmed Omran, Hannes Pichler, Soonwon Choi, Alexander S. Zibrov, Manuel Endres, Markus Greiner, and et al. Probing many-body dynamics on a 51-atom quantum simulator. *Nature*, 551(7682):579–584, Nov 2017.

[414] Frank Schindler, Nicolas Regnault, and Titus Neupert. Probing many-body localization with neural networks. *Phys. Rev. B*, 95:245134, Jun 2017.

[415] Jordan Venderley, Vedika Khemani, and Eun-Ah Kim. Machine learning out-of-equilibrium phases of matter. *Phys. Rev. Lett.*, 120:257204, Jun 2018.

[416] Yi-Ting Hsu, Xiao Li, Dong-Ling Deng, and S. Das Sarma. Machine learning many-body localization: Search for the elusive nonergodic metal. *Phys. Rev. Lett.*, 121:245701, Dec 2018.

[417] Wei Zhang, Lei Wang, and Ziqiang Wang. Interpretable machine learning study of the many-body localization transition in disordered quantum ising spin chains. *Physical Review B*, 99(5), Feb 2019.

[418] Evert van Nieuwenburg, Eyal Bairey, and Gil Refael. Learning phase transitions from dynamics. *Physical Review B*, 98(6), Aug 2018.

[419] Jun Li, Ruihua Fan, Hengyan Wang, Bingtian Ye, Bei Zeng, Hui Zhai, Xinhua Peng, and Jiangfeng Du. Measuring out-of-time-order correlators on a nuclear magnetic resonance quantum simulator. *Phys. Rev. X*, 7:031011, Jul 2017.

[420] K. A. Landsman, C. Figgatt, T. Schuster, N. M. Linke, B. Yoshida, N. Y. Yao, and C. Monroe. Verified quantum information scrambling. *Nature*, 567(7746):61–65, 2019.

[421] B. Vermersch, A. Elben, L. M. Sieberer, N. Y. Yao, and P. Zoller. Probing scrambling using statistical correlations between randomized measurements. *Phys. Rev. X*, 9:021061, Jun 2019.

[422] Manoj K. Joshi, Andreas Elben, Benoît Vermersch, Tiff Brydges, Christine Maier, Peter Zoller, Rainer Blatt, and Christian F. Roos. Quantum information scrambling in a trapped-ion quantum simulator with tunable range interactions. *Phys. Rev. Lett.*, 124:240505, Jun 2020.

[423] V. K. Varma, A. Raj, S. Gopalakrishnan, V. Oganesyan, and D. Pekker. Length scales in the many-body localized phase and their spectral signatures. *Phys. Rev. B*, 100:115136, Sep 2019.

[424] C. W. von Keyserlingk, Tibor Rakovszky, Frank Pollmann, and S. L. Sondhi. Operator hydrodynamics, otocs, and entanglement growth in systems without conservation laws. *Phys. Rev. X*, 8:021013, Apr 2018.

[425] Andreas Läuchli. New states of quantum matter – introduction to exact diagonalization. *Les Houches school on "Modern theories of correlated electron systems"*, May 2009.

[426] J M Zhang and R X Dong. Exact diagonalization: the bose–hubbard model as an example. *European Journal of Physics*, 31(3):591–602, Apr 2010.

[427] Elbio Dagotto. Correlated electrons in high-temperature superconductors. *Rev. Mod. Phys.*, 66:763–840, Jul 1994.

[428] J. Jaklic and P. Prelovsek. Lanczos method for the calculation of finite-temperature quantities in correlated systems. *Phys. Rev. B*, 49:5065–5068, Feb 1994.

[429] P. Prelovsek and J. Bonca. Ground state and finite temperature lanczos methods. *Springer Series in Solid-State Sciences: Strongly Correlated Systems*, 2013.

[430] Markus Aichhorn, Maria Daghofer, Hans Gerd Evertz, and Wolfgang von der Linden. Low-temperature lanczos method for strongly correlated systems. *Phys. Rev. B*, 67:161103, Apr 2003.

[431] Steven R. White. Density matrix formulation for quantum renormalization groups. *Phys. Rev. Lett.*, 69:2863–2866, Nov 1992.

[432] Ulrich Schollwöck. The density-matrix renormalization group in the age of matrix product states. *Annals of Physics*, 326(1):96–192, January 2011.

[433] Johannes Hauschild and Frank Pollmann. Efficient numerical simulations with Tensor Networks: Tensor Network Python (TeNPy). *SciPost Phys. Lect. Notes*, page 5, 2018.

[434] Jonas A. Kjäll, Michael P. Zaletel, Roger S. K. Mong, Jens H. Bardarson, and Frank Pollmann. Phase diagram of the anisotropic spin-2 xxz model: Infinite-system density matrix renormalization group study. *Phys. Rev. B*, 87:235106, Jun 2013.

[435] Matthias Gohlke, Ruben Verresen, Roderich Moessner, and Frank Pollmann. Dynamics of the Kitaev-Heisenberg Model. *Phys. Rev. Lett.*, 119(15):157203, Oct 2017.

[436] Ruben Verresen, Roderich Moessner, and Frank Pollmann. Avoided quasiparticle decay from strong quantum interactions. *Nature Physics*, 15(8):750–753, 2019.

[437] Sebastian Paeckel, Thomas Köhler, Andreas Swoboda, Salvatore R. Manmana, Ulrich Schollwöck, and Claudius Hubig. Time-evolution methods for matrix-product states. *Annals of Physics*, 411:167998, Dec 2019.

[438] Lawrence W. Cheuk, Matthew A. Nichols, Katherine R. Lawrence, Melih Okan, Hao Zhang, Ehsan Khatami, Nandini Trivedi, Thereza Paiva, Marcos Rigol, and Martin W. Zwierlein. Observation of spatial charge and spin correlations in the 2D Fermi-Hubbard model. *Science*, 353:1260–4, 2016.

[439] Andrew Ng. Machine learning by stanford university. *Coursera*, 2017.

[440] Ian Goodfellow, Yoshua Bengio, and Aaron Courville. *Deep Learning*. MIT Press, 2016.

[441] Pankaj Mehta, Marin Bukov, Ching-Hao Wang, Alexand re G. R. Day, Clint Richardson, Charles K. Fisher, and David J. Schwab. A high-bias, low-variance introduction to Machine Learning for physicists. *Physics Reports*, 810:1–124, May 2019.

[442] R. Herrmann, S. Samarin, H. Schwabe, and J. Kirschner. Two electron photoemission in solids. *Phys. Rev. Lett.*, 81:2148–2151, Sep 1998.

[443] N. Fominykh, J. Henk, J. Berakdar, P. Bruno, H. Gollisch, and R. Feder. Theory of two-electron photoemission from surfaces. *Solid State Communications*, 113(12):665–669, 2000.

[444] S. E. Nagler, D. A. Tennant, R. A. Cowley, T. G. Perring, and S. K. Satija. Spin dynamics in the quantum antiferromagnetic chain compound $kcuf_3$. *Phys. Rev. B*, 44:12361–12368, Dec 1991.

[445] Konstantin A. Kouzakov and Jamal Berakdar. Photoinduced emission of cooper pairs from superconductors. *Phys. Rev. Lett.*, 91:257007, Dec 2003.

[446] Debayan Mitra, Peter T. Brown, Elmer Guardado-Sanchez, Stanimir S. Kondov, Trithep Devakul, David A. Huse, Peter Schauß, and Waseem S. Bakr. Quantum gas microscopy of an attractive Fermi-Hubbard system. *Nature Physics*, 14(2):173–177, February 2018.

[447] Zheng Zhu and Zheng-Yu Weng. Quasiparticle collapsing in an anisotropic $t - j$ ladder. *Phys. Rev. B*, 92:235156, Dec 2015.

[448] Zheng Zhu, D. N. Sheng, and Zheng-Yu Weng. Intrinsic translational symmetry breaking in a doped mott insulator. *Phys. Rev. B*, 98:035129, Jul 2018.

[449] S. R. White and A. E. Feiguin. Real-time evolution using the density matrix renormalization group. *Phys. Rev. Lett.*, 93:076401, 2004.

[450] F. Verstraete, J. J. García-Ripoll, and J. I. Cirac. Matrix product density operators: Simulation of finite-temperature and dissipative systems. *Phys. Rev. Lett.*, 93:207204, 2004.

[451] F. Verstraete, V. Murg, and J. I. Cirac. Matrix product states, projected entangled pair states, and variational renormalization group methods for quantum spin systems. *Adv. Phys.*, 57:143–224, 2008.

[452] T. Barthel. Precise evaluation of thermal response functions by optimized density matrix renormalization group schemes. *New J. Phys.*, 15:073010, 2013.

[453] C. Karrasch, J. H. Bardarson, and J. E. Moore. Reducing the numerical effort of finite-temperature density matrix renormalization group transport calculations. *New J. Phys.*, 15:083031, 2013.

[454] S. Blanes and P. C. Moan. Practical symplectic partitioned Runge-Kutta and Runge-Kutta-Nyström methods. *J. Comput. Appl. Math.*, 142:313–330, 2002.

Colophon

This thesis was typeset using LaTeX, originally developed by Leslie Lamport and based on Donald Knuth's TeX. The body text is set in 11 point Arno Pro, designed by Robert Slimbach in the style of book types from the Aldine Press in Venice, and issued by Adobe in 2007. A template, which can be used to format a PhD thesis with this look and feel, has been released under the permissive MIT (X11) license, and can be found online at github.com/suchow/ or from the author at suchow@post.harvard.edu.